Corrosion Film Solubility and Suspended Particle Behaviour of Corroding SS316L Surfaces in Simulated Nuclear Plant Coolant

By

John M Hewett

A thesis submitted to
University of Birmingham
for the degree of
DOCTOR OF PHILOSOPHY

Metallurgy & Materials
University of Birmingham
June 2017

Acknowledgements

First of all, thank you to the sponsors, whose funding made this work possible – EPSRC and NNL for the Case Award studentship funding, and also the funders of Jonathan Morrison's EngD, EPSRC and Rolls-Royce, whose metal oxide solubility rig was the object of study in the current project.

I would like to thank everyone from industry who has helped, particularly my industry supervisor Jim Henshaw, NNL, for his expert advice and guidance; Shirley Dickinson, also of NNL; and Andy Banks, Rolls-Royce, for his encouragement, and enlightening discussions about modeling the rig, particularly the idea of using Stokes' law and buoyancy to estimate the maximum particle size entrained in upwards-flowing coolant.

I would like to thank my supervisors Brian Connolly, now at the University of Manchester, and Clive Ponton at University of Birmingham for their timely help and encouragement over the years of this PhD. I would also like to thank others at the University of Birmingham who have been instrumental in helping me along with the project – particularly Jonathan Morrison, who built the solubility rig, performed SEM analysis, and generally acted like a (younger) older brother in the world of doctoral research; Nathan Johnson, for helping take my samples while I was on holiday, among other things; and Christopher Cooper, whose intimate knowledge of the department and of whom can help with which tasks and analyses, as well as week-to-week help with the research, has been instrumental. Stephen Baker deserves a special mention for analysis of numerous samples by ICP-MS, which were central to the project, under stressful circumstances in which the instrument broke down at the most inconvenient times – thank you. Many thanks also to Daniel Reed for operating the Mass Spectrometer (and bespoke sample delivery system) for me, enabling analysis of effluent hydrogen content. Thanks to Alison Davenport for use of her pH meter, and Mary Taylor for help with SEM preparation and other tasks.

Others at the University provided practical help, use of equipment, and analyses, which were not used in the final write-up, but were nonetheless gratefully received. In particular: Mike Glynn, for assistance with HIPping metal oxide powers, and instruction on the lathe; Jeff Sutton, Jackie Deans and Louise Male for XRD spectrometry of magnetite granules and powders; and David Parker and others at the cyclotron for proton irradiation of metals.

I would also like to thank admin staff and anyone else I have not mentioned by name, particularly Tracy Parkes and others in Finance for efficiently processing the many purchases I made; Neville Adolphus from Met & Mat Stores; and Kay Jones and Anne Cabezas, the postgraduate administrators.

Lastly, I would like to thank my wife, Rachel, my family and friends, and God, for standing by me and supporting me through this PhD, even when I've been selfish at times and irrationally reluctant to take time out for fear of falling behind. Thank you all, I couldn't have done it without you!

Abstract

Deposition of corrosion product is a primary concern for the efficiency and safety levels of light water nuclear plant operation. Key to the understanding of the deposition process is 1) the solubility of generated corrosion product, and 2) the behaviour of particulate within the coolant. In this study a once-through flowing rig built entirely from 316L stainless steel (SS316L) was used to study the dissolution and particulate release behaviour of corrosion films on SS316L surfaces in simulated PWR primary coolant. Levels of the five most prevalent alloying elements – Fe, Cr, Ni, Mo, Mn – were analysed in rig effluent samples using ICP-MS. Nitrocellulose filters of three different pore sizes were used at the point of sampling in some runs (0.05 μm, 0.45 μm and 3.0 μm), to give an indication of the relative contributions from fully dissolved matter and particulates of several size ranges.

Simulated coolant was prepared from nitrogen-sparged ultrapure water, with a calculated pH_{25C} of 9 to 11 using LiOH, and slowly flowed through the rig at 200 to 300 °C, at flow velocity up to 6.4 mm/s, with Reynolds numbers of 150 and below. Hydrogen was not controlled, but is thought to have varied between around 0.0002 to 20 scc/kg, based on variation in parameters such as corrosion rate; total area of corroding surfaces; and coolant residence time.

In the first set of experiments, corrosion of the rig's SS316L surfaces provided the sole source of dissolved hydrogen, as well as the five metallic elements of interest to this study. Later experiments involved the addition of around 20 g of SS316L chips, resulting in an approximate 10-fold increase to the corroding surface area in the hot part of the rig.

Levels of Fe, Cr and Ni were in the low ppb or sub-ppb range, comparable with those measured in the primary coolant of LWRs. This is consistent with high temperature solubility, or in some cases a little higher, suggesting a contribution from suspended particles. Mo and Mn exhibited interesting behaviour, sometimes reaching high levels of 100s of ppb, suggesting a process of leaching from the alloy and corrosion film during the first few hundred hours of exposure. Little or no effect of the use of filters on effluent levels was discerned.

Few particles were observed on the filters, though in some instances significant deposits of micron sized multifaceted crystallites were observed on the plastic housing of filters. These crystallites were consistent with those seen on the corrosion film in the heated portions of the rig. The results could be understood in terms of a combination of equilibrium solubility of native corrosion films, at high temperature under reducing conditions, at room temperature under reducing conditions, and at room temperature under oxidising conditions possibly present in the last few mm of the sampling line. In addition to this we must consider the direct inclusion of particulates in the effluent, and release of ions from deposited high temperature oxide particles in the sampling line.

List of acronyms, abbreviations, and technical terms

BOC	Beginning Of Cycle (conditions employed at beginning of fuel cycle). Also the name of the company which supplied the nitrogen gas used for the current thesis project.
BWR	Boiling Water Reactor – a type of water-cooled nuclear reactor in which bulk boiling of coolant is allowed to occur in the core, raising steam to drive turbines and generate electricity.
CANDU	CANadian Deuterium Uranium reactor, so called because it is designed and principally operated in Canada, uses uranium metal as fuel, and uses heavy water (having the isotope deuterium in place of ordinary hydrogen) as its primary coolant
chromite	A family of normal spinel-type oxides having Cr(III) as the major trivalent cation, in addition to Fe(III). The divalent ions can be any metallic cation – mostly Fe(II) and Ni(II) in the context of corrosion films on Fe-Cr-Ni alloys.
CP	Corrosion Product(s)
CRR	Corrosion Rate Rig – a rig used in a sister EngD project by Jonathan Morrison, from which several effluent samples were taken in this project for ICP-MS analysis
CRUD, or crud	Deposits of corrosion products forming on fuel or at other locations in the coolant of LWRs. The origin of the term is the acronym “Chalk River Unidentified Deposit”, after the Chalk River CANDU reactor in Canada where it was first observed.
CVCS	Chemical and Volume Control System – system for the control of chemistry and filtration of particulate matter from primary coolant of PWRs
EPRI	Electric Power Research Institute
ferrite	In the context of this thesis, ‘ferrite’ refers to a family of inverse spinel-type oxides, having Fe(III) as the major trivalent cation, with up to a small amount of Cr(III). The divalent ions can be any metallic cation – mostly Fe(II) and Ni(II) in the context of corrosion films on Fe-Cr-Ni alloys. Magnetite is the end-member of this family containing purely the elements Fe and O (Fe_3O_4). The term ‘ferrite’ also describes one of the crystalline phases in which iron or steels can manifest. However, the word is never used in that context in this thesis.
HFT	Hot Functional Test - when a new PWR is first exposed to hot water and its systems are tested together at temperature for the first time
IX	Ion Exchange – IX resins are effective at removing ions of a certain type from solution, to be replaced by a different species of ion

LWR	Light Water Reactor (nuclear) – encompasses PWRs, BWRs, and VVERs, but not CANDUs
NPP	Nuclear Power Plant
PP	Polypropylene (plastic)
PWR	Pressurised Water Reactor – a type of water-cooled nuclear reactor in which primary coolant (which takes heat away from the core) is pressurised, and a secondary coolant circuit is used to raise steam and drive turbines to generate electricity (or direct drive, in naval applications).
PWSCC	Primary Water Stress Corrosion Cracking
RCS	Reactor Coolant System
SCC	Stress Corrosion Cracking
scc/kg	Standard cubic centimetres per kilogram – a measure of concentration of gas in a liquid, where 1 scc is the amount of gas filling a cubic centimetre under standard temperature and pressure conditions: 1 atm at 25 °C.
SG	Steam Generator
VVER	Vodo-Vodyanoi Energetichesky Reaktor (translates as Water-Water Power Reactor) – a Russian type of pressurised water reactor. These designs of reactor are different from other PWR reactors in a number of ways, such as the use of KOH as a base instead of LiOH, and the use of horizonal rather than vertical steam generators.
XPS/AIM	X-ray Photoemission Spectroscopy in conjunction with Argon Ion Milling – a technique used to measure the composition profile beneath a solid surface, in terms of elemental composition and also in terms of oxidation state of each element. XPS provides data at the surface, and when used in conjunction with successive applications of argon ion milling (in which bombardment by high energy argon ions removes a thin layer of material from the surface) can produce a through-depth composition profile.

Contents

List of Figures

List of Tables

1. Introduction

1.1. General Introduction

Pressurised Water Reactors (PWRs) are the most common type of nuclear reactor worldwide, used primarily for electricity generation, and for direct propulsion of naval vessels. They are so-named because the 'primary' coolant water that takes heat away from the core is pressurised to prevent boiling, necessitating the transfer of heat to a separate 'secondary' coolant loop to raise steam and drive turbines, in contrast with the second most common type of nuclear reactor, the Boiling Water Reactor (BWR) where a single body of coolant water held under slightly less pressure is used to serve both functions. Conditions in these three types of coolant circuit, though similar in some respects, such as high temperatures and pressures, are different in others, including materials of construction, chemical additions to the water, and the presence of lack of boiling and/or irradiation. The experimental study detailed in this thesis was designed to be most relevant to the primary coolant circuit of PWRs, and so the whole thesis is written from that perspective, though much of what is written is also applicable to BWRs and the secondary side of PWRs.

In the harsh environment of the primary coolant circuit of PWRs, corrosion of structural materials is inevitable, despite using some of the most corrosion-resistant alloys which are economically feasible and which have all the requisite characteristics such as strength and crack-resistance. However, it is not in general the structural components' 'weight loss' to corrosion which is of concern, the thickness of alloy lost to corrosion over the course of a plant's life is typically of the order of a few µm, the concern lies in the behaviour and fate of soluble and particulate corrosion products. Typical particles are nanometre to micron sized when released from the corrosion film into the coolant. These particulates accumulate in parts of the primary circuit, creating deposits which can cause problems, including reduced heat transfer efficiency, and high ex-core radiation fields [1]. The technical term for these deposits is "crud", from the acronym "Chalk River Unidentified Deposit" [2], named after the Canadian laboratory at which it was first observed. Crud deposits can occur on fuel assemblies, and their porous structure enables corrosive species and neutron poisons from the coolant (Li and B) to accumulate, potentially causing localised corrosion and uneven core wide power distribution in the reactor [1]. The former effect, known as Crud Induced Localised Corrosion (CILC) can cause fuel failure and release of fission products to the coolant in the most extreme cases.

Much research has been conducted over the years in order to better understand the mechanisms by which crud is transported through the reactor primary coolant circuit. Complex whole plant computer models have been developed, such as BOA [1], to try to take into account all the relevant processes. These processes include release and deposition of particulate material, dissolution of particulate, release and precipitation of soluble species. These can occur in the bulk coolant, on surfaces, in regions of boiling and non-boiling and where significant temperature variations exist. Data from experimental and theoretical research are used by these complex models, such as oxide solubility measurements and measurements of particulate deposition and release rates, as well as Nuclear plant data. Useful information can be obtained from crud scrape samples taken from plant, and measurements of the of levels of Fe, Ni and other elements in plant coolant.

The solubility of the oxides which make up crud is a key factor in describing its behaviour in the PWR primary circuit [2]. An important oxide is magnetite (Fe_3O_4), formed under reducing conditions in iron rich reactor systems. There is significant discrepancy between literature solubility data regarding magnetite in hydrothermal solutions of pH_{25C} 9 or 10 and above. In 1980, Tremaine and LeBlanc [3] recorded for high pH values a significantly lower solubility than found in previous studies, the most notable of which was that of Sweeton and Baes ten years previously [4], citing colloidal particles as the likely source of higher levels in the work of Sweeton and Baes. Tremaine and LeBlanc demonstrated that higher levels of Fe were present in their own experiment when the granules of magnetite were used for the first time, gradually settling to a constant value over several months of continuous flow. A later study by Ziemniak, Jones and Combs [5], studying solubility in the presence of complexing media: sodium phosphates; and ammoniated water, was in agreement with the data of Tremaine and LeBlanc, and leads to a reasonable set of self-consistent thermodynamics.

1.2. Project Aim, Objectives, and Approach

The overall aim of the project was:

- "To investigate the solubility behaviour of oxides present on corroding stainless steel surfaces in PWR primary coolant circuits, using a once-through flowing rig"

To achieve this aim, a once-through flowing rig was built by Jonathan Morrison, entirely from stainless steel 316L (SS316L), as part of a related EngD project. It was intended that further iterations of the rig be built in the future, from inert materials, building on an improved understanding and lessons learnt from the first iteration in terms of design modification.

Initial secondary aims of the current project were thus:

- "To ascertain whether the current iteration of the rig could be used for high temperature oxide solubility studies"
- "To develop capability and experience to inform any changes to design which may be beneficial to future iterations."

Control of dissolved hydrogen – a key variable determining the solubility of some oxides, including magnetite – was not possible due to health and safety rules within the lab. Initial experiments showed that levels of Fe and other elements released to coolant from the rig itself were comparable to or higher than the low ppb levels expected from oxide solubility studies. Therefore, it was ascertained that the current iteration of the rig was not suitable for high temperature studies of pure oxides under well-defined conditions. However, the levels of Fe and other elements were comparable with those expected due to reaching a dissolution/precipitation equilibrium with the coolant, especially given the uncertainty in dissolved hydrogen concentration.

The overall aim of the project remained unchanged, but instead of collecting data regarding high purity oxide solubility, the net release of Fe and other metals was measured from actual corrosion film on corroding SS316L surfaces (an alloy commonly used in PWR plant). Slow flow rates were adopted to promote full saturation of dissolved metals in the heated part of the rig, and to achieve reducing conditions due to hydrogen produced as a product of corrosion. Feedwater was prepared using ultrapure water, nitrogen sparged to remove any oxygen, with addition of LiOH to achieve required pH.

After deciding to study net release from corrosion film rather than the solubility of pure oxides, a set of adapted objectives was evolved, in terms of experimental and modeling work:

- Operate the rig, at varying flow rates (0.1 – 2 g/min), at a range of feedwater pH_{25C} values, and at a range of temperatures (200 – 300 °C);
- Take samples of effluent from the rig, and analyse for Fe, Cr, Ni, Mo and Mn by ICP-MS.
- Take equivalent samples of the feedwater before it enters the heated part of the rig.
- Use filters to investigate any particulate component to the levels of each metal which may be present in the simulated coolant.
- Characterise any particulates which may be present on filters, using SEM/EDX.
- Characterise the corrosion film on coolant-facing surfaces from the rig, using SEM/EDX.
- Characterise processes ongoing in the rig, by modeling the parameters of coolant within the rig, such as dissolved hydrogen concentration, coolant velocity, and progress towards saturation; and by taking measurements where possible.
- Develop a model to try to explain results observed

There were additional objectives in terms of developing capability:

- Investigate causes for problems such as pump stalls, and try to lessen their frequency
- Improve technique for analysing samples with minimal contamination
- Develop a method for measuring approximate hydrogen levels.

To complement results obtained from corroding surfaces of the rig alone, additional runs of the rig were performed in which a section of 1" tubing in the rig, known as the reaction chamber, was filled with 20 g of SS316L chips, resulting in a ten-fold increase in the surface area of corroding SS316L.

1.3. Overview of thesis structure

Chapter 2 gives a brief summary of the context and motivation for the current study. The research builds on the body of work undertaken by others to provide data and understanding of corrosion product transport in support of models of the formation of troublesome deposits.

In chapter 3, a review of the literature is undertaken regarding corrosion of stainless steels under hydrothermal conditions. The theory regarding mechanisms of corrosion is introduced, and the results of literature characterisations of the morphology and chemistry of corrosion films are presented.

In chapter 4 a review of the literature regarding solubility of metal oxides under conditions relevant to the present rig is presented and discussed. A fuller treatment of the literature is provided in an appendix.

Chapters 5 and 6 review the literature on particulates circulating in coolant, and mechanisms of deposit formation.

In chapter 7 the materials used and the methods adopted for the experimental work undertaken for this PhD project are described.

In chapter 8 the results of the ICP-MS analyses are presented and discussed, in terms of the results as a whole. A more in depth treatment, on a session by session basis, is provided in the appendices, along with full tables of results, and several models to aid in the interpretation of results.

Chapter 9 details the results of hydrogen measurement, and compares them to predictions from a simple model.

Chapters 10 and 11 present characterisations of corrosion films from exposed SS316L surfaces and of particulates from filters.

A summary, conclusions, and plans for future work are provided in chapter 12.

2. Industrial Context:

Efforts to Model the Formation of Troublesome Corrosion Product Deposits and to Mitigate their Effects

2.1. Overview of chapter, and relation to other chapters

Several serious problems are presented by the deposits which form at locations in the primary coolant circuits of Pressurised Water Reactors (PWRs). Models of ever-increasing sophistication are used as a tool for predicting the conditions under which the most serious problems will occur, so that these can be avoided or mitigated, through control of coolant chemistry and other means, such as ultrasonic cleaning of fuel rods during refuelling outages to remove deposits, and modified core reload design to control the extent and location of localised boiling in the core [6] (which can cause enhanced deposition, see sections 2.2.6 and 2.4.1).

This chapter introduces the reader to PWRs, particularly the primary coolant circuits thereof, before discussing processes of corrosion product transport, and describing some of the deposit types and the problems they can cause. A brief history is provided of efforts to model the underlying processes, and actions which have been taken so far to mitigate deposit-related problems. Models use data and qualitative findings from experimental and theoretical research regarding processes such as corrosion, particle release and deposition, and metal oxide solubility. The current state of knowledge on these topics is summarised in chapters 3 to 6.

2.2. An introduction to the primary circuit of PWRs

2.2.1. Generic description of PWRs

Nuclear power accounts for roughly 10% of electricity generation worldwide [7], and is an important low carbon alternative to fossil fuels. The major part of nuclear power generation worldwide is from the Pressurised Water Reactor (PWR) type of nuclear reactor.

PWRs use the heat generated by controlled fission reactions of U-235 atoms in uranium dioxide (UO_2) fuel to generate electrical power (in the case of commercial reactors), or propulsion (in the case of naval reactors). Each fission, or splitting, of a U-235 atom is induced by absorption of a neutron, and results in the release of several more neutrons – between 2 and 3 on average – which cause further fissions in a chain reaction. During fission the U-235 nucleus splits unevenly into two smaller nuclei (electrons are left behind due to high velocity), and these undergo further nuclear decay over various timescales, resulting in a total energy release of around 200 MeV per fission [8], which ends up as heat energy. The products of this process are called 'fission products'. The average number of neutrons from each fission which go on to cause further fission events (the multiplication factor, k_{eff}) is maintained at 1 in the reactor as a whole, by various mechanisms to maintain heating from fission at a safe and steady level, such as on one hand the use of a moderator – a material which is effective at slowing neutrons down due to collisions, so they can be absorbed by U-235 nuclei; and on the other hand the use of control rods, and a 'neutron poison' in the coolant or fuel, to absorb neutrons before they can cause further fissions.

In a PWR, water is used as both the coolant (to carry heat away from the core, where the fission occurs in fuel) and the moderator. There are two separate coolant circuits: in the secondary circuit, steam is raised from water in steam generators (SGs) and used to drive turbines to generate electrical power, in the same way as for conventional power plants; in the primary circuit, water is held under sufficient pressure (~155 bar) that boiling does not occur, despite temperatures up to ~325 °C – hence the name "Pressurised Water Reactor" – and is used to carry heat from the core to the secondary coolant in SGs. By contrast, Boiling Water Reactors (BWRs) have only one coolant circuit, as water boils directly in the core to produce steam to drive turbines.

A schematic of a typical PWR, the Westinghouse 4-loop design, is shown in Figure 2.1. Other designs are similar, typically having between 4 and 6 loops. Only the primary circuit is shown in the figure, though the secondary circuit is represented by annotations of its entry (from condenser) and exit (to turbine) from the steam generators, where thousands of thin tubes containing primary coolant act

as heating elements to raise steam in the secondary circuit. Each of the loops has its own steam generator (SG), and a 'hot leg' and 'cold leg' of pipes carrying coolant to and from the SG. Coolant from all loops meets and mixes together in the reactor vessel, where it is diverted first downwards, against the inside wall of the pressure vessel, then up through the core to carry heat away from fuel rods.

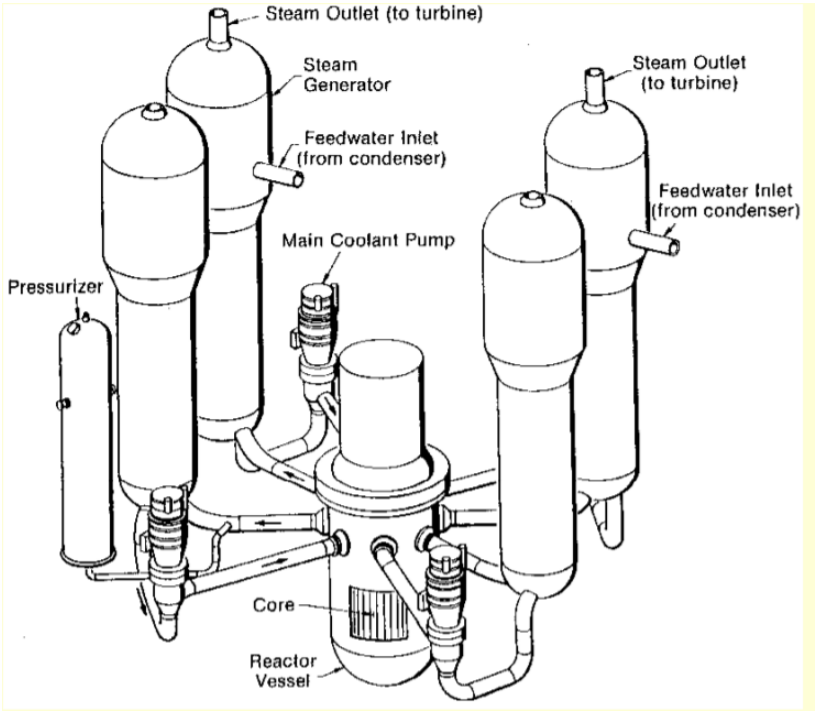

Figure 2.1. Schematic of a PWR. From [9].

2.2.2. Materials of construction

A significant proportion of the total surface area in the primary circuit resides in the SG tubing, ~ 70% [6], [10], due to the presence of thousands of thin tubes of ~ a centimetre in diameter. These are typically built from Inconels (nickel-based alloys), such as alloy 600 and alloy 690, whose corrosion release to coolant is much richer in Ni than that from stainless steels, reflecting the higher Ni content of the alloy. Fuel rods are clad in Zr alloy, which is selected due to its transparency to neutrons among other reasons. Corrosion of Zr alloy leads to a stable oxide, which does not interact with coolant (in contrast to the release of ions and particles from Fe and Ni alloys) [11]. The remainder of coolant-facing surfaces are built from stainless steels such as SS316L, with a few exceptions such as Stellite (a Co-based alloy) which is used for components which require a high

resistance to mechanical wear. The relevance of Zr alloy cladding to the problem of corrosion product transport is that any deposits of Fe, Cr and Ni oxide which form there is purely as a result of transport of corrosion products from Fe-Ni-Cr alloys. The relevance of Co alloys is that the Co released from these is a major source of radioactive isotopes of Co, which cause much of the activation problem. The relevance of Ni-based alloys being used as SG tubing, and stainless steels elsewhere, is that these are the main source of Ni in the circuit, and result in a higher Ni content in the corrosion film on stainless steel surfaces, circulating in the coolant, and on the deposits on fuel, than would be present due to the use of stainless steels alone.

2.2.3. Chemistry of primary coolant

Primary coolant is essentially demineralised, deoxygenated water, which has been thoroughly cleaned to achieve very high purity, to which a few chemical additions have been added for various operational reasons. It also contains corrosion products such as Fe and Ni ions and tiny particles of metal oxide, at very low concentrations. Within the core, strong radiation fields cause the splitting, or radiolysis, of water and other molecules, to produce various unstable species such as OH radicals, which are short-lived due to their high reactivity and instability. Some of these species are highly oxidising, which could cause elevated corrosion rates of structural materials, but hydrogen gas is added to the coolant to suppress their formation. Intense neutron flux within the core also causes transmutation of nuclei as neutrons are absorbed, forming a wide range of radioisotopes, some of which are incorporated in corrosion product deposits, such as Co-60, causing a radiation hazard to maintenance workers. Key chemical additions to the coolant are listed in the table below, with a brief explanation of their function (the list is not exhaustive):

Table 2.1. Principal chemical additions to primary coolant in PWRs

Chemical addition	reasons
Dissolved H_2 gas, 25 – 50 cm^3 H_2 at STP/ kg water	To ensure reducing conditions. The presence of dissolved oxygen could cause stress corrosion cracking (SCC) of stainless steels [12], endangering the integrity of reactor components. Hydrogen suppresses the formation of oxygen, and other oxidising species (such as caused by radiolysis).
Boric acid, H_3BO_3. Up to around 2000 ppm	Boron acts as a neutron poison, since it readily absorbs neutrons, enabling reactor power level to be controlled. Levels of boric acid are gradually decreased over the course of a fuel cycle (the time between refuelling outages), to offset the effect of a slight reduction in reactivity of the fuel over time as U-235 atoms are used up.
Lithium hydroxide LiOH. Up to around 2.1 ppm, or ~ 6 ppm, dependent on factors such as the particular alloy of Zr used in fuel clad.	To control the pH_T of the coolant and maintain alkaline conditions. Levels of LiOH are adjusted to take account of the current level of boric acid (a weak acid). An elevated pH helps to reduce the amount of deposit forming on fuel rods, and reduces the build-up of radioactivity outside the core.

2.2.4. Hot Functional Tests, and Shutdown Chemistry

Besides the chemistry applied during ordinary full power operation, there are different chemistry regimes applied at other times, for example during so-called Hot Functional Tests (HFT) when a new PWR is first exposed to hot water and its systems are tested together at temperature for the first time [10], or during plant shutdown for refuelling or for other reasons. Reductions in corrosion product transport and activity buildup can be achieved through well-chosen chemistry at these times. For example, Zn injected during HFT stabilises the passive oxide layers on surfaces of structural materials, providing better crud control subsequently under normal operating conditions. The process of plant shutdown includes a period of acid reducing conditions and a period of acid oxidising conditions [13], which can have a significant impact on crud transport [14] as the stability of oxides is much different under these conditions. At Sizewell B PWR, they used a modified HFT with both boric acid and hydrogen present in order to grow a passivating oxide film under appropriate (reducing) redox conditions, and have since benefitted from lower than usual shutdown releases and radiation fields.

2.2.5. Fluid dynamics of primary coolant

Coolant flow through the primary circuit is rapid and, in most parts of the circuit, turbulent [11], a typical speed in the core being 4 m/s [15] for example. The high turbulence, coupled with aspects of design which promote flow mixing (such as mixing vanes [15], [16]), results in a well-mixed bulk coolant, whose chemical composition is generally considered to be more-or-less homogeneous, at least in terms of distance from walls of the circuit. Effective flow mixing also improves the efficiency of heat transfer from fuel rods to coolant, resulting in lower temperatures of fuel cladding than would otherwise have been the case for the same power output, and thus reduced instances of nucleate boiling (see section 2.2.6) [15].

The assumption of homogeneity of bulk coolant, in terms of lateral position, is an important tool in the mathematical modeling of corrosion product transport in PWRs. In terms of longitudinal location within the circuit – i.e. whether the coolant volume under consideration is in the hot leg or cold leg, or how far it has progressed through the steam generator or the core if present there – there *are* some changes as the coolant progresses around the circuit. Temperature varies between ~ 290 °C at the core inlet, and ~ 325 °C at the core outlet [1], [6], [17], with corresponding changes to other parameters such as density and viscosity. Changes in temperature result in changes to the solubility of Fe-Cr-Ni oxides; this does not, however, necessarily result in corresponding changes to the levels of ions present. It takes just a few seconds for coolant to complete a full loop of the primary circuit, which is not sufficient time for full equilibrium to be attained between bulk coolant and corrosion film at all locations. A crude value of 13.9 s is calculated for transit time of primary coolant in a representative PWR (the AP-600), by dividing total mass of circulating coolant (volume [18] x density [19]) by flow rate [18]:

$$transit\ time = \frac{mass\ of\ circulating\ water}{mass\ flow\ rate} = \frac{193.7\ m^3 \times 715\ kg/m^3\ (at\ 300°C)}{9\ 940\ kg/s} = 13.9\ s$$

As equilibrium (saturation) concentrations change on flowing through the circuit, some progress towards equilibrium *is* achieved in the bulk coolant – this is illustrated schematically by the plots in Figure 2.2, taken from a description of the CRUDTRAN code, in an IAEA report on codes used to model corrosion product transport in PWRs [11]. Note that the plot shows qualitative trends only and is not to scale.

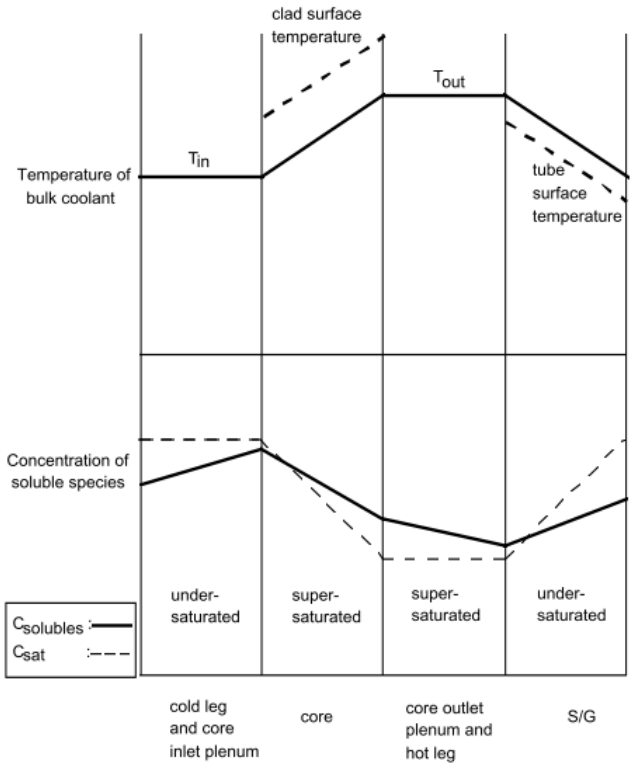

Figure 2.2. Qualitative schematic showing how the temperature of bulk coolant, and coolant-facing surfaces, varies at different locations of the primary circuit of a PWR; and also showing the resulting saturation and actual levels of soluble ions, according to the model underpinning the code 'CRUDTRAN'. From [11].
N.B.: Some models assume all the bulk primary coolant is at a constant 'background' solubility level, see reference [11]*. CRUDTRAN is a code developed in Korea, intended to predict the effect of coolant chemistry on transport of corrosion products and radioactivity, primarily in the form of soluble ions.*

By assuming the rate of mass transfer of ions between coolant and surfaces is controlled by diffusion across a 10 µm boundary layer (see the paragraph after next), a crude indication of the time constant, τ, for reaching equilibrium can be calculated for primary coolant in SG tubes, having a value 3.2 s, compared with approximate residence time, t_{res}, of 3.9 s. For the simple case of coolant entering at concentration C_0, and equilibrating to a fixed concentration C_{sat}, the progress to equilibrium is given by $\frac{(c(t)-C_0)}{(C_{sat}-C_0)} = 1 - e^{-\frac{t}{\tau}}$ (where $c(t)$ is the concentration at time t), resulting in 70% progress to the new equilibrium by the time the coolant exits the tube; a more realistic scenario would account for changes in solubility (C_{sat}) with changing temperature on progressing through the tube. The above quantities were calculated using the relations below, derived by the author, and plant data from [18], density of water $\rho_w(300\ °C) = 715$ kg m^{-3} [19], diffusivity of aqueous Fe^{2+} ions $D_{Fe2+}(300\ °C) = 1.2 \times 10^{-8}$ m^2 s^{-1} [20]–[22] (extrapolated from 25 °C data, see table 17.15):

$$\tau = \frac{d.\Delta r}{4.D_{Fe2+}} = \frac{15.5 * 10^{-3}\ m * \ 10 * 10^{-6}\ m}{4 * 1.2 * 10^{-8}\ m^2 s^{-1}} = 3.2\ s;$$

$$t_{res} = A.\frac{d.\rho_w}{4\dot{m}} = \frac{2 * 6986\ m^2 * 15.5 * 10^{-3}\ m * 715\ kg\ m^{-3}}{4 * 9940\ kg\ s^{-1}} = 3.9\ s;$$

where d is the diameter of tubes, Δr is the thickness of the viscous sublayer of the boundary layer (see Figure 2.3), $\dot{m}$ is the coolant mass flow rate, A is the total surface area of the insides of all SG tubes (which, when multiplied by $d/4$, gives total coolant volume in SG tubes), and other terms are as defined earlier.

These calculations are consistent with the qualitative form of Figure 2.2, in which concentrations of soluble species in the SGs and elsewhere make partial but not full progress towards equilibrating at saturation levels. Supersaturation may result in nucleation and growth of very small colloidal particles, which subsequently partially or completely dissolve under conditions of under-saturation. Additionally, there are some differences to chemistry in the core compared with the rest of the circuit, despite the short transit time, because of the presence of very short-lived products of radiolysis (as mentioned in section 2.2.3), which can influence the solubility of corrosion products through their effect on redox potential.

The term 'bulk' coolant refers to almost the whole of the circulating coolant. It excludes only a thin shell surrounding coolant-facing surfaces, known as the 'boundary layer', in which flow is slower and less turbulent than that of the bulk due to viscous drag forces, and whose chemistry and other properties (such as temperature) are influenced by those of the adjacent surfaces. The boundary layer forms a permeable barrier, between solid surfaces of the primary circuit on the one hand, and the turbulent, well mixed, bulk of the coolant on the other – through which chemical species, and heat, must migrate in order to transfer between the two. It therefore plays a crucial role in the processes of interaction between coolant and coolant-facing surfaces in the PWR primary circuit.

Figure 2.3 provides a schematic illustration of a boundary layer of flow developing under turbulent conditions. Where the boundary layer has developed from a laminar into a turbulent one, there still persists a very thin skin against the wall, on the order of tens of microns across [23] (depending on factors such as bulk flow velocity and properties of the fluid), for which flow is slow and laminar. It is this laminar, or 'viscous', sublayer which provides the strongest resistance to the transfer of mass and heat between coolant and walls, because in the absence of flow mixing such transfer can only occur via diffusion, which is a comparatively slow process, compared with the advective transport provided by turbulent flow mixing (in fact, some small contribution from turbulent eddies *is* thought to persist in the viscous sublayer [24]). The boundary layer requires a moderate distance to fully develop [25], and at some locations it can briefly separate from the wall, which has implications on corrosion product transport and deposit formations, via electrokinetic effects [26]. It can also be shed from the wall at any location, quasi-periodically, by turbulent bursts [24], [27].

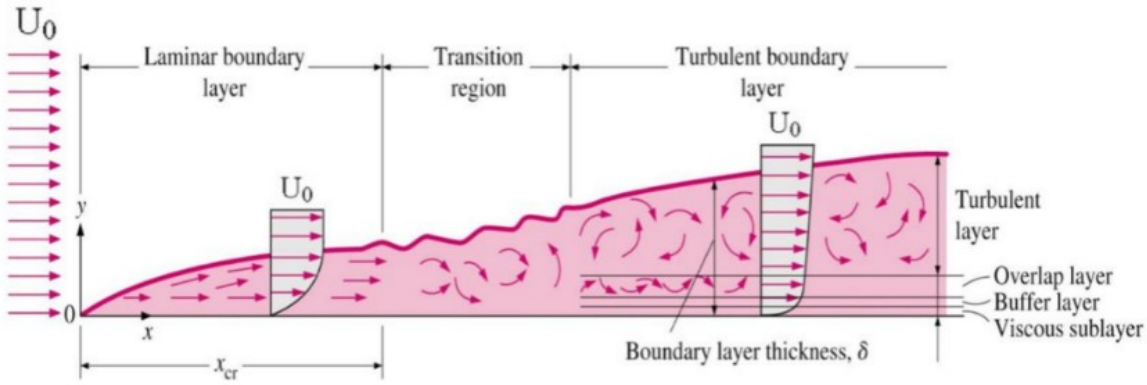

Figure 2.3. Schematic showing the development of a boundary layer against a surface under conditions of turbulent bulk flow. From [28].
The horizontal axis is compressed and the vertical axis stretched for clarity. The nominal limit of the boundary layer is typically taken to be the position at which velocity reaches 99% of that of the bulk. Arrows represent velocity, and U_0 denotes bulk coolant velocity. Within the turbulent boundary layer there exists a very thin viscous (or 'laminar') sublayer, on the order of tens of microns thick, in which mass transport occurs only by diffusion. Diffusion through the laminar boundary layer, or the viscous sublayer, is the rate limiting step for mass transfer of ions between coolant and corrosion film oxides (except where dissolution/precipitation kinetics are particularly slow such as for Ni/NiO).

Using the example of SG tubing in an AP-600 reactor again [18] (and the same sources of data), allows for some approximate dimensions to be calculated regarding the size of the boundary layer, and the distance the coolant must travel along the tube before fully developed turbulent flow is established, based on values of the Reynolds number. The Reynolds number (Re), a dimensionless number useful for describing the degree to which a flow is turbulent or not, features heavily in empirical relations regarding boundary layers, and is given by:

$$Re = \frac{\rho . U . L}{\mu},$$

Where μ is the dynamic viscosity of the fluid (8.64 x 10^{-5} Pa s for water at 300 °C [29]), U is the free stream velocity (mean velocity in the tube, calculated as 5.84 m/s for the current example), ρ is the density of the fluid (715 kg m^{-3} for water at 300 °C [19]), and L is a characteristic length scale selected according to the context.

Selecting the tube diameter, d, as the length scale gives Re_d = 7.5 x 10^5. Fully developed (steady state) flow in a tube is turbulent for values of Re_d greater than around 4000 [30], so flow is turbulent across the full diameter of the SG tubes (apart from a thin viscous sublayer, see Figure 2.3) once the coolant has travelled a certain distance along the tubes, known as the entry length, which is calculated below.

By selecting distance along the tube, x, as the characteristic length scale, the Reynolds number can again be calculated, this time as a function of x, providing a metric for the approximate location of transition of flow within the boundary layer, from laminar flow on first entering the tube, through a transition region, and on to a turbulent boundary layer as illustrated in Figure 2.3. The transition is complete at Re_x around 10^6 [30], corresponding to 2.1 cm in this example. The boundary layer then increases in thickness almost linearly with distance along the tube as it develops [30], until the layers from all sides meet in the middle, and from a short distance after that onwards the flow is fully developed, being independent of distance along the tube.

An empirical correlation for the turbulent 'entrance length', the distance into the tube at which turbulent flow becomes fully developed, is given as $\frac{L_e}{d} \approx 1.6\, Re_d^{1/4}$, valid for $Re_d < 10^7$ [30], which gives an entrance length of L_e = 73 cm for the SG tubes.

Other disturbances to flow, such as the bends in the SG tubes, may disrupt the fully developed turbulent flow profile, but the effects will not persist for longer than approximately the entry length given above, or less. Since the length of SG tubes as calculated from the data [18] is 22.7 m, the turbulent flow profile is fully developed over the majority of their length.

Even when turbulent flow is fully developed, the viscous sublayer continues to grow (see Figure 2.3). The thickness of the viscous sublayer, δ_0, increases much more slowly with distance than the rest of the turbulent boundary layer, and can be estimated by the following relation [31]:

$$\frac{U\delta_0}{\nu} = \frac{U\rho\delta_0}{\mu} = 206\, {Re_x}^{1/42}$$

This gives δ_0 = 5.9 µm around the point of transition to turbulent flow ($Re_x \sim 10^6$, around 2 cm into the tube), increasing very little by the end of the tube ($Re_x \sim 10^9$, around 22.7 m tube length, δ_0 = 7.0 µm). Turbulent eddies are thought to extend through the viscous sublayer, to some small extent, vanishing only at the wall [24]; at intervals, larger turbulent fluctuations 'suddenly penetrate very near the surface' [32], and the viscous sublayer then builds up from almost zero thickness until the next such event.

In the core, flow velocities and the diameter of flow channels are on a similar scale to the example above, so the values calculated above should be approximately representative.

Drag between coolant and oxide crystallites can cause erosion of crystallites – i.e. they are removed from the corrosion film and become entrained in the flow – especially if eddies of more rapid flow from the turbulent bulk flow impinge into the boundary layer.

2.2.6. Sub-cooled nucleate boiling

Sub-cooled nucleate boiling (SNB) is the process by which local boiling can occur in the superheated water immediately adjacent to fuel elements in certain parts of the core, giving rise to the continual release of tiny steam bubbles at nucleation sites. The bubbles are short-lived, as they condense once they reach the bulk coolant, which is sub-cooled (i.e. below boiling temperature under the coolant pressure of ~ 155 bar). This process has benefits as it offers enhanced heat transfer to the coolant [6], [33], and has increasingly been allowed or encouraged to occur [10], [16], [34], by employing higher coolant temperatures, and increased burnup and power output of fuel. There are also drawbacks, as SNB can cause enhanced crud deposition. As well as causing precipitation of dissolved ions, SNB causes enhanced deposition of particles [25], [35]. B and Li from the coolant incorporated in the thickest deposits of fuel crud forming under conditions of SNB can cause an imbalance in core power distribution known as Axial Offset Anomaly (due to the neutron absorber, B-10), and localised corrosion of the cladding (due to Li).

2.3. Mechanisms of corrosion product transport

Corrosion products circulating in coolant can be categorised according to size (see IAEA report [11])

- Solubles,
- Colloidal particles,
- Particulate matter.

Soluble species, such as metal cations and their hydrolysis products (see section 14.2) are governed by chemical processes, as described by thermodynamics and kinetics (see chapter 4).

Colloidal particles are very small particles, made from metals, metal oxides, and hydrated metal oxides in the context of PWRs. They are sufficiently small that surface effects have a significant impact on their behaviour, whilst inertial effects (due to their mass and their excess density compared with the coolant in which they reside) are minimal - this is because the surface area to volume (or mass) ratio of particles is inversely proportional to size.

Particulate matter consists of particles which are too large to be considered colloidal. For these particles behaviour is dominated by inertial effects as opposed to surface effects.

As implied by the above distinction between colloidal particles and particulates, the transition is gradual and to an extent context-dependent (transition may occur at a different size depending on

prevailing conditions or the effect considered); however, a particular cut-off size is generally defined for convenience, and to enable contributions from each class of corrosion product to be measured. In the context of PWRs, this is generally taken to be 0.45 µm, a standard pore size of filters used in on-line filtration of coolant. Particulates are then any particles which can be removed by filtration, whilst the filtrate consists of solubles and colloidal particles. For the same reasons, some studies include the very smallest particles in the category of solubles, because where present they cannot be excluded from any measurement of truly dissolved species concentrations if they are smaller than the smallest available filter pore size, for example 10 nm in the study of Bolz et al. [36] (see chapter 5).

Further details on each classification of corrosion product are provided below.

2.3.1. Soluble species

In the coolant immediately adjacent to the corrosion film forming on stainless steels and other Fe-Cr-Ni alloys in the PWR primary circuit, concentrations of metallic ions reach a steady state which is characteristic of the metal and metal oxide crystallites which make up the corrosion film, and is a function of coolant parameters (e.g., temperature, pH, and redox potential). This is similar to the solubility of those crystallites, though a little higher since the oxide crystallites of the protective 'inner' oxide film are continually undergoing selective dissolution of mostly Fe^{2+} and Ni^{2+} ions supplied by corrosion of the underlying alloy, whilst the Fe- and Ni- rich metal and metal oxide crystallites of the outer layer grow by precipitation from solution (see chapter 3 for further description of the corrosion film and process).

In the bulk coolant, the soluble concentrations may be significantly different from local concentrations against nearby Fe-Cr-Ni alloy surfaces. In some models, a single value of concentration is assumed for each metal in the bulk coolant; for others, concentration is assumed to vary with position in the circuit [11] (see Figure 2.2). In either case, concentrations in the coolant represent some kind of weighted average of saturation levels against oxides throughout the circuit, where the closest oxide surfaces may or may not receive extra weighting compared with the farthest; this is achieved by a net flux of aqueous ions through the boundary layer on each surface, by diffusion down a concentration gradient to or from the bulk coolant. In this way, material is removed from regions of high solubility, and precipitated in regions of low solubility.

2.3.2. Colloidal particles

In regions where the coolant is supersaturated, nucleation of very small, 'colloidal' particles (typically abbreviated to 'colloids') of metal or metal oxide may occur directly in the coolant. In addition, metal or metal oxide crystallites from corrosion film (see chapter 3) can be released to the coolant [37], of which a certain size fraction are small enough to be considered colloids. Definitions of 'colloidal' vary, but in principle it means sufficiently small that surface effects dominate over inertial effects, and can therefore be context dependent. In practice, for convenience and practical reasons, a fixed cut-off size of 0.45 μm is typically used in the context of PWR primary coolant, as explained at the start of section 2.3 above.

In general, oxide surfaces exposed to coolant have excess charge, which depends on the oxide, the coolant, and the temperature [38]; this results in a potential difference between the particle surface and the coolant far from the particle, which falls away exponentially towards zero on a length scale given by the Debye-Hückel length [26], which depends on (among other factors) the ionic strength of the solution, being shorter for solutions of higher ionic strength. The charge is primarily due to an imbalance of OH^- ions and H^+ ions adhering to the oxide surface, which in turn depends on pH [38]. The higher the pH, the further the imbalance shifts in the favour of OH^- ions. For a given oxide composition, at a given temperature, there exists a pH value for which the net charge from these ions is zero; this is known as the point of zero charge, or PZC. Taking other ionic species in the solution into account, and extending the surface to the 'slip plane', to include all ions which move with the particle as it moves through the coolant, yields the slightly different potential, known as the zeta potential, and corresponding pH at which this is zero, the isoelectric point, or IEP [38], [39], but this is specific to the coolant chemistry (other than simply the pH value), and is generally almost the same as the PZC in the context of LWRs [38].

At values of pH which are not close to the PZC (or more accurately, the IEP for a specific solution chemistry), there is mutual repulsion between particles of the same oxide, due to their like charges, as well as repulsion from any surfaces having the same polarity of charge. The resulting 'colloidal suspension', which refers to the homogeneous mixture of liquid and particles, can be very stable, as particles spread evenly to fill a volume and do not readily settle out or deposit from bulk flow. Where pH is close to the PZC (or IEP, as above) for oxides from which colloidal particles are formed, there is little or no repulsion between particles. In this case they can agglomerate together to form larger and larger particles, which are no longer in the colloidal regime, and more readily deposit on walls of the circuit. The band of pH values which can be considered as close to the PZC (or IEP) in this context, depends on the oxide and solution, being for example wider in solutions of higher ionic

strength – this is because of the shorter Debye-Hückel length (see above), so particles have to approach closer before feeling the same degree of repulsive force; once particles approach closer than a certain distance, Van der Waals forces, which are always positive and fall away sharply with distance, take over, and particles become attached [39]. Since different oxides have different values of PZC (or IEP), there may even be attraction between them at a pH intermediate between the two PZC (or IEP) values, causing particles to be actively attracted to oxide deposits, or to each other, where they are of differing oxide composition.

In general, because of the higher energy associated with atoms at the surface of a crystal than those in the bulk (positive 'surface energy'), the solution must be supersaturated for colloids of most crystalline phases to form – to a greater degree the smaller the particle size [38], [40]. Castelli [40] used an analytical relation from Glasstone [41], in which the degree of supersaturation is inversely proportional to particle size, to illustrate this effect, using representative values of surface energy and coolant parameters (the resulting plot showing degree of supersaturation versus particle size is reproduced in the appendices, Figure 14.11). From these illustrative values, Castelli contends that since colloids as small as 0.1 μm, for example, are unstable below a coolant supersaturation of ~ 25%, whilst elemental solubilities vary by only a few percent according to location in the plant, colloidal corrosion product particles of approximately that size are 'unstable and quickly dissolve' in the primary coolant loop, though mechanisms may indeed exist to create them. Note that for the very smallest size of colloid, less than around 10 nm, stability may shift from an oxide phase to a hydroxide phase, having lower surface energy, notwithstanding the fact that such a small particle of either phase has much higher solubility than a large particle of the stable oxide phase [38]. It has been argued elsewhere, however, that in the case of nickel ferrite, a major component of oxide deposits in PWRs, surface energy is negative and very small colloidal particles of a certain size (around 50 nm) are actually stable in the coolant [42].

Care must be taken when trying to ascertain the presence and composition of colloidal particles in PWRs experimentally - the presence of colloids in samples taken from primary coolant of operational PWRs does not necessarily reflect the situation at temperature, since it is possible that they form in the sampling line, when solubility decreases on cooling; conversely, colloids present at temperature may dissolve in the process of sampling if their solubility increases on cooling. Sampling line effects are discussed further in chapter 5. Despite some uncertainties regarding their measurement, colloids are believed to play an important role in corrosion product transport and deposition in the primary circuit.. In a fairly recent study, sub-micron sized particles of metallic nickel were observed directly in high-temperature coolant analyses (the problems associated with sample cooling prior to analysis

therefore not applying), and were concluded to be a common component in circulating crud in PWR primary coolant during operation [43].

Colloidal particles can deposit on surfaces, adding to crud deposits, and can also be re-released. Charge effects for colloids, and greater inertia for particulates, mean they behave differently in terms of their tendency to deposit and re-release. Particulates can more readily penetrate the thin viscous sublayer than colloids by carrying with them momentum towards a wall imparted by eddies in the turbulent boundary layer [24], [44].

2.3.3. Particulates

In addition to colloids, larger particles of oxide, known as 'particulates' are also transported in the coolant, for which size is sufficiently large that surface effects do not dominate their interactions. How large is "sufficiently large" depends on the context, and factors such as prevailing coolant conditions, but in practice a distinguishing size range is often chosen arbitrarily, or for convenience. For example, a figure of 1 µm might be used, being a round number, or a figure of 0.45 µm which represents a commonly used filter pore size, so that particulates are then any particles retained by filters. Particulates are typically borne of a different source from colloids, namely the entrainment into coolant flow of corrosion film oxide crystallites (see chapter 3), or spallation of larger flakes of oxide or swarf from alloy preparation, in the case of the largest particulates, as opposed to nucleation and growth directly in supersaturated solution as is thought typical of colloidal particles.

2.4. Some examples of deposit types, and problems they cause

2.4.1. Fuel crud

Crud forming on fuel can occur in a range of different forms and compositions, depending on factors such as the coolant chemistry, the mix of alloys used in the primary coolant system, and the extent to which sub-cooled nucleate boiling (SNB) occurs. Where the predominant materials of construction are stainless steels, the main corrosion product forming on corroding steel surfaces and circulating in the coolant is an impure magnetite, containing small amounts of Ni, Cr and other elements; this is also the nature of the oxide which deposits on the fuel.

Most commercial PWRs use Ni base alloys such as alloy 600 or alloy 690 for the steam generator (SG) tubing, which makes up the greater part of the coolant-facing surface area of the primary system, and this is reflected in a more Ni rich composition of fuel crud. Typical fuel crud consists of non-stoichiometric nickel ferrite, $Ni_xFe_{3-x}O_4$, having x = 0.45 to 0.75 [45], along with in some cases nickel metal and/or NiO, resulting in a ratio of Ni/Fe which varies between plants, at around 0.5 +/- 0.2 [46].

Adverse effects of fuel crud include decreased heat transfer efficiency, and resistance to coolant flow causing an increased pressure-drop across the core. Fuel crud becomes activated in the core neutron flux, and provides a major source of ex-core radioactivity after it is released and deposits throughout the primary coolant system. Therefore, it is desirable to keep deposits to a minimum.

Much thicker deposits may form locally where SNB is occurring. As water boils, entering the gas phase, dissolved species such as Li, B, and metallic cations, are left behind in the aqueous phase, becoming concentrated and forming deposits on the fuel, which can be thicker than those formed in the absence of SNB, and harbour aggressive chemicals (particularly Li) which cause accelerated corrosion of the clad. This so-called Crud Induced Localised Corrosion (CILC) [1] can even cause fuel failure in the most extreme cases. The presence of B in deposits (a neutron absorber) causes decreased neutron flux, and thus decreased power, in the upper regions of the core where the deposits reside. The resulting shift in power distribution towards the bottom of the core is particularly pronounced for deposits of thickness around 20 – 30 μm or greater (which may be due to conditions for the boron rich compound $LiBO_2$ to precipitate only being present at these depths) [47]; is known as Crud Induced Power Shift (CIPS), or Axial Offset Anomaly (AOA) [1], [6]; and has forced one plant for example to operate at only 70% power for the last 7 months of a fuel cycle, at a cost of tens of millions of US dollars [6].

Towards the base of the thickest deposits, conditions of high temperature and low hydrogen concentration allow the formation of compounds not otherwise found in fuel crud, such as bonaccordite (Ni_2FeBO_5) [47]. The resulting, low porosity, tenacious, crud cannot be removed by shutdown chemistry, whilst porous crud produced under non-SNB conditions can. As well as causing precipitation of dissolved ions, SNB causes enhanced deposition of particles [25], [35].

2.4.2. Deposition of activated crud on ex-core surfaces

Corrosion products are continually releasing and depositing from surfaces and deposits in the primary coolant system, both as soluble ions and as oxide (or metal) particles. In this way, radioisotopes which have been produced by activation of corrosion products in the core, either as circulating species in the coolant, or as fuel crud deposits, become incorporated in the corrosion oxide film on surfaces throughout the primary coolant system.

The gamma radiation fields that result, outside of the substantial radiation shielding surrounding the core, cause workers to be exposed to radiation doses, and necessitate expensive radiation protection measures to keep operational exposures to a minimum.

2.4.3. Deposition at entrances to flow restrictions

Deposits have been found to occur preferentially at the entrances to flow restrictions [26], including those used for instrumentation (venturis and orifice plates) and steam generator tubes [48]; in the former case, a narrowing of the opening due to deposits results in inaccurate measurement of flow velocity, typically an underestimation of ~1 % for orifice plates and overestimation of ~2.5 % for venturis, which can have implications for safety [48].

These deposits occur due to flow related effects [26]; research has been (and continues to be) conducted into improving understanding of the mechanism (for example, [26], [49]–[53]), which is thought to involve an electrokinetic effect occurring in regions of accelerated flow [49]. Deposition of colloids may be involved in addition to precipitation of ions [50].

2.5. Actions taken to mitigate effects of Corrosion Product deposits

As early as the 1950s, additions of dissolved hydrogen and a strong base, such as NaOH (or LiOH), have been shown to cause slower corrosion of stainless steels, and less transport and deposition of their corrosion products onto fuel pins, in experiments using a test reactor [11], [54]; along with boric acid, they remain the key additions to PWR primary coolant water (LiOH is used as the strong base in most PWR designs, whilst KOH is used in VVERs). Boric acid, H_3BO_3, is added to control reactivity in the core and smooth out the effects of decreasing fuel reactivity over the course of a fuel cycle as U-235 atoms are used up. Natural boron, B, contains the isotope boron-10 at typically around 19.8 at.% [55], which acts as a 'neutron poison', since it absorbs neutrons in the core which might otherwise lead to fission of U-235 nuclei. Over the course of a 12-month fuel cycle, levels of B in the coolant, as H_3BO_3, are typically decreased by around 100 ppm each month, from around 1200 ppm to 0 ppm [10], [56], [57].

In the 1960s to mid-1970s, during the early years of commercial PWR operation, Westinghouse recommended that Li, as LiOH, be maintained at between around 0.7 and 2.1 ppm in primary coolant to maintain alkaline conditions, whilst Siemens-KWU recommended between about 1 – 2 ppm Li. This advice was followed by almost all PWR plants [57]. The lower limit was set to avoid the formation of troublesome deposits on the fuel at low pH, whose effects could be perceived surprisingly rapidly (within 24 h) when LiOH was not applied to coolant, via an increased pressure drop through the core [57]–[59] and other effects [57], [60]; the upper limit was set to avoid excessive corrosion of Zircaloy-4 fuel cladding caused directly by Li [57]. Since then, a series of changes to recommended and applied chemistry in the primary coolant, and to the materials used, have been made as a result of extensive research and modeling efforts to understand, tackle and mitigate problems caused by crud deposits on the fuel, activity transport, and other problems in the primary coolant circuit.

Corrosion products from Fe-Cr-Ni alloys were known to be dissolved into the coolant, transported to the rest of the coolant circuit, and deposited preferentially in certain locations, particularly on fuel in the core. A key aim was to decrease the inventory of corrosion product sitting in fuel deposits, or transiting the core in the coolant at any given time, and thereby minimise the total inventory of radioisotopes activated by neutron flux in the core (which can subsequently be transported and deposited on out-of-core surfaces), as well as avoiding the problems caused directly by the fuel deposits themselves.

Two simple approaches were used to achieve this:

1. Minimise the quantity of corrosion product circulating in coolant, by selecting a coolant chemistry which minimises solubility of relevant metal oxides (at this point, effect of particulates was neglected).
2. Avoid the situation whereby a negative (or 'retrograde') temperature-dependence of solubility causes precipitation of oxides onto fuel as coolant is heated in the core, by selecting appropriate coolant chemistry.

Where stainless steels are the only metals present, magnetite is the oxide which controls soluble levels of corrosion product in coolant (see section 3.3.3), albeit with low levels of Cr and Ni and other elements incorporated into the oxide structure. The above two objectives, minimised solubility and non-negative temperature dependence of solubility, were found to be satisfied for magnetite at a pH_{300C} of around 6.9 or above for magnetite, as shown schematically in Figure 2.2 For this reason, in the 1970s a "coordinated boron and lithium" chemistry was recommended and applied, in which levels of Li were coordinated with those of B to maintain a constant pH_{300C} of 6.9. This is illustrated as the thick black curve in Figure 2.3, labelled "classic coordinated chemistry". Levels of Li were controlled slightly above the line where possible, to avoid any negative coefficient of solubility, and in many cases the upper and lower limits of 0.7 and 2.1 ppm were retained. Alongside other measures, classic coordinated chemistry has been attributed to significant improvements in dose rates and fuel crud thickness over the previously recommended regime [10].

From 1978 to 1984, Westinghouse conducted research under an EPRI contract, with a view to further reduce radiation field build-up in commercial PWRs, by improving further on the coordinated chemistry regime [57], [61]. Analysis of fuel crud scrapes showed the predominant oxides to be non-stoichiometric ferrites of nickel and cobalt [45] (and in later studies, Ni, NiO and other phases incorporating B and Li [10], [46], [62]), rather than magnetite. These mixed ferrite oxides were found by Kunig and Sandler [63]–[65] to have their minimum solubility, and zero temperature-dependence thereof, at a higher pH_{300C} of around 7.4 compared with the 6.9 of magnetite [66] – see Figure 2.4.

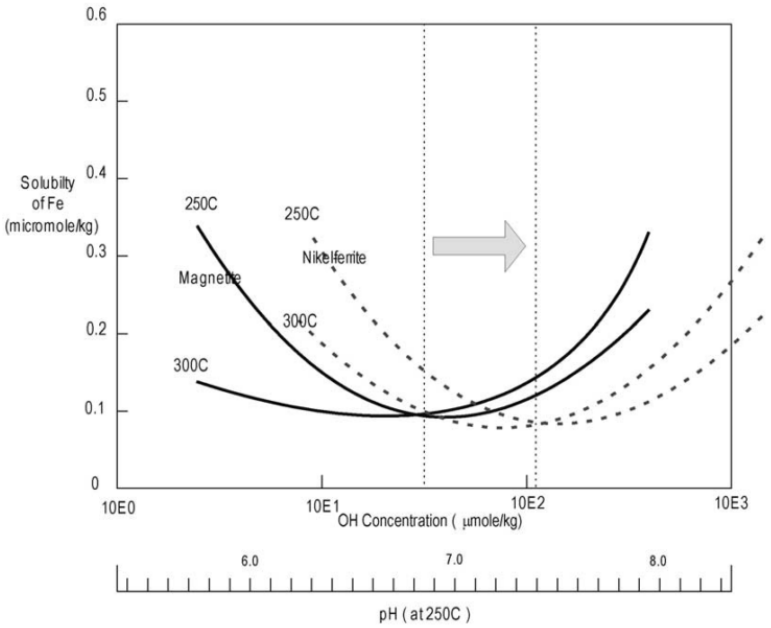

Figure 2.4. Solubility of Fe in magnetite and in nickel ferrite, versus pH_{250C}, at high temperatures. From [56].
The intersection of the 250 °C and 300 °C curves for magnetite gives the approximate pH_{250C} of minimal solubility in the range 250 – 300 °C (which is also the pH_{250C} above which temperature-dependence of solubility switches sign from negative to positive) as pH_{250C} 6.9, with the value of minimal Fe solubility being 0.1 µmole/kg. The equivalent values are also shown for nickel ferrite, being 7.4 and 0.1 µmole/kg respectively. Values of pH_{300C}, for the same minimal solubilities of magnetite and nickel ferrite at high temperature, which are the more typically quoted measures, are also 6.9 and 7.4 respectively.

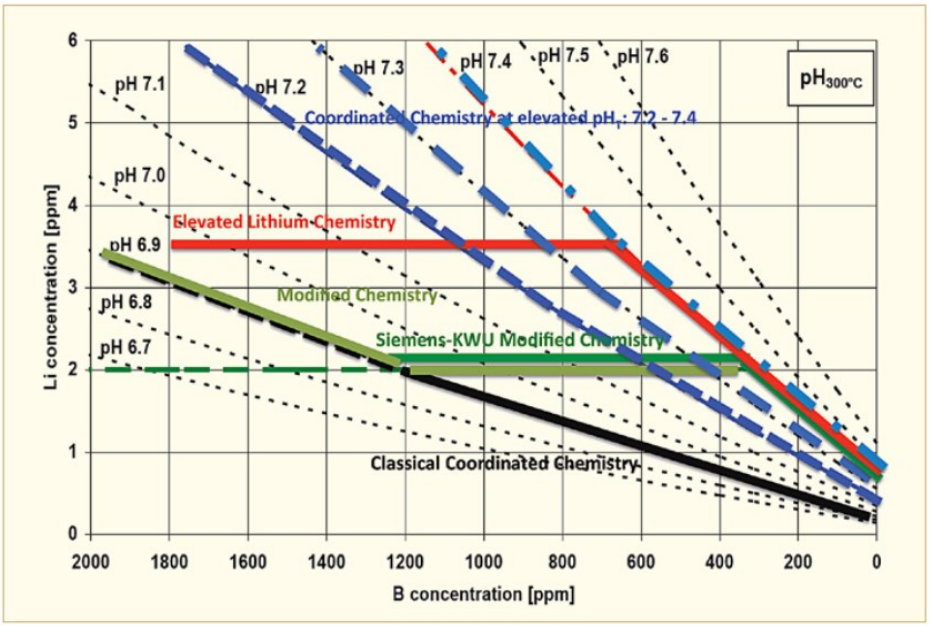

Figure 2.5. Coolant chemistry lithium / pH_{300C} strategies developed and used worldwide to optimise radiation field control. From [10].

In order to take advantage of this new knowledge to enable thinner fuel deposits and lower out-of-core dose rates, the demand for high pH_{300C} has to be reconciled with the ~ 2.1 ppm limit on Li concentration, imposed to prevent corrosion of fuel clad. In addition, there has been (and still is) a trend towards longer fuel cycles [56], to achieve greater burnup of fuel, resulting in higher beginning of cycle (BOC) levels of B, and correspondingly higher BOC levels of Li required even to maintain pH_{300C} 6.9. To this end, there have been several remedies suggested and applied. In the "Modified chemistry" regime (see Figure 2.5), Li is raised temporarily to concentrations up to 3.5 ppm at the start of a cycle, to ensure pH_{300C} does not fall below 6.9 at the beginning of an extended fuel cycle, once Li concentration falls to 2 ppm it is maintained at 2 ppm until B falls sufficiently that pH_{300C} reaches 7.4, then Li is adjusted to maintain pH 7.4 to the end of cycle. "Elevated lithium chemistry" employed a constant Li concentration of 3.5 ppm until B had fallen to about 700 ppm, before decreasing Li to maintain pH_{300C} 7.4 – this regime has been terminated because of fears that the prolonged exposure to 3.5 ppm Li may cause stress corrosion cracking of alloy 600 where present in steam generators, as well as Zircaloy clad corrosion. Replacement of Zircaloy-4 with new corrosion resistant fuel cladding alloys, like Zirlo™ and M5, has enabled Li concentrations up to around 6 ppm to be tolerated, making "coordinated chemistry at elevated pH_{300C}" of 7.2 to 7.4 possible, though not in plants where alloy 600 is present, for reasons described above. Finally, the use of boric acid enriched in boron-10 enables the same reactivity control with a smaller concentration of B [55], [56], making coordinated chemistry at pH 7.4 possible even for extended cycles. A mix of different regimes is currently in use, depending on the specific needs of each plant, but there is a clear trend towards the use of elevated pH, as shown in Figure 2.6.

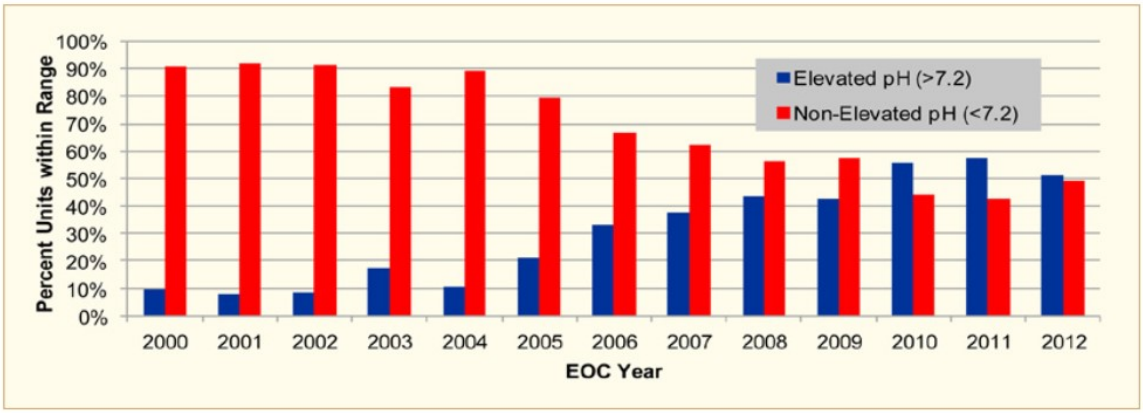

Figure 2.6. Evolution of PWR primary pH_T (elevated vs non-elevated) in the U.S. [67]

A relatively recent technique has been the injection of Zn into coolant, to help reduce radiation fields, and in some cases to mitigate SCC, by improvement of the passive oxide layer [68]. Injected Zn cations from the coolant replace cations such as Ni and Co in spinel-type oxides in the primary coolant circuit, including radioisotopes such as Co-58 and Co-60, and inhibit their incorporation into the oxide film from the coolant [68]–[70]. Radioisotopes which are thus removed from the oxide, or inhibited from incorporating into the oxide, are then removed by the CVCS in the usual way, resulting in a significant reduction [68], [69] in radioactivity build-up on out-of-core surfaces.

In summary, levels of B and Li utilised in primary coolant vary from plant to plant and over the course of a fuel cycle. There has been a trend towards coordinated chemistry at elevated pH_{300C} of 7.2 to 7.4 [67], [71] (see Figure 2.6), which is recommended by the industry [70], [71], but operators of some plants find it prudent not to exceed a certain level of Li because of materials corrosion concerns. For reference, for a solution containing strong base only, pH_{300C} of 6.9, 7.2 and 7.4 corresponds to pH_{25C} 9.8, 10.1, 10.3, or [Li] = ~ 0.23, 0.48, and 0.70 ppm (as read from the graph in Figure 2.5). An example of a typical overall chemistry in PWR primary coolant is 650 ppm B, 3.5 ppm Li, 35 scc/kg H_2, having pH_{300C} of 7.4.

3. Literature Review

Part I: Corrosion of SS316L and similar alloys in conditions of PWR primary coolant

3.1. Overview of chapter, and relation to other chapters

Mechanisms of corrosion relevant to this project are treated in section 3.2, with emphasis on the theory proposed by Robertson for stainless steels in high temperature aqueous environments [72], [73]. This has a bearing not only on interactions of metal and metal oxide corrosion products with the coolant, but also on the nature of hydrogen production and release to coolant.

As a result of exposure to hydrothermal environments, SS316L and related alloys form a duplex (double-layered) corrosion film consisting of a discontinuous layer of Fe-rich, spinel type, polyhedral crystallites, on top of a continuous, protective layer of Cr-rich spinel type oxide [26], [37], [74]–[87]. The morphology and chemistry of corrosion film is important as the film acts as a source of particulate material in coolant [37], which is known as crud in the context of nuclear plant (a source of many problems in the primary circuit of PWR's wherever deposits form [1], [26], [37], [42], [88]–[91]) and which was found to be present in simulated coolant in the rig of the current project. The outer layer oxide crystallites, although adherent, are not as tightly adherent as the inner layer oxide, and can become eroded by coolant flow, becoming a major source of suspended matter, whilst entrainment of particles from the inner oxide requires thermal-hydraulic conditions aggressive enough to result in spallation of the whole oxide film, and is therefore rare. Only the inner oxide layer conveys corrosion resistance. It controls the release of ions to coolant, which ultimately precipitate as outer layer oxide or on crud deposits on fuel, and in so doing it influences the chemical composition of those oxides.

The main, if not sole, source for the nucleation and growth of outer layer oxide crystallites is thought to be soluble metallic ions precipitating from solution, having diffused outward through the inner oxide layer and dissolved from its coolant facing surfaces [73], [81]. Corrosion products from local corroding surfaces mix with those carried by the coolant from different alloys corroding elsewhere in

the primary circuit, resulting in differences to oxide composition, driven by a reduction in Gibbs energy of the whole system. This means a net flux of soluble corrosion products can be transported from some regions of the primary circuit to others, driven by solubility differences in the corrosion film oxides with changing temperature and other coolant parameters (e.g. pH) which vary to some degree in the coolant around a primary system loop. Thus, solubility behaviour plays a key role in shaping the morphology and chemistry of the outer layer of a corrosion film.

The corrosion rate of the alloys used in the PWR system is diffusion controlled through the inner oxide, and is therefore inversely proportional to the thickness of the protective film, which results in parabolic kinetics over timescales of relevance to nuclear plant and this project [37], [73], [76], [77], [81], [84], [92], [93]. This means that generation and release of corrosion products is also to some degree controlled by parabolic kinetics and it is important to understand corrosion to appreciate material release.

All these topics are discussed in more detail below.

3.2. Corrosion mechanism of stainless steel in PWR Primary Coolant

Essentially, corrosion proceeds at the oxide-alloy interface, by the inwards diffusion of oxygen, and simultaneous outwards diffusion of Fe^{2+} and other metallic species through the protective inner oxide film.

A leading theory for mild steels and stainless steels [72], [73], is that oxygen is transported along micropores in the inner oxide as water, which reacts with metal at the oxide-alloy interface to form spinel oxide and hydrogen gas, and metals migrate outwards as divalent ions diffusing along grain boundaries. The outward diffusion of a little over half of the metal ions from the alloy makes room for oxide to form, which occupies a volume approximately double that of the metal it replaces. The model states that the outward diffusion of metal ions is the rate limiting step. This is based on the observation that the magnitude of the activation energy for the corrosion process is consistent with that expected for solid state diffusion in the inner oxide. In contrast with mechanisms of stainless steel corrosion under other regimes, such as high temperature gas oxidation (where Cr_2O_3 oxide grows by diffusion of Cr from the alloy, leaving nearby alloy depleted in Cr), oxidation under high temperature aqueous corrosion is essentially non-selective. This means that the metals in the alloy pass congruently into the oxide film, and there is no enrichment or depletion of alloying constituents in the alloy close to the oxide-alloy interface (though some minor Ni-enrichment [78], [79], [87] or Cr-depletion [77] has been observed by several authors within a few 10s of nm of the oxide film). There is, however, a difference in the composition of the two layers which make up the corrosion

film. The inner layer is strongly enriched in Cr, because of the difference in diffusivity of the alloy components, which vary in the order: Mn > Fe > Co > Ni >> Cr [73]. Elements which diffuse faster than the majority element (Fe) migrate through the protective (inner) oxide layer, becoming more concentrated in the outer layer, and those which diffuse more slowly remain and accumulate in the inner layer. The theory of Robertson accounts well for observed dependence of corrosion kinetics on pH and temperature, though pH dependent data for stainless steels is limited. Most of the content of his theory builds on and is in agreement with theories from other workers. However, alternative theories have been proposed, particularly regarding mechanisms for transport of oxygen and metal ions across the oxide film (see p341 of [83], and references therein).

Growth of oxide requires oxygen as a raw material; in the reducing conditions of the PWR primary circuit this ultimately comes from water, with excess hydrogen occurring as a result. The location at which hydrogen is produced or accumulates is to some extent dependent on the mechanism of corrosion, and may have important consequences in some situations, particularly where corrosion provides the only source of coolant hydrogen, such as in the current study. Two factors influence the location of hydrogen production and build-up.

1. Nature of the inward-migrating oxygen-bearing species. If oxygen migrates as water, then hydrogen is produced at the oxide-alloy interface, but if it migrates in the form of oxygen gas or oxide ions then the corresponding hydrogen is left behind in the coolant.
2. Nature of the charge carriers responsible for completing the electric circuit. An electric counter-current across the inner oxide is required, to balance the outward migration of metallic cations (and the inward migration of oxide anions where applicable). If this is provided by outward migration of electrons, then all the hydrogen associated with outer layer oxide formation is produced at the oxide-coolant interface, by the reduction of H^+ ions to form hydrogen gas (or equivalent reactions). However, due to the semiconducting properties of Fe-Cr-Ni spinels [79], electron conductivity is very low. Instead it has been proposed that H^+ ions are the charge carrier [73], [94]. This results in the evolution of hydrogen gas, or possibly atomic hydrogen, at the oxide-alloy interface where H^+ ions are reduced.

On the one extreme, inward transport of oxygen gas and outward transport of electrons would cause all the hydrogen to be released to the coolant. On the other extreme, H^+ ions as the charge carriers would cause almost all the hydrogen (~90% [94]) to be produced at the oxide-alloy interface (regardless of the oxygen-bearing species), the remainder being associated with oxidation of ions from the divalent state in which they diffuse across the inner oxide to the mixed divalent/trivalent state of Fe-Cr-Ni spinels. This figure, ~90% retention, has indeed been observed, for carbon steel and

low alloy ferritic steels, under hydrothermal conditions up to pH 11 [95] (in [94]). In much stronger alkalis, less hydrogen was retained, this was thought to be due to an increase in the porosity and hydrogen permeability of the corrosion film. Almost all (>99%) of the retained hydrogen was expected to diffuse through the alloy, to be released into the laboratory atmosphere, rather than passing through the protective oxide film [94].

3.3. Duplex corrosion film

The duplex oxide film forming on mild steel in hydrothermal solutions was first characterised by Potter and Mann in the early 1960s, [92], [96], described as a tightly adherent inner layer of small magnetite crystallites, which confers corrosion resistance, and a loosely adherent outer layer of larger magnetite crystallites. The inner layer was observed to occupy the same volume as the metal it replaces.

The oxide film forming on stainless steels is similar, being composed of spinel type oxides in both layers, but Cr from the alloy is concentrated in the inner layer, forming a Cr-rich inner layer (which conveys superior corrosion resistance compared with mild steels) and a Fe-rich outer layer, essentially magnetite, with some nickel and chromium content. Figure 3.1 and Figure 3.2 show typical examples of duplex corrosion films, in cross section on SS304 after up to 10 000 h exposure at 260 °C in hydrogenated, ammoniated water.

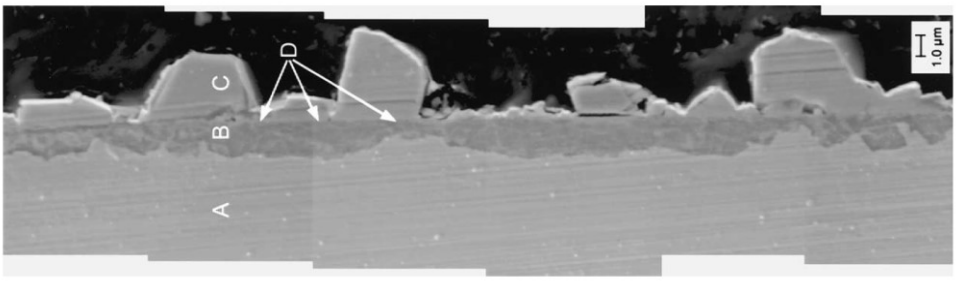

Figure 3.1. Cross section of corrosion film on SS304 (composite of SEM images) [84].
A: SS304 base metal; B: inner oxide layer; C: outer layer oxide crystallites; D: inner layer – outer layer interface. The bright layer on outer layer crystals is due to tungsten coating. The steel was exposed to hydrogenated ammoniated water for 10 000 h.

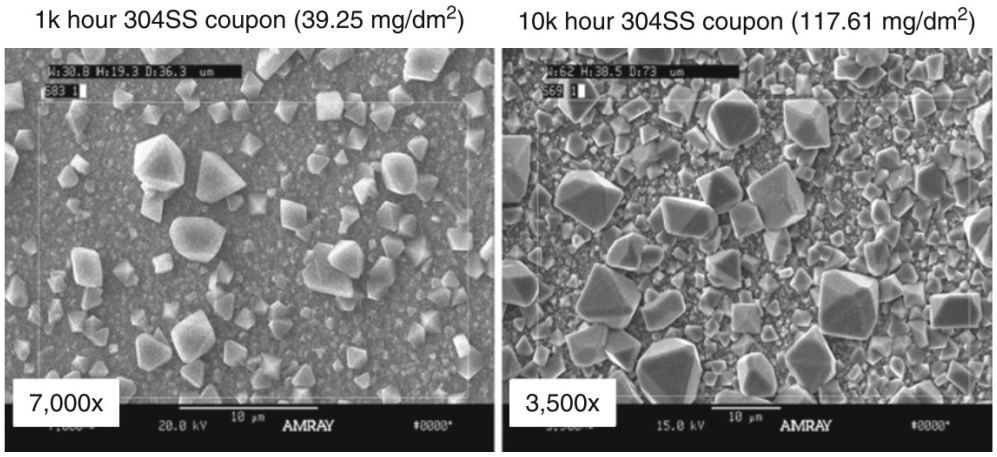

Figure 3.2. Corrosion films on SS304 after 1k and 10k hours of exposure to 260 °C hydrogenated ammoniated water in [84] (SEM images)*. The figure is taken from* [37]*.*

3.3.1. Factors which may determine the composition of inner and outer layers

Pilling-Bedworth ratios can be defined for each combination of alloy and oxide, as the ratio of oxide to alloy volume (assuming 100% of the alloy is retained in the oxide and there are no residual stresses) [97]. Pilling-Bedworth ratios for the oxidation of steels to form spinel oxides, such as magnetite, are around 2 [73], [86], which means that approximately half of the Fe in the steel must diffuse outwards through the inner oxide layer, and a similar flux of O atoms must diffuse inwards, via whatever mechanism, for newly formed inner oxide to maintain its adherent protective nature, with minimal porosity (i.e. close to full theoretical density of the oxide) and without significant stress, strain or movement. This fact was used in Robertson's model [72], [73], as described in the previous subsection, to explain the amount of release of metals to outer oxide layer, and the composition of inner oxide layer.

Ziemniak and Hanson [84] studied the corrosion film on SS304, and found that the inner layer was a spinel with the following composition: $(Ni_{0.2}Fe_{0.8})(Cr_{0.7}Fe_{0.3})_2O_4$. That is, ~ 47 +/- 3 at% Cr. Using a Pilling-Bedworth ratio of 2.1, and assuming that 100% of Cr from the alloy is retained within the inner layer oxide, an inner oxide layer of zero porosity occupying the same volume as the metal it replaces would have Cr content of 2.1 x 20.2 = 42.4 at%, based on the Ni, Cr, Fe composition of the oxide as stated in the paper (if the SS304 alloy they used had the maximum permissible amount of other elements for the grade, namely 2 wt% Mn and 1 wt% Si, this figure falls to 40.8 at%). Any release of Cr to the outer layer (observed to have ~ 3 +/- 2 at% Cr) would cause this percentage to decrease also. The Cr percentage observed was close to that expected from the Pilling-Bedworth

ratio, though a little higher, demonstrating that the amount of alloy released through the inner oxide to coolant and outer oxide is higher than the Pilling-Bedworth ratio alone would suggest. This additional release may be achieved by a slight retreat of the inner oxide – outer oxide interface from the original location of the alloy surface, or by the inner oxide having porosity of around 10 – 20%.

An alternative explanation proposed by Ziemniak and Hanson for what determines the amount and composition of metals released to the outer oxide layer, and thus the composition of the inner oxide layer, is that the inner and outer oxide layers are thermodynamically driven to take on compositions close to the solvus of immiscibility, as described in the following paragraph. Cremer ([98], as summarised in [85]) showed experimentally that ferrous chromite ($FeCr_2O_4$) and magnetite (Fe_3O_4) spinels are fully miscible only above the consolute solution temperature of around 900 °C. Below this temperature, mixtures with an intermediate Cr component separate over time into a Cr-rich phase (chromite) and a Fe-rich phase (ferrite), each having a Cr content described by the solvus of immiscibility. The results of their experiment are shown as curve (a) in Figure 3.3, where n represents the mole fraction of Cr at trivalent sites:

$$Fe\ (Fe_{1-n}Cr_n)_2\ O_4.$$

Cr content on a metals basis (at%) is given simply by 100 x 2/3 x n. The lowest temperature at which they produced data was 500 °C, presumably because of the prohibitively slow reaction kinetics, as described by Ziemniak et al. [74] for the Equivalent system $Ni\ (Fe_{1-n}Cr_n)_2\ O_4$ (see right hand side of Figure 3.3).

Grey circles on the plot show the composition of inner and outer oxide phase measured by Ziemniak and Hanson for SS304 [84], which indeed lie strikingly close to where one would expect the solvus of immiscibility to lie at the temperature employed, based on a linear extrapolation of the data plotted in curve (a).

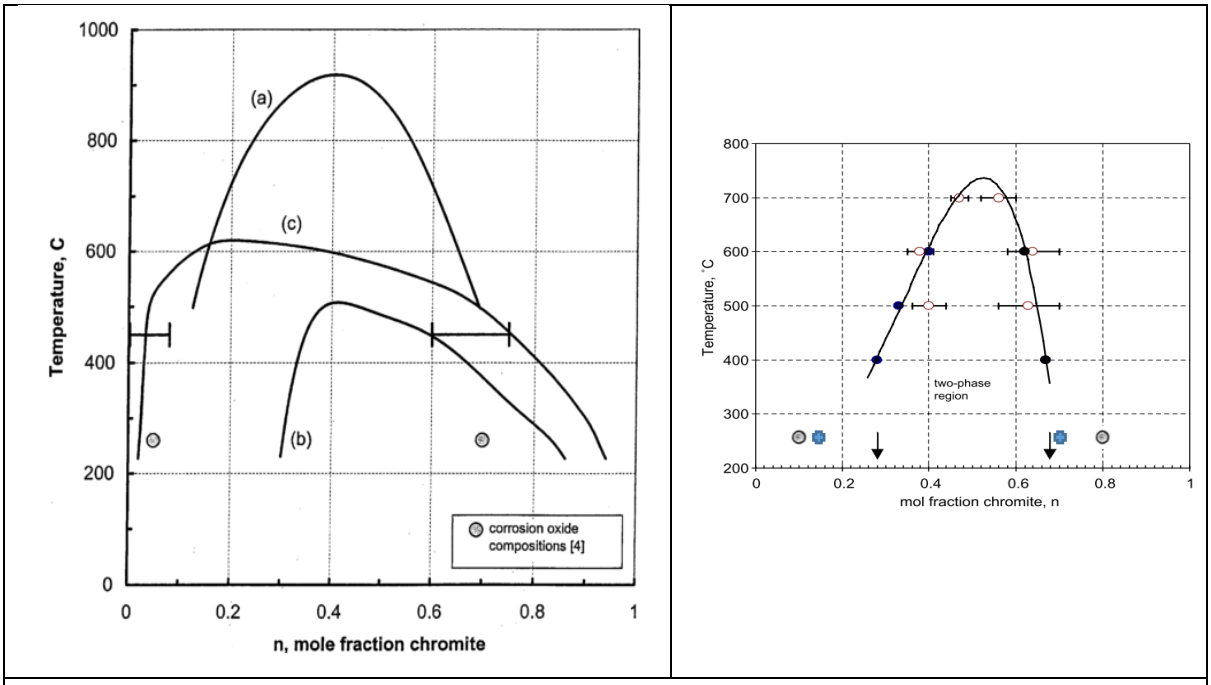

Figure 3.3 Solvi of immiscibility for $Fe(Fe_{1-n}Cr_n)_2O_4$ spinel binary (left) [84], [85], [98]–[100] and for $Ni(Fe_{1-n}Cr_n)_2O_4$ spinel binary (right) [74], [75], [86].
For $Fe(Fe_{1-n}Cr_n)_2O_4$ (left), the plot is taken from [85] unaltered. Curve 'a' represents experimental data from [98], whilst curves 'b' [99], [100] and 'c' [85] show predictions from theoretical models. Horizontal bars at 450 °C represent Weiser's analyses of naturally occurring minerals, as presented in [98]. Grey circles represent measured composition of oxides in the corrosion film of type 304 Stainless Steel (SS304) [84].
For $Ni(Fe_{1-n}Cr_n)_2O_4$ (right), the plot is taken from [74], and shows experimental data: EDX (open circles), EMPA (filled circles), and a fit to the data. Arrows represent a 'rough estimate' of the solvus at room temperature. At 260 °C, grey circles and pale blue symbols were added by the present author to show composition of oxides in the corrosion film of Ni base alloy 625 [86] and allloy 600 [75] respectively, as measured by Ziemniak et al. – the same team who produced data in [84].

The Pilling-Bedworth ratio is relatively insensitive to small changes in alloy composition, and therefore predictions based on Robertson's theory, assuming full density (zero porosity) of the inner oxide, give outer layer oxide Cr content of zero and an inner oxide Cr content which is strongly dependent on Cr content of the alloy:

$$c_{Cr,inner\ oxide}\ (at\%) = 2.1\ .\ c_{Cr,alloy}\ (at\%).$$

If porosity of the inner oxide is allowed (some porosity is indeed required for the inward transport of water through pores, as assumed in the model), then a fixed composition of the inner alloy is possible, but would require a level of porosity which depends on Cr content of the alloy, being more porous for alloys with lower Cr content.

At a given temperature, predictions based on solvus of immiscibility would give a fixed composition of inner (and outer) oxide, regardless of the Cr content of the alloy, which could result in a degree of

inner layer porosity which depends on Cr content of the alloy, for reasons given above. The temperature dependence of the solvus between 200 and 300 °C is a matter of guesswork, though a relative insensitivity to temperature, or a slight widening of the two-phase region with falling temperature would be the obvious inference. The latter effect would cause the inner oxide to be slightly more Cr-rich at lower temperatures, causing a greater fraction of the alloy to release to the solution and outer layer oxide, and thus potentially a more porous structure.

For the equivalent system of $Ni\ (Fe_{1-n}Cr_n)_2\ O_4$, experimental data regarding the solvus of immiscibility were produced by Ziemniak et al. [74]. The plot as it appeared in [74] is shown in Figure 3.3 on the right hand side, with the addition of grey dots to show the inner and outer layer spinel oxide composition for a Ni base alloy, alloy 625, measured by Ziemniak and Hanson [86], and pale blue dots for alloy 600 [75]. Again, levels of Cr in the inner and outer oxide layers are consistent with what would be expected based on extrapolation of the solvus of immiscibility data (though for alloy 625 the inner layer is a little more Cr-rich, and the outer layer a little more Fe-rich, than might be expected).

3.3.2. Inner layer oxide formed on stainless steels

The inner oxide layer is a Cr-enriched, compact, adherent, film which occupies the volume of the alloy it replaces [73]. It is composed of small equiaxed grains, around 10 – 30 nm [76], [78], [84], [87], of a non-stoichiometric Fe-Cr-Ni spinel having ~40 – 50 at% Cr on a metals basis [75], [77]–[79], [84], [86].

Fe-Cr-Ni spinel oxide has a Pilling-Bedworth [97] ratio of around 2 [73], [84]. Therefore as oxidation proceeds at the oxide-alloy interface, about half of the atoms once ionised must migrate across the inner oxide and into the outer oxide, to make room for new inner layer oxide to form, assuming full density (zero porosity) of the oxide. According to the model of Robertson [73], this migration occurs by solid state diffusion along grain boundaries of the inner oxide; since diffusivities in the oxide follow the order Fe > Ni >> Cr, Cr is effectively fully retained in the inner layer whilst the metal content of the outer layer is mostly Fe.

By applying the logic present in [73], namely that

i) The inner oxide occupies the same volume as the alloy it replaces;
ii) As oxidation proceeds at the oxide alloy interface, sufficient of the oxidised metal passes through the inner oxde into the outer oxide, for (i) to be exactly satisfied, and is replaced by oxygen to form oxide; and
iii) Approximately 100% of Cr is retained in the inner layer,

the concentration of Cr in the inner oxide can be expected to follow the following relation (not given in [73], but derived by the present author as a mathematical expression of the above three assumptions):

$$C_{oxide} = C_{alloy} \cdot R_{PB} \cdot \frac{1}{1 - \emptyset}$$

Where C_{alloy} (at%) is the Cr content of the alloy, C_{oxide} (at%) is the Cr content of the oxide, R_{PB} is the applicable Pilling-Bedworth ratio, and $\emptyset$ is the porosity of the inner layer oxide. If oxide porosity and R_{PB} are independent of alloy composition, then Cr composition of the oxide is proportional to Cr composition of the alloy. For stainless steels having a typical Cr content of ~ 17 – 22 at%, expected Cr content of the oxide assuming $R_{PB} = 2$ and $\emptyset = 0$ would be ~ 34 – 44 at%. Allowing for a slightly higher value of R_{PB}, and non-zero porosity, these values are consistent with values of ~50 at% observed on various stainless steels in the literature.

The observed value of ~50 at% Cr is close to the minimum value at which the oxide phase chromite is thermodynamically stable, as given by the solvus of immiscibility. Fe-Cr spinel type oxides of Cr content between ~5 at% and ~50 at% (based on extrapolation of data taken at ≥ 500 °C [98]) are thermodynamically driven to separate into a Cr-rich phase, chromite, and a Fe-rich phase, ferrite. This is largely due to the ordering of divalent and trivalent cations within tetrahedral and octahedral sites of the fcc lattice formed by oxide ions: ferrite has the structure of an inverse spinel, whereas chromite has the structure of a normal spinel. Whilst Fe-Cr spinels of intermediate composition are possible – having a disordered, partially inverse structure [101] – they are not thermodynamically stable. Corrosion is by nature a non-equiliubrium process, and processes such as diffusion can be slow in the solid state, even at 300 °C, so an unstable oxide composition is possible, but expulsion of Fe from the inner oxide layer to achieve sufficient Cr enrichment of the inner layer is likely to play a role in determining composition of the inner layer. Composition of the inner layer is consistent both with Robertson's theory (arguments relating to Pilling-Bedworth ratio in conjunction with slow diffusion of Cr), and with arguments relating to the solvus of immiscibility. Presence of these two factors working together has been noted by Ziemniak et al. (e.g. [76]). Composition of Cr observed in the *outer* layer is also consistent with both Robertson's theory and arguments based on the solvus of immiscibility.

The presence of other elements may affect whether a phase has normal or inverse spinel structure – for example Fe_3O_4 and $NiFe_2O_4$ are inverse spinels, but $MnFe_2O_4$ is a normal spinel [101].

Lister et al. [81] conducted experiments using corrosion product-free water, and found that the outer oxide layer was completely dissolved, but the inner oxide layer was not, remaining unaffected

in its ability to convey corrosion resistance (no significant change in corrosion rate was observed). Measurements made on the composition of inner layer oxide in this case yielded a Cr:Fe ratio close to 2, substantially higher than the ratio of ~1 measured in other studies in which the outer layer was present, and substantially higher than the measured Cr content measured for the inner oxide in the same study when corrosion product saturated coolant was used. Reading off the position of greatest Cr enrichment from a plot of Auger depth profile suggests an inner layer composition of 32 at% Cr, 23 at% Ni, and 45 at% Fe, after corrosion for 166 hours. Authors of the paper attributed this difference to interference from the Fe-rich oxide crystals precipitated from solution – which were not present in the corrosion product free case – and interference from the relatively Cr-poor underlying alloy. Accumulated data from other researchers since, consistently finding a composition of ~ 50 at% even at times as short as 5 h [79] (where Soulas et al. found a composition of ~ 42 +/- 6 % Cr, 11 +/- 4 % Ni) suggest that the inner oxide in Lister et al.'s experiment where outer layer was present had a similar composition, not the 2:1 ratio of Cr:Fe they expected to see.

The ratio of 2:1 observed in the inner layer oxide where no outer layer was present is interesting to note. Interference from the underlying alloy would only cause an under-reading of the Cr content, therefore such a high Cr content of the inner layer oxide seems genuine. This suggests that the presence of outer layer oxide, and of saturated coolant adjacent to the oxide film (one would not be present without the other) is responsible for the proportion of Fe and Ni (~ 50 at%) which is maintained in the inner layer oxide. In the case where dissolved corrosion products are effectively removed from the coolant adjacent to the oxide, the chromite suffers incongruent dissolution, as was observed in solubility experiments for stoichiometric $FeCr_2O_4$ [102], whereby Fe is released to solution at much higher levels than Cr. For chromite of only ~ 50 at% Cr or less, i.e. $Fe_{1.5}Cr_{1.5}O_4$, incongruent dissolution would cause Cr enrichement of the oxide, up to the stoichiometric limit of $FeCr_2O_4$. Further incongruent dissolution may result in a thin surface layer of CrOOH being present, for the following reasons. Under reducing hydrothermal conditions (30 scc/kg hydrogen), chromite is thought to be unstable at temperatures above about 170 °C with respect to decomposition into CrOOH and ferrite. This observation was made by Dickinson et al. [103], based on solubility experiments conducted by Ziemniak et al. on magnetite [5], and on chromite and other Cr(III) oxides [102]. A proposed mechanism by which this may occur is by the selective dissolution of Fe, leaving behind a Cr rich phase [103]:

$$FeCr_2O_4 + 2H^+ \rightarrow Fe^{2+} + 2CrOOH.$$

Therefore, the inner layer composition can be viewed as resulting from a combination of three effects which result in Cr-enrichment,

1. A tendency for Cr composition of inner layer to be enriched by a factor of ~ 2 from the base alloy due to formation of a fully dense inner layer of oxide having Pilling-Bedworth ratio ~2 (achieved by outward migration of divalent ions only, and therefore not Cr).
2. A thermodynamic driving force for the further Cr enrichment of the inner layer until it reaches the Cr level representative of the solvus of immiscibility, by release of additional Fe to the coolant, resulting in increased porosity of the inner oxide layer. For a fixed Cr concentration of inner layer, alloys with lower at% Cr would tend to produce inner oxide of higher porosity.
3. Incongruent dissolution of Fe rather than Cr from inner layer chromite oxide into coolant.

Against these three effects are effects which would tend to cause enrichment in Fe:

1. Constituents of the alloy enter the oxide film congruently, with levels of Cr and Fe being that of the alloy. Therefore, a diffusion flux of Fe^{2+} across the oxide film must be sustained at the rate at which corrosion proceeds, sufficient to maintain the level of Cr-enrichment of the inner layer (this diffusion flux is thought to be the rate limiting step of corrosion) – otherwise the inner layer becomes relatively Fe-enriched
2. Coolant adjacent to the oxide film builds to slightly supersaturated levels of Fe, Cr and Ni, as required to slow down the rate of Fe^{2+} dissolution from inner oxide, and speed up the rate of onward diffusion (away into bulk coolant or towards outer layer crystallites to precipitate new oxide) sufficiently that the two fluxes match.

Early on during corrosion, a rapid rate of Fe release to solution, coupled with limited surface area of nucleated outer layer crystallites on which to precipitate, would mean significant supersaturation in the coolant adjacent to oxide film, which might be expected to cause the inner oxide layer to be significantly less Cr rich. This was not observed by Soulas et al., at least after 5 h had passed, with inner oxide having ~ 42 +/- 6 at% Cr. This may be due to effects relating to PB ratio and the solvus of immiscibility overcoming any effect of coolant supersaturation.

3.3.3. Outer layer oxide formed on stainless steels

The outer layer on stainless steels is formed of large polyhedral crystallites, on the order of several µm across [81], [87], of Fe-rich spinel – essentially magnetite with up to ~ 10 at% each of Cr and Ni (metals basis). Ni content is much higher for Ni base alloys, at ~ 30 at% Ni [75], [86]. In at least one case, nickel ferrite has been observed on stainless steel, SS316L - ~ 25 at% Ni [82].

The crystallites have an appearance suggesting they grow chiefly from solution, from dissolved cations ejected from the inner oxide, or grow directly from the original surface [73], [84], and their

size tends to grow slowly over time, so is partly dependent on cumulative time of exposure, and on corrosion kinetics (which is itself dependent on many factors, see corrosion kinetics section). Lister et al. [81] showed that the outer layer can be fully removed by corrosion product free water, into which it dissolves, whilst the underlying Cr-rich oxide film was not affected (as determined by the fact that no change in corrosion rate was observed).

3.3.4. Intermediate oxide layer

Most workers refer to a duplex structure, of outer layer crystallites precipitated from solution and inner layer oxide replacing the volume of the alloy. However, the outer layer crystallites tend to be present in two distinct sizes, see Figure 3.4. The smaller crystallites of the outer layer are referred to variously as 'intermediate' layer [82], 'base layer' [104] or a 'uniform crystal layer' [81]. Due to their small size, their composition is difficult to measure without interference from the underlying alloy [84] and inner oxide layer.

3.3.5. Effect of surface finish of the alloy

Several studies have been conducted regarding the effect of the alloy's initial surface finish on corrosion rate, with processes such as electropolishing shown to achieve a dramatic reduction in corrosion rate – see section 3.4. Cissé et al. [77] instead studied the effect on the morphology and chemistry of the oxide film, comparing mechanically ground versus polished specimens of SS304L in steam at 400 °C, and in simulated PWR primary water at 340 °C. Schematic diagrams of the oxide films they observed are provided in Figure 3.4 below.

For both surface finishes, after exposure to the simulated PWR coolant for 500 h, they found a recrystallised area in the alloy beneath the oxide film, having much smaller size than the grains they replaced. This was proposed to be the cause of Cr depletion observed in the alloy close to the oxide film, as Cr migrated along grain boundaries, adding support to the solid state diffusion mechanism assumed by Robertson's theory [73]. The recrystallised area was thicker for the ground sample. The morphology and chemistry of the corrosion film was markedly different for the two surface finishes, particularly the thickness of inner oxide layer.

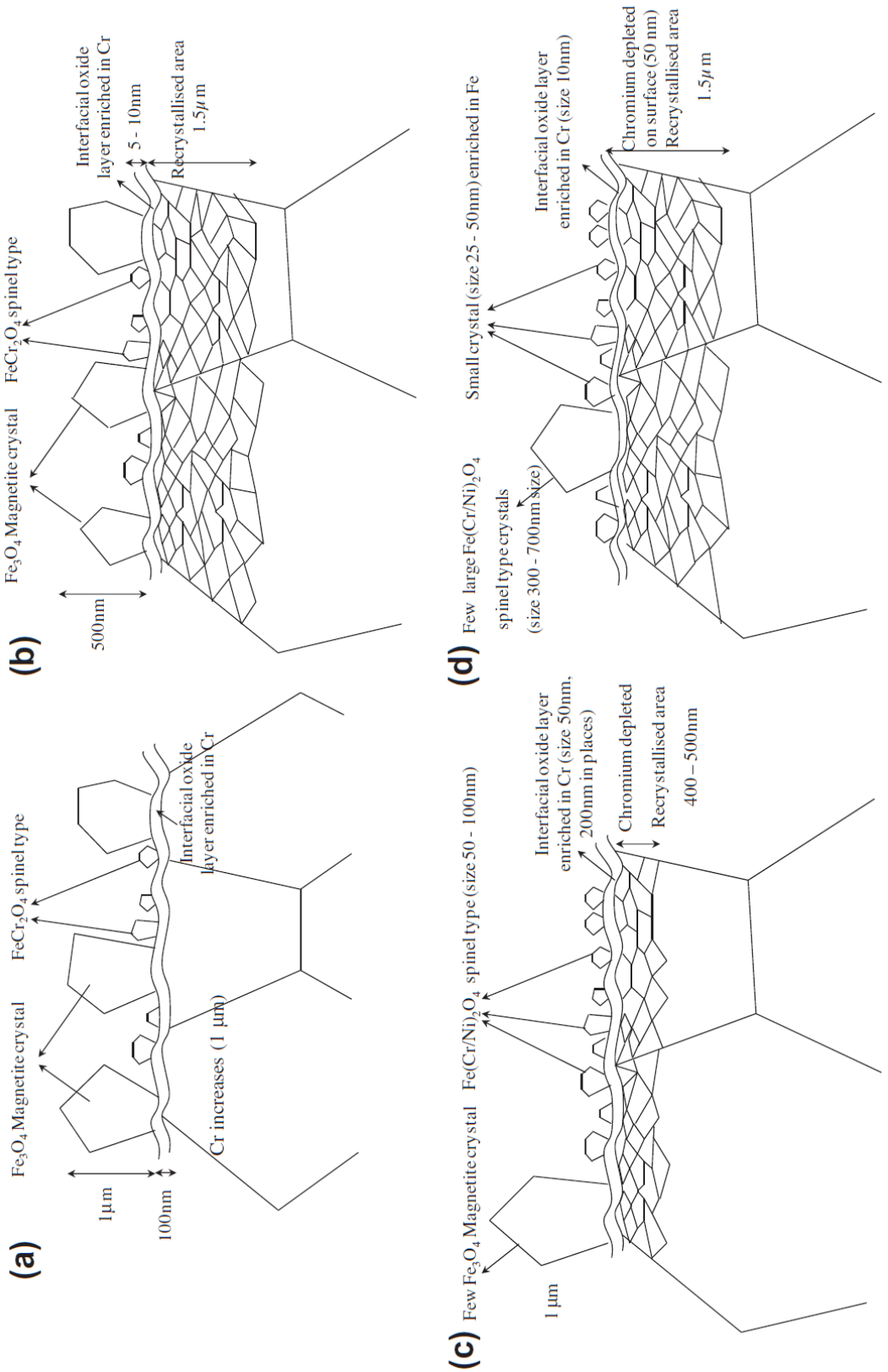

Figure 3.4. Schematic representation of the oxide formed on a SS304L sample. From [77].
(a) polished and exposed to 400 °C steam – for 500 h; (b) ground and exposed to 400 °C steam for 500 h; (c) polished and exposed to 340 °C simulated PWR primary water – for 500 h; and (d) ground and exposed to 340 °C simulated PWR primary water for 500 h.

3.4. Corrosion kinetics

The inner oxide layer acts as a barrier to slow down the oxidation of underlying alloy, since oxygen-bearing species and metallic cations must diffuse through it for oxidation of the alloy to proceed. Corrosion growth is measured in terms of the total mass of alloy oxidised (per unit area) since the alloy was first exposed to hydrothermal conditions, $w\ (mg\ dm^{-2})$. After some transient effects in the first few hundred hours of exposure, studies generally show a parabolic relationship between corrosion rate and time:

$$w = k_p t^{1/2} \qquad (3.1)$$

where t represents cumulative time in hours, and $k_p\ (mg\ dm^{-2}\ h^{-1/2})$ is the parabolic corrosion growth rate constant for the alloy.

This relationship arises because diffusion gradients, and therefore also corrosion rate, are inversely proportional to thickness of the protective oxide film. Differentiation of equation (2.1) to yield corrosion rate gives:

$$\frac{dw}{dt} = \frac{1}{2} k_p t^{-\frac{1}{2}} \qquad (3.2),$$

which can be expressed in terms of w by substituting for $t^{-\frac{1}{2}} = \frac{k_p}{w}$ to give

$$\frac{dw}{dt} = \frac{1}{2} . \frac{k_p^2}{w} \qquad (3.3).$$

The form of equation (2.3) shows explicitly the inverse relationship between corrosion rate and film thickness, where film thickness is proportional to the mass of alloy corroded, w.

An alternative formulation expresses corrosion kinetics in terms of the total thickness of alloy corroded, $x\ (cm)$:

$$x^2 = \kappa_p t \qquad (3.4),$$

Where $t\ (s)$ represents time, and $\kappa_p\ (cm^2 s^{-1})$ is the parabolic corrosion rate constant, giving the following equations for corrosion rate, by analogy with (3.2) and (3.3):

$$\frac{dx}{dt} = \frac{1}{2}\sqrt{\kappa_p}.t^{-\frac{1}{2}} = \frac{1}{2}.\frac{\kappa_p^2}{x} \qquad (3.5).$$

Corrosion rate constants from both formulations are used in this chapter, always accompanied by the units of measurement to make clear which is being referred to.

3.4.1. Effect of surface condition

When considering the release rate per unit nominal area of corroding surface, consideration must be taken of the surface roughness, which can cause greater actual surface area on the microscopic scale than the nominal area covered. More importantly though, the surface condition affects the mechanism of corrosion (see Figure 3.4 above) – and also the corrosion kinetics – via the degree of microstrain remaining as a result of cold work, as well as other defects in the crystal structure. This near-surface microstrain can be removed by electropolishing, resulting in fewer defects in the crystal structure. In hydrothermal solution this tends to result in slower diffusion due to a higher activation energy (less availability of diffusion short circuits using defects), and thus slower corrosion kinetics, though the associated lower activation energy (see section 3.4.2 below) means that this difference is lost at high enough temperatures – approaching critical temperature of water. The surface condition achieved by electropolishing (i.e. zero microstrain or cold work) enables the true corrosion rate inherent to the alloy to be observed [76], while any other surface state achieved by processes such as milling, grinding and polishing, though much more commonly encountered in engineering applications, is a deviation from this. Whilst there is often a large difference between the corrosion behaviour of electropolished surfaces versus mechanically treated surfaces (grinding, polishing etcetera), Warzee observed a relatively modest difference from one mechanical treatment to another in his study of SS304 [80] – despite significant differences in the depth and severity of surface cold work – compared with the significant difference between electropolishing and mechanical treatments.

The effect of surface condition is evident in Figure 3.6 to Figure 3.8 below, where corrosion kinetics of SS304 are plotted against temperature and pH_T.

3.4.2. Effect of temperature

Under some circumstances, an Arhhenius type plot of k_p $\left(mg\ dm^{-2}h^{-\frac{1}{2}}\right)$ or κ_p (cm^2s^{-1}) versus 1000/T yields a simple linear relationship, from which a single value of activation energy for the corrosion reaction can be derived. In this case, corrosion rate can be strongly dependent on temperature. Figure 3.5 shows an example of such a case, for Ni base alloy 600, for which the activation energy can be calculated as 47.5 kJ/mol. The corrosion kinetic is over 30 x faster at 350 °C than at 260 °C. Arrhenius plots were utilised by Robertson [73], to compare kinetics and activation energy of steel corrosion against growth rates of relevant oxides, as shown in Figure 3.6.

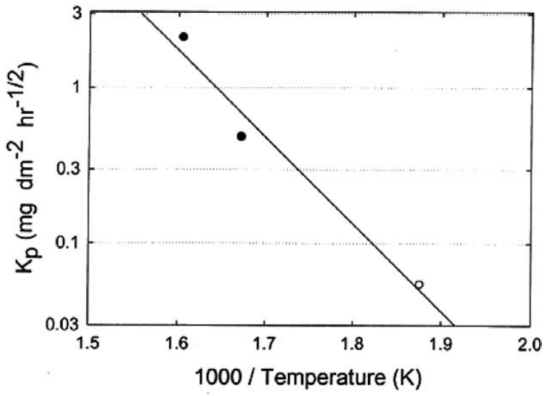

Figure 3.5. Effect of temperature on corrosion rate of alloy 600 in hydrogenated water. From [75]*, data from* [105]*.*
Approximate temperatures of the 3 data points, from left to right, are 350, 320 and 260 °C.

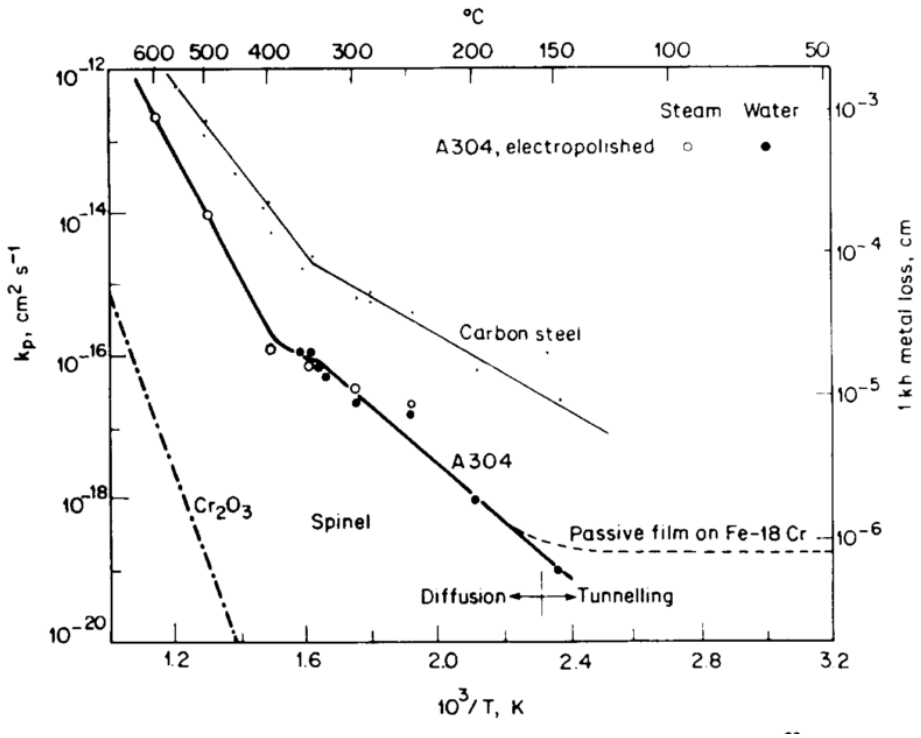

Figure 3.6. Arrhenius style plots comparing kinetics and activation energy (slope of curve) for carbon steel and stainless steel corrosion, against growth of Cr_2O_3 and spinel oxides. From [73]. *Data for the SS304 (A304) corrosion kinetics are from* [106].

Under other circumstances, temperature dependence of corrosion is not so simple. Figure 3.7 shows that SS304 corrosion kinetics can be apparently independent of temperature in the range 200 – 300 °C (milled surface finish, in water), or even have a negative dependence on increasing temperature (electropolished surface finish, in water). This is despite the fact that the same alloy with the same surface treatment (electropolished) had only positive temperature dependence of corrosion kinetics under the circumstances of Figure 3.6. In both cases, pure degassed water was used, therefore the difference demonstrates uncertainties relating to measurements, or effects of a factor which the researchers overlooked.

The underlying physical phenomena giving rise to apparently erratic temperature dependence of stainless steels in hydrothermal solutions are poorly understood, but the unusual temperature dependence itself can be characterised as a "local maximum which may appear within a rate which generally increases with temperature" [73]. This local maximum may be absent, as was the case for the electropolished specimens in the study of Maekawa et al. [106] (see Figure 3.6), or present at a temperature which varies widely between studies – for example 200 °C for the electropolished specimens in the study of Warzee et al. [80], a broad plateau (apparent lack of temperature

dependence) between 200 and 300 °C for the milled specimens of the same study [80], and a peak at around 300 °C for the abraded surface condition in the study of Maekawa et al. [106], reproduced in Figure 3.10.

Robertson offers a plausible explanation based on the interaction between three different corrosion sub-processes each having a different activation energy. Two of these processes operate in parallel, so that the one with the higher activation energy (steeper gradient) is the one which controls kinetics at high temperatures, whilst the one with lower activation energy dominates at lower temperatures. The process with lower activation energy works in series with another process having negative activation energy, resulting in a temperature dependence inversion at intermediate temperatures where this third process dominates. By way of a physical model, Robertson presents a speculative model adapted from Simpson and Evans [107], in which the nucleation of a chromia layer, which is more protective than spinel-type oxides, becomes easier at higher temperatures – in this model the temperature inversion is caused by the transition from the low temperature scenario, of a less protective spinel barrier oxide with patches of the more protective chromia oxide nucleated at certain locations, to a situation at higher temperatures where the chromia oxide forms a continuous protective barrier resulting in slower kinetics. Robertson's fits to the data of Warzee et al. using this model with fitted parameters are included in Figure 3.7.

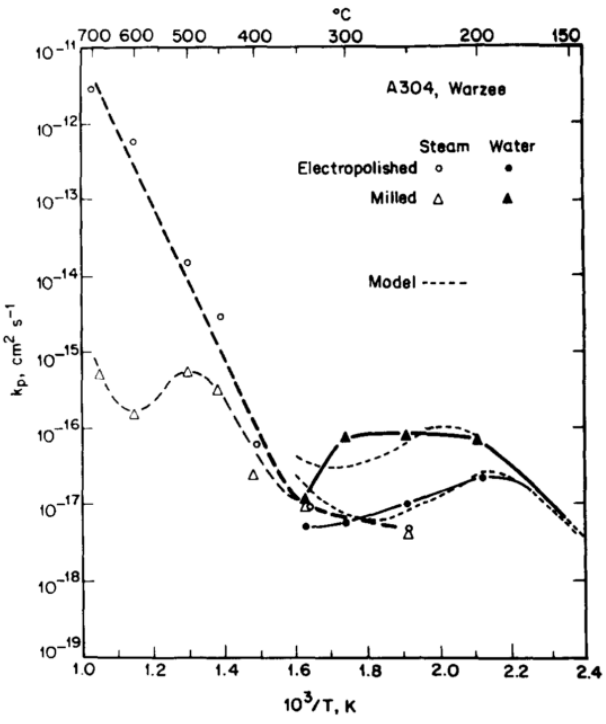

Figure 3.7. Temperature and surface finish dependence of SS304 corrosion rates, from [73]*, after Warzee et al.* [80]

3.4.3. Effect of pH

The effect of pH on corrosion rate is plotted schematically in Figure 3.8 for mild steel and for SS304 under two different surface conditions. The dependence of corrosion rate on pH can be explained by the solid state diffusion (pores - grain boundaries) model, since the concentrations of defects in the crystal structure, which facilitate diffusion of Fe^{2+} ions through the oxide, are dependent on pH [73].

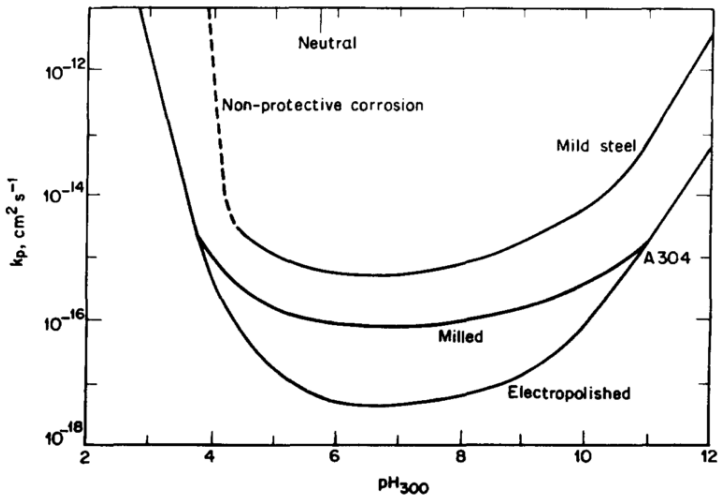

Figure 3.8. pH dependence of corrosion rate of carbon steel and SS304 at 300 °C, from [73].

In strongly alkaline solutions, vacancies dominate, and their concentration increases with pH, and in acidic solutions interstitials dominate with increasing concentration at decreasing pH. Corrosion rate passes a minimum at moderately alkaline pH, where populations of both vacancies and interstitials are low. There is a relatively flat dependence of corrosion rate on pH across a range which includes the pH values used for the current study (Li concentration ranging from 0.07 to7 ppm, giving pH_{300C} 6.4 to 8.4). According to Robertson, the minimum metal flux may be carried by protonated metal ion vacancies, $V^{2-}.2H^{+}$, whose concentration is independent of pH [72], [73].

3.4.4. Expected corrosion rates for SS316L rig of current project

There is some uncertainty regarding the surface state (degree of microstrain) of the steel rig of the current project, as well as the SS316L chips added to some of the runs. There is also uncertainty regarding the hydrogen concentration and any effect that may have. Even under well controlled conditions employed in literature studies, results are conflicting: a positive temperature dependence of corrosion rate was observed between 200 and 300 °C for SS304 in degassed pure water for one

group [106] (see Figure 3.6); whilst a zero or negative dependence was observed by another group under the same conditions [80] (Figure 3.7). Literature data for stainless steels suggests relatively flat pH dependence of corrosion rate within the range pH_{25C} 9 – 11 (Figure 3.8). The effects of pH, surface state, and temperature on corrosion kinetics appear to be to some extent unpredictable and inconsistent from one study to the next, as discussed in the preceding subsections above – particularly regarding temperature. The exact mechanisms behind these phenomena are not yet fully understood, though changes to the nature of the oxide film provide a plausible explanation.

In his EngD project, Jonathan Morrison [26] measured k_p for alloy 316L under the same conditions as used in the present project, in a sister rig to the rig of the current thesis (a once-through flowing rig). The following data in Table 3.1 are from gravimetric descaling performed on specimens mechanically ground to two different levels of roughness (120 grit and 1200 grit) after corrosion for up to 1000 hours in the rig. For the purposes of the current project, an average is taken of the two levels of roughness, though results were fairly similar, with corrosion being about 30% higher for the 120 grit compared with 1200 grit on the average. Crude estimates of standard error are given in terms of differences in results from the two surface finishes. Data for SS304 from other workers are included for reference.

Table 3.1. SS316L corrosion rate data from a sister rig to the rig of the current project [26], [90]*, assessed by gravimetric descaling after up to 1000 h corrosion.*
Data for SS304 [80], [84] *are shown for comparison, for hydrothermal corrosion of SS304 which has had mechanical surface treatment*

T/°C	Dissolved hydrogen	pH_{25C} (LiOH)	k_p (mg dm^{-2} $h^{-1/2}$)
300	[none added]	9.0 (pH_T 6.4)	0.52 +/- 0.03 (gravimetric descale)
300	[none added]	10.0 (pH_T 7.4)	0.44 +/- 0.04 (gravimetric descale)
300	[none added]	11.0 (pH_T 8.4)	0.23 +/- 0.10 (gravimetric descale)
300 (Warzee [80])	[none added]	[neutral] (pH_T 5.7)†	0.51 (hydrogen diffusion)* 0.41 (hydrogen reduction)**
250 (Warzee [80])	[none added]	[neutral] (pH_T 5.6)†	0.42 (hydrogen reduction)**
200 (Warzee [80])	[none added]	[neutral] (pH_T 5.6)†	0.39 (hydrogen reduction)**
260 (Ziemniak [76], [84])	45 scc/kg	pH_T 6.70, (NH_4). Equivalent to pH_{25C} 9.64 (LiOH)	1.16 +/- 0.06 (gravimetric descale)

* from 0.008 mg dm^{-2} h^{-1} corrosion rate at 1000 h;
** from mass of alloy corroded after 1000 h (mg dm^{-2})
† pH_T of high purity water is susceptible to deviate slightly in the presence of any dissolved ions

Measurements of k_p were also made in a separate set of experiments for the same EngD project [26], for SS316L coupons exposed in an autoclave for around 300 h at 200 °C and 250 °C as well as 300 °C; and at pH_{25C} values of ~ 9.5 and ~ 10.5 (~ 0.2 ppm Li and ~ 2 ppm Li). The k_p data for these specimens were determined by a different method to those exposed in the flowing rig – X-ray Photoemission Spectroscopy in conjunction with Argon Ion Milling (XPS/AIM). These results were consistently lower, at values around 0.1 to 0.2 mg dm^{-2} $h^{-1/2}$ for mechanically ground coupons (400 grit). For each set of conditions electropolished coupons were studied alongside the mechanically ground coupons for comparison: these had significantly lower corrosion rates than the ground coupons, in agreement with literature studies, in this case being 0.06 +/- 0.04 mg dm^{-2} $h^{-1/2}$. There was no clearly discernible trend with changing temperature, given the degree of scatter. For five of the six combinations of temperature and surface finish, the slower corrosion kinetics were observed at the lower Li concentration (0.2 ppm Li, pH_{25C} 9.5) in contradiction to the findings from the flowing rig study in which higher Li concentrations yielded slower kinetics.

Results from the two studies are shown graphically in Figure 3.9 below. These results are also plotted alongside other results from the literature for SS304 and mild steel, in Figure 3.10.

The corrosion rate data obtained from the flowing rig, using gravimetric descaling, were considered more reliable than those obtained from the autoclave, using XPS/AIM, for several reasons as described in the thesis [26]. As well as differences in the technique used (for example, in these particular XPS/AIM measurements, there was uncertainty in relating the number of etch cycles by AIM to an absolute depth measurement in nanometres to determine oxide film thickness and mass, whereas gravimetric descaling gave a more reliable measurement of corrosion depth), the XPS/AIM data were taken using an autoclave in which there was no refreshing of the chemistry, which could allow pH and redox conditions to deviate over time, whereas this issue is not relevant for the data subsequently taken from the once-through flowing corrosion rate rig in which chemistry was continually refreshed (from which the gravimetric descaling data were taken). In addition, flow conditions in the flowing rig, as opposed to the static conditions in the autoclave, were similar to those in the solubility rig of the current project and results are thus more directly applicable. It is not known why the data from the autoclave are consistently lower than those from the flowing rig; this may be due to a genuine difference in corrosion rates due to the effect of flow in the flowing rig, or possible changes to chemistry over time in the autoclave, or a difference in the quality of corrosion film due to unknown factors, or it may be a result of systematic errors in one or both of the studies.

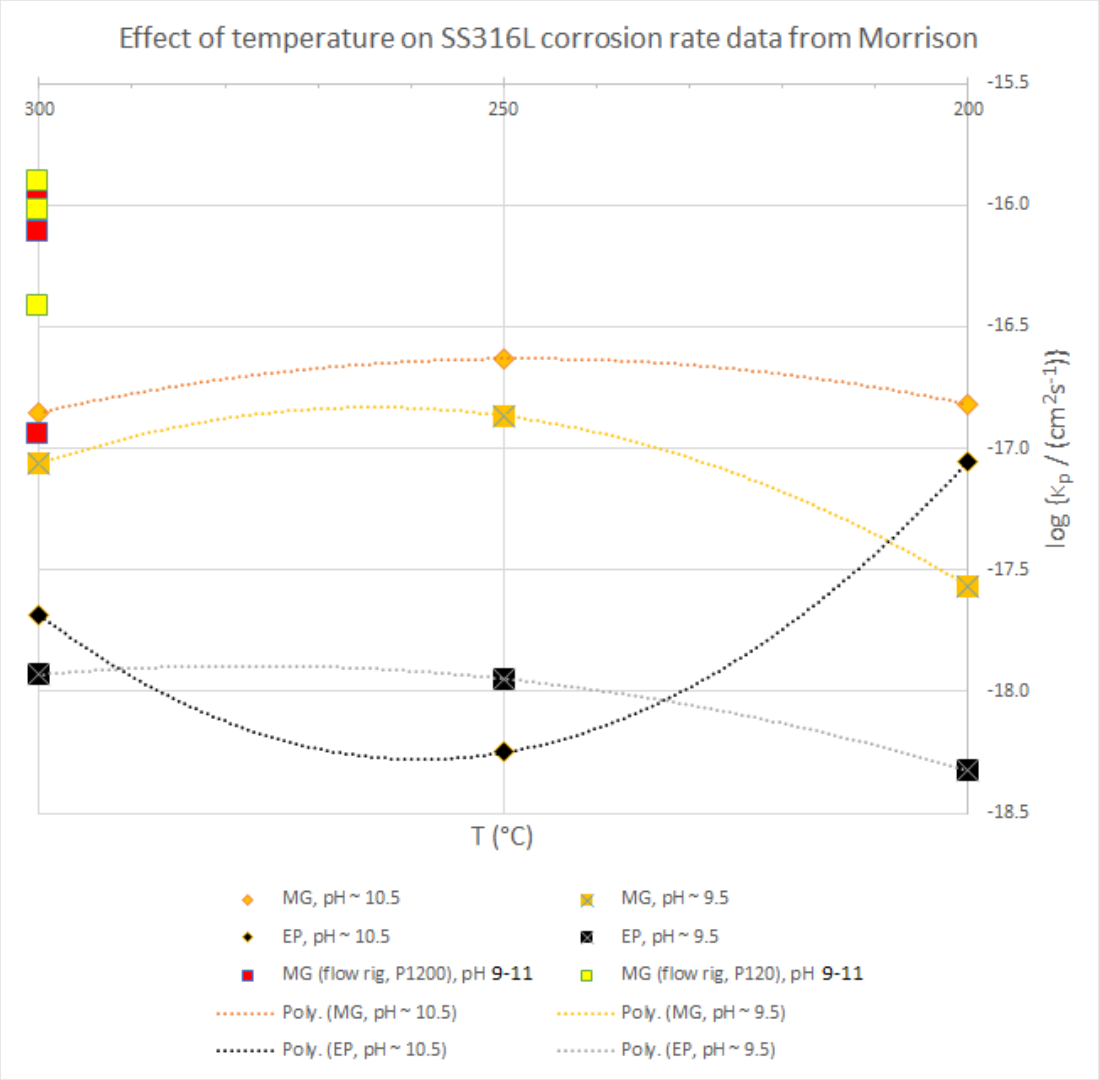

Figure 3.9. Data from the two sets of experimental work performed by Morrison [26] *on the parabolic corrosion kinetics of SS316L in basic hydrothermal solutions.*
The temperature scale has been reversed for easier comparison with the Arrhenius plot in figure 3.10.
The corrosion kinetic given, κ_p, is from an alternative expression of parabolic corrosion kinetics, $x^2 = \kappa_p.t$, where x is thickness of alloy corroded in centimetres and t is the time in seconds

Warzee et al. [80] showed that for SS304, whilst corrosion rates differed according to the type of mechanical surface treatment applied, the differences were not too great in comparison with scatter, and especially not in comparison with the difference made by electropolishing. This was corroborated by Morrison [26]. The solubility rig tubing of the present project was manufactured by extrusion [26], and the SS316L chips were prepared by CNC miller, presumably comparable to the lathe turnings which produced similar corrosion rate to other surface finishes [80]. Nevertheless, it is not known which surface condition most closely approximates that of the surfaces of the steel tubing used in the rig, and so k_p values are used as a guide only. The surfaces of SS316L chips used in the current project were very rough, so much faster corrosion rates might be anticipated. A lowering

of corrosion rates of stainless steels at higher pH (that is increasing from pH_{300C} ~ 6.5 and below to higher values such as the range 6.9 to 7.4 typically used in PWRs in recent years) was supposed by EPRI when considering the effects of primary chemistry on fuel crud deposition [35]. EPRI's assessment of the pH effect on corrosion kinetics follows the same trend as the Morrison data from the flowing rig, rather than the autoclave data.

For the purposes of the current thesis, Morrison's data from the flowing rig have been selected as the most appropriate baseline for estimating 316L corrosion kinetics in the flowing rig of the current project, since they are considered more reliable, and more directly applicable to the flowing conditions in the rig than the autoclave data, and since the same values of pH were used as in the current study (pH_{25C} 9,10,11 from 0.07, 0.7 and 7 ppm Li respectively). As these data were taken at 300 °C only, Morrison's data from the autoclave (taken at 200, 250 and 300 °C) were consulted to give an indication of temperature dependence, but no clear trend was discerned, therefore it has been assumed that corrosion kinetics are constant between 200 and 300 °C, in order to simplify corrosion rate calculations under changing pH and temperature conditions. The limited dependence on pH is as expected from the literature, and an apparent lack of dependence on temperature between 200 and 300 °C is consistent with the literature, given that this was in some cases observed (see Figure 3.7, and the discussion in section 3.4.2), though a strong dependence on temperature is also possible (see Figure 3.5 and Figure 3.6). Figure 3.10 shows data from various sources as plotted in [73] for the corrosion of stainless steels and mild steel as a function of temperature, to which Morrison [26] and Ziemniak et al. [76], [84] data have been added for comparison. It must be borne in mind that a pH dependence and temperature dependence quite different from that assumed may actually be present in the experimental rig, and the corrosion studies discussed above did not take account of the effect of cycling temperature and pH on the corrosion rate, therefore calculations of corrosion rates performed later in this thesis are as an illustrative guide only.

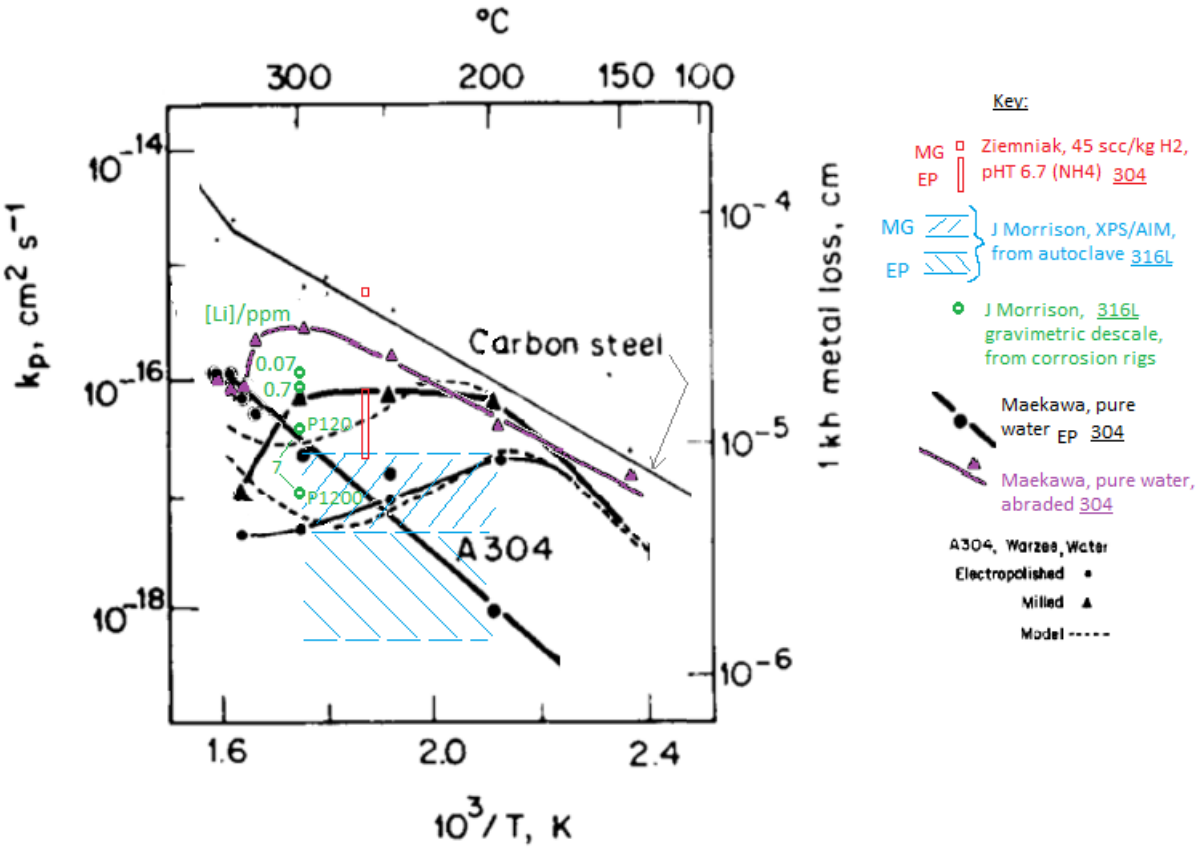

Figure 3.10. Temperature dependence of stainless steel corrosion kinetics in hydrothermal solutions. After Robertson [73].
This plot combines the data as plotted in [73]*, from several different figures (including those reproduced here as Figure 3.6 and Figure 3.7). In addition, data from Ziemniak et al.* [76], [84]*, and Morrison* [26] *have been added by the current author for comparison. MG represents mechanically ground, EP represents electro-polished, and the extent of the Ziemniak et al. data points in the y- axis is representative of the experimental uncertainty, which was large for the electro-polished (EP) specimen. For the Morrison data, the data for 0.07 and 0.7 ppm Li (i.e. pH_{25C} of 9 and 10) are an average of the (similar) values of the two surface roughnesses, whereas for 7 ppm Li (i.e. pH_{25C} 11), the difference was significant and so both data points are plotted separately. The blue hatched region shows schematically the approximate region occupied by Morrison's data from the autoclave study, as plotted in Figure 3.9. Dashed lines show Robertson's fit to the Warzee data, using a speculative model adapted from Simpson and Evans* [107] *to account for negative temperature dependence of kinetics between ~ 200 – 300 °C.*

3.5. Corrosion at room temperature

At room temperature, diffusion is so slow that a different mechanism of corrosion occurs, which is relatively independent of temperature. Corrosion in this regime is controlled by quantum tunnelling of ions through the corrosion film – which is relatively temperature-invariant. The film growth is initially rapid, until a layer of ~ 2-4 nm is formed, the approximate range of tunnelling [73]. Corrosion rate is then constant.

The film is made of a Cr_2O_3 based oxide, and a hydrated form of Cr(III) oxide is present on the coolant facing side [73], [83]. The film grows by the selective dissolution of components other than Cr from the alloy [73], [108]–[112], see Figure 3.11 for a schematic representation.

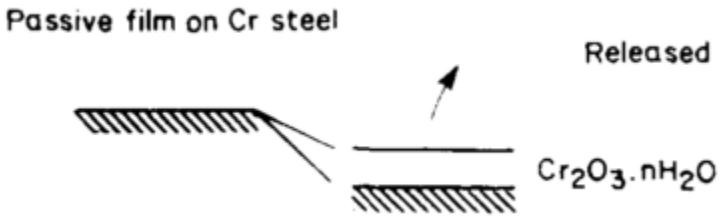

Figure 3.11 Schematic representation of passive film on Cr steel, as is formed under room temperature aqueous conditions. From [73].

4. Literature Review

Part II: Solubility and stability of metals and their oxides in PWR primary coolant circuits

4.1. Solubility and stability of metals and their oxides in PWR Primary Coolant Circuits

As discussed in earlier parts of the literature review (sections 2.3 and 2.5), solubility behaviour plays an important role in the transport of corrosion products (CPs). For example, a negative dependence of metal oxide solubility on temperature (affected by pH and other factors), can cause release of ions from corroding surfaces to the coolant in regions of decreasing temperature, such as steam generator (SG) tubing, whilst causing enhanced precipitation, and fortifying deposits, in areas of heating such as the core. It has been estimated that in excess of 1 mg of Fe per second is transported to the reactor core in this way [113].

The stability of metal and metal oxide phases is also important. Under changing conditions, such as during shutdown, a phenomenon of particulate and colloid release throughout the primary coolant circuit can occur, known as 'crud burst'; the switching of stability from one set of crystalline phases to another, and the resulting volume change, is thought to be one of the causes [36]. In the plant study referenced above [36], for example, this caused a doubling of particulates (as judged by particulate Co-58 levels) every ~3.3 hours for ~ 20 hours. This is discussed further at the end of section 4.1.2, preceding Figure 4.5. In addition, the presence of a different oxide as the solubility-controlling phase results in different solubility behaviour under changing conditions, for example Ni metal solubility has a dependence on hydrogen fugacity, whereas NiO solubility does not.

This subchapter describes the key findings in the literature regarding the stability and solubility of metals and their oxides, particularly in the context of their influence on CP transport in PWRs. Some of the most important studies regarding solubility are discussed in this context, with a discussion on

the causes of discrepancies between results from different studies, and the implications of this for subsequent studies and for the application of findings to practical applications.

A more in-depth treatment of stability and solubility theory is included in chapter 14 in the appendices, culminating in the presentation of various plots of fitted solubility as a function of pH, temperature and hydrogen fugacity for several oxides, working from equilibrium constant data for each soluble species, which are summed together to give total solubility. At the end of section 14.3.5 (on page 286), the solubility behaviour of magnetite is discussed in the context of the rig of the present study, including the effects of positive and negative temperature-dependence of solubility when a room-temperature sampling line is used.

A summary of the key information from this and other subsections of chapter 3, and from appendix 1, as they relate to expected conditions of the rig, is provided in section 17.3.

4.1.1. Thermodynamics

A theoretical treatment, incorporating experimental data, can be used to study the *thermodynamics* of a system - in other words the most stable configuration, which a system will take given infinite time to reach equilibrium. Key inputs in the present context are parameters such as coolant pH, temperature, and hydrogen fugacity; relative amounts of the various metallic elements; and the ratio of coolant mass to oxide mass. Key outputs include the types of oxide phase present at equilibrium (ferrite, chromite, bunsenite); the elemental composition and form taken by the oxides; and the concentration of each element in solution (broken down into each soluble species).

4.1.1.1. Applicability and limitations of thermodynamics

The degree to which a real system resembles the true equilibrium state, as given by thermodynamics, varies dependent on many factors, which can be considered broadly as belonging to one of the following categories

1. Kinetics – how quickly the system approaches equilibrium from a non-equilibrium state; and
2. History of changes to conditions, or other factors, which tend to take the system away from equilibrium.

The first category, kinetics, are strongly temperature dependent (faster at high temperature), and tend to be particularly fast for reactions in aqueous solution and between solution and oxide surfaces, and slow for processes in the solid state. Therefore, in almost all situations under normal operating conditions, equilibrium is achieved locally between oxide surfaces and adjacent coolant.

The oxide, however, is typically in a state which is metastable to some degree (see section 4.1.1.2), for example by having poor crystallinity or small crystal size compared with the most stable form described by thermodynamics, since the kinetics for 'ageing' towards the most stable state are slow (see Figure 4.8). Solubility depends on the stability of the oxide form, decaying slowly to the thermodynamically predicted value as the oxides age to the most stable form.

Regarding the second category, the primary coolant system of a PWR is an inherently non-equilibrium system, in which metals are separated from coolant – in which they are unstable – by only a thin layer of protective oxide. The temperature and other parameters of circulating coolant rapidly cycle as it transits the circuit every few seconds, and radiation in the core produces a number of short-lived unstable products of radiolysis, so that a true thermodynamic equilibrium is not possible despite the rapid kinetics. The transport of metal or oxide particles in the coolant can lead them to be deposited in locations where they are not the stable phase (for example Ni metal deposited in fuel crud, where stability transitions to NiO); and it is estimated that an Fe flux of around 1 mg/s is transported from out-of-core surfaces (by outward mass transfer to bulk coolant) to core deposits (by inward mass transfer through boundary layer, and precipitation) [113].

When a new reactor is first commissioned, the corrosion film on stainless steels and nickel base alloys is poorly developed, resulting in a relatively rapid corrosion release of ions (through the inner oxide layer) on the one hand, and a limited surface area of coolant-facing oxides (outer layer) on which to precipitate on the other hand. Soluble concentrations at the oxide-coolant boundary must reach a high level to provide sufficient driving force for the precipitation of oxides (in the outer layer, and directly in solution as colloids), and the mass transfer into bulk coolant, to keep pace with the build-up of ions from corrosion. Kinetics play a role in the form of oxide thus created, since meta-stable oxide forms, having small size and high solubility, can form at a faster rate than the thermodynamically most stable form. Over time, there is a slow fall in soluble concentrations as the corrosion film develops [114].

In addition to inherent non-equilibrium processes, changes to conditions may be externally applied by plant operators, for example the different chemistry and temperatures employed during shutdown, which are applied over relatively short timescales resulting in non-equilibrium conditions for which kinetics play an important role in the way the coolant system responds.

4.1.1.2. Meta-stable phases, and deviations from true equilibrium conditions

In the context of this chapter, by 'solubility' is meant the total concentration of a given metallic element or elements in solution, as various aqueous species, when equilibrium is attained between

the coolant and one or several oxides. The word is used fairly loosely here, as in other publications – true solubility is only defined in a system which is truly at equilibrium and is precisely defined. In many situations, not least in operational nuclear plant, the system is *not* at equilibrium and oxide phases are present which do not have the most stable form for the prevailing conditions [14]. The discrepancy may be manifest as subtle differences such as microstructure or elemental composition, or can be as significant as being an entirely different phase such as the presence of Ni when NiO is the more stable phase, and vice versa. Oxides will naturally 'age' over time towards the most stable state, by various mechanisms, for example by 'Ostwald ripening' where less stable phases dissolve and crystallites of the most stable phases are precipitated from solution, or by solid state processes involving diffusion of atoms within the lattice (generally a much slower process). In the meantime, oxide forms which differ from the most stable state by any degree, and persist for any appreciable time in the coolant, are known as 'meta stable' forms. These forms nonetheless reach equilibrium with the nearby coolant, having elevated solubility compared with the stable form - to an extent which is in accordance with the degree of instability (or in quantitative terms, the magnitude of elevated Gibbs energy of formation compared with the most stable form). In some cases slow kinetics can hinder even the establishment of equilibrium between oxide and nearby coolant.

4.1.2. Stability of oxides

4.1.2.1. Single metals and their oxides

For a system M-O-H, containing just a single metal (M), water, and any water-derived species (i.e., hydrogen or oxygen gas), the stable solid phase depends on the redox potential (as controlled by hydrogen concentration) and the temperature. Under sufficiently reducing conditions the metal itself is stable, and as conditions become more oxidising progressively more oxidised forms become stable. Figure 4.1 shows at the left the stable oxide phases for several transition metals, and the temperatures of transition from one to another, with hydrogen concentration at 17.7 scc/kg (a commonly used value in experiments and close to the concentration in PWR primary coolant of 25 – 50 scc/kg). On the right is plotted the equilibrium concentration of the neutral hydroxocomplex in solution for a selection of those oxides as a function of temperature, as calculated from thermodynamic data derived from solubility experiments. This serves effectively as an estimate or approximation of minimum solubility, at the pH of minimum solubility where the contributions from other aqueous species are minimal.

Table I. Stability of Metal Ion Oxidation States and Metal Oxides in Deoxygenated Water

Atomic Number	Symbol	Stable Oxidation State	Stable Solid Phase	Ref.
22	Ti	Ti(IV)	TiO_2 (rutile)	
23	V	V(V)	V_2O_5	
24	Cr	Cr(III)	CrOOH, Cr_2O_3 ($T > 693$), $Cr(OH)_3$ ($T < 333$)	4, 41
25	Mn	Mn(II)	MnO	
26	Fe	Fe(II)	$Fe(OH)_2$, Fe_3O_4 ($T > 393$)[a]	5
27	Co	Co(II)	$Co(OH)_2$, CoO ($T > 367$)	II
28	Ni	Ni(II)	$Ni(OH)_2$, NiO ($T > 468$)	6
29	Cu	Cu(II)	CuO	II
30	Zn	Zn(II)	$Zn(OH)_2$, ZnO ($T > 252$)	II

[a] Transformation temperature dependent on dissolved hydrogen level; indicated value based on 17.7 scc-kg^{-1} [$P(H_2) = 1$ atm at 25°C].

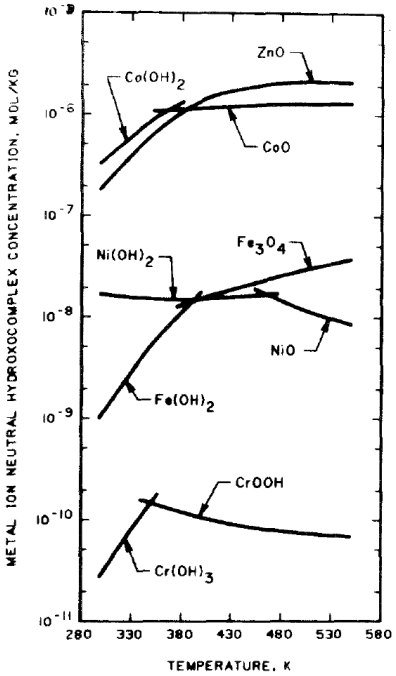

Figure 4.1. Left: table showing stable oxide phases, and temperatures of transition of stability, for selected metal oxides. Right: Predicted minimum solubilities of selected metal oxides as a function of temperature. Taken from [115].

Where the curve for one phase intersects with the curve for another phase of the same element, this represents a transition of stability from one phase to the other. For example at T/K = 333, stability transitions from CrOOH at higher temperatures, to $Cr(OH)_3$. It is possible for unstable oxides to exist and persist for a time which is dependent on kinetics and varies widely between oxide phases and depends strongly on temperature (see section 4.2), and this can also apply to other forms of instability such as crystal size, see later. The possibility of persistence of unstable phases is indicated by the overlap between the two curves in the figure, which may be extrapolated further than shown. This illustrates one route by which the phase change can occur: suppose that CrOOH and $Cr(OH)_3$ are both present at 330 K. The amount of Cr in solution is maintained at an intermediate level between the solubilities of the two oxides, as CrOOH dissolves into unsaturated solution whilst $Cr(OH)_3$ precipitates from supersaturated solution. In this way, the surface of the unstable oxide may become covered by precipitating crystals of the stable oxide until all the coolant-facing surfaces consist of the more stable oxide ($Cr(OH)_3$). Phase transformation can also occur directly in the solid state, by diffusion of ions through the crystal lattice, though this is generally much slower than the aqueous route mentioned above.

Another way to illustrate the stability of oxides, but this time with varying redox potential and pH, and holding temperature fixed, is the potential-pH diagram (or Pourbaix diagram). An example is shown in Figure 4.2 for the system Fe-O-H.

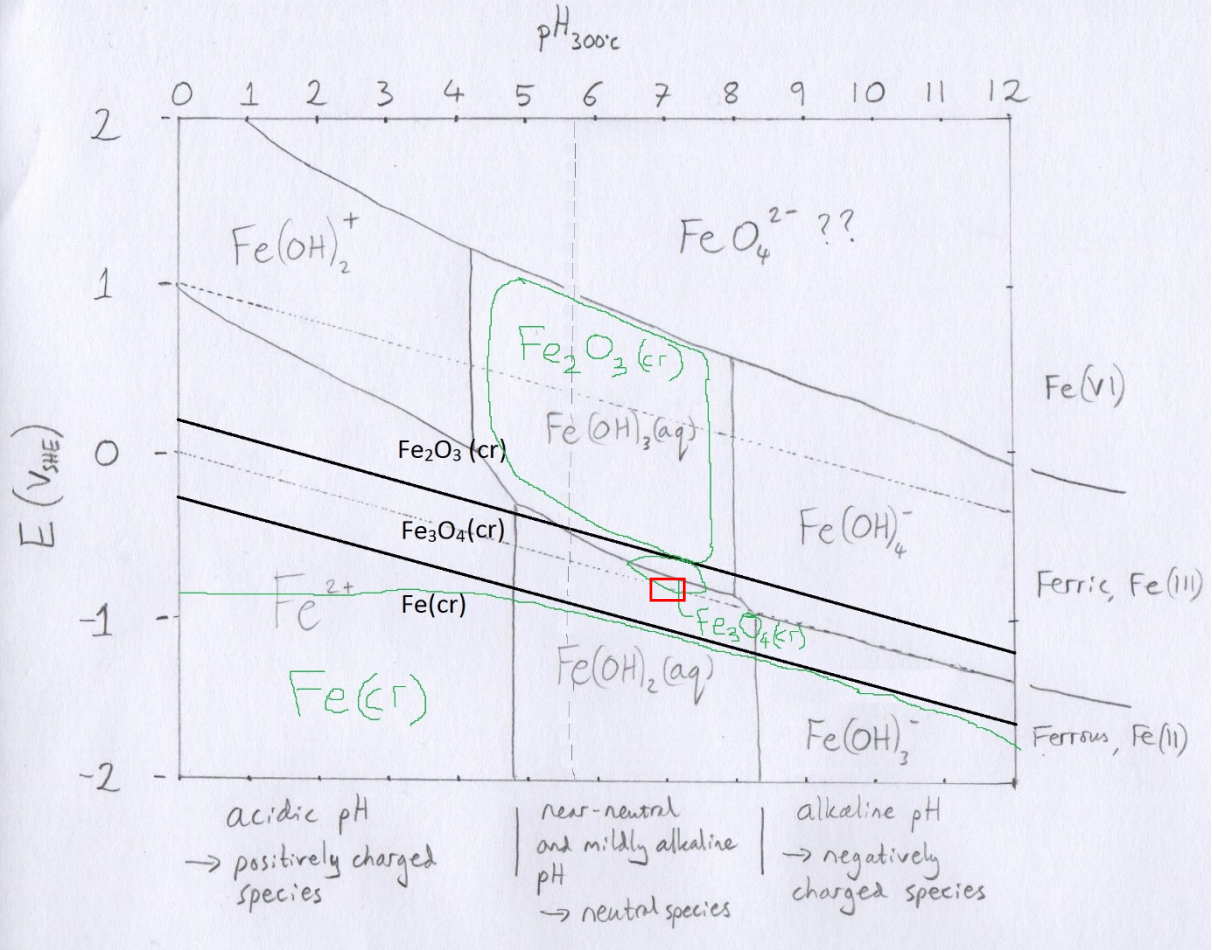

Figure 4.2. A variant of the potential-pH diagram for the system Fe-water at 300 °C, in which both the dominant soluble species and the most stable solid phase are shown for all regions. After [116], *with some additional annotations from the current author.*
The sloping lines, at zero and ~1 V_{SHE} respectively for pH 0, represent upper and lower stability limits for water against the formation of oxygen or hydrogen gas respectively.

In place of hydrogen fugacity, the redox potential is plotted on the vertical axis (though the two are closely related), against pH. The diagonal dotted lines depict oxidising (upper) and reducing (lower) conditions, representing one atmosphere of oxygen and hydrogen respectively, whilst the vertical line represents neutral pH at temperature. The computer-typed black font shows the regions of stability of the three solid phases, which depend only on hydrogen fugacity since the temperature is fixed. The hand-drawn navy-blue boundaries show the regions of predominance of the various aqueous species which together constitute Fe or Fe oxide solubility. Three regions are plotted and

labelled in green, showing the regions of 'stability' of the three solid phases, by which is meant the regions of potential-pH space in which the total concentration of dissolved ions is less than 10^{-6} molal. Approximate conditions in the primary coolant of PWRs are indicated by a red box.

Pourbaix diagrams for Ni show that the transition between stability of metallic Ni and the first oxidised form (being NiO at higher temperatures, $Ni(OH)_2$ at lower temperatures) is close to the hydrogen line – see Figure 4.3. Under normal operating conditions, the stable form in the primary coolant of PWRs is Ni metal, but under local conditions of increased temperature and decreased hydrogen fugacity on the upper spans of some fuel rods where SNB occurs, and throughout the primary RCS when there are oxidising conditions during shutdown, NiO can become the stable phase.

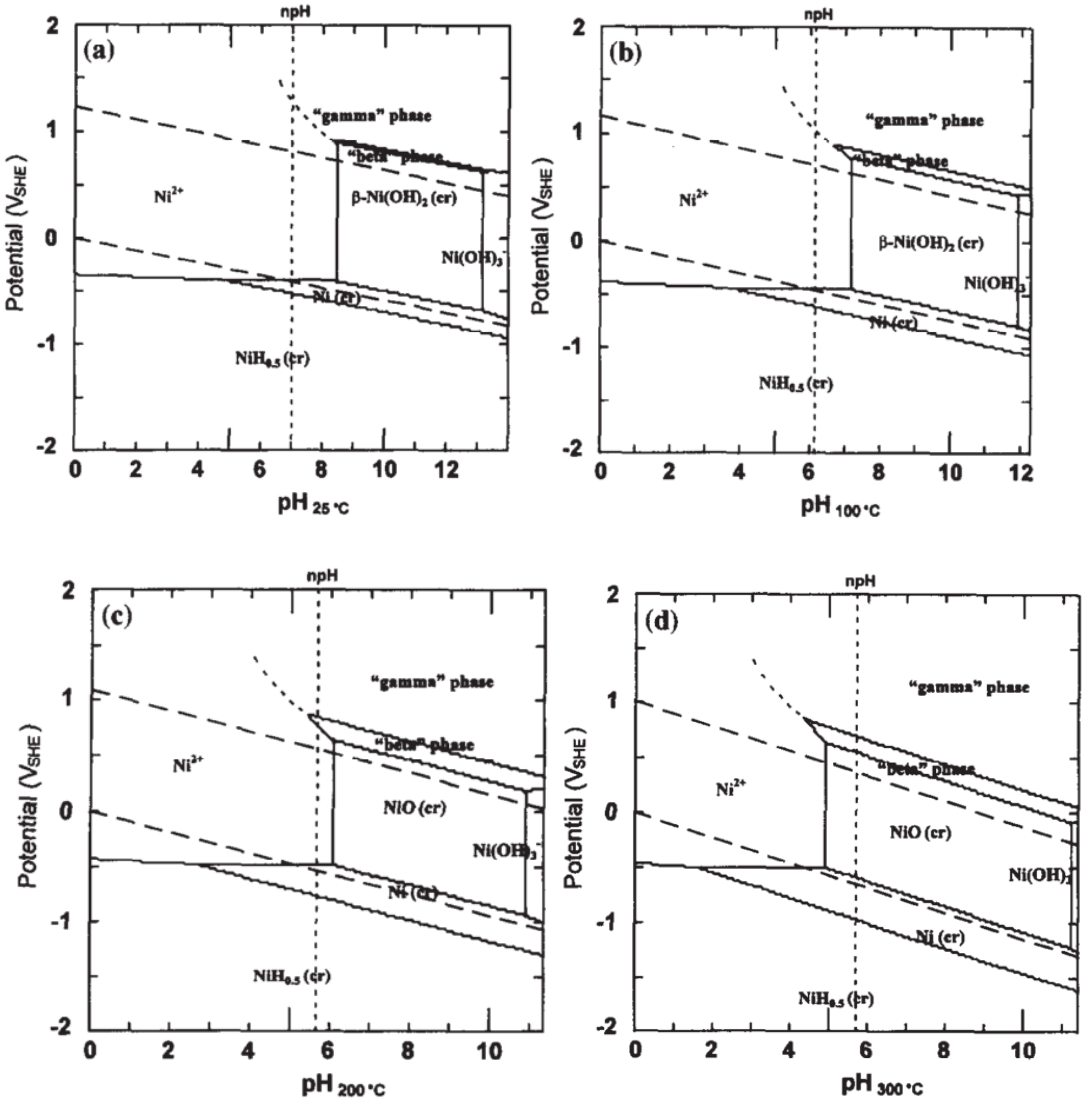

Figure 4.3. Pourbaix diagrams for Ni [117].

4.1.2.2. mixed metal oxides

For a system containing multiple metals in water, oxides containing more than one metal are often more stable than the single metal oxides of the previous subsection. In PWR Primary coolant conditions, the stable mixed oxides are of the spinel type. Spinels are oxides of the form $A^{(II)}B^{(III)}{}_2O_4$, where A and B are divalent and trivalent metal ions respectively. The oxide has approximately cubic form, consisting of a regular lattice of O^{2-} ions into which A and B ions are inserted into octahedral and tetrahedral sites in a complicated manner. There are two forms of spinel-type oxide – normal spinel and inverse spinel, determined by the ordering of metal ions in the octahedral and tetrahedral interstices.

Both forms are present in corrosion films of Fe-Cr-Ni alloys under PWR primary coolant conditions, as detailed in chapter 3.3, covering a range of different elemental compositions. Those for which the trivalent ion is predominantly Cr take the normal spinel form, and are collectively known as chromites; those for which the trivalent ion is predominantly Fe take the inverse spinel form and are collectively known as ferrites.

Ferrites and chromites of a wide range of different elemental compositions have been reported in studies of crud in PWRs. Chromite forms the inner protective layer of corrosion films on both stainless steels and nickel base alloys, as discussed in section 3.3, and tends to stay put where it is formed, with its composition being largely determined by the alloy on which it sits. Ferrite on the other hand precipitates from solution onto the chromite layer, from the mixture of corrosion release ions coming from the underlying alloy and ions from elsewhere in the RCS which have been transported in the coolant. In a typical PWR, the mostly Fe^{2+} ions released from stainless steel surfaces mix with the much higher proportion of Ni^{2+} ions (along with Fe^{2+} ions) from nickel base alloys, enabling some of the Ni metal outer layer crystallites on nickel base alloys to pick up extra Fe^{2+} ions to form nickel ferrite (nominally $NiFe_2O_4$) [75], [86], and enabling magnetite (Fe_3O_4, a member of the ferrite family) to pick up extra Ni^{2+} ions to form nickel ferrite [81]. Outer layer crystallites of ferrite (and Ni metal, on the surfaces of Ni base alloys) can release into the coolant flow relatively easily, becoming key components of crud deposits at other locations of primary RCS.

The mixed spinels are often represented by their end members – for example Fe_3O_4 (stoichiometric magnetite) and $NiFe_2O_4$ (stoichiometric nickel ferrite) representing the ferrites, and $FeCr_2O_4$ (stoichiometric ferrous chromite) and $NiCr_2O_4$ (stoichiometric nickel chromite) representing the chromites – from which any intermediate composition can be created by mixing the end members in various proportions in solid solution. Schemes have been devised for treating the properties (such as solubility or stability) of intermediate forms as linear interpolations between the end-members [66],

or according to more advanced models based on thermodynamics [12]. Figure 4.4 shows the limit of stability of Fe-Cr-Ni spinel-type oxides based on one such thermodynamic model [12]. Within the central bounded region (covering most of the plot area), overall Fe-Cr-Ni compositions are not achievable with a single *stable* oxide phase, instead consisting of two oxide phases on the limit of stability on their respective sides of the diagram existing in equilibrium – ferrite on the left hand side of the diagram and chromite on the right. However, it should be borne in mind that intermediate compositions are possible as *meta stable* phases, which may persist for a long time due to the very slow kinetics of ion diffusion in solids [74], whilst at the oxide surface (oxide-coolant boundary) the faster kinetics of dissolution / precipitation reactions enable faster transformation towards the most stable phase

There is a clear separation between the ferrites on the left and chromites on the right – this is because the normal spinels and inverse spinels are not fully miscible in each other, there is a positive energy of mixing (see appendix 1). Immiscibility of chromites and ferrites was demonstrated experimentally by Cremer [98], and Ziemniak et al. [74], as described in chapter 3.3.1. Essentially there is a 'consolute solution temperature', above which the two phases are fully miscible; below the consolute solution temperature there are a range of intermediate compositions which are thermodynamically unstable (the 'miscibility gap'); and the boundary between thermodynamically stable and unstable compositions is known as the solvus of immiscibility. Figure 4.4 is effectively a depiction of the solvus for Fe-Cr-Ni spinels, at 290 °C, as calculated according to a thermodynamic model.

Ziemniak et al. observed a similarity between the composition of inner and outer spinel oxides in corrosion studies [75], [76], [84], [86] and the solvus of immiscibility between the ferrites and chromites [74], [85], [98], concluding that composition of the oxides in the film is controlled by – among other factors – the thermodynamic driving force towards attaining the stable state of two phases at solvus compositions, in mutual equilibrium. As such, the compositions of the two spinel phases in corrosion films can be viewed as approximate measurements of the solvus of immiscibility for varying levels of Ni content. Results from these studies are summarised in Table 4.1 and plotted against Kurepin et al.'s model in Figure 4.4, as well as results from studies specifically designed for the study of solvus composition. Results from corrosion film analysis (open rectangles) match fairly well with the model at the Fe-rich solvus, but contain significantly more Fe than the model predicts for the Cr-rich solvus. One way to account for this discrepancy is by considering that corroding alloys represent an inherently non-equilibrium situation – the continual corrosion release flux of Fe^{2+} ions from the alloy at the oxide-alloy interface, into and through the chromite oxide layer, out into the coolant, driven by instability of the chromite layer. The chromite must remain unstable at a steady

state composition, for example by being more Fe-rich than the solvus composition, to provide the driving force for Fe release to the coolant and outer layer. As discussed in section 3.3.1, there are other kinetics factors besides the above argument which could help to control the inner oxide spinel at a non-equilibrium composition, such as considerations relating to the Pilling-Bedworth ratio, and relative diffusivities of the different ions in chromite.

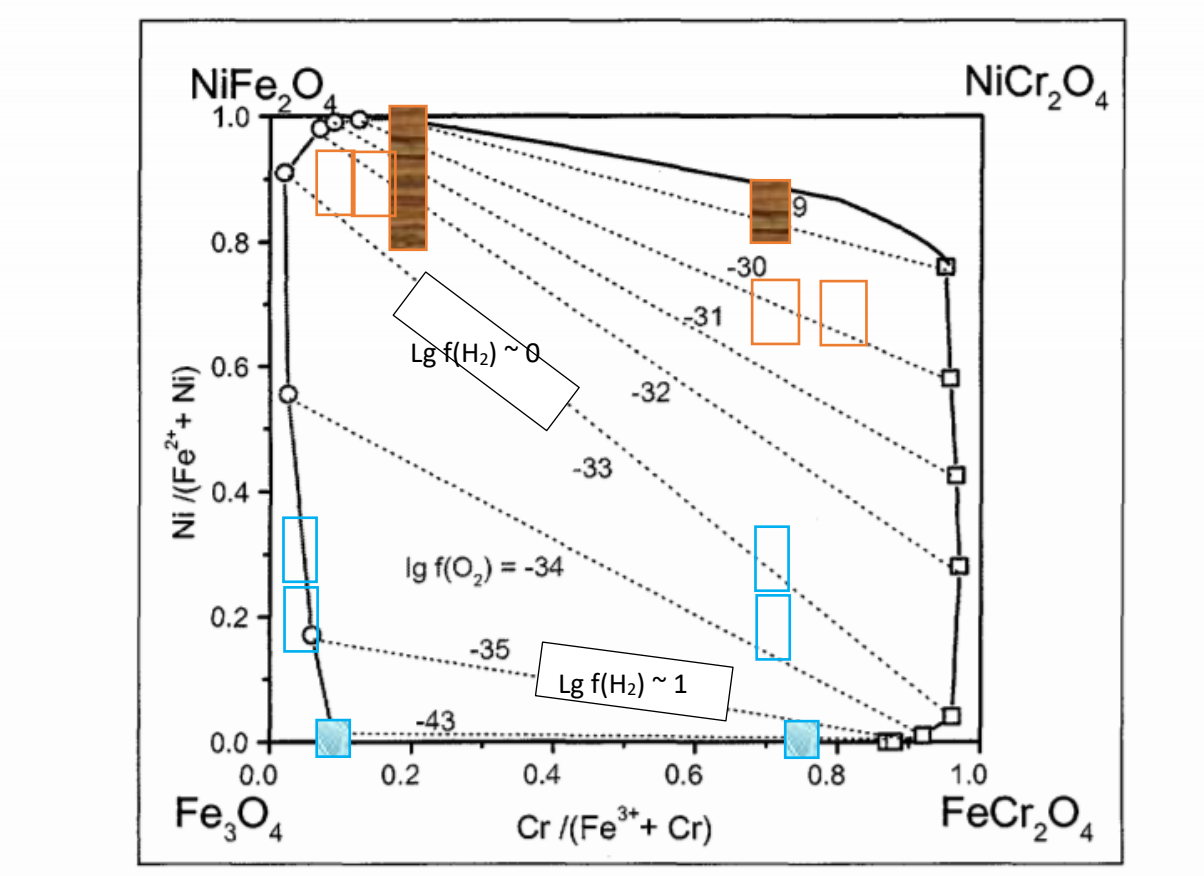

Figure 4.4.Calculated phase equilibria in the system Fe_3O_4 – $FeCr_2O_4$ – $NiFe_2O_4$ – $NiCr_2O_4$ at 290 °C, per the model of Kurepin et al. From [12].
The central bounded region indicates compositions which are thermodynamically unstable against decomposition into separate Fe-rich (ferrite) and Cr-rich (chromite) phases, at the left and right boundaries of the central region respectively. Lines of equal oxygen fugacity are shown, the two ends of which represent the pair of spinel compositions which are stable for that particular level of oxygen fugacity. This indicates that nickel content diminishes as conditions become increasingly reducing, due to the precipitation of Ni metal as a separate phase – under these conditions there is a much greater stability of Ni in ferrite than chromite, as shown. Very approximate equivalent hydrogen fugacities are indicated for reference. The boundary shown between single phase and two-phase stability is called the 'solvus of immiscibility'. Experimental determinations of the solvus, as plotted in Table 4.1, are plotted here as coloured boxes for comparison – open boxes for corrosion film studies (orange - Ni base alloys; blue – stainless steels), and shaded boxes for oxide decomposition studies (orange – $NiFeCrO_4$; blue – Fe_2CrO_4). In corrosion studies on Ni base alloys, there was excess Ni metal present in the inner oxide layer, demonstrating that the spinels were saturated with the highest concentration of Ni possible for the prevailing redox conditions, at least for the chromite phase. For the stainless steels, it can be seen that partition of Ni between ferrite and chromite was equal, within errors.

Table 4.1. Evaluation of the compositions of mixed Fe-Cr-Ni spinels at the solvus of immiscibility between inverse (ferrite) and normal (magnetite) types, per various studies.
These evaluations are derived from extrapolation of data from decomposition studies ([98]*,* [74]*), and characterisation of inner and outer oxides on corrosion films (based on an assumption that oxide compositions represent the solvus) (*[75], [76], [84], [86]*). x and y are parameters from the generic equation of an Fe-Cr-Ni spinel:*

$$Ni_xFe_{1-x}(Cr_yFe_{1-y})_2O_4.$$

These experimental evaluations or approximations of solvus compositions are plotted on Figure 4.4.

Study	***x (Ni)***		***y (Cr)***	
	ferrite	***chromite***	***ferrite***	***chromite***
Decomposition of $NiFeCrO_4$, extrapolated to ~300 °C [74]	~ 0.8 – 1.0	~ 0.8 – 0.9	0.2	0.7
Corrosion film on alloy 625 at 260 °C [86]	0.9	0.7	0.1	0.8
Corrosion film on alloy 600 at 260 °C [75] *N.B. Ni metal found alongside chromite in inner layer (so, Ni saturated), but not in outer layer due to pickup of aqueous Fe (so, may not be quite Ni saturated)*	0.9	0.7	0.15	0.7
Corrosion film on SS304 at 260 °C [76]	0.3	0.3	0.06	0.7
Corrosion film on SS304 at 260 °C [84]	0.2	0.2	0.05	0.7
Decomposition of $Fe_{1.5}Cr_{1.5}O_4$, extrapolated to ~300 °C [85], [98]	0	0	0.1	0.75

Where an excess of nickel metal is present in equilibrium with two spinel oxides, as Ni metal or NiO, the Ni content of each spinel at equilibrium (which can be said to be saturated with Ni under the prevailing conditions) is uniquely determined by the redox conditions. Compositions of the two spinels in equilibrium with nickel metal or oxide are shown on the plot for selected values of oxygen fugacity. As can be seen, saturation nickel contents of each phase decrease with decreasing oxygen fugacity. This is because of the increasing stability of nickel metal against dissolution, whose solubility is inversely proportional to hydrogen fugacity, or proportional to the square root of oxygen fugacity. The three crystalline phases together act as a weak buffer against changes to oxygen fugacity [12], since any increase in oxygen can be countered by the oxidation of Ni as it becomes taken up into spinel oxides, and vice versa for a decrease in oxygen fugacity.

Nickel ferrite and nickel chromite are said to be unstable against decomposition into nickel metal and the respective Ni-free spinels as oxygen fugacity falls below a certain level (or hydrogen above a certain level, see Figure 4.5 below and the accompanying discussion), though in practice this means a gradual decrease in saturation nickel content rather than a step-change to the Ni-free form, as

nickel leaches from the ferrite to precipitate as a separate phase – this is shown by the oxygen fugacity contours in Figure 4.4.

Where there is no excess of nickel, the nickel component of each phase is dependent on the ratio of total nickel present in relation to the total amounts of Fe and Cr. The model does not indicate the partition of nickel between the two phases in this case. The plotted results of corrosion film studies suggest a roughly equal partition of Ni between the two spinels on stainless steels, whilst on Ni base alloys, the presence of metallic nickel, at least in the inner layer, shows that the chromite was saturated with nickel, so the oxygen fugacity contours may apply in this case. The ferrite phase was formed by the pickup of Fe^{2+} ions released from stainless steels elsewhere in the experimental apparatus, co-precipitating with excess Ni from the Ni base alloy – it was not clear from the papers [75], [86] whether there remained any excess nickel metal in the outer layer or not, therefore it is possible that these oxides became nickel impoverished compared with the stable solvus phase ($x = 1.0$, $y \sim 0.1 – 0.15$) by excess uptake of Fe due to the plentiful supply of Fe ions from corroding stainless steels upstream. In operational PWRs, nickel ferrite is observed as the outer oxide layer composition on stainless steels due to pick-up of Ni^{2+} ions released from Ni base alloys in SGs, whilst the chromite of the inner layer remains at a composition closer to ferrous chromite than nickel chromite – though this may be related to the limited interaction between inner oxide layer and coolant, compared with the outer layer ferrites.

Under typical conditions in PWR, Ni and nickel ferrite are present concurrently as outer layer crystallites and in crud deposits. The stability of this mix of phases extends to only a relatively narrow band of conditions and is thus susceptible to changes in temperature and redox conditions (via hydrogen fugacity), as illustrated in Figure 4.5 [118]. At the higher temperatures on fuel crud deposits towards the top of the core, NiO replaces Ni as the stable oxide phase [119].

As mentioned at the start of the chapter, the changes in conditions which occur during shutdown are known to cause crud burst – the release of large quantities of loose crud to the coolant as particulates and colloids, and changing oxide stability is thought to be one of several causes [118]. Conditions in which corrosion products are highly soluble are intentionally applied during shutdown, to remove crud and outer layer oxides from the core and out-of-core surfaces (as aqueous ions) for the reduction of out-of-core radiation fields, among other reasons. However, the concurrent release of particulates and colloids is not desirable, since these include activated particles from fuel crud in the core which redeposit on out-of-core surfaces. Ions are removed effectively by the CVCS (a representative purification rate has a half-life of 8 h [120], but the CVCS is operated with increased letdown flow during shutdown [118]), so that any dissolved ions of radioisotopes released from the core which may precipitate or adsorb onto out-of-core outer layer crystallites are more than offset

by the release of radioisotope ions therefrom (along with the majority of ions released, which are not activated). Released particulates and colloids, on the other hand, redeposit onto surfaces throughout the primary coolant system, causing coolant concentrations to decay exponentially with a half-life that can be as little as 40 minutes [120], with which the CVCS purification rate cannot compete [10], [120]. In this way, activated particulates and colloids which were concentrated in the core are subsequently scattered through the whole circuit, and so steps are taken to try to avoid crud burst [118].

Crud burst is thought to be caused by the following factors [118]:

- thermal contraction of components (i.e. fuel clad), causing physical disturbance of oxides,
- Reduction in pH – higher solubiity, therefore bonds holding deposits together dissolve,
- Changes in hydrogen fugacity – changes to stability of oxides (as per Figure 4.5).

Any of these changes individually, as well as in combination, can cause release of particulate corrosion products. This is also relevant for the rig of the present study.

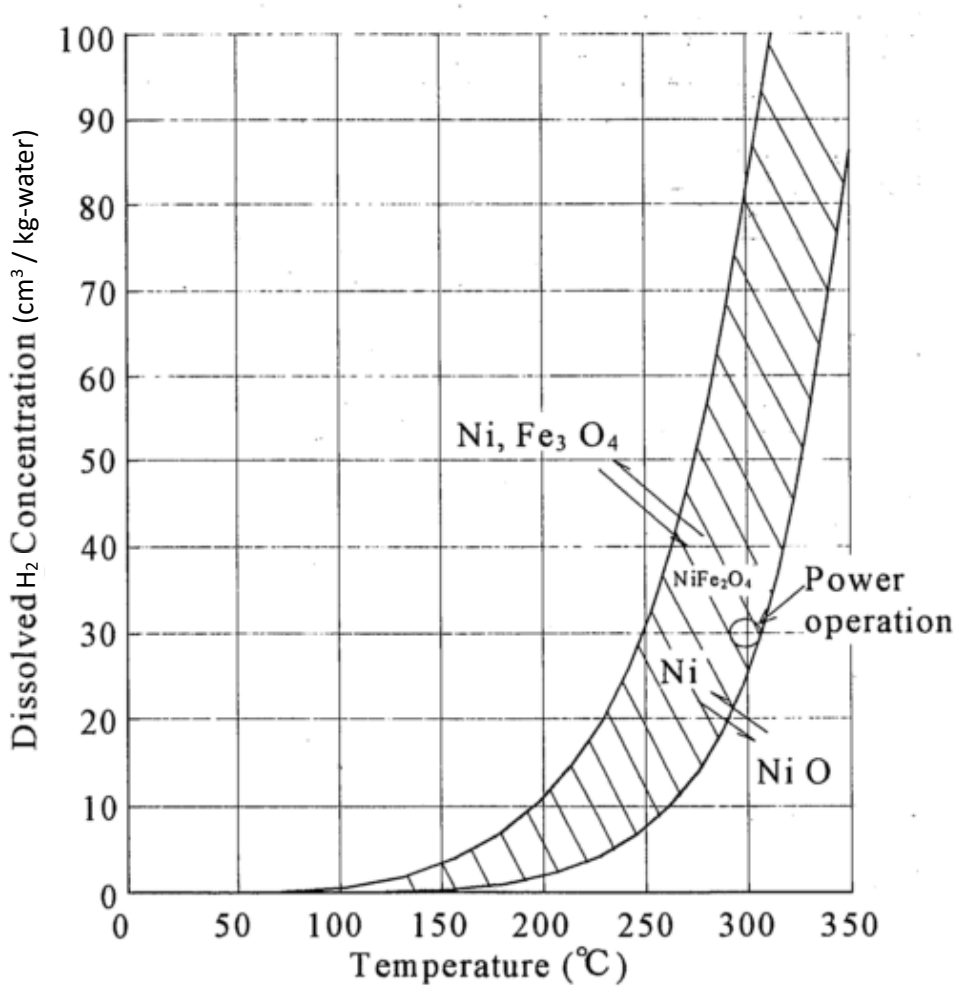

Figure 4.5. Region of stability of Ni metal and nickel ferrite, against oxidation to NiO and decomposition to nickel metal and magnetite respectively. From [118].

A review by Dickinson et al. [103] demonstrated that ferrous chromite ($FeCr_2O_4$) seems not to be a truly thermodynamically stable phase under conditions of PWR primary coolant, based on data and observations from studies by Ziemniak et al., of ferrous chromite [102] and magnetite ([5], which in turn made use of data from Tremaine and LeBlanc [121]), and also based on thermodynamic quantities, derived from the above references as well as other sources. Chromite is thought to undergo a decomposition reaction as

$$FeCr_2O_4 + \frac{4}{3}H_2O \rightarrow \frac{1}{3}Fe_3O_4 + 2CrOOH + \frac{1}{3}H_2$$

As far as the present author is aware there is no direct experimental evidence of the presence of the new phase (CrOOH) due to decomposition of chromite, though it can be inferred from changes to the solubility behaviour of $FeCr_2O_4$ as observed in the data of Ziemniak et al., and it may account for the oxide crystallites they observed to have crystallised from solution onto their chromite granules.

The charge of $FeCr_2O_4$ granules in Ziemniak et al.'s study, or the more stable surface oxide phases resulting from their exposure to hydrothermal solution, result in a much higher level of Fe in solution than Cr – this is explained by a process called incongruent dissolution:

$$FeCr_2O_4 \rightarrow Fe^{2+} + 2CrOOH$$

Fe^{2+} leaches from the chromite into solution, leaving behind a Cr oxide phase (CrOOH).

According to Wesolowski et al. [38], the solubility of Zn chromite and Co chromite have been studied in a collaboration between ORNL and Lockheed Martin, and were shown to also exhibit incongruent dissolution.

4.1.3. Solubility studies – design and methodology

Various methodologies and designs of apparatus have been used to study metal and metal oxide solubility under hydrothermal conditions. These are discussed briefly here. A review of those studies relevant to PWR primary RCS is provided in Morrisson's thesis [26], for example.

Although some studies were conducted in the early 20th and even 19th century [122], to inform the field of geology, a much greater frequency of studies have been conducted from the 1960s onwards, due to intense interest in the nuclear industry regarding the impact of coolant chemistry on oxide solubility behaviour (as discussed in section 2.2.3). Such interest remains, as the increased duty accompanying plant power uprates and life extensions, and future plant designs, requires further optimisation of coolant chemistry. As efforts to model crud transport processes using computer codes become more advanced, complete, and capable of quantitative predictions, there is need for increasingly accurate data and fuller understanding of solubility behaviour. Advances in study design, methodology, and analysis capabilities, and increased understanding from other related studies (such as speciation of aqueous ions, or behaviour of colloidal particles small enough to pass filters and affect solubility readings [36]), have enabled improvements in accuracy and precision of results. However, some questions remain, due to the difficulties inherent in measuring such low concentrations without contamination, sampling line effects or variable erroneous contributions from small colloidal particles.

Of particular note are the discrepancies in results of magnetite solubility for higher pH values, and uncertainties over the quantitative effect of additional metallic elements at low concentrations in the oxides.

Earlier solubility studies under hydrothermal conditions tended to focus on solubility in fairly strong acid or base solutions, in order to aid in the assessment of which species were dominant in solution

(via the manner in which solubility changes with pH), and because of difficulties in measuring the low dissolved concentrations present in near-neutral solutions. Improvements in methodology and analysis have enabled increasingly accurate assessment of solubility behaviour under conditions of minimal solubility.

Studies can be broadly categorised into four kinds, as detailed in Table 4.2. The method of sampling is an essential part of the process; Table 4.3 details the main types of sampling method which have been used.

Table 4.2. Types of apparatus used for solubility studies – adapted from the literature review of Morrison [26].

type	details
Static bomb / autoclave	Simulated coolant and oxide, and cover gas where applicable, are sealed in a heated autoclave, or a sealed vessel ('bomb') in a furnace), and left to reach equilibrium. Samples are taken by pressurised expulsion or quenched cold extraction.
Stirred autoclave	As per above, but the solution is stirred or otherwise agitated to improve kinetics of equilibrium between oxide and bulk solution. Teflon coated magnetic stirrers are a popular choice for this purpose.
Once-through flowing system	Most of the more recent studies, producing the most reliable results, have employed this method. Benefits include the continual refreshing of solution chemistry, and the ability to take samples online without causing any flow disturbances. Tremaine and LeBlanc [121] observed that stagnant conditions between samples could cause much higher apparent solubilities after recommencement of flow, due to fine suspended particulate matter, and so installed a bypass line to allow the system to equilibrate under flowing conditions before switching to the sampling line containing IX resins. More recent methodologies have tended to collect small samples from constant flow, negating the need even for diversion of flow.
Hydrogen Electrode Concentration Cell (HECC)	The HECC enables online measurement of pH at temperature. A salt solution, for example 0.1 – 4 M NaCl [123], is used in addition to pH reagent, to provide the ionic strength necessary for online pH measurements, though the more conventional mass balance approach can be used for pH determination in salt-free solutions or in strongly acid or alkaline solutions where online pH measurement is problematic. Electrochemical Potential (ECP) can also be measured online. In the most recent design [123], [124], multiple samples can be taken from the sampling line using a syringe, with system pressure being maintained by injection of additional hydrogen gas. The HECC can be used for other studies related to solubility, such as metal ion hydrolysis or complexation reactions [124].

Table 4.3. Sampling methods – adapted from the literature review of Morrison [26].

Sampling method	details
Direct extraction by pressurised expulsion	Samples are taken by pressurised expulsion through a valve, under the pressure of the hydrothermal fluid [125]. Helz used an evacuated tube for increased differential pressure [126].
Quenched cold extraction	Vessels are rapidly cooled by quenching in water, and samples are extracted by pipette after punching a hole in the top seals [127]
Ion exchange (IX)	Ion exchange beds consist of small spheres of organic polymer resin, packed in a column. These are effective at removing ions from a solution, while releasing other ions which were previously coordinated in the resin structure, and are often specific to either anions or cations. After completion of a sample, metal content is eluted from the IX beds with HCl solution, for analysis by any appropriate analytical chemistry method. Total metal content is divided by total cumulative flow during sampling time to give a concentration. Samples represent an average value from several litres or tens of litres taken over multiple hours of flow. Two IX beds may be used in series, providing confidence that no significant proportion of dissolved metal ions are missing from the sample so long as metals recorded in the second bed are only a small fraction of those from the first. Kanert et al. [128] used two oxide beds, with activated (radiolabelled) oxide in the first, and non-active oxide in the second, and measured the activity of the second bed against calibrated standards after the sampling time was over. The second oxide bed effectively acted as an ion exchange bed, but using oxide granules.
Direct collection from constant flow	Advances in analytical chemistry techniques have meant that small samples in the sub ppb range can be analysed directly without the need for a pre-concentration step, by methods such as ICP-MS. Effluent from the apparatus can be discarded when a sample is not being taken. This method allows the fluctuations in levels over short time / volume scales to be observed, enabling better monitoring of levels over time to observe changes such as occur in a corrosion study, or progress to equilibrium in a solubility study.

4.1.4. Solubility of Fe from magnetite and other spinels

4.1.4.1. Magnetite

Two of the most important studies regarding magnetite solubility are those of Sweeton & Baes in 1970 [4], and Tremaine & LeBlanc in 1980 [121]. Both used once-through flowing rigs, in which pressurised (~100 bar to prevent boiling), hydrogenated (typically 1 atm H_2 at 25 °C), pH-modified (HCl or KOH/NaOH) coolant flowed at temperature over magnetite granules, was cooled and depressurised, passed through filters, and passed over an IX bed for the collection of dissolved metal ions. Metal (Fe^{2+} and Fe^{3+}) ions were eluted from the IX beds using HCl solution, and the analysed total Fe content was divided by total integrated flow during the sample for an average concentration reading over that time period.

Results from the two studies agree well under acidic conditions, but those of the latter study are lower than the former (and other studies, e.g. [128]) by up to an order of magnitude under alkaline conditions. Figure 4.6 shows a representative comparison of results at 300 °C for a range of pH values. Tremaine and LeBlanc cite the following as likely causes for the discrepancies:

- Fines from the oxide: When oxide was freshly loaded in their apparatus for the first time, fine particulates were released which were collected by the IX resins along with dissolved ions. This was demonstrated by the use of 0.2 µm filters installed immediately after the oxide bed in some runs: whilst apparent solubility fell 'exponentially' from initial high values, particulates of ~ 1 µm were seen on the filters for the first 300 litres of flow. Under most conditions tested, apparent solubility settled to a steady value over a similar time frame. In studies by others where insufficient time was allowed, this could have affected results.
- Enhanced solubility due to very small particles: fixed, very small particulates (<0.1 µm) enhance the solubility due to their high free surface energy (see section 4.1.2) – even if they remain attached to oxide granules in the oxide bed. These may nucleate early on, then dissolve or grow larger over time, but sufficient time must be allowed for this to happen.
- Quality of magnetite granules: Tremaine and LeBlanc manufactured some granules according to a method similar to that of Sweeton and Baes, for comparison with their own, finding them to be 'visibly more poorly fused', and giving higher initial solubilities during some preliminary experiments.
- Colloids forming in stagnant conditions between runs: Results were spuriously high for the first few litres of flow after leaving the oxide bed under stagnant conditions between runs. A possible explanation is the build-up of colloids forming in solution due to temperature gradients (causing solubility gradients). See also [3], [113]. To combat this, an ion exchange

bypass feature was installed, to enable continuing flow and avoid stagnant conditions whilst the IX resins were replaced between runs.

- Time taken to establish new equilibrium at oxide surface after change in conditions: They observed that apparent solubility required about 2 – 10 litres of flow to decay down to steady values after each change in pH and temperature conditions, citing the need to establish a new equilibrium at the oxide surface as a likely cause. This can include the concentration of OH^- or H^+ ions adsorbed on oxide surfaces, and presumably particularly also the microstructure of the oxide near the surface. The bypass feature enabled the oxide to be 'pre-equilibrated with the flowing solutions at the measurement temperature' before switching flow to the IX bed, thus avoiding contaminating the IX bed with erroneously high Fe levels
- Ageing of oxides in solution: Apparent solubility values recorded at pH above about 10 continued to decay over time, until around 1000 litres of total flow had passed. This is despite the fact that particulates typically ceased to be observed in the filters after just 300 litres of total flow, with apparent solubilities in runs of lower pH decaying to steady levels over a similar timeframe (see the first bullet point above). They noted that the rate of decay over time was independent of flow rate, and therefore appeared to be 'a function of the time of exposure of the oxide to the flowing solution'. 1000 litres corresponds to several months (for example 3 months at a fairly typical flow rate of 7 ml/min) of time; a total flow of 2000 litres occurred during the whole study. It is interesting to note that solubility measurements from the same oxides produced steady results whenever acid to weakly alkaline conditions were employed, but a continuing decay towards steady levels whenever more strongly alkaline conditions were employed, over a period of several months.

These observations essentially equate to the same thing – readings of solubility or apparent solubility decay exponentially towards steady values, over rather long time periods: either by the flushing of fines from manufactured granules, or by the ageing of the crystalline phase to its most stable form under prevailing conditions. Studies prior to Tremaine and LeBlanc's had failed to allow adequate time for levels to fall when under alkaline conditions; and there were shown to be design advantages to having a flowing system, especially with flow bypass.

One possible flaw with the study could be the presence of Ti, as the material of construction of the apparatus. Incorporation of Ti to the magnetite crystal structure could cause it to become more stable, causing apparent solubility to be lower than that for pure magnetite. However, Ti was not observed in the magnetite after use in the rig. The results from another important study in 1995 by Ziemniak et al. [5], using a platinum lined flowing rig of similar design to the aforementioned studies,

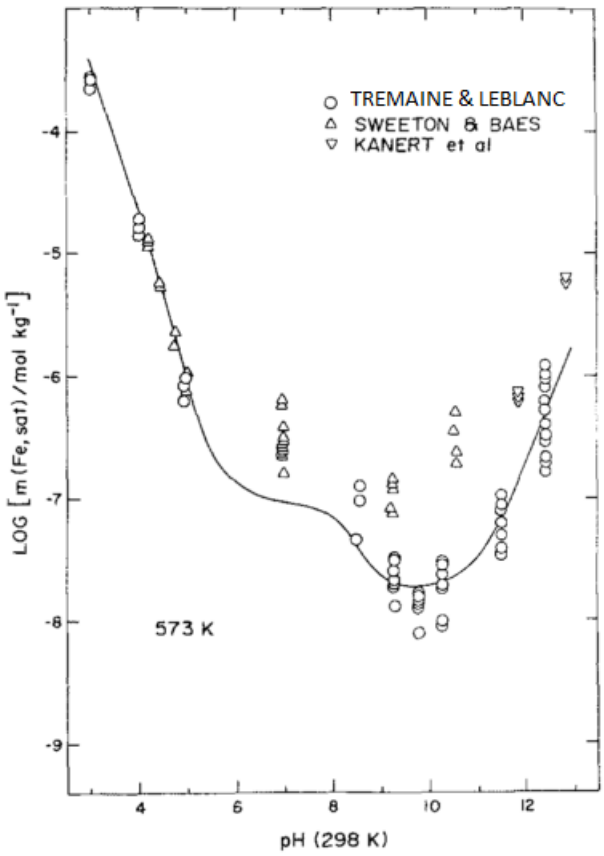

Figure 4.6. Tremaine and LeBlanc [121] *magnetite solubility data at 300 °C, 779 μ**m** H_2, as a function of initial pH_{25C} of feed solutions, plotted alongside results from Sweeton and Baes* [4]*, and Kanert et al.* [128] *for comparison. From* [121]*.*
Notice the agreement at low pH, and discrepancies at higher pH. Also note the much higher degree of scatter at pH above 6, and especially for the pH ~11.5 and pH ~12.5 data of Tremaine and LeBlanc. Results at those extreme pH values in Tremaine and LeBlanc's study continued to slowly decay over time for much longer than under other conditions, implying very slow progress to equilibration of oxide surfaces. The solid line represents a least squares fit to the data performed by the authors. The kink in the curve is an artefact of the use of pH_{25C} rather than pH_T – use of the latter produces a curve of monotonically increasing gradient.

were consistent with those of Tremaine and LeBlanc, whose data they combined with their own data in complexing media (alkaline sodium phosphate and ammonium hydroxide solutions) to provide equilibrium constants for forming ammino- and phosphate- complexes in solution. Further analysis has also tended to favour the Tremaine and LeBlanc / Ziemniak et al. results [38].

Unlike Sweeton and Baes, Tremaine and LeBlanc included ferric (Fe(III)) species in fits to their data, as well as ferrous (Fe(II)) species. They used some of their own measurements and fits to the data, combined with those of other studies, to quantify the equilibria between ferrous and ferric ions in solution. An example relative speciation plot as a function of pH, at 300 °C, is shown in Figure 4.7.

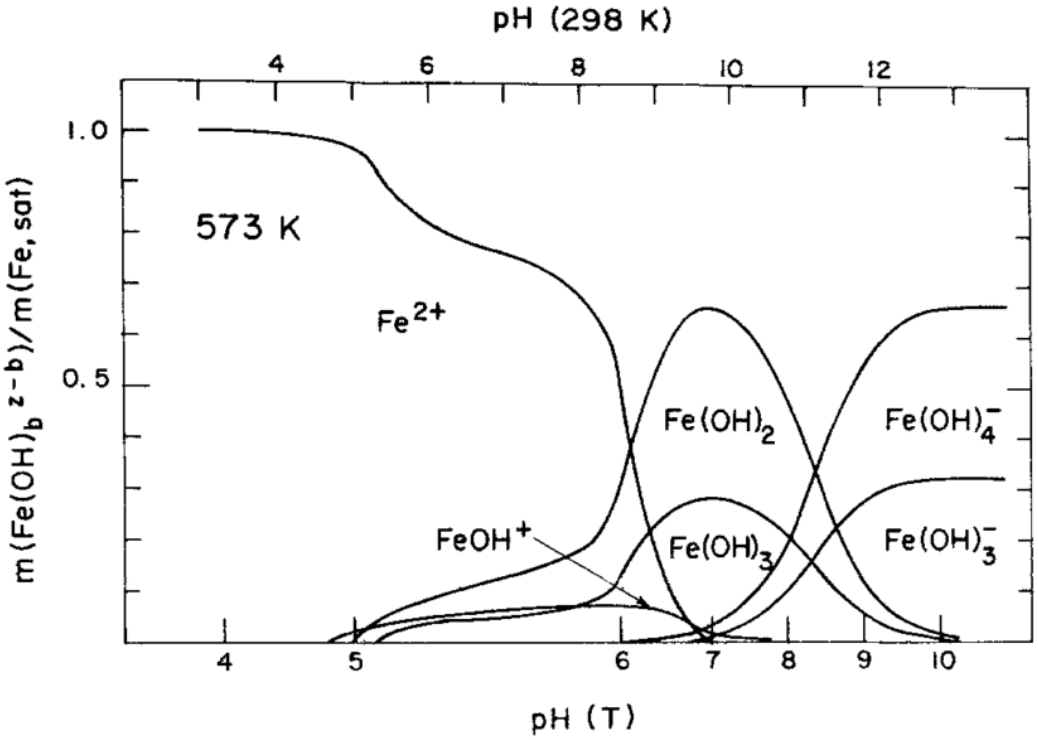

Figure 4.7. Relative speciation of soluble Fe ions at 300 °C, 1 atm H_2 (25 °C), as a function of pH. From [121].
Kinks in the curves are due to the fact they are plotted against equispaced pH_{25C} values (upper horizontal axis) resulting in a non-linear pH_T scale (lower horizontal axis). pH increases are associated directly with a shift towards predominance of more negatively charged species, as for any element. For Fe specifically, the relative stability of ferric species $Fe(OH)_4^-$ and $Fe(OH)_3$ compared with other ferric species, and the increased predominance of multiply hydrolysed forms at the highest temperatures, allows ferric species to predominate at the highest temperatures and pH values, even under the reducing conditions represented in the plot.

A study by Lambert et al. [113], looked at the link between coolant conditions, magnetite crystal size, and solubility, as part of an investigation into magnetite solubility, using magnetite powder in a titanium autoclave at up to 300 °C, at pH ~12 (10^{-2} M KOH) under 6 atm hydrogen (at 25 °C). They found that the grains in their magnetite powder evolved from a relatively regular distribution at several microns across, to a mixture of crystals of a much larger size surrounded by small crystals which were less than 1 micron across and were sometimes fused with the large crystals. This ageing of the magnetite was accompanied by a steady fall in apparent solubility over the course of ~300 days of experimentation, during which there were no signs of cessation of this continuing trend, as illustrated by the evolution of results taken at 300 °C, in Figure 4.8.

A crude observation of Tremaine and LeBlanc's results as plotted in Figure 4.6, by interpolating between measurements at pH ~11.5 and ~12.5, yields a mean value of log molality as -6.75, with a

range in data of about 0.75 log units. Since species at pH 12, 300 °C, 1 atm H_2 (25 °C) are ferric:ferrous in a ratio 2:1 (see Figure 4.7), the increase in solubility caused by increased ferrous ions (as H_2 pressure increases from 1 atm to 6 atm (25 °C)) is almost offset by a decrease in ferric ions – the overall effect is a roughly 10% increase for conditions used by Lambert et al.

In ppb units this equates to around 11 ppb solubility with a range of around 5 – 26 ppb, as might have been measured by Tremaine and LeBlanc, by crude extrapolation. By another crude extrapolation, the 2000 litres of total flow in their study would equate to around 200 days of total exposure of oxide to hydrothermal conditions, at a seemingly typical flow rate of 7 ml/min. High pH measurements only settled to steady levels (within scatter) after 1000 litres (100 days). Thus the Tremaine and LeBlanc fitted solubility of around 11 ppb (~5 to 26 ppb) from data taken after perhaps c. 100 – 200 days of exposure at temperature is broadly similar to data from Lambert et al. over the same time period. It thus seems that slow kinetics of transformation of the solid phase to its most stable form are a significant factor in determining apparent solubility of a particular sample of magnetite crystals at high pH and temperature, for which the state of the crystals at the time of measurement is an important consideration. Equilibrium solubility in this region may be lower than studies suggest, though perhaps unattainable in any practical application.

For a preliminary series of results, Lambert et al. had much higher apparent solubility readings than even the highest shown in Figure 4.8. They hypothesised that this was because they had to cool the autoclave down more frequently and for longer periods between sampling to keep hydrogen pressure maintained, to such an extent that the magnetite was not allowed to age to a stable form at temperature, contrary to the results observed in Figure 4.8 once the methodology had been improved. A further experiment was conducted in which as-prepared powder, and the powder having been aged in the autoclave for 300 days (as per above), were exposed in the autoclave at room temperature at a pH of around 7 to 8, for 8 weeks. This process resulted in very small crystals, often less than 0.3 microns, next to a few crystals of comparable size to the previous ones, as observed in SEM. The XRD pattern was clearly magnetite, as with all the other powders tested, but had broad peaks characteristic of an average grain size of less than 0.1 micron.

It was thus demonstrated that cool conditions can lead to the growth of small crystallites at the expense of large ones, in contrast with common experience at high temperatures. Slow kinetics were cited as a possible cause for the presence and persistence of such small crystallites – via variations in local hydrogen concentrations caused by slow homogenisation by diffusion, and via slow crystal growth.

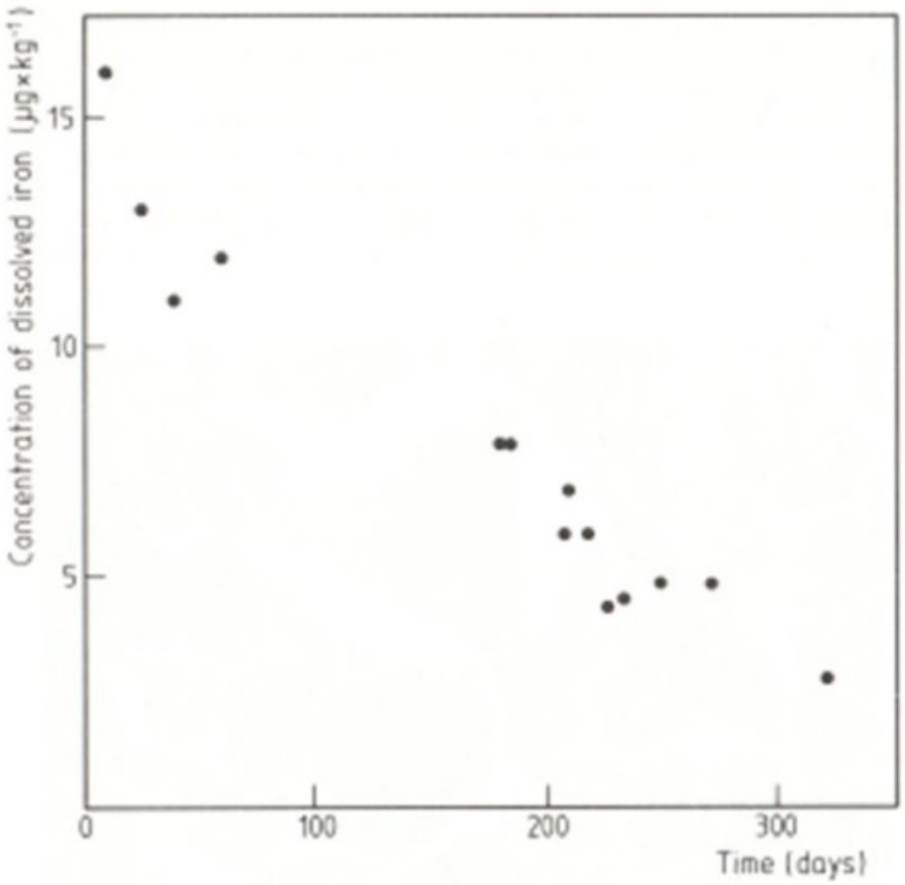

Figure 4.8. Decay over time of magnetite solubility measurements taken at 300 °C, as observed by Lambert et al. [113]. *Figure as translated to English taken from* [122].
Magnetite powder was dissolved in hydrothermal solution in a titanium autoclave at pH 12 (10^{-2} M KOH), 6 atm hydrogen (at 25 °C), at temperatures up to 300 °C. The powder was exposed to other test temperatures besides 300 °C, and between each set of samples the autoclave was cooled to room temperature to allow hydrogen to be replenished.

Figure 4.9 shows the transition from negative to positive temperature dependence of magnetite solubility with increasing pH.

A fuller description of the behaviour of magnetite solubility with pH, temperature and dissolved hydrogen levels is included in the appendices (chapter 14). Some representative values as relevant to the rig of the current study are included in section 17.3.

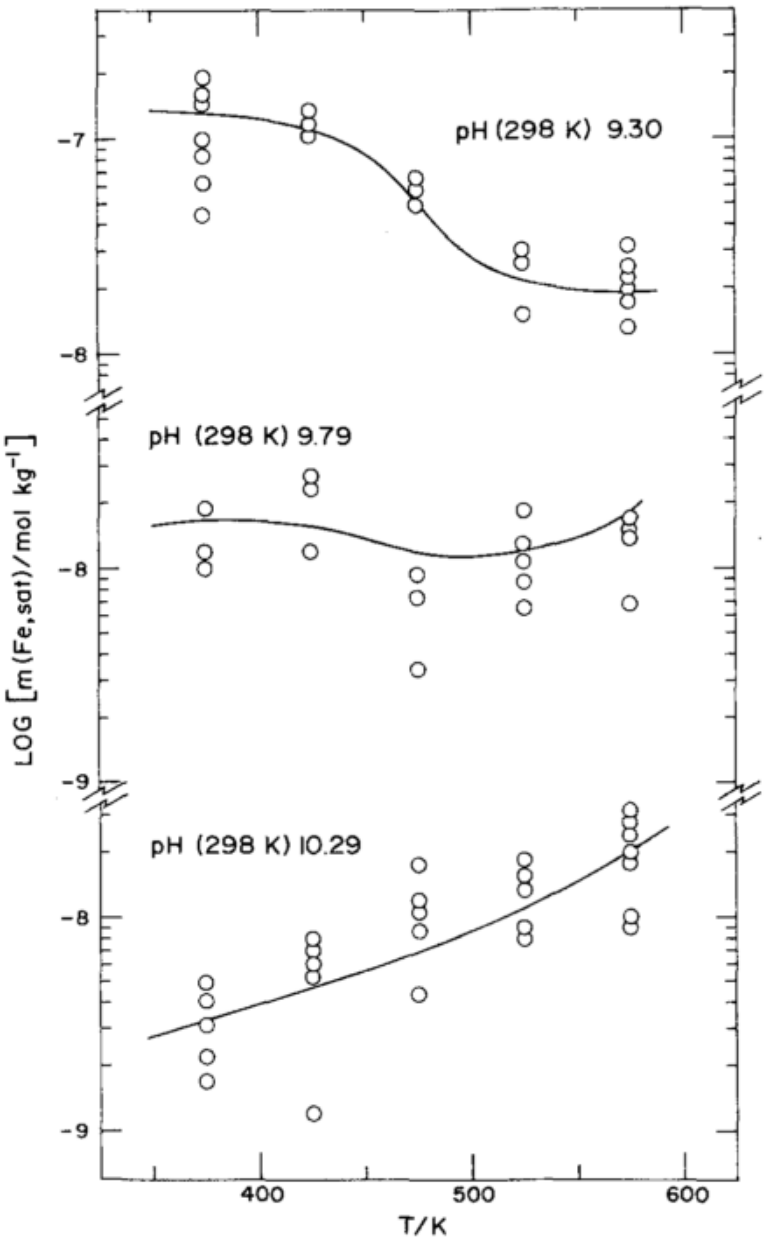

Figure 4.9. Temperature dependence of magnetite solubility, for solutions saturated with 1 atm hydrogen gas at 25 °C, showing transition from negative to positive temperature dependence with increasing pH. From [121].

4.1.4.2. Ferrites

A limited number of studies of solubility have been conducted on mixed ferrites. Results can be difficult to interpret, because composition of the oxide can change relatively rapidly with changing conditions For example, nickel ferrites saturated in nickel (and present alongside metallic nickel) have variable nickel composition at the surface, and thus controlling solubility, dependent on redox conditions. The equilibrium state to which a system of mixed oxides and coolant settles – both in

terms of equilibrium levels in solution, and in terms of oxide forms – is dependent on factors such as relative amounts of the different metals, and ratio of amounts of total oxide to total water, and cannot be described by single values of solubility, or even solubility products, as explained by Turner [14], and echoed by Kurepin [12].

The presence of other metal elements besides Fe in the ferrite lattice can modify the solubility of Fe from the oxide, generally to a lower value unless the oxide form is metastable. Kurepin's thermodynamic model suggests that with increasing additions of Cr up to saturation in solid solution, magnetite solubility at 290 °C steadily falls to about 80% the value of its pure form.

Experimental studies have been performed by for example You et al. [129], Bellefleur et al. [130], and Kunig and Sandler ([63]–[65]). A reanalysis [66] of studies of magnetite ([4], [121]), of NiO [3], and of non-stoichiometric Ni-Co-ferrites ([63]–[65]) used a thermodynamic/empirical model to arrive at a few key outputs from the data, such as the pH of minimum solubility and the pH of zero temperature dependence of solubility (or transition from negative to positive, with increasing pH), assessed at various temperatures. For some aspects of modeling, all Ni-Co-ferrites were considered as one irrespective of composition, such as for the determination of pH of minimum Fe solubility. Notwithstanding a high degree of uncertainty in results, they found that ferrites had the same pH_T of minimum Fe solubility as pure magnetite, ~6.9 – 7.0, at 280 – 300 °C. This contrasts with the findings of others that the solubility of Fe from stochiometric nickel ferrite is minimal at a higher pH than for magnetite. They found that at 292 °C, 1200 μmolal H_2, 100 – 1200 ppm B, sub-stoichiometric Ni-Co-ferrites had a higher pH_T for zero temperature dependence of Fe solubility than magnetite, at ~ 7.4 – 7.5 compared with ~ 6.2 – 6.4.

An example of Fe (and Ni) solubility data from sub-stoichiometric nickel ferrite is plotted in Figure 4.10. The magnitude of Fe solubility from ferrites in that study, and in the studies of Kunig and Sandler, was consistent with that for magnetite in the studies of Sweeton and Baes and others, being up to an order of magnitude greater than that for Tremeaine and LeBlanc, and Ziemniak et al. [66].

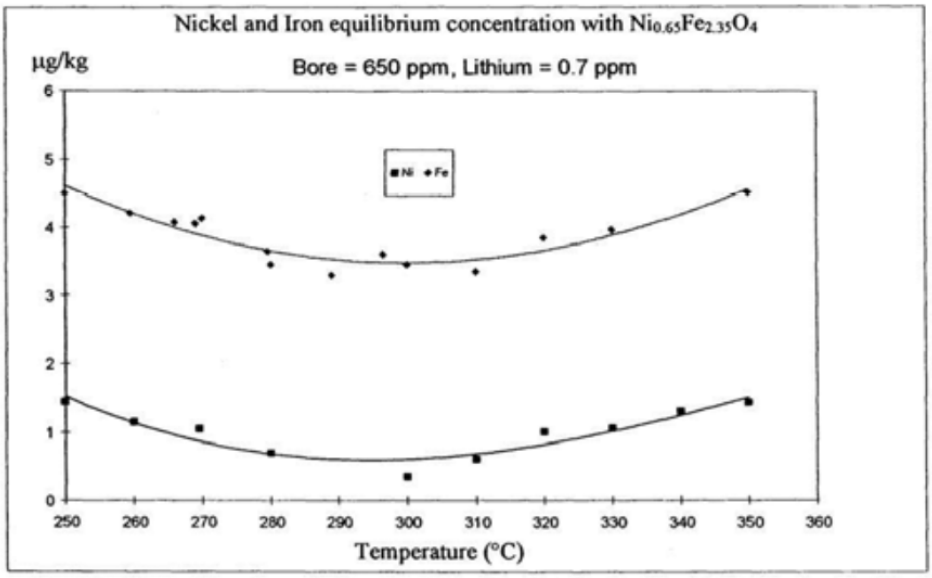

Figure 4.10. Sub-stoichiometric nickel ferrite solubility versus temperature, at pH_{300C} ~6.7. From You et al. [129]*, in* [11]*.*
At 300 °C, the pH_{25C} equivalent ~9.3, and this changes at different temperatures as the boric acid has different tendency to dissociate.

4.1.4.3. Chromites

In Figure 4.11, the model of Kurepin gives activity of Fe_3O_4 in Fe-saturated chromite as ~80% that of pure magnetite, which matches the activity of Fe_3O_4 in Cr-saturated magnetite, meaning a lower Fe solubility than for pure Fe_3O_4. The corresponding values of N (x axis) for equilibrium between the two phases at the solvus of immiscibility, at about 0.10 and 0.86, can be seen along the x axis of Figure 4.4, representing Ni free phases. In the context of corroding stainless steels, a continual flux of mostly Fe^{2+} ions is diffusing across the chromite protective film and releasing to solution, so the oxide is inherently Fe-rich causing a greater release than would be expected from the equilibrium solvus composition.

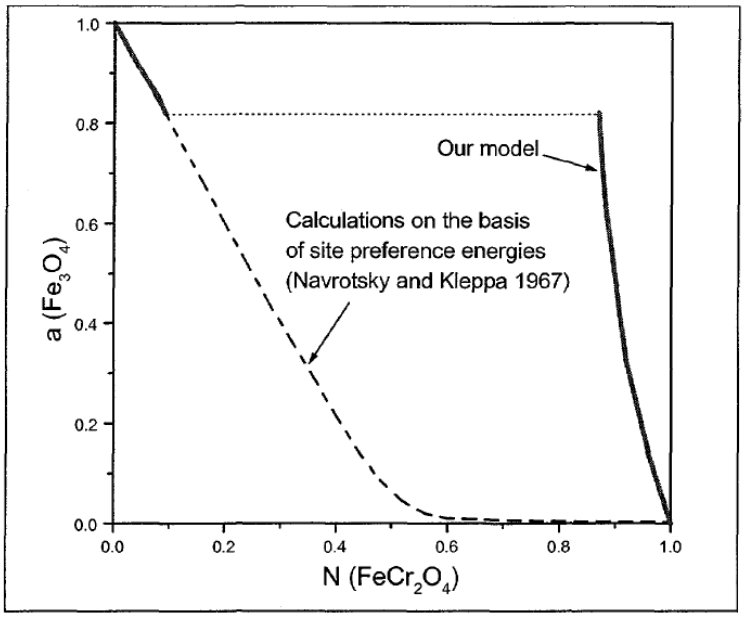

Figure 4.11. Dependence of activity of Fe_3O_4 on composition of Fe_3O_4-$FeCr_2O_4$ spinel at 290 °C, per model of Kurepin. From [12].

4.1.5. Solubility of Cr from spinels and other oxides

The solubility of Cr from various oxides is treated in chapter 14. for rig-relevant conditons, expected levels of Cr are almost invariant, especially considering the errors on measurement, at around 0.01 to 0.02 ppb.

Where chromite is metastable with respect to decomposition to magnetite and CrOOH, then levels of Cr in solution are controlled by the latter phase. Otherwise levels of Cr and Fe in solution can be considered to be related by a solubility product of $FeCr_2O_4$, in which $[Fe].[Cr]^2$ = constant. Levels of [Fe] and [Cr] are constrained to be at or below the solubility of their respective single-metal oxide phases (ferrite and CrOOH). For practical applications, a single solid phase at equilibrium is very unlikely and would require relative amounts of Fe and Cr in the system to match the equilibrium composition of the chromite under the prevailing conditions. An equilibrium between chromite and CrOOH (for an excess of Cr) or ferrite (for an excess of Fe) would be the more realistic outcome. In this case, equilibrium dissolved level for one metal is given by the single metal oxide, and for the other it is controlled by the chromite solubility product, a little lower than for the single metal oxide. The actual composition of the chromite at equilibrium is not stoichiometric, having for example about 15% magnetite in solid solution ($Fe(Cr_{0.85}Fe_{0.15})_2O_4$) according to Kurepin, or more according to Ziemniak et al., when in equilibrium with ferrite.

4.1.6. Solubility of Ni from Ni metal, nickel oxides, and spinels

Table 4.4 shows Ni solubility from various crystalline phases. At low levels of hydrogen, NiO is the stable Ni-based phase, having solubility of ~ 0.4 ppb at 300 °C across a wide range of pH values. Above approximately the level of hydrogen resulting from saturation with 1 atm at 25 °C (~17.7 scc/kg), Ni metal becomes the stable phase, having solubility which rapidly falls with increasing hydrogen fugacity, as [Ni] $\propto \frac{1}{\{H_2\}}$. With 25 – 50 scc/kg dissolved hydrogen, Ni is the stable phase, having solubility ~0.2 ppb at 300 °C. Transition between Ni and NiO is characterised by slow kinetics, particularly below 200 °C, so the high solubility of Ni under less reducing conditions is relevant even where it is not the thermodynamically stable phase.

Where spinel oxides are present alongside nickel metal, it is the nickel metal which controls Ni levels in the coolant, with Fe levels from the mixed ferrite oxide being comparable to or a little lower than that for magnetite. With increasing hydrogen fugacity, nickel solubility decreases; in turn, the lower Ni levels in solution reach equilibrium with a lower saturation concentration of NiO in solid solution in the ferrite (falling x in $Ni_xFe_{3-x}O_4$) – this can be seen in the Fe-rich solvus composition of Figure 4.4: At log $\{O_2\}$ = -33 (log $\{H_2\}$ ~ 0, ~ 18 scc/kg H_2), x = 0.9; whilst at log $\{O_2\}$ = -35 (log $\{H_2\}$ ~ 1, ~ 180 scc/kg H_2), x = 0.15. If the Ni content of the spinels is below saturation, then equilibrium levels of Ni in solution decrease accordingly from Ni solubility levels.

Table 4.4. A comparison of solubilities of Ni-based crystalline phases.
For NiO(cr), the stable phase under sufficiently oxidising conditions, hydrogen fugacity has no effect on solubility. The dominant ion in solution is indicated in the table, with $Ni(OH)_2(aq)$ providing a steady solubility having no dependence on pH and limited dependence on temperature. At lower temperatures and pH values Ni^{2+} dominates, having much higher solubility.
At higher hydrogen fugacities (as indicated in table), crystalline Ni becomes the stable phase, having a solubility which steeply diminishes to negligible values with increasing hydrogen fugacity, as shown in the table for 3 selected hydrogen fugacities. Red font is used to show conditions where Ni metal is not the most stable phase.
Below ~77 °C, $Ni(OH)_2(cr)$ replaces NiO as the stable phase in the presence of water, resulting in slightly lower solubility at 25 °C where present.

[Ni] (ppb) from NiO	*25 °C*	*200 °C*	*300 °C*	$Ni(OH)_2$(cr) at 25 °C
pH 9	150 Ni^{2+}	3 Ni^{2+}	0.4 $Ni(OH)_2$(aq)	20
pH 10	2 Ni^{2+}	0.3 $Ni(OH)_2$(aq)	0.4 $Ni(OH)_2$(aq)	0.3
pH 11	0.2 $Ni(OH)_2$(aq)	0.3 $Ni(OH)_2$(aq)	0.4 $Ni(OH)_2$(aq)	0.03

Critical log $\{H_2\}_{25C}$ of Ni/NiO transition	*25 °C*	*200 °C*	*300 °C*	
	-4.5	-1.4	0	

[Ni] (ppb) from Ni. $\{H_2\}_{25C} = 10^0$ atm.	*25 °C*	*200 °C*	*300 °C*	
pH 9	0.004	0.1	0.4	
pH 10	0.00004	0.01	0.4	
pH 11	0.000006	0.01	0.4	

[Ni] (ppb) from Ni. $\{H_2\}_{25C} = 10^{-3}$ atm.	*25 °C*	*200 °C*	*300 °C*	
pH 9	4	100	400	
pH 10	0.04	13	400	
pH 11	0.006	13	400	

[Ni] (ppb) from Ni. $\{H_2\}_{25C} = 10^{-6}$ atm.	*25 °C*	*200 °C*	*300 °C*	
pH 9	4000	100,000	400,000	
pH 10	40	13,000	400,000	
pH 11	10	13,000	400,000	

4.1.7. Solubility of Mo from MoO_2 and from mixed ferrites

Wang et al. [131] analysed solubility and thermochemical data for Mo and Mo oxides from various studies, including their own. They produced potential-pH diagrams, reproduced here in Figure 4.12. The boundary between MoO_2 oxide and soluble MoO_4^{2-} ions represents solubility of ~100 ppb in the upper plot and 1000 ppm in the lower plot. On each plot a red parallelogram has been added by the present author to indicate conditions expected in the sampling line of the rig. The lower boundary represents 1 atm H_2 and the upper boundary represents 10^{-6} atm H_2.

At pH 9, the boundary of MoO_2 in the upper plot representing 100 ppb solubility occurs at a hydrogen pressure of around 10^{-4} or 10^{-5} atm. At higher levels of hydrogen, solubility is lower, creating a possibility for precipitation of MoO_2 in the sampling line. At pH 10 and 11, and for lower hydrogen fugacity, MoO_2 solubility increases greatly, reaching around 1000 ppm for pH 11 at hydrogen pressure around 10^{-6} atm.

MoO_2 solubility has negative $\{H_2\}$ dependence, because on dissolving Mo is oxidised from Mo(IV) in the oxide to Mo(VI) in solution. MoO_2 solubility has positive pH dependence in the pH range 9 – 11, because on dissolving the negatively charged MoO_4^{2-} ion dominates in solution. The same arguments hold for Mo^{2+} or Mo^{4+} ions dissolving from magnetite or chromite at high temperature, where the dominant ions in solution are MoO_4^{2-} and $HMoO_4^-$, under conditions expected in the rig [132].

In reality, due to slow kinetics at room temperature, oxygen is not necessarily in equilibrium with hydrogen gas in the coolant (which would lead to around 10^{-72} to 10^{-84} atm O_2), and may instead persist at the same levels present in the high temperature part of the rig. For hydrogen concentration of 10^0 to 10^{-6} atm, this corresponds to ~ 10^{-24} to 10^{-45} atm oxygen, as indicated by the blue parallelogram in each plot. That is, 10^{-45} to 10^{-33} atm oxygen when the oven is at 200 °C, increasing to ~ 10^{-36} to 10^{-24} atm oxygen when the oven is at 300 °C. In this case, MoO_2 would not precipitate in the sampling line under any circumstances.

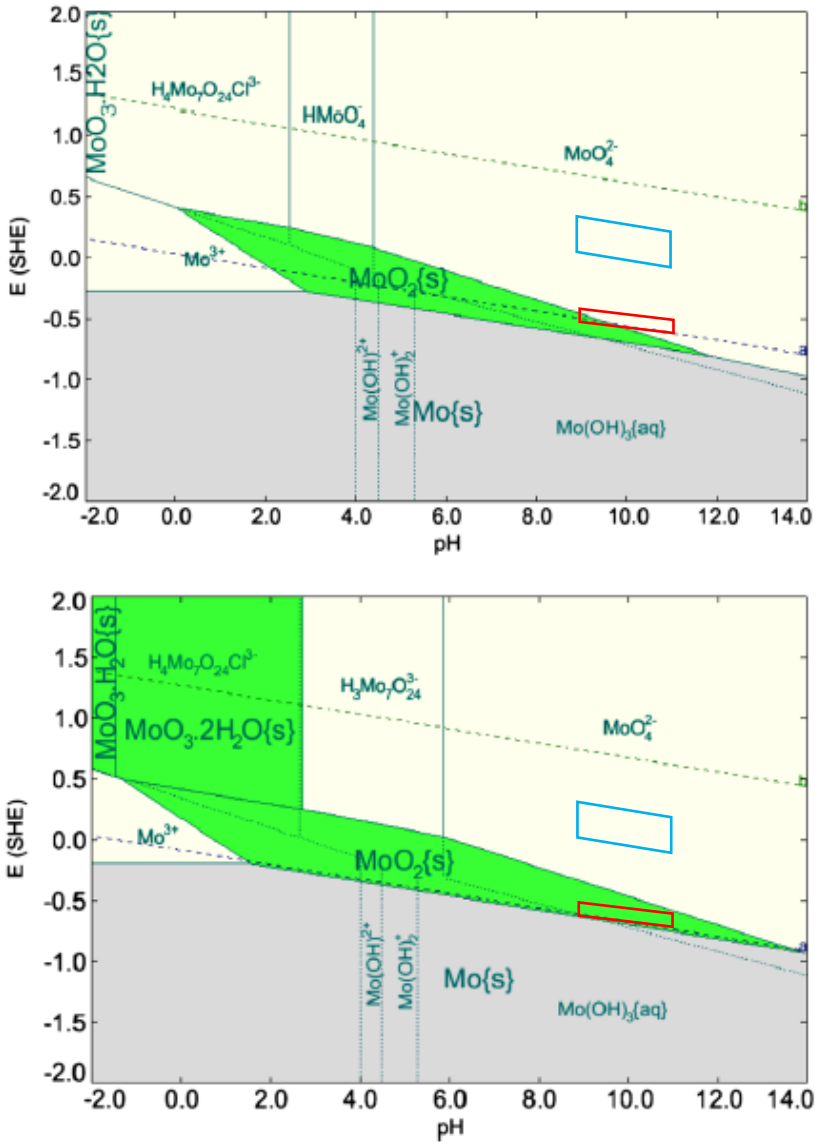

Figure 4.12. Potential-pH diagrams for Mo at 25 °C, for molal activities of dissolved Mo at 10^{-6} (top) and 10^{-2} (bottom). From [131].

4.1.8. Dissolution / precipitation behaviour of other elements within spinels

Other metallic elements can become incorporated within the spinel structure in small amounts, such as Co, Mn and Mo. Concerning coolant-oxide equilibria, there are some studies regarding Co and Zn in spinels, but a literature search did not yield any for Mn or Mo. In the absence of data, a simple assumption is that levels in solution are proportional to their composition in the oxide, for a given set of coolant conditions. For Ni in Co-Ni-ferrites, this assumption seems to hold reasonably well. However, for Co in Co-Ni-ferrites, this assumption does not seem to hold, as two oxides with very different Co compositions were found to have similar Co solubility [66].

4.2. Kinetics of reactions and processes involving coolant

When changes are applied to a system such as the primary circuit of a PWR, which take it out of equilibrium, chemical reactions and other processes occur as the system approaches a new equilibrium. If those changes are applied slowly, and the system has a high propensity to react to changes rapidly (i.e. fast kinetics), then global equilibrium as described by thermodynamics is a good approximation to the real situation. Under other circumstances, the effect of finite kinetics can cause the actual state of a system to differ significantly from that predicted by thermodynamics

The rate at which reactions proceed depends upon fundamental kinetics of the reaction, the rate constant, as well as other factors, particularly concerning geometry. This can be illustrated by the Kinetics of a typical reaction, where ROR is the rate of reaction, A is the active surface area, and k is the rate constant:

$$ROR\ (mole\ s^{-1}) = A\ (m^2).k(mole\ s^{-1}m^{-2})$$

Reaction rate constants tend to increase rapidly with temperature, as for example the corrosion rate of alloy 600, Figure 3.5, so that thermodynamics provide a useful guide to the state of hydrothermal systems such as found in PWRs under normal operating conditions. On the other hand, at room temperature long time periods may be needed for attainment of equilibrium, and predictions based on thermodynamics should be used with caution.

As the equation suggests, geometry can play an equally important role. As an example, precipitation of a crystalline phase from super-saturated coolant can occur readily when ample coolant-facing surface area of that phase is present. When none is yet present, this reaction pathway is not available, and nucleation must first occur on microstructural defects of other surfaces or directly in solution, requiring a greater degree of supersaturation and with initially slow rate of reaction. A different, metastable, phase may nucleate more readily or have crystallite surfaces already present, in which case it can become the dominant phase over intermediate time periods, before slowly transforming to the most stable phase over a longer timescale.

4.2.1. Oxide phase changes

Where changing conditions cause an oxide phase currently present to become unstable with respect to a different phase, the original phase may persist due to slow kinetics of transformation. This is especially the case in the solid state, where diffusion is slow. Ziemniak et al. observed incomplete phase separation of $NiFeCrO_4$ to Fe-rich and Cr-rich phases even after 1 year of air annealing at 600 °C [74].

Alternatively, a different phase may precipitate, which though more stable than the original phase, is not as stable as the most stable phase, as explained in the preceding paragraph. This has been observed in the case of, for example, $Ni(OH)_2$ precipitation on corroding Ni base alloys at 325 °C [133], despite being unstable, or meta stable, above around 77 °C.

4.2.2. Oxide form and composition

Subtle changes to an oxide's microstructure and stoichiometry can occur as it 'ages' over time towards the most stable form under prevailing conditions. This can be a slow process, taking weeks or months, with a corresponding gradual fall in solubility.

4.2.3. Dissolution and precipitation processes

Due to differing solubility in different parts of a PWR circuit, it is sometimes said that dissolution occurs from the corrosion film in some locations whilst precipitation occurs in others. It is perhaps more accurate to speak of respectively a net release to the bulk coolant, or uptake from the bulk coolant, of corrosion product ions. Ions dissolve from the inner layer oxide at the oxide-coolant interface (corrosion release flux), and concomitantly precipitate onto surfaces of outer layer oxide. Unless there is a particularly effective mass transfer of ions away from the vicinity of the oxide film, this process of concomitant dissolution and precipitation continues: during net release to the bulk coolant, precipitation of outer layer oxide occurs at a lesser rate than the corrosion release flux; the opposite is true in the case of net uptake of ions from bulk coolant. Through dissolution and precipitation processes, the corrosion film controls levels of dissolved ions in the adjacent coolant at equilibrium (solubility) levels, and there is a flux of ions transferred to or from the bulk coolant down the concentration gradient in the boundary layer. In this situation, kinetics of dissolution and precipitation at the oxide surfaces are not important as long as they are sufficiently fast to maintain a local equilibrium, it is the diffusion of ions across the boundary layer which determines the magnitude of soluble ion flux between reactor walls and bulk coolant. For a given concentration difference across the boundary layer, flux is inversely proportional to boundary layer thickness, and proportional to diffusivity of the ions in water.

A slightly simpler scenario, net dissolution of a single oxide phase, can be described as a two-step process, having two transport resistances in series [134]: transfer from solid phase to solution, also known as the 'surface reaction' or dissolution step,

$$\frac{dm}{dt}_{diss} = k_d . F^* . (C_{sat} - C_{os})$$

followed by transfer of dissolved species from solution at the oxide-solution boundary to bulk solution, through the boundary layer, known as 'mass transfer',

$$\frac{dm}{dt}_{mass} = k.(C_{os} - C_b)$$

where $\frac{dm}{dt}$ (g cm^{-2} s^{-1}) is mass flux, k_d (cm/s) is the dissolution rate constant, C_{sat} (g cm^{-3}) is oxide solubility, C_{os} (g cm^{-3}) is soluble concentration at the oxide-solution interface, F^* is a surface area factor, k (cm/s) is the mass transfer coefficient (across boundary layer), and C_b (g cm^{-3}) is the dissolved ion concentration in the bulk solution.

A steady state is set up where both processes occur at the same rate

$$\frac{dm}{dt}_{ss} = \frac{C_{sat} - C_b}{\left(\frac{1}{k_d F^*} + \frac{1}{k}\right)}$$

Under most commonly encountered scenarios at high temperatures, $k \ll k_d F^*$, so that kinetics are mass transfer controlled.

$$\frac{dm}{dt} \approx k.(C_{sat} - C_b)$$

The value of k varies depending on the thickness of the boundary layer, Δx, and the diffusivity of the ions in the coolant, D,

$$k = \frac{D}{\Delta x}.$$

5. Literature Review

Part III: Corrosion Products circulating in PWR primary coolant

5.1. Corrosion products circulating in PWR primary coolant

To better understand and model the processes which lead to crud deposits on fuel and elsewhere, there has been some effort in the industry to monitor and characterise the corrosion products circulating in operational PWR plants – this encompasses information such as the dissolved levels of each element; the concentrations and nature of particulates or colloids (crystallinity, phase, elemental composition and size distribution); and how these quantities change over time with changing conditions.

The more commonly collected data tend to be a breakdown of total circulating levels of each element (in mass ppb), broken down into 'particulate' (>0.45 μm) and 'soluble' (<0.45 μm) fractions, and therefore make no assessment of what proportion of the 'soluble' fraction is truly dissolved versus colloidal particles. These are typically collected during normal operation, at start-up, and during shutdown for each fuel cycle. There are some limitations of the standard sampling method as detailed in the sections that follow.

5.1.1. Method of sampling

Unfortunately, PWR coolant sampling systems 'were not designed with quantitative corrosion product sampling in mind' [6], instead being intended for monitoring levels of fully dissolved chemicals such as B and soluble fission products [135]. The main sampling line for circulating primary coolant is generally located in the hot leg (i.e. after passing through core), though there may be an additional line in the cold leg [135] – comparison of the two can be used to assess any differences in circulating corrosion product inventory according to location. Sampling lines are also present at other locations, such as the letdown line of CVCS, where the cooler temperature may be

advantageous for some applications due to the lack of stainless steel high temperature oxide film [10] (which has a tendency to adsorb trace elements).

5.1.1.1. Isokinetic sampling

To obtain a representative sample of suspended particles within a fluid, it is in some cases important that there be isokinetic conditions at the entrance to the sampling line, meaning that fluid in the sampling line has the same velocity as the fluid stream from which it is sampled. This is because larger particulates have sufficient inertia (relative to drag forces in the fluid) that they have a tendency to continue in the same direction briefly when flow changes direction, migrating to the outside of a bend like sediments in a river. The difference between isokinetic and anisokinetic sampling is illustrated in Figure 5.1. If fluid velocity in the sampling line is slower, then the flow diverges around the sampling line entrance, so that a smaller cross-sectional area of upstream flow is sampled than the cross-sectional area of sampling line. Particulates have a tendency to continue straight, and so particulates from a larger cross sectional area of upstream flow are sampled, compared with the fluid in which the particles are suspended – resulting in oversampling. The larger the particulate the greater the area of upstream flow sampled, up to the limit of the sampling line entrance area, and the greater the effect. By an analogous process, the opposite is true for faster flow in the sampling line. The non-negligible effect of inertial forces is one aspect which qualitatively separates larger particulates from colloidal particles, and also impacts on release and deposition behaviour in reactor coolant.

The nozzles of sampling lines for PWR primary coolant are not isokinetic, though in practice this does not pose a significant problem [135]. This is because conditions of coolant flow into a typical PWR

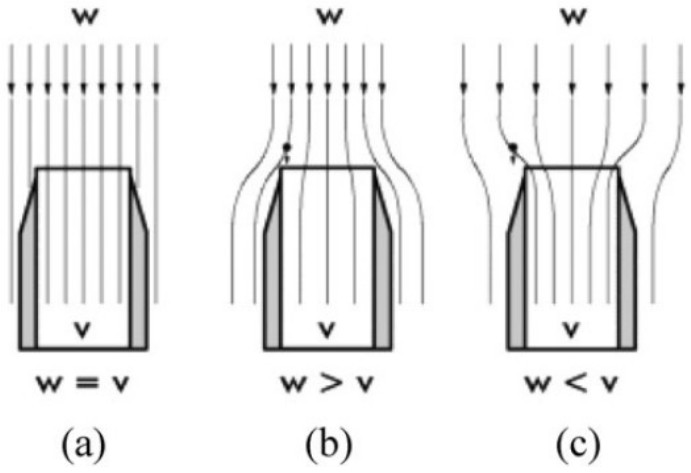

Figure 5.1. Illustrating isokinetic (a) and anisokinetic (b, c) sampling. From [136]

sampling line are such that viscous forces dominate, and the size above which the effect becomes noticeable is greater than the particulate size range of interest [137]; though the calculations provided in the reference do suggest that there may be a marginal effect for particles larger than 2 μm. In steam on the other hand, particle inertia is dominant and anisokinetic sampling can cause significant errors for ~1 μm magnetite particles [137].

5.1.1.2. Problems encountered with installed sampling lines at PWRs

An ANT International report on radiochemistry in LWRs [135] provides an informative introduction to the relevant aspects of sampling systems in PWRs, from which the pertinent points are reproduced in this paragraph. Sampling nozzles of sampling lines in PWRs are not isokinetic, though this is apparently not necessary for particulates in liquid sampling media [135], [137]. At most reactors in the U.S. the valve at the exit from the hot leg sampling line is not allowed to stay open due to safety considerations, and must be opened each time a sample is to be taken [135], making representative sampling problematic and continuous monitoring impossible. In Europe, the valves remain normally open, making relatively representative, continuous sampling possible [135]. Nevertheless, typical sampling line lengths can be up to 200 m long, made from 10 mm stainless steel tubing. This includes around 70 to 140 metres at high temperature within the reactor containment, followed by sampling coolers, pressure reducers, and the remainder of the sampling line [135]. In summary:

> 'The sample lines installed are long, have inadequate sampling nozzles, and are small diameter tubes, which have a high surface to volume ratio, so that significant interaction can occur between the sample medium and oxide layers on the sample line surface. This interaction and also uneven temperature distribution over the sampling line length can significantly affect the sampling composition' [135]

A major review into the subject of achieving representative samples has concluded that difficulties arise particularly when there are temperature and phase changes, and also that 'major sources of sampling deficiencies are deposition in the sample line, valves and coolers, and release of deposited material' ([138] in [137]).

Section 5.1.2 describes an example of a study in which the sampling system was modified to provide more representative sampling of coolant-borne particulates.

5.1.2. EPRI study conducted at Belgium

In the 1980s, EPRI conducted extensive research into the nature and behaviour of circulating particulates, using modifications to the installed sampling systems at four Belgian reactors [120]. Per their report, under normal operation the sampling system flows continuously, and routine sampling is carried out by 'diverting part of this flow through various sample bombs or filtration units, which can be isolated and removed from the laboratory for subsequent analysis.'

Figure 5.2 shows the modifications they made to the coolant sampling systems for the measurement of corrosion products [120]. The length of installed sampling line before the water cooler, 185 m, is consistent with the range of up to 200 m cited by the aforementioned ANT Report [135]. The residence time is not excessively long, at 159 s, thanks to the high flow velocity (0.44 to 1.8 m/s), despite the long length and high surface area (3.7 m^2).

A method of light scattering and absorption was used to detect suspended particles individually as they passed the 'sensitive volume', through which light from a small incandescent lamp was beamed onto a photodetector. The measured reduction in light was proportional to particle size. A complementary method was also used involving a laser and a measurement of scattered light from particles.

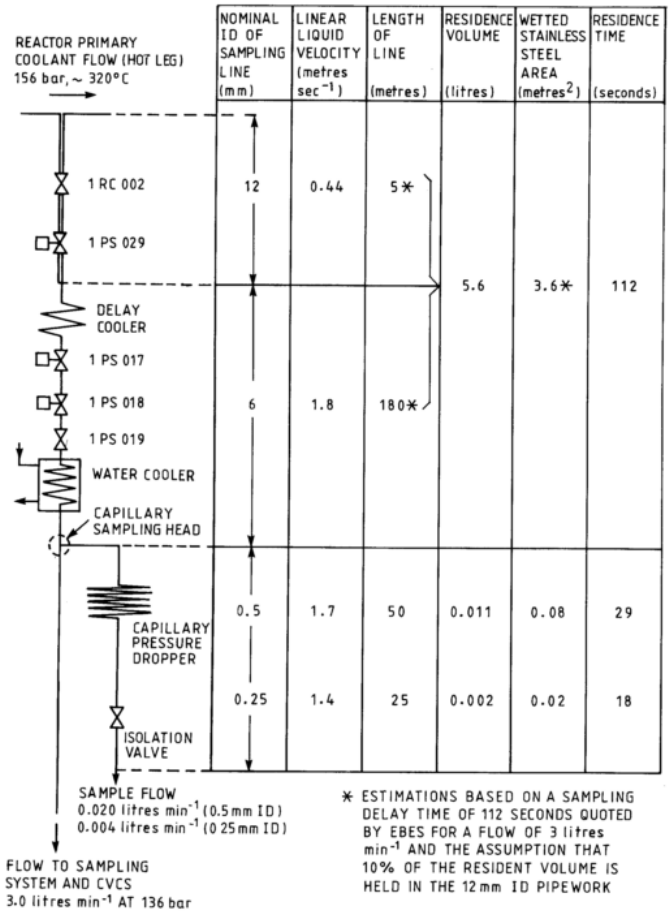

Figure 2-1. Typical Primary Circuit Sampling Flowsheet (Doel Unit 1) Showing Position of Capillary Sampling Line.

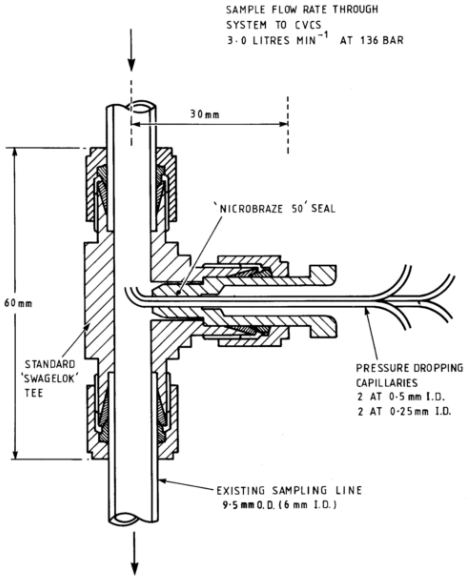

Figure 2-2. Detail of Capillary Sampling Head.

Figure 5.2. Schematic of isokinetic capillary sampling lines for analysis of circulating corrosion products, and the PWR sampling line for chemistry control from which the capillary lines are fed. From [120]*. Specifics of the figure relate to Doel unit 1, though a similar setup was used at the other 3 reactors.*

The team were careful to ensure sampling was as representative as possible, using approximately isokinetic sampling from the installed sampling line into 0.5 mm and 0.25 mm capillary tubing, to improve on non-representative sampling which had been reported in the past. The fact that transients in the reactor (such as the moving of fuel rods to effect power changes) were reflected rapidly in measured particle concentrations gave confidence that conditions within the primary circuit were accurately represented.

Additionally, activity of Co-60 and Co-58 was measured, for coolant samples as a whole and for the particulate (>2 µm) fraction, and SEM/EDX was used to measure size and analyse the elemental composition of individual particles.

5.1.2.1. Findings of the study

Figure 5.3 shows particle size distributions from one of the reactors during normal operation towards the end of cycle 3, both in terms of number density, and in terms of (estimated) relative contribution to total mass. It is interesting to note that across the size range covered, the mass contribution per micron of size range was more-or-less constant. The factor of ~ 2 decrease for larger sizes is not large in this context – indeed, the equivalent size distribution for the same reactor, towards the end of cycle 2, showed a factor of ~2 *increase* for larger sizes. If this trend continues to the smallest sizes, then the contribution from particles of 0.2 μm can be simply determined. A similar (flat) trend of mass distribution was observed by Degueldre et al. [139] over 2 orders of magnitude (~0.05 μm to ~ 5 μm) in BWR and PWR coolant.

Figure 5.4 shows changes to coolant-borne particulate concentrations over time during the startup of cycle 3, of the reactor which features in Figure 5.3. It can be seen that disturbances cause large releases of particulates, with particle concentrations peaking then decaying over time. A fit to one such period of decay is shown, giving a half-life around 4 h. Other fits were performed at various times, giving a range of half-life values, suggesting competition between deposition and other processes (such as removal by CVCS), and measurement errors caused by concomitant release by other events during the deposition. Although the plot shows only total number density, this typically correlates reasonably well with mass concentration (ppb), since the mass distribution typically remains more-or-less flat, despite the factor of ~ 300 difference between peak concentration (4.8 x 10^6 litre^{-1}, distribution plotted in Figure 5.4) and steady state concentration (1.5 x 10^4 litre^{-1}, distribution plotted in Figure 5.3. The study also revealed that even minor changes to chemistry resulted in peaking of particulate concentrations.

Figure 5.5 shows that the particle size mass distribution was not flat during cycle 1 shutdown, instead being dominated by the smaller particles.

Another point to note from the study was that particulates were not heterogeneous – for example some were Fe rich and some were Ni rich, with the latter dominating early in cycle 1 due to early release from Ni base alloys, and the former dominating thereafter, and different elements dominated at different size ranges. Less particulates were released and present in coolant at the elevated pH_{300C} value of 7.4 compared with lower pH_{300C} values.

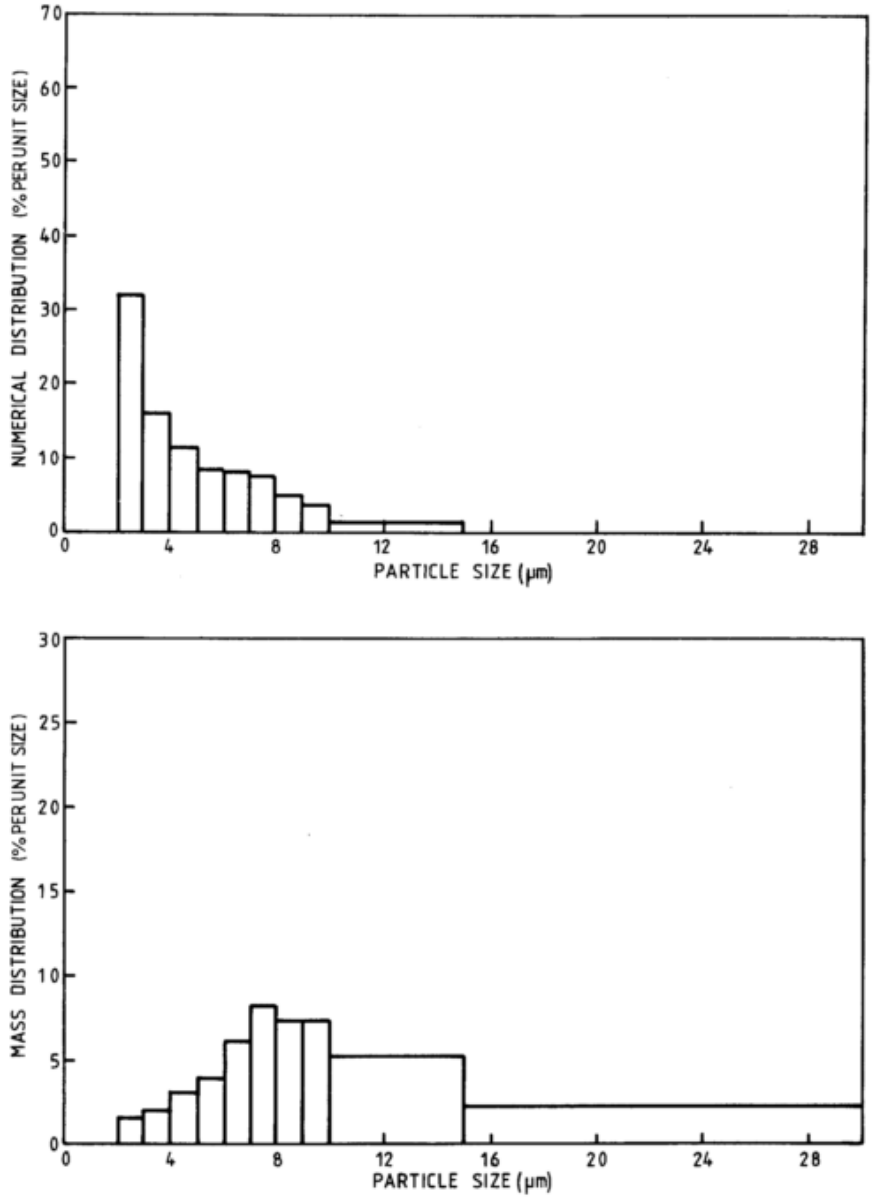

Figure 5.3. Frequency histograms, showing numerical distribution (top) and calculated mass distribution (bottom) against particle size, during normal operation of Doel unit 3 at the end of cycle 3. From [120].

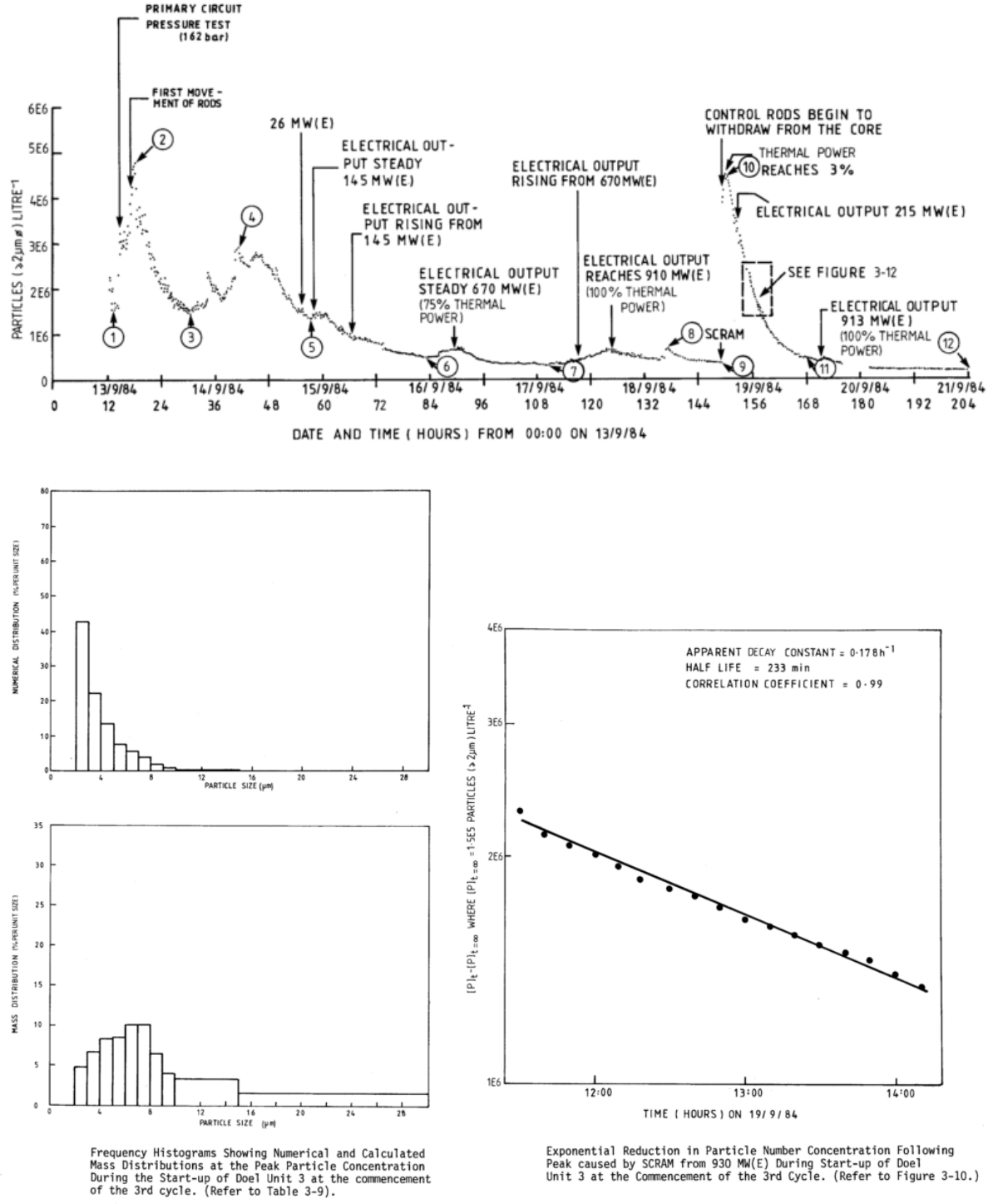

Frequency Histograms Showing Numerical and Calculated Mass Distributions at the Peak Particle Concentration During the Start-up of Doel Unit 3 at the commencement of the 3rd cycle. (Refer to Table 3-9).

Exponential Reduction in Particle Number Concentration Following Peak caused by SCRAM from 930 MW(E) During Start-up of Doel Unit 3 at the Commencement of the 3rd Cycle. (Refer to Figure 3-10.)

Figure 5.4. Monitoring of coolant-borne particulates over time in Doel unit 3 early in cycle 3 [120]*. Top: monitoring of particle number density over time during start-up of cycle 3 (first ~200 h). Notice the peaks occurring due to disturbances, such as withdrawing of control rods, and the exponential fall-off between disturbances. Left: number distribution (above) and estimated mass distribution (below), taken at the highest peak concentration (position 2 in top plot). This is comparable with that taken under normal conditions, see Figure 5.3. Right: Exponential fit to concentration fall-off following the peak caused by withdrawal of fuel rods (marked by rectangle in top plot), showing a good fit with half-life ~ 4 h. From* [120].

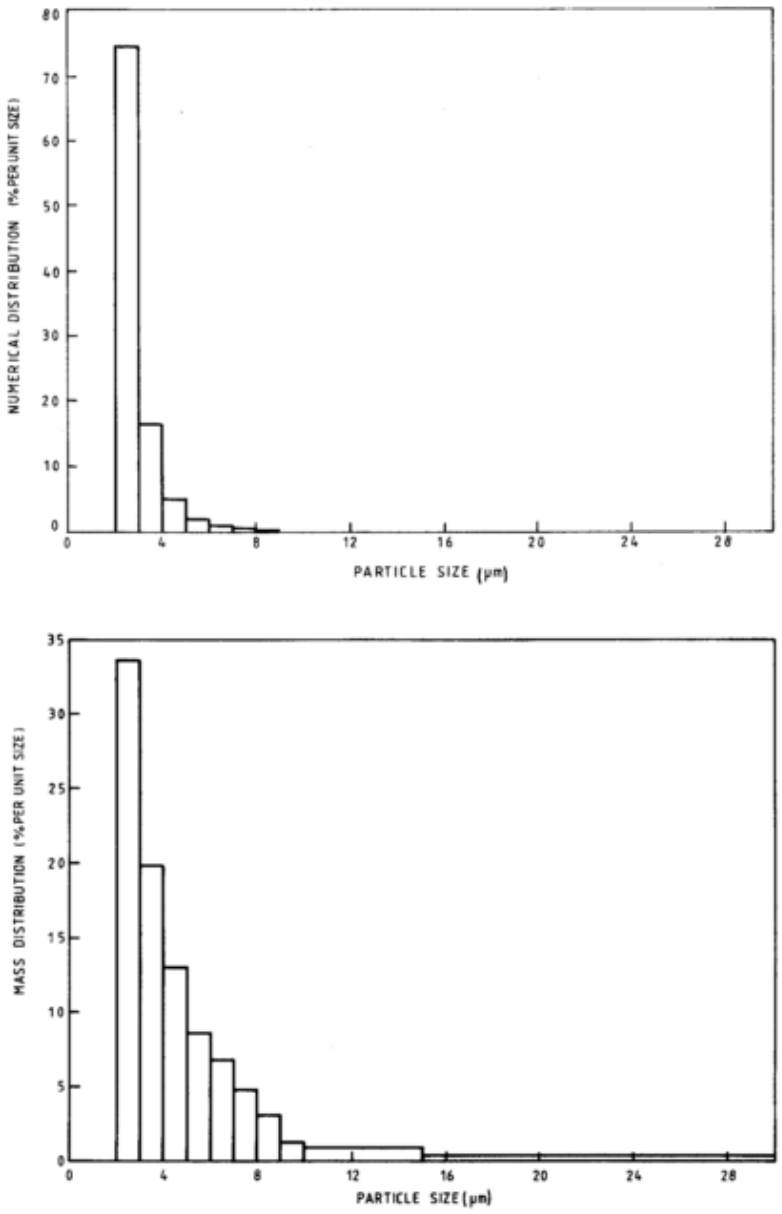

Figure 5.5. Particle size distribution for cycle 1 shutdown, Doel unit 3. In this particular case, the mass distribution is dominated by the smallest particles. From [120].

5.1.3. Study performed by Bolz et al.

One limitation of the EPRI project at Doel (section 5.1.2) was that for the most part they only studied the particulate size distribution for particles of 2 µm and above (apart from a few size distributions to 0.6 µm measured at one of the reactors). Typical measurements of circulating corrosion product from operational plant are split into 'soluble' (<0.45 µm) and insoluble (>0.45 µm) fractions, but with

no indication of the relative contributions of truly dissolved ions versus small particulates in the 'soluble' fraction. Where 'soluble' levels of a particular element exceed those expected from solubility data or models, there is uncertainty as to whether the difference is achieved through supersaturation alone or the presence of small particles (<0.45 μm), or whether the solubility data or models are wrong. Indeed, there is disagreement between different studies of magnetite solubility in hydrothermal solutions at pH_{25C} above around 9 or 10, with suspended particulate matter being proposed as the reason.

Bolz et al. [36] conducted a study to address this uncertainty about the role played by small particles in the levels of corrosion product measured in PWR primary coolant, with 'special attention to the differentiation between particulate and dissolved species' at the very lowest end of the size range, and to plot colloidal particle size distributions to complement the larger particulate size distributions of the EPRI project [120].

Numerous analytical techniques were used in this very challenging study, involving concentrations as low as the low mass ppt (part per trillion) range and particles sizes down to 10 nm.

5.1.3.1. Findings of the study

In the study, various size fractions were measured using a stack of membrane filters and ion exchange filters ('discriminating filtration'), as illustrated on the left of Figure 5.6. Results are shown in the uppermost table of the figure. Other techniques were used to complement these measurements.

The group had the surprising finding that even the tiniest size fraction of particles, less than 10 nm across, made a significant contribution to total mass: 'it was found that about 70% of iron with diameter smaller than 10 nm was dissolved', as determined by a process of 'standard addition', with the remaining 30% (about 0.3 ppb) being colloidal particles of < 10 nm.

For particle sizes above about 11 nm, Laser Induced Photoacoustic Breakdown Detection (LIPBD) was used, showing a peak number density for particles of around 11.5 nm diameter, see Figure 5.7.

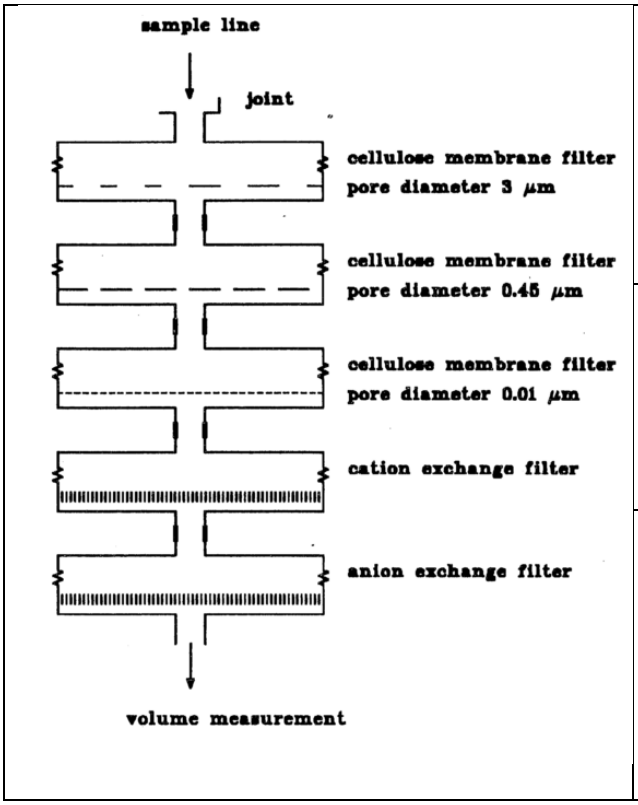

Table 1: Concentration of insoluble corrosion products classified according their diameter d [µg/kg].

Diameter/Species	Cr	Mn	Fe	Ni	Co
d< 3 µm	0.15	0.012	0.8	0.19	0.0030
0.45 µm<d<3 µm	0	0.008	0.4	0.03	0.0011
0.01 µm<d<0.45 µm	0.003	0.004	0.7	0.02	0.0002
Sum	0.153	0.024	1.9	0.24	0.0043

Table 2: Concentration of dissolved corrosion products (Ni, Co, Index "s") or particles with diameters smaller 10 nm respectively [µg/kg].

Cr	Mn	Fe	Ni	Co
< detection limit (0.05)	0.06 - 0.1	0.7 - 1 70% (s)	0.1 0.03 - 0.05 (s)	0.01 0.001 - 0.003 (s)

Table 3: Total concentration of dissolved and undissolved elements in primary coolant determined by ICP-MS [µg/kg].

Cr	Mn	Fe	Ni	Co
0.15 - 0.3	0.08 - 0.12	2 - 4	0.25 - 0.35	0.01 - 0.015

Figure 5.6. Discriminating filter apparatus used by Bolz et al. [36].
Diagram and tables taken from [36].

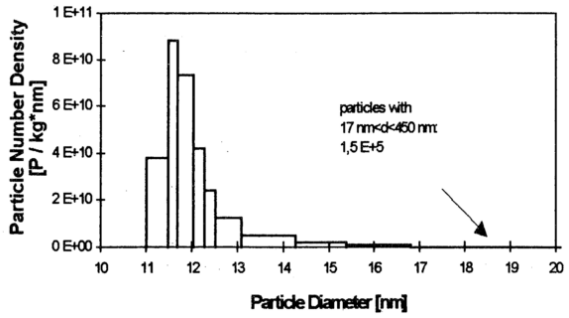

Figure 5.7. Particle size distribution, by LIPBD. Figure taken from [36].

It was observed that 'if during the discriminating filtration the filtration velocity is very slow (filtration time several hours) nearly no particulates penetrate the 0.45 µm filter', because spinels dissolve and new oxide phases are formed. (i.e. the smaller particles do penetrate but are then dissolved).

6. Literature Review

Part IV: Particle release and deposition mechanisms

6.1. Deposit formation, and deposition and release mechanisms

Various mechanisms of particle deposition and release have been shown to occur, and modelled by various authors. A common theme in these models is the consideration of deposition as a two-step process: transport of particles from bulk coolant to wall; and attachment to the wall on arriving there [11], [24], [140]. Accounting for re-entrainment, the net deposition flux can be found from

$$\frac{dm}{dt} = \varphi_d - \varphi_r$$

Where m is the mass of deposit per unit area, φ_d is deposition flux (gross) and φ_r is the re-entrainment (or release) flux from deposit back to the bulk coolant.

6.1.1. Transport of particles to (and from) walls

Most models of relevance to the nuclear industry assume turbulent bulk flow separated from walls by a thin boundary layer of coolant, across which species must be transported or transferred. There are many different phenomena which can contribute to this transport, whose relative effects can differ widely per the size of particle, as well as other particle properties such as surface charge and density.

The smallest particles, colloids, move with the fluid, and diffuse randomly (down concentration gradients) by Brownian motion. In addition, colloids may have a drift velocity towards or away from the wall, due to effects such as the following:

- Electrophoresis – net migration through fluid with (or against) electric field, for particles of positive (or negative) surface charge

- Thermophoresis – net migration down temperature gradients, due to higher energy bombardments from molecules on the higher temperature side.

Larger particles, particulates, are characterised by their non-negligible inertia in the flow. Brownian diffusion diminishes with increasing particle size, being replaced by turbulent diffusion. Particles in the inertial regime are sufficiently large that turbulent eddies can give some particles enough momentum to transit the viscous sublayer directly. Inertia also contributes to mass transfer where accelerating flow heads towards a surface briefly, by analogy to non-isokinetic sampling concerns as discussed in a previous subsection. Other effects which can provide a drift velocity for larger particles more readily than smaller ones, include:

- Gravity – terminal velocity of falling is proportional to d_p^2.
- Turbophoresis – net migration down a turbulence intensity gradient, towards walls.

6.1.2. Attachment at walls

Attachment can be characterised simply by a sticking probability, S [24]

$$\varphi_d = k_t c_b S = k_t (c_b - c_s)$$

Where φ_d is deposition flux; k_t is the mass transfer coefficient (m/s); and c_b and c_s are particle concentration in the bulk and at the surface respectively.

Alternatively, one can consider the process of attachment, for example by attractive London-van der Waals forces at close range dominating the repulsive electrostatic forces of like-charges, as one of overcoming an energy barrier by analogy with the treatment of chemical reactions, see Figure 6.1. In this case, deposition is seen as the result of two processes occurring in series: transport, with mass transfer coefficient k_m; and attachment, with the particle-wall equivalent of a kinetic rate constant, k_r. The deposition coefficient is then given as:

$$k_d = (k_m^{-1} + k_r^{-1})^{-1}$$

Where $k_m \gg k_r$, the deposition process is controlled by the attachment step,

$$k_d \approx k_r$$

whilst in other scenarios the opposite is true and the process is mass transfer controlled.

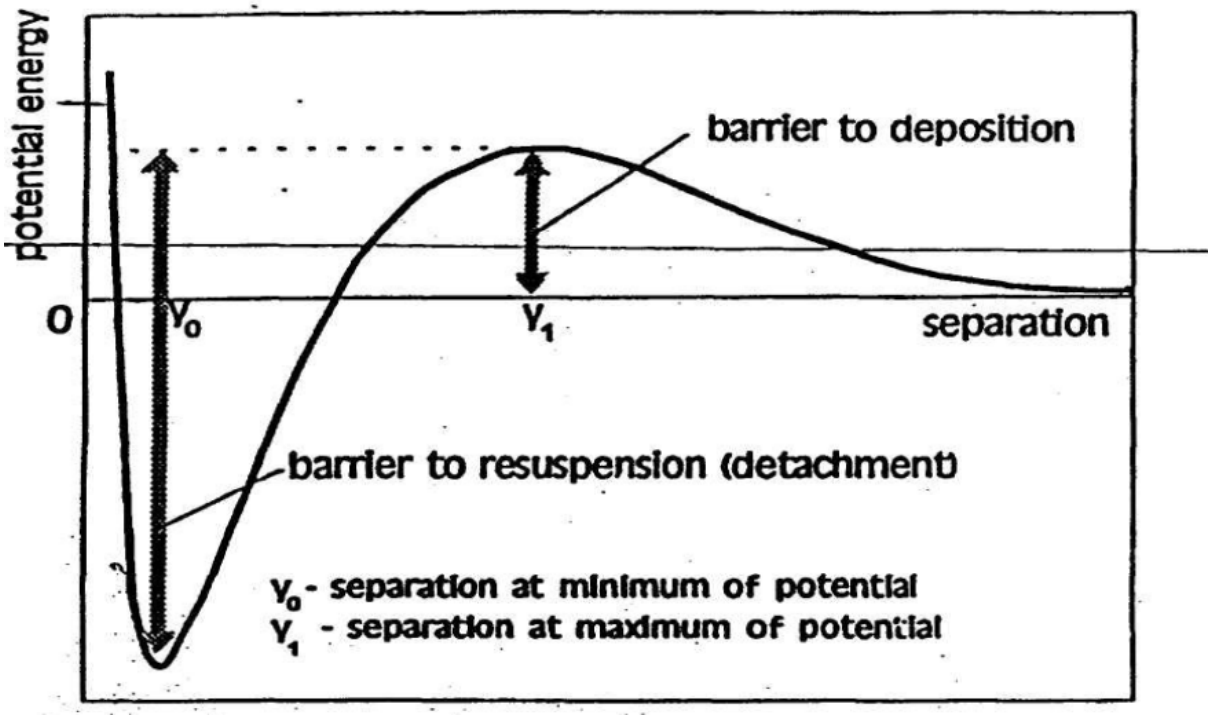

Figure 6.1. from [11]*. Energy barrier to particle deposition.*
By analogy with activation energy barrier, for chemical reactions, a kinetic rate constant for deposition can be derived from this.

6.1.3. Re-entrainment of particles

A simple assumption that re-entrainment flux, φ_r, is proportional to deposit mass, m, was made by Kern and Seaton

$$\varphi_r = bm$$

where b is the re-entrainment constant. Combined with an independent deposition flux, this gives an exponential approach to steady state deposit thickness, m^*, as

$$m = m^*\left(1 - e^{-bt}\right)$$

A characteristic time constant, $t_c = 1/b$, can be defined, giving average residence time of particles in the deposit

For deposits of appreciable thickness, it has been observed that the deposit becomes progressively more adherent with increasing depth from the surface [11]. This can be more simply modelled by splitting the deposit into two regions: a 'transient' (or labile) outer region obeying the first order kinetics of Kern and Seaton, having thickness up to a certain maximum value; and a 'permanent' (or

consolidated) layer for anything beneath that, from which particles do not release – or more complex kinetics can be used to better match experimental findings [140]. This is illustrated in Figure 6.2.

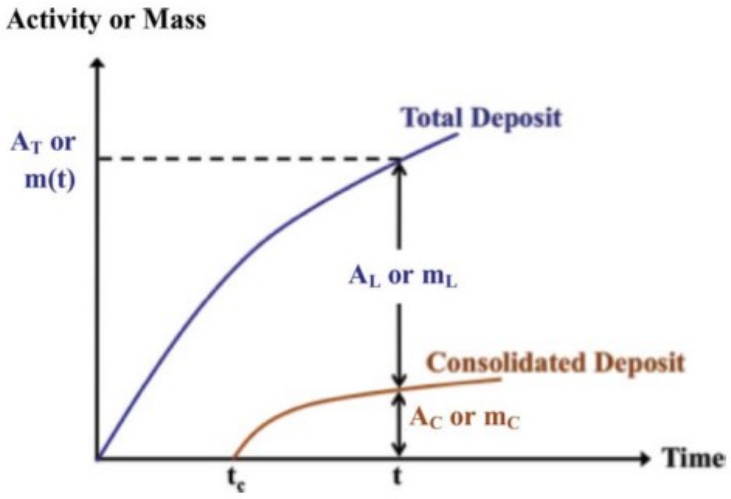

Figure 6.2. Schematic diagram showing time evolution of deposit mass, as consolidated and labile components. From [140].

6.2. Application to rig

Much of the reviewed literature concerns well-mixed, high velocity, turbulent flow; mass transfer across only a thin boundary layer; and thick deposits. This is in stark contrast with conditions of the rig. Typical conditions in the rig entailed very slow, laminar flow, with a very limited inventory of deposited particles observed. Nonetheless, there may have been more substantial deposits in tubing at locations not characterised, and levels of some elements in the coolant, such as Ni, were indicative of the presence of particles.

Under steady conditions, erosion of outer layer crystallites was not expected, but colloidal particles precipitated from solution were expected (and indeed observed on corrosion films). Gravity could be expected to be a key effect, with the uphill flow in the oxide chamber and adjacent tubing acting as settling chambers in which larger particles settle and do not pass onward. In horizontal tubing settling along the bottom surface may be expected. Electrophoresis may have caused different effects under the different pH values used in different runs, or perhaps as hydrogen concentration changed leading to a change in pHpzc. This could be the cause of unexpectedly high levels of Cr during session 6, though the steadiness of this value across many samples is suggestive of a (unexpected) solubility effect. Thermophoresis may have caused localised repulsion of particles from

the walls at the entrance to oven, and deposition at the exit. Convection currents at points of entry to and exit from the oven may have stirred up particles.

Much of the transport of particles would likely have happened during transient conditions, such as after a change in flow rate or temperature. In addition, there were a few occasions where boiling occurred, which could conceivably have been the source of crystallites of a few µm across seen on filter housing at the sampling point which appeared to be from the outer oxide layer in a heated part of the rig.

Downward force due to gravity gives particles an average drift velocity downwards relative to the coolant flow, whose magnitude can be found by equating gravitational force (net of buoyancy provided by the coolant) with drag, per Stokes' law. Assuming spherical particles of diameter d_p, density ρ_p, gives:

$$F_{grav} = (\rho_p - \rho_w).\frac{\pi d_p^3}{6} g; \qquad F_{Stokes} = -3\pi\mu v_p d_p$$

Where ρ_w and μ are density and dynamic viscosity of coolant water, g is gravitational acceleration. The condition of zero net force gives v_p as a function of d_p, and other terms, or vice-versa:

$$v_p = (\rho_p - \rho_w).\frac{d_p^2 g}{18\mu}; \quad d_p = \left(\frac{18\mu v_p}{(\rho_p - \rho_w)g}\right)^{\frac{1}{2}}$$

At 1 g/min, 200 – 300 °C, coolant flows upwards at around 10^{-7} m/s in the oxide cell, 10^{-6}, m/s in the ¼" tubing, with μ ~ 10^{-4} kg m^{-1} s^{-1}. Assuming particle density of ~ 3.5 – 4 g/ml, this gives a maximum particle size of ~ 0.25 µm which can be carried in the flow in the oxide cell, and 0.75 µm in the upward flowing portion of ¼" tubing, falling to ~0.1 µm and ~0.25 µm at 0.1 g/min. In horizontal tubing, sedimentation would be expected to be faster for larger and heavier particles, though other effects such as electrophoresis may be stronger for smaller particles.

Where deposition is not inhibited, the propagation of particles along horizontal tubing may be slow, relying on build-up of sufficient deposit along the entire length of tube to give a re-entrainment flux comparable to that for steady state. Generic precipitation of particles onto the oxide film is shown in Figure 6.3.

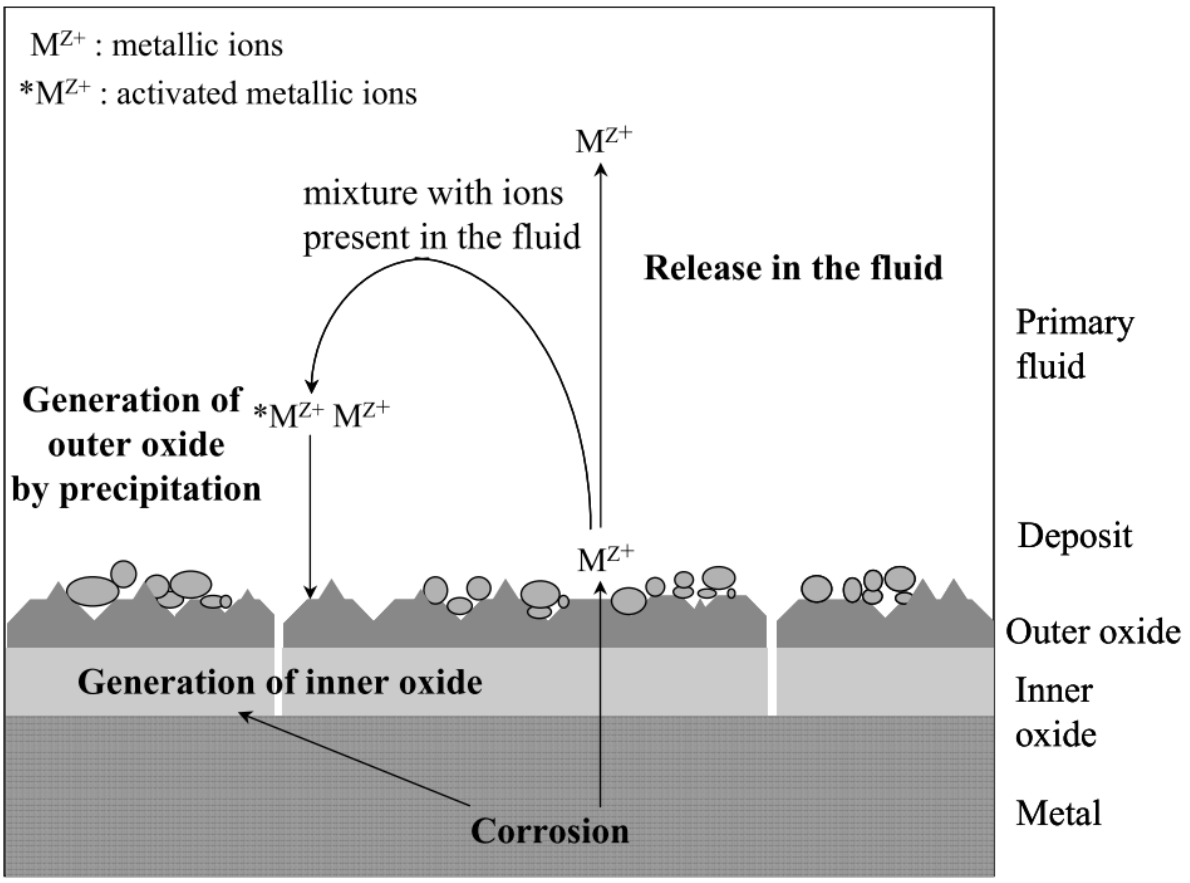

FIG. 3. Growth of the 'double' layer of inner and outer layers of oxide.

Figure 6.3. From [11]. *This is the most relevant plot to the situation in rig – deposition of colloids onto outer oxide layer*

7. Materials & Experimental Methods

7.1. Scope of work

The primary aim of the PhD project was to use a bespoke flowing Metal Oxide Solubility (MOS) rig to investigate the solubility behaviour of metal oxides which form on corroding surfaces in the primary coolant of PWRs (the motivation for improved knowledge in this area, in an industrial context, is provided in chapter 2). Within that framework, the specific methodology and objectives of the study evolved over time as discussed in section 1.2 and section 7.3.2: essentially, initial plans to study pure oxide solubility under well-defined equilibrium conditions in an inert rig, evolved into a study of the release of corrosion products from corroding surfaces of stainless steel 316L (SS316L, an alloy widely used in PWR primary circuits), which represents a non-equilibrium system in which corrosion kinetics, dissolution and precipitation kinetics, and the release and deposition of metal oxide particles, all have an effect on coolant concentrations of corrosion products, in addition to the metal oxide solubility behaviour which was the initial focus of the study.

The rig was designed and built by Jonathan Morrison, as part of his EngD project [26], for which he built a suite of experimental rigs commissioned by Rolls-Royce and National Nuclear Laboratory (NNL) for the study of corrosion product deposition and related processes in the primary coolant of PWRs. The aim of the overarching experimental programme was to provide improved understanding and data for relevant processes such as solubility and dissolution/precipitation kinetics, with a view to develop whole-plant computer models of corrosion product transport.

The rig underwent 6 sessions of use, at pH_{25C} values of 9, 10 and 11, and temperatures of 200 – 300 °C. Section 7.3 presents the metal oxide solubility rig and the methodology of its use, as originally designed and built and as modified. Section 7.4 details the methodology used for analysis of effluent from the rig, to measure concentrations of the five most prevalent alloying elements in

SS316L, by inductively-coupled plasma mass spectrometry (ICP-MS). This was the primary mode of study of the rig during operation. Additionally, a small number of effluent samples were taken in a pressurised, sealed vessel, and analysed for the volume of hydrogen gas contained therein by gas mass spectrometry, using a bespoke system designed and operated by Daniel Reed at the University of Birmingham, as described in section 7.6. These measurements were used as a validation of a model used to estimate hydrogen concentration in the rig resulting from corrosion, an important factor in determining solubility of certain metal oxides such as magnetite; the basis for this model is briefly outlined in section 7.7, and provided in full in section 17.2 in the appendices.

For all except the second and third sessions of rig use, fresh as-yet unoxidized tubing was used for the 1" section of the rig, allowing the surfaces of the 1" tubing from previous sessions to be studied and characterised under SEM. The methodology of this process is provided in section 7.9.

Section 7.2 describes the materials used over the course of the project.

7.2. Materials

7.2.1. Solid Materials, as received

The MOS rig was constructed almost exclusively of stainless steel 316L (SS316L). Manufacturer quoted composition of some of the tube stock used is provided in Table 7.1.

Table 7.1. Chemical composition of SS316L materials used for the rig

Heat# / lot # (form)		Chemical composition (weight %), as per TW Metals Ltd									
		C	Si	Mn	P	S	Cr	Ni	Mo	N	Fe
530938/36318 (1" tubing)	a	0.016	0.37	1.69	0.031	0.009	17.30	13.15	2.52	0.035	Bal.
	b	0.017	0.35	1.70	0.030	0.007	17.22	13.14	2.52	0.033	Bal.
531994/41982 (1" tubing)	a	0.018	0.42	1.69	0.029	0.009	17.31	13.12	2.53	0.036	Bal.
	b	0.023	0.42	1.67	0.030	0.01	17.25	13.12	2.53	0.032	Bal.
530598/36226 (1/8" tubing)	A	0.017	0.40	1.68	0.031	0.009	17.33	13.13	2.53	0.046	Bal.
	B	0.018	0.40	1.67	0.031	0.008	17.29	13.08	2.54	0.041	Bal.
530789/37443 (1/8" tubing)	A	0.017	0.37	1.61	0.029	0.009	17.34	13.16	2.54	0.034	Bal.
	B	0.018	0.37	1.59	0.030	0.007	17.27	13.05	2.51	0.034	Bal.
530839/37893 (1/8" tubing)	A	0.017	0.38	1.65	0.031	0.011	17.34	13.18	2.53	0.042	Bal.
	B	0.018	0.38	1.64	0.030	0.009	17.31	13.11	2.50	0.035	Bal.
Mean average	B	0.019	0.38	1.65	0.03	0.01	17.27	13.10	2.52	0.035	64.98
Standard error	B	0.002	0.03	0.04	0.00	0.00	0.03	0.04	0.02	0.004	0.08

a = unprocessed material; b = product.

The alloy was purchased from TW Metals Ltd, as 'Seamless stainless cold finished instrument tubing' and bar stock, the details of which are shown in Table 7.2. The rig was put together using Swagelok® SS316L connectors and valves. Frits for use in the reaction chamber were cut from "3AL3" sintered SS316L sheets in the Bekipor® range, manufactured by Bekaert. These frits have manufacturer quoted pore size of 3 µm.

Table 7.2. Dimensions of the SS316L bar stock and tubing used for the rig

	Bar stock dimensions (mm)		
	5 x 60 x 1000		
Tubing:	**Inner diameter (mm)**	**Outer diameter (mm)**	**Wall thickness (mm)**
1" tubing	21.082	25.400	2.159
1/4" tubing	3.048	6.350	1.651
1/8" tubing	1.397	3.175	0.889

Disc shaped nitrocellulose filters and re-usable polypropylene filter holders (from the Swinnex ® range) were purchased from Merck Millipore, in two sizes – according to filter diameter – and three different pore sizes. Properties of the filters are tabulated in Table 7.3.

The filters were all similar to one another in many respects. All were hydrophilic membranes, made from mixed cellulose esters, and of comparable thickness and porosity. The key differences were in the pore size and overall filter size. These properties combine to determine the rate of water flow through the filter, which was important since it precluded the use of the 1.3 cm filter of 0.05 µm pore size on any of the faster flow rate runs. The bubble point is an indirect measure of pore size, and is essentially the minimum differential pressure at which a continuous stream of bubbles can be pushed through the filter against a liquid – the smaller the pores, the larger the pressure that's required to prevent the liquid from filling the pores by capillary action. Another property which differed among the filter types is the level of gravimetric extractables. Extractables are defined as contaminants which are present in the final filtrate that originate from the filter or derive from the filter material. According to the website of Merck Millipore [141] extractables from filters can be of three types:

- Materials that are shed by the filter material itself.
- Residual chemicals carried over from the filter manufacturing process.
- Secondary chemistries that washed off the filter.

Aside from the shedding of organic polymers from the filters, it was not clear from the information available online which chemical elements are represented in the extractables, and whether there is a significant quantity of the metallic elements under study in this project. Study under SEM, in conjunction with EDX, showed that the filters as-received contained crystalline particles of mixed oxides containing Na and other metals. Over the course of the project, no effect was discerned on ICP-MS results due to the presence or absence of either of the three filter types of larger diameter (4.7 cm). Two ICP-MS samples were taken of ultrapure (type I) water which had been passed slowly through a recently used filter, exhibiting levels of each element only marginally above that of the type I water which had not passed through a filter. Of the smaller diameter filters (1.3 cm), only the 3.0 µm pore size was used (except for a brief period of a few hours when a 1.3 cm filter of 0.45 µm pore size was in series with said filter, in a separate housing, and was then removed because of its disruptive effect on effluent flow); levels of Fe were higher for the two effluent samples analysed with the filter installed, but this was interpreted as being due to the continuation of a trend of increasing Fe which began before the filter was installed, thought to be caused by particulates and/or colloids, and this interpretation was corroborated by Fe-rich particulates observed on the filter under SEM/EDX, which were not seen on filters before use in the rig (dissolution of particulates caught in the filter could have accounted for increased Fe levels in effluent even when particulates were too large to pass through the filter).

The website also states [142] that MF-Millipore™ filters without Triton® surfactant 'contain minimum amounts of wetting agent and have a lower water extractable content than standard MF-Millipore™ filters', therefore although the level of gravimetric extractables was not stated, it can be assumed to be less than for the other filters.

For early sample collection from the rig, and for a few other purposes, glass vials with plastic screw tops and a nominal volume of 40 ml were used. Other glassware such as pipettes, beakers and syringes were used in the early stages of the project, but their use was almost entirely eliminated by the end of session 3 of rig use.

In an effort to minimise sample contamination, glassware was replaced wherever possible by plastic equipment, on the advice of Stephen Baker (ICP-MS operator), corroborated by the absence of glassware on the list of suitable materials for trace metals analysis listed in the ASTM standard for Handling of High Purity Water Samples [143]. The elimination of glassware, in conjunction with other changes, resulted in much lower contamination in blank samples (see Table 7.8). In most or all cases, polypropylene (PP) was used, due to its wide-ranging chemical compatibility and suitability for high purity analytical chemistry.

Polypropylene (PP) test tubes of nominal volume 16.5 ml were purchased, with matching PP stoppers, from Sarstedt AG & Co., for taking rig effluent samples. Tri-pour® ultra clear PP beakers of various sizes were used for preparing chemical solutions. An adjustable volume pipettor (1-10 ml), with 1 – 10 ml PP tips, was purchased from Cole-Parmer Instrument Co. Ltd., for accurate addition of acid to samples as part of the sample preparation procedure. Disposable 10 ml piston syringes were purchased from Terumo Medical Corporation. The syringes comprise a PP barrel and plunger, and a gasket made from a highly inert thermoplastic elastomer material [144].

When preparing samples for study in the Scanning Electron Microscope (SEM), the following materials were used:

- Clear adhesive tape, for acquiring tape pull samples – Scotch® Matte Finish Magic™ Tape manufactured by 3M, 13 mm width
- Carbon adhesive discs for mounting samples
- Aluminium SEM stubs for mounting samples
- Bakelite for mounting samples
- Finely sputtered Pt or Au applied using a sputter coater, to minimise charging of samples.

Table 7.3. Properties of the filters used. Values given are as quoted by the manufacturer, except where otherwise stated. All filters below are hydrophilic

Cat. No.	Pore size	Dia.	material	Thickness	Porosity	Water flow rate (ml / min x cm^2)	Water flow rate abs. (ml / min) ‡	Bubble point at 23°C (air with water)	Gravimetric extractables
SSWP04700	3.0 µm	4.7 cm	MF-Millipore™: *cellulose acetate & cellulose nitrate*	150 µm	83%	320	5552	≥ 0.7 bar	6 %
SSWP01300	3.0 µm	1.3 cm	MF-Millipore™: *cellulose acetate & cellulose nitrate*	150 µm	83%	320	425	≥ 0.7 bar	6 %
HAWP04700 F1	0.45 µm	4.7 cm	MF-Millipore™: *cellulose acetate & cellulose nitrate*	150 µm	79%	60	1041	≥ 1.8 bar	2.5 %
HATF01300	0.45 µm	1.3 cm	Immobilon®: *cellulose acetate & cellulose nitrate, Triton®-free* †	150 µm	79%	60	80	≥ 2.1 bar	Value not given
VMWP04700	0.05 µm	4.7 cm	MF-Millipore™: *cellulose acetate & cellulose nitrate*	100 µm	72%	0.74	13	≥ 17.6 bar	1.5 %
VMWP01300	0.05 µm	1.3 cm	MF-Millipore™: *cellulose acetate & cellulose nitrate*	100 µm	72%	0.74	0.98	≥ 17.6 bar	1.5 %

† Triton is a surfactant

‡ as calculated by the author according to nominal surface area of the filters (pi * (dia./2) ^2)

7.2.2. SS316L chips manufactured using CNC milling machine

Chips of approximate dimensions 1 x 10 x 0.05 mm^3 were produced from the SS316L bar stock using a CNC milling machine, see Figure 7.1. CNC's consist of a cutting tool and a computer-controlled stage, which can be programmed to move relative to the cutting tool to carve out complex shapes from a block of metal, but in this case the product of interest was the millings, or chips (which would ordinarily be regarded as waste). A simple program was utilised in which the machine advanced a small distance between straight passes. No coolant was applied to the cutting tool, to prevent contamination of the chips, which were collected directly into a cardboard tray and transferred to glass vials until needed.

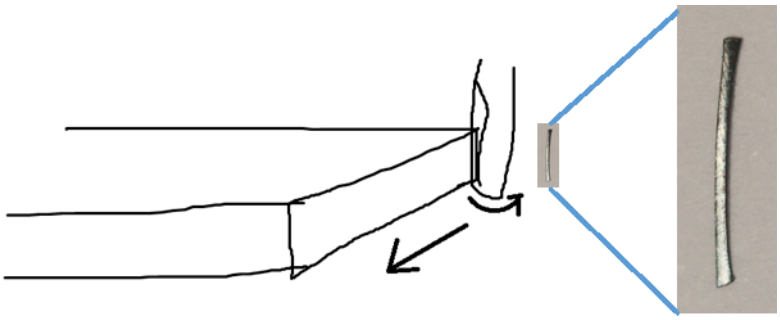

Figure 7.1. Method for producing SS316L chips.
The cutting tool rotated rapidly while moving across the face of the bar stock, removing a fraction of a millimetre from the bar on each pass, in the form of small chips. To the right of the figure is a photograph of a typical chip, showing its original orientation in the bar – the 10 mm long dimension corresponds to the thickness of the bar.

7.2.3. Chemicals and fluids

For earlier experiments, de-ionised water from a Millipore Elix® Essential 3 Water Purification System was used. This water is designated as type II [145], [146], and has a typical conductivity of 10 – 15 MΩ.cm as quoted by the manufacturer. Part-way through the project, a Milli-Q® Integral Water Purification System from Millipore was installed in the laboratory in which experiments were undertaken [147]. This type I system produced ultrapure water with a consistently maintained conductivity of 18.2 MΩ.cm – the same as theoretical fully pure H_20 – as measured online by the system's integrated instrumentation. On the rare occasions that the conductivity temporarily decreased (to 15.6 MΩ.cm on the most extreme occasion), the water was continuously extracted

from the system for a few seconds or minutes, however long it took until conductivity recovered; water extracted during this period was not used for any experiments.

Concentrated nitric acid (68 wt%) was purchased from Romil Ltd in two forms according to purity – SpA™ (Super Purity Acid) and UpA™ (Ultra Purity Acid). Elemental compositions are tabulated in Table 7.4, for all the elements of interest to this project. For the earliest experiments, concentrated nitric acid (69 wt%) of 99.999% purity from Sigma Aldrich was used. Although the total metallic impurities as stated by the supplier is ≤ 10.0 ppm, a breakdown by element is not available due to being below the detection limits of the assay technique employed. However, it is very likely that the levels of metallic impurities are considerably higher in this acid than in those from Romil: total metallic impurities in the SpA™ amount to less than 20 ppb, and less still in the UpA™ acid. For example, if impurities were shared among the various elements in the same proportions in the Sigma Aldrich acid as for the SpA acid, there would be < 500 ppb Fe as received by the customer. This is roughly consistent with Fe levels found in the blank analysed with the first batch of samples: indicative of ~ 600 ppb Fe in the acid before dilution, assuming the glass vial and the glassware used for acid transfer introduced no more than the 1.5 ppb typical of PP test tubes and plastic-ware used in later batches of analysis. In reality glassware is known to introduce more impurities, and also lower purity (type II) water was used, so the actual contribution from the acid is likely to be lower.

Table 7.4. Assay of acids purchased for the project, carried out by the manufacturer

Acid Type	Nature of assay	Chemical composition (ppb), as per Romil						
		Fe	Ni	Cr	Mo	Mn	Co	Ti
Romil-SpA™ nitric acid	Typical, at time of manufacture	<0.5	<0.1	<0.5	<0.1	<0.1	<0.1	<0.1
	Typical, as received by customer	<1	<0.5	<1	<0.1	<0.1	<0.5	<0.5
Romil-UpA™ nitric acid	Typical, at time of manufacture	<0.01	<0.01	<0.01	<0.001	<0.002	<0.001	<0.01
	Actual – Certificate of Analysis	<0.005	<0.005	<0.01	<0.001	<0.001	<0.001	<0.005

Lithium hydroxide was purchased in anhydrous powder form from two suppliers. Sessions 1 – 3 of use of the MOS rig (plus earlier runs of the corrosion rig, see Table 7.5), used powder of 98+% purity (metals basis) from Sigma Aldrich whilst powder of 99.995+% purity from Alfa Aesar was used to prepare feed water from session 4 onwards (plus later runs of the corrosion rig). The manufacturers did not provide a breakdown of elemental impurities for these powders; however, a very rough indication can be derived by assuming that the relative proportions of chemical impurities are similar

to those in Romil's nitric acid. This assumption yields indicative levels of around 2 ppb or less for the elements of interest, in a pH 11 solution prepared from the 98+% purity powder – all other solutions used would be orders of magnitude lower. Samples taken from feedwater at pH 11 contained comparable levels, though it is not known what bearing the LiOH had on these levels since the water had first been exposed to the feedwater barrel during several days of sparging. Equivalent samples from pH 9 feedwater prepared using the purer LiOH (where no contribution is expected from the LiOH) were in many cases comparable, suggesting the impurity levels may rather be representative of an equilibrium between feedwater and barrel, or the amount of particulate matter released from the steel of the feedwater barrel and 1/8" tubing.

All nitrogen gas used for the project was oxygen free nitrogen (OFN) purchased from BOC.

7.3. Metal Oxide Solubility (MOS) Rig

7.3.1. Initial Design & Build

The MOS Rig was designed and built from SS316L as the prototype model of a rig design for pure metal oxide solubility studies under hydrothermal conditions [26].

Figure 7.2 shows schematically the design of the rig. Simulated coolant is pumped against a back-pressure of around 100 bar by a High Performance Liquid Chromatography (HPLC) pump. Back pressure is maintained by a Back Pressure Regulator (BPR) close to the outlet from the rig, and a manometric module is used to smooth out any minute oscillations in pressure that may be caused by the action of the pump. The manometric module also provides online measurement of pressure, and communicates with the pump to allow a maximum pressure auto-cutoff as an additional safety feature, as well as providing feedback to the operator. The simulated coolant is heated to desired temperature in a furnace, where it resides for ~1 to 20 hours depending on the flow rate. Upon leaving the furnace, the coolant is cooled to room temperature in ¼" tubing, passes through the BPR and exits as rig effluent. During sampling, effluent drips directly into sampling vessels under gravity; at all other times effluent is collected in dump vessels for monitoring of mass flow rate.

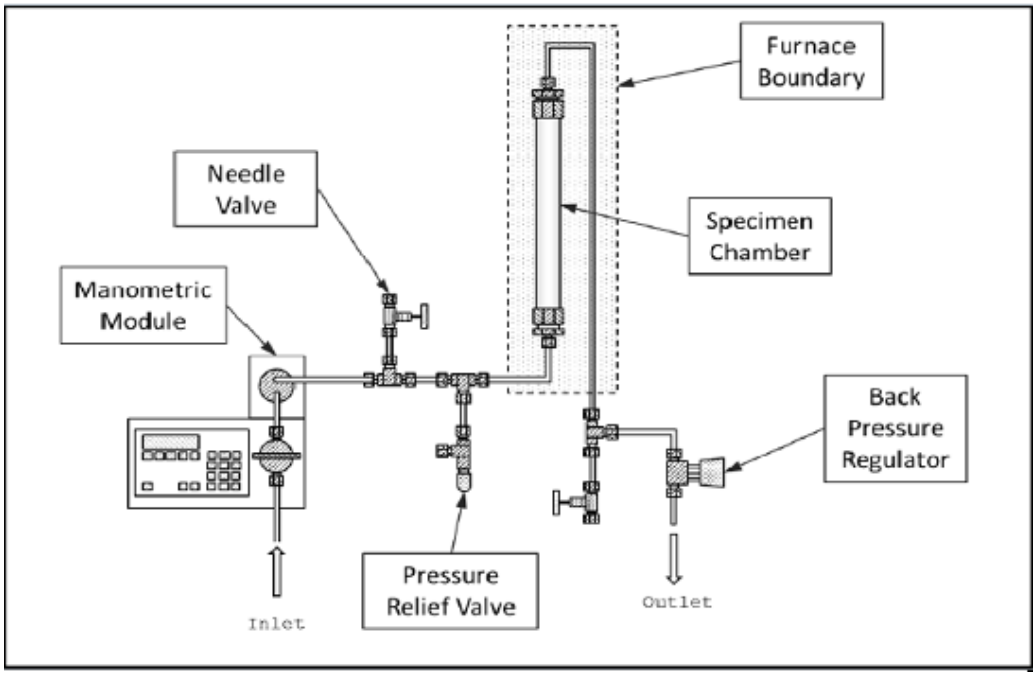

Figure 7.2. Idealised rig design for inert MOS rig, with hydrogen control and charge of oxide granules

7.3.2. Evolution of Project Aims

As well as proof of concept for the overall rig design, one of the project aims was to produce data – or at least increased understanding – of the solubility behaviour of oxides present in light-water cooled nuclear reactors, such as magnetite, or to ascertain if such studies are feasible given the fact that the material of the rig itself is not inert under hydrothermal conditions.

Initial tests were conducted to characterise the elemental impurities coming from the rig itself – with no charge of oxide added. These tests showed levels comparable with the solubility of magnetite and other oxides of interest, as well as high and time-varying levels of impurities such as Mo and Mn which could influence the solubility and create poorly-defined test conditions. There was also evidence that particulates formed a significant proportion of the elemental contributions of Fe, Ni and Cr. For these reasons, combined with a lack of the anticipated control of hydrogen (due to health and safety rules within the lab), it was determined that the rig in its current iteration was not suitable for studying solubility of pure oxides under well-defined conditions. Instead, the rig was adapted for the study of net dissolution and particulate release from corroding SS316L under conditions relevant (but not identical) to the primary coolant system of PWRs.

There are some key differences between conditions in the rig, and those in the primary coolant of a PWR, particularly regarding the coolant flow but also the simplified coolant chemistry, absence of

other materials than SS316L, absence of radiation effects, and lack of hydrogen control, among other things. There are also some key aspects of the complex, interdependent processes occurring in a PWR which are present in the rig, but absent in more fundamental research such as equilibrium solubility studies for pure oxides. In this respect, the rig acts as a half-way house between fundamental studies (for example, providing information on solubility of pure oxide phases at equilibrium) and the complex situation in a PWR (where levels of dissolved ions depend on a number of factors, including solubility of mixed oxides occurring on corrosion film, which may be metastable compared with the equilibrium phase, and kinetics limited processes in a dynamic system which is not at equilibrium – see section 2.2.5, for example). Findings from the study may be of interest to workers modeling corrosion product transport processes in PWRs, due to the possibility to study some of the processes occurring in PWRs under simplified conditions where particular phenomena may be easier to single out. Processes involving removal of oxide crystallites from the oxide film by high shear forces are unlikely to occur in the rig, meaning any processes of particulate or colloid release are likely due to other effects, to be explored as one of the aims of the project.

The rig changed over time as the corrosion film developed, affecting corrosion rates and the nature of the oxide crystallites on coolant facing surfaces, which in turn affected the net release of metal ions to the coolant and the nucleation or release, and behaviour, of colloidal and particulate matter.

7.3.3. Rig Modifications

The rig underwent several sessions of use, as detailed below. Various modifications were made to the rig itself, and the methodology of operation, in order to produce more consistent and reliable results. The c. 3 m of 1/8” flexible plastic tubing connecting the feedwater barrel to the pump inlet was replaced with 1/8” SS316L tubing between sessions 1 and 2, after a persistent problem with pump stalls due to bubble formation at the pump inlet. This change, along with other minor modifications such as increasing the pump draw time, resulted in a marked improvement in mean time to pump stall from around 10 hours in session 1 to around 100 hours in sessions 3, see Figure 7.3. Mean time to pump stall was greater than 100 h in sessions 4 to 6. In order to explore the relative contributions of Fe and other elements from different processes at the corrosion film/coolant boundary (e.g. particulate release versus release of dissolved ions), and the effect of surface area, later sessions employed a charge of SS316L chips to enable comparison with earlier sessions having an empty reaction chamber. The last two sessions also made use of filters at the point of sampling, to explore the size distribution of any particulates that may be present. During

sessions 1 to 2 the use of a sealed SS316L sampling cell was trialled, but subsequently abandoned. The cell was later used for collecting pressurised samples, from which hydrogen readings were made. The sampling cell is described in more detail in section 7.3.6.

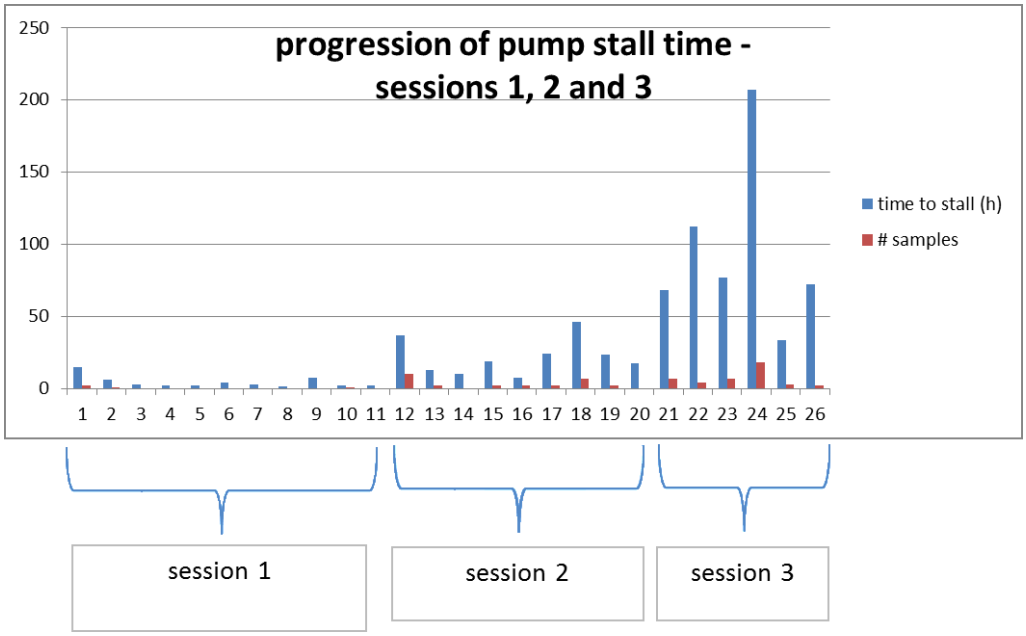

Figure 7.3. Bar chart showing improvement of pump time to stall, by session.
After session 3 there were few, if any, pump stalls

7.3.4. Feed Water Preparation

Feed water was prepared in a 50 litre SS316L barrel, using high purity water and LiOH. Table 7.5 details the source of these substances (see section 7.2.3) for each session, and the amounts used to achieve the nominal pH values listed. Since LiOH is a strong alkali with a pK_b of around -0.36 [148], rising to 1.6 at 300 °C [149], 100% dissociation was assumed, and required LiOH concentration was calculated according to the following equation

$$\text{mass (mg) of LiOH per 1 kg water} = [\text{LiOH}] * \frac{1}{\rho} * 10^6 * \text{RMM}_{\text{LiOH}}$$

Where ρ (kg/m^3) is the density of water at lab temperature, RMM_{LiOH} is the relative molar mass of a molecule of LiOH, in grams, and $[\text{LiOH}]$ (mole/litre) is the required concentration of LiOH for the pH needed, given by

$$[\text{LiOH}] = 10^{\text{pH}-\text{pK}_\text{w}}$$

For pH values of 9, 10 and 11, this gave concentrations of 0.2424, 2.424 and 24.24 ppm LiOH respectively, though for sessions 2 and 4 the values of 25 and 0.25 ppm were aimed for instead, with minimal effect on pH.

The feed water barrel was filled to around 40 – 50 kg, then the required mass of LiOH was calculated and measured out in a glass vial using a 5 point balance and added to the feed water. For sessions 2, 3 and 6 the LiOH powder was added to the water directly in the feed water barrel; for session 6, some water was held back, used to thoroughly rinse the glass vial which had held the LiOH powder, then added to the barrel, to ensure that no LiOH residue was left behind. In either case, the glass vial was checked for any visible LiOH powder remaining, none of which was observed. In preparing feed-water for session 4, which was subsequently used for session 5 as well, the LiOH was added to 40 ml of water in the sampling cell and injected into the feed-water barrel using nitrogen gas pressure. In this case, the water in the feedwater barrel and sampling cell had been pre-sparged with nitrogen in an effort to prevent any Li ions being lost from solution to salts such as $LiHCO_3$ or Li_2CO_3 by reacting with carbonic acid in solution. CO_2 from the atmosphere dissolves in water, forming carbonic acid (HCO_3^- and CO_3^{2-} ions and H_3O^+ counter-ions); it was suspected by the author that nitrogen sparging over several days (as practiced) could remove these ions, and subsequent salts formed, but results from sessions 4-5 and session 3 were compared for any differences which might suggest that pre-sparging before LiOH addition was beneficial.

Table 7.5. Variations in feedwater preparation methodology according to session #

Session info		Source chemicals		Quantities			Measurements	
#	pH	Water	LiOH, % purity	Water (kg)	LiOH (mg)	pH (calc)	Cond. (µS/cm)	Other (pH, O_2 conc.)
1	7*	Type II	-	25	-	-	2.5-4.5 † (effluent) 3.5 (pump inlet)	-
2	11	Type II	98+	49.85	1247 (1)	11.01 (0)	190, 274 (effluent)	pH ~ 10-11 (f'w' from barrel, UI paper)
3	9	Type I	98+	40.02	9.7 (2)	9.00 (1)		~pH 7 - 9 UI paper
4 / 5	9	Type I	98+	49.20	12.4 (2)	9.02 (1)	1.4 (effluent)	O_2 conc. < 10 ppb (feed water)
6	10	Type I	99.995+	49.40	119.7(1)	10.00 (0)		~9.7
CR 1 #1	10	Type I	98+	~100?	[To 2.5 ppm]	~10.01		
CR 2#1	10	Type I	98+	~100?	[To 2.5 ppm]	~10.01		
CR 1 #2	9	Type I	98+	~100?	[To 2.5 ppm]	~9.01	1.3 - 1.4 (effluent)	
CR 2#2	11	Type I	98+	~100?	[To 2.5 ppm]	~11.01	110 (effluent)	

† session 1 conductivity readings are probably overestimates because the technique of measuring low conductivity had not yet been perfected at that stage (as judged by inability to get readings of the type I water of lower than about 1 µS/cm, when measurements of 0.2 and below were achieved later after very thorough rinsing of beakers and the conductivity probe)
* pH of high purity water is susceptible to deviate slightly in the presence of any dissolved ions

Since LiOH is known to be hygroscopic [150], exposure to the air was limited as far as possible to ensure that weighing remained an accurate method. The 99.995% purity LiOH was only ever opened in a dry atmosphere of nitrogen in a glove bag, to extract a little more than was required, before weighing out the required amount from that subsample as described above.

Feed water was sparged with nitrogen for at least 1 hour per kg of water before use in the rig, and sparging continued throughout the course of each session of rig use, see Figure 7.4.

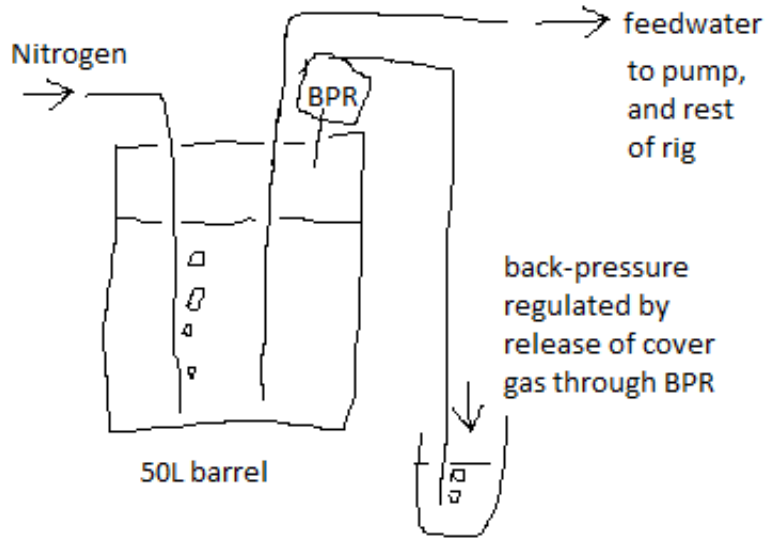

Figure 7.4. Nitrogen-sparging of feed water and feed water barrel setup.
It was initially intended that hydrogen would be used instead of nitrogen, but this was not possible in the time-frame of the project due to health and safety rules within the lab.

The room temperature pH was measured for a few samples of feedwater and found to be as expected, within errors, which were unfortunately quite large due to the effect of carbonic acid on pH values of feedwater and effluent, on contact with CO_2 from the atmosphere. Conductivity readings were also taken at room temperature using a Jenway 4520 conductivity meter. Table 7.5 also includes some information about the feedwater used in the corrosion rate rigs from which a few samples were taken, for completeness. Feedwater was prepared in these rigs in the same way as for the MOS rig. At 25°C, the molar ionic conductivity of LiOH in pure water can be calculated as 237 mS/cm $(mol/L)^{-1}$ for dilute solutions, using data from [151], giving conductivity values 237 µS/cm, 23.7 µS/cm and 2.37 µS/cm for pH 11, 10 and 9 respectively, but full equilibration with CO_2 in the air causes conductivity to fall to 87 µS/cm, 8.7 µS/cm and 1.0 µS/cm respectively (using data from [152]) as pH values fall to 8.3, 7.3, and 6.3. The decrease in conductivity occurs because the number of Li^+ ions remains the same, whilst the counter ions which are initially OH^- ions (with a high value of ionic equivalent conductivity, at 198 mS/cm $(mol/L)^{-1}$) are replaced, primarily by HCO_3^- ions (with a lower value of ionic equivalent conductivity, at 44.5 mS/cm $(mol/L)^{-1}$). The fact that pH readings, and in some cases conductivity measurements, were lower than would be expected for a LiOH solution as prepared, can be explained by the above effect; higher than expected readings may be due ions released from the stainless steel tubing, or contamination from the vessels holding the coolant. The above calculations neglected the effects of non-zero ionic strength on calculated

conductivities, since even the largest deviation (for Li^+ ions in pH 11 coolant) would only have been 3% (according to equation (16) in [151]).

Before each session, the rig was flushed with nitrogen gas to displace any oxygen in the tubing. Upon opening the 3-way valve at the pump inlet, the rig naturally part-filled with water under back-pressure from the feedwater barrel (typically ~0.7-0.8 barg). The pump was then switched on and primed using a syringe of water at the inlet, before switching the 3-way valve back to the line from the feedwater barrel. After around an hour, depending on the flow rate, the nitrogen within the rig began to be pressurised by the advancing coolant, and the pressure increased, rising relatively rapidly once the rig was filled with water – at this point, water started to release through the BPR and exit the rig. The oven was set to the desired temperature and the session commenced. In the first few sessions of use samples were taken in the first few hours to compare with later samples and ascertain the timescale over which results begin to settle.

7.3.5. Reaction Cell

Figure 7.5 shows the reaction cell, or reaction chamber, in more detail. The cell was around 30 cm tall, constructed from 1" SS tubing, and connected with Swagelok fittings to ¼" tubing at each end. A 3µm sintered SS316L frit was fitted at the top and bottom of the cell, and a charge of SS316L chips was added to the cell in sessions 5 and 6 only. In all sessions, the sole source of Fe and other metallic elements (except for Li) was the corroding surfaces of SS316L, particularly in the hot part of the rig where dissolution kinetics are much faster. The frits, fittings and ¼" tubing within the oven all contribute to this, as well as the walls of the reaction cell. The vast majority of the residence time in the oven is spent in the reaction cell due to its large volume, but in the ¼" tubing there is less distance to diffuse from the wall to the centre of the flow. The implications of the geometry in terms of simple dissolution are explored in chapter 8. The corrosion film can be seen as a source of Fe and other metallic elements via dissolution; more accurately however, the prevailing view in the literature is that metallic ions diffuse through the protective inner layer oxide from the underlying alloy, and the outer oxide layer grows from saturated or slightly super-saturated solution in the boundary layer (so the oxide film is a net sink of ions, although it is thought to be a source of particulate matter).

7.3.6. Sampling Cell

The sampling cell (Figure 7.6) was of a similar design to the reaction cell, and was originally intended for taking samples. Instead of dripping directly into a sampling vessel, effluent from the rig was collected in the sampling cell until it became full and pressure started to build. At this point the valve to the sampling line was closed, causing any subsequent effluent to flow along an alternative line known as the 'dump line', via a BPR set at slightly higher pressure than that of the sampling line. This setup took on board advice from previous studies to ensure a flow bypass, so that particulates would not build up during a period of no flow (stagnation) between samples. However, there was still stagnation in the section of tubing leading from the tee to the sampling cell, and the cell itself, between samples. Samples taken in this way could not avoid any transient present when flow first starts along a section of tubing which was previously dry or stagnated. Indeed, early samples taken in this way proved unreliable.

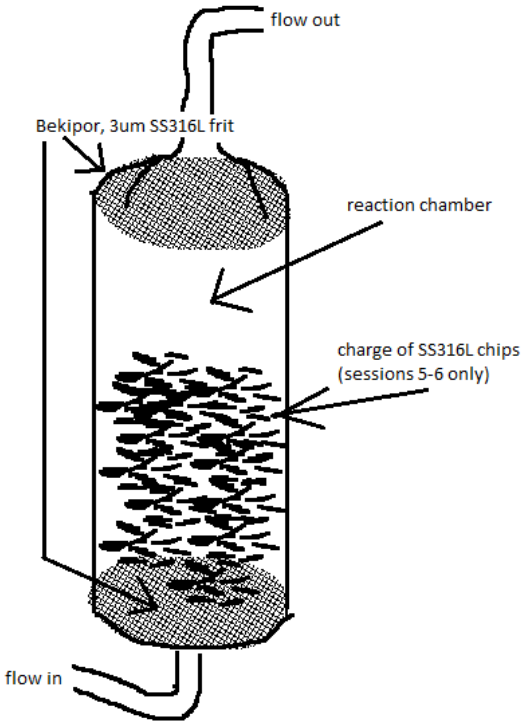

Figure 7.5. Reaction Cell.
The cell was approximately 33 cm tall, with a nominal wetted surface area of ~2 dm^2. Internal volume of ~120 ml made up the bulk of the rig's volume, and thus also residence time of the coolant. During sessions 1 – 4, the chamber was left empty of any oxide charge save for the oxide film naturally forming on the stainless steel walls. For sessions 5 and 6, a charge of SS316L chips was added resulting in a ten-fold increase to the nominal surface area of corroding steel. For sessions 1-3 the same reaction cell was used; from session 4 onwards a fresh reaction cell was used for each session of rig use.

After session 2, no further use was made of the sampling cell or the dump line for these purposes, with effluent instead dripping directly into sampling vessels. This ensured that there could no longer be any transient effects on the flow as a direct result of sampling. The dump line was retained as an additional safety feature but not used under normal operation. As discussed in chapter 9, the sampling cell was used later for taking pressurised samples, from which the dissolved hydrogen content could be measured, and also for feed-water preparation in session 4.

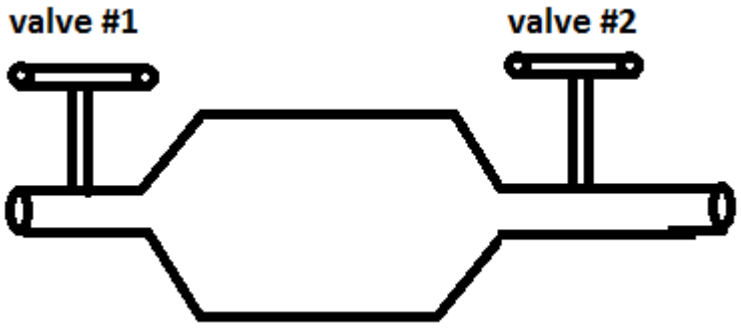

Figure 7.6. Sampling Cell.
Constructed entirely of SS316L, the thinner tubing was from ¼" stock and the thicker tubing in the central portion was 1". Total volume was around 40 ml.

7.3.7. Scope of Rig Use for this Project

The rig underwent 6 sessions of use, as detailed in Table 7.6. During sessions 1 and 2, modifications were made regarding the operation of the rig, as well as methods of sampling and preparing samples for analysis by ICP-MS. These early sessions did not produce reliable results (apart from Mo and Mn levels), and served as practice for later sessions of rig use. They are important to bear in mind, to give context to later results, as the history of the rig could influence its later behaviour – particularly with regards to the pH and temperature conditions previously used and the amount of time allowed for a corrosion film to develop under hydrothermal conditions in the hot parts of the rig. For session 3, the condition of the oxide film on the reaction cell was influenced by conditions in sessions 1 and 2. From session 4 onwards, a new reaction cell was used for each session, along with new frits, to allow better comparison between the different sessions. Elapsed time under hydrothermal conditions (in this case: ≥200 °C) was considered for each reaction cell as one of the variables of interest when analysing the results. Other independent variables considered were the flow rate, and the presence or absence of SS316L chips in the reaction cell and filters at the point of sampling – as well as the primary variables of temperature and feedwater pH.

Table 7.6. Sessions of testing

#	pH	T (°C)	flow (g/min)	filters	chips	new cell	duration, T≥200 °C	#samples analysed
1	7	Room temp, 260	1, 2	No	No	Yes	6 days	4
2	11	300	2	No	No	No	12 days	10
3	9	200, 250, 300	0.1, 0.5, 1, 2	No	No	No	28 days	30
4	9	200, 250, 300	0.1	No	No	Yes	70 days‡	43
5	9	200, 250, 300	0.1, 0.5, 1	Limited	Yes	Yes	85 days*	39
6	10	200, 250, 300	0.1, 0.5, 1	Yes	Yes	Yes†	77 days	79

‡ only samples taken during the first 70 days of flow were analysed. This period was followed by a further 78 days under flowing conditions at ≥200 °C, and 12 days under zero flow – of which 6 days were at room temperature. The session ended with 12 days at 315 °C, 0.05 g/min, followed by 2 days at 315 °C, zero flow.
* followed by 21 days at 200 °C, zero flow.
† in addition, the section of ¼" tubing leading up to the reaction cell was replaced, due to damage.

The initial tests undertaken with no additional charge of oxide showed interesting time-varying dependence on factors such as flow rate and temperature. A decreased level of Fe and Ni at slower flow (despite laminar conditions) was indicative of the presence of particulates, at levels which seemed to be fortuitously close to those expected from literature studies of solubility (i.e. fully dissolved), at least under some conditions. In order to investigate this further, conditions employed during sessions 3 and 4 were replicated in session 5, but with a charge of SS316L chips – millings from a CNC Miller. The chips served to increase the surface area of alloy held at temperature by a factor of about 10-fold, and also decrease the distance dissolved cations must diffuse through to saturate the flow. Comparison of results from these tests against the earlier tests enabled the investigation of questions such as "is the level of particulates in flow proportional to corroding surface area or does it reach a steady state?" Session 6 replicated session 5, but using pH 10 feedwater. Filters of different pore sizes were used at the point of sample collection in these later tests: to get an idea of the size distribution of any particulates present, based on the impact of filtration on the elemental analysis of rig effluent; and to get a qualitative characterisation of the particulates present, based on SEM and EDX observation of the used filters. Filters of the smaller diameter (1.3 cm) were used to a limited extent during session 5, and also on the corrosion rate rig, but problems were experienced with pressure build-up behind the filters, sporadically released by a burst of flow. During session 6, the use of larger-diameter (4.7 cm) filters eliminated these problems and filters were used extensively. For each set of conditions within the rig, at least two samples were taken under each of four filter conditions at the sampling point: no filter; 3.0 µm filter; 0.45 µm filter; and 0.05 µm filter.

7.3.8. Supplementary Samples Taken from Other Similar Rigs

In addition to the samples taken from the MOS rig, a few samples were taken from other rigs of a similar construction, used by Jonathan Morrison [26]. The two corrosion rate rigs had the same overall design as the MOS rig, including an identical setup for the preparation of feedwater, an identical pump and BPR, identical SS316L ¼" tubing and fittings, and the same method for heating the water (i.e. residing in a furnace). The key differences lay in the configuration of the tubing within the oven. In the corrosion rate rigs, the large-volume (~120 ml) reaction cell was absent, and instead there were several smaller cells containing rectangular corrosion coupons, of SS316L or in some cases SS304. There was a complex system of valves to allow online removal of coupons, with the result that the simulated coolant left and re-entered the oven several times during its transit through the rig. Another rig used by Jonathan Morrison, known as the 'Hot Loop', was designed for the study of electrokinetic deposition of magnetite at flow restrictions under high velocity flow in hydrothermal conditions. Conditions were very different from those of the MOS rig, but two samples were taken to give an indication of the level of particulate or colloidal Fe and Ni can be present under conditions more favourable to their formation.

In all, 8 samples were taken from the corrosion rate rigs, including two with filtration at the point of sampling. Two samples were taken from the 'Hot Loop'.

7.4. Elemental Analysis of Rig Effluent, by ICP-MS

Rig effluent was primarily analysed for total elemental levels of various metallic elements by Inductively Coupled Plasma Mass Spectrometry (ICP-MS).

7.4.1. Collection of Samples

During early use of the rig (sessions 1 and 2), a variety of sampling methods were trialled. The initial design of the rig involved the use of a sampling cell (s.c.), which was filled until it became pressurised. Some of the contents were then decanted into a glass or plastic sampling vessel for analysis. Other techniques employed involved: direct collection – sample drips from the exit point of the rig into sampling vessel under gravity; or using the sampling vessel to scoop a sample from a much larger 'dump' beaker (which is used to catch the effluent exiting from the rig, for mass flow rate monitoring and eventual disposal). Various sampling vessels were used: glass vials, and several different types of plastic test tube. There were two different exit points from the rig, known as the

'dump line' and the 'sampling line'. To begin with, the dump line was used for ordinary flow, for mass monitoring; and the sampling line was used for taking samples in the s.c. In this way, the dump line acted as a bypass, so that it was not necessary to stop the flow when not taking a sample.

After the first two sessions, the procedure for taking samples was standardised, having explored different methodologies in the previous sessions and chosen the most appropriate one. Sarstedt test tubes of 16.5 ml nominal volume were used (see section 7.2.1), to collect samples of between ~4 and ~12 ml dripping directly from the 'sampling line'. From session 4 onwards, the dump line was never used (except immediately before and after one-off hydrogen samples in the s.c., see section 7.6.1), and all samples were taken directly from the sampling line. Any effects from stagnant water in the sampling lines were thus avoided. During session 3, however, flow was ordinarily routed along the dump line, but diverted to the sampling line up to around 20 minutes before each sample was taken to provide some flushing of the stagnant water in the sampling line. For samples where the shortest amount of flushing time was allowed, elevated levels of Cr and Mn were observed, as discussed in section 8.2.7. The number of samples from each session which were analysed by ICP-MS is listed in Table 7.6.

Dust shields were fashioned from A4-sized plastic punched pockets, and periodically replaced, to protect samples from airborne dust.

Each sampling vessel was weighed to 0.01 g precision before and after filling with the sample: in this way the sample mass was determined.

Feedwater samples were taken during sessions 4, 5 and 6 by the following method. At the entrance to the pump, a 3-way valve was located, for the purposes of priming the pump in the event of a stall. A Terumo disposable plastic syringe was thoroughly rinsed, first with the highest available purity water (the outside was rinsed and the inside was flushed by drawing and ejecting water), and then with feedwater (by drawing and ejecting feedwater from the 3-way valve), before taking a sample of feedwater from the 3-way valve. The sample was then ejected into a Sarstedt 16.5 ml PP test tube, and treated like any other sample.

To investigate the possibility of any contamination being introduced to feedwater samples by collection and ejection via syringe, samples called "syringe blanks" were taken shortly before or after some of the feedwater samples, by rinsing and flushing the syringe with type I water drawn directly from the source, then drawing a sample directly from the source (i.e. from the stream of water as it fell under gravity into a plastic tray rather than from the water collected in the plastic tray). The results of these were used for direct comparison, and no adjustment was made to feedwater samples based on the results of syringe blanks.

For session 2 a glass syringe was used to take one feedwater sample in the manner described above, decanted into a glass vial rather than a test tube. In a similar manner, a sample was taken from the feedwater barrel, drawn into a glass syringe at a valve there.

7.4.2. Preparing test tubes

The glass vials and plastic test tubes used for the earliest samples (sessions 1 - 2) were simply water-rinsed before use. During session 3, Sarstedt PP test tubes were used having been soaked for at least a week beforehand in type 1 water in a 5 litre glass beaker, followed by several water rinses prior to use.

For session 4 onward, all samples were taken in Sarstedt PP test tubes which had been acid soaked per the procedure described below, which is an adaptation of ASTM D4453-11 [143]:

Test tubes were left to soak in a covered 5L glass beaker filled with type I water for at least a week, followed by a 48 hour soak in 1:1 (by volume) concentrated nitric acid:water mix, and finally a soak of at least 48 hours in type I water. After the minimum 48 hour period, test tubes remained in water soak until needed. Apart from the initial water soak in a glass beaker, 'soak' stages involved the internal surfaces of the test tubes only. Between each stage, and immediately prior to use, test tubes were rinsed at least three times in type I water. This process utilised PP tripour beakers, the pipettor with PP tip, and SpA nitric acid from Romil. Test tubes were prepared in sets of around 30 and a note was made of which samples and blanks were from which set, in case of significant variance between sets. Since no such significant variance was found, samples were not discriminated according to which set they came from when analysing the results.

7.4.3. Acidifying Samples

Samples were acidified in batches using nitric acid in order to prepare them for analysis in the ICP-MS instrument. As well as modifying the pH, and ensuring that all the cations in the sample stay in solution, nitric acid acts as a matrix modifier and is an important part of the preparation for ICP-MS analysis. For batch 1, the nitric acid from Sigma Aldrich was used; for batches 2 and 3, SpA nitric acid from Romil was used; and for batches 4 and 5, Romil's UpA nitric acid was used. Estimated upper limits of Fe contributions from each of the acid types to the samples are ~10 to 20, ~0.01 to 0.02, and ~0.00 (i.e. <0.005) ppb respectively.

Table 7.7 summarises each batch of samples analysed, including which sessions (or other rigs) samples were taken from, and any distinguishing features of the batch; a full sample by sample listing with ICP-MS results is provided in the Appendices (Chapter 18).

Table 7.7. Batches of rig samples sent for analysis.
The use of the terms session 3a and session 3b is for convenience, merely indicating that early samples were processed in one batch and the remainder were processed in the following batch

Batch Number	Feed water conditions	Number of samples	Features of the batch / sessions covered
1	pH 7, 260 °C (session 1)	3	High contamination of blank Practice of technique
	pH 7, 24 °C (session 1)	1	
	[blanks]	1	
2	pH 9 (session 3a)	10	Used plastic test tubes. 4 blanks for average and s.e. One duplicate sample analysed to indicate error from the ICP-MS instrument
	'Hot loop' rig	2	
	[blanks]	4	
3	pH 9 (session 3b)	19	Tested a procedure for cleaning the test tubes with acid – levels of Fe and other elements significantly decreased in blanks utilising the new procedure.
	pH 11 (session 2)	10	
	pH 11 feedwater	2	
	Corrosion rate rigs	4	
	[blanks]	9	
4	pH 9 (session 4)	75	Session 4 used 0.1 g/min flow rate (c.f. 1 – 2 g/min previously), and testing over several weeks at same conditions.
	pH 9 feed water	6	
	[blanks]	11	
5	pH 9 (session 5)	39	Limited use of filters, on samples from corrosion rigs and session 5. Extensive and systematic use of filters on session 6 samples. Session 5 replicated sessions 3-4, but with 10x more surface area due to SS316L chips. Session 6 replicated session 5, but at pH 10.
	pH 9 feed water	8	
	pH 10 (session 6)	89	
	pH 10 feed water	10	
	Corrosion rate rigs	4	
	[blanks]	18	

The methodology for acidification was developed and improved with each batch. Essentially, a stock solution of 10% (v/v) concentrated nitric acid was prepared freshly for each batch (that is, as-received "concentrated" nitric acid, of ~68-69 wt%, diluted to one-tenth of its concentration volumetrically). This stock solution was then added to samples in the volume ratio 1 part acid to 4 parts sample, to give an overall matrix of 2% concentrated nitric acid (v/v) as required by the ICP-MS technique. Strictly speaking, the ratio of importance – 5 ml of acidified solution for every 1 ml of 10% conc nitric acid added – does not equate to exactly a 4:1 ratio of sample:acid, because some volume can be gained or lost on mixing fluids; however, the discrepancy is small in this case, especially compared to other sources of uncertainty and error.

Batch 1 was prepared quickly, as a trial run of the technique of preparing samples for ICP-MS analysis, and to give an early indication of the levels of each element to expect from the rig. Due to a

misunderstanding, the required acidification of samples was taken to be 2% of the anhydrous nitric acid (i.e. 100% w/w rather than as-received "concentrated" 68-69% w/w), and on a w/w basis (rather than v/v as was actually required); in addition, to simplify the method for this first batch, the density of nitric acid was assumed to be 1.0 g/ml at all concentrations. As a result, the acidified samples had a concentration of around 3% (v/v) concentrated nitric acid.

Using glass beakers and glass pipettes, 20 ml concentrated nitric acid was added to 120 ml type II water to make the stock solution, of which 5 ml was added to 20 ml of fluid from each sample (from each ~ 25 – 35 ml sample, 20 ml was transferred to another glass vial for acidification). The relatively high levels of contamination for batch 1 compared to later batches were thought to be largely due to the lower purity acid and water used compared with later batches.

For batch 2, a high precision volumetric glass flask of 1000 ml volume was used to mix the stock solution of 10% concentrated nitric acid. The volumetric flask was filled to about half way with type I water. Around 150 ml of nitric acid was poured into a glass beaker, from which 100 ml was transferred to the volumetric flask using a 20 ml glass pipette. Water was carefully added until the flask was filled to 1000 ml, after allowing time for mixing; the last few drops were added by pipette. The flask was weighed before and after filling, and thus the density of the stock solution was measured, at around 1.05 g/ml. All samples and blanks acidified for batch 2 were filled to exactly 12.0 g (which equals 12.0 ml at lab temperature), by trial and error in the case of blanks, and by careful monitoring of mass during sampling for the rig effluent samples. In this way, exactly 3 ml of stock solution was required to be added each instance for acidification – a 3 ml glass pipette was used for this purpose – and the volume transferred was also monitored by mass, ensuring the mass increase was close to the expected value of 3.15 g each time. All samples and blanks were in water-rinsed Sarstedt test tubes. After acidification, samples from batch 2 were split into two, by pouring half of the sample into a fresh (water-rinsed) test tube, as it was mistakenly believed that two separate samples would be needed in order to cover the full range of seven elements analysed for; in the event, this was achieved by simply running each sample twice. One such duplicate sample (JH-03-08-dupl) was analysed along with its partner to corroborate or otherwise the quoted standard error of ~ 5% for the ICP-MS instrument; another (JH-03-09-Mo) was analysed along with batch 3 after being left un-refrigerated in the lab for several months, to investigate the effect of being left un-refrigerated for extended periods.

Batch 3 contained samples in various vessels from session 2 – these were all transferred to water-rinsed Sarstedt test tubes before acidification; the remainder of samples were from session 3 and thus already contained in water-rinsed Sarstedt test tubes. Glassware was replaced by plastic-ware wherever possible in the preparation of samples. ~50 ml of concentrated nitric acid was poured into

a tripour PP beaker, from which 20 ml was transferred to another tripour PP beaker (with volume graduations to 250 ml) containing ~150 ml water, using a pipettor with PP tip. This was topped up with more water to reach 200 ml total volume of stock solution. For each sample (and blank), the required addition of 10 % conc nitric acid was calculated using the ratio 1.05 g acid per 4 g sample (that is, 1:4 volume ratio, using the 1.05:1 ratio of densities as measured during batch 2 preparations), and then added using the pipettor. Desired and actual masses of stock solution added were recorded, and were observed to be within at most 2 % of each other for every sample.

Batches 4 and 5 were prepared in like manner to batch 3 with minor modifications. Larger volumes of stock solution were required due to greater numbers of samples; stock solution was prepared in an empty used bottle of SpA nitric acid, known to be very clean since it had been used to store ultra-clean acid; and the nitric acid used to prepare the stock solution was poured directly into the used SpA bottle, thus avoiding unnecessary contact with any surfaces where leaching of metallic elements may occur. Several hundreds of grammes of water were introduced to the used SpA bottle, directly from the source, then sufficient nitric acid to make up the required amount of stock solution, or more, was poured directly from the nitric acid bottle, then the mixture was topped up with water to the required mass, based on how much nitric acid had been added. The pipettor was used for the last few grammes of water, with water drawn directly from the stream of water coming from the source of type I water. Tables of nitric acid w/w concentration versus density data were used to infer the mass ratio of concentrated nitric acid to water required for a 10% (v/v) concentrated nitric acid stock solution. A ratio of 13.35 : 86.65, i.e. 13.35% (w/w) concentrated nitric acid, was determined and used for preparation of stock solution for batches 4 and 5.

With each batch a number of blank samples were acidified, using the highest available purity of water (type I from batch 2 onwards) in place of rig effluent, in order to give an indication of the levels of each element introduced by the sampling and acidification process, and the variances thereof. Typical Fe levels achieved by blanks in each batch are summarised in Table 7.8 for indicative purposes; full details for each element are provided in chapters 15 and 18 in the appendices. Two sets of blanks were acidified for batch 3: one set used test tubes which had been prepared by various stages of water rinsing, to provide the most accurate assessment of contamination levels introduced to session 3 samples (which had been prepared in like manner); the second set trialled the acid soak procedure for preparing test tubes, which was shown to be effective and employed for the test tubes used in all subsequent samples and blanks (as analysed in batches 4 and 5).

Table 7.8. Improvements made to Fe levels in blanks.
Note that the higher blank level of (1.5 +/-0.3) ppb Fe applies to the samples analysed in batch 3, which were taken in water-rinsed test tubes; the acid soaked blanks were analysed to inform procedure in subsequent batches

Batch Number	Number of blanks	[Fe] (ppb)	Notes
1	1	19	Contamination due to glassware and acid used
2	4	1.5 +/- 0.5	Contamination due to test tubes (after water rinsing)
3	4	1.5 +/- 0.3	Contamination due to test tubes (after water rinsing)
	4	0.17 +/- 0.09	Marked improvement due to acid soak of test tubes
4	11	0.11 +/- 0.07	Acid soaked test tubes
5	18	0.04 +/- 0.14 0.18 +/- 0.33	Acid soaked test tubes – excluding 5 rejected test tubes Acid soaked test tubes – all 18 test tubes

Once acidification of all the samples and blanks in a batch was complete, they were put in refrigerated storage at approximately 3 – 5 °C after between 12 and 24 hours. The reason for insisting on a minimum time was to give the acid time at room temperature to fully dissolve any particulates, and also to prevent any short-term time dependence of leached concentrations from affecting some samples more than others. Time in storage varied from batch to batch, but could be anything up to around 11 months in the most extreme case due to problems with the ICP-MS instrument. There was no evidence of problems caused by such periods of refrigerated storage, with levels in blanks showing no relation to time spent in storage.

7.4.4. Analysis in ICP-MS instrument

An Agilent 7500ce instrument was used for ICP-MS analysis. Several methods were used to calibrate the results, by the operator of the ICP-MS instrument in line with standard practice (such as calibration curves using standards solutions, and internal standards used with each sample), and also by the author (the use of blank samples, as detailed in the following sections).

Once the results were received from the ICP-MS operator, the levels and variance in blank samples submitted at the same time as the samples of interest were taken into account, as was the dilution effect on the samples due to acidification; the values reported for the results (in chapters 8, 15 and 18) are as-adjusted in this way, as detailed in section 15.2.1. The assumption that values from the blanks can simply be subtracted is valid, provided that:

- There is no significant impurity in the type 1 water itself; and

- Samples did not receive additional airborne contamination due to their extended time with no stopper.

These can both be assumed true for the majority of samples, though high levels were measured in some blanks analysed for batch 5 which had higher levels than the feedwater samples analysed at the same time, suggesting slight contamination of the type I water source at that time.

7.4.4.1. A brief description of how the ICP-MS instrument works

A peristaltic pump draws solution (~4 ml) from the sample. In the nebuliser, a stream of Ar gas nebulises the sample solution into a fine mist. Larger droplets are rejected and the remainder is transferred to the Inductively Coupled Plasma (ICP) torch. In the ICP torch, argon gas is converted to a plasma by electromagnetic induction. The nebulised sample, now an aerosol, is instantly desolvated and ionised on contact with the argon plasma. The sample ions pass through a small hole in the back of the ICP torch to a vacuum chamber, and through another orifice to a second, higher vacuum chamber, manipulated by ion optics. A quadrupole mass analyser selects for a specific mass:charge ratio (effectively, simply the mass number, since all the ions are singly charged), allowing only ions of that value to pass through to the detector. Voltages applied to the four rods of the quadrupole – which control which mass:charge ratio is allowed through – are ramped very rapidly, enabling the entire mass range of 2-260 amu to be scanned every 100 ms. Thus, spectra of mass versus intensity can be obtained for all elements effectively simultaneously. In the 7500ce, but not all ICP-MS instruments, there is also an Octopole Reaction System (ORS) between the vacuum chambers and the quadrupole mass analyser, which removes polyatomic ions, which can cause interferences with the monatomic ions of interest from the sample.

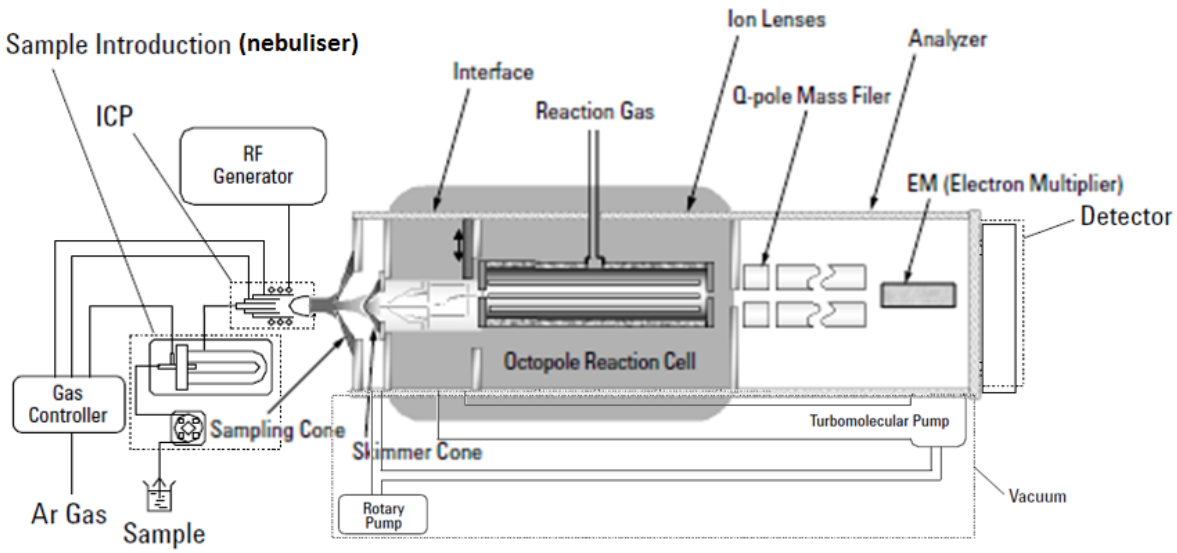

Figure 7.7. System diagram for the Agilent 7500ce ICP-MS instrument. Adapted from two figures in [153] *(figures 7, 8 therein).*
Sample solution is pumped to a nebuliser (marked 'sample introduction'), the resulting nebulised aerosol enters the ICP torch where it is completely desolvated and ionised. After passing through vacuum systems and ion optics, the quadrupole mass filter and detector enable spectra of mass versus intensity to be recorded. The octopole reaction cell removes polyatomic interferences.

7.5. Further Analysis of Results

The effects of many different variables were explored by plotting their value against the ICP-MS results. The most interesting or important of these are presented in the results section.

Some samples were taken to test a specific effect, such as two duplicates taken from the same sample and analysed at the same time, or one duplicate analysed after an extended time in the acidified but not refrigerated state. Samples like this treated in a way which is not consistent with the others were not included in general plots of the results.

Plots were made of samples against cumulative time of rig operation – these plots are to be borne in mind when looking at any of the other variables, as the rig appeared to take several days to react to changes and so results at the present condition may be influenced by the previous conditions of the rig – the rig's history.

7.6. Dissolved Hydrogen (DH) Measurement, Using Mass Spectrometry

To obtain approximate representative measurements of DH concentration in the rig, two sealed samples of rig effluent were taken in the sampling cell, and later analysed for hydrogen content of gases released on opening the cell. More specifically, the measured ratio of hydrogen to nitrogen in the released gas, in conjunction with a model which accounted for any gas not released in the mass spectrometer due to retention in the cell, was used to provide an estimate of hydrogen concentration in the effluent at the time of sampling. The model is described in chapter 16.

7.6.1. Taking pressurised samples from the oxide solubility rig

Using oxygen-free nitrogen gas, the sampling cell (SC), to which a pressure gauge had been attached, was flushed through thoroughly to remove any residual air, then filled to atmospheric pressure. It was then connected to the rig exit at the end of the sampling line before opening the valve at the entrance to the SC. It took around 7.5 to 8 hours for the SC to fill to ~ 90% with rig effluent at 0.1 g/min, at which point the pressure rose fairly rapidly. Once the pressure reached around 15 bara in the SC, the valve to the dump line exit from the rig was opened. Since the BPR on the dump line was set at a lower pressure than the BPR on the sampling line, this caused flow to divert away from the SC and the pressure in the SC stopped rising. The valve at the entry end of the SC was then closed, and the SC was removed from the rig and stored, ready for analysis in the Mass Spectrometer. After the sample was taken, mass and pressure readings were periodically taken to track any loss of mass or pressure that may occur over time before the Mass Spectrometer was available for use.

7.6.2. Measuring gas contents of cell, using mass spectrometry rig

The SC was attached, as shown in Figure 7.8, to a bespoke system of stainless steel tubing and valves built by Dr. Daniel Reed for gas measurements made in his research group, which was connected to a ProLab Benchtop Mass Spectrometer via capillary tubing. A needle valve was slowly opened to introduce gas from the SC to a stream of Ar carrier gas, which was controlled at a steady flow rate. Approximately 0.4 m downstream of the sample introduction point, a small proportion of the mixed gas stream was continuously sampled and fed to the mass spectrometer along capillary tubing.

The mass spectrometer measured the partial pressure of each gas (or each value of charge:mass for ionised molecules) every 6 seconds, in arbitrary units. It has dual detection capability [154]: the Faraday cup had been set up to measure Ar; and the Channeltron® electron multiplier (which scans across the range of charge:mass ratios once every 6 seconds) had been set up to measure all other gases.

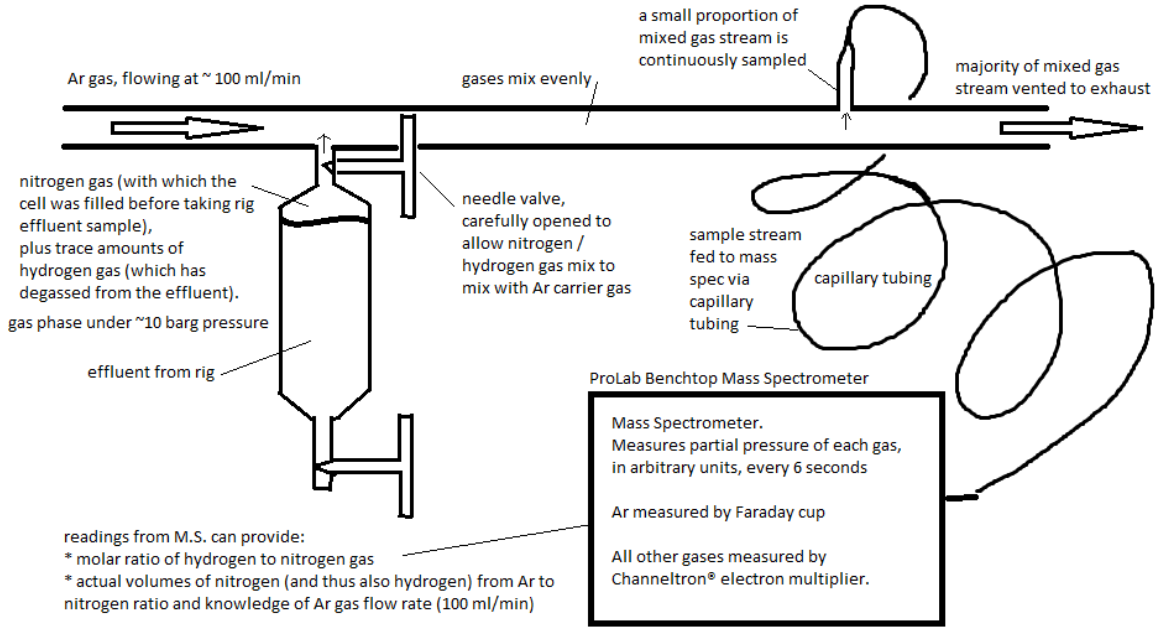

Figure 7.8. Bespoke setup for feeding gas mixtures with trace amounts of certain gases to a mass spectrometer, for measurement of very small gas volumes.
The mass spectrometer provides information on the ratio of partial pressures of the different gases. These ratios can be used to ascertain absolute volumes (at STP) through prior knowledge of the volume of the main component of measured gas mix, or through knowledge of the Ar gas flow rate.

The system was monitored and allowed to settle for several minutes between attaching the sampling cell to the apparatus and introducing gases from the cell for measurement. Continuous measurement and logging of the data from the mass spectrometer occurred during this period, once readings had settled, and continued during introduction of gases from the cell, and for around an hour afterwards, for background readings and to observe any drift in readings.

Since the readings given are in arbitrary units, the only definite information which can be gleaned from the readings alone is the relative proportion of each gas in the mixed stream at the sampling point (i.e. entrance to capillary tubing), determined at 6 s intervals. Assuming a constant flow rate of the Ar carrier gas, and effective mixing with introduced gases from sample, these relative proportions also represent relative flow rates in arbitrary units, which can be integrated over time to give relative volumes of each gas released from the sample.

Calibration against known volume flow rate of the Ar carrier gas (100 ml/min) was used to provide an estimate of actual volumes of hydrogen and nitrogen released during measurement. The measure of released nitrogen volume thus obtained was compared against the value predicted by a model, and attempts were made to account for any discrepancy.

7.6.3. Interpretation of results to determine hydrogen concentration in rig

The same model used to predict nitrogen volume released from the cell was also used to estimate hydrogen concentration in the effluent at the time of sampling – and by extension the hydrogen concentration in the pressurised part of the rig – from measured ratio of hydrogen to nitrogen gases.

The model uses data from observations made on the SC during and after sample acquisition, such as time taken to fill and pressure changes over time, and Henry's law coefficients for gas solubility [155], to provide a conversion from the ratio of hydrogen to nitrogen measured (from gases released to the MS) to the ratio of total hydrogen to nitrogen in the cell when first filled. Differences arise due to the slightly higher solubility of hydrogen compared with nitrogen. Simple relationships are used to determine the ratio of total nitrogen to mass of water in the cell, which is multiplied by estimated ratio of total hydrogen to nitrogen to give hydrogen concentration.

7.7. Estimates of DH levels, using corrosion rate data

It is known that corrosion of stainless steel under reducing hydrothermal conditions causes the release of hydrogen. For each mole of oxide produced, (AB_2O_4), 4 moles of hydrogen gas are produced.

$$3Me + 4H_2O \rightarrow Me_3O_4 + 4H_2$$

By assuming about 10% of hydrogen is released to coolant, and 90% is retained in the metal [94], [95] (see lit review), and using data on corrosion rate of SS316L under similar conditions [26], estimates were made of the rate of release of hydrogen gas to the coolant in the rig, over the course of experiments. To account for the effect of differing corrosion kinetics over the course of experimentation, as differing values of coolant pH_{25C} were used, it was assumed that corrosion rate at any given time was inversely proportional to oxide thickness (this relationship is implied by the parabolic kinetics observed). Equations for cumulative corrosion growth and corrosion rate were re-arranged and expressed in terms of oxide film thickness and time. From the estimated rate of

hydrogen release to coolant, and the rate of dilution by inflow of fresh coolant into the hot part of the rig, a steady state level of expected hydrogen concentration was calculated, and plotted against time. The kinetics with which steady state would be approached was also modelled, briefly.

7.8. pH and Conductivity Measurements

Measurements of pH were made on the rig effluent and feed water using a Hanna 210 pH meter, and also using UI paper. Problems were encountered with CO_2 from the atmosphere, which is known to dissolve in de-aerated water at room temperature, producing carbonic acid and causing a rapid decrease in pH. Difficulties were also encountered in measuring pH of low salinity solutions; an addition of high purity KCl was used to obtain more stable readings.

For pH measurements, only test tubes which had been thoroughly cleaned by the adapted ASTM procedure (see section 7.4.2), and subsequently rinsed many times to remove any acid residue, were used. The test tube was first flushed with nitrogen gas at high flow rate and the stopper replaced (to exclude carbon dioxide gas, as far as possible). Next, a small amount of KCl was quickly added, sufficient for a final conductivity of around 1 – 10 m S/cm. More nitrogen gas was directed at the entrance of the test tube, at sufficiently slow flow to not eject the KCl powder, and the test tube was covered with ParaFilm as quickly as possible. A second test tube was prepared in the same way. Around 7 ml of feed water was drawn into the plastic syringe at the pump inlet, and the end sealed quickly with Parafilm “M” ®. A similar amount of type I water (known to be at room temperature, as per the feed water) was drawn into another plastic syringe.

For each test tube a sharp implement was used to puncture the parafilm lid, the end of one of the syringes was inserted into the hole, and the solution was injected. The electrode probe of the pre-calibrated pH meter was then inserted into the feedwater solution and the temperature probe into the pure water – in each case replacing the syringe, and ensuring a tight seal. The purpose of the pure water test tube was to give an idea of temperature over time, due to the exothermic effect of salt dissolution, and to calibrate the pH reading – since there was insufficient space in one test tube for both probes. Since the heating effect from the salt was quite minor, temperature variations had no material effect on the pH, and temperatures in the two test tubes were compared afterwards and found to be very close.

pH readings were made on samples of feedwater, and found to be fairly unstable, changing over time. Considering the uncertainty and variability on measurements, pH readings from the feed water at a theoretical value of pH 10 were found to be consistent with the theoretical value. Over a period

of up to an hour, readings took time to adapt to the pH of the solution, settling at around 9.7, before gradually falling to lower values, presumably as CO_2 continually seeped in to the solution.

Conductivity readings were taken periodically in feed water and rig effluent, using a Jenway 4510 bench conductivity probe, providing typical readings summarised in Table 7.5. Conductivity readings were also taken of type I water directly as it first flowed from the MilliQ system, over the minutes that followed (showing a rapid increase due to contamination from the thoroughly cleaned vessel in which it was collected and from CO_2 in the atmosphere), and after equilibrating with the atmosphere for several days.

pH of very low salinity water cannot be reliably measured directly. This can be overcome with the addition of salt, but results are still vulnerable to the extreme sensitivity to contamination from the container – ions of a particular charge need only be present to a concentration of ~ 1 micro molal to change the pH of neutral solution by 2 units. Conductivity measurement can be a useful alternative to pH for monitoring such solutions. In either case, without a system for online measurement isolated from the lab atmosphere, the presence of CO_2 makes results unreliable whenever pH is not controlled by an effective buffer solution. Therefore, the pH readings can only be viewed as an approximate corroboration of calculated values, and the conductivity readings as a means to monitor levels and be aware of any major changes, of which none were noted.

7.9. Optical and Scanning Electron Microscopy (SEM) Analyses of Components from Rig and Filters

Various components used in or with the MOS rig were characterised before and after use, by various techniques as described below.

7.9.1. Scope of Work

This subsection summarises the types of sample studied and what was characterised. Samples were taken from various coolant-facing SS316L surfaces in the hot part of the MOS rig, to characterise their form, and to study the corrosion oxide film present on them. This is important because the corrosion film controls levels of dissolved and particulate corrosion products in the coolant in the hot part of the rig, by solubility and by deposition and release mechanisms respectively; although characterisation can only assess the oxides in their present state, which may have changed over the course of each session and during the time since the last coolant samples were taken. Also the

sampling line was thought to have had a significant effect on dissolved and particulate levels in effluent samples, see chapter 8.

Samples were taken from frits, chips (before and after use in the rig), and the 1" tubing of three of the four reaction chambers used (from sessions 1-3; 4; and 5).

These samples enabled characterisation of the following, using an SEM for imaging, and SEM/EDX for elemental analysis:

- Oxide film surface morphology, on samples from reaction chambers and chips
- Morphology and elemental composition of a cross-section through oxide thickness and underlying alloy, on a reaction chamber sample, prepared by Jonathan Morrison by cutting using a slow speed diamond saw without lubricant, mounting in Epofix, grinding, and polishing using 0.25 µm diamond paste.
- Morphology and elemental composition of oxide crystallites, removed from reaction chamber samples using adhesive tape to prevent interference from underlying alloy
- Morphology of frits, after their use in the rig, and their oxide film
- Surface morphology and overall shape of chips before use in the rig, and their oxide film after use in the rig

Having studied the supposed source of rig effluent particulate matter – the oxide film in the hot parts of the rig – it was important to also study any particulates captured from the effluent, to compare against those present in the oxide film. Nitrocellulose filters were used routinely in session 6, and several were also used during session 5 and on the CRR rigs, to assess particulate contribution to rig effluent samples. As well as observing their effect on the levels of metals, in filtered effluent samples, the filters themselves were examined under SEM and EDX for any particulates which may be visible. In a few cases a residue of particulate was unexpectedly found in the polypropylene housing of the filters; this was analysed under SEM/EDX also, as well as under optical microscope to observe the colour of the particles.

7.9.2. Procedure for terminating each session of rig use

At the end of sessions 1 and 2, no further action was taken after the draining of water from the rig, and rinsing with DI water, until the next session. After sessions 3 and 4, the oxide chamber was removed and replaced with a fresh one, and samples were taken from it for SEM/EDX analysis as described above.

At the end of sessions 5 and 6, to avoid any change to the morphology and composition of the corrosion film in the presence of water under room temperature (and potentially oxidising) conditions, nitrogen gas was flushed through the rig in reverse direction to the normal route of water flow, to flush out all water from the rig and thoroughly dry the walls and chips over several days. From the oxide chamber in use during session 5, chips were carefully removed so that representative samples of chips from near the top, mid-level, and bottom of the chamber could be selected for characterisation as described above.

7.9.3. Optical microscopy and close-up photography

For close-up photography, D-SLR cameras were used (Canon EOS 70D, and Canon EOS 250D) with a 60 mm macro lens, tripod, and remote shutter. For optical microscopy, various microscopes were used, with 100 x objective and 10 x eyepiece [double check] Some photomicrographs were taken using a smartphone (Samsung Galaxy LTE Prime), since the lens is small enough to be used in place of an eye in conjunction with an ordinary eyepiece. Other photomicrographs were taken using a D-SLR camera, in the microscope's slot intended for such a purpose.

Photographs were taken of chips for characterisation. A combination of photographs and photomicrographs were taken of the deposit found on one of the filter holders, enabling the shape of the whole deposit to be mapped out in its entirety, so that higher magnification images could be placed in the context of the overall deposit shape. The use of a white light source allowed colours to be distinguished, with some particles appearing black and some orange – presumed to be magnetite or nickel ferrite (black) and hematite or other Fe(III) oxide (orange). Individual crystallites were identified, and information about them from SEM / EDX was combined with that obtained from optical imaging.

7.9.4. SEM and EDX

SEM / EDX characterisations were performed by a colleague, Dr Jonathan Morrison, using a Jeol 7000F SEM, fitted with an Oxford Instruments Inca EDX spectrometer. Some images were also taken using a Hitachi S4500-FEG SEM (Figure 10.2 a; Figure 10.3 a,b). Images were taken using the secondary electron detection mode with a beam energy of 20 kV and working distance of 10 mm, and EDX analyses were also performed using a beam energy of 20 kV and working distance of 10 mm. Apart from samples of the rig walls, samples were mounted on an Al stub. Tape pull samples and filter samples were prepared by Au or Pt sputter coating to mitigate the effects of charging, prior to use in the SEM.

8. Results:

Levels of Fe, Cr, Ni, Mo, Mn and Co in Rig Coolant – ICP-MS Analysis of Effluent and Feed-water Samples

8.1. Summary of experimental work

Effluent samples were taken over the course of six sessions of rig use, and analysed for Fe, Cr, Ni, Mo and Mn content. All coolant-facing surfaces in the heated part of the rig, and almost all coolant-facing surfaces at ambient temperature, were of alloy SS316L, whose corroding surfaces acted as the sole source of the elements measured in the coolant, and also of dissolved hydrogen in the coolant, a by-product of the corrosion process. The Model 305 piston pump with Model 10 WTi titanium pump head, and the Model 308 manometric module, all manufactured by Gilson, were specifically designed for high purity applications, 'where the leaching of metal ions from stainless steel may cause undesirable interference' [156], and so were not expected to introduce significant levels of ions to the coolant. Liquid-facing materials in these components were limited to: grade 2 titanium; SS316L; sapphire/ceramic; ruby; nitrile rubber (O ring); and engineering plastics (such as PTFE) [156]–[158]. Ti levels were measured for the first 9 samples of session 3, yielding 0.0 +/- 0.1 ppb, i.e. no different from blank samples. The only other coolant-facing surfaces which were not SS316L were: nitrocellulose filters used at the point of effluent sampling; and engineering plastics used at room temperature for filter holders, for the dump line and feedwater line in earlier runs, and for a short section (~10 cm) of capillary tubing and 3-way valve leading to the pump inlet, from which feedwater samples were taken.

While it was hoped that measured levels of Fe and Cr would be indicative of the solubility of the coolant-facing oxide phases, ferrite and chromite (or possibly CrOOH) respectively, in the heated part of the rig, it was suspected that the rig may not provide accurate data, due to contributions of Fe, Cr and other elements from all parts of the rig, including the portions held at room temperature (feed-water barrel, feed-water lines, sampling line).

Based on findings from other workers studying pure magnetite solubility [4], [121], it was anticipated that an additional contribution from iron particulate or colloidal matter *may* be present initially, before decaying over a period on the order of months (1000 h) of cumulative flow, (particularly with the addition of SS316L chips to the latter runs, which could have introduced small fragments or 'fines' to the system), though the corrosion film forming on stainless steel, having individual micron sized crystals growing from solution, is qualitatively different from the ~ 100 μm to 1 mm sintered granules used in solubility studies. Since the source of ferrite crystals in the present work was the corrosion film on corroding SS316L (rather than granules used in pure solubility studies), it could also be anticipated that crystallites in the outer layer of oxide may release from the corrosion film [1], [2], [44], [159]–[161] and contribute to effluent samples, though the very slow laminar flow in the present study (Re ranging from 0.002 to 77, maximum velocity in heated part of rig 6.4 mm/s), is qualitatively very different from the high velocity turbulent flow employed in nuclear plant.

Soluble levels were also expected to fall from high initial values, as the oxides 'age' to the most stable microstructure [113], [121]. This effect is compounded, on surfaces undergoing corrosion such as the rig, by the continual flux of corrosion ions, primarily Fe^{2+}, through the protective inner layer of oxide to the coolant-facing surface, and onward to the outer layer oxide by a dissolution and re-precipitation process. In the absence of such flux, corrosion products from SS316L would approach the (metastable) equilibrium of Cr-saturated ferrite with Fe-saturated chromite at the solvus of immiscibility [74], [76], [84]–[86] (see Figure 4.4 and Figure 17.11), and eventually the true equilibrium in which CrOOH replaces chromite as the stable Cr-rich phase [162]. At equilibrium, concentrations of dissolved Fe and Cr ions would be in equilibrium with both oxide phases, and there would be no net dissolution or precipitation. As the oxides slowly 'age' towards their state of minimised Gibbs energy, their solubility (and thus the concentrations of dissolved Fe and Cr), slowly decays to the true equilibrium value. In the presence of corrosion flux, however, there must be a driving force for Fe^{2+} ions to dissolve from the chromite crystallite surfaces, and subsequently to precipitate onto ferrite outer layer crystallite surfaces. Therefore the coolant must be to some extent supersaturated in Fe and Cr ions with respect to the outer layer ferrite crystallites, yet undersaturated with respect to the inner layer chromite crystallites, whose solubility is elevated because of their small size, ~ 10 – 30 nm [76]. Solubility of the inner layer chromite crystallites may also be elevated from true equilibrium by virtue of not being the most stable Cr-based phase under conditions of the rig or PWR primary coolant, CrOOH. However, it is possible that a thin layer of CrOOH may form on the surfaces as a solubility controlling phase – for example a layer of less than 10nm thickness was detected on the surfaces of Cr_2O_3 after exposure to hydrothermal solutions in

solubilty experiments [102], and the dissolution reaction for FeCr2O4 proposed by Dickinson et al has CrOOH as a reaction product ($FeCr_2O_4 + 2H^+ = Fe^{2+} + 2CrOOH$) [103].

The coolant very close to the corrosion film (within a few microns) may have spatially varying concentration according to whether it is closer to chromite surfaces (Fe source) or ferrite surfaces (Fe sink), with concentration gradients supporting diffusion through the coolant from source to sink, though at a greater distance the concentration would become uniform, being somewhere intermediate between solubility (or surface concentrations) of the two phases. Early on in the corrosion process the corrosion release flux is fast, yet there is limited surface area of outer layer crystallites on which to precipitate, therefore a great degree of supersaturation is required before the precipitation rate can keep pace with the release rate (per dm^2 of corroding alloy). Supersaturation increases until nucleation of new crystallites occurs, directly in coolant (as colloids) and atop chromite crystallites, as well as growth of existing crystallites. As corrosion progresses, the combined effects of a slowing corrosion flux and an increased surface area of outer layer crystallites on which to precipitate mean that the degree of coolant supersaturation relative to outer layer crystallites falls over time. Concurrently, as the outer layer crystallites grow and age, their solubility decreases over time.

In summary, just as with magnetite granules used in solubility studies, one might expect some loose particulate matter to be present from the start, such as small stainless steel pieces broken off from the chips, and colloids may form in the coolant under certain scenarios; in addition, and unlike those solubliity studies, the outer layer crystallites may act as a source of particulates and colloids if they release from the surfaces, with the potential inventory for release increasing over time as the film develops. Solubility of the outer layer crystallites may be expected to decrease over time as they grow and age, in like manner to the study of Lambert et al. and Tremaine and LeBlanc; however, in contrast with those studies, where equilibrium is approached from a point of *under*saturation by dissolution, the ferrite (approximately magnetite) crystallites of the present study approach equilibrium with the adjacent coolant by precipitation from *super*saturated solution (one can neglect diffusion away from the corrosion film to the bulk of the coolant in the rig, as the bulk coolant easily becomes saturated at the same concentration as is present near the corrosion film, due to the long residence times used). The precipitation reaction generally yields slower kinetics than the dissolution reaction, so that for a given reaction rate, the former yields a greater deviation from saturation concentrations [163], which is one reason why dissolution reactions are favoured for solubility studies. However, as corrosion flux slows over time the rate of precipitation, and thus the degree of supersaturation, will fall also. Another difference from solubility studies is the the presence of the two Fe-Cr oxide phases ferrite and chromite concurrently, which may be expected to cause a slight

reduction of soluble levels of Fe and Cr compared with the pure stoichiometric phases tested separately. Overall, the soluble Fe and Cr concentrations are expected to be similar to those from solubility studies using granules of magnetite, chromite, or Cr_2O_3 with surface CrOOH as the solubility controlling phase [102] (or at least the levels that they would have seen had dissolved hydrogen been present at the low levels present in the rig, based on the thermodynamic data they obtained, see section 14.3), and exhibit decay over time as observed with magnetite solubility studies, the only difference being that corrosion flux would prevent the decay all the way to equilibrium levels.

The presence of other elements in amounts which vary over time due to corrosion flux and varying coolant conditions introduces another layer of complexity. Whilst soluble levels of Fe and Cr were controlled at close to saturation levels, by phases which approximate to equilibrium Fe-based and Cr-based phases, levels of Mo and Mn (and for the most part Ni, except perhaps very early on when dissolved hydrogen in the rig was highest and corrosion release was fast) were lower than the solubility of their respective single metal or single metal oxide phases. Therefore, soluble levels in the rig were controlled by kinetics in terms of diffusion to the surface from deeper within the corrosion film or underlying alloy, solubility in terms of release at the surface (via the partition coefficient – the ratio of equilibrium soluble concentration to concentration in the solid phase), and again, kinetics in terms of removal into the effluent according to the coolant flow rate.

As discussed in sections 1.2, 12.1 and 12.2, the aims of the project shifted from initially trying to make the best of the rig, mitigating or accounting for the effects of particulate or colloidal matter on total effluent levels of each element to try to measure the solubility of the Fe-Cr-Ni oxides present on corroding stainless steels, to finally embracing the richness of the rig and the opportunities it provides to study the time-varying release of corrosion products as flow is disturbed, and under steady conditions, as parameters such as temperature, pH, flow rate and amount of corroding material are changed. The rig represents a half-way-house between the simplicity of equilibrium oxide solubility studies for pure oxides, and the complexities of a nuclear power plant. Although conditions are not identical to the primary coolant of PWR, several interacting factors from PWRs are present in the rig, such as ongoing corrosion, which changes as it progresses over time; dissolved levels of metal ions controlled by a dissolution / precipitation process of the stainless steel and corrosion film (rather than dissolution of pure oxides); and native oxide crystallites on the corrosion film, which may release (as colloids and particulates) or deposit in different ways as conditions change, or as a pseudo-random function of time regardless of changes to conditions. For these reasons, data from the rig could be of great interest to plant modelers.

The key variables on which oxide solubility depends, in dilute solutions in the absence of complexing agents, are pH, temperature, and – for the case of oxides whose average oxidation state of the metal changes on dissolution (such as magnetite) – hydrogen fugacity. The six sessions of rig use covered a range of values of coolant pH_{25C} (9, 10, 11), and a range of temperatures in the heated part of the rig (200, 250, 300 °C). Hydrogen concentration was not known nor controlled, but was modelled according to corrosion rate data and flow rate of coolant. Modelled hydrogen fugacity varied between amounts equivalent to ~ 10^{-4} and 10^{-1} bar at 25 °C. Two effluent samples were analysed for hydrogen content; the results agreed broadly with the model, being about an order of magnitude above and an order of magnitude below the modelled value respectively for the two samples – therefore hydrogen concentration was known only very approximately.

Results of ICP-MS analyses are provided in full in chapter 18, in the form of data tables.

An in-depth analysis of all ICP-MS results is provided in chapter 15, including relevant information regarding the method of processing the data, and the particular circumstances under which samples were taken (for example, noting the recent history of changes to conditions in the rig, including pump stalls and restarts, and drawing attention to cases where this may have had an impact on results). In section 15.2, results are discussed and analysed on a session-by-session basis, referring primarily to tabulated data. In section 15.3, results are plotted against cumulative time for each element for sessions 1 to 4, allowing trends over time and responses of the rig to changing conditions to be observed, and the plots are discussed and analysed. In section 15.4, the topic of overall variability of the results is discussed, and an attempt is made to assess the repeatability of findings. In chapter 17, the varying levels of dissolved hydrogen over the course of the experiment are modeled (section 17.2), and used to predict soluble levels of each element under several different scenarios, including levels of hydrogen close to the top end, middle, and lower end of the expected range, pH_{25C} values of 9, 10 and 11, and temperatures of 25 °C, 200 °C, 250 °C and 300 °C. Solubilities under oxidising conditions at room temperature are also presented, as these may be present within the last few mm of the sampling line due access of air to the end of the sampling line. Qualitative effects of kinetics considerations are also presented, in section 17.3.4, and a discussion of possible particulate behaviour is presented in section 17.4.

The key findings from the ICP-MS data are summarised below, drawing on the analysis from chapter 15.

8.2. Main findings from the first four sessions

8.2.1. Session 1 – practice run using pure water

Session 1 was used mostly as a practice for the use of the rig and taking and analysing samples. Through this process it became clear that multiple blanks would be needed and cleanliness measures enacted to control contamination in order to obtain acceptable levels of standard error on samples.

8.2.2. Session 2 – similarity between feedwater and effluent

Session 2 results showed that levels of some elements could change over time. For example, levels of Mn fell from between 0.3 and 0.7 ppb in the first three samples to 0.0+/-0.1 ppb thereafter. It was found that average levels for each element were consistent with those measured in the feedwater sample, except for Mo, see Table 8.1. Various sampling methods were used to find which worked best, though this made comparison of results taken by different means problematic.

It is not known why levels of Cr were so high in these samples, for both the feedwater and the effluent. It may be due to the fact the surfaces of the rig had not been exposed to hydrothermal conditions for as long, during session 2, as they had for later sessions. However, levels of Cr were lowest during session 5, after the addition of fresh unoxidised SS316L chips, so if this were a factor it would have to be due to the sampling line or feedwater barrel rather than the high temperature parts of the rig. Another possible factor is the feedwater pH, since consistently high levels of Cr also occurred at a feedwater pH of 10 (session 6), but were much lower for most of sessions 3 to 5 where the feedwater was at pH 9. A pH effect is not expected for the solubility of Cr from chromite or CrOOH, with solubility remaining at around 0.01 ppb for all the conditions employed in this study, therefore the high levels are probably due to oxide particles as well as some degree of supersaturation.

Table 8.1. Summary of average results at pH 11 (session 2), pH_{300C} 8.4

Condition / element	[Fe] (ppb)	[Ni] (ppb)	[Cr] (ppb)	[Mo] (ppb)	[Mn] (ppb)
pH11, 300 °C, 2 g/min – effluent	~ 0.8	~ 1.0	~ 1.6 (or 1.1 if outlier is removed)	~ 200	~ 0.2 (0.0 excluding first three results)
pH11, 25 °C, 2 g/min – feedwater	~ 1.0	~ 1.3	~ 0.6	~ 1	~ -0.1

Levels of Mo were also much higher than expected, given the fact that the mass of Mo released during session 2 (estimated by integrating the product of flow rate and effluent concentration over time) was about eighty-four times that expected from a process of non-selective oxidation of the alloy and zero retention of Mo within the oxide film (using Morrison [26] corrosion kinetics); this figure falls to thirteen times the expected mass of Mo if it is assumed that Mo was fully retained in the corrosion film during prior operation in pH neutral water at 260 °C, session 1, before releasing fuly during session 2 (see section 17.7, and in particular Table 17.19). Levels of Mo were higher than expected during other runs also, as discussed in the sections that follow, and in section 17.2.

One possible source which has been suggested is the release of Mo from the pump, if, for example molybdenum sulphide (a lubricant), or some other Mo-bearing phase were present and able to leach into the coolant. As discussed at the beginning of this chapter, the pump, pump head, and manometric module were designed specifically for use in high purity applications, and would not be expected to release high levels of Mo ions. Correspondence with a representative from Gilson UK (Tim Bunce, August 2018) confirmed that the rig coolant used in the experiments should not come into contact with any lubricant which may be used in the pump, by design, as long as the pump seals are intact. Likewise, the fluid in the manometric module, which is methanol with a blue dye (and could conceivably contain Mo), should not come into contact with the coolant unless the unit fails. In either case, failure should be easily identified by leakage into the laboratory. There was no sign of failure in either unit, and Mo was also seen at relatively high levels in the two corrosion rate rigs, which used the same model of pump, pump head and manometric module as the current experiment (~15 - 20 ppb at 1.5 - 2 ml/min flow, Table 18.7), and also in the high velocity recirculating coolant of the hot loop, which used a regenerative turbine pump (~700 ppb, higher than all the other elements tested – see Table 18.8). Release from the stainless steel 316L tubing into the heated coolant (200 - 300 °C) is therefore considered the most likely source of Mo, despite representing up to a factor of ~ten more Mo than could be explained by non-selective oxidation of the alloy and full release from the oxide film (see above).

8.2.3. Session 2 – Mo levels falling over time

It was observed that levels of Mo fell smoothly and fairly rapidly from around 500 ppb to around 60 ppb over the 12 days duration of session 2, as shown in Figure 8.1. Due to different sampling methods, some samples were considered less representative (coloured orange on the plot) than others (coloured blue). A power law curve was fitted through the more representative points, yielding a good fit, suggesting a relatively high affinity for Mo in the aqueous state compared with

the oxide at pH 11, leading to leaching of Mo present in the corrosion film after prior corrosion in high purity water coolant during session 1.

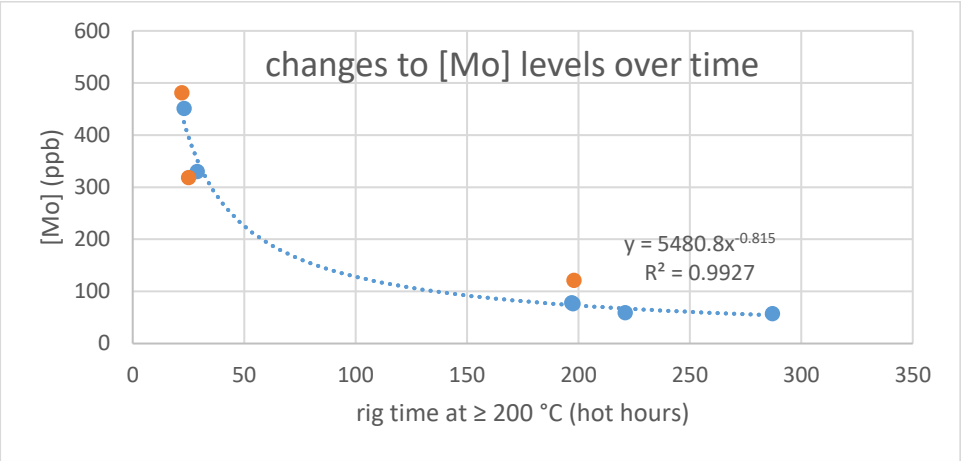

Figure 8.1. Changes to [Mo] levels over time during session 2

8.2.4. Sessions 2–3 – Effect of rig pH history on Mo levels

Over the first 2 days of session 3, at pH 9, levels of Mo rose relatively steeply from ~5-10 ppb to 26 ppb, then stayed fairly constant – decaying slightly to 22 ppb over the next 8 days, see Figure 8.2.

It can be hypothesised that at pH 9, the partition of Mo ions between oxide and coolant is less heavily weighted in favour of coolant than at pH 11; thus, little Mo was released from the corrosion film at the start of session 3 because it was still Mo-depleted after its prior exposure at pH 11. The Mo component of corrosion release flux from the oxide-alloy interface (see chapter 3) allowed the build-up of Mo at the coolant-facing surface of the inner oxide until a steady state was reached between supply of Mo to the oxide surfaces and its dissolution release to the coolant.

The subsequent gradual fall in Mo levels could be explained by the gradual decay in corrosion rate, causing a decrease in corrosion release flux. This assumes soluble Mo levels are more controlled by the balance between rate of supply by corrosion, and rate of dilution by coolant flow, rather than a fixed solubility.

To test this hypothesis, ppb effluent levels have been converted to Mo release rates, and plotted against the release rates predicted by a simple model in Figure 8.3. The model assumes non-selective oxidation (i.e. all alloying elements pass congruently into the oxide film – and/or onwards as effluent in the present case), and zero retention of Mo in both the inner and outer oxide layers. The model simply finds the molybdenum component of the rate of alloy oxidation (using data from Morrison [26] and the corrosion rate model in section 17.2.3), and assumes all is released to solution instantly.

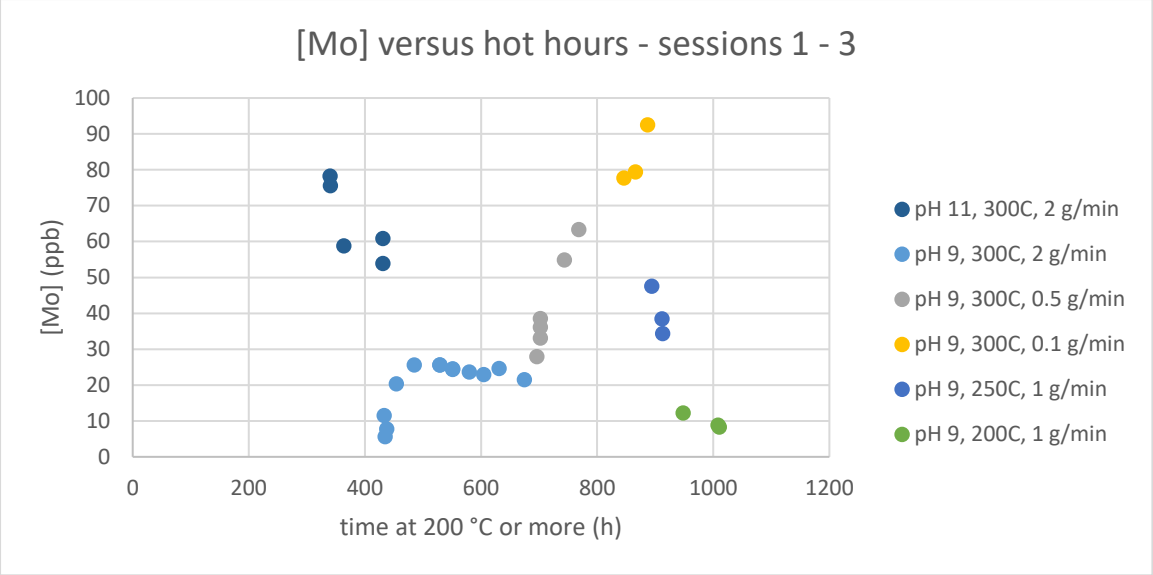

Figure 8.2. [Mo] levels versus time at 200 °C or more, in rig effluent during sessions 1 to 3. No data were taken for Mo during session 1, but the origin of the time axis corresponds with the start of session 1, when the oxide chamber and other SS316L surfaces of the rig were first exposed to high temperature coolant. Much of the session 2 (pH 11) data is outside the range of the plot (see Figure 8.1), with the reduced scale allowing lower values from session 3 to be discerned more clearly. Error bars were plotted, but cannot be seen as they are smaller than the data point markers.

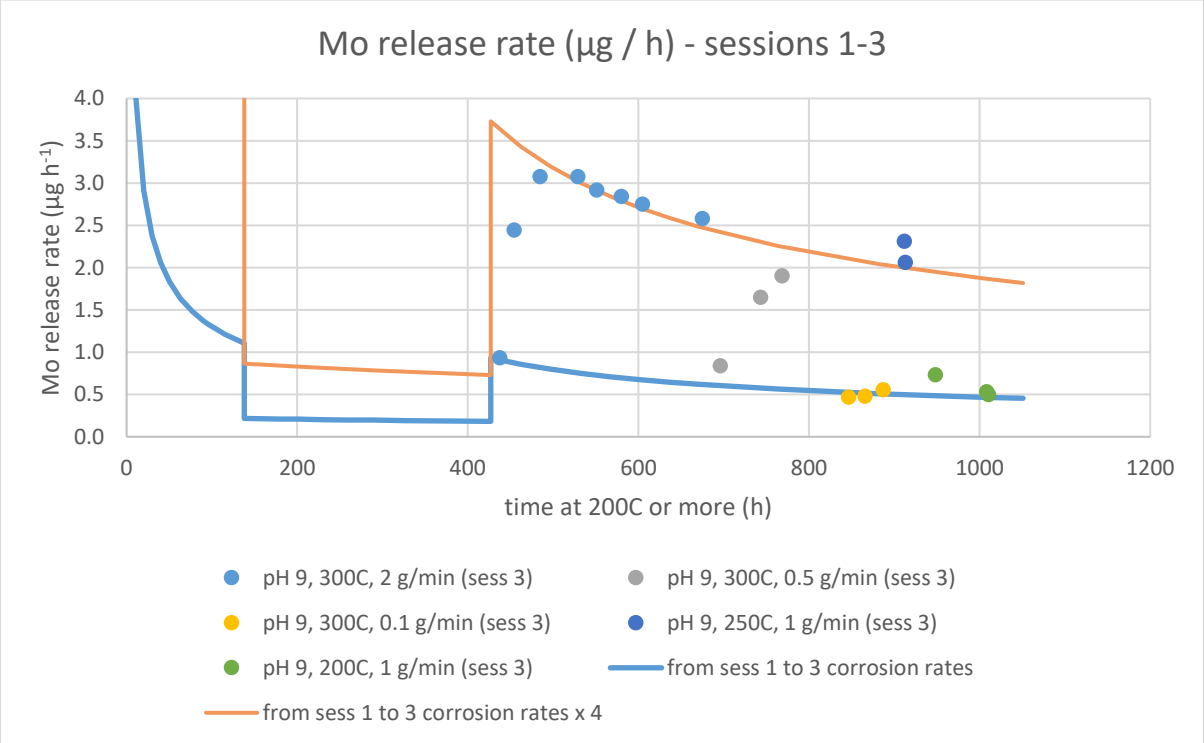

Figure 8.3. Mo release rate to rig effluent during session 3, according to ICP-MS data (release rate = coolant mass flow rate x average concentration in effluent), compared against a simple model.

It can be seen that the Mo release rate during the majority of session 3 was greater than or equal to the modelled value. If the model is adjusted to allow retention in the corrosion film then elevated release rates *can* be sustained, over a relatively short time period, as the inventory of Mo, built up in the corrosion film during a prior period of retention, is leached into the coolant – for example, after conditions have changed from relatively low to high solubility of Mo ions, as appeared to be the case in session 2. However, mass balance calculations, which were performed by integrating the release rate over the full time period of each session of rig use, have shown that Mo release to the effluent was many times greater than the maximum value permitted by the model, for sustained periods – see Table 17.19 in the appendices. If it is accepted that the Mo component of corrosion flux is greater – by a factor of ten, say – than the model value (either by faster than anticipated corrosion, or by selective oxidation of Mo), and a variable degree of retention within the corrosion film is allowed (dependent on conditions), then the time variation of the first ~ 100 h of session 3 can be well modelled by the release of a fixed proportion of the Mo component of corrosion flux, after a time lag during which the inventory of Mo in the corrosion film is built up to a higher level of retention compared with the previous use of the rig, see the orange (higher) curve.

8.2.5. Session 3 – negative effect of flow rate on Mo levels

Mo levels increased steeply for several days after each reduction in flow rate during flow at 300 °C, pH 9, from 2 to 0.5 and from 0.5 to 0.1 g/min, see Figure 8.2. Not enough time was allowed at either 0.5 g/min or 0.1 g/min to see what concentrations would have been reached at steady state. If it is assumed that the Mo component of oxides is negligible, though still proportional at the oxide surface to the concentration in solution, then approximately 100% of the Mo component of corrosion release flux is released to solution as a dissolution flux, with the two fluxes matching at steady state. In this scenario, one would expect steady state levels of [Mo] to be inversely proportional to flow rate – a constant release rate diluted to varying extents by coolant flow. If the Mo component of oxides is not negligible, compared with the ~2.5 wt% composition of Mo in the alloy, then the steady state Mo dissolution flux will be less than 100% of Mo corrosion release, as a certain proportion is incorporated into freshly precipitated ferrite, or retained in new growth of chromite – this proportion would be expected to increase with Mo concentration in coolant, resulting in a sub-linear relationship of [Mo] concentration with coolant residence time (i.e. the inverse of flow rate). These effects are obfuscated by the increase over time of the inner oxide film thickness, resulting in slowing corrosion flux over time, as illustrated by the model plots in Figure 8.3. The relationship becomes clearer when Mo concentration is converted to release rate and

compared against the model representing full release, as per Figure 8.3. If Mo release were consistent with the corroding surface area; non-selective oxidation of the alloy; and a certain proportion of the Mo being retained in the corrosion film (the remainder being released to the effluent), then one could expect the Mo release rate to follow the fitted curve (blue) in the plot, or a certain proportion of that value dependent on the degree of retention in the oxide film. After a change in flow rate, a new steady state may be approached with a lower proportion of the blue fitted curve, due to higher concentrations in the coolant and thus higher retention in the oxide film, or a similar proportion, if a similar proportion were retained. This latter scenario appears to be the case on changing from 2 g/min to 0.5 g/min, showing that the *form* of the Mo release time dependence is consistent with a solid state diffusion rate, falling over time as expected by the thickening corrosion film, only the *amount* of Mo release is higher than expected from non-selective oxidation, suggesting selective oxidation from the underlying alloy, as has been suggested in other parts of this chapter and in section 17.7. This process appears to be driven by the high affinity of Mo ions for the aqueous phase, especially at the higher pH values used, leading to a low concentration of Mo in the corrosion film oxides near the coolant-facing surfaces, which in turn creates a relatively large concentration gradient, driving diffusion across the barrier formed by the inner oxide layer.

8.2.6. Session 3 – positive effect of flow rate on Fe levels

During session 3, at 300 °C, a decrease in flow rate led to a decrease in observed Fe levels, which was unexpected. The positive relationship between flow rate and Fe levels cannot be explained by solubility behaviour in the heated part of the rig alone. Diffusion at 200 – 300 °C should be comfortably fast enough for levels of Fe to reach full saturation in the heated part of the rig, but should also be fast enough for appreciable progress to be made towards a new solubility equilibrium with oxides in the room temperature tubing downstream of the oven. Particulates were anticipated to occur under at least some conditions, based on findings of literature studies [4], [121], and might reasonably be expected to be at lower levels during periods of slower flow due to settling out, and at higher levels at faster flow. If the flow rate effect is caused by particulates only, one might expect measured levels of Fe to give the best representation of high temperature solubility at the *slowest* flow rates, being increasingly inflated by particulates as flow rate increases. If the flow rate effect is caused only by precipitation of dissolved Fe on the SS316L tubing downstream of the heated part of the rig, then one might expect measured levels to give the best representation of high temperature solubility at the *fastest* flow rates, with levels tending towards the room temperature solubility value as flow rate decreases. Therefore it was not clear from this finding whether a fast or slow flow rate should be employed for representative results.

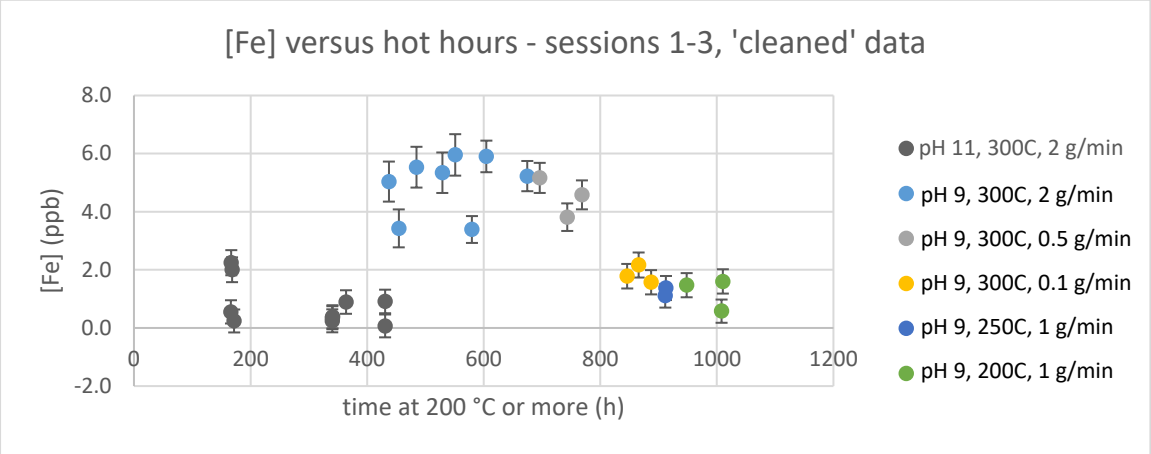

Figure 8.4. [Fe] levels versus time at 200 °C or more, in rig effluent during sessions 1 to 3. This plot shows only 'cleaned' data, after removal of data points considered to be unreliable based on a set of rules, see section 15.3.1. Per this set of rules, all data points from session 1 were removed. Nonetheless, the origin of the time axis corresponds with the start of session 1, when the oxide chamber and other SS316L surfaces of the rig were first exposed to high temperature coolant. As with all the ICP-MS data plotted in this thesis, a process was followed to account for contamination introduced by the sampling test tubes, and to provide estimates of experimental error (see section 15.2.1); consistent application of these methods have resulted in error bars which extend below zero for some data points, though negative concentrations are of course not possible.

8.2.7. Session 3 – Variability of results, and elevated Cr levels after leaving sampling line under stagnant conditions

For session 3, It was observed that levels were very variable from one sample to the next (i.e. scatter), especially for Fe and Ni; that levels changed over the course of days and weeks (i.e. actual changes to levels occuring in the rig effluent); and that samples taken shortly after a change in conditions could have erratic results compared with typical samples. Effluent was ordinarily routed along plastic tubing into a dump beaker, but diverted to the SS316L sampling line typically up to 20 minutes before sampling to allow any stagnant effluent to flush through. Comparison of samples for which varying amounts of flushing time had been allowed, consistently showed that Cr levels were high and sometimes erratic if insufficient flushing time was allowed. Tremaine and LeBlanc found that levels of Fe (from magnetite [121]) and Ni (from $Ni/NiO/Ni(OH)_2$ [3]) built up, due to supposed colloidal particles, under similar circumstances of stagnant conditions – these experiences from solubility studies show examples of build-up during stagnant conditions, though the elements concerned in those studies – Fe and Ni – did not show a clear effect of insufficient flushing of the sampling line in this study. Another possible explanation for Cr could be the effect of oxidising conditions in the sampling line by inward oxygen diffusion from the air, or by bulk air ingress from

the open end of the sampling line as coolant drips out, affecting Cr oxide solubility (see for example [14]), and chapter 3). For the 3 most extreme cases of insufficient sample line flushing, levels of Mn were also clearly elevated compared with other samples, having levels of ~ 60 – 100 ppb compared with ~ 20 – 50 ppb.

For all subsequent sessions of rig use, flow was continuously routed along the sampling line, and never diverted along the alternate route (plastic tubing), avoiding the problems of insufficient flushing of the sampling line. The above observations, regarding the effect of leaving the sanpling line under stagnant conditions followed by varying amounts of flushing time before sampling, provide a crude indication of the effect that passage of rig effluent through the sampling line may have on sample levels of each element in later sessions – for elements which had a clear increase when coolant was left in the sampling line for long periods and only partially flushed, it can be inferred that passing through the sampling line in the normal course of sampling may have caused an increase too, albeit to a lesser extent. In this context there is only evidence of an effect on Cr and Mn. Surrounding the rig with a nitrogen atmosphere, to investigate the extent to which sampling line effects may have been due to oxidising conditions in the last few mm of sampling line, (or further, when the sampling line had been left stagnant) may have been theoretically possible, but would have made sampling extremely difficult and was not attempted.

8.2.8. Sessions 3 and 4 – build-up, peaking, and decay of Ni levels over time

For both sessions 3 and 4, it was observed that levels of Ni seemed to rise over a period of several days, reach a peak value, and then start to fall (see Figure 8.5 and Figure 8.6), and this seemed to be occurring independently of temperature and flow rate conditions – at least to some extent, though it was difficult to determine the effect, if any, of changing conditions. This behaviour, along with the fact that Ni levels were higher than expected from solubility considerations, was indicative of the presence of particulates, and time-dependent levels in effluent controlled by deposition and release mechanisms.

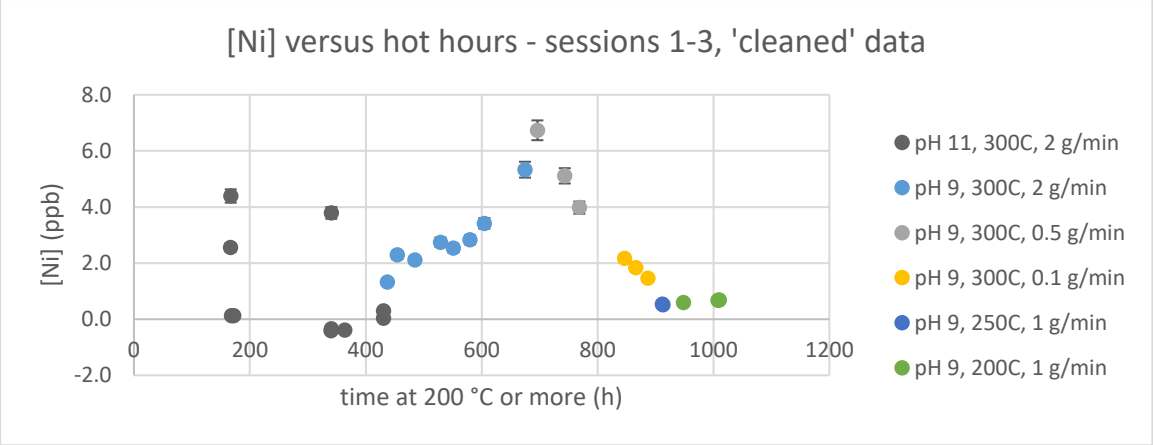

Figure 8.5. [Ni] levels versus time at 200 °C or more, in rig effluent during sessions 1 to 3. This plot shows only 'cleaned' data, after removal of data points considered to be unreliable based on a set of rules, see section 15.3.1. Per this set of rules, all data points from session 1 were removed. Nonetheless, the origin of the time axis corresponds with the start of session 1, when the oxide chamber and other SS316L surfaces of the rig were first exposed to high temperature coolant. The pH 11 data were taken during session 2, and were not very reliable, due to the effects of inconsistent sampling techniques, but did not contravene the rules and are included to give context for trends seen in later data; apparent negative Ni concentrations are a result of the method used to account for the effect of contamination from test tubes, by subtracting the mean levels of blanks from each result (see section 15.2.1), though negative concentrations are of course not possible – negative data merely show that some samples had lower levels of Ni than the average blank sample.

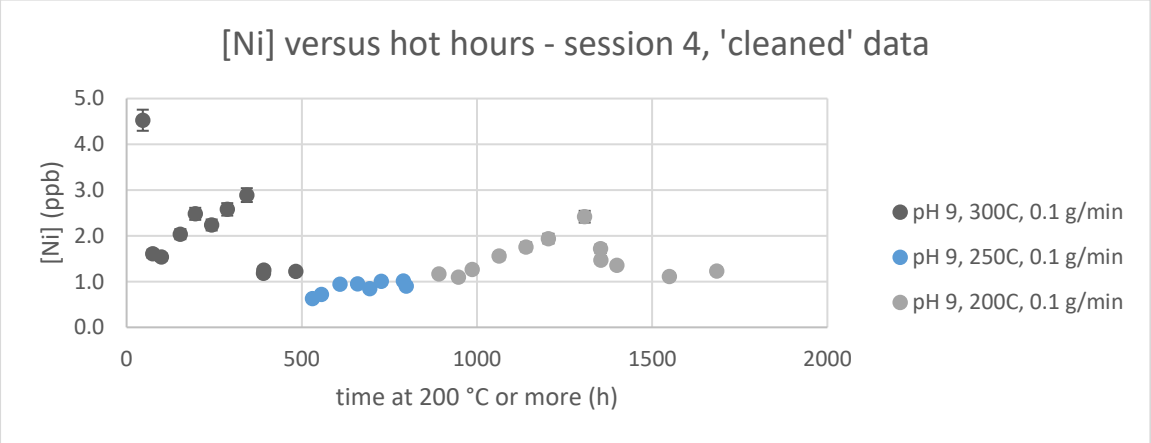

Figure 8.6. [Ni] levels versus time at 200 °C or more, in rig effluent during session 4. This plot shows only 'cleaned' data, after removal of data points considered to be unreliable based on a set of rules, see section 15.3.1.

8.2.9. Session 4 – statistical distribution of sample [Fe] levels

In response to findings from session 3, a large number of samples were taken during session 4 (to mitigate high degree of scatter), over long periods of time at the same temperature (to see more clearly if there are long term trends in the data), for three temperatures (to see whether levels of Fe bear any relation to differing solubility conditions in the heated part of the rig), and flow rate was not altered from 0.1 g/min for the whole session. Several feedwater samples were also taken, to give an indication of the levels of Fe and Ni which one might expect to see from samples controlled by passage through room temparture tubing alone. Results were plotted as histograms, to indicate the statistical distribution of the data, and are shown below in Figure 8.7 - Figure 8.9.

Levels of Fe were similar for each temperature, being clustered around the range 0 – 1 ppb but with relatively frequent samples at much higher levels. By plotting the distribution Fe levels of samples for all three temperatures combined, in bins of 0.1 ppb width, and comparing against distribution of the feedwater blanks prepared in the same way, it became apparent that the distributions were very similar, with the same modal range and similar appearance of scatter (though the number of feedwater samples was very small). Distribution of effluent samples had significant positive skew,

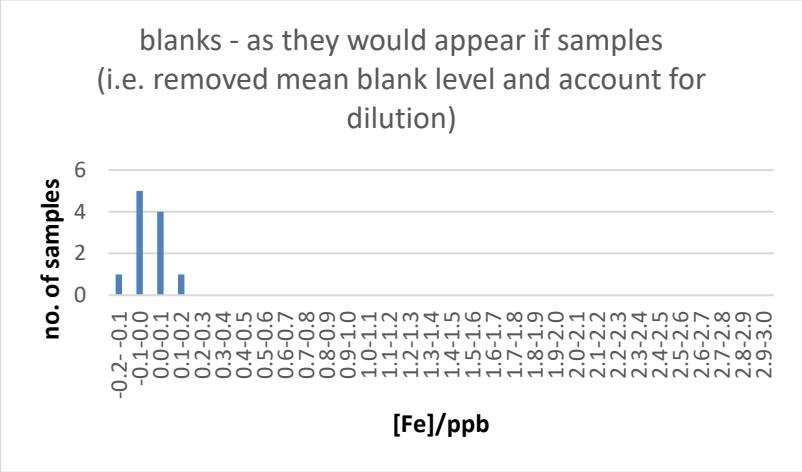

Figure 8.7. Histogram of [Fe] levels in blanks used for session 4 – as they would appear if samples. i.e. each reading was multiplied up to account for dilution by the addition of nitric acid, after subtracting the mean level on blanks, by the same process that was applied to samples

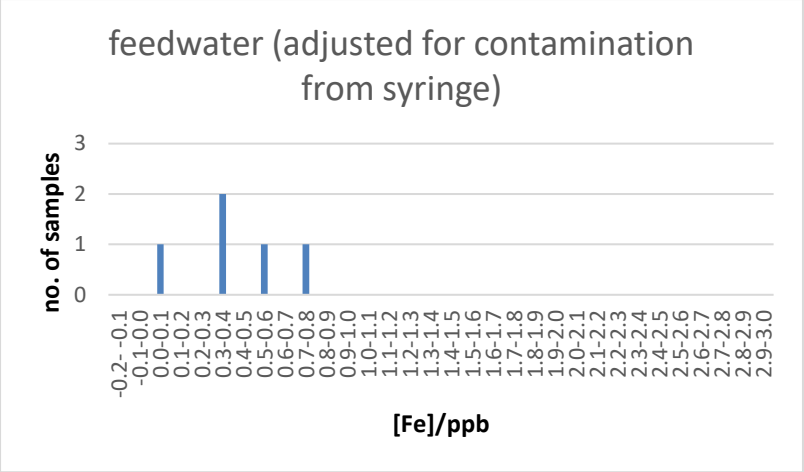

Figure 8.8. Histogram of [Fe] levels in feedwater samples taken during session 4, adjusted for contamination from syringe.

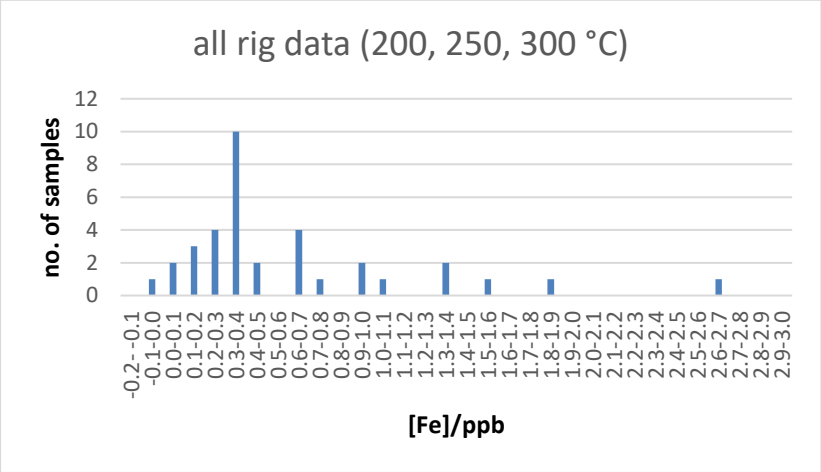

Figure 8.9. Histogram of [Fe] levels in all rig effluent samples taken throughout session 4, i.e. for runs at 200, 250 and 300 °C.

suggesting that taking a mean average could be susceptible to over-representation of high value outliers, with the modal range providing a useful alternative measure of average or typical value. This may have implications for past solubility studies, where ion exchange beds were used to measure integrated dissolved iron levels over large volumes of flow.

The fact that levels of Fe during session 4 were consistent between effluent samples at all three temperatures tested, and also consistent with feedwater samples, suggests that data taken at 0.1 g/min is representative of room temparture conditions rather than the solubility equilibrium attained in the heated part of the rig, unless high temperature solubility happens to be relatively temperature-insensitive – and similar to the levels observed in feedwater – at the prevailing conditions of hydrogen fugacity. By happenstance, solubility of magnetite at pH 9, at log H_2 = -3, is 1.0, 0.5, 1.0, and 0.6 at 300, 250, 200 and 25 °C (see Table 17.7). That is, relatively insensitive to temperature, and similar to levels observed in feedwater. However typical levels both in feedwater

and in rig effluent samples were slightly lower, at the modal range of 0.3 to 0.4 ppb Fe. It is possible that the values calculated from literature data are overestimates, and these effluent data truly reflect conditions in the heated part of the rig. Also, the additions of Cr and Ni give ferrite extra stability over pure magnetite. Indeed there are slightly lower levels for 250 °C than 200 or 300 °C, reflecting the trend in literature solubility data, though this may be adventitious. If the literature data do not give overestimates, then prevailing hydrogen fugacity must be at a lower value, at which room temperature solubility is below 0.3, as no mechanism could cause Fe levels to fall below solubility levels. Solubility of magnetite at pH 9, at log $\{H_2\}$ = -4, is 1.4, 0.5, 0.5, and 0.3 at 300, 250, 200 and 25 °C. At a comparable hydrogen fugacity to this, particulate Fe from corroding SS316L at room temperature, or from the heated parts of the rig, plus ~0.3 ppb dissolved Fe, could maintain Fe at the levels observed. Calculations on diffusion in this thesis suggested that most of the hydrogen would be retained in the effluent until a distance on the order of a cm from the exit point. If this is not the case, then a ~ 30 cm section of tubing at very low hydrogen fugacity would enable equilibration with Fe at rig walls having a very low solubility (<0.005 ppb), regardless of the hydrogen fugacity in the pressurised part of the rig as far as the BPR.

In summary, typical levels of Fe observed in the effluent during session 4 were surprisingly low, requiring log $\{H_2\}$ to be -4 or less to achieve such low values, despite the prediction of ~ 10^{-2} to 10^{-3} bar H_2 given by the model.

8.3. Main findings from sessions 5 and 6

8.3.1. Session 5 – Showing that results are not very repeatable from one session to the next, and readings which appear particulate-based are not changed by the presence of filters

The table below shows results across the three sessions which used pH 9 feedwater. Though session 3 showed a positive flow rate dependence on Fe levels, the opposite was true for session 5, though this can be seen in the light of an apparent surge in particulate matter which happened to start mid-way through the time spent at 300 °C, 0.1 g/min, continuing until 250 °C data was taken and perhaps

also present at 200 °C. A 3.0 µm filter was installed at the time of the highest Fe levels, and particulates were seen on it.

Across the 3 sessions, levels of Ni and Cr are typically consistent with those seen in the feedwater. Levels of Mn are sometimes comparable, sometimes higher. Levels of Mo are consistently much higher in effluent samples than in the feedwater.

Table 8.2. Summary table for pH 9 results. Session 5 data, with session 3 and 4 data below for comparison.

Element ***(solubility , 25 °C)*** †	**T:300** $\dot{m}$**: 2**	**T:300** $\dot{m}$**: 1**	**T:300** $\dot{m}$**: 0.5**	**T:300** $\dot{m}$**: 0.1**	**T:250** $\dot{m}$**: 1**	**T:250** $\dot{m}$**: 0.1**	**T:200** $\dot{m}$**: 1**	**T:200** $\dot{m}$**: 0.1**	**Feed-water**
[Fe], ppb ***(0.00)***		3 to 4	2	6, rising to 30-40		20		4	~.5 – 2.5
(sess 3)	6		5	2	1-1.5		1-1.5		
(sess 4)				~0.8 (.3–1.5)		~0.2 (.0-.4)		~0.5 (.1-1.4)	~0.6 (.1-1.0)
[Cr], ppb ***(0.01)***		0.00	0.00	0.01		0.02	0.01		~0.02
(sess 3)	.3 falls to .05		0.1	.16 falls to .10	0.00		0.00		
(sess 4)				.1-.2, falls to 0.01		0.03 climbs to 0.30		0.01 falls to 0.00	.00-.02
[Ni], ppb ***(27)***		0.4	0.3	~0.65 (0.4 to 0.9)		1.3		0.7	~0.4 – 0.9
(sess 3)	1-3, climbs to 5		7, falls to 4	2.2 falls to 1.5	0.4		0.7		
(sess 4)				~2, (5-8 early on)		0.5 climbs to 1.0		~1.4 (.8-2.4)	~0 – 2.5
[Mo], ppb		1 rises to 100	~90 – 100	~ 40 – 70		20		10	~0.7
(sess 3)	Rises to 25, falls to 20		30 rises to 60	80 rises to 90	50 falls to 35		12 falls to 8		
(sess 4)				40-100, settles at ~ 55		30, falls to 20		10	~0.5
[Mn], ppb		1.5	1.9	3.2		8.3		20.5	~4 – 7
(sess 3)	30-100, settles at 20		40, falls to 25	17, falls to 13	7		14		
(sess 4)				90, settles at 5.3		3, falls to 2		4, rises to 25, falls to 13	~2 – 6

† For Fe, Cr and Ni, solubility of the most stable oxide phase at pH9, 25 °C, under neutral redox conditions is provided for reference. Solubility of magnetite is 0.3 ppb under those conditions; 0.00 ppb under mildly reducing conditions (hematite/magnetite equilibrium); and 58 ppb in the presence of air (i.e. 0.2 bar oxygen)

8.3.2. Session 6 – Showing that filters have no effect on observed Fe levels, finding particulates from hot part of rig on filter holders

Levels of all 5 elements studied were not significantly different with filters in place than when there was no filter. Elevated Fe levels could be due to very small colloidal particulates (smaller than the 0.05 µm filter), or simply supersaturated solution. However, small particles are known to dissolve on filters whe filtration is performed over a timescale of hours or more [36].

Levels of Ni in effluent were comparable with feedwater for both sessions 5 and 6, but the level was only 0.1 for sess 6 (pH 10) compared with 0.4 to 0.9 for sess 5 (pH 9).

For session 6, pH 10, levels of Cr were consistently ~ 2 ppb, which was surprising as they stayed very close to 0.01 ppb at pH 9. Solubility is expected to be around 0.01 ppb at both pH 9 and pH 10. This is discussed further in section 8.3.3. Levels of Fe were maintained at low levels at pH 10, consistent with feedwater for most conditions, except at 250 °C, 0.1 g/min.

Deposits of oxide crystallites, of the same form as observed on corroding surfaces in the hot part of the rig, were observed on the plastic housing of some of the filters used during session 6, demonstrating that such particulates were being transported in the coolant.

*Table 8.3. C*omparison of results from the two sessions which employed SS4316L chips.
Levels of each element which are significantly different in the effluent compared with feedwater are highlighted in red and italicised.

	Fe	Cr	Ni	Mo	Mn
Sess 5 (pH 9)	*2 to 40*	0.01	0.4 to 0.9	*~ 10 to 100*	*1 to 3, or 21*
Feedwater	.5 to 2.5	0.02	0.4 to 0.9	0.7	4 to 7
Sess 6 (pH 10)	0.1 to 0.3	*2*	0.1	*~ 30 to 700*	*0.1*
feedwater	0.2	0.01	0.1	0.1	0.03

Table 8.4. Summary table of ICP-MS results for rig with chips (session 5 and 6).

Element ***(solubility , 25 °C)*** †	**T:300** $\dot{m}$**: 2**	**T:300** $\dot{m}$**: 1**	**T:300** $\dot{m}$**: 0.5**	**T:300** $\dot{m}$**: 0.1**	**T:250** $\dot{m}$**: 1**	**T:250** $\dot{m}$**: 0.1**	**T:200** $\dot{m}$**: 1**	**T:200** $\dot{m}$**: 0.1**	**Feed-water**
[Fe], ppb ***(0.00)*** **(s5)**		3 to 4	2	6, rising to 30-40		20		4	~.5 – 2.5
(sess 6)		0.1	0.1	0.3		0.8		0.3	0.2
[Cr], ppb ***(0.01)*** **(s5)**		0.00	0.00	0.01		0.02		0.01	~0.02
(sess 6)		0.8	0.6	2.1		2.3		2.2	0.01
[Ni], ppb ***(27)*** **(s5)**		0.4	0.3	~0.65 (0.4 to 0.9)		1.3		0.7	~0.4 – 0.9
(sess 6)		0.1	0.0	0.1		0.1		0.1	0.1
[Mo], ppb (sess 5)		1 rises to 100	~90 – 100	~ 40 – 70		20		10	~0.7
(sess 6)		700 falls to 60	90 falls to 60	~ 150		~ 80		~ 30	0.1
[Mn], ppb (sess 5)		1.5	1.9	3.2		8.3		20.5	~4 – 7
(sess 6)		0.1	0.1	0.1		0.1		0.1	0.03

† For Fe, Cr and Ni, solubility of the most stable oxide phase at pH9, 25 °C, under neutral redox conditions is provided for reference. Solubility of magnetite is 0.3 ppb under those conditions; 0.00 ppb under mildly reducing conditions (hematite/magnetite equilibrium); and 58 ppb in the presence of air (i.e. 0.2 bar oxygen)

8.3.3. Session 6 – Comparing effluent levels, and inferred net release rate to coolant, of Mo and other elements

Throughout the study, levels of Mo and Mn were often found to be high, in some cases reaching 100 ppb or over, despite their low concentration in the alloy compared with other elements (2.5 and 1.7 wt% respectively). This indicates relatively high solubility of the respective single metal oxides (thought to be MnO and MoO_2 under conditions of the rig), whose precipitation would otherwise maintain low levels, and high 'solubility', or partition coefficient, for dissolution from the corrosion film (i.e. high ratio of concentration of the metal in aqueous solution to concentration of the metal in solid solution in ferrite or chromite at equilibrium). MoO_2 solubility is known to be high, see section 4.1.7.

Figure 8.10 shows the effluent concentrations of Mo and Mn which would be expected in the limiting case of zero retention of these two elements in the corrosion film, with 100% of each element's contribution to corrosion release flux being released to the coolant, against which are plotted measured data. Data for Mn suggests almost full retention in the corrosion film under these conditions. On the other hand, Mo had higher than expected levels, which fell almost linearly from about 400 ppb at 70 hours to 60 ppb at 500 hours. This suggests leaching of Mo from any corrosion film already present, or even preferentially from the underlying alloy. Although the oxide chamber was freshly replaced for session 6, some ¼" tubing was present from previous sessions, with oxide film established under mostly pH 9 conditions. As for previous results, Mo increases at slower flow rates, but to a lesser extent than would be expected from a constant net release rate. This behaviour can be interpreted per solubility considerations: if Mo is present in the 2+, 3+, or 4+ oxidation state in the spinel, then dissolution is oxidative, since soluble Mo exists in the 6+ oxidation state under the rig conditions (as predominantly $HMoO_4^-$ or MoO_4^{2-}) [132]. Therefore a 5-fold slowing of the flow rate could be expected to produce a 5-fold increase in hydrogen concentration, and thus decrease in solubility or partition coefficient. A situation intermediate between corrosion rate control (zero retention in film, [Mo] $\propto$ 1/flow rate, ~constant Mo release rate to solution), and solubility control (~full retention in film, ~constant [Mo], release rate to solution $\propto$ flow rate), may produce this behaviour with changing flow rate.

An alternative explanation for the [Mo] behaviour can be seen in Figure 8.11 in which the data from Figure 8.10 are adjusted to provide net release rate to coolant. At around 865 hours, the continuity of [Mo] concentration data shortly before and after the change in flow rate causes a discontinuity in apparent release rate, but this effect is short-lived, on the order of rig residence time. There appears

to be a long-term trend of falling release rate, falling more rapidly than expected by corrosion kinetics.

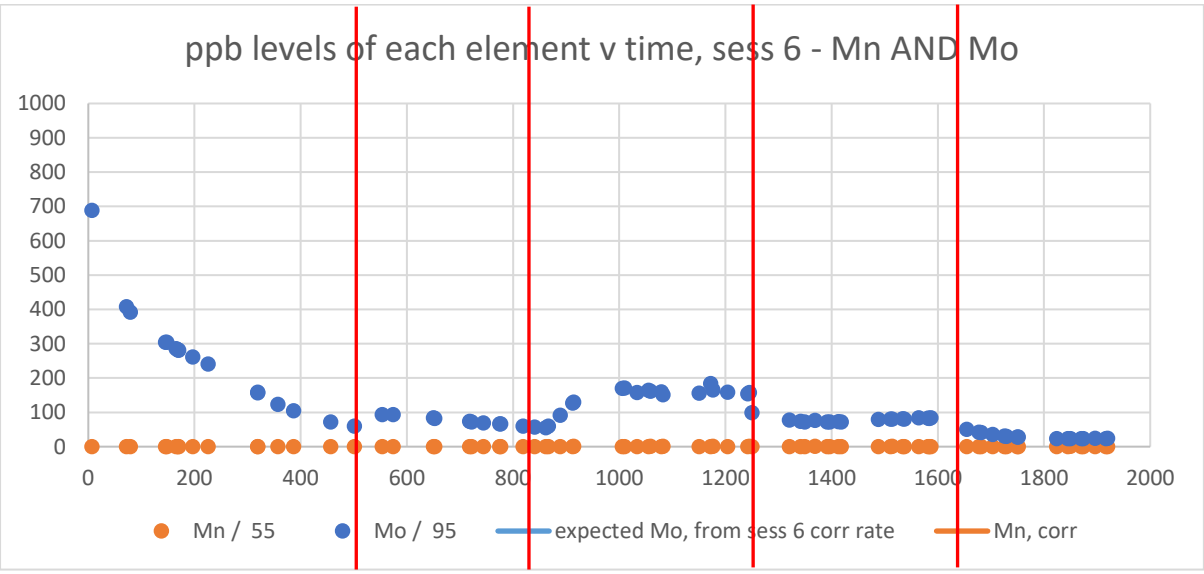

Figure 8.10. Levels of Mo and Mn measured during session 6 (ppb), against time (h).
Solid lines show levels expected if 100% of the Mo and Mn components of corrosion release flux were to release immediately to solution. Vertical lines demarcate the 5 sets of conditions employed: 300 °C, 1 g/min; 300 °C, 0.5 g/min; 300 °C, 0.1 g/min; 250 °C, 0.1 g/min; and 200 °C, 0.1 g/min.

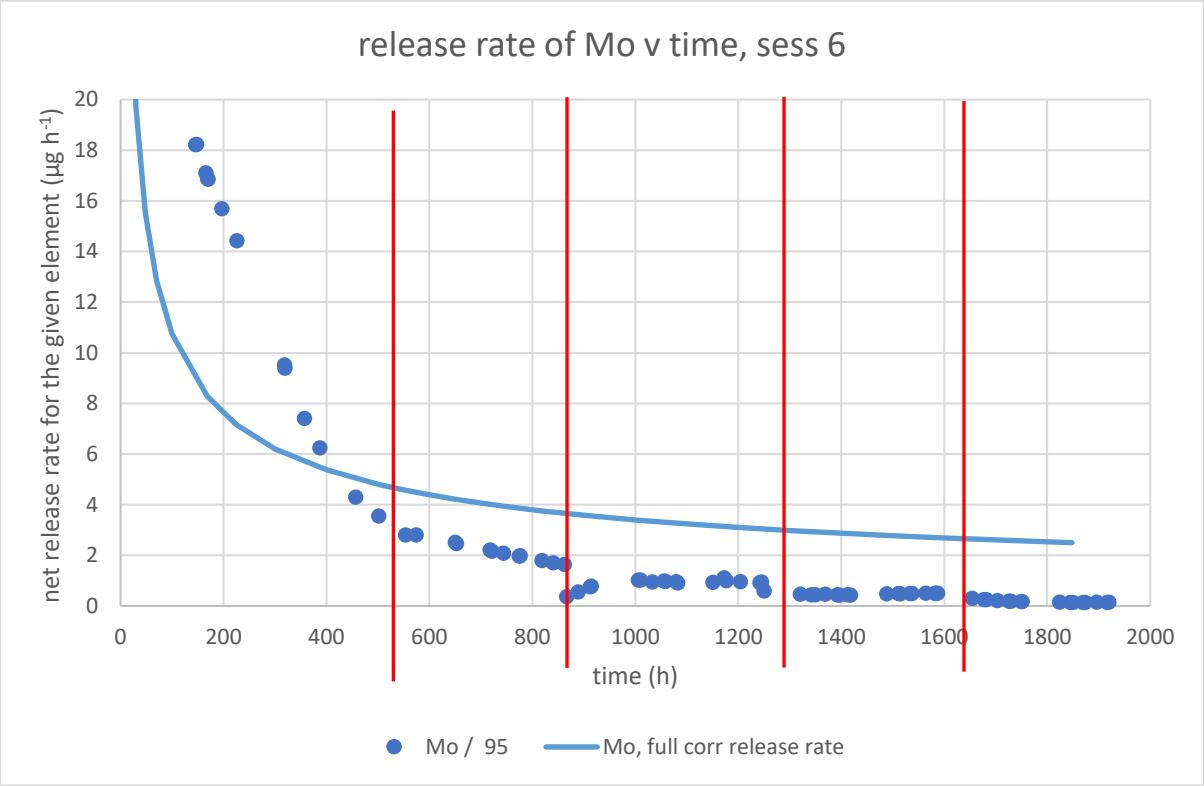

Figure 8.11. Net release rate of Mo versus time during session 6 (pH 10, chips).
The data and fit from Figure 8.10 are shown here as converted to a release rate, taking into account the coolant flow rate. Vertical lines demarcate the 5 sets of conditions employed: 300 °C, 1 g/min; 300 °C, 0.5 g/min; 300 °C, 0.1 g/min; 250 °C, 0.1 g/min; and 200 °C, 0.1 g/min.

Figure 8.12 and Figure 8.13 are analogous to Figure 8.10 and Figure 8.11, but for Fe, Cr, Ni and Mn. Higher Cr concentrations at slower flow (Figure 8.12) can be interpreted in terms of a (net) release-rate controlled mechanism: release rate of Cr can be seen to slowly decay over the first 1000 hours, before maintaining a steady rate (Figure 8.13). The smoothly varying nature of net Cr release rate suggests a dissolution process rather than direct sampling of coolant-borne particulates. Ingress of oxygen to the rig is one possible explanation, though this would cause Fe solubility to be very low at room temperature, with a tendency to cause lower results at slower flow rate where residence time in the sampling line is longer, but the opposite effect occurs. Spallation of particulate matter is another possible cause. The high Cr:Fe ratio would suggest a pure Cr-based phase, such as $Cr(OH)_3.xH_2O$ from corrosion film in the sampling line, or CrOOH in the heated part of the rig if present. It was known that particulates were present near the end of the sampling line, from deposits found on the plastic filter housing, and a few particulates found on filters, therefore the most likely explanation is perhaps the leaching of Cr from ferrite and/or chromite particulates deposited on the filter holder or on filters, in the oxidising conditions close to the sampling point. Under steady flowing conditions, oxygen is expected to diffuse a few mm or cm upstream, see 0.

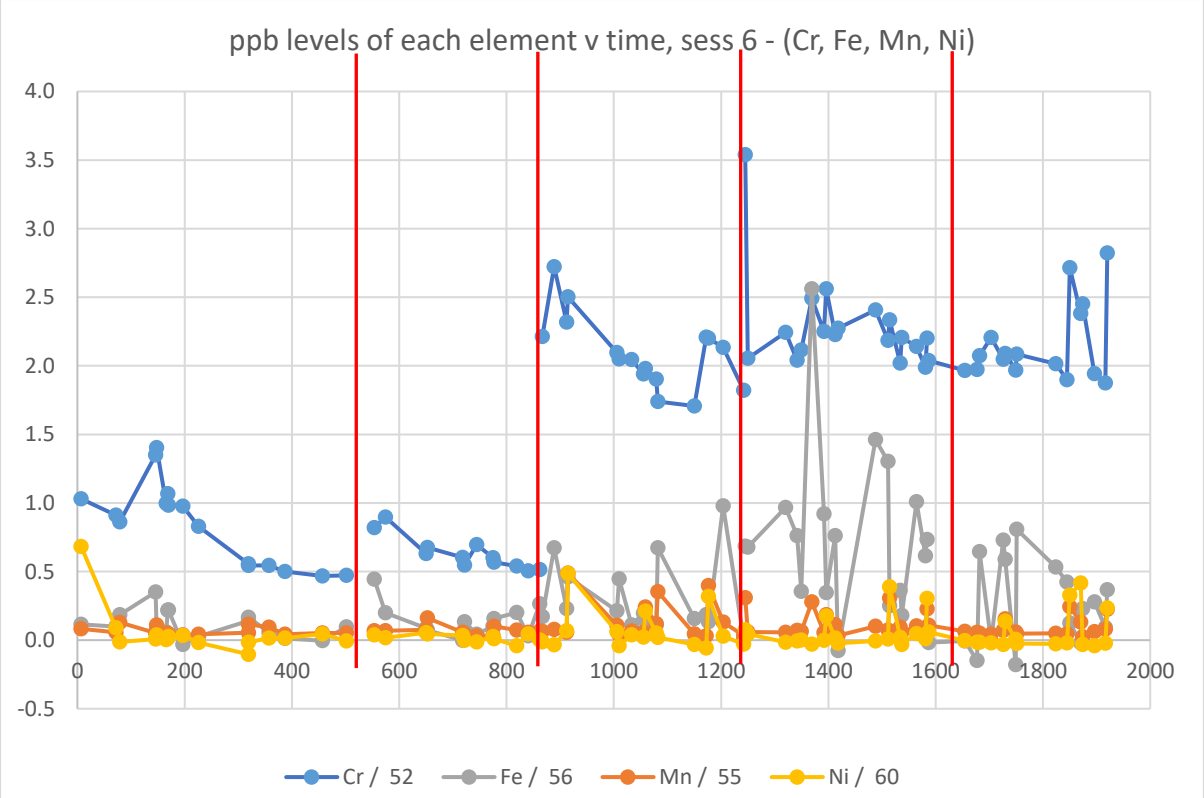

Figure 8.12. Levels of all elements except Mo measured during session 6 (ppb), against time (h). Vertical lines demarcate the 5 sets of conditions employed:
300 °C, 1 g/min; 300 °C, 0.5 g/min; 300 °C, 0.1 g/min; 250 °C, 0.1 g/min; and 200 °C, 0.1 g/min.

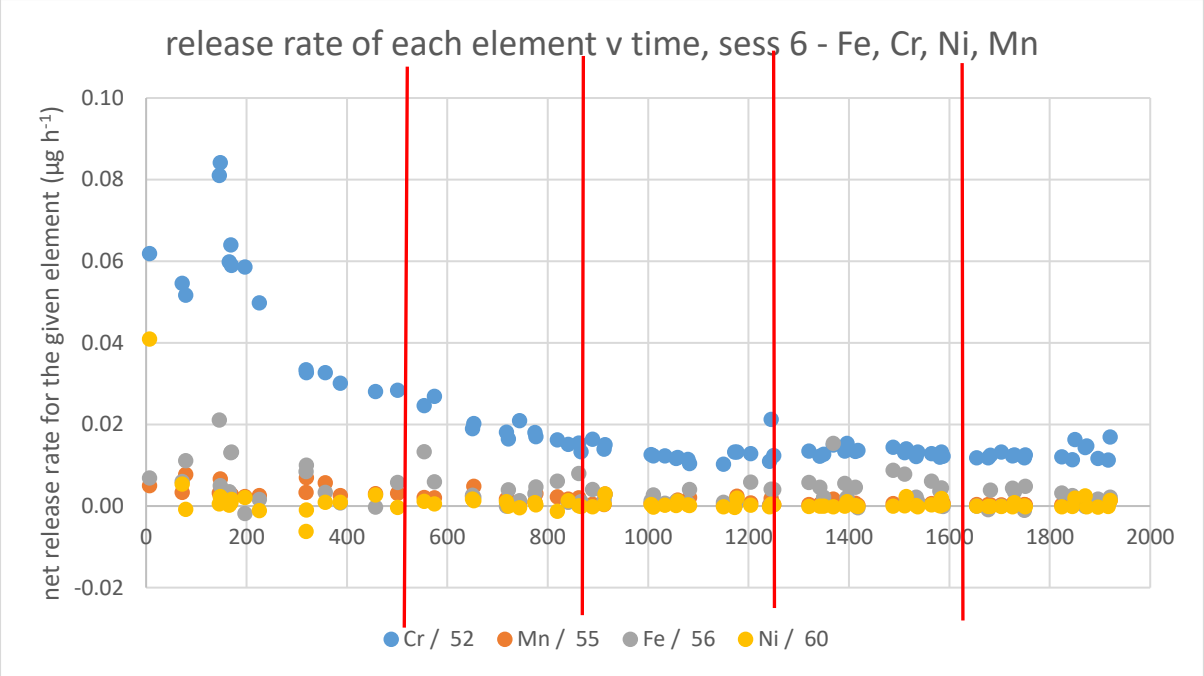

Figure 8.13. Net release rate of Fe, Cr, Ni and Mn versus time during session 6 (pH 10, chips). The data from Figure 8.12 are shown here as converted to a release rate, taking into account the coolant flow rate. Vertical lines demarcate the 5 sets of conditions employed: 300 °C, 1 g/min; 300 °C, 0.5 g/min; 300 °C, 0.1 g/min; 250 °C, 0.1 g/min; and 200 °C, 0.1 g/min.

9. Results:

Dissolved Hydrogen Levels in Coolant – Mass Spectrometry of Effluent Gases

In this chapter, results are presented from the analysis of gases released from two rig effluent samples, using a mass spectrometer. A model was used to interpret the findings to give an estimate of dissolved hydrogen level in the rig effluent at the time of sampling. Full details of the model are provided in the appendices (chapter 16).

In Figure 9.1, the two measurements of effluent hydrogen levels made in this way are plotted on the same graph as predictions according to the effluent hydrogen model, which is provided in the appendices (section 17.2).

9.1. Overview of method

Two sealed samples of rig effluent were taken during sessions 5 and 6 in the sampling cell, and analysed in a mass spectrometer (MS) for hydrogen content, as described in section 7.6. Another sample was taken beforehand, from which the total quantity of released gas was measured.

The MS and accompanying apparatus enabled measurement of released volumes of nitrogen (with which the sampling cell was filled before sampling), and hydrogen, from the pressurised gas phase in the sampling cell. Calibration to absolute quantities was not explicitly performed, and the apparatus appeared to underestimate total volumes (though this could alternatively have been due to gas leakage from the cell); however, independent measurement of released volume from the cell, together with a model to account for gas retention in the aqueous phase, enabled the absolute volume of hydrogen in the cell – and in turn the effluent hydrogen concentration – to be determined from only a ratio of measured hydrogen to nitrogen gases, which could be accurately measured.

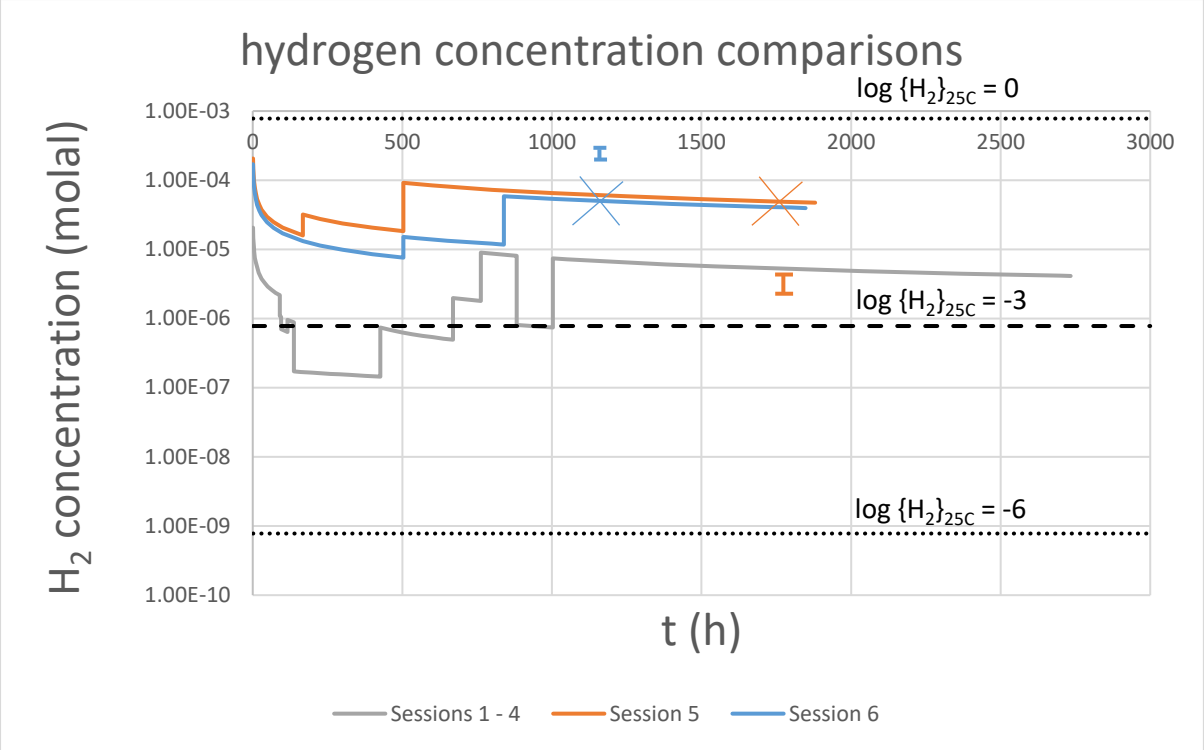

Figure 9.1. Modelled steady state hydrogen concentrations in the rig during sessions 1 to 6, and hydrogen concentration measurements made during sessions 5 (pH 9, chips) and 6 (pH 10, chips). Approximate values from the two measurements are indicated, by error bars, and for each measurement the corresponding modelled hydrogen concentration is marked with a colour-coded cross – the orange cross at ~1750 h represents the first reading, taken during session 5, and the blue cross at ~ 1200 h represents the second reading, taken during session 6. Lines are plotted at selected values of log{H_2}$_{25C}$ for ease of reference. 10^{-3} molal represents 22.7 scc/kg hydrogen.

9.2. Taking pressurised samples

Key information regarding the taking of pressurised samples for dissolved hydrogen analysis is summarised in Table 9.1 below.

Table 9.1. Key information regarding pressurised effluent samples for hydrogen gas analysis

Sample #	Time to fill	Pressure when first filled	Subsequent readings (time since sample taken)	Other information according to model †
Sample "0"	469 min	15.8 bara immediately	N2_prompt gas volume measured (26 d) 43 +/- 2 scc *	V_liquid = 47 cc Fill fraction, F, = 0.91 ⇒ V_gas = 5 cc ⇒ V_tot = 52 cc N2_tot = 54 scc N2_gas = 47 scc N2_prompt = 42 scc
Sample 1	452 min	15.8 bara immediately	Mass spec (0.75 d)	V_liquid = 45 cc Fill fraction, F, = 0.88 ⇒ V_gas = 6 cc ⇒ V_tot = 52 cc N2_tot = 53 scc N2_gas = 48 scc N2_prompt = 42 scc
Sample 2	470 min	15.2 bara immediately 14.4 bara after 46 min	11.2 bara (5 d) 11.2 bara (18 d) 11.0 bara (113 d) Mass spec (114 d)	V_liquid = 47 cc Fill fraction, F, = 0.91 ⇒ V_gas = 5 cc ⇒ V_tot = 52 cc N2_tot = 54 scc N2_gas = 46 scc N2_prompt = 42 scc

* included a small amount of water

† see appendix for explanation of the terms

9.3. Analysis of gas released to MS, from sample 1

As described in section 7.6.2, gas from the sample was released into a steady stream of Ar carrier gas, and the mixed gas stream was continuously sampled and analysed in a benchtop MS. Readings from the MS, produced every 6 seconds, represented the volume flow rate of each gas (that is, total volume flow rate of the gas mix multiplied by mole fraction of the particular gas), in arbitrary units (a.u.); integration of these values over the course of the 'surge' of gas release from the cell allowed the determination of total volume of each gas released, in a.u.; and the measured ratio of hydrogen to nitrogen volumes was used in conjunction with a model to determine hydrogen concentration in the rig.

Ar flow rate had previously been calibrated at 100 ml/min for other work. Flow was controlled at a steady rate, though it was uncertain whether that rate still equated to 100 ml/min. Absolute volumes of nitrogen and hydrogen, assuming 100 ml/min Ar flow rate, are provided for reference, and compared to the nitrogen volume predicted by model.

9.3.1. Raw data from mass spectrometer

In Figure 9.2 the raw data are plotted on a logarithmic scale, in arbitrary units. Some data points were negative, and so are absent from the plot, but are present in later plots on a linear scale. A clear peak is seen in nitrogen readings over the first five minutes or so.

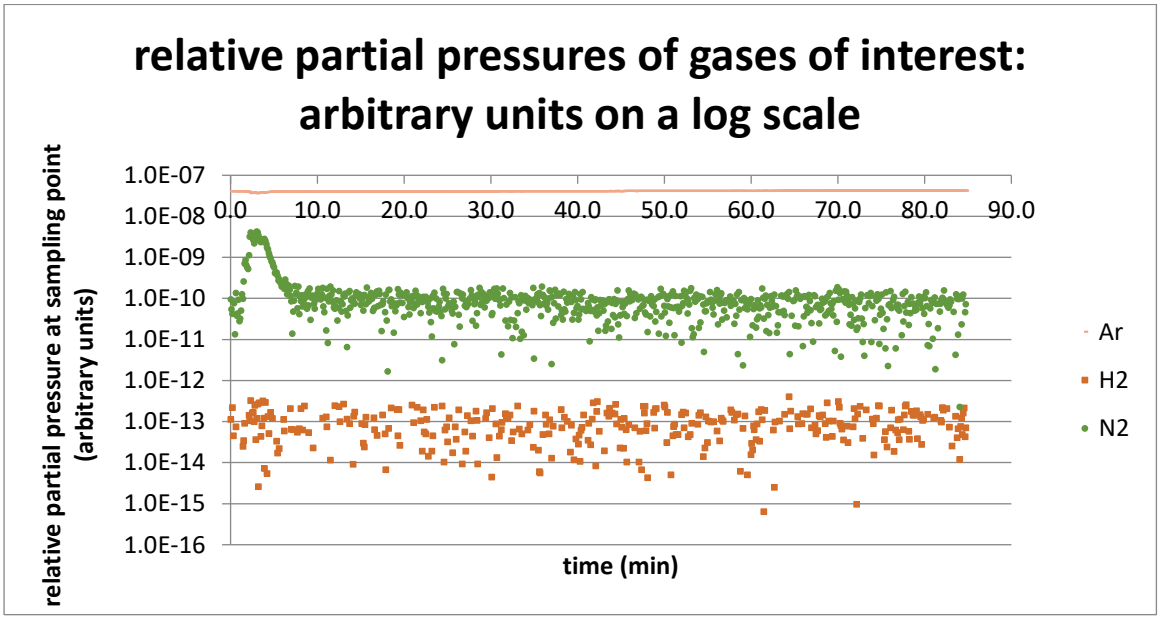

Figure 9.2. Raw data from mass spectrometer, for argon, hydrogen and nitrogen, on analysing gases from pressurised rig effluent sample #1. Data given in arbitrary units, on a log scale.

9.3.2. Comparison of argon and nitrogen data on a linear scale, to test whether the two sensors in the MS are calibrated consistently

Data for the major gas components, Ar and N_2, are plotted in Figure 9.3 on a linear scale, representing relative partial pressure of each gas at the sampling point. The sum of all partial pressures for the raw data at t = 0 min, in arbitrary units (4.06×10^{-8} a.u.) was used as a reference value: all data points were normalised, by dividing by this value and multiplying by 100, to provide a more intuitive scale of arbitrary units compared with the raw data.

The peak in nitrogen readings was almost exactly mirrored by a dip in Ar readings, such that overall pressure obtained by summing their partial pressures remained almost constant. An apparent slight rise in overall pressure observed, of around 1%, is consistent with the effect which might be expected from addition of gas from the sample to the constant flow of carrier gas. It is therefore concluded that calibration of the Faraday cup (which measured Ar) was consistent with that of the electron multiplier (which measured all other gases) in the MS, so that 1 a.u. of Ar represents the same amount of gas as 1 a.u. of the other gases.

Over the full 85 minutes during which readings were taken, the total pressure at sampling point as indicated from the data exhibited a drift over time, to lesser and then greater values. This may be an artefact of the MS and sampling system, or may indicate a change in Ar flow rate. However the readings for (N_2 + Ar) were relatively stable over the five minutes or so during which gases were released from the sample.

9.3.3. Data converted to volume flow rate by assuming Ar flow rate of 100 ml/min

For illustrative purposes, the data as converted to volume flow rate (ml/min) are plotted on a linear scale in Figure 9.3 for Ar and N_2, assuming Ar flow rate of 100 ml/min. It was also assumed that the two sensors in the MS were calibrated consistently with each other, see above. For each 6 s time interval, conversion was achieved by dividing raw values for each gas by the raw value for Ar gas and multiplying by 100 ml/min.

If Ar flow rate was not necessarily 100 ml/min, but was nevertheless maintained at a relatively constant value during the release of gas from the sample, then the units of flow rate in the figure can be treated as arbitrary units.

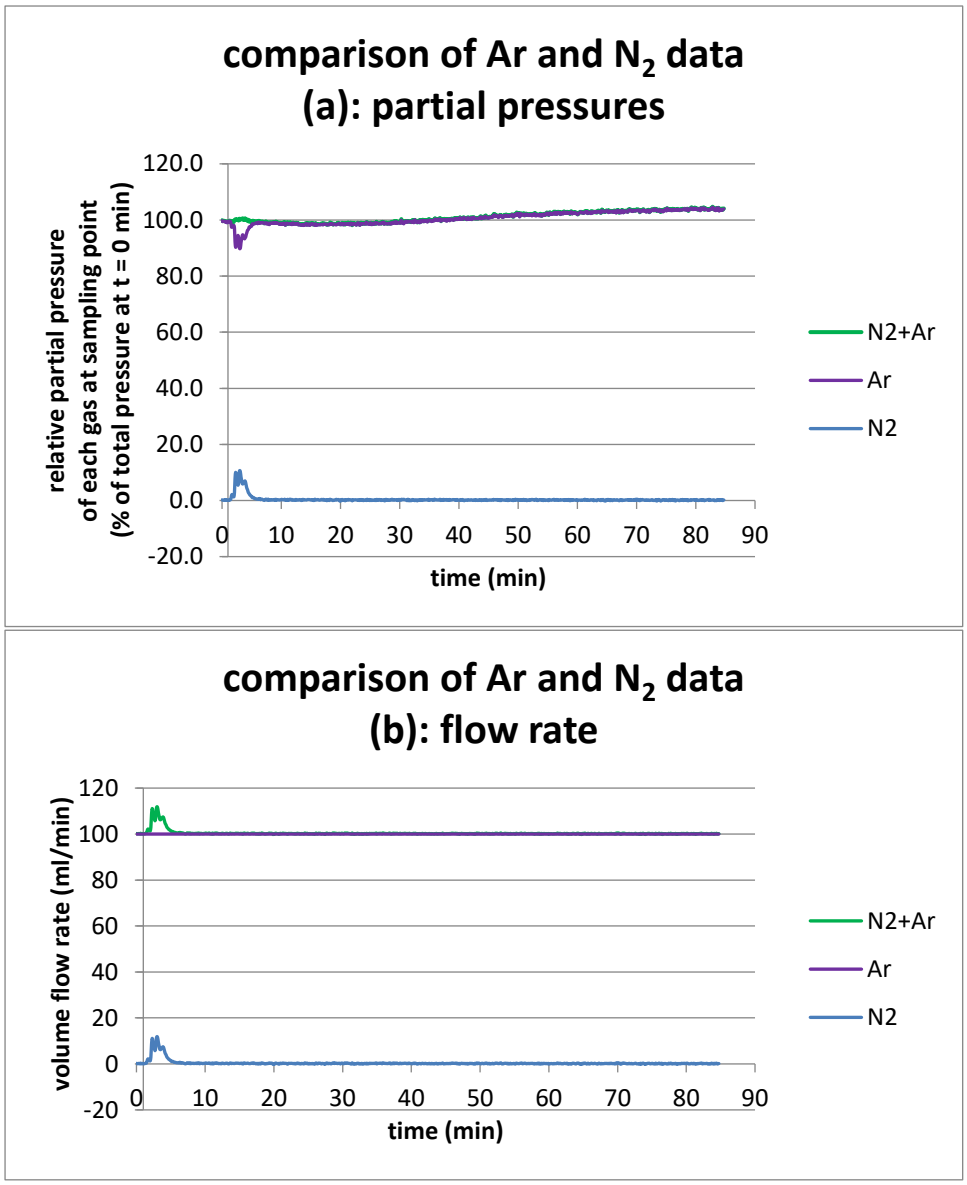

Figure 9.3. Comparison of Ar and N_2 data from mass spectrometer, on analysing gases from pressurised rig effluent sample #1. Data given on a linear scale in units of partial pressure (a); and in units of flow rate assuming a constant Ar flow of 100 ml/min (b).

9.3.4. Estimates for actual volumes of hydrogen and nitrogen released from sampling cell, and their ratio, using assumption of 100 ml/min argon flow rate

Data for the first 20 minutes are shown in Figure 9.4 for nitrogen and for hydrogen, after converting to volume flow rate by assuming a constant 100 ml/min Ar flow rate (see above). Hydrogen data are scaled up by a factor of 10^4 for ease of comparison. The nitrogen data show a composite peak lasting around five minutes, composed of four sub-peaks, which demonstrate the methodology used by the operator to introduce gas gradually by opening the needle valve between the sampling cell and the measurement apparatus incrementally. Trends in the hydrogen signal are difficult to discern, due to the low signal to noise ratio. Using a 6 period moving average in Excel® software, a clear peak can be discerned coinciding with the timing of the nitrogen (composite) peak. The background level of hydrogen was on average less than zero, implying a slight zero offset error. However, this should not cause a problem as long as background levels are accounted for and as long as sensitivity to hydrogen maintains linearity at these concentrations, which was assumed to be the case.

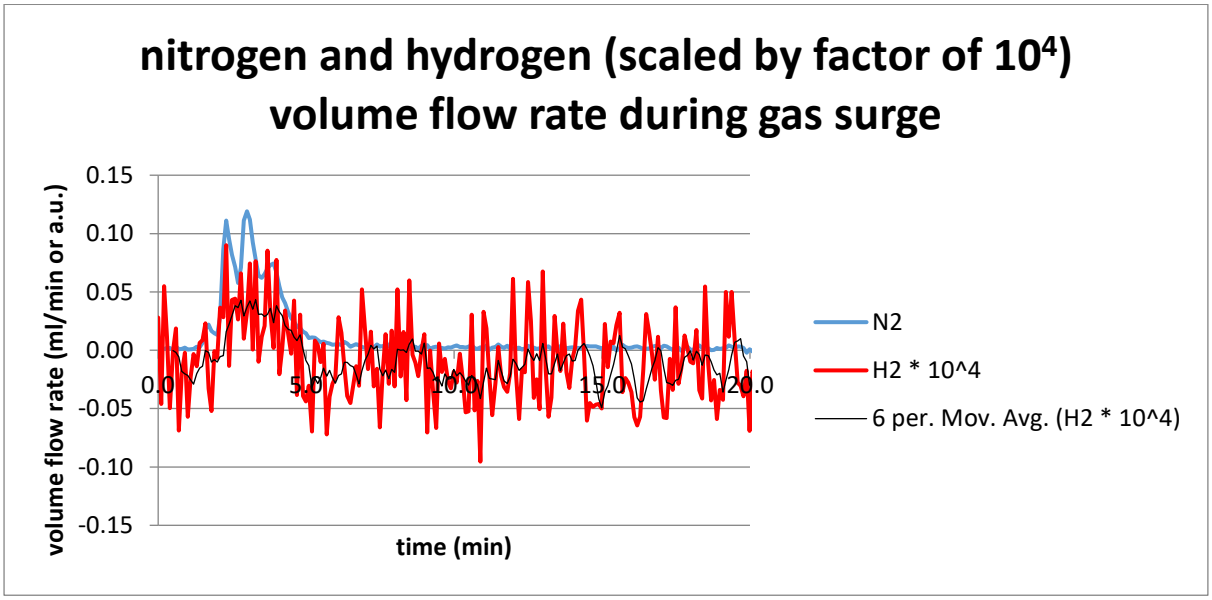

Figure 9.4. Nitrogen and hydrogen readings from the mass spectrometer, on analysing gas from pressurised rig sample #1, around the time of the gas surge from sample, showing an increase in levels of each gas detected over a period of around 3 minutes.
For the hydrogen data a 6 period moving average is also shown (plotted using Excel®) to show trends in the data more clearly.

Figure 9.5 illustrates the method used to fit the peak in nitrogen and hydrogen levels, by removing the background level to estimate the integrated volume of each gas released from the sample. The duration of the gas surge from the sampling cell was around 5.5 minutes, from around 1.5 minutes to 7.0 minutes, as seen from the nitrogen data. During this time period, the averaged nitrogen flow rate was 3.81 ml/min. Background readings over the following 5.5 minutes, and preceding 1.5 minutes, corresponded to a flow rate of 0.23 ml/min. The difference, multiplied by the 5.5 minute duration gives a reading of 19.7 ml of nitrogen gas.

Applying the same method to the hydrogen surge, the averaged flow rate without accounting for background was found to be 5.8 x 10^{-5} ml/min, and the background was found to be -15.1 x 10^{-5} ml/min, giving a reading of 1.15 x 10^{-3} ml of hydrogen gas over the 5.5 minute time period. This reading is sensitive to the level of background, therefore the variation in background readings was explored. Background readings for hydrogen were found to drift upwards slightly over the course of the 85 minutes the apparatus was left running. The average over the full 85 minutes, apart from data taken during the gas surge, was -9.7 x 10^{-5} ml/min: when this value is used as the background reading, a value of 0.85 x 10^{-3} ml hydrogen gas is provided. Since the drift in background levels took place over a fairly long time period after the gas surge, more weighting was given to the earlier figure, and a value of (1.1 +/- 0.2) x10^{-3} ml was chosen.

The key result from these measurements is the ratio of hydrogen to nitrogen volumes. The measured value of this ratio is (5.6 +/- 1.1) x10^{-5}.

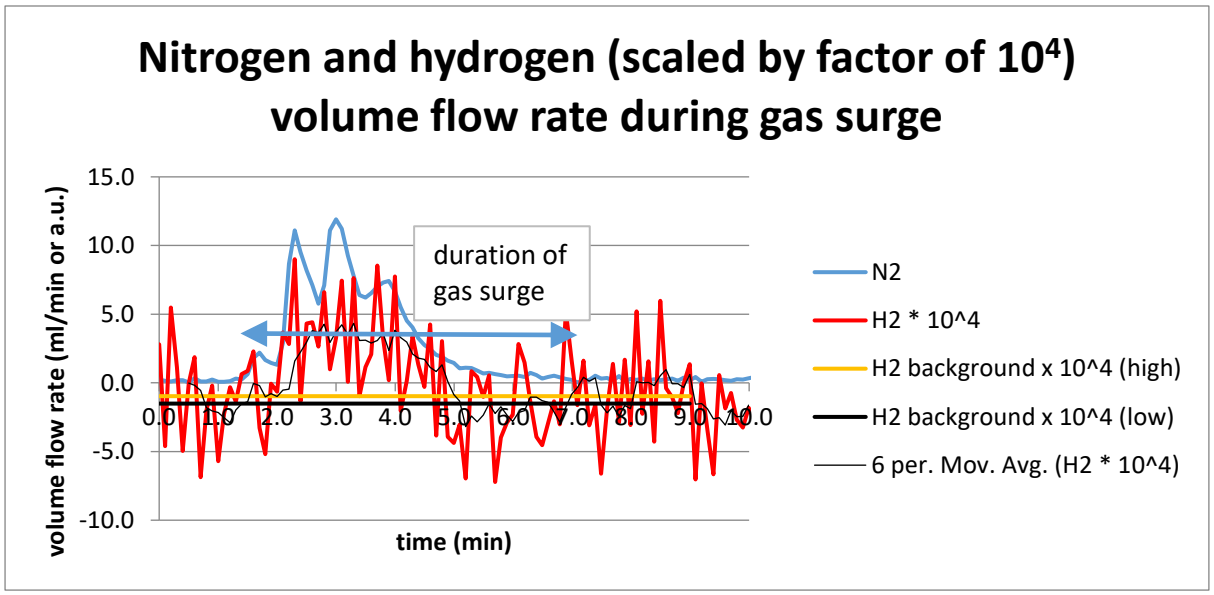

Figure 9.5. Plot illustrating the method used to fit the peak in hydrogen and nitrogen levels, to estimate the integrated volume of each gas released from pressurised rig effluent sample #1. Integrated volume is calculated as actual volume (ml), assuming 100 ml/min Ar flow rate is correct, or in arbitrary units (a.u.) if not.

9.4. Analysis of gas released to MS, from sample 2

Sample 2 was analysed in like manner to sample 1. However, in this case the results indicated that the two detectors in the MS were calibrated inconsistently with each other, so a conversion factor of about 20 was used between results for Ar, and results for other gases, in a.u.

9.4.1. Comparison of argon and nitrogen data on a linear scale, to test whether the two sensors in the MS are calibrated consistently

Data for the major gas components, Ar and N_2, are plotted in Figure 9.6 (a) on a linear scale, representing relative partial pressure of each gas at the sampling point. In contrast with the data for sample 1 (Figure 9.3(a)), where the surge in hydrogen was almost exactly mirrored by a dip in Ar readings, there is a dip in argon levels but no appreciable peak in nitrogen is apparent on the same scale.

Comparison of the relative sizes of the Ar dip, the N_2 peak and the H_2 peak is provided in Figure 9.6 (b). The data for Ar were shifted downward by 4.55×10^{-8} a.u. (the value for Ar just before gas mix was introduced), and multiplied by negative one before plotting. Data for nitrogen were multiplied by a factor of 20 before plotting, and hydrogen multiplied by a factor of 5000 before plotting, to display all three peaks on a similar scale. In this way it can be seen that the sizes of the peaks (or dip) for the three gases (Ar : N_2 : H_2) were in the approximate ratio 1 : 0.05 : 0.0002. Since nitrogen dominated the mix of gases released from the cell, it was concluded that the two detectors in the MS – the Faraday cup for detecting Ar and the electron multiplier for detecting all other gases – were inconsistently calibrated, and 1 a.u. of any gas other than Ar was taken to represent the same partial pressure as approximately 20 a.u. of Ar.

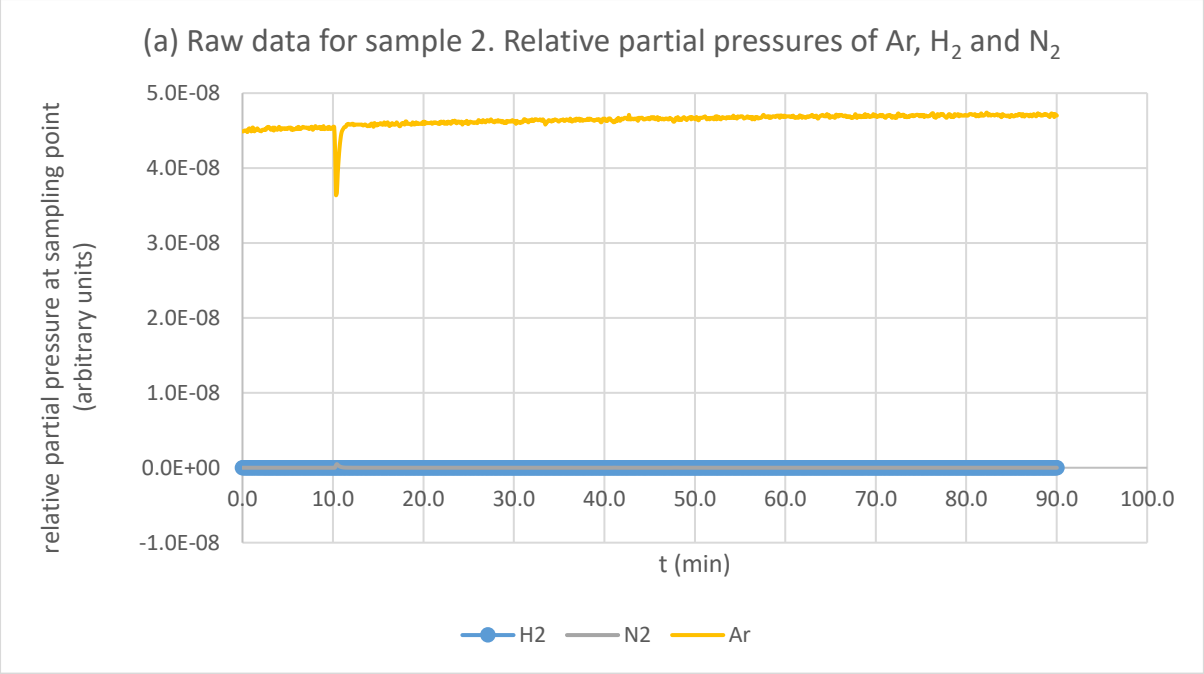

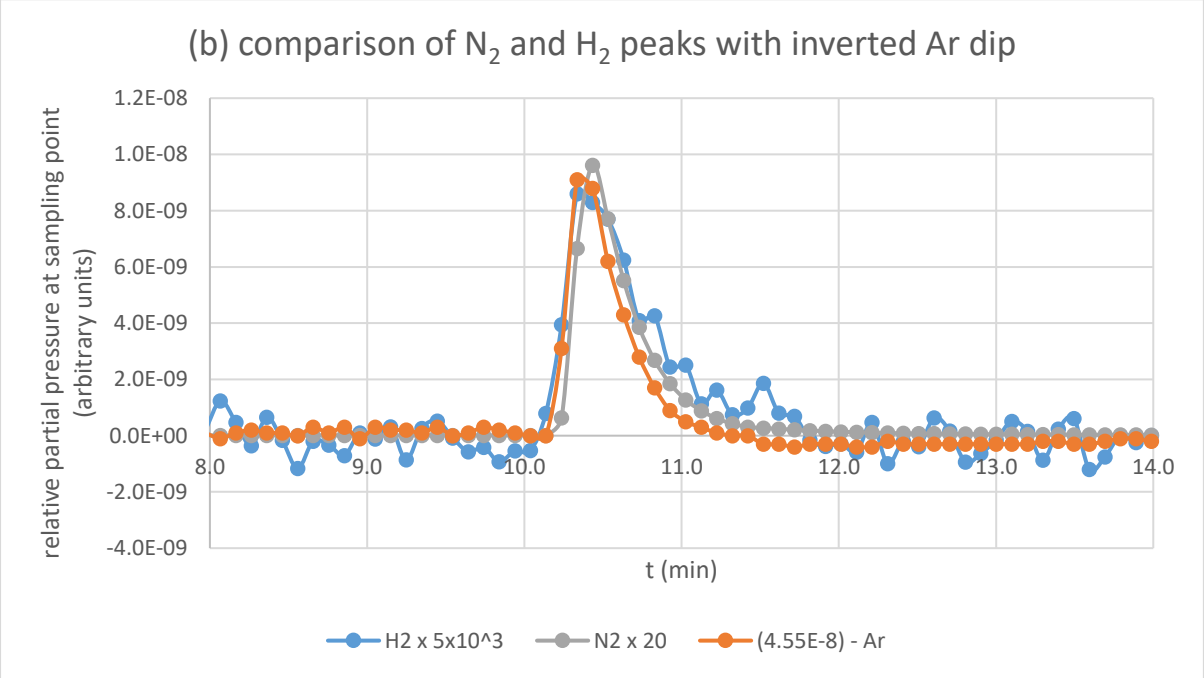

Figure 9.6. (a) Raw data from mass spectrometer for pressurised rig effluent sample #2 – relative partial pressures of Ar, N_2 and H_2 at sampling point; (b) Comparison of the nitrogen and hydrogen peaks with the argon dip, from the raw data as displayed in part (a).
In plot (a), since the dip in Ar is not matched by a similar-sized peak in N_2, this suggests that the two detectors in the MS were not consistently calibrated and 1 a.u. of Ar represents a much lower partial pressure (~20x) than 1 a.u. of any other gas. In plot (b), hydrogen and nitrogen data are multiplied by 5000 and 20 respectively; argon data is subtracted from its value at the beginning of the dip in Ar (or at the beginning of the peak in values of nitrogen and hydrogen).

9.4.2. Data converted to volume flow rate, by assuming Ar flow rate of 100 ml/min

For illustrative purposes, the data as converted to volume flow rate (ml/min) are plotted on a linear scale in Figure 9.7 for Ar, H_2, and N_2, assuming Ar flow rate of 100 ml/min. A sensitivity ratio of 20 was used to compare raw data for Ar with raw data for other gases, as discussed above. The hydrogen data as presented are multiplied by 250 and shifted upwards by 50 units for clarity. For each 6 s time interval, conversion was achieved for H_2 and N_2 by dividing raw values for each gas by the raw value for Ar gas, multiplying by sensitivity ratio of 20, and multiplying by 100 ml/min.

If Ar flow rate was not necessarily 100 ml/min, but was nevertheless maintained at a relatively constant value during the release of gas from the sample, then the units of flow rate in the figure can be treated as arbitrary units.

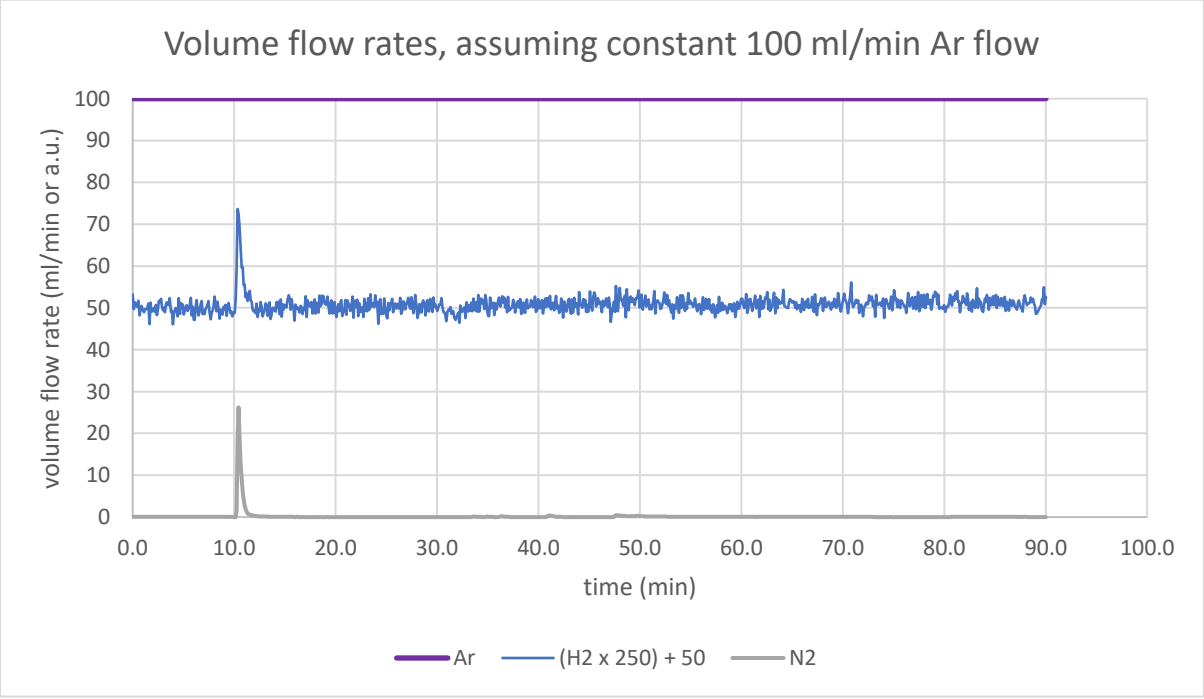

Figure 9.7. Volume flow rates of Ar, N_2 and H_2, as measured by the mass spectrometer, on analysing gas from pressurised rig effluent sample #2.
A constant Ar flow of 100 ml/min is assumed. Hydrogen data are multiplied by 250 and shifted up by 50 units for clarity

9.4.3. Estimates of actual volumes of N_2 and H_2 released by SC, by assuming Ar flow rate of 100 ml/min

Volume flow rate data, as derived above, are plotted in Figure 9.8 for the time period of the gas surge. Integrating the peaks in nitrogen and hydrogen between 10 and 12 minutes gives volumes of 10.7 +/- 0.1 ml and (53 +/- 2) x 10^{-3} ml respectively, where the error is indicative of the difference depending on whether background is taken from an average of data 10 minutes before and after the peak, or just 2 minutes before and after the peak.

The key result from these measurements is the ratio of hydrogen to nitrogen volumes. The measured value of this ratio is (5.0 +/- 0.2) x10^{-3}.

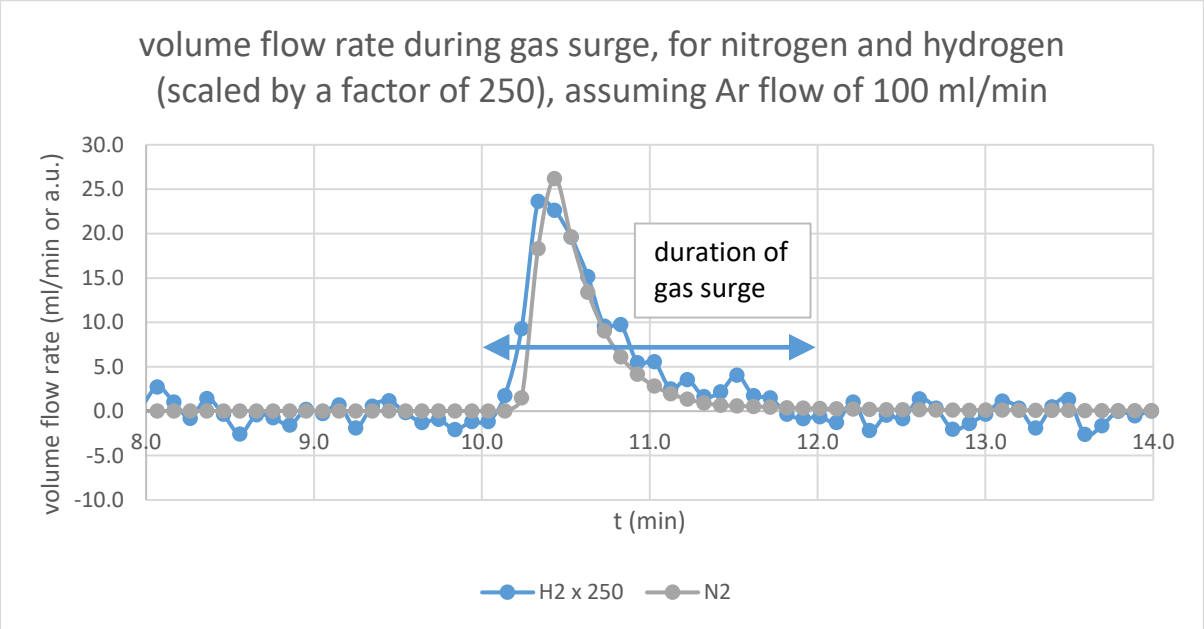

Figure 9.8. Plot illustrating the method used to fit the peak in hydrogen and nitrogen levels, to estimate the integrated volume of each gas released from pressurised rig effluent sample #2. Gas was released from the sample over a period of around 1 to 2 minutes.
Integrated volume is calculated as actual volume (ml), assuming 100 ml/min Ar flow rate is correct, or in arbitrary units (a.u.) if not.

9.5. Comparison of measured N_2 volumes with that expected from model

Measured nitrogen volumes for samples 1 and 2, assuming Ar flow rate of 100 ml/min, were (19.7 +/-0.1) ml and (10.7 +/- 0.1) ml respectively. These are a factor of about two and four

respectively less than the value of ~42 ml predicted by the model in each case, which was verified by the measurement of (43 +/- 2) ml released from another sample taken in the SC in similar manner.

One possible explanation is that Ar flow rate was actually a factor of two to four times lower than the 100 ml/min value assumed. It is unlikely that a significant quantity of nitrogen was lost through slow leakage from the cell, since pressure readings only showed loss of around 0.2 bar pressure over 100 days for sample 2. The formation of froth could explain the discrepancy, since gas enclosed within small bubbles could release from the cell, but sit on the bottom of the gas stream tubing and thus not be included in the surge of gas sampled by the MS. Some froth was indeed observed in a previous pressurised sample from the rig, on decanting into a test tube. Also, mass difference before and after use in the MS indicated in each case that 1.7 g of liquid water had released from the cell into the rig attached to the MS. Water vapour and other gases released from the cell, according to volumes measured, only accounted for about 0.04 g of mass loss..

9.6. Interpretation of results to determine hydrogen concentration in the rig

A model was developed in order to estimate of the hydrogen concentration in the rig, based on the ratio of gas volumes released from samples of rig effluent as measured in the MS. For this purpose, the following equation was derived:

$$H2_{effluent} = \frac{H2_{tot}}{V_{water}} = \left(\frac{H2_{prompt}}{N2_{prompt}}\right)_{MS} . \left(\frac{N2_{frac}}{H2_{frac}}\right) . \left(\frac{N2_{tot}}{V_{water}}\right)$$

Full details on the derivation of the formula, and the meanings of the terms, are provided in the appendix. Essentially, the first term in parentheses is the ratio of hydrogen to nitrogen measured in the MS; the second term in parentheses is a factor which accounts for the slightly higher solubility of hydrogen in water compared with nitrogen, and modifies the measured ratio of released gases to give a ratio of total amounts in the cell (including gas dissolved in the aqueous phase); and the third term – total amount of nitrogen per ml of water in the cell – converts the ratio of gases to hydrogen concentration, in units of scc (gas) / ml (water).

The hydrogen concentration given by the formula is units of scc/ml, since mass did not feature in the model. The result is simply multiplied by room temperature specific volume of water, 1000 ml/kg, to give hydrogen concentration in more familiar – and density invariant – units of scc/kg.

The second and third terms in parentheses are dependent on the fill ratio of the cell, which is determined from cell pressure measurements according to a correlation provided by the model. The

product of these two terms acts as a conversion factor between measured ratio of gases and hydrogen concentration (in units of scc/ml), and is plotted as a function of fill ratio in Figure 9.9. The fill ratio as given by the model was 0.88 for sample 1 and 0.91 for sample 2.

Estimates of hydrogen concentration in the rig at the time samples were taken, as determined by the ratio of gases measured and relations provided by the model, are shown in Table 9.2.

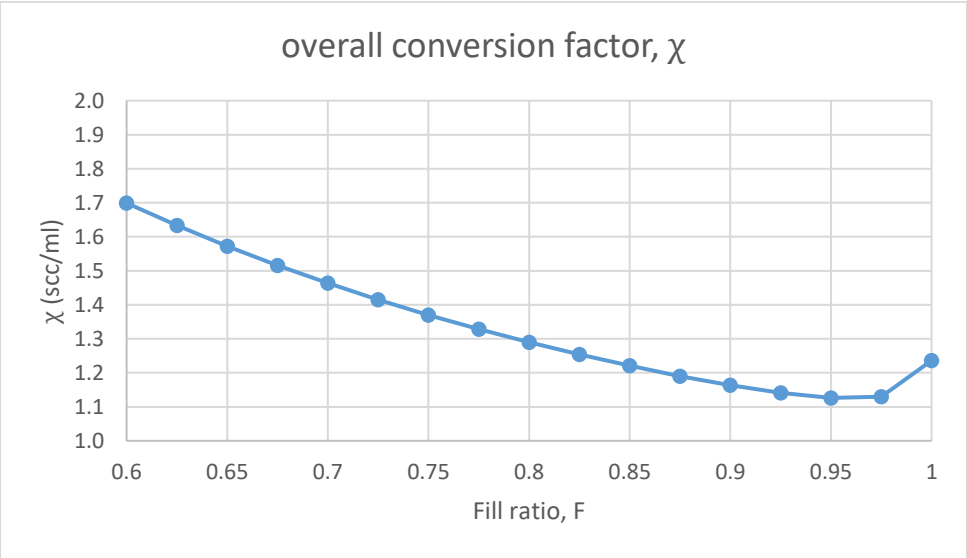

Figure 9.9. Plot of χ for F between 0.6 and 1, as calculated by the model. χ is the overall conversion factor by which the measured ratio of hydrogen to nitrogen is multiplied to give an estimate of hydrogen concentration in rig effluent (in units of scc/ml).

Table 9.2. Estimates of dissolved hydrogen (DH) concentration in the rig coolant at the time samples were taken, based on analysis of gases released from sealed samples of rig effluent.

Sample #	Fill ratio	conversion factor, χ (scc/ml)	Measured ratio of gases	Hydrogen concentration (scc/ml)	Hydrogen concentration (scc/kg)	Log({H_2}/bara) at 25 °C
1	0.88	1.19	(5.6 +/- 1.1) x10^{-5}	(6.7 +/- 1.3) x10^{-5}	0.067 +/- 0.013	-2.42 +/- 0.09
2	0.91	1.16	(5.0 +/- 0.2) x10^{-3}	(5.8 +/- 0.2) x10^{-3}	5.8 +/- 0.2	-0.49 +/- 0.02

10. Characterisation of Wetted Surfaces of Rig

10.1. Overview of Chapter 10

This chapter presents the results from analysis of wetted SS316L components of the rig, using a Scanning Electron Microscope (SEM) to characterise the surface morphology before and after exposure in the rig. Energy Dispersive X-ray Spectrometry (EDX) was also used, where mentioned, in conjunction with electron imaging to give semi-quantitative elemental analyses. Samples analysed were as follows:

- Samples cut from reaction cell wall after exposure in the rig, to characterise the corrosion film surface morphology;
- A cross-section sample prepared from reaction cell wall after exposure in the rig, to image the through-depth profile of corrosion film, and to provide semi-quantitative elemental analysis from a through-depth EDX line scan and EDX spot scans;
- Samples of corrosion film oxide crystallites removed from reaction cell walls after exposure in the rig, using adhesive tape (referred to here as tape-pull samples), to enable semi-quantitative elemental analysis from EDX spot scans (in the absence of underlying SS316L, which interferes with EDX readings where oxide is present in situ);
- SS316L chips, before exposure in rig, to characterise surface morphology of the chips;
- SS316L chips, after exposure in rig, to characterise surface morphology of corrosion film;
- SS316L Bekipor ® frits, after exposure in the rig, to characterise surface morphology of corrosion film there.

10.2. Corrosion film on reaction cell walls

10.2.1. Surface imaging using SEM

Four different Reaction Chambers were used in the course of the project, as detailed in Chapter 7. Using the SEM, samples were studied from the first three reaction chambers: as used during sessions 1 to 3; during session 4; and during session 5.

SEM surface images from these reaction chambers taken at three different length scales are shown below in Figure 10.1, illustrating typical morphology of the coolant-facing (outer layer and intermediate layer) oxide crystallites.

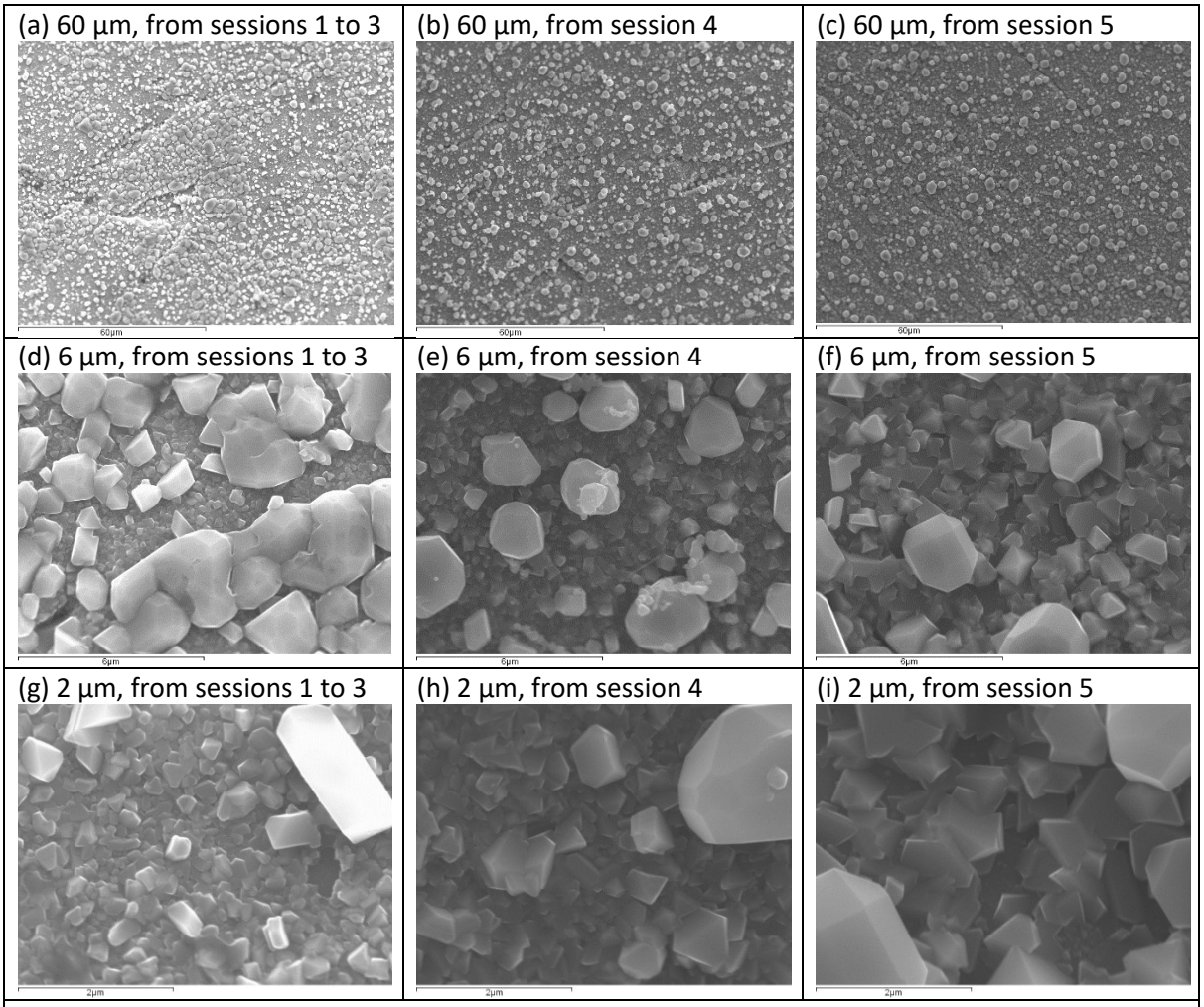

Figure 10.1 (a) to (i). SEM surface images from the three used reaction cells studied, at three different length scales.
Length scale refers to the scale bar at bottom left of each image, occupying about half the width of each image. For Session 5, there seem to be a lesser number of intermediate layer crystals (f, i), compared with for sessions 1 to 3 (d, g), but each one is much larger and more angular. Session 4 represents an intermediate case (e,h).

Images look broadly similar across the three reaction chambers studied – especially bearing in mind that oxide film morphology can vary slightly based on orientation of the underlying metal crystallite [164], as well as slight general variation from one region to another. A representative size for such metal crystallites is ~60 µm [164], though crystallography of the metal used in the current project was not studied. Despite similarities, the intermediate layer crystallites (deemed to be those significantly smaller than the largest ones, being typically less than or approximately 1 µm across) appeared to be significantly larger and less numerous on the samples from session 5 than those from sessions 1 to 3, with the samples studied from session 4 representing an intermediate case.

The observed morphology of the oxide film surface was consistent with that described in previous studies for similar alloys under similar conditions. (for example [73], [77], [78], [81], [84], [87]). Figure 10.2 shows a comparison of SEM images of oxide film from this project with those from Perrin et al. [78].

(a) – from sessions 1 to 3

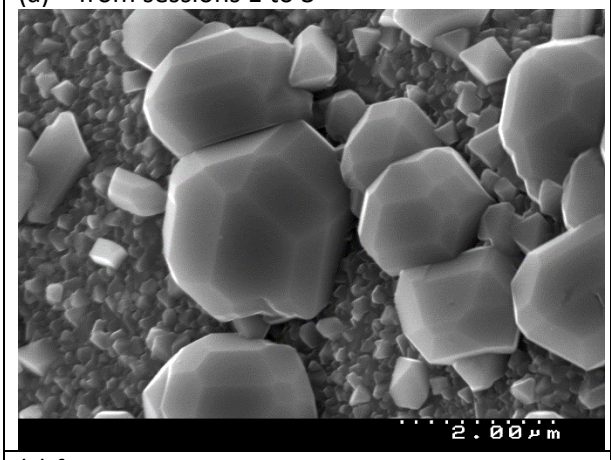

(b) from session 4

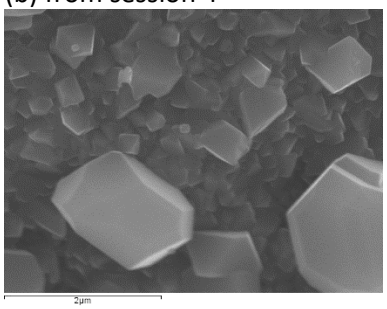

(c) from sess 5

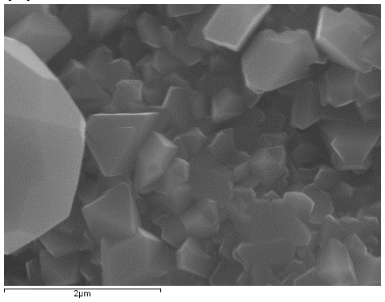

(d) image from Perrin et al. after 1024 h

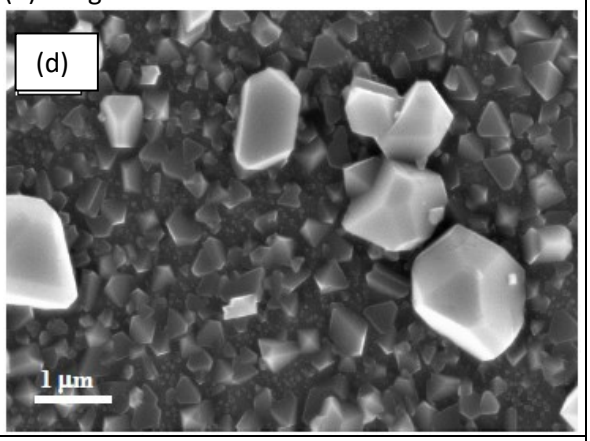

Figure 10.2. Comparison of SEM images of oxide film from the current project with those from Perrin et al. [78] *under similar conditions and timescale.*
Images (b) and (c) occupy a smaller area on the page, to achieve the same length scale across all four images, for ease of comparison.

On some samples from the used reaction chambers, agglomerations of crystallites were observed, which appeared to have deposited from elsewhere having been transported via the coolant. Figure 10.3 compares a typical example from the reaction cell used during sessions 1 to 3 with what may be small deposits on the reaction cells used during sessions 4 and 5.

(a) – from sessions 1 to 3

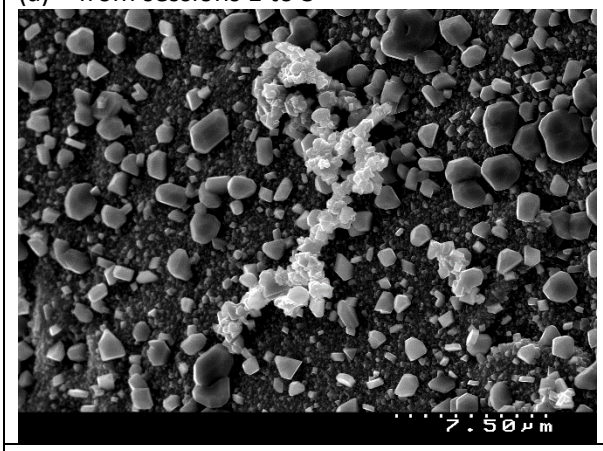

(b) close-up from sessions 1 to 3

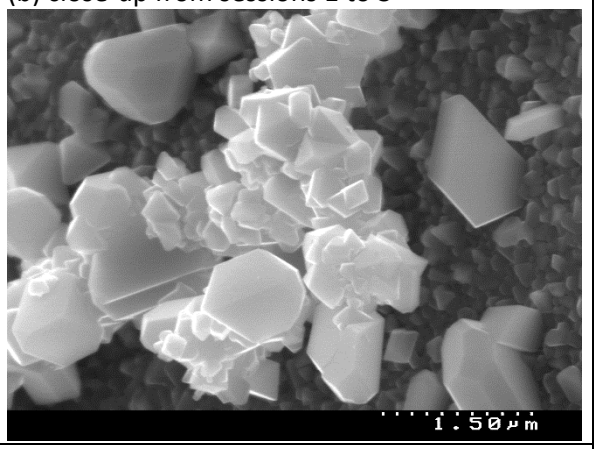

(c) from session 4 (scale bar = 6 µm)

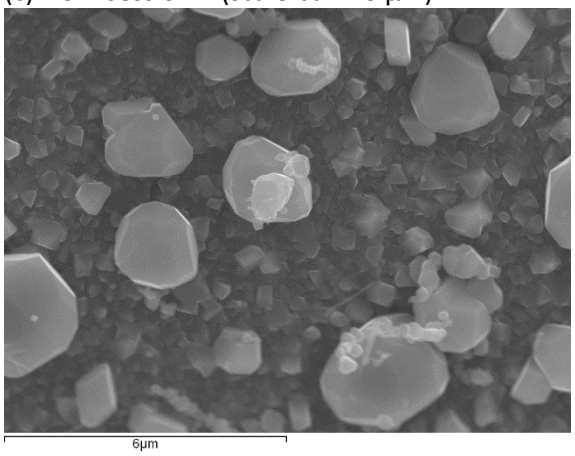

(d) from session 5 (scale bar = 10 µm)

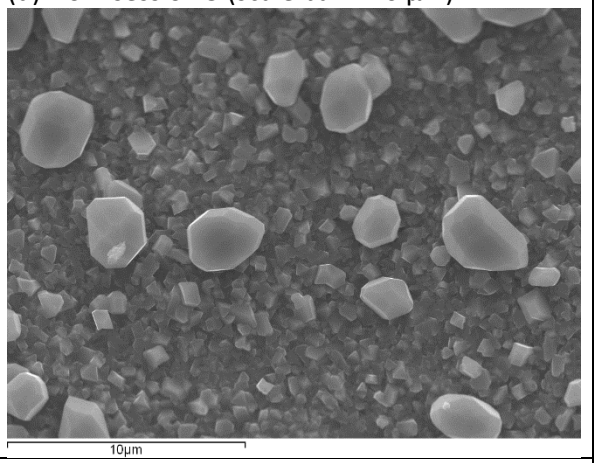

Figure 10.3. Agglomerations of deposited particulates visible on SEM images of oxide film. Deposits observed were most prevalent and substantial (consisting of a large number of individual crystallites and occupying a large volume) on the first sample taken from the reaction cell after use during sessions 1 to 3 – images (a) and (b). However, none were observed on the second sample taken from the sessions 1 to 3 reaction cell. Smaller deposits were observed on the reaction cell from session 4, (c), and a deposited crystallite appears to be present in the image shown of the reaction cell from session 5, (d), on the large crystallite left of centre. Owing to the difference in prevalence of deposited agglomerations between the first and second samples analysed from the reaction cell in use during sessions 1 to 3, it is concluded that such agglomerations may have been present to a similar extent for all sessions – a more detailed analysis would be required to properly compare one reaction chamber to another.

10.2.2. Through-depth imaging of corrosion film using SEM, and elemental analysis using EDX

The through depth profile of a transverse section of corrosion film was studied using SEM and EDX. The sample was taken from the reaction cell used during sessions 1 to 3.

Results of the EDX line scan are shown in Figure 10.4. Intensity for each element is in arbitrary units. Sensitivity is different for each element. For all elements shown other than oxygen, intensity can be calibrated against known composition of the alloy; for oxygen it can be inferred from deficit in readings from the other elements. Oxygen intensity did not fall to zero, perhaps because of very thin (~ 2-4 nm) protective oxide film formed in air [73], [165] at room temperature after the cross section sample was prepared. Also, different phases and surface conditions such as surface roughness have different sensitivities, therefore the technique is only semi-quantitative. Nevertheless, evidence for the duplex oxide film can be qualitatively seen in the EDX line scan.

At the location of the line scan, the thickness of the outer oxide layer was determined to be about 1.1 µm, and thickness of the inner oxide layer was determined to be about 0.2 – 0.3 µm. The inner oxide thickness is consistent with the value of ~ 0.2 µm expected, based on 15 mg alloy dm^{-2} corroded as determined from corrosion rate data in section 7.6, with the assumption that 100% of Cr is retained in the inner oxide layer. Location of the outer boundary of outer oxide layer was determined from the SEM image, and aligns with a point about 0.4 µm from one end of EDX line scan (Figure 10.4 (c), (d)). Location of the inner oxide layer was judged from the region of Cr enrichment (on a metals basis, i.e. excluding oxygen), as seen most clearly by the dip in Fe levels, and the fact that Fe signal has fallen more significantly than the Cr signal, relative to their respective signals coming from the alloy (Figure 10.4 (c)). Surprisingly, the outer layer appears to be enriched in molybdenum, although Mo was seen to release at high concentrations to the coolant (see chapter 8). This also is in contrast to the line scan of Perrin et al. [78] where it looks like Mo is enriched in the internal oxide, but depleted in the external oxide.

Results of additional EDX spot scans performed at 0.5 µm intervals along the route of the line scan are shown in terms of at% in Figure 10.5, and in terms of wt% in Figure 10.6. The approximate supposed location of inner oxide layer is marked on plots for indicative purposes.

(a) overview of region analysed

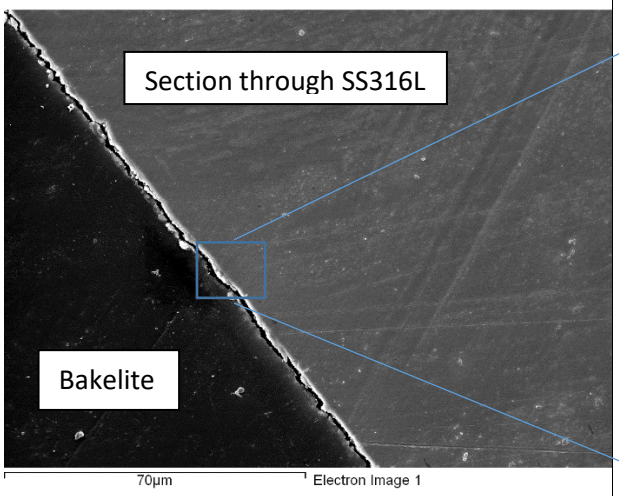

(b) close-up, showing path taken by EDX line scan

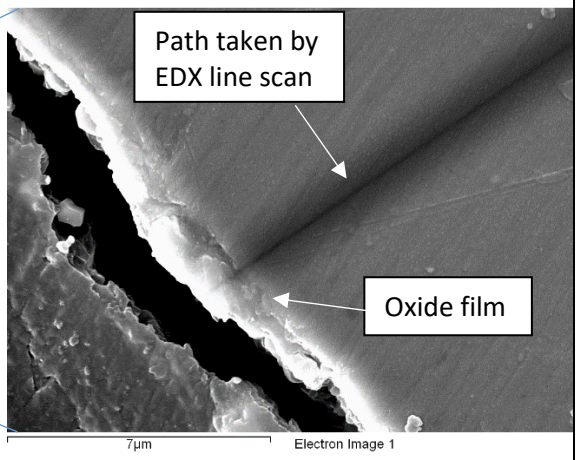

(c) Results of EDX line scan

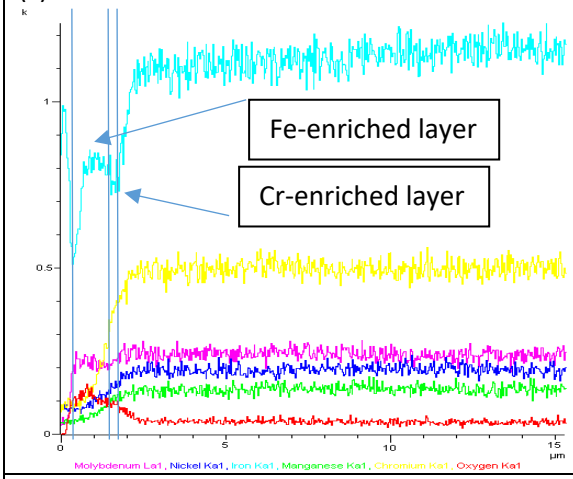

(d) EDX line scan, superposed on SEM image

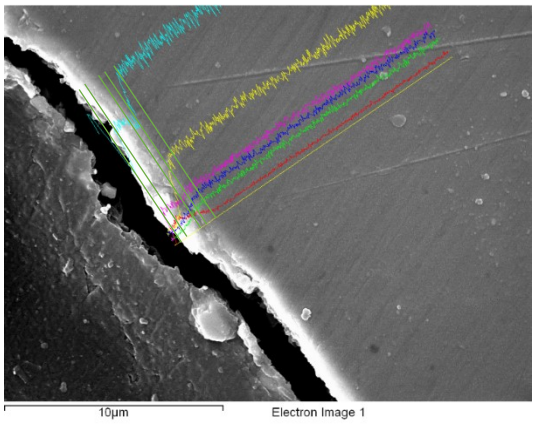

(e) SEM image of transverse section of oxide film, from Castelli [37], for comparison

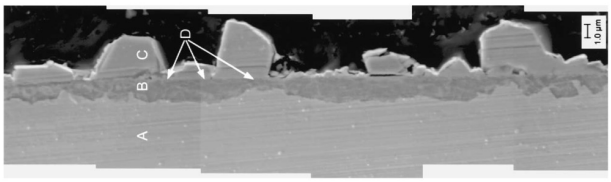

(f) TEM / EDX of oxide film from Perrin et al. [78], for comparison

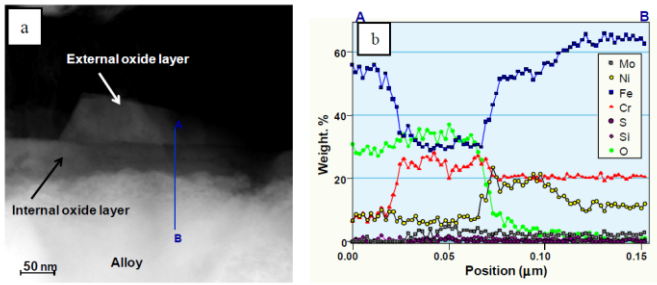

FIGURE 1. Structure of the oxide layer on non irradiated sample after the two corrosion sequences observed by TEM in HAADF mode (a) coupled to EDX analysis (b)

Figure 10.4. Through depth imaging of oxide film from sessions 1 to 3, using SEM; and through-depth elemental analysis using EDX line scan.

(a) Results of EDX point scans (at%)

Spectrum	In stats.	O	Cr	Mn	Fe	Ni	Mo
point(1)	Yes	35.0	4.5	0.0	53.1	7.5	0.0
point(2)	Yes	28.0	5.0	0.6	58.8	7.6	0.0
point(3)	Yes	20.5	13.4	1.4	54.8	9.8	0.0
point(4)	Yes	8.6	20.4	1.7	56.0	13.3	0.0
point(5)	Yes	0.0	20.6	1.9	63.6	13.8	0.0
point(6)	Yes	0.0	19.7	2.4	64.5	13.3	0.0
point(7)	Yes	0.0	20.0	2.1	64.6	13.3	0.0
point(8)	Yes	0.0	19.7	1.9	65.0	13.3	0.0
point(9)	Yes	0.0	20.1	2.1	64.8	13.0	0.0
point(10)	Yes	0.0	19.8	2.1	65.0	13.2	0.0
point(11)	Yes	0.0	19.7	2.0	65.5	12.8	0.0
point(12)	Yes	0.0	20.1	2.0	65.1	12.8	0.0
point(13)	Yes	0.0	20.0	2.2	64.9	12.9	0.0
point(14)	Yes	0.0	20.5	2.1	64.0	13.4	0.0
point(15)	Yes	0.0	19.8	2.1	64.6	13.4	0.0
point(16)	Yes	0.0	20.0	2.4	63.7	14.0	0.0
point(17)	Yes	0.0	19.8	2.3	64.3	13.7	0.0
point(18)	Yes	0.0	19.4	1.9	65.4	13.3	0.0
point(19)	Yes	0.0	19.6	2.5	64.8	13.1	0.0
point(20)	Yes	0.0	19.3	2.1	65.0	13.6	0.0
point(21)	Yes	0.0	19.3	2.1	65.2	13.4	0.0

(b) Location of EDX point scans, superposed on SEM image

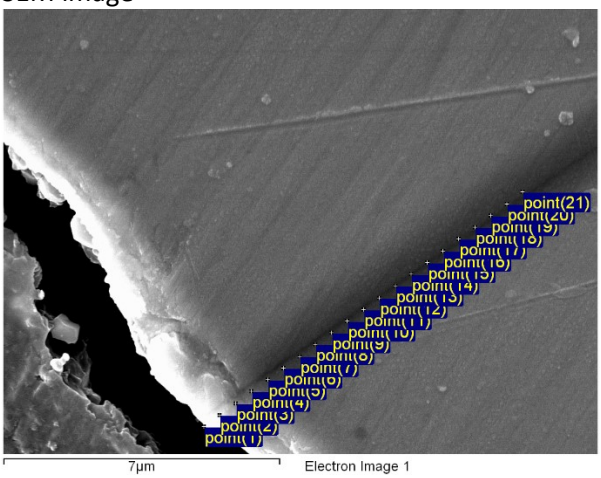

(c) at%, all elements

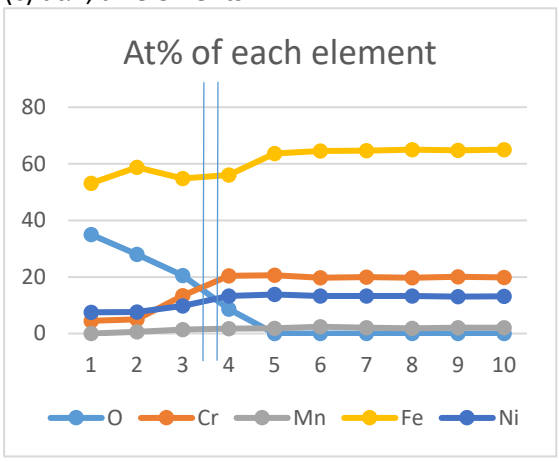

(d) at%, metals only

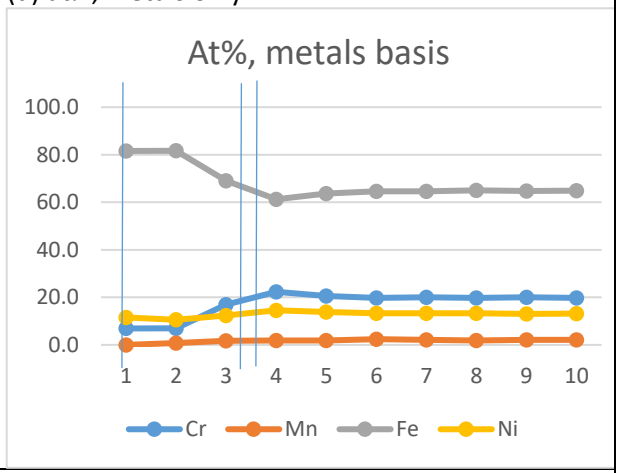

(f) TEM / EDX of oxide film from Perrin et al. [78], for comparison. About 10% of Cr and Ni seen in external oxide layer, same as observed for the current project (see (a) above)

Figure 10.5. EDX Spot scans following the same path as the EDX line scan, showing through depth elemental analysis – results given in at%.

Looking at wt% (Figure 10.6), we see that oxygen should take up ~30%, but instead is measured as 13%. If it was correctly measured at 30%, then levels of Ni and Cr would be ~ 8.6 and 4.5 wt% at the outer oxide surface, which is similar to the Perrin et al. value of ~9% and 9% respectively. It is also similar to the levels reported by Ziemniak et al. [84], [85]: $(Fe_{0.8}\ Ni_{0.2})\ (Fe_{0.95}Cr_{0.05})_2\ O_4$, giving 5 wt% Ni, and 2 wt% Cr. In terms of at% (Figure 10.5), adjusting oxygen readings to the ~57 at% expected for a spinel type oxide would give 5.0 at% Ni and 3.0 at% Cr

→ Or other way around: we have 5.0 at% Ni and 3.0 at% Cr if oxygen was as high as it's supposed to be for spinel. Calculating on a metals basis, using only Fe, Cr, and Ni, gives 11.5 at% Ni and 6.9 at% Cr for the data in Figure 10.5, yielding approximate chemical formula $(Fe_{0.7}Ni_{0.3})\ (Fe_{0.9}Cr_{0.1})_2\ O_4$, similar to that determined by Ziemniak et al. [84], [85].

(a) Results of EDX point scans (wt%)

Spectrum	In stats.	O	Cr	Mn	Fe	Ni
point(1)	Yes	13.3	5.5	0.0	70.7	10.5
point(2)	Yes	10.0	5.8	0.8	73.4	9.9
point(3)	Yes	6.9	14.7	1.6	64.6	12.2
point(4)	Yes	2.6	20.4	1.8	60.2	15.0
point(5)	Yes	0.0	19.4	1.9	64.1	14.7
point(6)	Yes	0.0	18.5	2.4	65.0	14.1
point(7)	Yes	0.0	18.8	2.1	65.1	14.1
point(8)	Yes	0.0	18.5	1.9	65.5	14.1
point(9)	Yes	0.0	18.8	2.1	65.3	13.8
point(10)	Yes	0.0	18.5	2.0	65.5	14.0
point(11)	Yes	0.0	18.5	2.0	66.0	13.6
point(12)	Yes	0.0	18.8	2.0	65.6	13.6
point(13)	Yes	0.0	18.8	2.2	65.4	13.7
point(14)	Yes	0.0	19.2	2.1	64.5	14.2
point(15)	Yes	0.0	18.6	2.1	65.1	14.2
point(16)	Yes	0.0	18.7	2.3	64.1	14.8
point(17)	Yes	0.0	18.5	2.2	64.8	14.5
point(18)	Yes	0.0	18.1	1.9	65.8	14.1
point(19)	Yes	0.0	18.4	2.5	65.3	13.9
point(20)	Yes	0.0	18.1	2.1	65.4	14.4
point(21)	Yes	0.0	18.1	2.1	65.7	14.2

(b) Plot of EDX point scans (wt%)

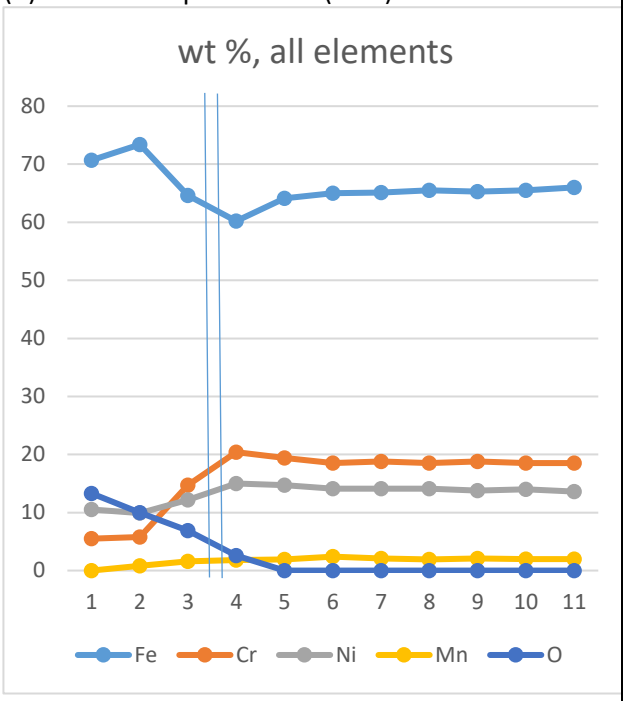

(c) Figure from Perrin et al. [78]. About 9% of Ni and 9% Cr seen in external oxide layer, compared with ~ 10% and 5% respectively for the current project (see (a) above)

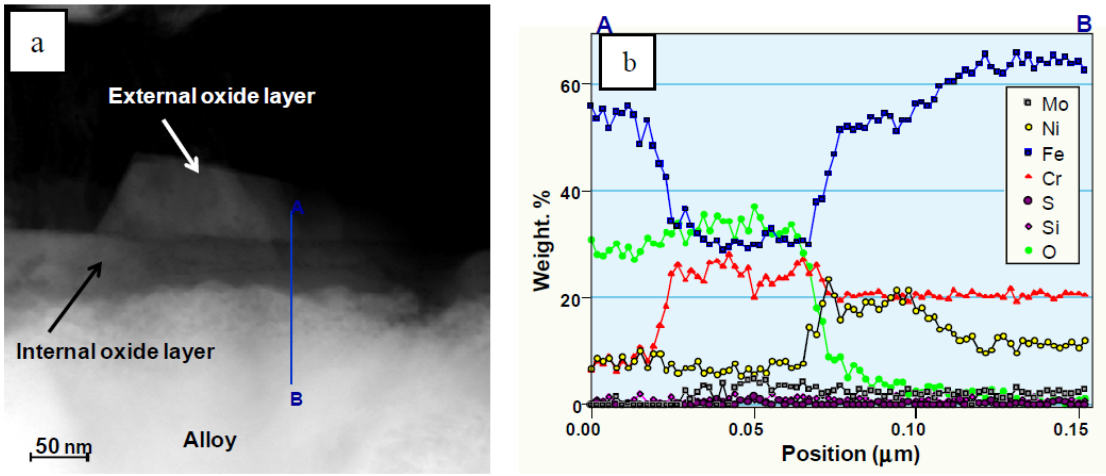

Structure of the oxide layer on non irradiated sample after the two corrosion sequences observed by TEM i HAADF mode (a) coupled to EDX analysis (b)

Figure 10.6. EDX Spot scans following the same path as the EDX line scan, showing through depth elemental analysis – same results as provided in Figure 10.5, in this case given in wt%.
A through depth elemental analysis from [78] is also shown for comparison.

10.2.3. Elemental analysis of oxide film crystallites sampled using adhesive tape

Tape pull samples were collected by the process shown in Figure 10.7, and prepared in the same manner as filter samples (see chapter 7.9.4). In the figure below is shown an SEM image containing examples of inner oxide, intermediate layer oxide crystallites, and outer layer oxide crystallites. Representative spot scans were performed in each of these areas, at locations indicated in Figure 10.8; results are summarised in Table 10.1, and compared with literature data.

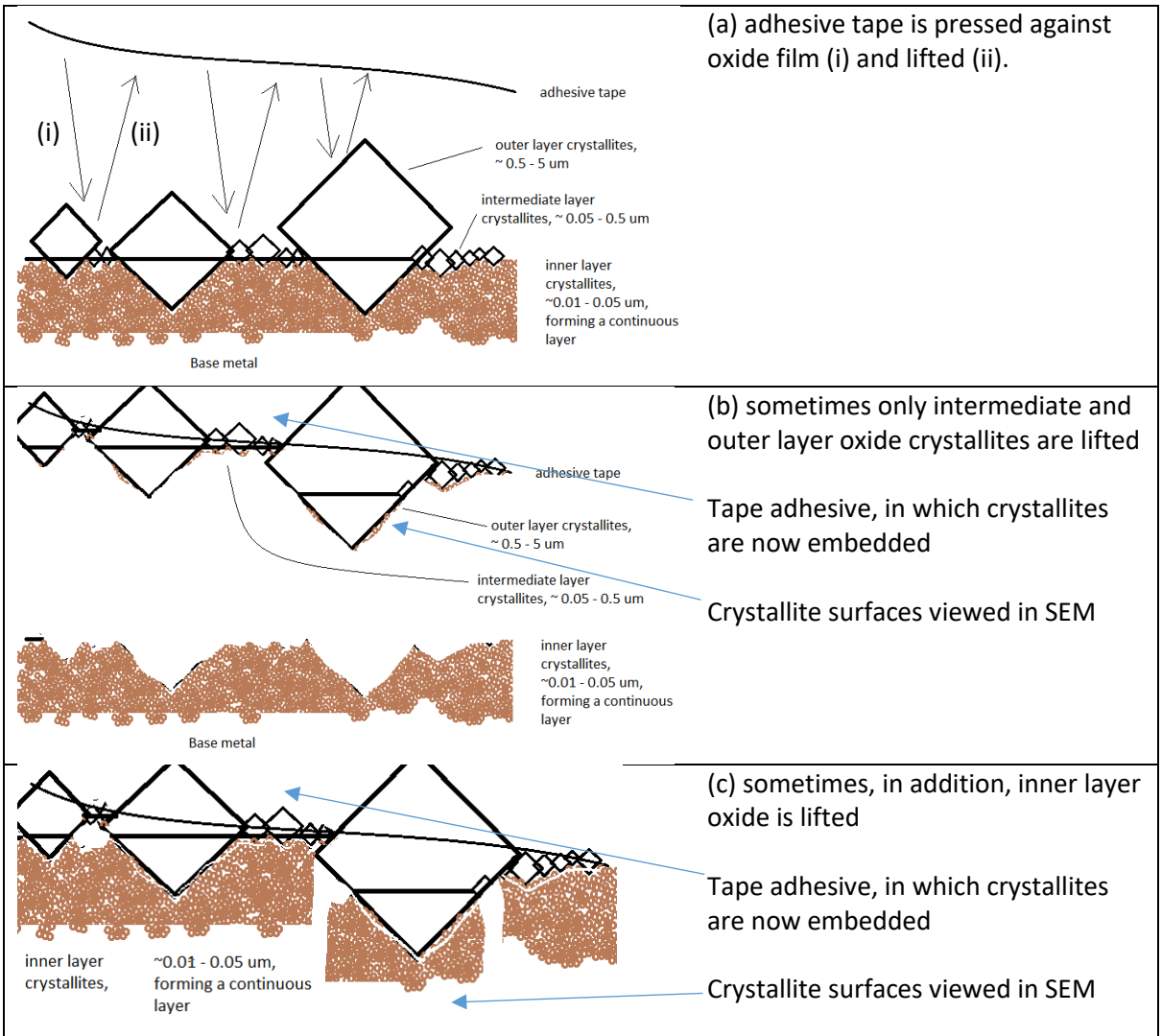

Figure 10.7. Schematic, showing process by which tape pull samples were obtained. Notice how outer and intermediate layer oxide crystallites may move relative to one another, and it is their internal (interface with inner oxide) surfaces which are imaged under SEM. Where outer and intermediate layer crystallites only are present, tape pull samples enable their elemental analysis by EDX without interference from the underlying SS316L substrate. Where inner layer oxide is also present, elemental analysis is affected by composition of the outer and intermediate layer crystallites which lie beneath the inner layer oxide on the tape adhesive.

Data quoted from Ziemniak et al. [84] for the inner and outer oxide compositions were converted to wt% composition on a metals basis, and stoichiometric oxygen at% for spinel oxides was used in this case. Data quoted from Perrin et al. [78] was read off from their plot of EDX analysis (on a scale of overall wt%), adjusted appropriately to give the various values quoted in Table 10.1.

Relative levels of Fe, Cr and Ni in the outer layer crystallites matched well to those reported by Ziemniak et al. Relative levels of Ni were consistent with both literature sources, given the error, but levels of Cr and Fe conformed more closely to those reported by Ziemniak et al. than the 10 wt% Cr seen in Perrin et al.

Intermediate layer crystallites had Cr content of ~ 23 +/- 5 wt%, roughly in the middle of the thermodynamically forbidden region according to Ziemniak et al., between that of Cr- saturated ferrite (3 wt% Cr, metals basis) and Fe- saturated chromite (46 wt% Cr, metals basis). Relative levels of Fe, Cr and Ni in the inner layer oxide were the same, within errors.

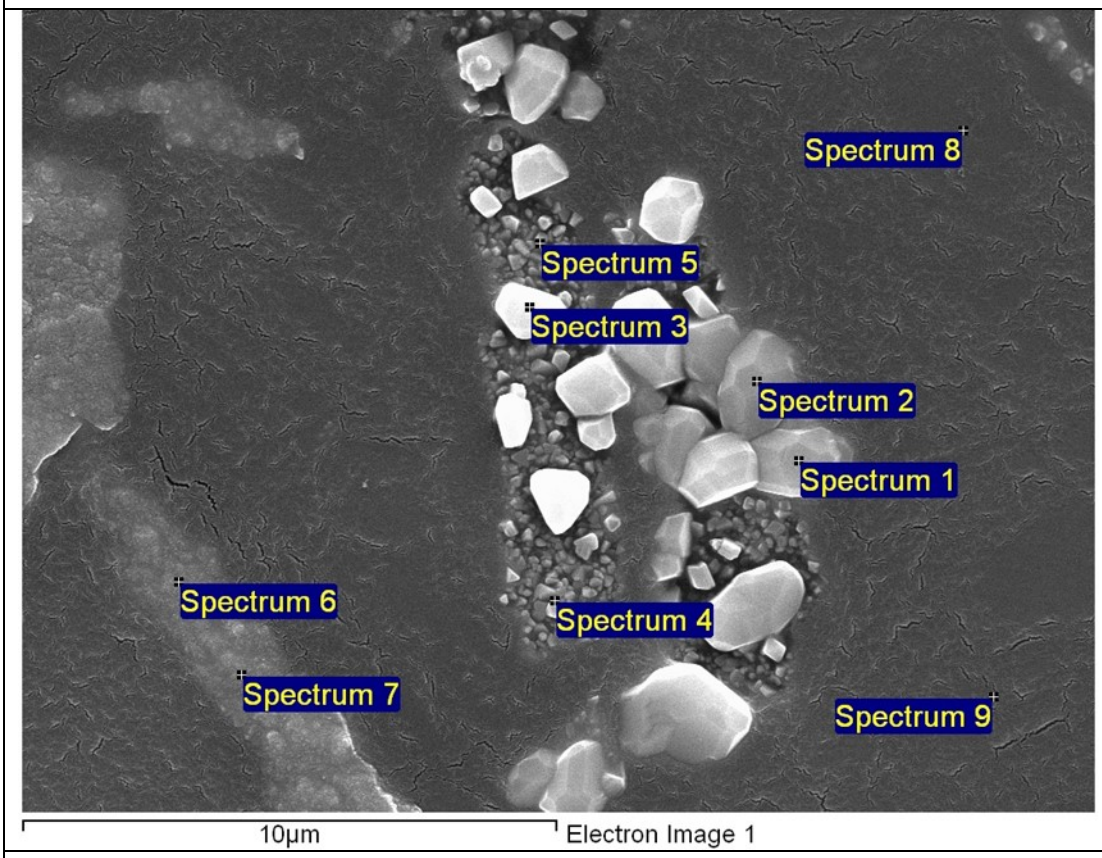

Figure 10.8. SEM image from a tape pull sample, showing locations at which EDX spot scans were performed.
Spot scans were performed in regions of inner oxide (spectrum 6, 7); intermediate layer oxide crystallites (spectrum 4, 5); outer layer oxide crystallites (spectrum 1, 2, 3); and regions where no oxide was present, representing background signal from tape adhesive and/or sputter coating (spectrum 8, 9).

Table 10.1. Summary of results of EDX spot scans on oxide crystallites

spectra	region	Rel. wt % of the alloying elements Fe, Ni, Cr			Rel. at % of O (all elements other than O, Fe, Ni, Cr excluded from analysis)
		Fe	Ni	Cr	
8-9	background	0	0	0	N/A
N/A	SS316L composition	68	14	18	0
N/A	Outer layer oxide (Perrin) [78]	79 (1)	10 (2)	10 (2)	60 (1)
N/A	Ziemniak et al. – outer [84]	90 (4)	7 (3)	3 (3)	Not reported, but close to stoichiometry (i.e. 57)
1-3	Large (outer layer) crystallites	87 (3)	9 (3)	3 (1)	~ 45 (8)
chip	4 µm outer layer crystallite	95	3	2	~ 28
N/A	Inner layer oxide (Perrin) [78]	50(2)	11 (2)	39(2)	64 (3)
N/A	Ziemniak et al. – inner [84]	46(bal)	7 (3)	43(6)	N/A (much lower than expected, indicating EDX contribution from base alloy)
N/A	Cissé et al. – inner [77]	~52		~48	
4-5	Intermediate size (intermediate layer) crystallites	61(3)	16 (2)	23 (5)	~ 53 (2)
6-7	Small (inner layer) crystallites	60 (4)	15 (1)	26 (5)	~ 32 (7)
chip	Inner oxide / alloy	70	11	19	~ 3
-	Session 6 particulate	88	0	12	~ 54

Note: Oxygen readings were highly variable. Levels of other metallic elements such as Mo and Mn were not consistently measured in this project, since levels were often below detection limit, nor are they consistently reported in the literature.

*For the reasons above, levels of Fe, Cr and Ni are given as relative weight percent from those 3 elements only in order to avoid high scatter introduced by the scatter in oxygen data and to enable consistent comparisons across studies. The EDX line scan of this study (*Figure 10.4*) suggested enrichment of Mo in the oxide relative to the alloy, but for the corresponding spot scans (*Figure 10.5 *and* Figure 10.6*) Mo was below the detection limit so a numerical value of atomic or weight percent could not be attached to this. In the EDX spot scans summarised in this table, Mo and Mn were not detected.*

Levels of oxygen are given as at%, as a fraction of the whole from Fe, Cr, Ni and O only. In this way, levels can be compared against the expected stoichiometric value of 57 at% for spinel type oxides (normal and inverse), which does not vary with composition, whereas the wt% of oxygen varies with Cr content since Cr is lighter than Fe and Ni. The effect of any Mo or Mn which may thus been excluded is that measured O may be expected to be slightly higher than the stoichiometric value.

According to the proposed mechanism of transfer of oxides to the tape, XRD spectra on the intermediate layer should be sampling intermediate layer crystallites only, though at their interface with the inner oxide layer rather than their coolant facing surfaces. It is possible for oxides which are not thermodynamically stable to form, for reasons of faster kinetics. However, this situation would be in stark contrast to other studies, such as that of Perrin et al. under similar conditions. An

alternative explanation is that fragments of oxide which adhered to the adhesive tape included inner oxide in every case: some of these fragments rolled over so that coolant facing surfaces of intermediate and outer layer crystallites became the exposed surfaces viewed in the SEM; and others did not, so that the inner surface of the inner oxide was exposed to be viewed in the SEM. In this case, the amount of Cr observed could be explained by roughly equal signals coming from the small intermediate layer crystallites and the inner oxide hidden from view underneath.

In either case, one would expect spectra from the inner layer oxide to be affected by intermediate and outer layer crystallites present beneath the inner oxide layer, which is thought to be around 0.2 µm thick.

Measured amounts of oxygen were lower than the value of 57 at% expected from spinel-type oxide stoichiometry, though within approximately two standard errors for intermediate and outer oxide layers. For the inner oxide layer, despite levels of Fe, Cr and Ni being the same as for intermediate crystallites, the level of oxygen was significantly lower, at just 32 +/- 7 at%. It is possible that the location of fracture between inner oxide and alloy was located at a region of transition – though images of clear dividing lines have been reported in literature between oxide and alloy (for example TEM images in [164]), so too have regions in which there are concentration gradients of species such as oxygen beneath the oxide film been reported (for example the oxygen through-depth profile in [78]).

The high levels of Ni in inner and outer layer crystallites are interesting to note, and not expected from literature findings regarding stainless steels. For Ni base alloys, Ni has been reported in both (?) oxide layers as pure nickel metallic phase. This would help to explain the low levels of oxygen observed, if some of the Ni were present as Ni^0 rather than Ni^{2+}.

Figure 10.9 shows a close-up of the inner oxide layer, in which can be seen what appear to be crystallites. Image (a) shows the 'fuzzy' appearance of surfaces, due to particles of gold deposited by the sputter coating process. These are less than ~ 10 nm in diameter, and therefore difficult to resolve individually under SEM. In contrast, the roughly spherical particles making up the surface of image (b), thought to be inner layer oxide, are around 10 – 50 nm in diameter – consistent with literature findings ([78], [164] etc.) concerning inner layer crystallites.

(a) SEM image showing the 'fuzzy' appearance of intermediate layer oxide crystallites, which is likely due to the process of sputtering samples with inert metal (in this case gold), as observed also on the tape adhesive at the left and right edges of the image.

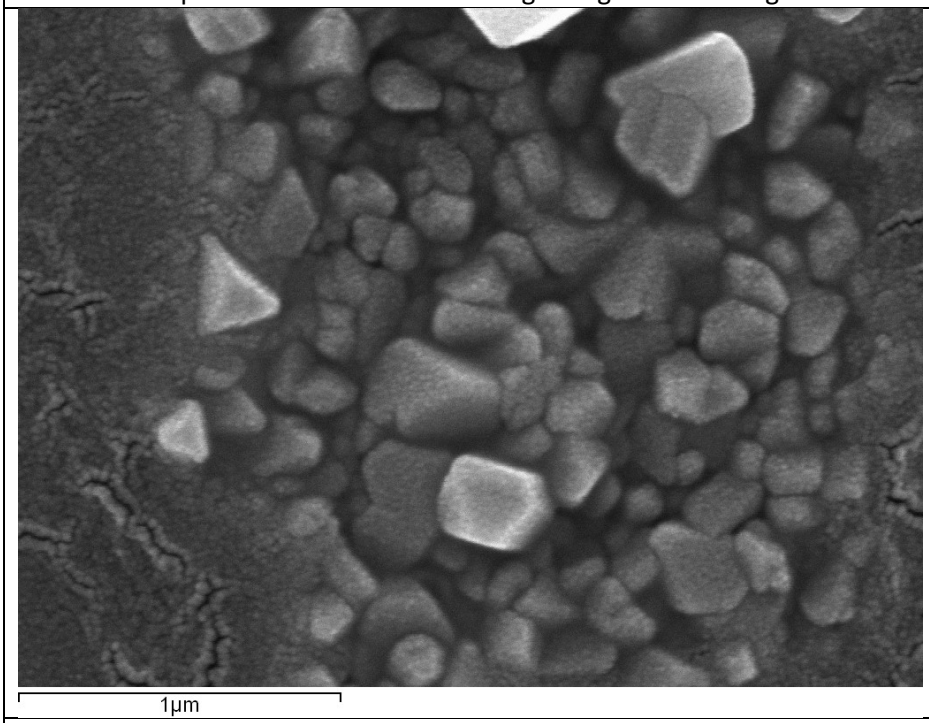

(b) SEM image on the same scale, showing inner oxide, and presumed crystallites of the oxide. Notice that these grains are much larger than the fuzz observed in image (a).

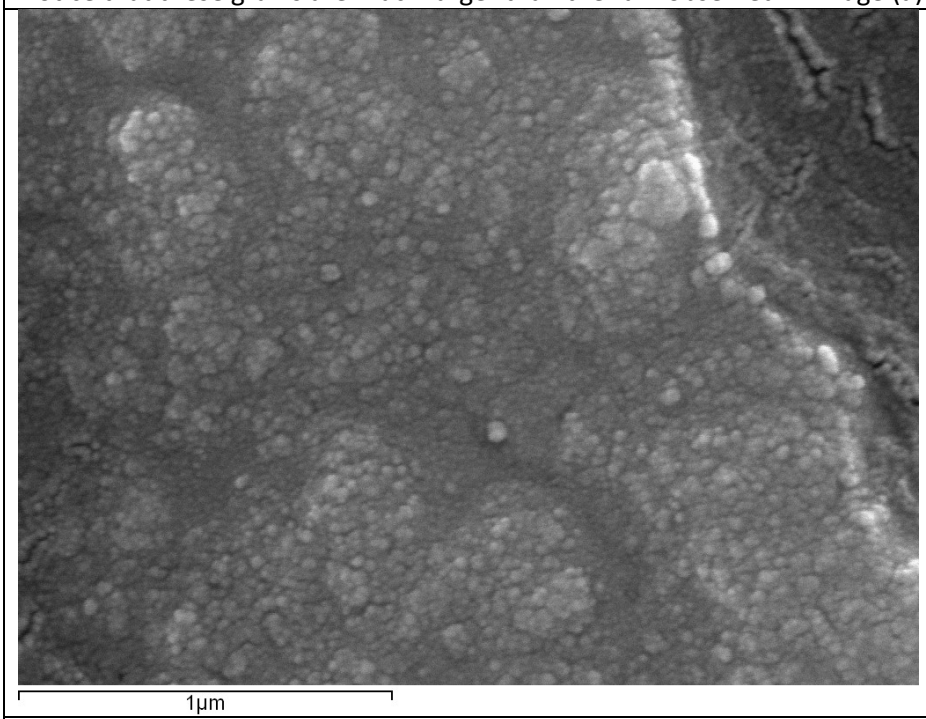

Figure 10.9. SEM images showing the size of presumed crystallites in the inner oxide layer (b), compared with the 'fuzzy' appearance caused by Au sputtering (a).

10.3. SS316L chips

10.3.1. Morphology of chips – optical photography

The chips were not of uniform size and shape, though all were fairly similar. Several different morphological variants were identified – some of which were very narrow for example – in each case chips were observed to have a smooth/shiny side and a rough/dull side. This is related to the method by which they were made, see section 7.2.2: during each cut, the side furthest from the blade curls in a concave manner, causing ridges to form under compression. Some chips had feathered edges, which were a possible source for SS316L particulates within the rig. Indeed, particulates of a similar size were observed when emptying the last few chips from the reaction cell after use during session 5. Photos of some typical chips are shown in Figure 10.10.

10.3.2. Surface morphology of chips, and oxide film thereon – SEM imaging

SEM images in Figure 10.11 show the surface morphology of a typical SS316L chip before use in the rig, over various length scales, for both sides of the chip. Figure 10.12 and Figure 10.13 show the equivalent images for a chip selected from the bottom and the top of the reaction cell respectively, after use in the rig during session 5, enabling comparison between the different locations and the two qualitatively different sides of the chips.

Surface morphology on the rough side of chips is very rough, with pillow-like formations resulting from the ridges which form primarily lengthways (along the long dimension of the chip, of length ~10 mm) but also widthways (along the short dimension of the chip surface, of length ~1 mm). The smooth side of the chips is much smoother than the other side, as viewed under SEM, and has no ridges like the rough side, but machining marks running across the chip widthways.

On the rough side of chips from both bottom and top of reaction cell, number density of large outer layer crystallites is much higher than on the smoother side, suggesting a higher corrosion rate, as one might expect given the much higher surface roughness – see section 3.4.1.

On the smooth side of chips, outer layer crystallites are clearly aligned along the direction of machining marks, with a high number density along particular lines, and often a very low number density elsewhere.

By modelling the crystallites as spheres of density 5.2 g/cm^3 (the density of ferrite and chromite spinel type oxides), and finding an approximate size distribution using these SEM images, approximations of outer layer mean film thickness and mass thickness (mg dm^{-2}) were made (see section 17.7.1). For the smooth side of a chip used during session 5, this yielded 0.13 µm (6.7 mg dm^{-2}), and for the rough side of a chip used during session 5 this yielded 0.53 µm (27.3 mg dm^{-2}); taking an average from the two sides gives 0.33 µm (17.0 mg dm^{-2}).

The expected film thickness using Morrison [26] kinetics was 0.66 µm (34.6 mg dm^{-2}) for the full film, so ~ 0.33 µm (~ 17.3 mg dm^{-2}) for the outer layer assuming approximately equal mass of the two layers. This provides some corroboration that the corrosion rates are indeed consistent with the kinetics described by the data of Morrison.

(a) chip with feathered edge; (i) dull / rough side	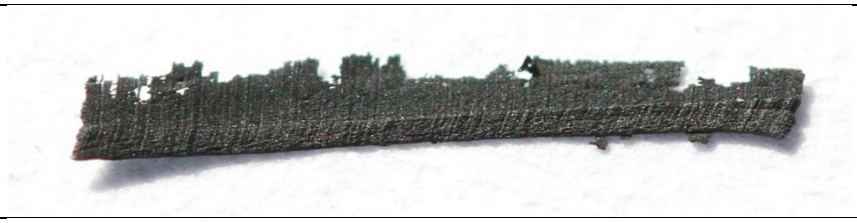
(a) chip with feathered edge; (ii) shiny / smooth side	
(b) curled chip; (i) dull / rough side	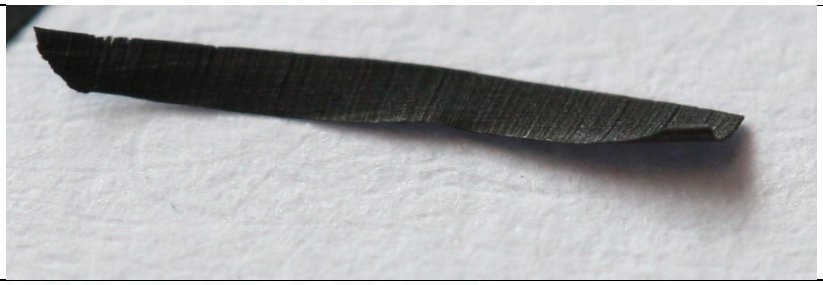
(b) curled chip; (ii) shiny / smooth side	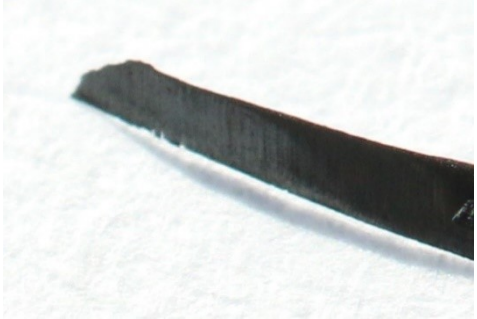
(c) Uniform chip, dull / rough side	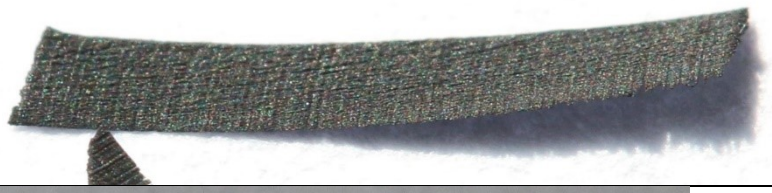
(d) a chip (with feathered edge) before exposure in the rig – shiny / smooth side	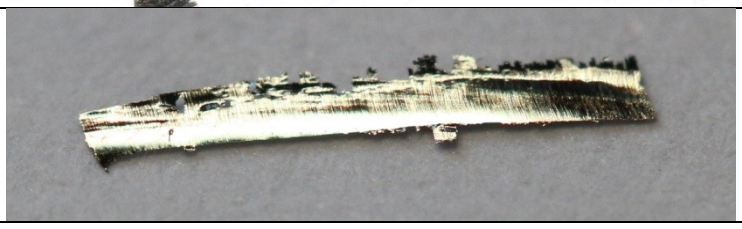

Figure 10.10. morphology of a selection of chips, as viewed by optical photography.
Chips (a) to (c) are as-oxidised, after exposure in rig during session 5. Chip (d) is photographed prior to exposure in the rig. Approximate dimensions are 10 x 1 x 0.05 mm^3.

Rough side	Smooth side
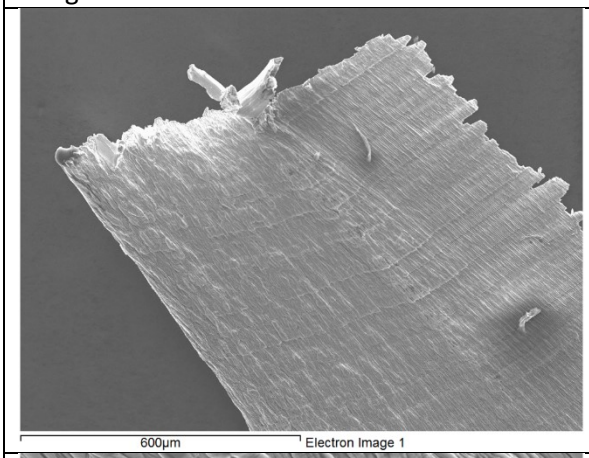	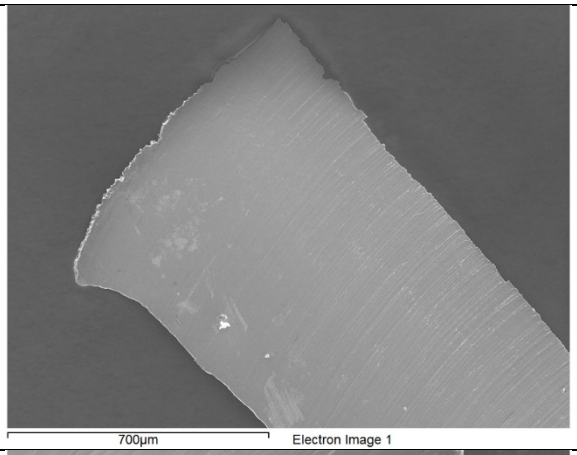
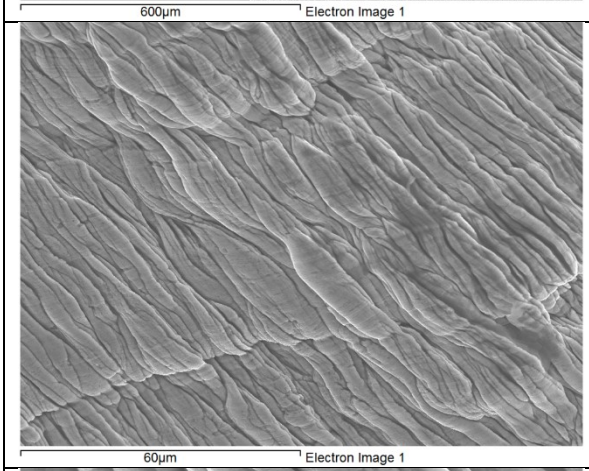	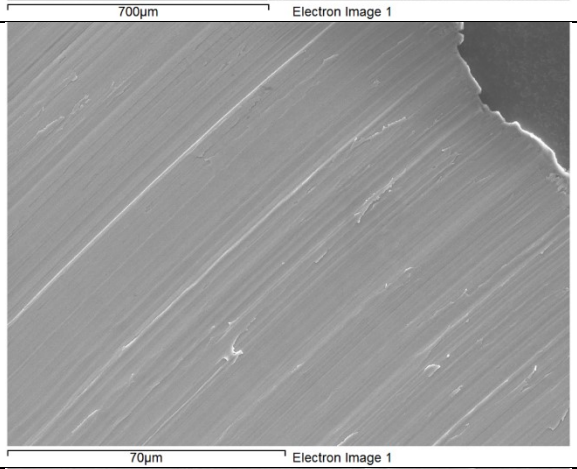
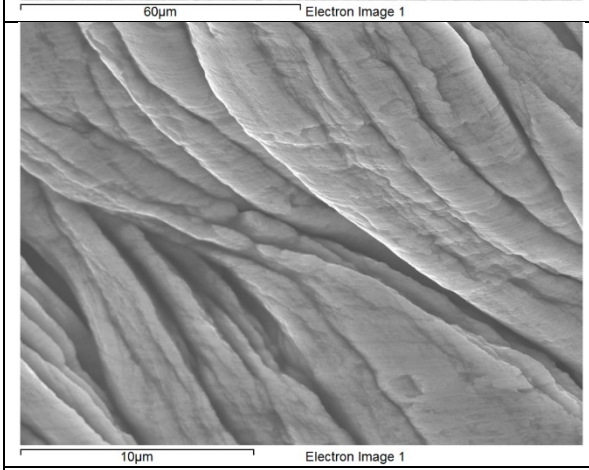	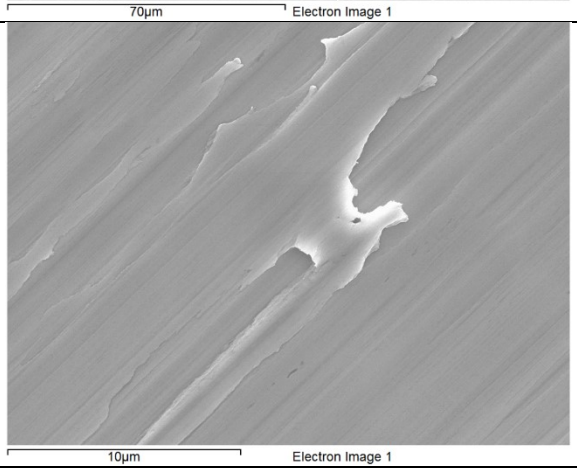

Figure 10.11. surface morphology of chips before exposure in the rig

Rough side	Smooth side
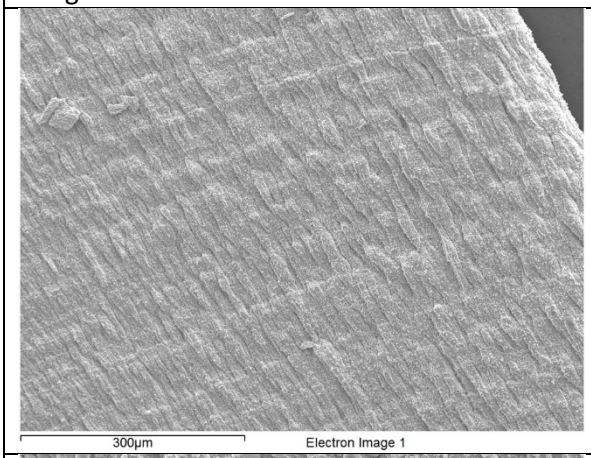	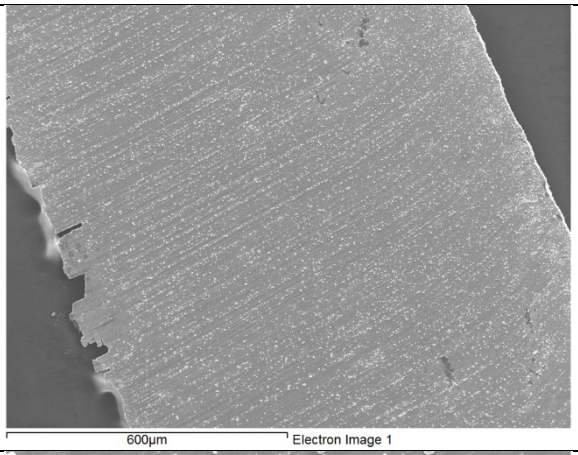
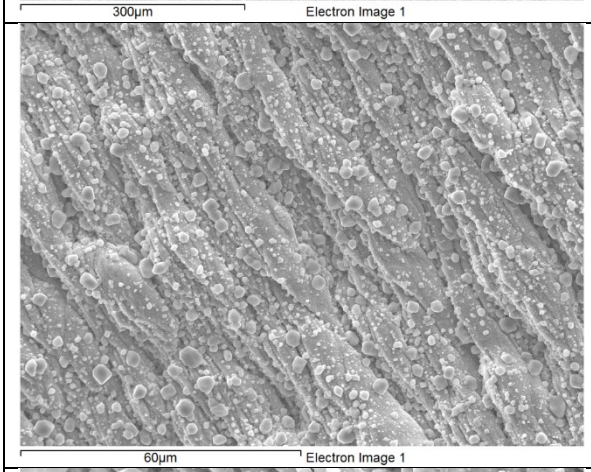	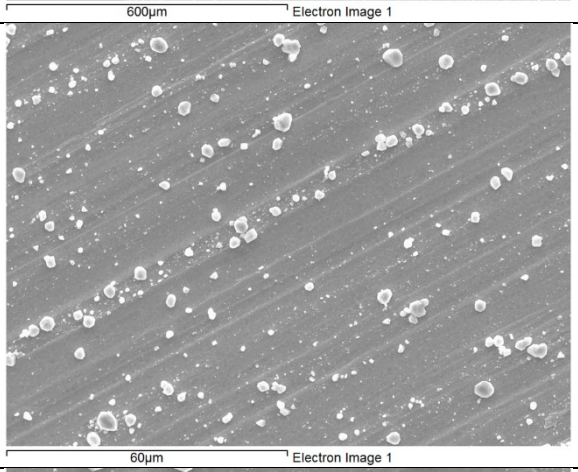
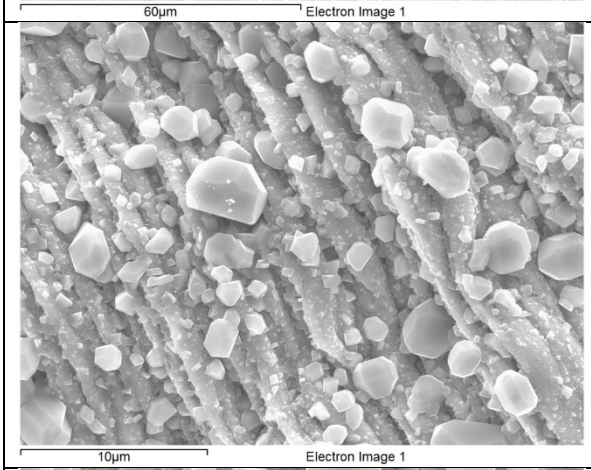	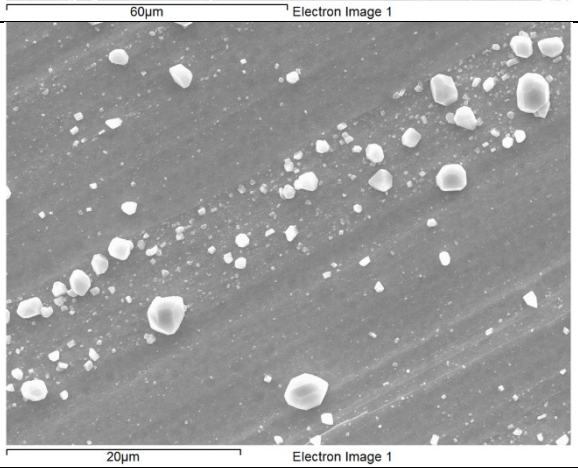
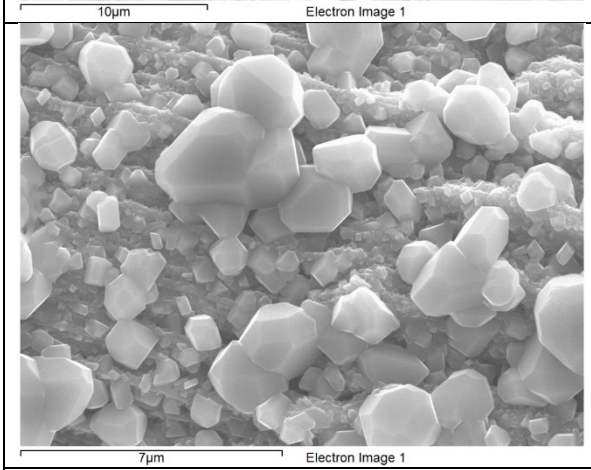	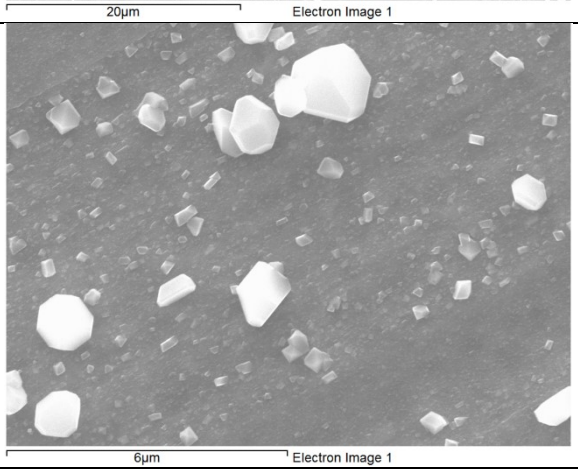

Figure 10.12. Surface morphology of oxide film on chip from bottom of reaction cell

Rough side	Smooth side
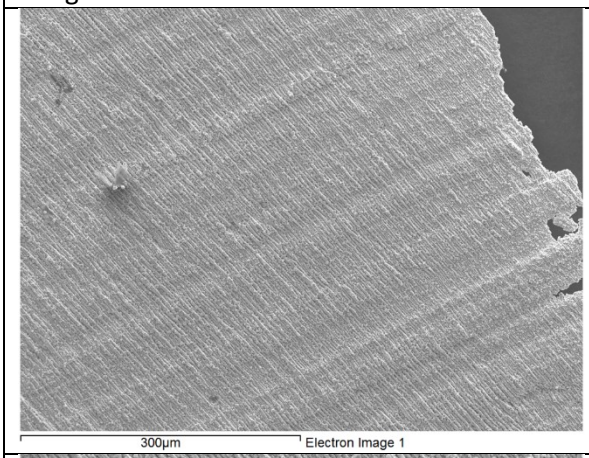	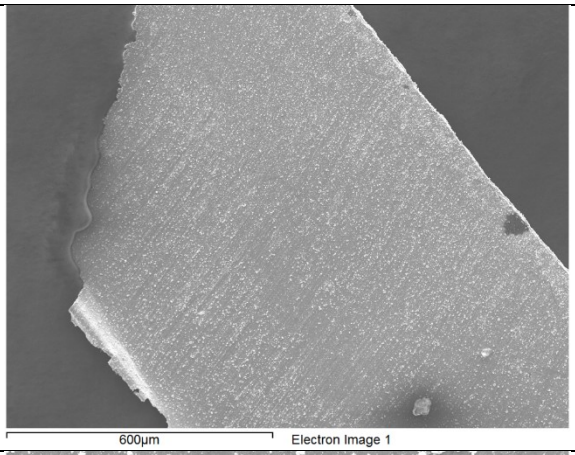
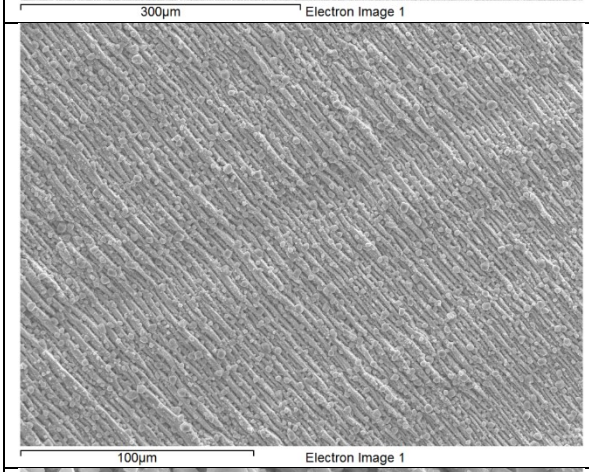	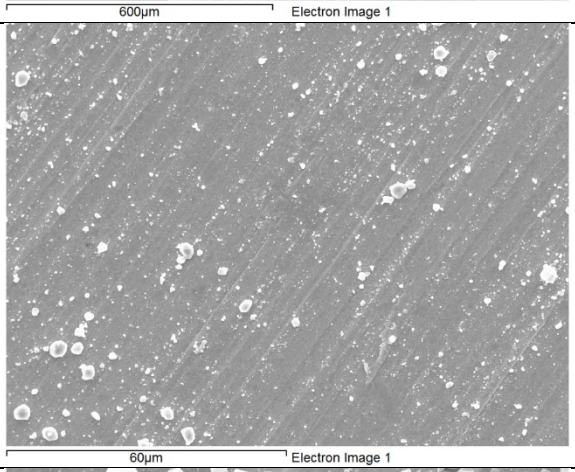
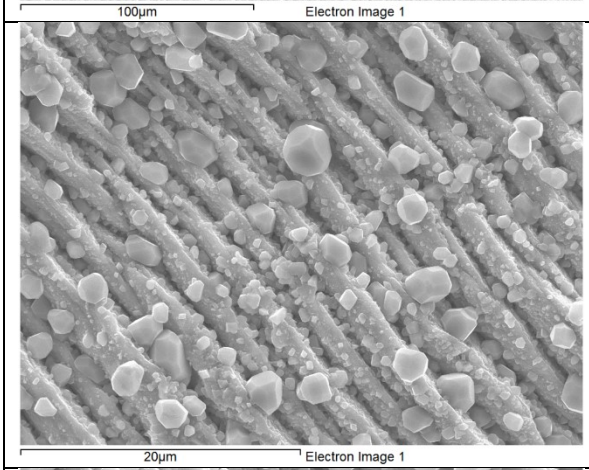	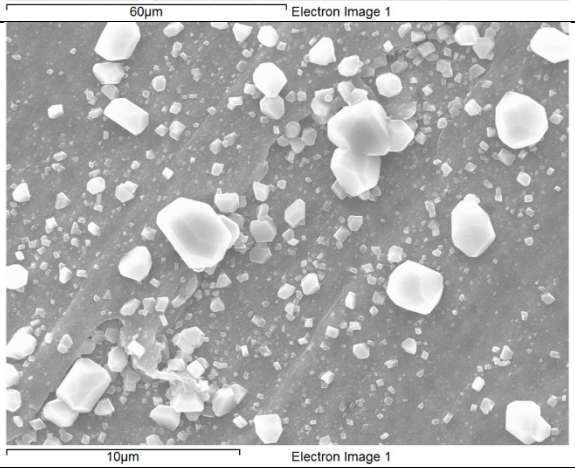
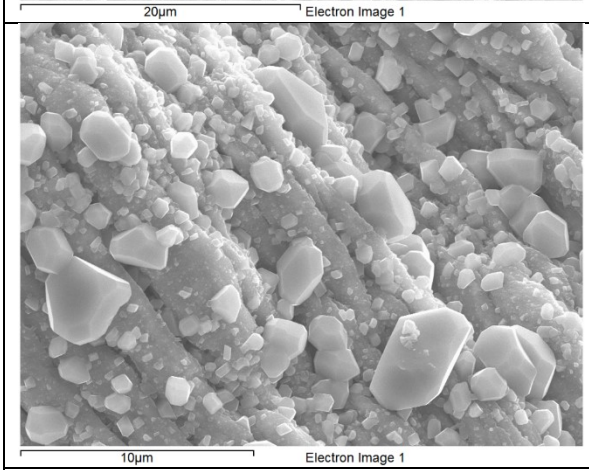	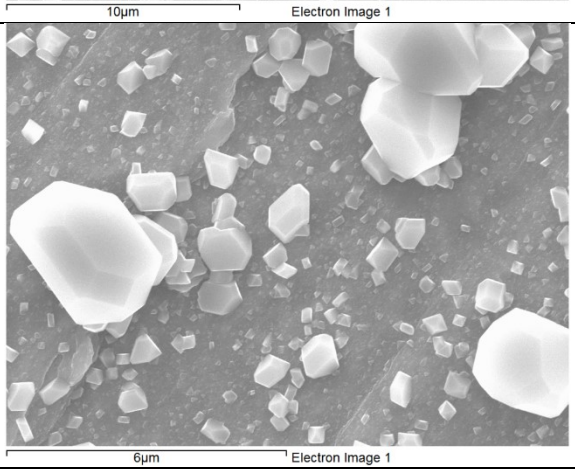

Figure 10.13. Surface morphology of oxide film on chip from top of reaction cell.

10.4. Bekipor ® SS316L frits after use in the rig

The Bekipor ® SS316L frits, used at the top and bottom of the reaction chamber within the rig, were studied under optical microscope after use in the rig. The results are shown below in Figure 10.14.

(a) frit after use in the rig, under optical microscope. Oxide crystallites on the order of 1 µm across are just about visible.	
(b) frit after use in the rig, under optical microscope, close-up.	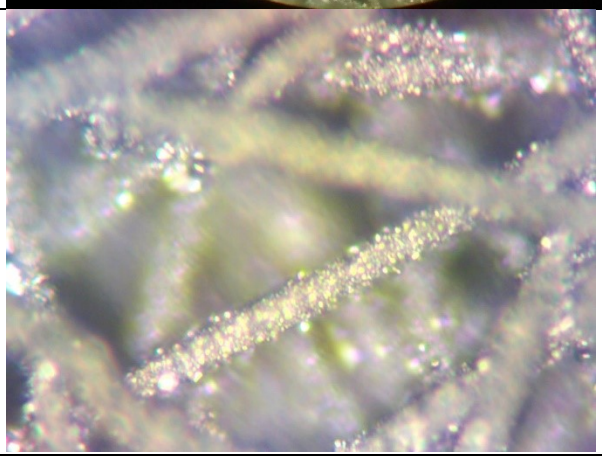

Figure 10.14: optical microscope images of SS316L Bekipor ® frit after use in the rig.

11. Characterisation of Particulates on Used Filters

11.1. Overview of Chapter

This chapter presents the results of analysis of filters used at the rig exit point/sampling point, particularly with regard to the particulates present. SEM was used in conjunction with Energy Dispersive X-ray Spectrometry (EDX). Some optical images using microscopes and photography were also captured.

Filters of 13 mm diameter were used during session 5, and on the CRR. These filters caused problems by disrupting the flow, causing effluent to leak through the filter housing and bypass the filter, or to flow through or possibly around the filter in punctuated bursts in which several minutes of flow went past the filter during only a few seconds.

11.2. Filter used on the Corrosion Rate Rig (CRR)

One filter was used on the corrosion rate rig. Details of the filter, and photographs, are provided in Figure 11.1. A selection of the particulates observed are shown in Figure 11.2, at the same scale for ease of comparison, with a more detailed image of one of the particulates shown in Figure 11.3. Alumina spacers used in the rig crumbled and released particulates into the rig. The particulates observed were of various forms and interesting to observe, though probably not relevant to the Metal Oxide Solubility (MOS) rig because of the role played by the alumina, which was not present in the MOS rig.

Right: 13-mm filter of 0.45 µm pore size used on CRR rig. The filter was in place for 8 days during 1.5 g/min flow of pH_{25C} 10 coolant (17.3 litres of integrated flow); the heated part of the rig was at 300 °C (?)

Below: the sample as mounted

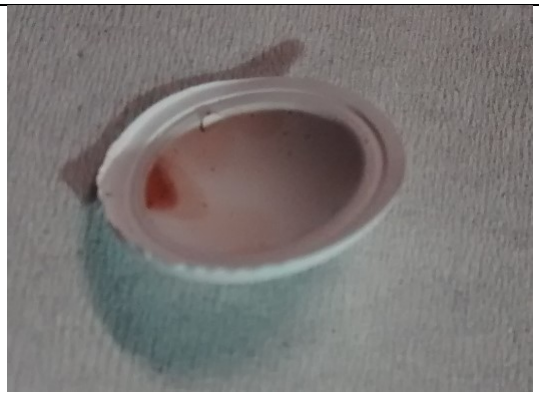

Figure 11.1. Filter used on CRR rig.
Notice the orange/brown staining over some regions of the filter. Alumina spacers which were used to electrically isolate the specimens used in that rig by Jonathan Morrison as part of his EngD project [26] *turned the same colour and began to crumble after a long time of exposure in the CRR rig. This material is believed to be the source of the orange/brown staining on the filter.*

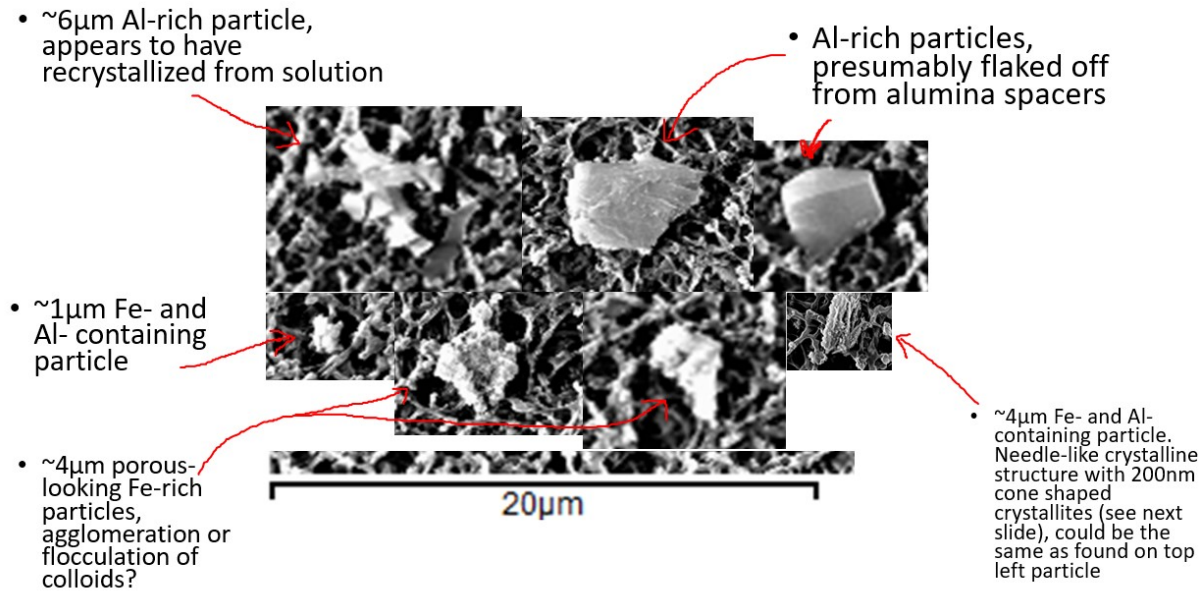

Figure 11.2 Annotated SEM images of a selection of the Fe- and Al- rich particulates observed on the filter used on the CRR rig.
EDX was used in conjunction with the SEM to determine the key elemental components of each particulate.

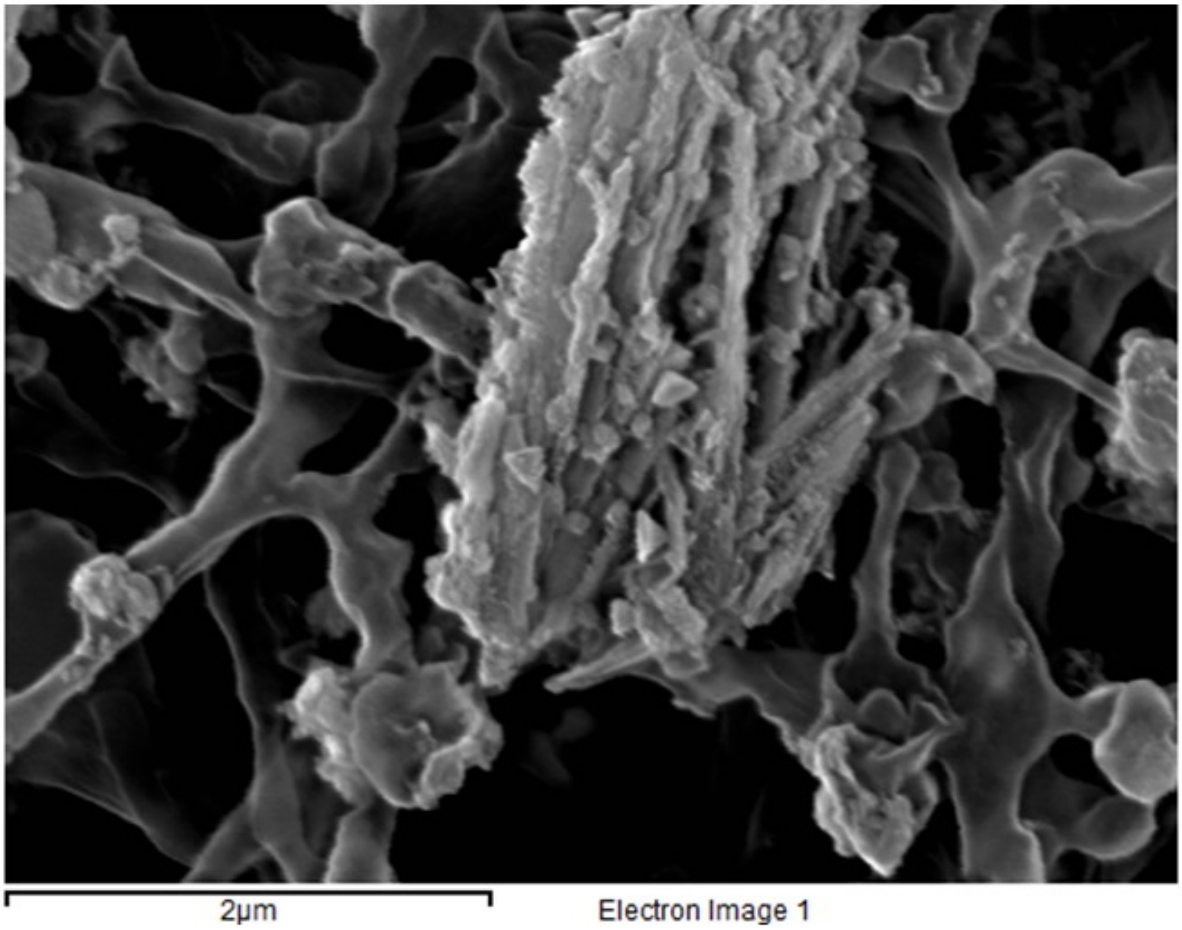

Figure 11.3. SEM image detail of one of the particulates shown in Figure 11.2.

11.3. Filter used during session 5

During session 5 only one filter was used for more than a few hours. The caption for Figure 11.4 provides details about the use of the filter. Several particulates of various sizes were observed on this filter, as shown in Figure 11.5. The filter did not prevent high levels of Fe from entering the two effluent samples which were taken while it was in place. Since the pore size was 3.0 µm, particulates up to a reasonable size could have passed through (for example, one possible source of particulates is from outer layer oxide crystallites released to the coolant from heated parts of the rig, these are typically less than 3 µm across.

(a) 13-mm filter of 3.0 µm pore size used during session 5. The filter was in place for 3 days during 0.1 g/min flow of pH_{25C} 9 coolant (450 ml of integrated flow); the heated part of the rig was at 300 °C	(b) filter within filter holder, connected to the rig exit point. A drip of water is observed to leak from the side of the holder. This problem occurred intermittently. At other times, build-up of pressure was released by punctuated flow through filter, or possibly around the filter but within filter housing
	

Figure 11.4. filter used during session 5.
A faint orange staining is visible on the filter, of a different hue to that observed on the filter used on the CRR rig where alumina was present.

(a) 7 µm x 2 µm Fe-rich oxide particulate. The crystal growth pattern is plate-like, unlike the polyhedral forms of spinel oxide crystallites precipitated in the hot parts of the rig.	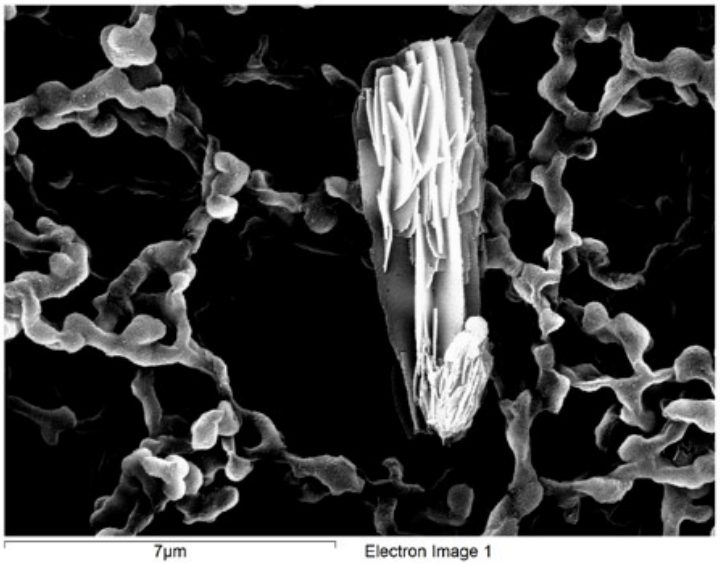
(b) 4 µm x 4 µm Fe-rich particulate. The shape appears to be very approximately spherical, with delicate oxide growth only covering the outermost ~ 0.1 µm. This outermost oxide covering is likely to have formed in situ on the filter, where close proximity to air from the laboratory causes steel or magnetite to have a high solubility (up to 58 ppb Fe in the case of magnetite), whilst Fe(III) oxides, goethite and hematite, have < 0.01 ppb solubility.	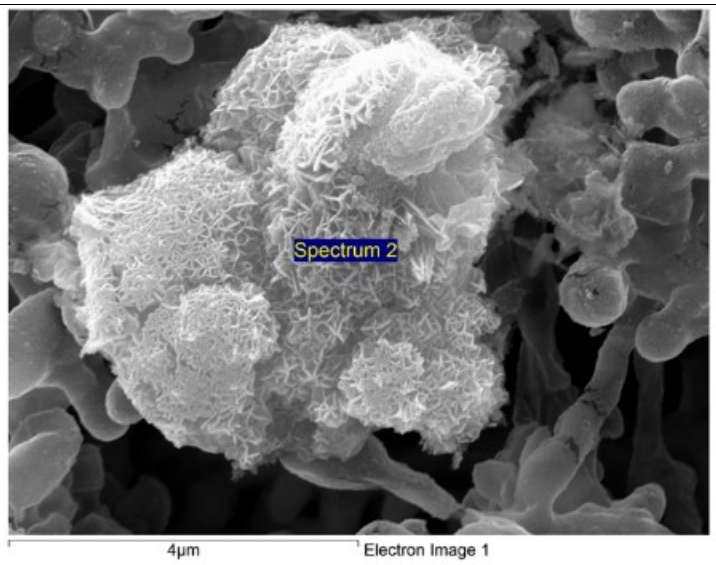
(c) ~ 15 µm x 10 µm Fe-rich oxide particulate. An outer oxide covering appears to have recrystallised from solution in situ on the filter, in like manner to the particle (b), though in this case the re-precipitated oxide appears more well-developed, having a thickness on the order of ~ 1 µm.	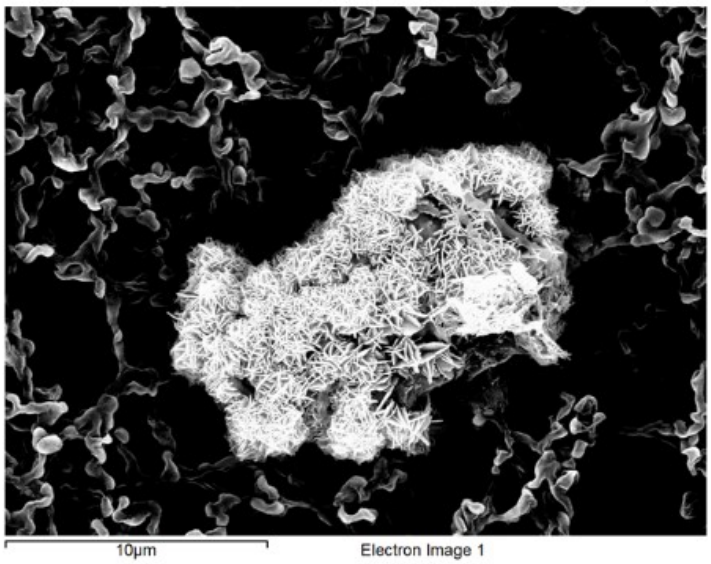

Figure 11.5. A selection of particulates observed on the 3.0 µm filter used during session 5. For each particulate, size is indicated according to the two observable length dimensions – depth cannot be determined from these images, though it is likely to be comparable with the other two dimensions.

11.4. Filters used during session 6

Filters were used extensively during session 6. By using larger filters, of 47 mm diameter, it was possible to keep the filters in place continuously without any disruption to the flow of effluent from the rig. Examples of filters used during session 6 are provided in Figure 11.6. Filters of all three pore sizes were used, in turn, under each set of conditions, and samples were also taken with no filter present for comparison.

No discernible difference was observed in the elemental analysis of effluent samples – for filters of any pore size – compared with results taken when no filter was present. However, levels of Fe, Ni, Mo and Mn were on some occasions elevated for the first sample taken soon after a filter was installed at, or removed from, the rig sampling point.

(a) One of the 47-mm filters used during session 6.
Filters were typically in place for around 3 days, during flow of pH_{25C} 10 coolant at either 1. 0.5, or 0.1 g/min (typically ~ 500 ml of integrated flow); the heated part of the rig was at 300 °C, 250 °C and 200 °C over the course of session 6.

(b) Filter within filter holder, connected to the rig exit point. These larger diameter filters did not cause disruptions to flow as the smaller ones did. In some cases deposits of oxide crystallites from the hot part of the rig were observed at the top of the plastic filter housing, at the point indicated by the arrow

Figure 11.6. Example of filters used during session 6.

Two samples, of around 5 mm x 5 mm, were taken from each filter, and studied extensively under SEM for any particulates. Aside from native particulates present on the filters themselves, which

consisted of various elements such as Al and Ca, only one particulate was found on any of the filters. An SEM image of that particulate, along with results from EDX analysis, is provided in Figure 11.7.

(a) 3 µm x 1 µm Fe-rich oxide particulate. The crystal growth pattern is plate-like, unlike the polyhedral forms of spinel oxide crystallites precipitated in the hot parts of the rig.

The growth pattern is different from the particulate shown in Figure 11.5 (a), though it also bears some similarities.

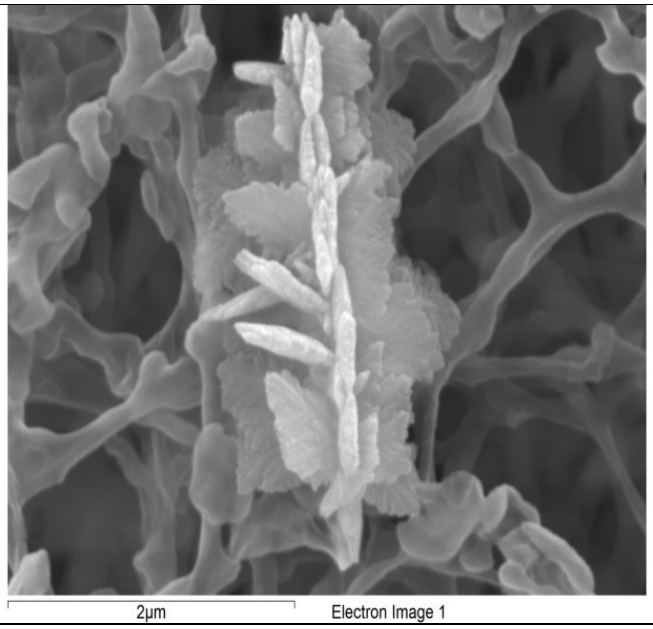

(b) Results of EDX spot scan performed on the particulate, and comparison with calculated solubility of single oxide phase.

Fe, wt%	Cr, wt%	Ni, wt%	Mo, wt%	Mn, wt%	O, wt%
61.1	8.4	0.2	1.8	4.8	23.7

EDX results, metals basis: (plus O at 52.1 at%), versus alloy composition

	Fe, wt%	Cr, wt%	Ni, wt%	Mo, wt%	Mn, wt%
Particle	80.1	10.9	0.3	2.4	6.3
Outer ox.	79.3	10.4	10.4	0	0
alloy	64.9	17.3	13.1	2.5	1.7

Levels of each element in effluent when the filter was installed – measured vs solubility

	Fe, ppb	Cr, ppb	Ni, ppb	Mo, ppb	Mn, ppb
Meas.	0.2	0.8	0.0	90	0.1
Sol.	0.00	0.01	<0.3	?	?

Figure 11.7. SEM image and EDX spot elemental analysis from the only particulate observed on filters during session 6.
No other particulates were observed on the filters themselves during session 6, despite extensive use of filters. Size is indicated according to the two observable length dimensions – depth cannot be determined from these images, though it is likely to be comparable with the other two dimensions. EDX shows that the particle is very poor in Ni, but strongly enriched in Mn. This suggests that partition coefficients for Mn and Ni are weighted heavily in favour of Mn uptake into, and Ni release from, the oxide phase from which the particle is formed – at pH 10, room temperature, oxidising conditions. Mo is present to the same levels as found in the alloy, and Fe and Cr are at levels reported by Perrin et al. in their outer oxide [78].

Though only one particulate was found on filters during session 6, substantial deposits of polyhedral crystallites were discovered on the plastic (PP) housing of the 47 mm filters on several occasions. The largest of these deposits was studied by digital photography and optical microscopy. Findings are summarised in Figure 11.8.

(a) macroscopic view of whole deposit, using digital photography	
(b) view of some of the deposit under optical microscope	
(c) digital photograph taken through optical microscope. The object at the left of this image provides an example of the two types of crystallite observed in this deposit using the optical microscope. There is a faceted octahedral large crystallite (on the order of ~ 1 µm across), together with an agglomeration of much smaller crystallites, on the order of 0.1 µm across. The smaller crystallites have an orange hue, suggesting the possibility of hematite or similar phase. The larger crystallites are black, suggestive of magnetite	

Figure 11.8. Images of deposit on one of the filter holders, using photography and optical microscopy.

12. Summary, conclusions and future work

12.1. Initial aims, and scope of work

1. A prototype once-through flowing rig was built by Jonathan Morrison for the study of metal oxide solubility in conditions relevant to PWR primary coolant. The rig was built entirely of SS316L, with the intention that later iterations might be built of more inert materials such as titanium alloy.
2. Operation of the rig served partly as a feasibility study, to ascertain whether the current iteration of the rig could be used for high temperature oxide solubility studies, and partly as a means for developing capability and experience, to inform any changes to the design which may be beneficial in future iterations. If initial testing showed the rig to be suitable for such studies, it was intended to use a bed of high purity oxide granules held in a reaction cell in the rig, in conjunction with simulated coolant, of controlled pH, hydrogen concentration, and temperature. A particular point of interest was the discrepancy between the data of Sweeton and Baes [4], and those of Tremaine and LeBlanc [121], regarding solubility of magnetite under reducing, alkaline, hydrothermal conditions, and the role which might be played by colloidal material.

12.2. Initial findings, and revised aims and scope of work

1. In order to ascertain the level of contamination released by the rig itself, three initial sessions of use of the rig were conducted without any oxide granules in the reaction cell. Samples of effluent were analysed by ICP-MS for Fe, Cr, Ni, and Mn, as well as Mo and/or Co. A range of conditions of temperature (200 – 300 °C), flow rate (0.1 – 2 g/min), and pH_{25C} (neutral, 11, and 9) were employed, to explore the effect on levels in the effluent. Other

factors were also considered in terms of their potential impact on effluent levels, such as total time, and time since the latest flow disturbance.

2. It was found that the rig in its current form would not be suitable for studying the solubility of pure metal oxides in high temperature aqueous solutions. This was partly because a planned procedure to introduce a known amount of dissolved hydrogen in the feedwater, an important factor in the solubility of oxides such as magnetite, was not implemented due to health and safety concerns. In addition, the rig was found to introduce Fe, Cr and Ni into the simulated coolant at unpredictable and variable levels, which were comparable to or higher than the range of values expected from solubility of corrosion film oxides forming on stainless steel under hydrothermal conditions, but which did not follow the pattern expected in terms of dependence on temperature and pH, being seemingly more influenced by flow rate and time since the latest disturbance to flow. Mo and Mn were also released to the coolant, at levels sometimes as high as several hundred ppb, and Co was found in the samples where it was included in the analysis. These elements may have affected the solubility of pure oxides.
3. Instead of studying the solubility of pure oxide granules under well-defined conditions, it was decided to study the levels of the five major alloying components of SS316L released into simulated coolant from the walls of the rig itself. A small amount of dissolved hydrogen was present in the coolant as a by-product of the steel corrosion process. This was modelled according to expected corrosion rates [26], corrosion mechanism [73], [94], [95], and coolant flow rate. Two rig effluent samples were analysed for hydrogen content, and were found to be about one power of 10 above and below the modelled value respectively.
4. A fourth session of rig use without any oxide granules in the reaction cell was conducted, to answer questions which arose from results of the previous sessions. Results from the first three sessions were observed to change over time, over a period of days and weeks, and there was a high degree of scatter between samples. The few samples taken from feedwater had values for some elements which were consistent with effluent samples, suggesting that levels may be controlled by room temperature processes in the sampling line. Therefore, during the fourth session many samples were taken over a long period of time under each set of conditions, and several feedwater samples were taken. During session 3, lower levels were observed at slower flow rates, which suggested either the presence of particulates at levels which increased with flow rate, or the effect of a new equilibrium being approached with the room temperature SS316L tubing of the sampling line, at much lower Fe levels than

were present at high temperature. In order to explore this further, a slow flow rate of 0.1 g/min was used throughout the fourth session of rig use.

5. A fifth session of rig use employed 20 g of SS316L chips in the reaction cell, increasing the corroding surface area by a factor of 10. pH 9 feedwater was used, and a range of temperatures and flow rates, to enable comparison with the third and fourth sessions.
6. A sixth session of rig use was employed, following the same methodology as session 5 but at pH 10. Filters of several pore sizes were used to ascertain the presence and size distribution of any particulates that might be present, both in terms of the effect of filtration on effluent samples and in terms of analysis of any particulates found on filters themselves by SEM and EDX.
7. Particulates found on filters were studied by SEM and EDX. Samples of corrosion film from exposed surfaces of the rig were characterised by SEM and EDX, and the results compared with literature studies.

12.3. Overall findings from solubility measurements

1. For each element, levels were on some occasions observed to follow trends over time, rather than a clear step change on each change of conditions. This made it difficult to determine whether different results under different conditions arose due to the change in conditions, or due to some process which was occurring over time anyway.
2. In many cases levels of Cr matched very well with the expected level of ~ 0.01 ppb. On other occasions they were much higher, a sign of the presence of particulates. It was difficult to say with a high degree of certainty what levels of Fe would be expected, due to uncertainty over hydrogen levels. However, levels sometimes were lower than expected and sometimes significantly higher than expected. Ni was occasionally at expected levels, at the solubility of NiO or lower, but typically was much higher. Mo and Mn levels were sometimes very high (>100 ppb), but tended to vary smoothly and monotonically over long periods of time, suggesting that they were present in soluble form and not as particulates. Other workers have found that Mn has a high diffusivity in chromite [73], [166], [167] (the protective oxide on corroding stainless steel in hydrothermal solutions), therefore it would be expected to release fully through the protective oxide and into solution and the outer oxide crystallites. This, coupled with a high solubility would explain its high levels in some samples.
3. Various problems were encountered, and mitigated, such as: frequent pump stalls; contamination introduced by method of sample collection; and high scatter introduced to results from variable contamination levels during sample preparation.

4. Calculations were performed on a spreadsheet to determine the potential effect on pH_T of elements released from the steel during session 1, assuming levels measured in effluent represent dissolved level in the rig. It was found to be feasible that pH_{260C} could have risen from neutral, ~ 5.58, to between ~ 5.64 and ~ 6.09, i.e. equivalent to pH_{25C} (LiOH) between 8 and 9. At pH_{25C} (LiOH) 9 and above, as used in all subsequent sessions, the effect on pH_T from soluble metallic species was expected to be relatively minor. For example, rising from pH_{25C} (LiOH) equivalent 9.00 to 9.06, or pH_{300C} actual from 6.27 to 6.32 for sample 03-06, which had 104 ppb Mn.
5. Levels from sessions 1-3 at comparable flow rates and temperature can be summarised as follows, in units of ppb:

Session/element	Fe	Cr	Ni	Mo	Mn	Co
Session 1 (pH 7) 1 g/min, 260 °C	14 +/- 4	1.3 +/- 0.4	4 - 57	-	67 - 527	0.8 - 30
Session 2 (pH11) 2 g/min, 300 °C	0.8 +/- 0.4	8 samples: 0.9 +/- 0.3 Last two: 6.3, 2.4	7 samples: -0.1 +/- 0.2 3 samples: 2.6 – 4.4	Falling, 450 to 50	first 29 h, falling: 0.7 to 0.2 >29 h: 0.0	-
Session 3 (pH 9) 2 g/min, 300 °C	~ 6	Falling, 0.3 to 0.05	Initially: 1 – 3 Then climbs to 5	Rises to 25, falls to 20	30 – 100, then settles to 20	0 to 0.3, where measured

- Levels of Fe, Ni, and Mn appeared to have a positive dependence on H^+ ion concentration, having the highest levels during session 1 (pH ~7) and the lowest during session 2 (pH 11).
- Levels of Cr at pH 7 and pH 11 were about 1 ppb, aside from two outliers, but fell from 0.3 to 0.05 ppb at pH 9. This may have been an effect of the passage of time, as the rig was in the early stages of corrosion during sessions 1 and 2, where more transient effects might be expected.
- Levels of Co were perhaps surprising given that Co was not even listed as an impurity element in the manufacturer quoted SS316L composition.
- Levels of Mo were found to be particularly high, and varying with time.
- During session 3, the effects of flow rate and temperature were studied. It was found that when results from sessions 1 to 3 were plotted against time, levels of Mo were seen to vary smoothly over time, with changes appearing to take place within the rig over the course of several days. Levels of Mo seemed to be affected by levels present under previous conditions of rig operation, slowly reaching a new equilibrium with new conditions over a period of several days. Levels of Ni also changed with time, reaching a peak and then falling

away, apparently due to processes more related to the passage of time than to the prevailing conditions. Levels of Fe fell with decreasing flow rate, suggesting either a flow rate-dependent contribution from particulate matter, or the approaching of a new equilibrium at room temperature with the SS316L walls of sampling line, having lower solubility (~ 0.0 ppb Fe) than in the hot part of the rig.

- Results from session 5 were similar to those from sessions 1 to 3, though Fe rose to higher levels. Results from session 6 were surprisingly high in Cr, consistently about 2 ppb.

12.4. Findings from SEM and EDX studies

1. Outer layer oxide crystallites had composition similar to that observed by other workers [78], [84], namely magnetite with 3 +/- 1 wt% Cr and 9 +/- 3 wt% Ni. Inner layer oxide was enriched in Cr. However, observed levels of Cr were lower than found in the literature, being 26 +/- 5 wt% Cr compared with 43 +/- 6 wt% Cr [84] and 39 +/- 2 wt% [78]. This may have been due to interference from outer layer crystallites, or base alloy, residing behind the inner oxide film, whose thickness was expected to be around 0.2 µm. Similar problems were experienced by other workers [84], who used different techniques to obtain more accurate assessment after a positive bias was found in the proportion of Fe measured by EDX.
2. Crystallites which appeared to have been released to solution and subsequently redeposited were observed on some of the corrosion film samples
3. A few Fe-Ni oxide particulates of unknown origin were found on filters used at the rig sampling point, though the quantity was not nearly enough to account for the high degree of supersaturation observed in some effluent samples.
4. A deposit of polyhedral crystallites was found on the polypropylene housing of some of the filters used during session 6 (pH 10, 200 – 300 °C). These had the same morphology as those observed on the outer oxide layer. The larger crystallites (several microns across) appeared black under optical microscope, as expected for ferrite (although chromite can also appear black) [168]. Much smaller crystallites were also present in clusters (each crystallite several tenths of a micron across), consistent with the assumed deposits observed on oxide film samples. These were unexpectedly observed to have an orange/red hue under optical microscope, suggesting an Fe(III) oxide. The difference in colour could be due to preferential oxidation of the smaller, less stable crystallites under oxidising conditions at the point of deposition or in the period between deposition and observation under microscope, or they may have oxidised in the hot part of the rig itself. Alternatively the coloration could be an artefact of the small length scale, comparable with the wavelengths of visible light.

12.5. Limitations of the current study

There were many factors which could have affected the levels of Fe, Cr, Ni, Mo and Mn observed in effluent samples taken from the rig. It is therefore difficult to draw conclusions from the results. Levels of hydrogen, a key factor in the solubility behaviour of magnetite, were not accurately known. In order to ensure reducing conditions and saturated coolant in the heated part of the rig, and in an effort to minimise the contribution from particulate matter, slow flow rates were employed, between 2 g/min and 0.1 g/min. This may have also enabled a new equilibrium to be approached in the room temperature SS316L tubing of the sampling line. The use of inert material in the sampling line, such as PTFE, would have been advantageous. Levels of Fe and Ni were in many cases fairly high in the feedwater, comparable to the levels in effluent. A Teflon lining may have decreased such levels.

There was a significant lag time of several months between taking samples and receiving ICP-MS results, which made it difficult to learn from one session of testing to inform the next.

12.6. Future work

One possible adaptation planned for future iterations is the injection of nitric acid to the coolant at the point of exit from the heated part of the rig, to ensure that there is no precipitation of oxide on the walls of the rig on cooling. This would only be viable for a rig built of inert material such as titanium alloy, or stainless steel with a platinum lining, at least from the point of acid insertion onwards. Use of a rig built entirely from inert materials would also enable studies of pure oxides to be made.

Addition of dissolved hydrogen to the feedwater would enable more certainty over the redox conditions, instead of relying on uncertain and varying concentrations of hydrogen produced by corrosion of the walls of the rig; this would be essential for studies of pure oxide solubility (in an inert rig), if the findings from previous well controlled studies are to be improved upon. It is regrettable that this was not possible for the work performed herein.

It was initially anticipated that particulate and colloidal matter may cause total levels of Fe and other elements to be higher than solubility levels, and erratic, making meaningful results difficult to record, but that this may be minimised by using very slow flow velocities; it was also anticipated that the low surface area to volume ratio present when using the corroding rig itself as a source of metal oxides may necessitate a long residence time, afforded by slow flow velocities (or equivalently, slow

flow rate). A range of slow flow rates were used (0.1 – 2 g/min), and yielded some interesting results. However, calculations using a model of the rig showed that saturation of the coolant could be achieved at faster flow rates, and that there could be some progress being made towards a new equilibrium in the room temperature SS316L tubing of the sampling line. It would, therefore, be interesting to extend the experiments to conditions of faster flow as this may enable the effects of the sampling line to be minimised, if indeed they are significant, and may also introduce a flow-rate dependent contribution from oxide particles. Perhaps a better way to eliminate or minimise sampling line effects would be to use a PTFE or Teflon lined sampling line, as well as PTFE or Teflon lining of the feedwater barrel and room temperature tubing between the feedwater barrel and the oven, and a lithiated ion exchange column to remove any remaining metal ions before the entrance to the pump. Methods such as the above and the use of platinum lining were considered for the current project, but could not be implemented due to time and cost constraints.

The use of nickel metal chips mixed in with chips of SS316L would provide an interesting extension to this work, to investigate the effect on levels of Ni and other metals in the effluent, and on the composition and form of metal or metal oxide crystallites forming on the chips and the walls of the rig. Another extension to the work could be provided by comparing the effect of using different pH raisers, such as ammonia, instead of LiOH, or combinations of LiOH and boric acid, to better simulate the chemistry employed in a PWR.

Six pieces of SS316L polished to a mirror finish were added to the reaction chamber along with SS316L chips during session 6, so that they may be analysed for corrosion film thickness at a later date, though there was insufficient time during the PhD project. These pieces were cut from unused specimens prepared for the corrosion rate studies of Jonathan Morrison [26]; their flat finish would facilitate analysis of corrosion film profile and depth by imaging of a cross section in SEM/EDX, or by XPS/AIM. The mass of each of each one was recorded prior to exposure in the rig, as well as the total mass of SS316L chips, which may facilitate a crude form of gravimetric analysis by measuring the total mass afterwards and comparing with the total mass before and thus estimate the extra mass from oxide ions (O^{2-}) in the oxide film and from this the extend of corrosion. This would be problematic though due to the possibility of chips becoming left behind in the reaction chamber, for example.

SS316L chips used during session 6 were not analysed afterwards, this would be interesting to do, to compare with those exposed during session 5.

13. References

[1] J. Deshon, D. Hussey, B. Kendrick, J. McGurk, J. Secker, and M. Short, “Pressurized water reactor fuel crud and corrosion modeling,” *JOM*, vol. 63, no. 8, pp. 64–72, 2011.

[2] R. A. Castelli, *NUCLEAR CORROSION MODELLING: The Nature of CRUD*. Elsevier Inc., 2010.

[3] P. R. Tremaine and J. C. Leblanc, “The solubility of nickel oxide and hydrolysis of Ni2+ in water to 573 K,” *J. Chem. Thermodyn.*, vol. 12, pp. 521–538, 1980.

[4] F. Sweeton and C. Baes, “The solubility of magnetite and hydrolysis of ferrous ion in aqueous solutions at elevated temperatures,” *J. Chem. Thermodyn.*, vol. 2, pp. 479–500, 1970.

[5] S. E. Ziemniak, M. E. Jones, and K. E. S. Combs, “Magnetite Solubility and Phase Stability in Alkaline Media at Elevated Temperatures,” *J. Solution Chem.*, vol. 24, no. 9, pp. 837–877, 1995.

[6] “PWR Axial Offset Anomaly (AOA) Guidelines, Revision 1,” EPRI, Palo Alto, CA: 2004. 1008102.

[7] World Nuclear Association, “World Nuclear Performance Report 2016,” 2016. [Online]. Available: http://world-nuclear.org/getmedia/b9d08b97-53f9-4450-92ff-945ced6d5471/world-nuclear-performance-report-2016.pdf.aspx.

[8] S. J. Zinkle and G. S. Was, “Materials challenges in nuclear energy,” *Acta Mater.*, vol. 61, pp. 735–758, 2013.

[9] A. V. Nero Jr., *A guidebook to nuclear reactors*. University of CA Press, 1979.

[10] S. Odar and P. Rudling, “CRUD in PWR / VVER Coolant Volume II – Control of CRUD in the PWR / VVER Coolant and Mitigation Tools,” Mölnlycke, Sweden: ANT International, 2015.

[11] IAEA, “Modelling of Transport of Radioactive Substances in the Primary Circuit of Water-Cooled Reactors,” Vienna: International Atomic Energy Agency, 2012.

[12] V. A. Kurepin, D. A. Kulik, A. Hiltpold, and M. Nicolet, “Thermodynamic modeling of Fe-Cr-Ni spinel formation at the light-water reactor conditions,” Villigen, Paul Scherrer Institut, PSI-Bericht No. 02-04, 2002.

[13] C. Bates, K. Garbett, K. Hinds, G. Lancaster, M. Mantell, and G. Renn, “Development of

Corrosion Product Behaviour and Radiation Fields at the Sizewell B PWR from 1995 to 2008," *VGB PowerTech*, vol. 88, no. 12, pp. 52–60, 2008.

[14] D. J. Turner, "Thermodynamics and the transport of corrosion products in PWR primary circuits," *Nucl. Energy*, vol. 31, no. 4, pp. 327–333, 1992.

[15] M. A. Navarro and A. A. C. Santos, "Evaluation of a numeric procedure for flow simulation of a 5 × 5 PWR rod bundle with a mixing vane spacer," *Prog. Nucl. Energy*, vol. 53, no. 8, pp. 1190–1196, 2011.

[16] B. Cheng and R. L. Yang, "Fuel Failure Experiences in U.S. Light Water Reactors," in *International Conference on Global Environment and Advanced Nuclear Power Plants, Kyoto, Japan*, 2003.

[17] R. Reiss and S. Odar, "LCC-8 Special Topic Report,, PWR/VVER Primary Side Coolant Chemistry, Volume II - Water Chemistry Tool to Mitigate the Concerns," 2012.

[18] IAEA, "Status of Advanced Light Water Reactor Designs."

[19] W. Wagner, J. R. Cooper, A. Dittmann, J. Kijima, H.-J. Kretzschmar, A. Kruse, R. Mareš, K. Oguchi, H. Sato, I. Stöcker, O. Šifner, Y. Takaishi, I. Tanishita, J. Trübenbach, and T. Willkommen, "The IAPWS Industrial Formulation 1997 for the Thermodynamic Properties of Water and Steam," *J. Eng. Gas Turbines Power*, vol. 122, no. 1, p. 150, 2000.

[20] O. Eiff, "Environmental Fluid Mechanics Course notes: 1 . Concepts , Definitions , and the Diffusion Equation," in *Environmental Fluid Mechanics Course notes*, vol. 1, Karlsruhe, pp. 1–22.

[21] C. R. Wilke and P. Chang, "Correlation of diffusion coefficients in dilute solutions," *AIChE J.*, vol. 1, no. 2, pp. 264–270, 1955.

[22] R. Taylor and R. Krishna, *Multicomponent mass transfer*. John Wiley & Sons, Inc., Canada, 1993.

[23] A. Sleigh, "Notes For the First Year Lecture Course: An Introduction to Fluid Mechanics," *School of Civil Engineering, University of Leeds, UK*, 2001. [Online]. Available: http://www.efm.leeds.ac.uk/CIVE/CIVE1400/PDF/Notes/section_all2.pdf. [Accessed: 01-Jun-2017].

[24] N. Epstein, "Elements of Particle Deposition onto Nonporous Solid Surfaces Parallel to Suspension Flows," *Exp. Therm. Fluid Sci.*, vol. 14, no. 4, pp. 323–334, 1997.

[25] M. Basset, N. Arbeau, J. Mclnerney, and D. H. Lister, "Deposition of magnetite particles onto

alloy-800 steam generator tubes," in *3rd Int. Steam Generator and Heat Exchanger Conference, Toronto, Canada*, 1998, pp. 677–693.

[26] J. J. Morrison, "Corrosion, Transport, and Deposition in Pressurised Water Nuclear Reactor Primary Coolant Systems," [EngD thesis], University of Birmingham, UK, 2016.

[27] N. T. Vatistas, "Effect of Adhesion Time on Particle Deposition : Reentrainment and Rolling," *Ind. Eng. Chem. Res.*, vol. 31, no. 6, pp. 1549–1554, 1992.

[28] "Boundary layer - nuclear power," *nuclear-power.net*. [Online]. Available: http://www.nuclear-power.net/nuclear-engineering/fluid-dynamics/boundary-layer/. [Accessed: 16-Mar-2017].

[29] "Release on the IAPWS Formulation 2008 for the Viscosity of Ordinary Water Substance," Berlin, Germany: The International Association for the Properties of Water and Steam (IAPWS), 2008.

[30] H. Schlichting and K. Gersten, *Boundary-Layer theory*. Springer-Verlag, 2017.

[31] B. Lautrup, "Chapter 25: Boundary Layers," in *Physics of Continuous Matter, Exotic and everyday Phenomena in the Macroscopic World*, Revision 7., 2004, p. 500.

[32] R. L. Meek and A. D. Baer, "The periodic viscous sublayer in turbulent flow," *AIChE J.*, vol. 16, no. 5, pp. 841–848, 1970.

[33] I. U. Haq, "Heat and mass transfer analysis for crud coated PWR fuel," [PhD thesis]. London, UK: Imperial College London, 2011.

[34] R. Yang, B. Cheng, J. Deshon, K. Edsinger, and O. Ozer, "Fuel R & D to Improve Fuel Reliability," *J. Nucl. Sci. Technol.*, vol. 43, no. 9, pp. 951–959, 2006.

[35] "Impact of PWR Primary Chemistry on Corrosion Product Deposition on Fuel Cladding Surfaces," EPRI, Palo Alto, CA. TR-108783 1250-27, 1997.

[36] M. Bolz, W. Hoffmann, W. Ruehle, and F. Becker, "Characterization of Colloids in Primary Coolant," in *Water Chemistry of Nuclear Reactor Systems 7*, 1996, pp. 42–46.

[37] R. A. Castelli, "The Corrosion Source," in *Nuclear Corrosion Modeling: The nature of CRUD*, 2009, pp. 1–31.

[38] D. Wesolowski, S. Ziemniak, L. Anovitz, M. Machesky, P. Benezeth, and D. Palmer, "Solubility and surface adsorption characteristics of metal oxides," in *Aqueous Systems at Elevated Temperatures and Pressures: Physical Chemistry in Water, Steam and Hydrothermal Solutions.*, D. Palmer, R. Fernandez-Prini, and A. Harvey, Eds. 2004, pp. 493–595.

[39] B. Cox, “ZIRAT-6 SPECIAL TOPICS REPORT Water Chemistry and Crud Influence on Cladding Corrosion,” 2001.

[40] R. A. Castelli, “Chapter 3: Building Block Fluxes for the General Equation Set,” in *Nuclear Corrosion Modeling: The nature of CRUD*, Elsevier Inc., 2009, pp. 43–63.

[41] S. Glasstone, *Thermodynamics for chemists*. New York: Van Nostrand Reinhold, 1947.

[42] C. J. O’Brien, Z. Rak, E. Bucholz, and D. Brenner, “First Principles Calculations Predict Stable 50 nm Nickel Ferrite Particles in PWR Coolant,” *J. Nucl. Mater.*, vol. 454, no. 1–3, pp. 77–80, 2014.

[43] EPRI, “Evaluation of fuel clad corrosion product deposits and circulating corrosion products in pressurized water reactors,” 2004.

[44] M. Vepsäläinen and T. Saario, “Magnetite dissolution and deposition in NPP secondary circuit (VTT Report),” 2010.

[45] Y. L. Sandler, “Structure of PWR Primary Corrosion Products,” *Corrosion*, vol. 35, no. 5, pp. 205–208, 1979.

[46] J. A. Sawicki, “Analyses of crud deposits on fuel rods in PWRs using Mossbauer spectroscopy,” *J. Nucl. Mater.*, vol. 402, no. 2–3, pp. 124–129, 2010.

[47] J. Henshaw, J. C. McGurk, H. E. Sims, A. Tuson, S. Dickinson, and J. Deshon, “A model of chemistry and thermal hydraulics in PWR fuel crud deposits,” *J. Nucl. Mater.*, vol. 353, no. 1–2, pp. 1–11, Jul. 2006.

[48] M. L. Calvar, J. L. Bretelle, J. P. Cailleaux, R. Lacroix, M. Guivarch, N. Gay, S. Taunier, F. Gressier, P. Varry, G. Corredera, and M. Dijoux, “Effect of Water Chemistry on Deposition for PWR Plant Operation,” *Nucl. Plant Chem.*, 2012.

[49] J. Mcgrady, “The Effect of Water Chemistry on Corrosion Product Build-Up under PWR Primary Coolant Conditions,” [EngD thesis]: Manchester (UK); University of Manchester, 2016.

[50] F. Scenini, G. Palumbo, N. Stevens, A. Cook, and A. Banks, “Investigation of the role of electrokinetic effects in corrosion deposit formation,” *Corros. Sci.*, vol. 87, pp. 71–79, 2014.

[51] M. Guillodo, P. Combrade, T. Muller, G. Berthollon, N. Engler, C. Brun, and G. Turluer, “Formation of Deposits in HT Water under High Velocity Conditions : a Parametric Study,” in *Water Chemistry of Nuclear Reactor Systems*, 2004, pp. 1941–1949.

[52] C. Brun, N. Engler, G. Berthollon, T. Muller, B. Sala, P. Combrade, and G. Turluer,

"Investigation on the relation between pressure drops and fluid chemical treatment," 2002.

[53] D. J. Morris and I. S. Woolsey, "Studies of Oxide Deposition in Boiler Flow Control Orifices," in *Water Chemistry of Nuclear Reactor Systems 7*, 1996, pp. 243–246.

[54] C. Wohlberg and F. W. Kleimola, "Factors which Affect Formation and Depostion of Transport Corrosion Products in High-temperature Recirculating Water Loops," Argonne National Laboratory, USA, report no. ANL 5195, 1953.

[55] C. Cosse, F. Jolivel, and M. Berger, "Enriched boric acid as an optimized neutron absorber in the PWR primary coolant," in *Nuclear Plant Chemistry Conference, Paris, France*, 2012.

[56] M. C. Song and K. J. Lee, "The evaluation of radioactive corrosion product at PWR as change of primary coolant chemistry for long-term fuel cycle," *Ann. Nucl. Energy*, vol. 30, no. 12, pp. 1231–1246, 2003.

[57] P. Rudling and S. Odar, "LCC-12 Special Topic Report on Effects of WC on Corrosion," 2016.

[58] Picone, "The in-pile test of chemical shim," 1963.

[59] BAPL (Bettis Atomic Power Laboratory), "Pressurized water reactor (PWR) project technical progress report for the period January 24, 1964 – April 23, 1964," 1964.

[60] J. Weisman and S. Bartnoff, "The Saxton chemical shim experiment," 1965.

[61] C. A. Bergmann, D. E. Durkosh, W. T. Lindsay, and J. Roesmer, "The Role of Coolant Chemistry in PWR Radiation-Field Buildup," 1985.

[62] J.-W. Yeon, I.-K. Choi, K.-K. Park, H.-M. Kwon, and K. Song, "Chemical analysis of fuel crud obtained from Korean nuclear power plants," *J. Nucl. Mater.*, vol. 404, no. 2, pp. 160–164, Sep. 2010.

[63] Y. L. Sandler and R. H. Kunig, "The Solubility of Nonstoichiometric Nickel Ferrite in High-Temperature Aqueous Solution," *Nucl. Sci. Eng.*, vol. 64, no. 4, pp. 866–874, 1977.

[64] Y. L. Sandler and R. H. Kunig, "The Solubility of Nickel Ferrite in Aqueous Boric Acid Solution," *Nucl. Sci. Eng.*, vol. 77, no. 2, pp. 211–218, 1981.

[65] R. H. Kunig and Y. L. Sandler, "The solubility of simulated PWR primary circuit corrosion products," 1986.

[66] S. M. Walker and E. W. Thornton, "Reanalysis of oxide solubility data," in *Water chemistry of nuclear reactor systems 5. V. 1*, 1989, pp. 89–95.

[67] K. Fruzzetti, S. Garcia, N. Lynch, and R. Reid, "BWR and PWR Chemistry Operating Experience

and Perspectives," 2014.

[68] C. Haas and D. Perkins, "Zinc injection update," *NE Magazine, Nuclear Engineering International*, 2011.

[69] H. Ocken, K. Fruzzetti, P. Frattini, and C. J. Wood, "Recent Developments in PWR Zinc Injection," in *Proceedings of Chemistry 2002: International conference on water chemistry in nuclear reactors systems - operation optimisation and new developments*, 2002, pp. 1–7.

[70] R. Reiss, S. Odar, J. Kysela, and F. Nordmann, "LCC-7 SPECIAL TOPIC REPORT PWR / VVER Primary Side Coolant Chemistry Volume I – Technical Basis and Recent Discussions PWR / VVER Primary Side," 2011.

[71] F. Nordmann, "LCC10. Key Emerging Issues and Recent Progress Related to Plant Chemistry / Corrosion in PWR / VVER / CANDU Reactors," 2014.

[72] J. Robertson, "The Mechanism of High Temperature Aqueous Corrosion of Steel," *Corros. Sci.*, vol. 29, no. 11, pp. 1275–1291, 1989.

[73] J. Robertson, "The Mechanism of High Temperature Aqueous Corrosion of Stainless Steels," *Corrosion*, vol. 32, no. 4, pp. 443–465, 1991.

[74] S. E. Ziemniak, a. R. Gaddipati, and P. C. Sander, "Immiscibility in the NiFe2O4–NiCr2O4 spinel binary," *J. Phys. Chem. Solids*, vol. 66, no. 6, pp. 1112–1121, Jun. 2005.

[75] S. E. Ziemniak and M. Hanson, "Corrosion behavior of NiCrFe Alloy 600 in high temperature, hydrogenated water," *Corros. Sci.*, vol. 48, no. 2, pp. 498–521, Feb. 2006.

[76] S. E. Ziemniak, M. Hanson, and P. C. Sander, "Electropolishing effects on corrosion behavior of 304 stainless steel in high temperature, hydrogenated water," *Corros. Sci.*, vol. 50, pp. 2465–2477, 2008.

[77] S. Cissé, L. Laffont, B. Tanguy, M.-C. Lafont, and E. Andrieu, "Effect of surface preparation on the corrosion of austenitic stainless steel 304L in high temperature steam and simulated PWR primary water," *Corros. Sci.*, vol. 56, pp. 209–216, Mar. 2012.

[78] S. Perrin, L. Marchetti, C. Duhamel, M. Sennour, and F. Jomard, "Influence of Irradiation on the Oxide Film Formed on 316 L Stainless Steel in PWR Primary Water," *Oxid. Met.*, vol. 80, no. 5–6, pp. 623–633, Feb. 2013.

[79] R. Soulas, M. Cheynet, E. Rauch, T. Neisius, L. Legras, C. Domain, and Y. Brechet, "TEM investigations of the oxide layers formed on a 316L alloy in simulated PWR environment," *J. Mater. Sci.*, vol. 48, pp. 2861–2871, 2013.

[80] M. Warzee, J. Hennaut, M. Maurice, C. Sonnen, J. Waty, and P. Berge, “Effect of Surface Treatment on the Corrosion of Stainless Steels in High-Temperature Water and Steam,” *J. Electrochem. Soc.*, vol. 112, no. 7, p. 670, 1965.

[81] D. H. Lister, R. D. Davidson, and E. Mcalpine, “The Mechanism and Kinetics of Corrosion Product Release from Stainless Steel in Lithiated, High Temperature Water,” *Corros. Sci.*, vol. 27, no. 2, pp. 113–140, 1987.

[82] M. D. A. C. Belo, M. Walls, N. E. Hakiki, J. Corset, E. Picquenard, G. Sagonb, and D. Noel, “Composition, Structure and Properties of the Oxide Films Formed on the Stainless Steel 316L in a Primary Type PWR Environment,” *Corros. Sci.*, vol. 40, no. 2, pp. 447–463, 1998.

[83] B. Stellwag, “The Mechanism of Oxide Film Formation on Austenitic Stainless Steels in High Temperature Water,” *Corros. Sci.*, vol. 40, no. 2/3, pp. 337–370, 1998.

[84] S. E. Ziemniak and M. Hanson, “Corrosion behavior of 304 stainless steel in high temperature, hydrogenated water,” *Corros. Sci.*, vol. 44, no. 10, pp. 2209–2230, Oct. 2002.

[85] S. E. Ziemniak and R. a. Castelli, “Immiscibility in the Fe3O4–FeCr2O4 spinel binary,” *J. Phys. Chem. Solids*, vol. 64, no. 11, pp. 2081–2091, Nov. 2003.

[86] S. E. Ziemniak and M. Hanson, “Corrosion behavior of NiCrMo Alloy 625 in high temperature, hydrogenated water,” *Corros. Sci.*, vol. 45, no. 7, pp. 1595–1618, 2003.

[87] T. Terachi, K. Fujii, and K. Arioka, “Microstructural Characterization of SCC Crack Tip and Oxide Film for SUS 316 Stainless Steel in Simulated PWR Primary Water at 320 °C,” *J. Nucl. Sci. Technol.*, vol. 42, no. 2, pp. 225–232, 2005.

[88] K. Dinov, K. Ishigure, C. Matsuura, and D. Hiroishi, “Solubility of magnetite in high temperature water and an approach to generalized solubility computations,” *J. Nucl. Mater.*, vol. 207, no. C, pp. 266–273, 1993.

[89] T. Tone, N. Suzuki, Y. Yoshizawa, K. Iida, K. Haraguchi, and K. Maeda, “Crud removal performance and application of developed ion exchange resins,” in *Water Chemistry of Nuclear Reactor Systems 7, Bournemouth, UK*, 1996, pp. 269–271.

[90] J. J. Morrison, “Corrosion, Transport, and Deposition in Pressurised Water Nuclear Reactor Primary Coolant Systems,” University of Birmingham, 2014.

[91] J. Mcgrady, F. Scenini, N. Stevens, N. Bryan, and A. Banks, “Characterisation of Particulate Material in PWR Primary Coolant,” in *Proceedings of Nuclear Plant Chemistry Conference*, 2014.

[92] E. C. Potter and G. M. W. Mann, “Oxidation of Mild Steel in High Temperature Aqueous Systems,” in *Proc. 1st Int. Congress on Metallic Corrosion*, 1962, pp. 417–426.

[93] J. Morrison, J. Hewett, C. Cooper, C. Ponton, B. Connolly, and A. Banks, “Corrosion and Deposition of Metal Oxides in the Primary Coolant System of PWR’s,” in *Nuclear Plant Chemistry Conference, Sapporo, Japan*, 2014.

[94] L. Tomlinson, “Mechanism of Corrosion of Carbon and Low Alloy Ferritic Steels by High Temperature Water,” *Corrosion*, vol. 37, no. 4, pp. 591–596, 1981.

[95] S. H. Smith and M. C. Bloom, “NRL Report 6887,” Washington, D.C., 1969.

[96] E. C. Potter and G. M. W. Mann, “The Fast Linear Growth of Magnetite on Mild Steel in High-Temperature Aqueous Conditions,” *Corrosion*, vol. 1, no. 1, pp. 26–35, 1965.

[97] N. B. Pilling and R. E. E. Bedworth, “The oxidation of metals at high temperatures,” *J. Inst. Met.*, vol. 29, pp. 529–582, 1923.

[98] V. Cremer, “The miscibility gap in the system FeCr2O4 - Fe3O4 - FeAl2O4 between 500 and 1000 °C,” *Neues Jahrb. für Mineral. - Abhandlungen (Journal Mineral. Geochemistry)*, vol. 111, pp. 184–205, 1969.

[99] H. S. C. O’Neill and A. Navrotsky, “Simple spinels: crystallographic parameters, cation radii, lattice energies, and cation distribution.,” *Am. Mineral.*, vol. 68, no. 1–2, pp. 181–194, 1983.

[100] H. S. C. O’Neill and A. Navrotsky, “Cation distributions and thermodynamic properties of binary spinel solid solutions,” *Am. Mineral.*, vol. 69, no. 7–8, pp. 733–753, 1984.

[101] G. C. Allen and J. A. Jutson, “Characterisation of manganese-chromium-iron spinel-type oxides,” *J. Nucl. Mater.*, vol. 160, pp. 34–47, 1988.

[102] S. E. Ziemniak, M. E. Jones, and K. E. S. Combs, “Solubility and Phase Behavior of Cr (III) Oxides in Alkaline Media at Elevated Temperatures,” *J. Solution Chem.*, vol. 27, no. 1, pp. 33–65, 1998.

[103] S. Dickinson, M. Bachet, R. Eaker, J. Henshaw, D. Hussey, C. Marks, and P. R. Tremaine, “Solubility of Chromium (III) Oxide and Metal Chromates: Development of Multieq Models,” in *Nuclear Plant Chemistry*, 2012, no. Iii.

[104] S. E. Ziemniak, P. a. Guilmette, R. a. Turcotte, and H. M. Tunison, “Oxidative dissolution of nickel metal in hydrogenated hydrothermal solutions,” *Corros. Sci.*, vol. 50, no. 2, pp. 449–462, Feb. 2008.

[105] L. Guinard, O. Kerrec, D. Noel, S. Gardey, and F. Coulet, “Influence of initial surface condition

on the release of nickel alloys in the primary circuit of PWRs," *Nucl. energy*, vol. 36, no. 1, pp. 19–27, 1997.

[106] T. Maekawa, M. Kagawa, and N. Nakajima, "Corrosion Behavior of Stainless Steels in High Temperature Water and Superheated Steam," *Trans. Japanese Inst. Met.*, vol. 9, pp. 130–136, 1968.

[107] P. W. G. Simpson and H. E. Evans, "Method for calculating the quantity of spalled oxide released from AGR fuel cladding," in *Nuclear Fuel Performance, Proceedings of the Conference.*, 1985, p. 265.

[108] K. Asami, K. Hashimoto, and S. Shimodaira, "An XPS study of the passivity of a series of iron-chromium alloys in sulphuric acid," *Corros. Sci.*, vol. 18, no. 2, pp. 151–160, 1978.

[109] C. Calinksi and H. H. Strehblow, "ISS Depth Profiles of the Passive Layer on Fe/Cr Alloys," *J. Electrochem. Soc.*, vol. 136, no. 5, p. 1328, 1989.

[110] G. Hultquist, M. Seo, T. Leitner, C. Leygraf, and N. Sato, "The dissolution behaviour of iron, chromium, molybdenum and copper from pure metals and from ferritic stainless steels," *Corros. Sci.*, vol. 27, no. 9, pp. 937–946, 1987.

[111] I. Olefjord, "The passive state of stainless steels," *Mater. Sci. Eng.*, vol. 42, no. C, pp. 161–171, 1980.

[112] A. E. Yaniv, "The Composition of Passive Films on Ferritic Stainless Steels," *J. Electrochem. Soc.*, vol. 124, no. 4, p. 490, 1977.

[113] I. Lambert, J. Montel, P. Beslu, and A. Lalet, "Thermodynamique de solubilisation de la magnetite en milieu basique," in *Thermodynamics of nuclear materials*, 1979, pp. 89–104.

[114] C. Bates, K. Garbett, K. Hinds, G. Lancaster, M. Mantell, and G. Renn, "Development of corrosion product behaviour and radiation fields at the Sizewell B PWR from 1995 to 2008," *VGB PowerTech*, vol. 88, no. 12, pp. 52–60, 2008.

[115] S. E. Ziemniak, "Metal Oxide Solubility Behavior in High Temperature Aqueous Solutions," *J. Solution Chem.*, vol. 21, no. 8, pp. 745–760, 1992.

[116] B. Beverskog and I. Puigdomenech, "Revised Pourbaix diagrams for iron at 25–300 C," *Corros. Sci.*, vol. 38, no. 12, pp. 2121–2135, 1996.

[117] B. Beverskog, "Revised Pourbaix diagrams for nickel at 25-300 C," *Corros. Sci.*, 1997.

[118] A. Ito, "Study on improvement in shutdown chemistry for radiation exposure reduction in nuclear plants," in *Water Chemistry of Nuclear Reactor Systems 7*, 1996, pp. 22–26.

[119] S. Dickinson, J. Henshaw, H. Sims E., and K. Garbett, “Some aspects of Ni behaviour in PWR primary coolant,” in *Proceedings of Water Chemistry of Nuclear Reactor Systems 8*, 2000, vol. 40, pp. 306–309.

[120] D. A. Bridle, K. R. Butter, P. Cake, G. C. W. Comley, and C. R. Mitchell, “The Nature and Behavior of Particulates in PWR Primary Coolant,” 1989.

[121] P. R. Tremaine and J. C. LeBlanc, “The solubility of magnetite and the hydrolysis and oxidation of Fe2+ in water to 300°C,” *J. Solution Chem.*, vol. 9, no. 6, pp. 415–442, 1980.

[122] G. Bohnsack, *The solubility of magentite in water and in aqueous solutions of acid and alkaline*. Essen: Vulkan-Verlag, 1987.

[123] D. A. Palmer, P. Bénézeth, and D. J. Wesolowski, “Aqueous high-temperature solubility studies. I. The solubility of boehmite as functions of ionic strength (to 5 molal, NaCl), temperature (100-290°C), and pH as determined by in situ measurements,” *Geochim. Cosmochim. Acta*, vol. 65, no. 13, pp. 2081–2095, 2001.

[124] S. N. Lvov and D. A. Palmer, “Electrochemical processes in high-temperature aqueous solutions,” in *Aqueous Systems at Elevated Temperatures and Pressures: Physical Chemistry in Water, Steam and Hydrothermal Solutions.*, D. A. Palmer, R. Fernandez-Prini, and A. H. Harvey, Eds. Elsevier Ltd, 2004.

[125] M. A. Styrikovich, O. I. Martynova, I. F. Kobyakov, V. L. Men’Shikova, and M. I. Reznikov, “The Solubility of Magnetite in Water at High Temperature, in a Reducing Medium,” *Therm. Eng.*, vol. 19, no. 9, pp. 127–130, 1972.

[126] Helz, “Hydrothermal Solubility of Magnetite,” The Pennsylvania State University, 1971.

[127] W. T. Holser and C. J. Schneer, “Hydrothermal magnetite,” *Bull. Geol. Soc. Am.*, vol. 72, no. 3, pp. 369–385, 1961.

[128] G. Kanert, G. Gray, and W. Baldwin, “The solubility of magnetite in basic solutions at elevated temperatures,” 1976.

[129] D. You, J. Lambert, and D. Feron, “Dissolution and solubility of cobalt and nickel ferrites in PWR primary conditions,” in *7th International Conference on Water Chemistry of Nuclear Reactor Systems, Bournemouth, UK*, 1996, pp. 486–488.

[130] A. Bellefleur, M. Bachet, P. Bénézeth, and J. Schott, “Solubility of Nickel Ferrite (NiFe2O4) from 100 to 200 ° C,” in *Proceedings of Nuclear Plant Chemistry Conference, Paris, France*, 2012.

[131] P. Wang, L. L. Wilson, D. J. Wesolowski, J. Rosenqvist, and A. Anderko, “Solution chemistry of Mo(III) and Mo(IV): Thermodynamic foundation for modeling localized corrosion,” *Corros. Sci.*, vol. 52, no. 5, pp. 1625–1634, 2010.

[132] Z. Minubayeva and T. M. Seward, “Molybdic acid ionisation under hydrothermal conditions to 300 °C,” *Geochim. Cosmochim. Acta*, vol. 74, no. 15, pp. 4365–4374, 2010.

[133] M. Sennour, L. Marchetti, F. Martin, S. Perrin, R. Molins, and M. Pijolat, “A detailed TEM and SEM study of Ni-base alloys oxide scales formed in primary conditions of pressurized water reactor,” *J. Nucl. Mater.*, vol. 402, no. 2–3, pp. 147–156, Jul. 2010.

[134] L. D. de Pierrefeu, “The dissolution behaviour of magnetite electrodes in high-temperature water,” University of New Brunswick, 2009.

[135] R. Riess, W. Ruhle, and S. Odar, “LCC6 STR. Radiochemistry in Nuclear Power Reactors (Light Water Reactors). Volume I.”

[136] D. Lister and S. Uchida, “Determining water chemistry conditions in nuclear reactor coolants,” *J. Nucl. Sci. Technol.*, vol. 52, no. 4, pp. 451–466, 2015.

[137] P. Srisukvatananan, D. H. Lister, C. Ng, R. Svoboda, and K. Daucik, “Corrosion Product Sampling in Power Plants under Water / Steam Cycle Conditions,” in *ICPWS XV*, 2008.

[138] P. Srisukvatananan, D. H. Lister, R. Svoboda, and K. Daucik, “Assessment of the State of the Art of Sampling of Corrosion Products from Water/Steam Cycles,” *Power Plant Chem.*, vol. 9, no. 10, pp. 613–626, 2007.

[139] C. Degueldre, H. Wedda-Nobbenhuis, and E. Schenker, “Investigation of the colloid characteristics in the water of boiling water reactors,” in *Water Chemistry of Nuclear Reactor Systems 7*, 1996, pp. 112–119.

[140] K. Khumsa-Ang and D. Lister, “Initial Oxide Particle Deposition Under Low-Temperature Cooling Water Conditions: Experiments Under Subcooled Boiling at High pH,” *Heat Transf. Eng.*, vol. 34, no. 8–9, pp. 702–711, 2013.

[141] “Extractables | Life Science Research | Merck Millipore,” 2016. [Online]. Available: https://www.merckmillipore.com/GB/en/life-science-research/chromatography-sample-preparation/membrane-learning-center/Extractables/AI2b.qB._ToAAAFMvv988eJ0,nav. [Accessed: 30-Sep-2016].

[142] “MF-Millipore (TM) Membrane Filters - Sample Preparation,” 2016. [Online]. Available: http://www.merckmillipore.com/GB/en/product/MF-Millipore™-Membrane-Filters,MM_NF-

C152. [Accessed: 30-Sep-2016].

[143] ASTM, “Standard Practice for Handling of High Purity Water Samples 1,” pp. 11–13, 2014.

[144] “Terumo 3 part syringes.” [Online]. Available: http://dencor.ziltsysteem.nl/customers/dencor.ziltsysteem.nl/documents/syringes_3_part.pdf. [Accessed: 01-Jun-2017].

[145] “Standard specification for reagent water. D1193 - 06,” *ASTM International*. 2011.

[146] “Elix (R) Essential Water Purification System - Elix (R),” 2016. [Online]. Available: https://www.merckmillipore.com/GB/en/product/Elix-Essential-Water-Purification-System,MM_NF-C105153. [Accessed: 30-Sep-2016].

[147] “Milli-Q (R) Integral Water Purification System - Type 1 (Ultrapure) Water Purification System.” [Online]. Available: http://www.merckmillipore.com/GB/en/product/Milli-Q-Integral-Water-Purification-System,MM_NF-C72876. [Accessed: 30-Sep-2016].

[148] K. Lew, *Acids and Bases*. Infobase Publishing, 2009.

[149] P. Tremaine, K. Zhang, P. Benezeth, and C. Xiao, “Ionization equilibria of acids and bases under hydrothermal conditions,” in *Aqueous Systems at Elevated Temperatures and Pressures: Physical Chemistry in Water, Steam and Hydrothermal Solutions*, D. A. Palmer, R. Fernández-Prini, and A. H. Harvey, Eds. Elsevier Ltd, 2008.

[150] A. Hermann, N. W. Ashcroft, R. Hoffmann, A. Hermann, N. W. Ashcroft, and R. Hoffmann, “Lithium hydroxide, LiOH, at elevated densities,” *J. Chem. Phys.*, vol. 141, no. 2, 2014.

[151] R. Pawlowicz, “Calculating the conductivity of natural waters,” *Limnol. Oceanogr. Methods*, vol. 6, pp. 489–501, 2008.

[152] N. N. Greenwood and A. Earnshaw, *Chemistry of the Elements (2nd ed.)*. Butterworth-Heinemann, 1997.

[153] Agilent Technologies Inc, “Agilent 7500 Series ICP-MS Hardware Manual.” 2008.

[154] “Product Specifications: Thermo Scientific ProLab Bechtop Mass Spectrometer.” Thermo Scientific, 2010.

[155] R. Fernández-Prini, J. L. Alvarez, and A. H. Harvey, “Henry’s constants and vapor-liquid distribution constants for gaseous solutes in H2O and D2O at high temperatures,” *J. Phys. Chem. Ref. Data*, vol. 32, no. 2, pp. 903–916, 2003.

[156] Gilson, “WTi-type Piston Pump Heads User’s Guide.” 2003.

[157] Gilson, “305 Pump. User’s Guide.” 2003.

[158] Gilson, “805, 806, 807 Manometric Modules User’s Guide.” 2001.

[159] M. Barale, “Study of colloidal particle behaviour in PWR primary circuit conditions (in French),” PhD thesis, Chimie ParisTech, 2007.

[160] K. Ishigure, N. Fujita, T. Tamura, and K. Oshima, “Effect of gamma-radiation on the release of corrosion products from carbon-steel and stainless-steel in high-temperature water,” *Nucl. Technol.*, vol. 50, no. 1, pp. 169–177, 1980.

[161] G. C. W. Comley, D. A. Bridle, K. R. Butter, K. DeRanter, and R. Roofthooft, “Nature and behaviour of particulates in PWR coolants,” in *Water chemistry of nuclear reactor systems 5. V. 1*, 1989, pp. 297–300.

[162] G. M. W. Mann and P. W. Teare, “The oxidation of iron-chromium alloys in ferrous chloride solution at 300C.,” *Corros. Sci.*, vol. 12, no. September 1971, pp. 361–369, 1972.

[163] D. J. Wesolowski, S. E. Ziemniak, L. M. Anovitz, M. L. Machesky, P. Bénézeth, and D. A. Palmer, *Chapter 14 - Solubility and surface adsorption characteristics of metal oxides*. Elsevier, 2004.

[164] R. Soulas, M. Cheynet, E. Rauch, T. Neisius, L. Legras, C. Domain, and Y. Brechet, “TEM investigations of the oxide layers formed on a 316L alloy in simulated PWR environment,” *J. Mater. Sci.*, vol. 48, no. 7, pp. 2861–2871, Nov. 2012.

[165] R. Soulas, M. Cheynet, E. Rauch, T. Neisius, L. Legras, C. Domain, and Y. Brechet, “TEM investigations of the oxide layers formed on a 316L alloy in simulated PWR environment,” *J. Mater. Sci.*, vol. 48, no. 7, pp. 2861–2871, 2013.

[166] R. Dieckmann, “Defects and cation diffusion in magnetite (iii) tracer diffusion of foreign tracer cations as a function of temperature and oxygen potential,” *Berichte der Bunsengesellschaft für Phys. Chemie*, vol. 82, no. 8, pp. 778–783, 1978.

[167] R. Dieckmann, “Point defects and transport properties of binary and ternary oxides,” *Solid State Ionics*, vol. 12, pp. 1–12, 1984.

[168] “Geology.com - Geoscience News and Information.” [Online]. Available: https://geology.com/minerals/. [Accessed: 13-Jul-2018].

[169] C. F. Baes and R. F. Mesmer, “The thermodynamics of cation hydrolysis.,” *American Journal of Science*, vol. 281, no. 7. pp. 935–962, 1981.

[170] D. P. Fernández, A. R. H. Goodwin, E. W. Lemmon, J. M. H. Levelt Sengers, and R. C. Williams,

"A Formulation for the Static Permittivity of Water and Steam at Temperatures from 238 K to 873 K at Pressures up to 1200 MPa, Including Derivatives and Debye–Hückel Coefficients," *J. Phys. Chem. Ref. Data*, vol. 26, no. 4, p. 1125, 1997.

[171] I. Persson, "Hydrated metal ions in aqueous solution: How regular are their structures?," *Pure Appl. Chem.*, vol. 82, no. 10, pp. 1901–1917, 2010.

[172] J. Kielland, "Individual Activity Coefficients of Ions in Aqueous Solution," *J. Am. Chem. Soc.*, vol. 59, no. 3, pp. 1675–1678, 1937.

[173] J. R. Cooper and R. B. Dooley, "Revised Release on the IAPWS Industrial Formulation 1997 for the Thermodynamic Properties of Water and Steam," Lucerne, Switzerland: The International Association for the Properties of Water and Steam, 2007.

[174] D. W. Brenner, S. Lu, C. J. O'Brien, E. W. Bucholz, and Z. Rak, "A particle assembly/constrained expansion (PACE) model for the formation and structure of porous metal oxide deposits on nuclear fuel rods in pressurized light water reactors," *J. Nucl. Mater.*, vol. 457, pp. 209–212, 2015.

[175] M. L. Machesky, D. J. Wesolowski, D. A. Palmer, and K. Ichiro-Hayashi, "Potentiometric Titrations of Rutile Suspensions to 250 °C," *J. Colloid Interface Sci.*, vol. 200, no. 2, pp. 298–309, 1998.

[176] D. J. Wesolowski, M. L. Machesky, D. A. Palmer, and L. M. Anovitz, "Magnetite surface charge studies to 290 °C from in situ pH titrations," *Chem. Geol.*, vol. 167, no. 1–2, pp. 193–229, 2000.

[177] M. L. Machesky, D. J. Wesolowski, D. a. Palmer, and M. K. Ridley, "On the Temperature Dependence of Intrinsic Surface Protonation Equilibrium Constants: An Extension of the Revised MUSIC Model.," *J. Colloid Interface Sci.*, vol. 239, no. 2, pp. 314–327, 2001.

[178] D. A. Kulik, "Thermodynamic properties of surface species at the mineral-water interface under hydrothermal conditions: A gibbs energy minimization single-site 2pK(A) triple-layer model of rutile in NaCl electrolyte to 250??C," *Geochim. Cosmochim. Acta*, vol. 64, no. 18, pp. 3161–3179, 2000.

[179] M. A. A. Schoonen, "Calculation of the point of zero charge of metal oxides between 0 and 350 °C," *Geochim. Cosmochim. Acta*, vol. 58, no. 13, pp. 2845–2851, 1994.

[180] Y. G. Berube and P. L. Debruyn, "Adsorption at Rutile-Solution Interface .I. Thermodynamic and Experimental Study," *J. Colloid Interface Sci.*, vol. 27, no. 2, p. 305-, 1968.

[181] L. G. J. Fokkink, A. De Keizer, and J. Lyklema, “Temperature Dependence of the Electrical Double Layer on Oxides. Rutile and Hematite,” *J. Colloid Interface Sci.*, vol. 127, no. 1, pp. 116–131, 1989.

[182] D. A. Sverjensky and N. Sahai, “Theoretical prediction of single-site enthalpies of surface protonation for oxides and silicates in water,” *Geochim. Cosmochim. Acta*, vol. 62, no. 23–24, pp. 3703–3716, 1998.

[183] M. K. Ridley, M. L. Machesky, D. J. Wesolowski, and D. A. Palmer, “Calcium adsorption at the rutile-water interface: A potentiometric study in NaCl media to 250 degrees C,” *Geochim. Cosmochim. Acta*, vol. 63, no. 19–20, pp. 3087–3096, 1999.

[184] B. Beverskog and I. Puigdomenech, “Pourbaix diagrams for the ternary system of iron-chromium-nickel,” *Corrosion*, vol. 55, no. 11, pp. 1077–1087, 1999.

[185] S. Ziemniak, A. R. Gaddipati, and P. C. Sander, “Immiscibility in the NiFe2O4–NiCr2O4 Spinel Binary,” 2004.

[186] R. Robie and B. S. Hemingway, “Thermodynamic Properties of Minerals and Related Substances at 298.15 K and 1 Bar (10^5 Pascals) Pressure and at Higher Temperatures,” *U.S. Geol. Surv. Bull.*, no. 2131, 1995.

[187] D. A. Palmer, P. Bénézeth, C. Xiao, D. J. Wesolowski, and L. M. Anovitz, “Solubility measurements of crystalline NiO in aqueous solution as a function of temperature and pH,” *J. Solution Chem.*, vol. 40, no. 4, pp. 680–702, 2011.

[188] S. E. Ziemniak and M. a. Goyette, “Nickel(II) Oxide Solubility and Phase Stability in High Temperature Aqueous Solutions,” *J. Solution Chem.*, vol. 33, no. 9, pp. 1135–1159, Sep. 2004.

[189] “Impact of Nickel Oxide Solubility on PWR Fuel Deposit Chemistry,” EPRI, Palo Alto, CA and U.S. Department of Energy, Washington D.C.: 2002. 1003155, 2002.

[190] “Behavior of Nickel / Nickel Oxide in PWR Environments,” EPRI, Palo Alto, CA: 2001. 1001397, 2001.

[191] B. J. Thamer, R. M. Douglass, and E. Staritzky, “The Thermal Decomposition of Aqueous Chromic Acid and Some Properties of the Resulting Solid Phases,” *J. Am. Chem. Soc.*, vol. 79, no. 3, pp. 547–550, 1957.

[192] A. Stefánsson and T. M. Seward, “A spectrophotometric study of iron(III) hydrolysis in aqueous solutions to 200 °C,” *Chem. Geol.*, vol. 249, no. 1–2, pp. 227–235, 2008.

[193] “Personal communication from Stephen Baker, the ICP-MS operator.” .

[194] P. A. Nikolaychuk and A. G. Tyurin, “The Revised Pourbaix Diagram for Molybdenum,” *Butlerov Commun.*, vol. 24, no. 2, pp. 101–105, 2011.

[195] X. Cao, “Solubility of molybdenite and the transport of molybdenum in hydrothermal solutions,” 1989.

[196] A. V. Kudrin and V. I. Rekharsky, “Experimental-Study of Solubility of Tugarinovite MoO2 in Aqueous-Solutions at 250-degrees-C and 450-degrees-C,” *Geokhimiya*, vol. 12, pp. 1825–1834, 1980.

[197] A. V. Kudrin, “Experimental-Study of Solubility of Tugarinovite MoO2 in Aqueous-Solutions at High-Temperatures,” *Geokhimiya*, vol. 6, pp. 870–883, 1985.

[198] J. E. Post, “Manganese oxide minerals: Crystal structures and economic and environmental significance,” *Proc. Natl. Acad. Sci.*, vol. 96, no. 7, pp. 3447–3454, 1999.

[199] H. J. van Hook and M. L. Keith, “The system Fe3O4-Mn3O4,” *Americ. Miner.*, vol. 43, no. 56, pp. 69–83, 1958.

[200] F. Carrette, “Relâchement des produits de corrosion des tubes en alliage 690 de générateur de vapeur du circuit primaire des réacteurs à eau pressurisée,” (PhD thesis, in French), Polytechnic National Institute of Toulouse, 2002.

[201] T. O. Passell and C. L. Perry, “Upstream Diffusion in Hagen-Poiseuille Flow,” *Phys. Fluids*, vol. 4, no. 4, p. 444, 1961.

[202] W. M. Haynes, Ed., *CRC Handbook of Chemistry and Physics*, 97th editi. Boca Raton, FL, USA: Taylor and Francis Group, LLC, 2017.

[203] B. Jähne, G. Heinz, and W. Dietrich, “Measurement of the diffusion coefficients of sparingly soluble gases in water,” *J. Geophys. Res. Ocean.*, vol. 92, no. C10, pp. 10767–10776, 1987.

[204] H. SATO, M. YUI, and H. YOSHIKAWA, “Ionic Diffusion Coefficients of Cs + , Pb 2+ , Sm 3+ , Ni 2+ , SeO 2- 4 and TcO − 4 in Free Water Determined from Conductivity Measurements,” *J. Nucl. Sci. Technol.*, vol. 33, no. 12, pp. 950–955, 1996.

[205] D. T. Kallikragas, A. Y. Plugatyr, and I. M. Svishchev, “High Temperature Diffusion Coefficients for O 2 , H 2 , and OH in Water, and for Pure Water,” *J. Chem. Eng. Data*, vol. 59, no. 6, pp. 1964–1969, 2014.

14. Appendix 1:

Literature Review and theory: Solubility of metal oxides in PWR primary coolant

14.1. Overview

In order to understand and accurately model the interactions between structural materials and coolant in nuclear reactors, it is essential to have accurate quantitative knowledge of the solubility behaviour of the oxides which form on those structural materials. This entails not only the total dissolved concentrations at equilibrium for a given set of coolant conditions, but also the manner in which these quantities change with varying parameters such as temperature and pH; and the kinetics of dissolution or precipitation when not at equilibrium.

By combining experimental solubility data – taken across a comprehensive range of values for the parameters of interest such as T and pH – with known thermochemical data, the values for further thermodynamic quantities can be extracted. These can be used to independently predict the concentrations of each soluble species of interest (such as Fe^{2+}, $Fe(OH)^{+}$, $Fe(OH)_2$ (aq), etc.) under any given set of conditions, which are summed to provide a theoretical prediction of solubility. This information is not simply built up from tabulated data of total dissolved levels of metallic elements, but the best use is made of thermodynamic theory and whatever thermochemical data and relations are available in order to interpolate and extrapolate numerically to any set of conditions.

Additional complexities arise when considering the presence of mixed, non-stoichiometric oxides, and the effect of having crystals which have elevated Gibbs energy compared with the most stable form, in terms of crystallinity and size, and also in other ways ([37], [38]), – all of these effects are present in the inherently non-equilibrium situation of corroding materials in nuclear plant.

The typical apparatus used for modern studies involves a bed of oxide granules, over which simulated coolant is passed, and the effluent analysed for content of the relevant metallic elements [115]. Earlier studies, such as those of Styrikovich et al. [125] used autoclaves. For some very

sparingly soluble oxides, solubility can reach a minimum in the sub part per billion range, this can cause difficulties in accurately measuring the solubility, especially in the case of magnetite where the presence of suspended or colloidal particulate matter has proved very difficult to avoid [121]. Sweeton and Baes [4] built on the work of many prior researchers in their careful study, which was one of the first and most comprehensive studies to use a once through flowing system. A review of such previous studies as they relate to magnetite solubility has been written by Bohnsack [122].

14.1.1. Explanation of chapter subsections

In this chapter, an overview of theory relating to metal oxide solubility is presented, with particular reference to magnetite. A brief discussion is made of the evolution of the current state of knowledge with the most recent few studies. The literature on solubility of other relevant stoichiometric oxides is then reviewed: namely nickel / nickel (II) oxide; nickel ferrite; pure chromium (III) oxides (chromia, CrOOH, $Cr(OH)_3$); ferrous chromite; and nickel chromite. Finally, the effects of non-stoichiometric and non-equilibrium (meta-stable) oxides are discussed.

14.2. Theory of Metal Oxide Solubility

The solubility of a metal oxide in a solvent is simply the total concentration of the metal in solution in that solvent, when it is at equilibrium with the solid oxide phase. It is generally made up of contributions from several soluble species.

A dynamic equilibrium is established, in which metal and oxide ions – along with hydroxide ions in the case of hydroxides and oxy-hydroxides – are solvated and released from the crystalline phase to solution, at the same rate at which species from solution precipitate onto the crystalline (metal oxide) phase. Regardless of which particular soluble species are the most active participants in this exchange, an equilibrium is rapidly attained between *all* the possible species in solution via reactions such as the deprotonation reaction in water,

$$M(OH)_n^{(z-n)+} + H_2O \rightleftharpoons M(OH)_{n+1}^{(z-(n+1))+} + H^+ \qquad (1);$$

via redox reactions,

$$M(OH)_n^{(z_1-n)+} + \frac{1}{2}H_2 \rightleftharpoons M(OH)_n^{(z_2-n)+} + H^+ \quad ; \quad z_2 = z_1 - 1 \qquad (2);$$

and via complexation with other chemicals in the water, where present. This is illustrated schematically in Figure 14.1 for magnetite and the scheme of six ferrous and ferric ions to which Tremaine and LeBlanc [121] fitted their solubility data.

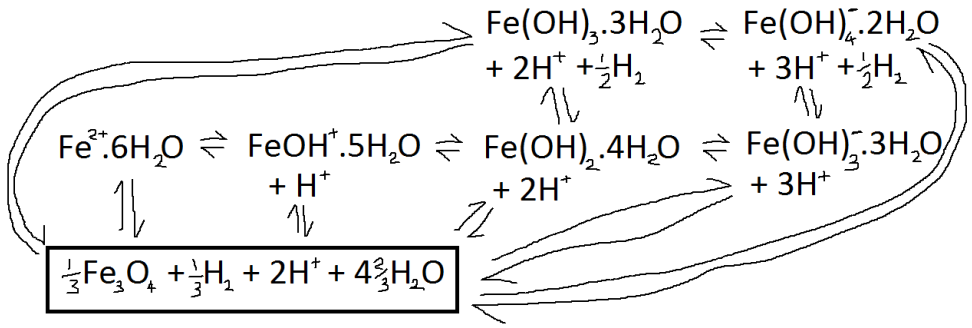

Figure 14.1. A schematic illustration of the multiple equilibria that exist, connecting a solid phase with all the soluble species in a solvent – in this case, magnetite with the scheme of six ferrous and ferric species to which Tremaine and LeBlanc [121] *fitted their data on solubility in hydrothermal solutions.*
Some equilibrium symbols have been included to illustrate that equilibria can be defined linking any *two species*.

In Figure 14.1 the co-ordination water molecules of the first solvation shell have been included for clarity, for example $Fe^{2+}.6H_2O$, where ordinarily the short-hand form, $Fe^{2+}(aq)$, is used.

It is not a simple matter to determine which species are most important in the mechanisms of dissolution and precipitation. This is covered in more detail in Bohnsack [122]. In terms of thermodynamics however, it is irrelevant: since all species in solution are in equilibrium with each other, the oxide phase is in equilibrium with each of them also.

14.2.1. Characterising multiple equilibrium reactions

It is not necessary to describe each equilibrium independently. Instead, a minimum spanning set of equilibria can be chosen in a logical manner according to preference, and any other equilibria can be constructed from combinations of these. A common convention is to define the dissolution / precipitation reaction as that between the oxide (or oxy-hydroxide) and the unhydrolysed solvated metal cation, with one mole of metal per mole of reaction, and balanced by water and hydronium ions:

$$\frac{1}{i}M_iO_{iz/2}\,(cr.)\;+\;z\,H^+ \rightleftharpoons M^{z+}\;+\;H_2O \qquad (3);$$

Step-wise hydrolysis reactions are then defined, in the manner of eq. (1), as well as other reactions such as redox reactions and complexation with other species. Other similar conventions may be used, such as equilibria between the bare metal cation and each progressively more hydrolysed species, rather than step-wise hydrolysis reactions; or a dissolution reaction between the oxide and a neutral hydrolysed species, rather than eq. (3).

Choosing a spanning set in this way – with just one equilibrium involving the solid phase – takes advantage of the fact that the same equilibria apply between soluble species regardless of which oxide phase is present, or indeed whether any oxide phase is present. These purely aqueous-phase equilibria only give relative activities, of one species compared with another: absolute activities (and from these, the solubility) are fixed by the aforementioned equilibrium with the oxide phase, where one is present; otherwise they are unconstrained, or constrained only by total dissolved concentration of metal.

A convention used in many solubility studies is to define multiple dissolution reactions for a particular oxide – one for each soluble species.

Equilibrium constants

Equilibria are characterised by their equilibrium constants, which are defined for a generic reaction, $aA + bB \rightleftharpoons cC + dD$, as

$$K_{eq} = \{C\}^c.\{D\}^d.\{A\}^{-a}.\{B\}^{-b} \qquad (4),$$

where K_{eq} is a function of T only, and curved brackets denote thermodynamic activity. Having knowledge of K_{eq} at a particular temperature means that the activity of any particular species, say D in equation (4) above, can be uniquely described in terms of activities of the other species involved in the reaction, whatever their values may be:

$$\{D\} = \left[K_{eq}.\{A\}^a.\{B\}^b.\{C\}^{-c}\right]^{1/d} \qquad (5).$$

Using the relations below,

$$\Delta G^0 = -RT \ln K_{eq} \quad (6a); \qquad \text{and} \qquad \Delta G = \Delta H - T\Delta S \quad (6b),$$

values for each K_{eq} can be related to thermodynamic data. In this way, by making appropriate assumptions and simplifications, values of K_{eq} can be extrapolated to different temperatures from those at which measurements were made. Equally, the manner in which experimentally determined K_{eq} – and thus ΔG^0 – values change with temperature in solubility studies is an important method by which thermodynamic data can be determined. More on this later in section on temperature dependence.

Whilst K_{eq} is a generic term to describe equilibrium constants, various conventions – sometimes conflicting – are adopted in the literature for the naming of specific equilibrium constants.

Table 14.1 summarises some of these conventions.

Baes and Mesmer [169] conducted a review of all thermodynamic data available at the time on cation hydrolysis reactions, and drew some interesting generalisations and conclusions which are applicable across the whole range of soluble cations. For example, they found that the equilibrium constant for the first hydrolysis step at 25 °C, which is also the concentration of hydronium ions below which the bare cation is no longer dominant compared with the first hydrolysed species, can be related to the oxidation state and size of the solvated bare cation, as well as a parameter which relates to the 'softness' (susceptibility) of the cation to hydrolysis:

$$\log K_{11} = A + 11.0\ (z/d) \qquad (7),$$

where z is the valence of the cation; d is the bond length between the cation and oxygen centres of the first solvation shell of water molecules; and A is a parameter representing 'hardness' to hydrolysis. Elements from similar regions of the periodic table tend to have similar values of A for their soluble cations. They also found that the enthalpy change of the first hydrolysis step was always positive, and usually near the value of enthalpy for dissociation of water. These two findings make intuitive sense, since the energy (enthalpy) required to split water molecules is relatively great, and dominates the overall entropy of the reaction; and the strong electric field in the vicinity of the cation (especially for large z/d) can be expected to reduce slightly the energy required to eject a proton from solvation shell water molecules.

Table 14.1. Notation for equilibrium constants.
Where the solid phase is involved, equilibrium constants have the form "K_sny", where s denotes 'solubility', 'n' describes whether the soluble species is polynuclear (n ≠ 1), or mononuclear (n = 1) – polynuclear species being those with two or more metallic cations being complexed together in one entity; and y denotes the number of OH^- ions in the soluble species. Where the equilibrium is between two soluble species, equilibrium constants have the form "K_(n,y)", where the reactant is the bare metallic cation and n and y have the same meanings as above

Equilibrium constant	**Symbol used for reaction**	
	B & M [169]	This thesis
Dissolution to bare cation: $\boldsymbol{M(OH)_z(cr.) + zH^+ \rightleftharpoons M^{z+} + zH_2O}$	K_{s10}	K_{s10}
First hydrolysis step $\boldsymbol{M^{z+} + H_2O \rightleftharpoons M(OH)^{(z-1)+} + H^+}$	K_{11}	K_{11}
(y+1)st hydrolysis step: $\boldsymbol{M(OH)_y^{(z-y)+} + H_2O \rightleftharpoons M(OH)_{y+1}^{(z-y-1)+} + H^+}$	$K_{1,y+1}/K_{1,y}$	$K_{1,y+1}/K_{1,y}$
y cumulative hydrolysis steps from bare cation $\boldsymbol{M^{z+} + yH_2O \rightleftharpoons M(OH)_y{}^{(z-y)+} + yH^+}$	$K_{1,y}$	$K_{1,y}$
Dissolution directly to y-times hydrolysed cation $\boldsymbol{M(OH)_z(cr.) + (z-y)H^+ \rightleftharpoons M(OH)_y{}^{(z-y)+} + (z-y)H_2O}$	K_{s1y}	K_{s1y} $K_{z,l}^{phase}$

14.2.2. Effects of key parameters on solubility, at fixed temperature

In order to illustrate the effects of various parameters on solubility, consider the equilibrium of a dissolution/precipitation reaction between a generic oxide, M_iO_j, and a generic solvated and hydrolysed soluble species, $M_k(OH)_l^{(kz-l)+}$, where M represents a metal, subscripts *i*, *j*, *k*, *l* represent composition of the respective species, and have non-negative integer values (also, non-zero for *i* and *k*), and *z* represents the oxidation state of M in the soluble species. The equilibrium equation can be written, with one mole of M per mole of reaction, as follows:

$$\frac{1}{i}.M_iO_j + \frac{1}{k}\left(l - \frac{jk}{i}\right).H_2O = -\frac{1}{k}(kz-l).H^+ + \left(z - \frac{2j}{i}\right).\frac{1}{2}.H_2 + \frac{1}{k}M_k(OH)_l^{(kz-l)+} \quad (8)$$

If one neglects the possibility of polynuclear species (since they do not feature for any of the sparingly soluble metal oxides under consideration in thus study), *k* becomes 1 and is dropped from the equations; the equilibrium constant can then be written as:

$$K_{z,l}^{phase} = \{H^+\}^{l-z} \,.\, \{H_2\}^{\frac{1}{2}\left(z-\frac{2j}{i}\right)} \,.\, \left\{M(OH)_l^{(z-l)+}\right\} \quad (9),$$

where $K_{z,l}^{phase}$ is a function of T, and is specific to the oxide phase (M_iO_j) and aqueous species ($M(OH)_l^{(z-l)+}$) in question. Activity of the aqueous species can thus be written as:

$$\left\{M(OH)_l^{(z-l)+}\right\} = K_{z,l}^{phase} \,.\, \{H^+\}^{z-l} \,.\, \{H_2\}^{-\frac{1}{2}\left(z-\frac{2j}{i}\right)} \quad (10).$$

Or in terms of logs, as follows:

$$\log\left(\left\{M(OH)_l^{(z-l)+}\right\}\right) = \log\left(K_{z,l}^{phase}\right) - \,(z-l).pH \, - \frac{1}{2}\left(z-\frac{2j}{i}\right).\log(\{H_2\}) \quad (11).$$

Equation (11) can be modified slightly to find *concentration* of each aqueous species – and from this the solubility – where $\gamma_{(z-l)+}$ is the activity coefficient for a species with charge $(z-l)$:

$$\log\left(\left[M(OH)_l^{(z-l)+}\right]\right) = \log\left(K_{z,l}^{phase}\right) - \,(z-l).pH \, - \frac{1}{2}\left(z-\frac{2j}{i}\right).\log(\{H_2\}) \, - \log\left(\gamma_{(z-l)+}\right) \quad (12);$$

$$\text{solubility} = \sum_{z,l}\left[M(OH)_l^{(z-l)+}\right] \stackrel{\text{def}}{=} \sum_{z,l} c_{z,l} \quad (13)\,.$$

Using equation (12), the values of log $c_{a,l}$ (and thus also $c_{a,l}$, the equilibrium concentrations) can be determined at any given temperature, as long as pH_T, and $\{H_2\}$ are known for the solution as a whole, and $\gamma_{(z-l)+}$ and log K are known for each species. For dilute solutions, as used in most studies applicable to nuclear power, values of log γ tend to be close to zero

Effect of pH on solubility

Inspection of eq (12) shows that where other variables are held constant (T, $\{H_2\}$, ionic strength of solution), the concentration of each soluble species varies with pH as:

$$c_{z,l} = constant - (z - l).pH \quad (14).$$

Thus the most hydrolysed (most negatively charged) species tend to dominate at high pH, the least hydrolysed species at low pH, and species of neutral charge at intermediate pH. Figure 14.2 illustrates a typical scenario for the case of z=3, from Baes and Mesmer's observations (figure taken from [169]). Individual straight lines are shown for the various species, and the thick black line represents their sum (the solubility). Note that different values of the 'constant' term in equation (14), determined by values of log K and log $\{H_2\}$, mean that in actuality, for some cations, there may be aqueous species which never dominate at any pH, and others which dominate over a much greater pH range.

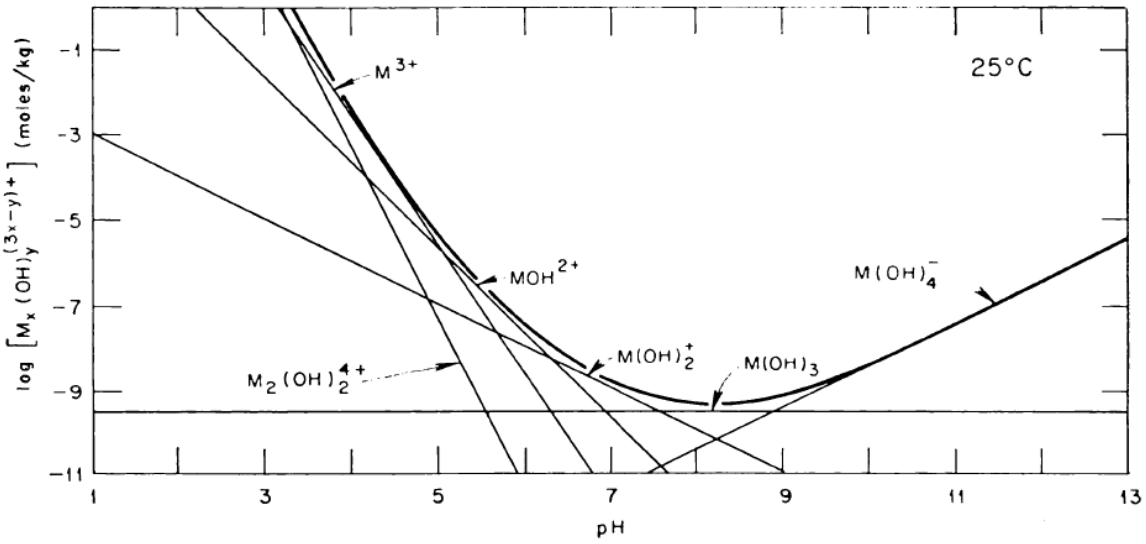

Figure 14.2. Distribution of hydrolysis products in solution at equilibrium with a hydroxide solid phase for a hypothetical trivalent cation. Taken from [169].
The heavy curve is the total concentration of M(III) in solution

In summary, solubility reaches a minimum at intermediate pH, where it is typically close to the equilibrium concentration of uncharged species, $M(OH)_z(aq)$. At higher or lower pH the solubility rises exponentially, due to the dominance of more- or less- hydrolysed species respectively. The pH of minimum solubility, and the exact form of the solubility versus pH plot, varies depending on the metal, oxidation state, and other parameters of the solution.

Effect of hydrogen activity on solubility

Inspection of eq (12) yields the following relationship regarding the effect of hydrogen, where other variables are held constant:

$$c_{z,l} = constant - \frac{1}{2}\left(z - \frac{2j}{i}\right).\log(\{H_2\}) \qquad (15).$$

The term $\left(z - \frac{2j}{i}\right)$ represents the change in oxidation state experienced by a metal cation, on entering solution as the species of interest (valence: z), from the oxide (valence: $\frac{2j}{i}$). Where there is no change in oxidation state, the term involving hydrogen drops out of equation (12), and therefore hydrogen activity has no effect. However, as long as other oxidation states of the metal ion are possible, there will always exist a hydrogen concentration at which dominance transitions to species in that other oxidation state, at least in principle. As will be discussed in later sections, at this aforementioned critical hydrogen activity the oxide in question may no longer be the stable solid phase, therefore in some cases the effect of other oxidation states may be neglected for a particular oxide.

Figure 14.3 shows the effects of these considerations schematically. Concentrations represented by straight lines are themselves the sum of all aqueous species of that oxidation state, and may be dominated by ions in a particular hydrolysis state depending on the pH (see Figure 14.2). Overall solubility is given by the thick curve, which represents the sum of contributions from the various oxidation states present.

In Figure 14.3 (a) is shown the situation for a metallic element for which the cations M^{n+}, $M^{(n+1)+}$, and $M^{(n-1)+}$ all have a hydrogen activity range at which they are stable, and for which the solubility-controlling phase has metal ions in the oxidation state n+. The scheme of species for which $z - \frac{2j}{i} = 0$ dominate across a wide range of $\{H_2\}$ values, resulting in there being no effect of $\{H_2\}$ across that range; but the exponential dependence of the other two species on $\log(\{H_2\})$ means they must eventually become dominant at high or low enough values of $\log(\{H_2\})$, respectively. This approximately describes the situation for hematite solubility, for n=3, though the species for which z = n + 1 (i.e. z=4) does not exist in nature for iron.

In Figure 14.3 (b) is shown the dependence of solubility on $\log(\{H_2\})$ for an oxide in which the average oxidation state of metal cations is not an integer. In this case soluble species either increase exponentially or decrease exponentially as $\log(\{H_2\})$ is increased/changed, therefore there is no range of $\{H_2\}$ across which $\log(\{H_2\})$ has no effect. This describes the situation for magnetite solubility, with ferric species dominating at low $\log(\{H_2\})$ and ferrous species dominating at high $\log(\{H_2\})$.

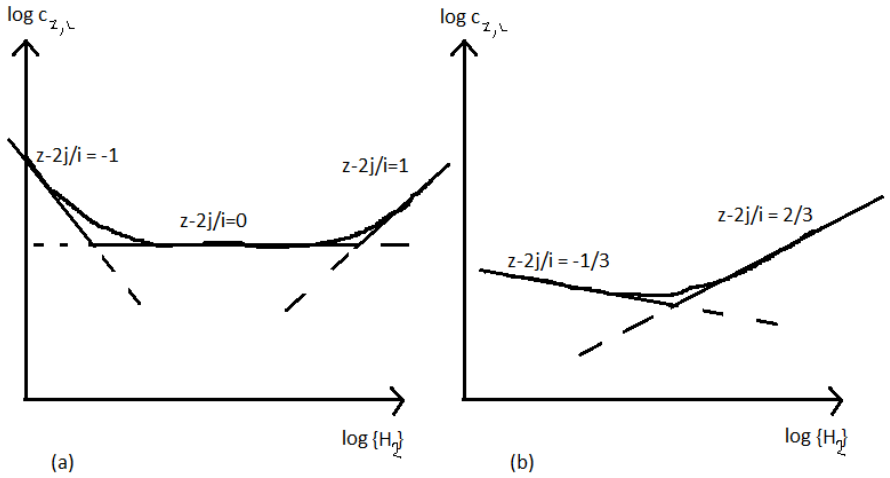

Figure 14.3. Effect of hydrogen activity on solubility, for (a) integer and (b) non-integer average oxidation state of the metal ion in oxide.

In either case, in summary there exists a critical activity – or in many cases a wide range of activities – of hydrogen, for which solubility is at a minimum with respect to hydrogen. At higher or lower values of $\log(\{H_2\})$, solubility increases exponentially.

Whenever metallic species exist in solution in more than one oxidation state, the straight black lines in Figure 14.2 would represent the sum of all species having that charge, rather than a single species (in analogy with the straight lines in Figure 14.3 representing the sum of all aqueous species having a particular oxidation state on the metal cation. In either case, the effect of the variable *not* featuring on the x-axis (that is, $\{H_2\}$ in the case of Figure 14.2, pH for Figure 14.3), manifests in the raising or lowering of the straight lines of the plot in question.

Effect of activity coefficients, $\gamma_{(z-l)+}$, on solubility

It may seem surprising to the uninitiated reader that activities of the various aqueous species are found to be dependent on the activities of key components of the solution in such a *simple* manner, but that is because this is the very way in which thermodynamic activity is defined. The real world complexity and non-linearity is tied up in the way concentrations vary, and how activity coefficients deviate from unity to reflect this.

At moderate to high ionic strength activity coefficients vary dramatically, in ways which must be experimentally measured. Nonetheless, various techniques have been developed over the years to approximate them from first principles, each valid in their own finite range of conditions. Thankfully, at the low ionic strength of primary coolant of PWRs, BWRs and CANDUs, and in the most directly relevant oxide solubility studies, activity coefficients can be assumed to be unity without introducing too much error and within error of most solubility studies.

Relationship between equilibrium constants and solubility behaviour, at fixed temperature

The remaining term in equation (12) to be discussed is $\log\left(K_{z,l}^{phase}\right)$, which expresses the effect of equilibrium constants on the activity of each species, and ultimately, on the solubility. As alluded to in preceding subsections, it is the magnitude of each $\log\left(K_{z,l}^{phase}\right)$ which determines the *precise form* (rather than a schematic illustration) of plots of log c versus pH (as per Figure 14.2) or versus log ($\{H_2\}$) (as per Figure 14.3). Where pH, log ($\{H_2\}$), and each log γ are set, or assumed, equal to zero, $K_{z,l}^{phase}$ gives the equilibrium concentration of each species directly. Therefore, for a plot of log c versus pH, where log ($\{H_2\}$) is fixed at zero, straight lines representing each aqueous species intercept the y-axis (i.e. pH = 0) at y = $\log\left(K_{z,l}^{phase}\right)$; and an analogous statement can be made about plots of log c versus log ($\{H_2\}$). As noted earlier, the values of these K_{eq}, and their relation one to another, have been observed to follow trends [169].

Combined effect of changing various parameters at fixed temperature – potential-pH plots

In order to plot the effects of several parameters simultaneously – namely $\log(\{H_2\})$ and pH – a three-dimensional plot could be constructed, with pH on the x-axis, $\log(\{H_2\})$ on the y-axis, and log c on the z-axis. Such plots can be difficult to represent in two dimensions however, and become cluttered.

A much more commonly used method is to label the regions of dominance of the various aqueous species on a plot of $\log(\{H_2\})$ (or equivalent quantity) against pH. In this way one can determine at a glance which species dominates in solution under a given set of conditions, and thus the approximate solubility dependence on key parameters of the solution – $\log(\{H_2\})$ and pH – under those conditions. By convention, the quantity 'reduction potential', or just 'potential', is used instead of $\log(\{H_2\})$, hence the term potential-pH plots. Potential is related to $\log(\{H_2\})$ in the following way.

$$\frac{1}{2}H_2 = H^+ + e^- \qquad (15)$$

Potential on the Standard Hydrogen Electrode (SHE) scale is defined to be zero, at pH = 0 and $\log(\{H_2\})$ = 0. For each unit increase in pH, there must be a 10-fold increase in activity of e^-s, which equates to a decrease in potential of … (to do with Faraday's number and stuff – Nernst equation?)

On the same set of axes can be plotted regions of dominance of the various oxides of a particular metal, in terms of the hydrogen activity (via its effect on potential). Information on the oxidation state of the metal in the prevailing oxide phase is necessary when determining the solubility behaviour of a particular aqueous species with respect to hydrogen activity (or potential), as discussed above.

In the context of corrosion, potential-pH plots are commonly produced depicting *only* the dominant aqueous species, when concentration in solution is above a threshold amount (say 10^{-6} M), and *only* the stable solid phase otherwise. In this way it can be seen, where concentration in solution is at the threshold amount, regions of potential and pH in which the solid phase is stable against dissolution and regions in which it is not. Where the solid phase unstable against dissolution, the dominant species in solution is shown. This type of potential-pH diagram is often referred to as a Pourbaix diagram, after the Russian-born Belgian chemist who invented it.

14.2.3. Effect of temperature on solubility behaviour

It is of great importance to operators of nuclear plant to understand the conditions under which solubility increases or decreases as temperature is increased, and the magnitude of the change in solubility for a given temperature change. In other words, the magnitude and sign of the temperature coefficient of solubility. This quantity determines whether deposition or dissolution is expected under conditions of changing temperature – such as in the steam generators or the core of a PWR – for a particular solution chemistry and temperature range.

At a given temperature, equilibrium constants for the dissolution of the oxide to its various aqueous species are all that is required to determine solubility, as long as one has knowledge of a few key parameters to characterise the solution: pH_T; log $\{H_2\}$; activity coefficients; and the activity of any other chemicals in solution which may enhance solubility through forming complexes with the metal ions.

The temperature dependence of equilibrium constants is not simple, and is related to thermodynamic quantities as discussed in the following sections. Various assumptions and simplifications can be made, as discussed later. Each equilibrium constant has a different

dependence on temperature, and so the behaviour of solubility with changing solution parameters is generally different at high temperatures than at lower temperature, though still following the same overall trends detailed in section 14.2.2 above.

Assuming that the values of solution parameters such as pH_T are not constrained to be fixed as temperature changes – which would be difficult to achieve physically, and is not ordinarily attempted – these parameters also change with temperature. Since the temperature dependence of pH_T (and each $\gamma_{(z\text{-}l)+}$) depends on the chemical make-up of the solution, it is not uniquely defined and must be determined on a case by case basis for the particular chemistry of the solution. The temperature dependence of hydrogen fugacity, where an unchanging concentration is present in solution, is significant and is more or less independent of solution chemistry (and is therefore uniquely defined for a given temperature and hydrogen concentration). It is determined by the temperature dependence of the Henry's law coefficient for hydrogen solubility.

Temperature dependence of equilibrium constants

As mentioned previously, each K_{eq} can be related to thermodynamic quantities. Ziemniak [115] provides a concise summary of how to treat temperature dependence, from which the following few paragraphs gain inspiration. Rearranging equations (6a) and (6b) and solving for log K gives:

$$\log K(T) = -0.434\frac{\Delta G^0(T)}{RT} = 0.434\left(\frac{\Delta S^0(T)}{R} - \frac{\Delta H^0(T)}{RT}\right) \qquad (16).$$

To give the exact temperature dependence of log K(T), under isobaric conditions, heat capacity differences between products and reactants must be known as a function of temperature.

$$i.e. \qquad \Delta H^0(T) = \Delta H^0(298.15) + \int_{298.15}^{T} \Delta C_p(\tau)d\tau \qquad (17),$$

$$and \qquad \Delta S^0(T) = \Delta S^0(298.15) + \int_{298.15}^{T} \left(\frac{\Delta C_p(\tau)}{T}\right)d\tau \qquad (18).$$

Although tabulated data for $\Delta C_p(T)$ are available (e.g. ref OECD Fe) over wide temperature ranges and to a high degree of precision for many reactions, equations to describe $\Delta G^0(T)$ are often more

convenient, and sometimes *are* necessary due to a lack of $\Delta C_p(T)$ data. Various equations are used in the literature for the dependence of ΔG^0 on T, $\Delta G^0(T)$, depending on empirical goodness of fit to the data. Two of the commonest, laid out below, are based directly on physical considerations and simple approximations. The first one takes into account temperature dependence of ΔH^0 and ΔS^0, and thus uses equations (17) and (18), but assumes a constant value of ΔC_p across the temperature range of extrapolation. This results in an equation of the form:

$$\Delta G(T) = A - BT - CT\ ln\ T \qquad (19),$$

$$\begin{aligned} where \qquad A &= \Delta H^0(298.15) - 298.15\ \Delta C_p \\ B &= \Delta S^0(298.15) - (1 - \ln 298.15)\,\Delta C_p \\ C &= \Delta C_p \end{aligned}$$

Therefore log K has the form

$$\log K(T) = \frac{0.434}{R}\left(B - \frac{A}{T} + C \ln T\right) \qquad (20).$$

The second equation form treats ΔH^0 and ΔS^0 as being independent of temperature, and thus is fully described by equation (16), but with $\Delta H^0(T)$ and $\Delta S^0(T)$ being replaced by fitted average values across the temperature range of interest, ΔH^0_{av} and ΔS^0_{av}. This class of equations has the form:

$$\Delta G(T) = A - BT \qquad (21),$$

$$\begin{aligned} where \qquad A &= \Delta H^0_{av} \\ B &= \Delta S^0_{av} \end{aligned}$$

In this case, log K has the form:

$$\log K(T) = \frac{0.434}{R}\left(B - \frac{A}{T}\right) \qquad (22).$$

The two resulting equations for log K have similar form, with the addition of the "$+C \ln T$" term in brackets for the former equation being the only difference between them. This does not mean log K in the former case is always greater than in the latter case by an amount "$C \ln T$", because the parameters of fit are different in either case: according to values of the thermodynamic quantities chosen, or to give best fit to data taken across a range of temperatures for the two different shapes of fit. Temperature dependence will look similar in either case for low to moderate T, but at the highest values of T the "$+C \ln T$" term will prevent fitted values of log K from settling at a constant value, as they do in the alternative case.

Tremaine and LeBlanc [121] used essentially the latter method in their study of magnetite solubility to fit thermodynamic constants to their solubility data, but instead of treating both ΔH^0 and ΔS^0 as independent parameters of the fit, they constrained their fit to pass through the point (T = 298.15 K, $\Delta G^0_{fit}(T) = \Delta G^0_{298.15K}$), and enabled the gradient to vary, as ΔS^0_{fit}.

In Figure 14.4 is shown a schematic example comparing genuine $\Delta G^0(T)$ (the curved black line) with a linear line of best fit (the straight red line), as per equation (21) but constrained to have the value $\Delta G^0_{298.15}$ at 298.15 K. The red line is fitted across a specific temperature interval – in this case 298.15 K to 573.15 K – and so is shown as a dashed line outside of this interval. For the genuine curve of $\Delta G^0(T)$, the values of $-\Delta S^0(T)$ and $+\Delta H^0(T)$ are given respectively by the gradient and intercept of a tangent to the curve at temperature T. Figure 14.5 shows examples of log K(T) resulting from 3 different fits of the form shown in Figure 14.4.

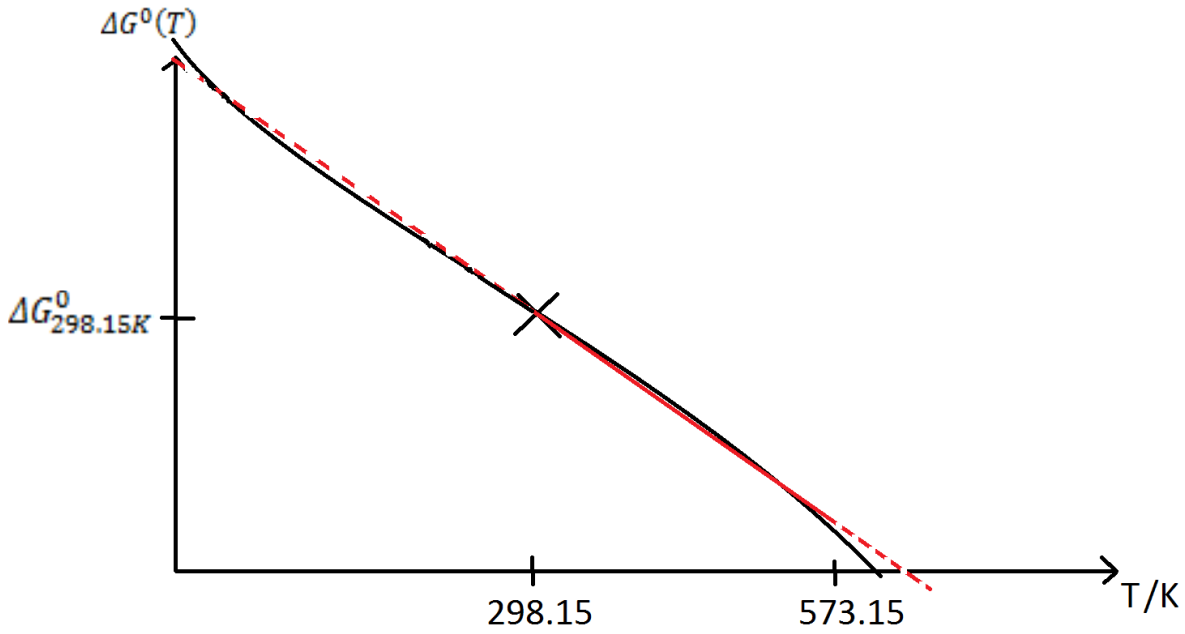

Figure 14.4. A schematic diagram showing a linear fit to $\Delta G^0(T)$ (red line) compared with actual temperature dependence of $\Delta G^0(T)$ (black curve).

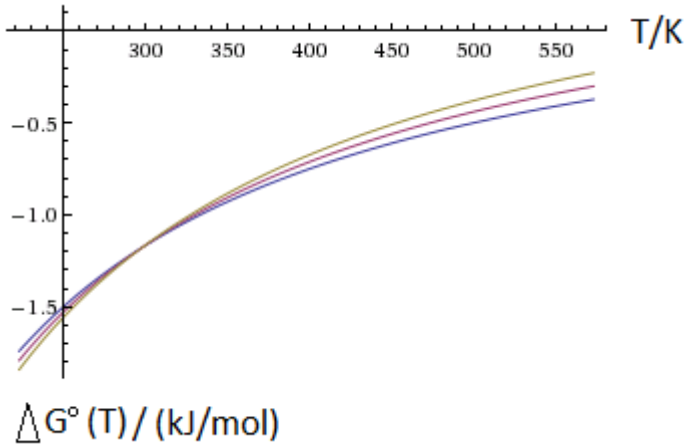

Figure 14.5. Examples of log K(T) resulting from 3 different fits of the form shown in Figure 14.4.

Temperature dependence of activity coefficients

It is beyond the scope of this thesis to talk in detail about the various schemes used to model temperature dependence of activity coefficients. The activity coefficients below were calculated by the author for a simple solution of pure water plus LiOH, under 100 bara pressure, using the extended Debye Hückel equation, a power-5 fit (performed by the current author using Excel® software) to dielectric constant data from [170], and using data on radii of solvated ions [171], [172].

In this regime, of fairly dilute solutions, γ's tend towards 1.000 as solution strength tends towards zero, but deviate further from unity – to ever-smaller values – as concentration increases. Where the major source of ions in solution is the pH reagent, conditions of extreme pH result in higher γ's, purely because of the increased ionic strength of solution. In addition, γ's for the more strongly ionised aqueous species (i.e. $\gamma_{2+/2-}$, $\gamma_{3+/3-}$), which tend to dominate at extremes of pH, experience the most extreme deviation from unity. Therefore under these conditions, the behaviour of activity coefficients would cause plots of solubility versus pH (such as Figure 14.2) to become ever-steeper as pH becomes more extreme, compared to the case where ionic strength of solution is maintained by a buffer solution or where effects of γ's are ignored. The effect becomes more noticeable at higher temperature. Nevertheless, the effect on an ion of +3 or -3 net charge, at 300 °C in 7070 ppb LiOH (pH_{25C} 11) results only in a 2-fold increase in concentration (according to a pH calculator developed by the present author). This results in a contribution to log $c_{z,I}$ of only +0.31. In Table 14.2 are plotted γ's for representative conditions experienced by the rig (pH_{25C} 9-11, temperature up to 300 °C, soluble species of charge magnitude up to 2). Values of $\gamma_{3+/3-}$ are also included for reference. The value of γ_0 remains at 1.00 under the conditions used in the rig. For more concentrated solutions, γ's can become much *larger* than unity.

	100 °C	200 °C	300 °C
pH_{25C} 9 (71 ppb LiOH)			
$\gamma_{+/-}$	1.00	0.99	0.99
$\gamma_{2+/2-}$	0.98	0.98	0.96
$\gamma_{3+/3-}$	0.96	0.95	0.92
pH_{25C} 11 (7070 ppb LiOH)	100 °C	200 °C	300 °C
$\gamma_{+/-}$	0.96	0.95	0.92
$\gamma_{2+/2-}$	0.85	0.81	0.72/0.73
$\gamma_{3+/3-}$	0.70	0.62	0.49

Table 14.2. Activity coefficients for a few selected conditions, under 100 bara pressure. Species of charge +/-3 were absent from the present study, so values for $\gamma_{3+/3-}$ are provided for illustrative purposes only. The most extreme deviation from unity likely to have been encountered in the rig of the present study is 0.72, for pH_{25C} 11, 300 °C temperature, species of charge 2+/- - for example $Fe^{2+}(aq)$. It means there is about 40% more Fe^{2+} in solution under those conditions than direct use of the activity figures (i.e. an assumption that γ = 1) would suggest.

Temperature dependence of pH_T

The value of pK_w for water, and thus also the neutral pH_T (which is simply $pK_w/2$), changes significantly with temperature – see Figure 14.6.

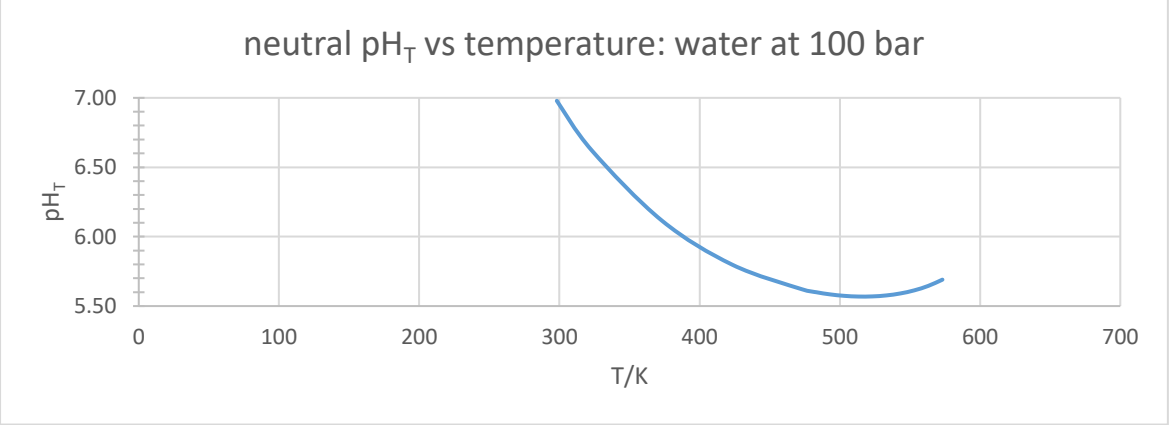

Figure 14.6. Neutral pH_T versus temperature, for pure water at 100 bara pressure

Figure 14.7 below illustrates the advantage of using pOH_T instead of pH_T for a strong base. Where alkalinity is controlled by a fixed molal concentration of a strong base, the concentration of OH^- ions in solution, and therefore the value of pOH_T, remains fairly constant, as it is very close to the concentration of base in solution (grey line). The pH_T however varies significantly with temperature (blue line). This is because the average of pH_T and pOH_T is constrained to be equal to neutral pH_T (orange line).

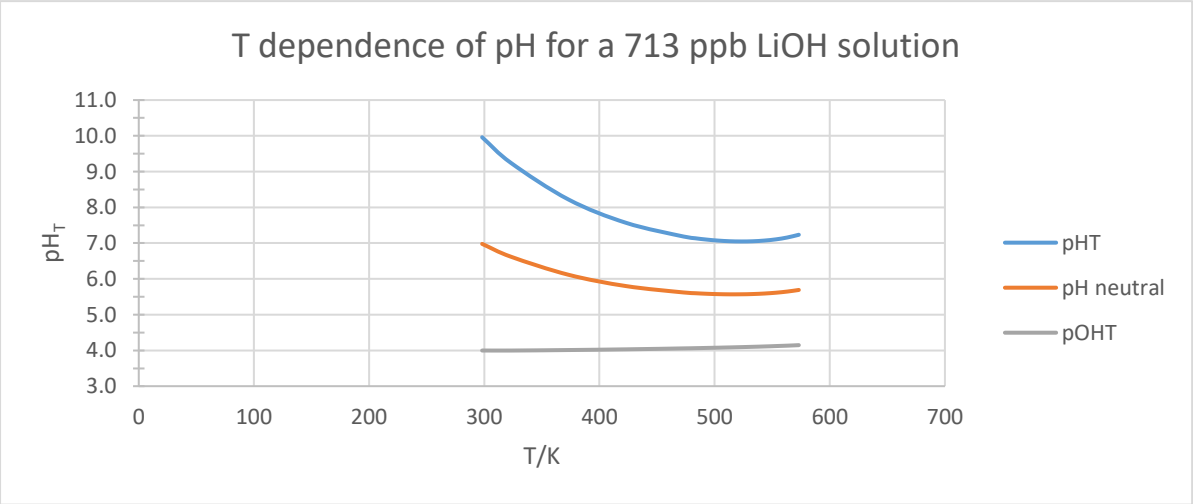

Figure 14.7. Illustrating the constancy of pOH_T compared with pH_T, for a strong base

As temperature changes, the position of equilibrium of various reactions changes, including that for the dissociation of water itself (see the two figures above), and dissociation of any pH reagents used. Since LiOH is a strong base, its dissociation was more or less complete for all the experiments of this thesis, and in most situations in plant. However, boric acid, as used in PWR primary coolant, is a weak acid, and the extent to which it dissociates to form ions varies considerably with temperature and pH_T. Where the ionic strength of a solution is weak enough, the presence of metal ions resulting from oxide dissolution can have an influence on pH_T, which varies with temperature according to the solubility and the hydrolysis reactions between the various soluble species. The presence of other impurities, such as metals other than those accounted for, can also affect pH_T, causing it to differ from calculated values.

Temperature dependence of log $\{H_2\}$

Hydrogen has greater solubility at higher temperature, as shown in Figure 14.8. Consequently, a given amount of hydrogen dissolved in water at 25 °C has lower fugacity on heating to higher temperature (say 200 to 300 °C), see Figure 14.9. This results in a change to log $\{H_2\}$ of -0.75 log units, on heating from 25 to 300 °C, as shown in Figure 14.10.

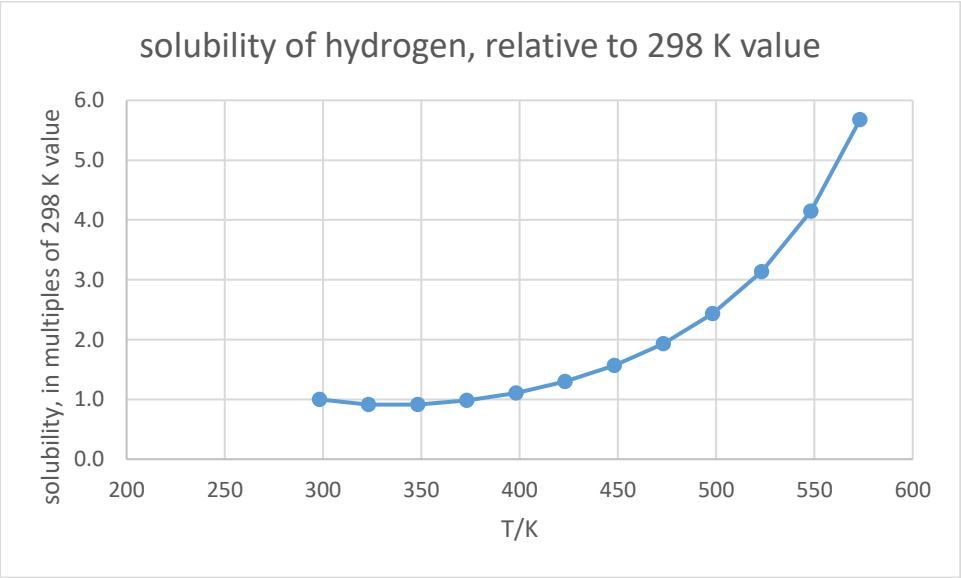

Figure 14.8. Relative solubility of hydrogen as a function of temperature. Using Henry's law data from ref. [155] *and temperature dependent properties of water from ref.* [19], [173]. *Solubility at 298 K was calculated as 0.793 mmol kg^{-1} atm^{-1}.*

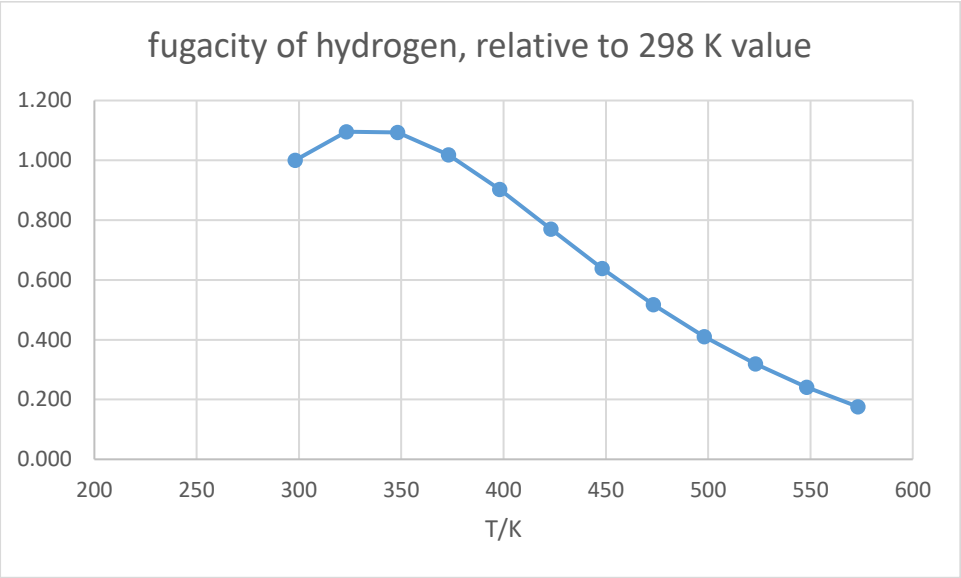

Figure 14.9. Relative fugacity of hydrogen as a function of temperature, for aqueous solution into which a fixed concentration of hydrogen has been dissolved.
This is simply the reciprocal of data plotted in Figure 14.8.

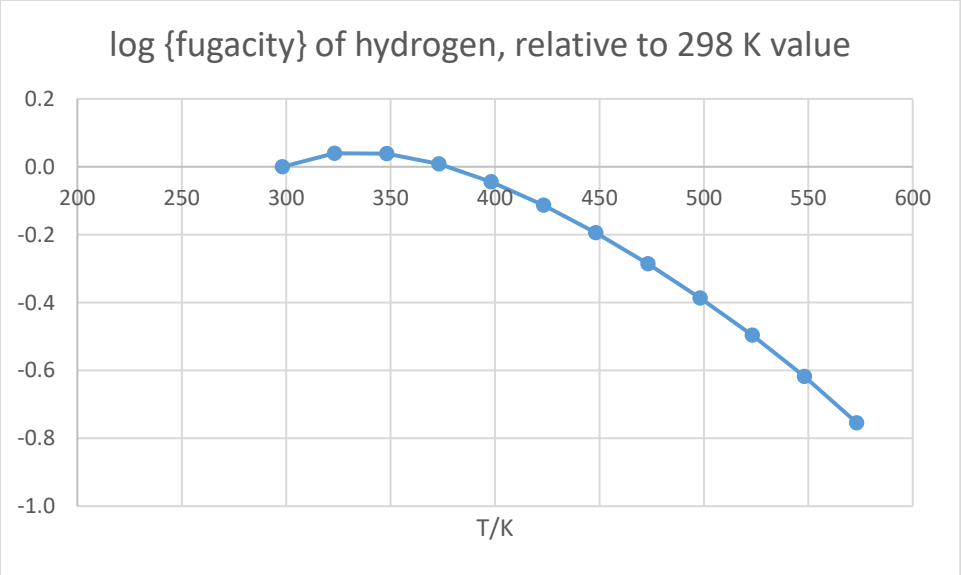

Figure 14.10. The logarithm of relative hydrogen fugacity (relative to 298 K value) as a function of temperature, for aqueous solution into which a fixed concentration of hydrogen has been dissolved.
This is simply the logarithm of data plotted in Figure 14.9.

Overall effect of temperature on solubility

All of the above effects combine to produce an overall dependence of solubility on temperature. As mentioned earlier, this dependence has important applications, and must be determined on a case by case basis for a particular chemistry and with particular assumptions made.

14.2.4. Meta-stable versus true equilibrium

So far, consideration has been made only of true equilibrium, achieved after a system has been left for infinite time to acquire perfect equilibrium. In later sections, kinetics – the rates at which reactions happen – will be explored in more detail. For this section an understanding that some reactions occur on faster timescales than others is sufficient. Also, kinetics increase rapidly with temperature, and so thermodynamic stability is a useful tool in predicting which phases will be present under hydrothermal conditions, but is less useful or reliable at room temperature.

As a general rule, reactions in the solid state occur slowly, and aqueous reactions proceed to equilibrium much more rapidly. Although true equilibrium requires that both the solid oxide and the aqueous species are in their equilibrium state, an apparent equilibrium can exist where changes to the oxide are so slow as to appear non-existent whilst exchange (dynamic equilibrium) between metal species in solution and metal ions in the oxide rapidly attains a steady state. In this case, the metal oxide may deviate only slightly from the thermodynamically stable state for current conditions, for example by an excess or deficiency of metal ions compared with oxide ions, or an excess of lattice defects; or it may persist as an entirely different oxide phase from the stable one.

Whereas the true equilibrium state is uniquely defined for a well-defined system, there are an infinite number of meta-stable situations, as for example a non-equilibrium oxide slowly decays, smoothly over time, to be ever-closer to the thermodynamically stable ideal. In some cases a meta-stable situation could be relatively well defined, for example where a well characterised oxide is first introduced to a solution in which a different oxide is the stable phase (but is not present). Over time, however, the formation of crystals of the stable phase from solution will interfere with dissolved levels of the metal in a difficult to define way.

For the reasons above, it is generally the one true value of solubility which researchers hope to measure. However, it is important to be aware of the various causes of deviation from this situation, both in order to eliminate their effects when measuring solubility, and to take their effects into account when modeling a real-life situation based on solubility data. Below are a few examples of deviation from equilibrium dissolution / precipitation reactions. In general, true equilibrium is approached over time. Therefore, workers refer to “ageing” of oxides towards a truly stable form by leaving them under appropriate hydrothermal conditions for several months. Once crystallites of a stable phase have nucleated and reached a relatively stable size, they grow from solution as crystallites of a less stable phase or size dissolve, in a process known as Ostwald ripening.

Imperfectly crystalline material

Oxides which have poor crystallinity – for example a considerable excess of lattice defects compared with the stable form of the oxide – have an effective thermodynamic activity of greater than one, and elevated meta-stable solubility. The activity gradually falls to 1 over extended time scales as the crystal ages in hydrothermal solution.

Stability of small crystallites

Surface energy becomes a significant factor for small crystallites or particulates, resulting in enhanced solubility (and therefore instability). Castelli [40] illustrates this effect using a simple analytical form from Glasstone [41], as shown in Figure 14.11 below.

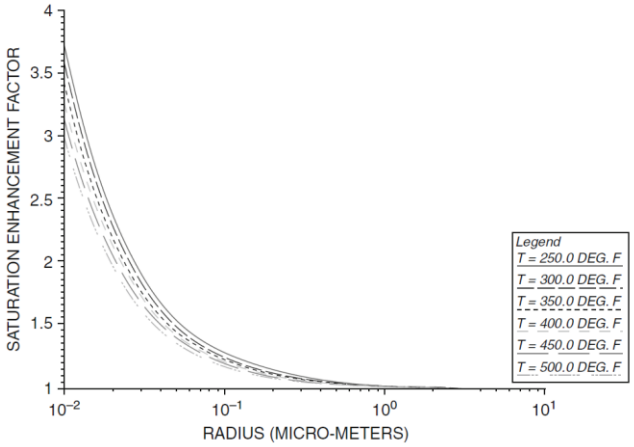

Figure 14.11. Particulate crystallisation/dissolution saturation enhancement factor taken from [40]. *A metastable equilibrium between solution and these sub-micron sized particulates results in solution which is supersaturated with respect to perfectly stable, larger crystallites.*

The general trend of decreasing stability with decreasing size is consistent with the observation that crystallites on corroding steels grow over time [78], [84], and also that dissolved levels of soluble species may be elevated in the presence of small suspended particulates or colloidal particles.

However, recent research using first principles calculations [42] has shown that for the oxide phase nickel ferrite there is a *negative* free energy of formation from solution for several surface orientations, particularly {1 1 1} surfaces. This is true even under conditions and cation concentrations for which the Gibbs energy of formation of the bulk phase is positive: in this case, there is an optimum size of octahedral crystallite (whose surfaces are exclusively {1 1 1} planes) resulting from the trade-off between increased total surface area and increased bulk volume as the

size of crystallite is increased – see Figure 14.12. Note that the free energy in this case is a summative quantity, not measured per mole, therefore the effect of each additional deposited ion is to lower the global free energy as long as the gradient of the curve is negative, and thus the most stable crystallite size is given by the position of the minimum.

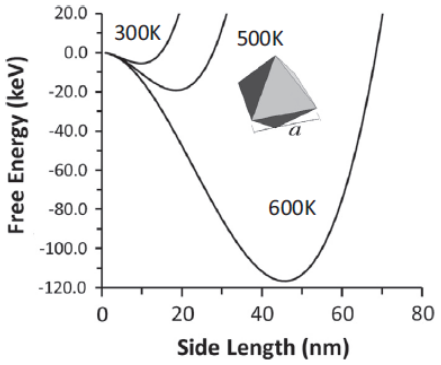

Figure 14.12. Change in the free energy for the formation of an octahedral nickel ferrite particle in solution from dissolved ions, as a function of characteristic length at different water temperatures. From [42].
The characteristic 'side length' in this case is the length of one edge, labelled 'a' in the inset diagram.

The same research group applied these findings further, to develop a model describing the structure of fuel crud [174]. This model was shown to accurately predict the porous nature of nickel-ferrite-based crud by assuming a network of optimum-sized octahedral crystallites joined at the vertices. It also correctly predicted the observed decrease in porosity with sub-surface depth, based on the assumption that the crystallite-to-crystallite spacing is constrained to stay constant whilst optimum crystal size grows over time, in line with local temperature and pH increases under an ever-thickening crud layer.

The implications are that colloidal-sized crystallites of nickel ferrite can circulate in coolant as the thermodynamically stable phase, not just as a meta-stable suspension; and also that the porous nature of nickel ferrite deposits is also thermodynamically driven and stable.

For nickel ferrite to form, there must be sufficient Ni present in solution relative to Fe. For the case of corroding stainless steels (such as the SS316L used for the project in this thesis), there is only sufficient Ni for a ferrite of composition approximately $(Ni_{0.2}Fe_{0.8})Fe_2O_4$ to form. In PWR primary circuit, a considerable portion of the metal surface area in contact with the coolant is in the steam generator tubing, made from Ni base alloys, for which the native outer layer oxide is nickel ferrite.

Coolant circulates around the whole coolant loop so fast that dissolved levels of each element in the bulk coolant represent an average of the conditions in different parts of the loop, and so sufficient dissolved Ni species reach the core to precipitate nickel ferrite there, in addition to circulating nickel ferrite crystallites.

Surface charge effects, pH_{pzc}

Another surface effect which manifests in small crystallites or other oxide particles is surface charging. Water molecules and other ions from solution adsorb or chemi-sorb onto oxide surfaces: at low pH, the abundance of H^+ ions is such that surfaces become positively charged; at high pH surfaces become negatively charged by the adsorption of OH^- ions (alternatively one can picture the protonation or deprotonation of chemisorbed water molecules). Each oxide phase has a characteristic pH at which the net charge density is zero (pH_{pzc} – the pH of zero charge), or the surface potential matches that of bulk solution (pH_{iep} – the isoelectric pH). The two quantities are a function of temperature, and for the purposes of this thesis can be considered interchangeable.

At pH values sufficiently far from pH_{pzc}, all surfaces of a given oxide phase have like charges, and so particulates are repelled from the walls of the coolant loop (assuming the coolant-facing oxide is of the same type, or has the same charge polarity), and from each other. The consequence is that particles which are sufficiently small that surface effects dominate ($\lesssim 1\ \mu\mathrm{m}$) can persist for extended periods in a colloidal suspension, as they seek to become evenly spaced from each other and are repelled from settling on surfaces. Over sufficiently long time periods they may dissolve, assuming the simple analytical dependence of solubility on size, from Glasstone's equation [41] (see above), though solubility may be elevated while they are present, and if they are small enough to pass through filters then they may interfere with solubility measurements directly.

When pH is close to pH_{pzc}, there is little or no repulsion and colloidal particles may agglomerate as they come into contact with each other, forming ever larger particulates until they settle onto surfaces due to gravity, or inertia effects where coolant changes direction. The settling out on surfaces is also no longer inhibited in this case. Where different oxide phases are present, and the solution pH is intermediate between the pH_{pzc} values of two phases, different charge polarities may cause attractive forces, resulting in preferential deposition in certain areas, and the formation of agglomerate colloidal particles of multiple oxide phases.

Figure 14.13 shows some data on pH_{pzc} for magnetite and nickel ferrite. Note that the data for nickel ferrite was for a fine powder rather than well aged crystallites, and this was the main reason for an elevated pH_{pzc} for nickel ferrite compared with magnetite. Therefore a pH_{pzc} closer to the one for

magnetite is expected for the aged crystallites found in plant and in the rig used for this thesis study. This serves to demonstrate that caution should be exercised when applying results from laboratiory experiments to plant, or to other experiments, especially since difficulties with high temperatures and pressures mean that experimental data are in some cases scarce and not well corroborated.

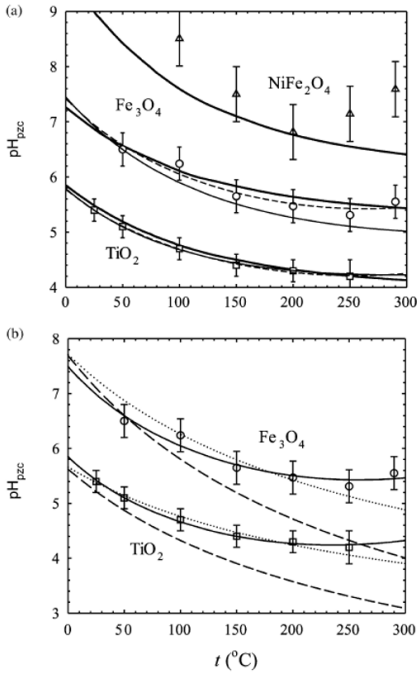

Figure 14.13. Figure taken from [38]*. Comparison of experimental pH_{pzc} values for rutile (squares* [175]*), magnetite (circles,* [176]*), and nickel ferrite (triangles, unpublished), with estimates based on (a) the MUSIC Model (heavy curves,* [177]*),* [178] *(thin solid curves), and* [179] *(dashed curves); and (b)* [180] *(solid surves),* [181] *(dotted curves) and* [182] *(dashed curves).*

Surface adsorption of other species from solution

Oxide surfaces become increasingly negatively charged, as pH is set at increasingly alkaline values (above pH_{pzc}). As a result, there is a tendency for cations to adsorb onto those surfaces. Quantitative research into this field under hydrothermal conditions has only begun in earnest relatively recently, utilising emerging experimental techniques such as the Hydrogen-Electrode Concentration Cell (HECC). Wesolowski et al. have been instrumental in this work, and provide a helpful introduction to the topic [38].

Figure 14.14 shows adsorption properties of powdered rutile (TiO_2) with varying pH. The dashed lines indicate pH_{pzc}. For each cation species, there is a pH at which 50% of the metal introduced to the solution is adsorbed on oxide surfaces, known as the pH_{50}. The degree of adsorption changes relatively rapidly with pH, to around 0% at lower pH and around 100% at higher pH, in the shape of a sigmoid function. The pH region over which this transition occurs is known as the ‘sorption edge’. It

is interesting to note the difference in pH_{50} from one species to the next: At 150 °C at the pH_{pzc}, Nd^{2+} is strongly adsorbed, whereas Ca^{2+} is not adsorbed at all.

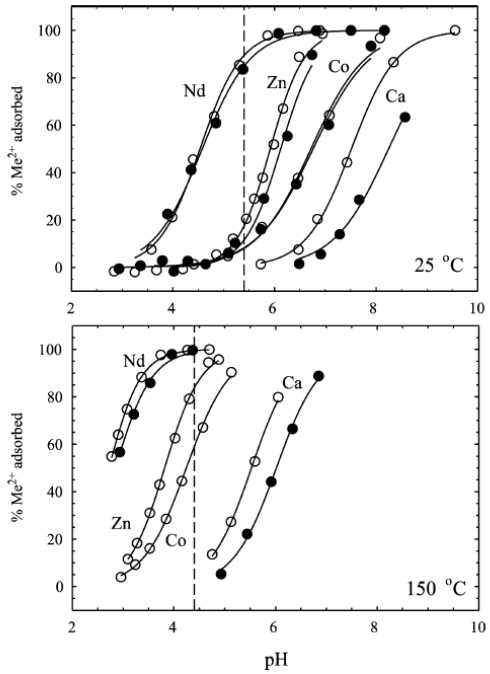

Figure 14.14. Figure taken from [38]*. Percent Nd^{3+}, Zn^{3+}, Co^{2+}, Ca^{2+} adsorbed as a function of pH and temperature. Dashed vertical lines indicate the pHpzc of rutile* [175] *at each temperature (Ca^{2+} data from* [183]*). Smooth curves are 4-parameter sigmoid functions which asymptote to 0 and 100%.*

On rutile there is increasing tendency for adsorption of cations with increasing temperature, even when changes in pHpzc are accounted for, see Figure 14.15. Due to a lack of data at high temperature, it is difficult to ascertain to what extent these findings of extrapolation to higher temperature may be applicable to other oxide phases such as magnetite and nickel ferrite. In some cases adsorption can alter the solution chemistry by adsorbing added chemicals.

Cr in particular may exhibit significant sorption tendencies under plant relevant conditions. According to Turner [14], at room temperature Cr(VI) (which is present under oxidising conditions, such as may be present at the back-end of the rig used for this thesis project after passing through the back-pressure regulator), has a strong tendency to be adsorbed onto many solid surfaces. Beverskog & Puigdomenech [184] also mention Cr(VI), citing chromium sorption data at 25 °C on iron hydrous oxides for which Cr(III) was sorbed at near neutral to high pH (>5), and Cr(VI) was sorbed instead at low pH (<5). Extrapolating to the hydrothermal regime, they suggest that at neutral solutions oxidation of Cr(III) to Cr(VI) should induce a complete Cr desorption. This hypothetical explanation was put forward to explain a phenomenon observed in BWR's on changing

from HWC (reducing) to NWC (oxidising), in which Cr concentration may initially rise to 100 ppb, where it would normally be at most a few ppb, defying any thermodynamic solubility explanation.

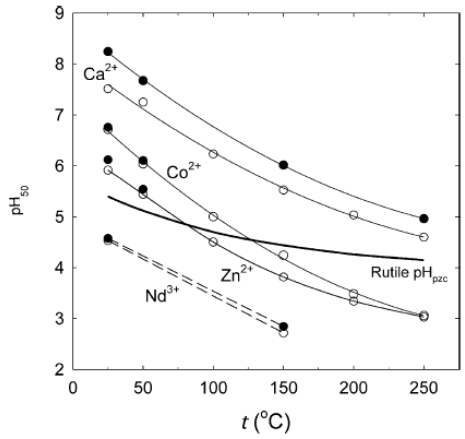

Figure 14.15. Figure taken from [38]*. Variation of pH50 for Nd^{3+}, Zn^{3+}, Co^{2+}, Ca^{2+} on rutile powder surfaces in NaCl or NaTr solutions at ionic strength 0.03 mol/kg (open circles) or 0.3 mol/kg (filled circles). Data for Ca^{2+} from* [183]*. Rutile pH_{pzc} from* [175]*.*

14.2.5. Mixed oxides, and non-stoichiometric-oxides (theory)

Figure 14.16 illustrates the interplay between single metal oxides and mixed oxides in controlling levels of each dissolved metal, at equilibrium or metastable equilibrium, using chromite as a case study.

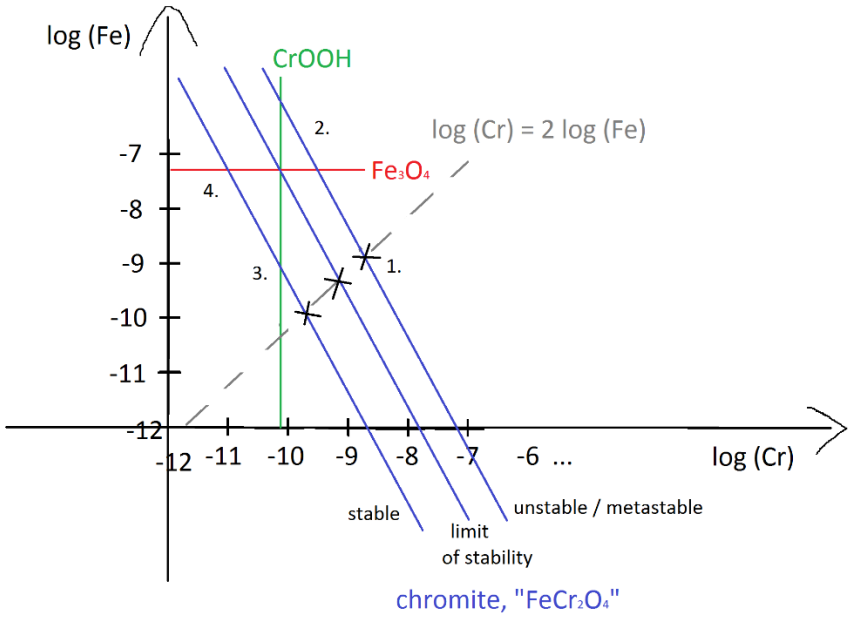

Figure 14.16. Schematic illustration of incongruent dissolution for chromite

In the absence of a mixed oxide phase, Cr levels are controlled at the solubility level of CrOOH (vertical line in figure), where present, otherwise at any lesser or equal concentration; and likewise for Fe levels and the magnetite phase (horizontal line in figure). The intersection of the two lines represents soluble levels when both oxides are present at equilibrium. If the two phases are miscible in each other, they may not have fully stoichiometric composition at equilibrium; lines representing solubility of the two phases may therefore deviate very slightly from a linear trend. In this case, it is known that there is some accommodation of Cr(III) in ferrite when in equilibrium with Cr(III) oxide. A literature search did not reveal data on the solubility of γ-FeOOH in γ-CrOOH at hydrothermal conditions: the two phases are isomorphous, but pure γ-FeOOH is significantly unstable under hydrothermal conditions.

Solubility behaviour of the mixed oxide phase (chromite) is treated differently, as follows. Consider the solubility product of $FeCr_2O_4$, involving the dissolution to neutral hydrolysed species:

$$FeCr_2O_4(cr) + 4H_2O(l) = Fe(OH)_2(aq) + 2Cr(OH)_3(aq) \qquad (1)$$

$$\mathrm{K}_1 = \{Fe(OH)_2\}.\{Cr(OH)_3\}^2 \qquad (2)$$

This equation does not define activity of the Fe species nor the Cr species uniquely, but rather the product of their activities (raised to the power two in the case of Cr species here). For given conditions of temperature, pH and hydrogen fugacity, contributions from other soluble Fe and Cr species will be fixed relative to those featuring in equation (2), as long as concentration is low enough that activity coefficients do not deviate significantly from zero. Thus, in terms of total dissolved concentrations of iron, [Fe] and chromium, [Cr], we have:

$$[Fe].[Cr]^2 = \kappa(T, pH, \{H_2\}) \qquad (3)$$

Where κ is a constant for a given set of solution conditions. Thus

$$\log[Fe] = \log\kappa - 2\log[Cr] \qquad (4)$$

Equation (4) is plotted schematically in Figure 14.16, for three different scenarios – where chromite is stable; where chromite is unstable or metastable; and at the limit of stability for chromite.

At true equilibrium, chromite can only exist where it is stable with respect to decomposition:

$$FeCr_2O_4 + \frac{4}{3}H_2O = \frac{1}{3}Fe_3O_4 + 2\,\gamma CrOOH + \frac{1}{3}H_2 \qquad (5)$$

This is illustrated by the line marked ‘stable’ in Figure 14.16, up as far as the line marked ‘limit of stability’. Where chromite is stable under conditions of interest, a range of [Fe] and [Cr] levels are possible, as illustrated by the line connecting points “3” and “4” in the plot. At the limit of stability, all three oxide phases can co-exist in equilibrium, and levels of [Fe] and [Cr] are given uniquely by solubility of their respective single oxide phases.

Where soluble levels of Fe are particularly high relative to those of Cr, the composition of each oxide may be slightly more Fe-rich and less Cr-rich than otherwise, and vice-versa where the ratio is lower. The extent to which this occurs depends on the oxide phase. Figure 4.4 in chapter 4 shows the deviation from stoichiometry for chromite in equilibrium with magnetite. A search of literature did not yield the composition of chromite in equilibrium with CrOOH for comparison, but composition between positions 3 and 4 is likely to be similar. Therefore, unless Cr and Fe are introduced to a system in precisely controlled proportions to yield a composition between those limits, there will in general be an excess of either Cr or Fe, resulting in equilibrium of $FeCr_2O_4$ with CrOOH (position 3) or Fe_3O_4 (position 4) respectively. In the former case, [Cr] is controlled by CrOOH and the level of [Fe] is less than the solubility of magnetite, to an extent which depends on how stable the chromite is (how positive Δ_rG is for equation (5) at prevailing hydrogen fugacity). In like manner, [Fe] is controlled by magnetite in the latter case, with [Cr] being less than the solubility of CrOOH.

Where chromite is present as a metastable phase, the oxide reaches, or approaches, a metastable equilibrium with solution locally. Levels of [Cr] and [Fe] at the oxide surface may be in the approximate vicinity of position 2 in the plot, on the solubility curve for chromite labelled 'unstable / metastable'. Whether this position lies closer to the CrOOH line or Fe_3O_4 line depends on kinetics and available surface area of each phase. The level of [Cr] near to any CrOOH is controlled close to the CrOOH solubility value, and likewise for [Fe] and magnetite, and so by diffusion of aqueous Cr and Fe species down the concentration gradient from chromite to the respective single metal oxides, the chromite is gradually replaced by the other oxides in a process of Ostwald ripening.

In Ziemniak et al.'s solubility study [102], stoichiometric chromite was used. An initial net dissolution must have occurred before equilibrium could be achieved, which might be expected to involve Cr:Fe in the ratio of roughly 2:1 (over longer timescales, whichever ion becomes scarce at the surface could be replaced by diffusion from beneath the surface, resulting in a slight change in bulk composition, but not over short timescales). This situation is marked by a cross in Figure 14.16, for each of the three illustrative chromite solubility curves, representing metastable equilibrium in each case because the solution is supersaturated with respect to CrOOH. As CrOOH phase precipitates, a net flux of Cr ions from chromite to CrOOH via solution is established, and the remaining chromite begins to become increasingly Cr-poor, (or Fe-rich). It is this change in stoichiometry which causes the solution chemistry near the surface of chromite to move upwards and left (in the plot), along the chromite solubility curve, until the ratio of Cr:Fe in solution near the chromite is orders of magnitude lower than the value of 2 initially assumed, and the level of [Cr] reaches the solubility value of CrOOH. At this point the iron-rich chromite is in equilibrium with CrOOH (position 3). Ziemniak et al. reported that the CrOOH manifested as a thin continuous layer over the surface of the chromite crystals. Therefore, the surface layer of CrOOH may alternatively have been formed by incongruent dissolution, by the leaching of Fe^{2+} ions to solution and the uptake of protons from solution, accompanied by a solid state transformation, instead of a dissolution and precipitation process.

Since the chromite of said study was in equilibrium with CrOOH, it may have been slightly less Fe-rich than the compositions of chromite in equilibrium with magnetite, reported in studies of stainless steel corrosion [76], [84] and in a studies of magnetite-chromite equilibrium specifically [85] – see Figure 4.4. The chromite in this latter study had x = 0.7 for $Fe(Cr_xFe_{1-x})_2O_4$ which is a significant deviation from stoichiometry.

Solid solution and immiscibility

In small amounts, any impurity metal ions can be incorporated into a given oxide phase. Although the word 'solubility' does not apply for those impurity elements, strictly speaking, an equilibrium is achieved at any given coolant conditions, in which the molar concentration of the metal in the oxide phase corresponds to the metal's concentration in solution. A rise in the impurity concentration in the metal corresponds to a rise in the solution concentration, but the relation is not necessarily simple. The two activities (in the solid, and in aqueous solution) are related by a partition constant. There is limited data available on these.

For some pairs of oxides, the oxide structure is the same for each, and there is full miscibility between the two phases, forming a continuous solid solution. This is the case for Fe_3O_4 and $NiFe_2O_4$, with the combined phase being known as 'ferrite'; and between $FeCr_2O_4$ and $NiCr_2O_4$, known generically as 'chromite'. There is some considerable miscibility between chromite and ferrite also, but not full miscibility – except at temperatures above about 750 – 880 °C (depending on Ni content). The reason for this is that ferrite is an inverse spinel, and chromite is a normal spinel, and the two phases are not compatible. The Gibbs energy of mixing reaches a local maximum for a composition of ~50% $NiCr_2O_4$, 50% $NiFe_2O_4$: any composition having mole fraction of $x \approx 0.2 – 0.7$ $NiCr_2O_4$ is unstable with respect to decomposition into a Cr rich phase having $x \approx 0.7$, and an Fe-rich phase having $x \approx 0.2$. A similar situation is true for the Ni free equivalent phases, $FeCr_2O_4$ and Fe_3O_4, see Figure 14.17.

Where ferrite and chromite phases – of a given nickel composition – are in equilibrium, the proportions of Fe and Cr are uniquely determined for each phase, dependent on temperature. The partition of Ni between the two oxides is also constrained – i.e. if the Ni proportion of one phase is known, the Ni proportion of the other is uniquely determined – and the partition is roughly equal. The overall Ni proportion is dependent on relative abundance of Ni, but is uniquely determined if levels of Ni in solution are sufficient to precipitate a separate Ni(cr) phase.

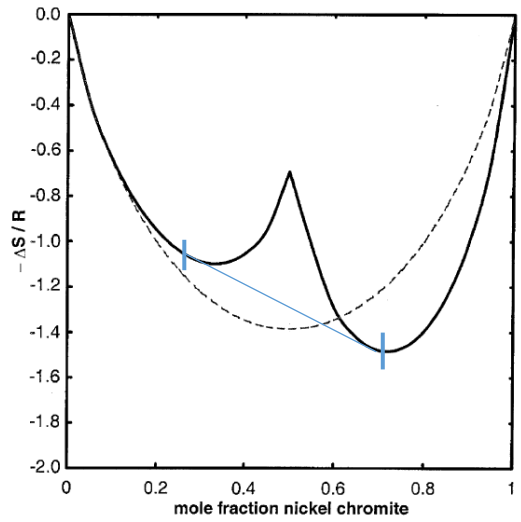

Figure 14.17. Estimated entropies of mixing (ΔS_{mix}) in the nickel ferrite-nickel chromite spinel binary based on changes in configurational entroy. Ideal entropies of mixing are shown as a dashed line. Figure adapted from [74].
A blue straight line connecting the tangent to the curve at two points has been added by the present author. The end points of this line, shown by blue markers, represent oxide composition at the solvus of immiscibility. Any intermediate composition is not stable as a single oxide, and instead exists at equilibrium as a combination of Fe rich (ferrite) and Cr rich (chromite) phases, with compositions as indicated by the markers. End points of the plot represent stoichiometric $NiFe_2O_4$ (left, chromite mole fraction = 0) and $NiCr_2O_4$ (right, chromite mole fraction = 1).

14.3. Literature data on solubility for selected oxides

14.3.1. Overview

For a given oxide, the key data describing solubility are the temperature dependent solubility constants, K_{eq}, defined for specified equilibria between the oxide and each soluble species. Using these, the concentration of each species – and thus the solubility – can be determined for any solution using equations (12) and (13), provided that key parameters of the solution are that solution. In general, these key parameters of the solution have their own temperature dependence, which is largely independent of the particular oxide in question (except under conditions where the solution is particularly sensitive to the effects of the dissolved metal oxide itself, such as in near-neutral solutions with no pH modifier).

For a particular metal, the thermodynamically stable solid phase at prevailing hydrogen fugacity and temperature may be one of several oxide phases, or a crystalline phase of the metal itself. Data and plots pertaining to the stability field of each oxide phase is given in section 14.3.2.

Data for the temperature dependence of log K values are given in sections 14.3.5 onwards for the selected oxides, along with plots of temperature dependent solubility as calculated using equations (12) and (13) for selected solution conditions, and other plots from the literature which help to illustrate solubility behaviour. Further explanation of the format in which these data and plots are presented is given in section 14.3.4. In section 14.3.3 the temperature dependence of solution parameters is explored for a model solution, having fixed molality of both hydrogen gas and a strong acid / base. Temperature dependence of parameters thus modelled is used in some of the plots of sections 14.3.5 onwards.

14.3.2. Stability of oxides

Hydrous versus anhydrous forms

In the presence of water or steam, oxides persist in their anhydrous form only at sufficiently high temperature. As temperature is decreased, increasingly hydrated forms become stable. In the case of magnetite, the temperature of transition to $Fe(OH)_2$ is a function of hydrogen fugacity, owing to the change in oxidation state of the Fe. Figure 14.18 (a) lists the various hydrated oxides forms of various elements relevant to nuclear power generation, and temperatures of transition. In Figure 14.18 (b) is shown a plot of concentration versus temperature for neutral hydroxocomplexes of selected elements in equilibrium with the stable oxide phase. Transition of stability from one phase

to the next is accompanied by a discontinuity in the solubility curve for the neutral hydroxocomplex, as can be seen most clearly for Cr oxides. Since equilibria between species in solution are independent of any oxide phase which may be present, total solubility under particular conditions (of pH and hydrogen fugacity etc.) is proportional to the concentrations of neutral hydroxocomplexes, which generally give a fairly good approximation of minimum solubility at conditions of intermediate pH where such species dominate. In this respect the plot also serves to demonstrate relative stability against dissolution for several single-metal oxide phases present in primary coolant system of nuclear reactors.

a

Table I. Stability of Metal Ion Oxidation States and Metal Oxides in Deoxygenated Water

Atomic Number	Symbol	Stable Oxidation State	Stable Solid Phase	Ref.
22	Ti	Ti(IV)	TiO_2 (rutile)	
23	V	V(V)	V_2O_5	
24	Cr	Cr(III)	CrOOH, Cr_2O_3 ($T > 693$), $Cr(OH)_3$ ($T < 333$)	4 41
25	Mn	Mn(II)	MnO	
26	Fe	Fe(II)	$Fe(OH)_2$, Fe_3O_4 ($T > 393$)[a]	5
27	Co	Co(II)	$Co(OH)_2$, CoO ($T > 367$)	II
28	Ni	Ni(II)	$Ni(OH)_2$, NiO ($T > 468$)	6
29	Cu	Cu(II)	CuO	II
30	Zn	Zn(II)	$Zn(OH)_2$, ZnO ($T > 252$)	II

[a] Transformation temperature dependent on dissolved hydrogen level; indicated value based on 17.7 scc-kg^{-1} [$P(H_2) = 1$ atm at 25°C].

b

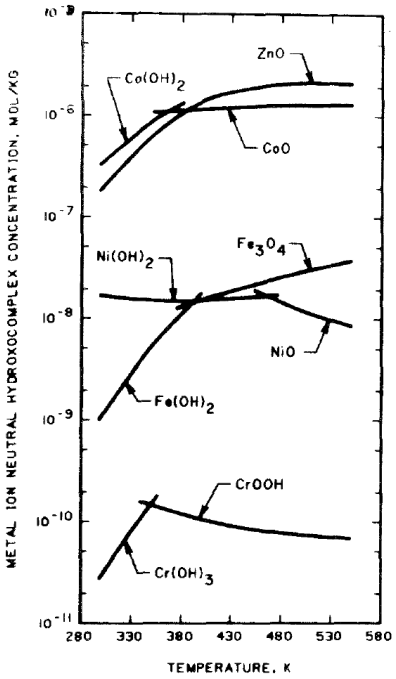

Figure 14.18. Taken from [115]*. (a) table showing stable oxide phases, and temperatures of transition of stability, for selected metal oxides.(b) Predicted minimum solubilities of selected metal oxides as a function of temperature.*

There is also a pressure dependence of stability, with more hydrated phases preferring higher pressure, though there is generally very little change in the transition temperature between saturation pressure of water and the pressures of around 100 bar (10 MPa) employed in the primary circuit of PWR's and in studies such as the one performed for this thesis. In Figure 14.19 is plotted the pressure dependence of the temperature at which a selection of these transitions occur.

Polymorphs

For oxides of a given chemical formula, several different polymorphs may be possible at different temperatures. Strictly, these are designated with a greek letter in front of the formula, or by giving the mineral name of the oxide form. For example, the stable form of Cr oxide between about 333 and 693 K is γ-CrOOH, which has no mineral name and is isomorphous with γ-FeOOH, known as lepidocrocite. A transition between two such phases occurs for NiO at around 250 °C, which can be observed as a kink in the NiO/$Ni(OH)_2$ transition curve in Figure 14.19.

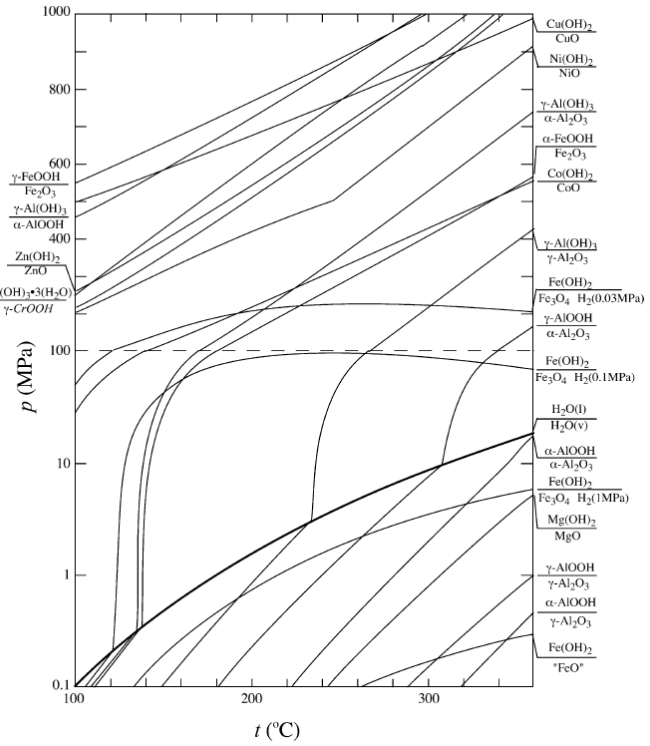

Figure 14.19. From [38]. *Pressure dependence of the temperature at which a selection of metal oxide dehydration reactions occur.*
The dashed line indicates a scale change from logarithmic to linear. The heavy curve is the liquid-vapour saturation surface. The kink in the curve for NiO occurs at the solid-state phase transition, NiO → $Ni(OH)_2$. Curves for the $Fe(OH)_2$ – Fe_3O_4 reaction are shown for fluids saturated at 25 °C with a gas having hydrogen partial pressure, $pH_2(g)$, of 30, 100 and 1000 kPa.

Different oxidation states – the effect of oxygen (or hydrogen) fugacity

At sufficiently low oxygen fugacity (or sufficiently high hydrogen fugacity), a crystalline phase of the bare metal is the stable form; as oxygen fugacity is increased, progressively more oxidised forms become stable.

If the oxidation reaction between two oxides is written with the less oxidised form on the left, and 1 mole of oxygen per mole of reaction, the equilibrium oxygen fugacity for the reaction can be

determined from $\Delta_R G^0$ for the reaction. This is demonstrated below for the example of hematite oxidation to magnetite.

$$3Fe_3O_4(cr) + O_2(g) = 6Fe_2O_3(cr) \qquad (1)$$
$$\Delta_r G^0 = 6\Delta_{f,hematite} G^0 + 4\Delta_{f,magnetite} G^0 \qquad (2)$$

For each oxidation reaction written in this way, the value of $\log\{O_2\}$ when the two phases are in equilibrium is found from $\Delta_r G^0$ and T as follows:

$$\log K = -\log\{O_2\} = -\Delta_r G^0/(2.3026RT) \qquad (3)$$

Several different parameters can be used to measure the extent to which conditions are oxidising or reducing, besides oxygen fugacity. Equation (3) shows that for a given temperature $\Delta_r G^0$ is higher (more positive) at more oxidising conditions, being proportional to $\log\{O_2\}$. Lower $\log\{H_2\}$ represents more oxidising conditions, at a given temperature and fugacity of water vapour, according to the equation for the redox stability of water:

$$H_2(g) + \frac{1}{2}O_2(g) = H_2O(g) \qquad (4)$$
$$\log\{O_2\} = 2\left(\log\{H_2O(g)\} - \log\{H_2\} - \log K_4\,(T)\right) \qquad (5).$$

For the case of liquid water $\{H_2O(g)\}$ is uniquely determined by the vapour pressure at any given temperature, and so there is a one-to-one correspondence between oxygen fugacity and hydrogen fugacity.

Since hydrogen fugacity can be related to hydrogen concentration, redox conditions can be controlled or measured by controlling or measuring the hydrogen concentration, under conditions for which oxygen concentration would be so low as to prohibit such measures. In addition, the confirmed presence of a particular oxide phase under hydrothermal conditions provides some evidence that oxygen fugacity was within the range for stability of that oxide. The presence of oxides from both sides of an oxidation reaction implies that oxygen fugacity was controlled at least locally at close to the characteristic value for that reaction, perhaps due to redox conditions in bulk solution straying outside the region of stability for one of the oxides already present which had previously been the stable form, with oxygen fugacity controlled locally by consumption or production in the oxidation reaction and the resulting buildup or consumption of hydrogen gas via the $H_2O(g) \leftrightarrows H_2(g) + \frac{1}{2}O_2(g)$ reaction. This is the case for corroding steel: conditions in bulk solution are outside the range of stability for the unoxidised metal phase (steel), which forms a protective oxide layer of the chromite phase. Oxygen fugacity is buffered locally to a level several orders of magnitude lower than in bulk solution by the steel to chromite oxidation reaction.

Plots of $\Delta_r G^0$ versus temperature can be drawn for many such oxidation reactions on the same set of axes, and are known as Ellingham diagrams. Onto these plots other quantities of interest can be superimposed for informative purposes, such as contours of fixed oxygen fugacity, fixed hydrogen fugacity (in saturated water, or for steam at a fixed pressure), or a ratio of steam to hydrogen fugacity. Figure 14.20 is an example of an Ellingham diagram, with contours for hydrogen fugacity (MPa).

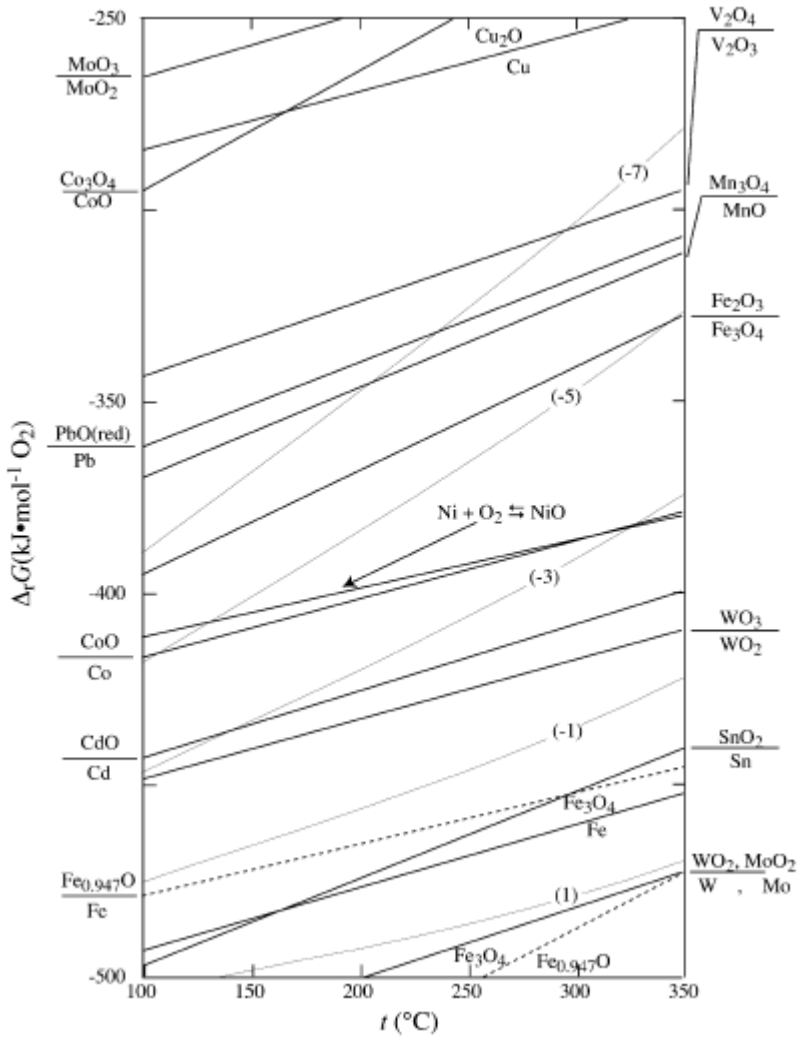

Figure 14.20. From [38]. *Gibbs energies of anhydrous oxidation reactions as a function of temperature.*
Solid lines are stable reaction boundaries, dashed lines are metastable reaction boundaries, thin contours are labeled with the redox state imposed at high temperature by liquid water saturated at 25 °C with a gas having the log$_{10}$ [pH$_2$(g)/p] inidicated (p* = 1 MPa).*

Mixed oxides

Dickinson et al. [103] reviewed literature studies and thermodynamic data regarding the solubility and stability of chromite spinels. They concluded that under conditions of PWR coolant (30 scc/kg hydrogen), $FeCr_2O_4$ is unstable above about 160 °C, and $NiCr_2O_4$ is unstable below about 330 °C.

This is in contrast with well-established observation that chromite oxides form the protective oxide layer on corroding stainless steels (Ni-poor chromite) and Ni base alloys (Ni-rich chromite) in PWR coolant circuit. One possible explanation is that hydrogen fugacity is higher within the protective oxide layer, especially at the oxide-alloy boundary where it is controlled at the characteristic fugacity of the oxidation reaction.

The mixed oxides are unstable with respect to the following decomposition reactions, from which the critical hydrogen fugacity can be derived, and has been plotted in Figure 14.21 (i) and (ii):

$$FeCr_2O_4 + \frac{4}{3}H_2O = \frac{1}{3}Fe_3O_4 + 2CrOOH + \frac{1}{3}H_2(g)$$

$$NiCr_2O_4 + H_2(g) = Ni + 2CrOOH$$

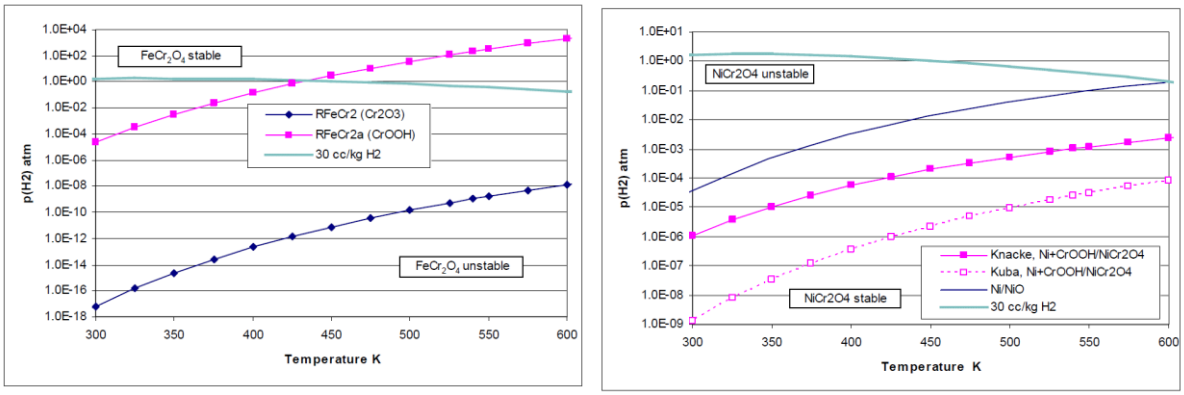

Figure 14.21. (i) Equilbrium H_2 pressure for $FeCr_2O_4$ (ii) Equilbrium H_2 pressure for $NiCr_2O_4$ decomposition and Ni oxidation. Both from [103].

Taking account of elevated hydrogen fugacity within the oxide makes the local stability of ferrous chromite more plausible, but makes nickel chromite even less stable.

A better explanation is that the respective mixed oxide phases genuinely are thermodynamically unstable, and that the solubility controlling phase at the surface of chromite oxide surfaces is actually CrOOH. CrOOH was observed as a surface phase on $FeCr_2O_4$ crystallites used in Ziemniak et al.'s solubility study [102]. Solid state oxide decomposition reactions are known to be extremely sluggish [74], [185], and the continual corrosion of Fe-Cr-Ni alloys is inherently a non-equilibrium process. Kinetics considerations may limit the formation of CrOOH at the oxide alloy interface.

The negative Gibbs energy of mixing for non-stoichiometric oxide compositions was not considered. Published expressions for $ZnCr_2O_4$ and $CoCr_2O_4$ indicated they were much more stable than $NiCr_2O_4$ and unlikely to decompose in PWR coolant.

Summary – phase diagrams

The stable phases for any solid state composition can be depicted by a phase diagram such as the one shown in Figure 14.22. The lower-left corner represents 100% Ni, the lower-right corner represents 100% Fe, and the top corner represents 100% Cr.

The three corners represent the purest (monometallic) form of the most stable phase of their respective element, being Ni metal, CrOOH, and Fe_3O_4. The ferrite phase, of which Fe_3O_4 is an end-member, is fully miscible with $NiFe_2O_4$, and also has a reasonably high solid solubility of Cr(III).

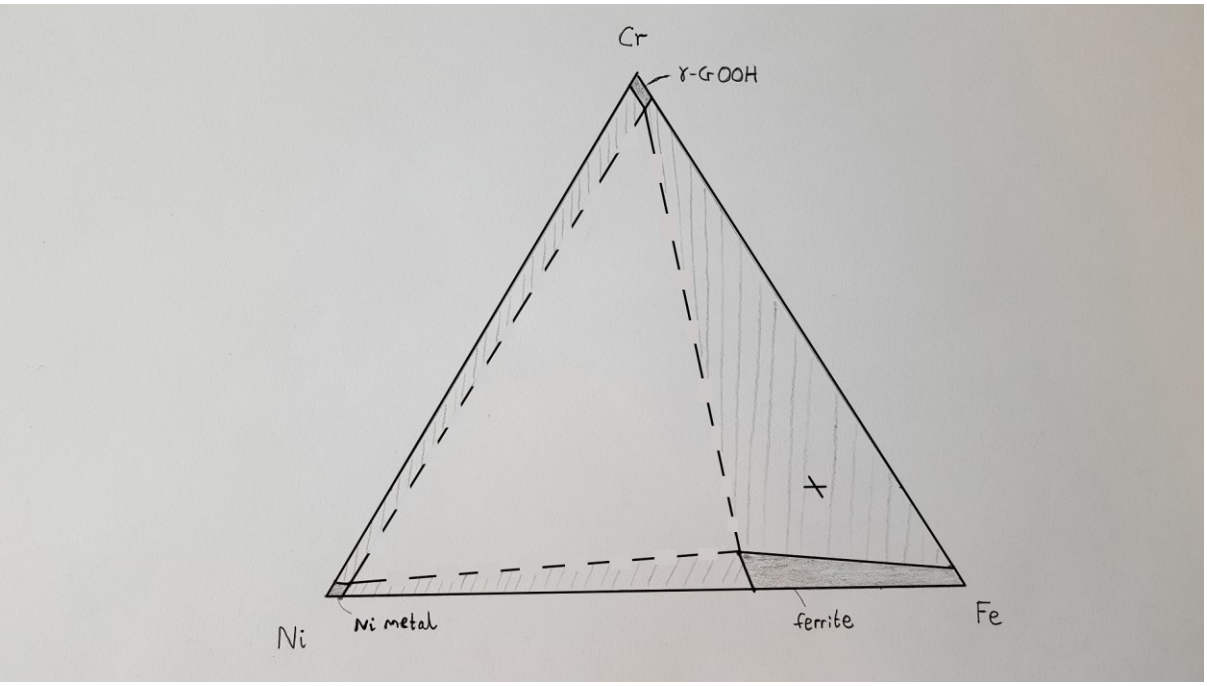

Figure 14.22. Approximate phase diagram for the Fe-Cr-Ni-H_2O system at 300 °C, 100 bar pressure, 1 bar hydrogen fugacity.
Shaded regions represent the presence of a single solid phase. Hatched regions represent compositions which cannot be accommodated by a single phase, and therefore indicate the simultaneous presence of the two adjoining phases. The unshaded region of composition space is achieved by the simultaneous presence of all three phases, at compositions represented by the three vertices of its triangular shape.

Just three stable phases are included in Figure 14.22 above: nickel metal; γ-CrOOH; and ferrite. The decision to omit the chromite phase is based on the findings of Dickinson et al. [103].

For the phases CrOOH and Ni metal, a brief literature search did not yield information on the solid state solubility of each other phase in those phases, so a nominal solubility of around 3% (metals basis) was assumed in each case for illustrative purposes.

For ferrite, the two end-member phases, magnetite (Fe_3O_4) and trevorite ($NiFe_2O_4$), are known to be fully miscible, as is also the case for the equivalent chromite end-member phases. Equilibria between magnetite and the ferrous chromite phase (nominally $FeCr_2O_4$), and between trevorite and the nickel chromite phase (nominally $NiCr_2O_4$) were modelled by other workers [74], [85], based on an experimental study, and this data was the basis for the extent of the ferrite region in the diagram. Although the equilibrium in this case is with CrOOH, the relatively small negative value of ΔG^0_R (573.15 K) for the reaction $FeCr_2O_4 + \frac{4}{3}H_2O = \frac{1}{3}Fe_3O_4 + 2CrOOH + \frac{1}{3}H_2$, as per the data used in the Dickinson et al. paper, means that the chromium content of ferrites in equilibrium with a Cr(III)-containing oxide phase will be similar whether that phase is CrOOH or $FeCr_2O_4$. In the same paper, the equivalent decomposition reaction of nichromite, $NiCr_2O_4 + H_2 = Ni(cr) + 2CrOOH$, was found to have a more negative value of ΔG^0_R (573.15 K), of around -20 to -40 kJ/mol, based on purely thermodynamic considerations. This more significant instability could result in a noticeably lesser Cr content in nickel ferrite when in equilibrium with CrOOH (and Ni metal) instead of nickel chromite (and Ni metal), but this was not reflected in the diagram for the sake of simplicity. Indeed, the greater maximum Cr content of nickel ferrite compared with magnetite (7% versus 3%, metals basis) in the studies of Ziemniak et al. may be due in part to the fact that the nickel saturated end-member of the nickel/ferrous chromite phase (nickel chromite) was more unstable than the nickel-free end member (magnetite), and would therefore be at equilibrium with a greater activity of Cr(III) ions in solution.

A second phase diagram is included below, under the same conditions, but with chromite included as a stable or meta-stable phase (Figure 14.23). The chromite composition in equilibrium with ferrite is as per the Ziemniak et al. studies mentioned above, having (on a metals basis) 0% or 33% Ni for the respective end-members, ~47% Cr in either case, and the balance as Fe. A linear interpolation between end-members is assumed in the plot, and a nominally slightly more Cr-rich composition is plotted for the equilibrium with CrOOH for illustrative purposes.

A cross is marked on each diagram, representing the composition of SS316L, if elements other than Fe, Cr Ni are neglected. The other alloying elements may incorporate more readily in some phases than others, depending on their dominant oxidation state under prevailing conditions, altering the effective composition slightly, but this should not affect the conclusion from the diagrams that for corroding SS316L in PWR primary coolant or equivalent conditions, the alloy should oxidise over

time to become ferrite in metastable equilibrium with chromite (Figure 14.23), provided the kinetics of chromite formation are favourable compared with γ-CrOOH (as is observed), and the corrosion products would eventually become ferrite in solid state equilibrium with γ-CrOOH (Figure 14.22), given sufficient time.

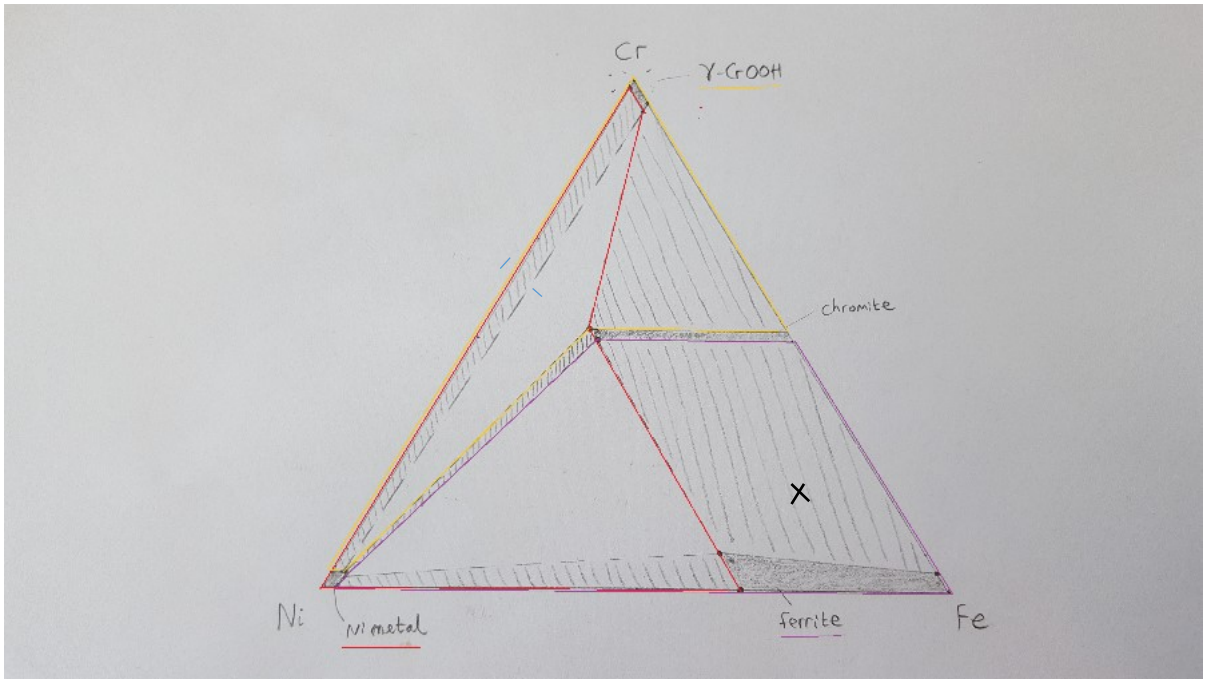

Figure 14.23. Approximate phase diagram for the Fe-Cr-Ni-H_2O system at 300 °C, 100 bar pressure, 1 bar hydrogen fugacity.
This phase diagram follows the same logic as the previous one, but with the chromite phase included as a meta-stable phase. Chromite is also present as a stable phase under higher hydrogen fugacity and/or lower temperatures.

Fe oxides

On increasing redox potential, the stable Fe-based solid phase changes from Fe^0 metal or alloy, to $Fe(OH)_2$, to Fe_3O_4, and finally to Fe_2O_3.

On increasing temperature under reducing conditions, $Fe(OH)_2$ is replaced by Fe_3O_4 as the stable phase. The temperature of transition depends on redox conditions, and is 120 °C for solutions saturated in 1 atm. of H_2 at 25 °C (17.7 scc/kg H_2).

Cr(III) oxides

Up to around 50 °C, $Cr(OH)_3.xH_20$ is the stable phase. This is an amorphous phase resulting from the aging of stoichiometric crystalline $Cr(OH)_3.3H_20$ in solution [102]. The stable phase on up to around

300 to 325 °C is γ-CrOOH. This phase has no mineral name, and is isomorphous with γ-FeOOH, lepidocrocite [102].

14.3.3. Temperature dependence of solution parameters

The key parameters of the solution which feature in equation (12) – pH_T, log $\{H_2\}$ and log $\gamma_{z+/z-}$ – have a temperature dependence which in general depends on the entire chemical make-up of the solution, and any changes to that composition with changing temperature (for example a change in the molality of dissolved metal oxide due to temperature dependence of solubility). In many contexts, however, the solution can be well approximated by a model solution having fixed hydrogen molality, a fixed molal concentration of either strong acid or strong base, and no other constituents besides water. 100% dissociation of the acid or base is assumed.

Equations describing temperature dependence of solution parameters for a model solution

Ignoring the effect of gammas, simple relationships for pH_T or pOH_T are obtained for the use of acidic or basic solutions respectively:

$$pH_T = -\log[acid]_{\underline{m}} + \log \rho_w(T). \quad (23)$$

$$pOH_T = -\log[base]_{\underline{m}} + \log \rho_w(T). \quad (24).$$

Since it is pH_T rather than pOH_T which features in equation (12), it is necessary to express alkalinity in terms of pH_T for the alkaline case described by eq (24), as follows:

$$pH_T = pK_w(T) + \log[base]_{\underline{m}} - \log \rho_w(T). \quad (25)$$

From the relation $\{H_2\}(T) = K_H(T).\frac{[H_2]_{\underline{m}}}{[H_2O]_{\underline{m}}}$, where $K_H(T)$ is the Henry's law coefficient of solubility, the temperature dependence of hydrogen fugacity can be derived:

$$\log\{H_2\}(T) = \log K_H(T) + \log[H_2]_{\underline{m}} - \log[H_2O]_{\underline{m}} \quad (26)$$

Equations (23) or (25), and (26), can be used in conjunction with (12) and (13) to explore temperature dependence of log c values and log solubility for realistic solutions of particular composition, rather than for pH_T and log $\{H_2\}$ constrained to be constant.

Splitting solution parameters into temperature independent and temperature dependent components

It can be instructive to consider separately the effects of a baseline change in pH_T and log H_2 from zero – which produces an upward or downward shift in the various log c(T) curves compared with log K(T), but preserves their temperature dependence, from the temperature-dependent aspect of these solution parameters – which alters the temperature-dependence of log c(T) curves (and ultimately the solubility). Here, the baseline change is evaluated at 298.15 K, though a different temperature such as 573.15 K could equally have been chosen. Solution parameters can now be written as:

$$pH_T = pH_{298K} + \Delta pH_T \quad (27)$$

$$\log\{H_2\}_T = \log\{H_2\}_{298K} + \Delta \log\{H_2\}_T \quad (28).$$

Temperature dependent component of $\log\{H_2\}_T$, $\Delta\log\{H_2\}_T$

The curve for $\Delta \log\{H_2\}_T$ is the same for all solutions, and is plotted in Figure 14.24 below.

$$\Delta \log\{H_2\}_T = \log K_H(T) - \log K_H(298K) \quad (29).$$

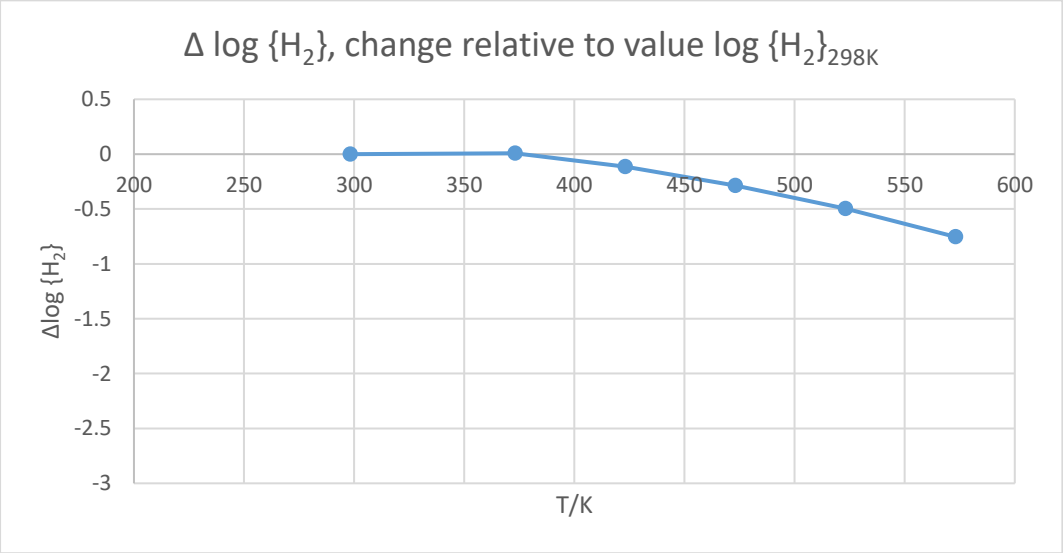

Figure 14.24. Plot of Δ log {H_2} as a function of temperature. That is, the change in log {H_2} on bringing a solution of fixed hydrogen concentration up to a given temperature from 25 °C.

Temperature dependent component of pH_T, ΔpH_T

The curve for ΔpH_T depends on what kind of pH reagent is added to the solution (acid or base), and to what extent it dominates the temperature dependent contribution of H^+ ions already present from the dissociation of water. Three equations and curves are presented below, for the cases of: (i) strong acid, with pH_T significantly lower than the lowest value of neutral pH_T; (ii) strong base, with pOH_T significantly lower than the lowest value of neutral pOH_T; and (iii) neutral solution, no pH reagent added. Curves are presented in Figure 14.25.

$$Acid: \quad \Delta pH_T = 0 \qquad (30);$$

$$Base: \quad \Delta pH_T = pK_w(T) - pK_w(298K) \qquad (31);$$

$$neutral: \quad \Delta pH_T = \frac{1}{2}\left(pK_w(T) - pK_w(298K)\right) \qquad (32).$$

Where the molality of acid or base is low – say, below ~ 10^{-6} m – the curve of ΔpH_T is intermediate between the case presented below for acid or base, and the neutral pH case.

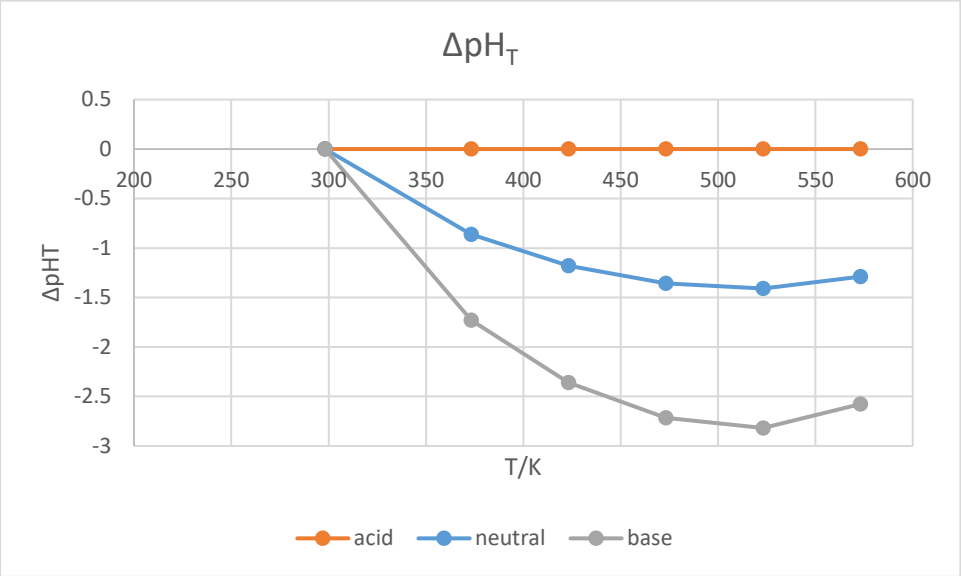

Figure 14.25. Plot of ΔpH_T as a funtion of temperature, for three cases of model solution (strong acid, strong base, pH neutral). That is, the change in pH_T on bringing a model solution up to a given temperature from 25 °C.

14.3.4. Format used for presenting data and plots for each oxide

In the following sections – one for each oxide – data, plots and explanations regarding specific solubility behaviour of the oxide and its soluble species follow the format outlined below.

Temperature dependent solubility constants, $K_{eq}(T)$

For each oxide, just one source of data is selected for producing a full set of temperature dependent K values for the soluble species, to ensure a self-consistent data set. The data generally come in the form of thermodynamic quantities ΔH^0, ΔS^0, and ΔC_p, as parameters in either a two- or three-parameter fit as described by equations (22) and (20) respectively, see section 14.2.3.

The form of the fit is stated, and the parameters listed in a table. The K values are defined for the production of each soluble species from the oxide, as per equations (8) and (9). For hydrous oxides – i.e. those containing hydrogen atoms – the quantity 2j/i in equations (8) and (9) and related equations (such as (12)), can be replaced by the mean oxidation state of the metal ions in the hydrous oxide. Curves for log K(T) are plotted against T for each species on a single set of axes.

Temperature-dependent solubility, for fixed pH_T and log $\{H_2\}_T$

Plotted curves of log K(T) versus T give the activity of each species directly, for the specific conditions where pH_T and log $\{H_2\}_T$ are both fixed at zero. Applying the approximation log $\gamma \approx 0$ for dilute solutions, the curves represent a good approximation of log $c_{z,l}$ curves, and thus also temperature-dependence of solubility via eq (13). These results can be extrapolated to any other conditions of fixed pH_T and log $\{H_2\}_T$, simply by shifting the curve of log c for each species up or down, according to eq (12) – the same temperature dependent form is maintained for each species, though the absolute values and temperature-dependence of solubility changes as different species come to dominate under different conditions.

A full set of log c's and the log of the resulting solubility, as derived in the manner described above, are plotted against T for selected conditions of pH_T and log $\{H_2\}_T$.

Temperature-dependent solubility, for a model solution of fixed composition

As discussed in section 14.3.3, parameters of the solution, such as pH_T and log $\{H_2\}_T$, vary with temperature in general, in a way which depends on the full chemical composition of the solution, yet in many applications this temperature dependence can be well described by that of a model solution having fixed molality, both of hydrogen gas, and of a strong acid or base. Temperature dependent pH_T and log $\{H_2\}_T$ can each be split into constant and temperature-dependent parts, as per equations (27) and (28). In this way, plots can be produced in the manner of section 14.3.4.(ii) above, with pH and log $\{H_2\}$ fixed at their 298.15 K values; and the temperature-dependent form of each log c can then be modified by the appropriate curves of ΔpH_T and Δlog $\{H_2\}_T$, as plotted in Figure 14.24 and Figure 14.25.

A full set of log c's and the log of the resulting solubility, as derived in the manner described above, are plotted against T for selected conditions of pH_{298K} and log $\{H_2\}_{298K}$. Similar plots taken directly from the literature are also presented, where available.

Solubility behaviour at fixed temperature, with changing solution parameters

A selection of plots from the literature are included, to further elucidate the solubility behaviour – for example Pourbaix diagrams, at selected temperatures.

Discussion

Implications of the above on solubility behaviour are discussed.

14.3.5. Magnetite, Fe_3O_4

Temperature dependent solubility constants, K_{eq}

Temperature-dependent Keq values for magnetite are (re)produced here using temperature-independent values of ΔH^0 and ΔS^0, published by Tremaine and LeBlanc [121], which were fitting parameters in a least squares fit to their high temperature solubility data, according to relations similar to equations (12) and (13). Solubility data were taken across a wide range of temperatures and $pH_{298.15K}$ values: at 373.15 K – 573.15 K; and $pH_{298.15K}$ ~ 3 – 13, controlled by a strong base (LiOH) or a strong acid (HCl). Most data were taken at 779 µm hydrogen (1 atmosphere at 25 °C), though some were taken at 77.9 µm and 8570 µm.

The resulting fit for each species follows the form of equation (22). The fit was performed over the range 298.15 K – 573.15 K, and constrained by the relation $\Delta H^0_{fit} - 298.15.\Delta S^0_{fit} = \Delta G^0_{298.15K}$ for each species. Values of $\Delta G^0_{298.15K}$ were selected by Tremaine and LeBlanc from literature data available at the time. Some use was also made of other literature data and measurements of the dissolved Fe oxidation state, especially regarding redox reactions between ferric and ferrous species. The resulting temperature dependent K(T) curves are plotted below in Figure 14.26.

The fitting parameters for each species are provided in Table 14.3 below, along with coefficients of pH_T dependence, -(z-l), and log $\{H_2\}_T$ dependence, -1/2(z-2j/i), for each log c. Tremaine and LeBlanc presented their two parameter fit to $\Delta G^0(T)$ in an equivalent but different form to equation 21, as $\Delta G^0(T) = \Delta G^0_{298.15K} - (T/K - 298.15)\Delta S^0_{fit}$, and so these were the only two paramaters for which data and errors were published. In addition to these, calculated ΔH^0_{fit} values are included in Table 14.3 for illustrative purposes, without an assessment of error.

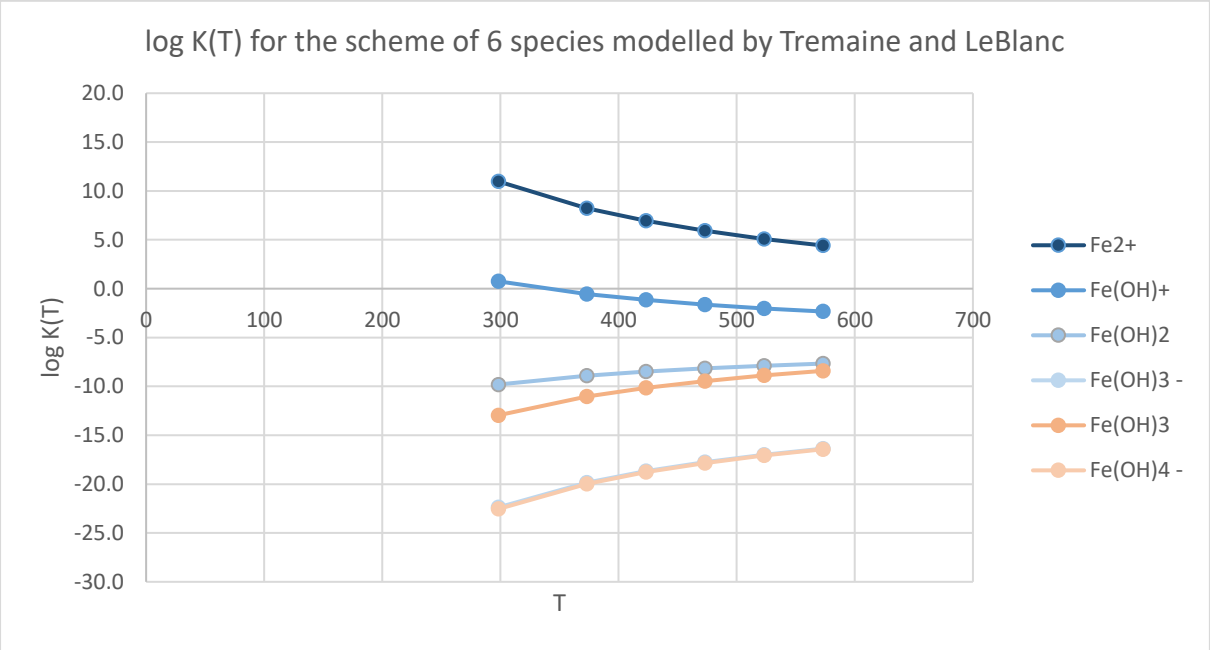

Figure 14.26. Temperature dependence of log K(T) for the various aqueous species whose combined concentrations make up the solubility of the iron oxide magnetite. Using data from [121].
Note the similarity between the two species of neutral charge, $Fe(OH)_2$ and $Fe(OH)_3$, and the species of single negative charge, $Fe(OH)_3^-$ and $Fe(OH)_4^-$ (which are so close as to be indistinguishable on the graph). This shows that at a hydrogen fugacity of 1 bar, the negatively charged species are present at almost equal activity. The neutrally charged species are present at equal activity for a hydrogen fugacity of around 10^{-4} bar at 150 °C. This falls to ~ 10^{-6} bar at 25 °C, and rises to ~ 10^{-1} bar at 300 °C.

Table 14.3. Thermodynamic data [121] *and other related data pertaining to magnetite solubility*

Soluble species	$\Delta G^0_{298.15K}\ (kJ/mol)$	$\Delta H^0_{fit}\ (kJ/mol)$	$\Delta S^0_{fit}\ (J/mol/K)$	$-(z-l)$	$-\frac{1}{2}\left(z-\frac{2j}{i}\right)$
Fe^{2+}	-62.70 +/- 0.43	-78.09	-51.63 +/- 3.29	-2	1/3
$FeOH^+$	-4.30 +/- 1.77	-36.52	-108.96 +/- 17	-1	1/3
$Fe(OH)_2$	56.03 +/- 0.78	25.51	-102.35 +/- 3.61	0	1/3
$Fe(OH)_3$	≤74.0	≤54.14	-66.60 +/- ~ 3.3	0	-1/6
$Fe(OH)_3^-$	127.84 +/- 1.66	71.58	-188.71 +/- 6.71	1	1/3
$Fe(OH)_4^-$	128.80 +/- 1.0 (sic.)	27.82	-187.76 +/- ~ 3.3	1	-1/6

Temperature-dependent solubility, for fixed pH_T and log $\{H_2\}_T$

As discussed in section 14.3.4, curves of temperature dependent log c(T) (neglecting effect of gammas), for conditions of fixed pH_T and log $\{H_2\}_T$, can be produced by simply shifting log K(T) curves in Figure 14.26 above, according to equation (12). For convenience, the last two columns of Table 14.3 show the extent to which curves of log c for each soluble species shift up or down, according to pH_T and log $\{H_2\}_T$ respectively.

Figure 14.27 below shows plots of log c for each species, from equation (13), for selected conditions of fixed pH_T and log $\{H_2\}_T$.

Moving from left to right, in the middle row of plots in Figure 14.27 (log H_2 = 0), dominance shifts from Fe^{2+} at low pH, to $Fe(OH)_3^-$ / $Fe(OH)_4^-$ at high pH (curves for the two species are almost identical at log H_2 = 0, reflecting their very similar thermodynamic quantities, see Table 14.3). At intermediate pH, dominance is shared between several species, depending on the temperature. For pH 8, Fe^{2+} becomes increasingly the dominant species as temperature decreases to the lower end of the range, and $Fe(OH)_2$ (aq), having positive temperature dependence, dominates at higher temperatures, above about 150 °C.

At higher or lower values of log H_2, curves for the ferric species – $Fe(OH)_3$ and $Fe(OH)_4^-$ – shift vertically by an amount -1/6 log H_2, and curves for ferric species – the remainder of species – shift by +1/3 log H_2. At low pH, where Fe^{2+} ions dominate by a large margin, solubility behaviour has unchanged temperature dependence, but increases with log H_2. When conditions are sufficiently oxidising however (low log H_2, < -6), $Fe(OH)_3$ becomes dominant at the higher temperatures even at pH values as low as 4. This causes a solubility minimum with respect to log H_2, as decreasing log H_2 causes solubility to decrease until such a point as the ferric $Fe(OH)_3$ ions take over, at which point solubility increases on decreasing log H_2 further. A similar effect is observed at pH 8, with $Fe(OH)_3$

and $Fe(OH)_4^-$ jointly becoming dominant species around log H_2 = -6 and lower, at the expense of / taking over from Fe^{2+} and $Fe(OH)_2$; and $Fe(OH)_4^-$, and at pH 12, with $Fe(OH)_4^-$ becoming dominant species below log H_2 = 0, taking over from $Fe(OH)_4^-$.

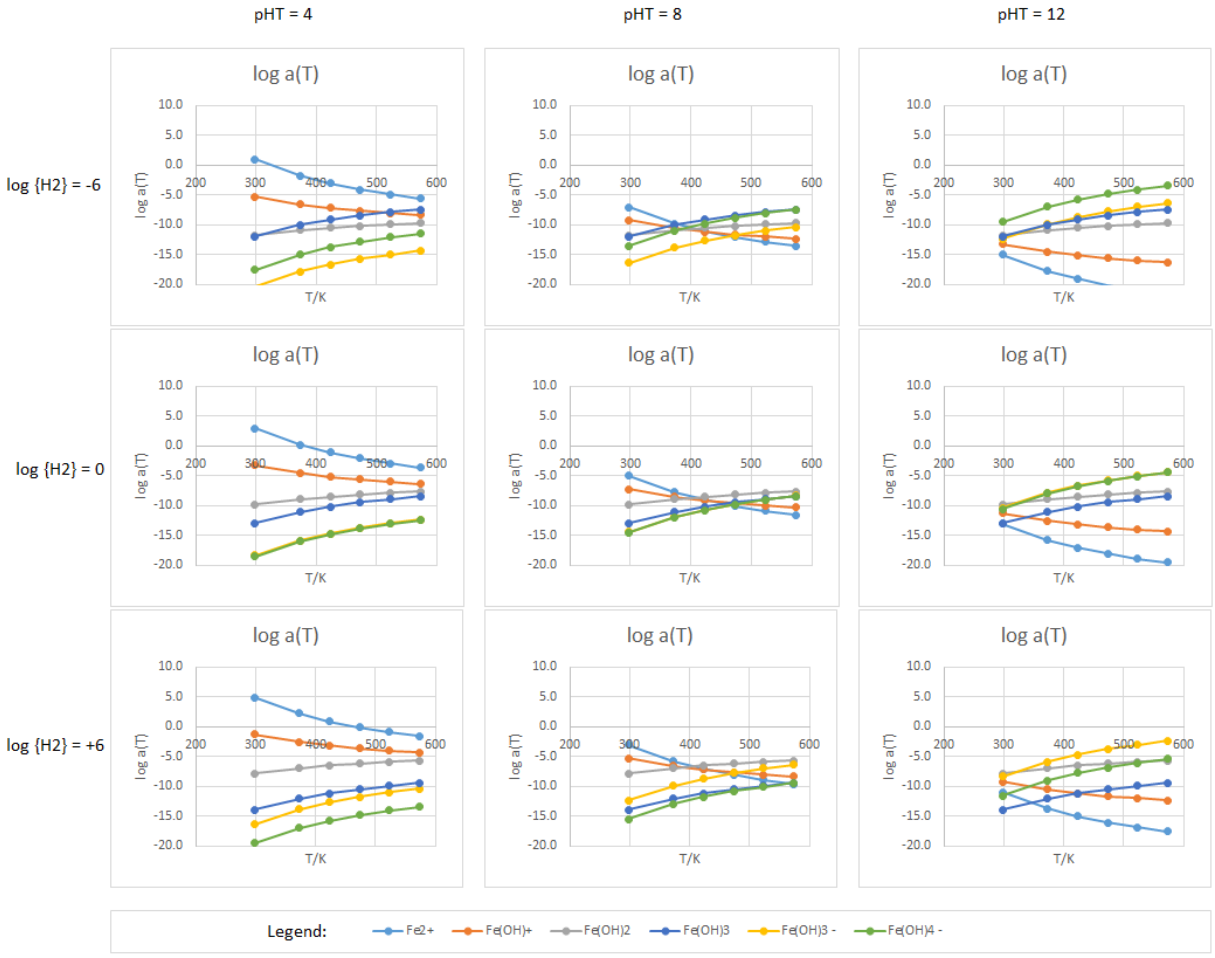

Figure 14.27. Temperature dependent log(a) for selected conditions of fixed pH_T and log $\{H_2\}_T$, where a is the equilibrium activity. Where unitary activity coefficients are assumed, this is equal to equilibrium concentration (solubility) in molal units.

Temperature-dependent solubility, for a model solution of fixed composition

For the plots in this section, values of pH_T and log $\{H_2\}_T$ have been allowed to vary with T as they would for a model solution of fixed composition, as discussed in section 14.3.4. Figure 14.28 shows the resulting plots under a range of conditions. Under neutral or basic conditions, the negative temperature dependence of the two positively charged species, and the positive temperature dependence of both negatively charged species, are in each case somewhat mitigated by the tendency of pH to decrease with temperature, causing higher log c for the positively charged species and lower log c for the negatively charged species than would otherwise have been.

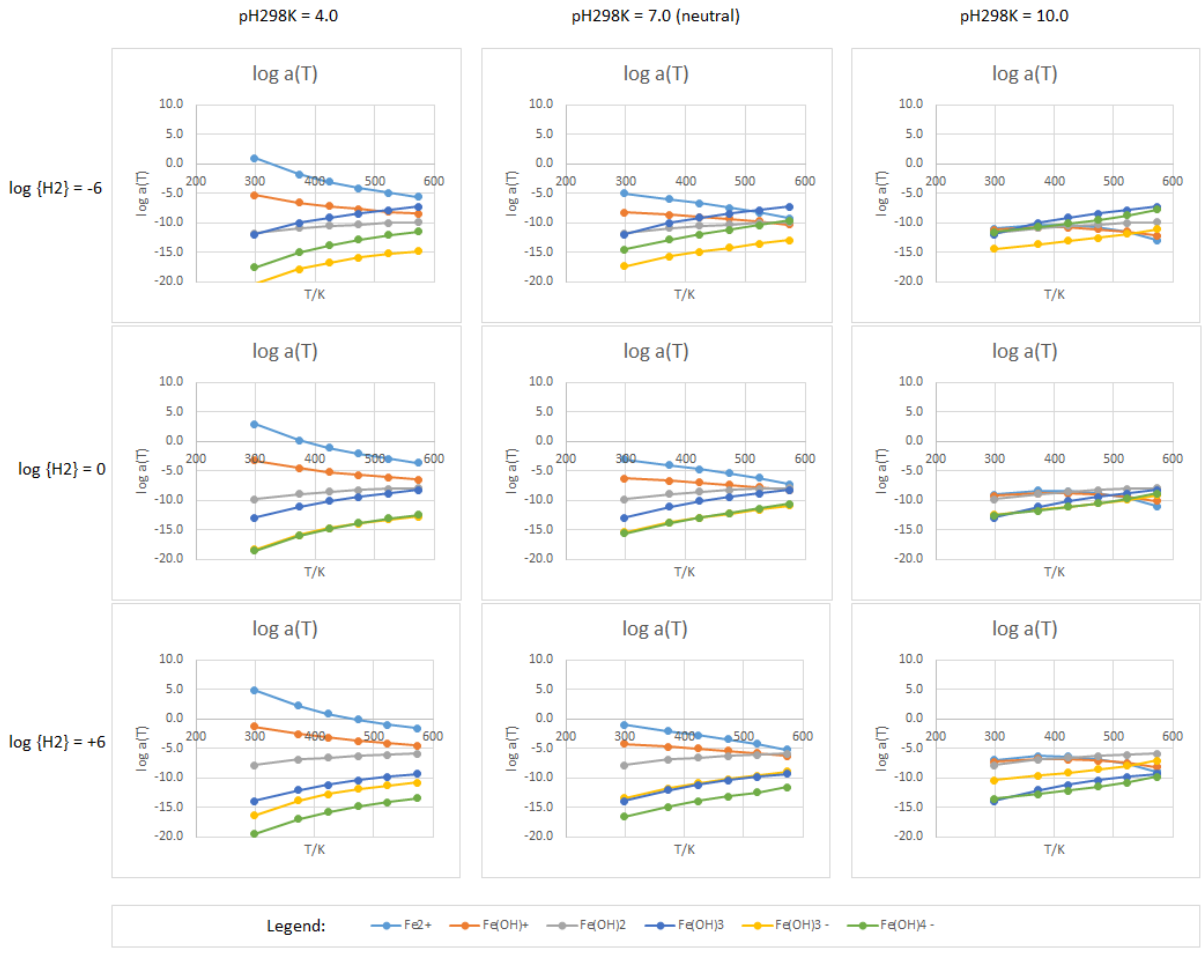

Figure 14.28. Log c curves for model solution, under acidic (pH_{298K} = 4.0), neutral (pH_{298K} = 7.0), and basic (pH_{298K} = 10.0) conditions

The temperature dependence of all species (under any solution conditions) is also affected by the tendency of log H_2 to decrease with temperature, causing log c for ferric species to have a higher at higher temperatures and causing log c for ferrous species to have a lower value at the higher temperatures, compared with what it would otherwise have been.

The combined result of these effects is a different temperature dependence of solubility. At intermediate pH values, where species with a more negative temperature dependence (such as Fe^{2+}) dominate at the lower temperatures, and species with a more positive temperature dependence dominate at higher temperatures, the transition is more gradual; and where one species dominates, the gradient of log c with temperature is less extreme. Compare: the pH_{298K} = 10, log H_2 = 0 plot from Figure 14.28 with pH_T = 8, log H_2 = 0 plot in Figure 14.27 (the solution having pH_{298K} reaches pH_T = 8 at around 125 °C).

In Figure 14.29, curves were plotted in the same manner as for Figure 14.28, for model solutions having the three pH_{298K} values employed in the present study, and two different possible values of log H_2 for comparison. It is thought that actual log H_2 in the hot part of the rig was typically between the two scenarios illustrated, though changes to cumulative corrosion time; flow rate; pH_T; total corroding surface area; and temperature throughout the study will have caused significant variations through the course of the study.

The relatively high levels of ferric species which are likely to have been present at these comparatively low hydrogen concentrations (compared with literature studies, which typically employed log H_2 = 0 at 25 °C), result in lower solubility at 25 °C, higher solubility at 300 °C, and thus a much stronger positive temperature coefficient of solubility. This is problematic, since it greatly increases the tendency for dissolved Fe species from the hot part of the rig to precipitate out as a solid phase in the cold back end of the rig, which is exacerbated by the fact that slow flow rates were employed to minimise particulates, or suspected particulates.

The low level of hydrogen present also means that hematite as a possible stable phase under some conditions experienced by the rig must be considered. This is treated in the next subsection.

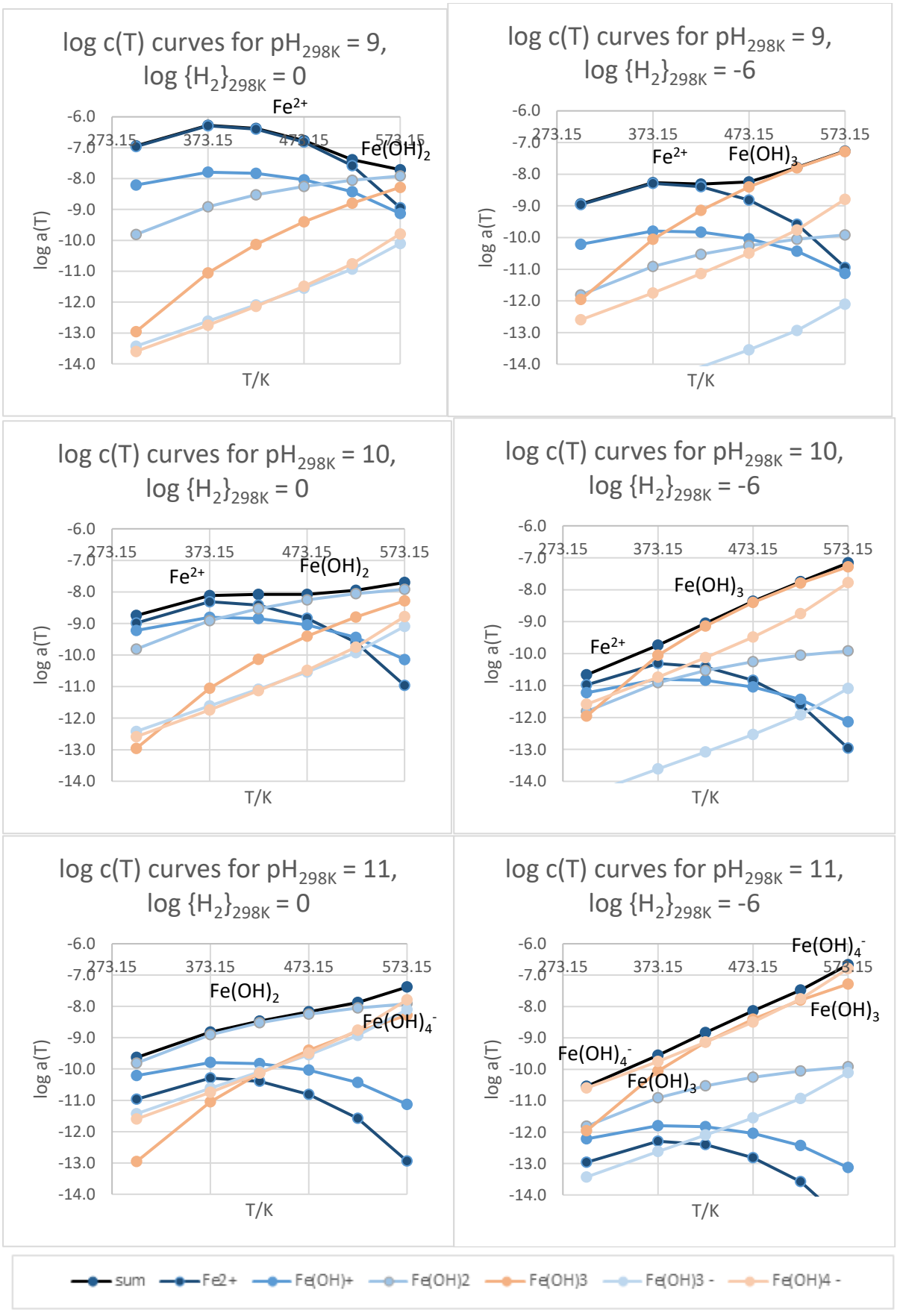

Figure 14.29. Curves for log c(T) for each species, and log sol(T), for selected model solutions.

Figure 14.30 shows the transition from negative to positive temperature dependence of solubility, over the region 373 – 573 K, as pH_{298K} is increased from 9.30 to 10.29.

Figure 14.31 shows solubility as a function of pH_{298K} for magnetite at 300 °C, 1 bar of H_2 at 25 °C. The kink in the curve, observed between around pH_{298K} 6 to 8 is a distortion due to the choice to plot against equi-spaced pH_{298K} values – when plotted against pH_T the plot shows the same form as Figure 14.2 (i.e. monotonically increasing gradient), as expected.

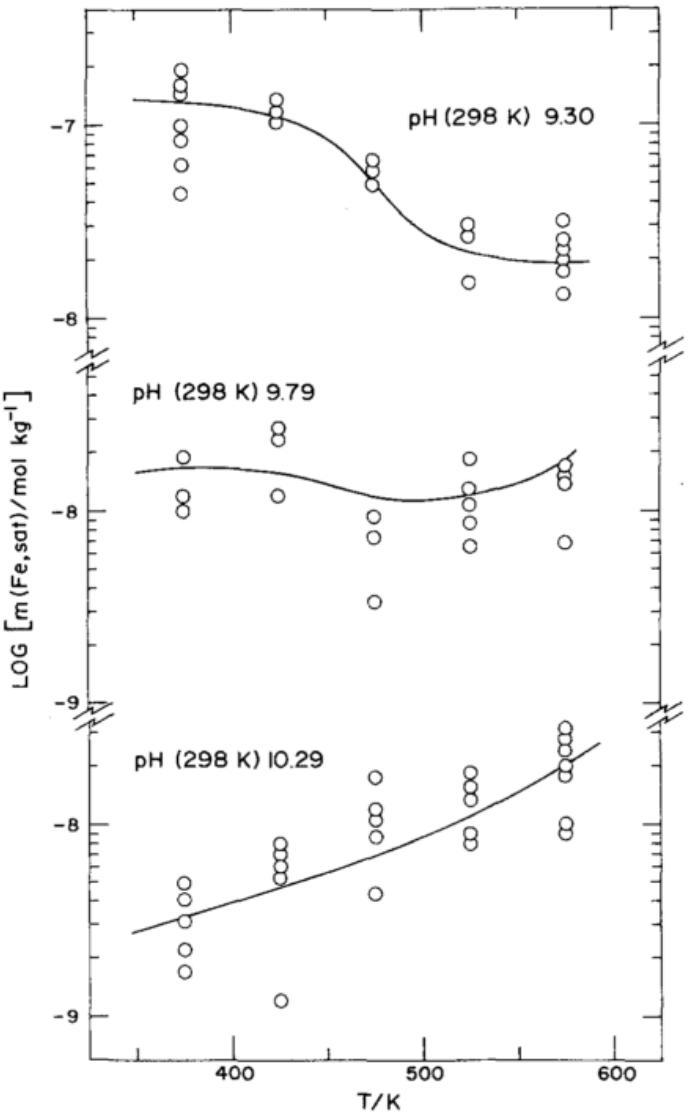

Figure 14.30. Temperature dependence of Fe_3O_4 solubility at log $\{H_2\}_{25C}$ = 0, at pH_{25C} 9.30, 9.79, and 10.29, with least squares fit to the data. From [121].

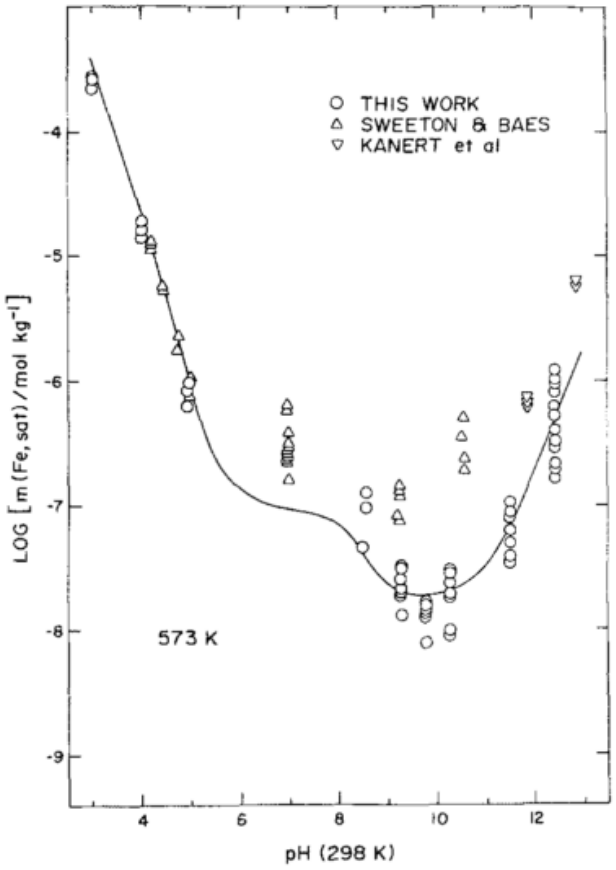

Figure 14.31. Experimental solubilities of magnetite at 300 °C and 1 bar of H_2, against initial pH of the feed solutions. The solid line corresponds to a least squares fit to the data provided by authors of the paper. From [121].

Solubility behaviour at fixed temperature, with changing solution parameters

A figure from Tremaine and LeBlanc illustrates things well in an equivalent way (Figure 14.32). See the 573.15 K end of each curve in Figure 14.30. Now look at Figure 14.32: For log H_2 = 0, the most dominant few species match in either case, except at pH 11, where $Fe(OH)_4^-$ takes over the dominant role slightly earlier in Figure 14.29 than below. This slight discrepancy is probably due to the authors taking into account the effect on pH_T from the soluble species themselves, acting as a weak buffer to bring pH_T closer to the value at which neutral species are most dominant – about pH_T 7 at 573.15 K.

The scale bars at the top (pH_{298K}) and bottom (pH_T) of the figure show how room temperature pH and high temperature pH correspond for the same solution. Neutral pH at 298.15 K (7.0) lines up approximately with neutral pH at T (~5.7), acidic pH values roughly align (though high temperature pH is a little higher due to the strong concentration of Fe^{2+} ions), and basic pH values are lowered at temperature by around 2.6 units – two times the difference in neutral pH values, as expected. The choice to present equal spaced pH_{298K} values (rather than equal spaced pH_T) is the reason for warped appearance of the plot between pH_T 5 and 6.

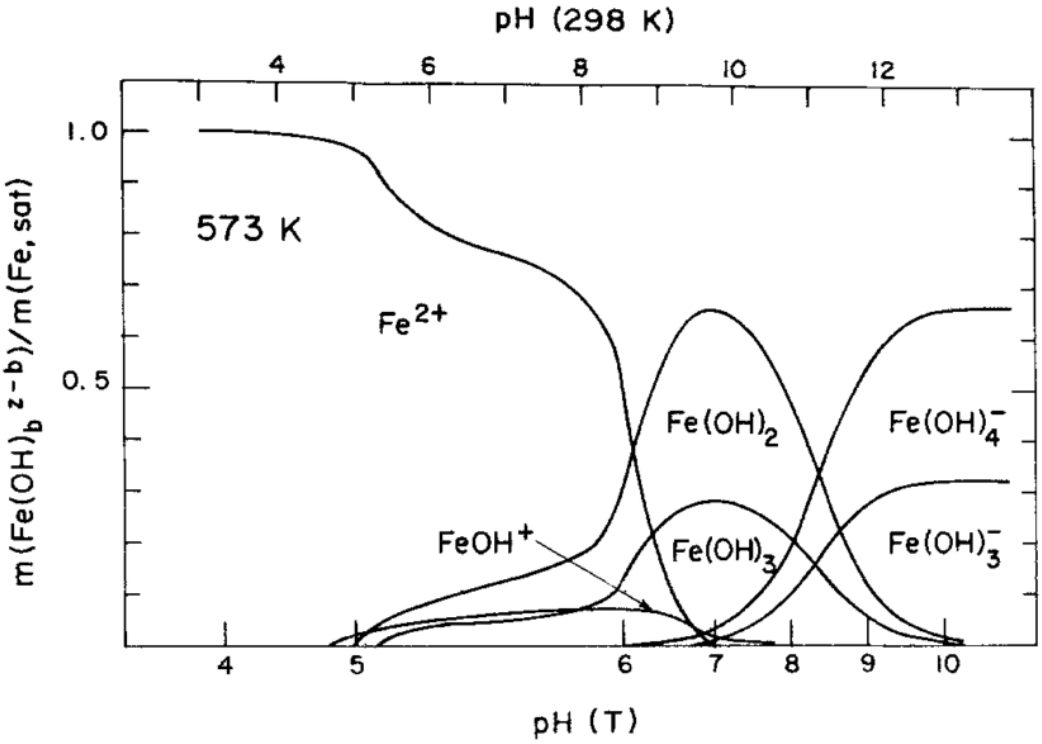

Figure 14.32. Speciation of soluble iron species in equilibrium with magnetite, as a function of pH. Solution contains 1 atm of hydrogen at 25 °C. From [121].

As log $\{H_2\}_{298K}$ is decreased below zero, concentration of ferric species increases whilst concentration of ferrous species decreases. This can be observed in Figure 14.29, but is perhaps illustrated more clearly in Figure 14.32, from [121]. At pH_{298K} 5 and below, Fe^{2+} dominates by a large margin, so solubility $\propto \{H_2\}^{1/3}$; at higher pH values the simultaneous presence of ferrous and ferric species creates a less straightforward dependence on $\{H_2\}$. Where the ratio of ferric:ferrous species is 2:1, the respective dependencies on $\{H_2\}$, of $\{H_2\}^{-1/6}$ and $\{H_2\}^{1/3}$, result in a locally flat dependence on hydrogen activity, and a solubility minimum. The plot below can be thought of as having three different regions of pH_T: ≤ 6, having positively charged ferrous species and a positive dependence of solubility on $\{H_2\}$, being $\propto \{H_2\}^{1/3}$; 6 – 8.3, for which the neutral species dominate, having a slight positive temperature dependence of solubility on $\{H_2\}$, but with $\{H_2\}$ not very much higher than the position for minimum solubility; and ≥ 8.3, for which singly negatively charged species dominate, having a ferric : ferrous ratio of ~ 2:1, and thus temperature dependence of solubility on $\{H_2\}$ is more or less flat and $\{H_2\}$ is at the level for minimum solubility at that pH range.

To summarise the effect of $\{H_2\}$ and pH_T simultaneously, in terms of which species dominates at a given temperature, a potential-pH plot is included in Figure 14.33 below, for T = 573.15 K

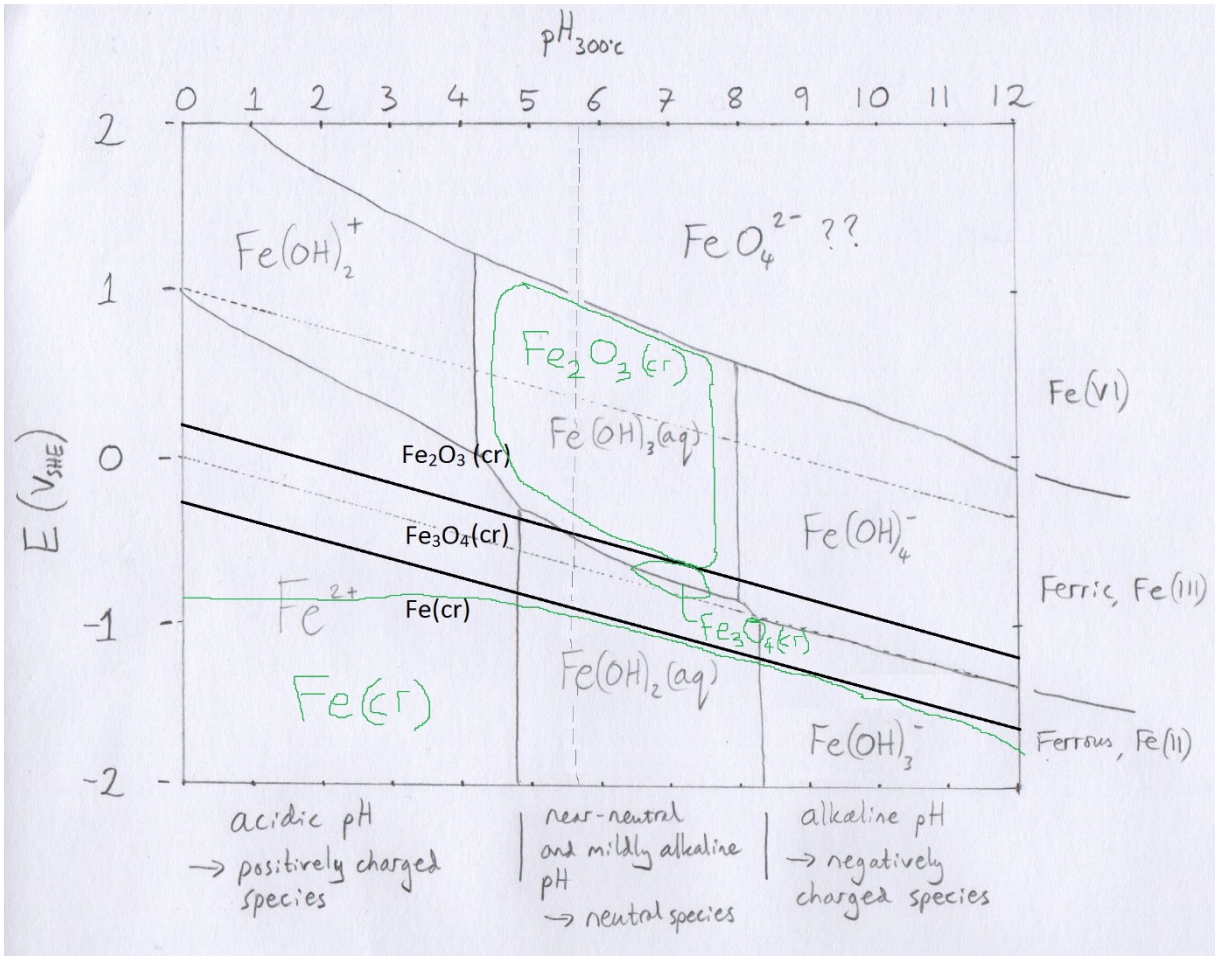

Figure 14.33. A variant of the potential-pH diagram for the system Fe-water at 300 °C, in which both the dominant soluble species and the most stable solid phase are shown for all regions. After [116]*, with some additional annotations from the current author.*
The sloping lines, at zero and ~1 V_{SHE} respectively for pH 0, represent upper and lower stability limits for water against the formation of oxygen or hydrogen gas respectively.

The black lines and typed formulas give regions of stability of oxide phases, and the grey lines and hand-written species names give regions of dominance for the various soluble species. A vertical line is shown at pH_T ~ 5.7, denoting neutral pH_T. Under conditions used in PWR primary coolant, potential is close to but slightly above the lower limit for stability against hydrogen evolution, therefore at near-neutral pH the dominant soluble species is $Fe(OH)_2$ (aq), closely followed by $Fe(OH)_3$ (aq). At 300 °C, the minimum solubility for magnetite is achieved at a pH_T of around 7.2 (pH_{25C} of 10 using LiOH), with redox potential close to that of the dominance boundary between $Fe(OH)_2$ (aq) and $Fe(OH)_3$ (aq). Indeed these are the approximate conditions used in plant, with magnetite solubility considerations being one of the key reasons for that.

The regions bounded in green show where the three respective solid phases are considered most stable in solution, as total solubility in those regions is < 10^{-8} molal.

Discussion

In summary, the combination of prevailing log $\{H_2\}$ and T determines which oxide of iron is thermodynamically stable. These parameters, in addition to pH_T, also determine which species dominate in solution. This is demonstrated for a particular T in the potential-pH diagram.

Where a particular species dominates strongly, the dependence of solubility on various parameters, as well as the solubility itself can be calculated using equation (12), with values of 2j/i and K selected for the appropriate oxide. Otherwise, contributions from each species must be summed, using equations (12) and (13).

The key data for the purposes of determining solubility of a particular oxide are the values of K for the reaction between the oxide and solution to form each soluble species. Differing explicit T dependence of K from one species to another is one reason why different species may dominate as a solution is heated to different temperatures. Another reason is due to the temperature-dependence of solution parameters such as pH_T, which can vary according to the exact solution composition, but for dilute solutions is often dominated by temperature dependence of the dissociation of water. In near neutral to alkaline solutions this effect tends to favour positively charged species at higher temperatures (such as Fe^{2+}), more so than would otherwise have been the case.

In conditions relevant to PWR primary coolant – that is, T ~300 °C, log $\{H_2\}$ ~ 0, and pH_T ~7.2 (equivalent to pH_{298K} ~10 for a simple solution of strong base and hydrogenated water) – magnetite is the stable pure oxide phase for iron. Its solubility reaches a minimum at approximately those conditions (but with $\{H_2\}$ a few orders of magnitude lower), with the dominant species in solution being $Fe(OH)_3$ and $Fe(OH)_2$. Since $\{H_2\}$ is a little higher than the value for minimum solubility, there is a slight positive dependence of solubility on $\{H_2\}$. There is a slight positive temperature dependence of solubility, owing to the presence of $Fe(OH)_2$ complexes, though this temperature dependence becomes flat or slightly negative at lower pH values, owing to the presence of Fe^{2+} ions – see Figure 14.30 and earlier plots.

Under more strongly alkaline conditions of $pH_T > 8$ ($pH_{298K} > 11$), $Fe(OH)_4^-$ and $Fe(OH)_3^-$ become dominant, in a ratio of approximately 2:1. In this case there is more or less flat dependence on $\{H_2\}$, since it is at the value for minimum solubility. Increases of pH_T in this region cause increase in solubility, and there is a strong positive temperature dependence of solubility.

Under less alkaline conditions, where $Fe(OH)_3$ and $Fe(OH)_2$ remain the dominant species at 573.15 K the effect of pH and $\{H_2\}$ remains similar, though the dominance of Fe^{2+} at lower temperatures causes a distinct rise in solubility at lower temperatures (negative temperature dependence of

solubility). As pH is decreased further, Fe^{2+} becomes the dominant species at 573.15 K, and so solubility has a strongly positive dependence on $\{H_2\}$ and negative dependence on temperature.

Implications for the current study

For the current study, solutions having pH_{298K} values of 9, 10 and 11 were used. The feed water was deoxygenated, but no hydrogen was added – the only hydrogen present was that which resulted from corrosion of the SS316L rig. Literature studies suggest that the majority (~90%) of hydrogen produced by corroding steel in a hydrothermal environment is retained within the steel and not released to solution [94], [95]. Conditions of flow rate, temperature, pH, total surface area of corroding alloy, and cumulative corrosion time, will have caused greatly varying levels of hydrogen throughout the course of experimentation. Plots in Figure 14.29 show log H_2 = 0 and log H_2 = -6 scenarios. According to a simple model, hydrogen concentrations were typically between these two limits. The plots suggest a lower solubility at room temperature than high temperatures at pH_{25C} 10 and 11, resulting in precipitation of dissolved iron on walls of the sampling line. At pH_{25C} 9 precipitation of Fe on the sampling line walls may be expected for hydrogen concentrations at the lower end of the range, whereas during periods of high hydrogen fugacity this would not occur, and ionic release from the native corrosion film may occur in the sampling line.

14.3.6. Hematite, Fe_2O_3

Consider the redox reaction between magnetite and hematite, in the presence of hydrogenated water:

$$\frac{1}{3}Fe_3O_4(cr) + \frac{1}{6}H_2O(l) = \frac{1}{2}Fe_2O_3(cr) + \frac{1}{6}H_2(g) \qquad (33).$$

For a certain hydrogen activity, dependent on temperature, the two oxides may co-exist at equilibrium; otherwise only one phase is thermodynamically stable under any given conditions (magnetite where $\{H_2\}$ is greater than the critical value; hematite where it is lower). The solubility for either phase can be defined for any conditions, but refers to a meta-stable equilibrium whenever the other phase is the stable phase.

The critical hydrogen fugacity for equilibrium can be found from thermodynamic data as follows:

$$\log K_{33}(T) = \frac{-0.434}{RT}\Delta G^0_{33}(T) = \frac{1}{6}\log\{H_2\}_{crit,T}\,; \qquad \log\{H_2\}_{crit,T} = \frac{-0.434}{R}.6.\frac{\Delta G^0_{33}(T)}{T} \qquad (34).$$

Due to slow reaction kinetics, there is great uncertainty over the value of ΔG^0 for reaction (33) at room temperature, but less so under thermodynamic conditions. Temperature-dependent $\log\{H_2\}_{crit,T}$ for the above reaction, according to equations (33) and (34), is displayed in Figure 14.34 below, using data from [38] – by comparing parametric fits to ferric ion solubility from magnetite versus hematite, in "table 14.2" of that reference. For illustrative purposes, two representative hydrogen concentrations are also plotted, and 'neutral' hydrogen concentration – that is, concentration in pressurised (one-phase) water with no excess of hydrogen or oxygen and therefore a ratio $[H_2]$:$[O_2]$ of 2, using $H_2O(g)$ dissociation data [186].

Figure 14.35 shows the degree of supersaturation of hematite relative to magnetite at representative hydrogen concentrations. Curves of log K(T), and thus log c(T) for each species, as plotted for magnetite (Figure 14.26 to Figure 14.29), are shifted up by the above curve to give the various log K(T) curves for hematite. Hematite was not stable for any of the conditions employed in the rig of the current project, upstream of the back pressure regulator (BPR). Downstream of the BPR, in the last few mm of sampling line tubing and especially in filters, oxidation from atmospheric oxygen may have caused oxidation to hematite or other Fe(III) oxide phase – see chapter 17 in the appendices.

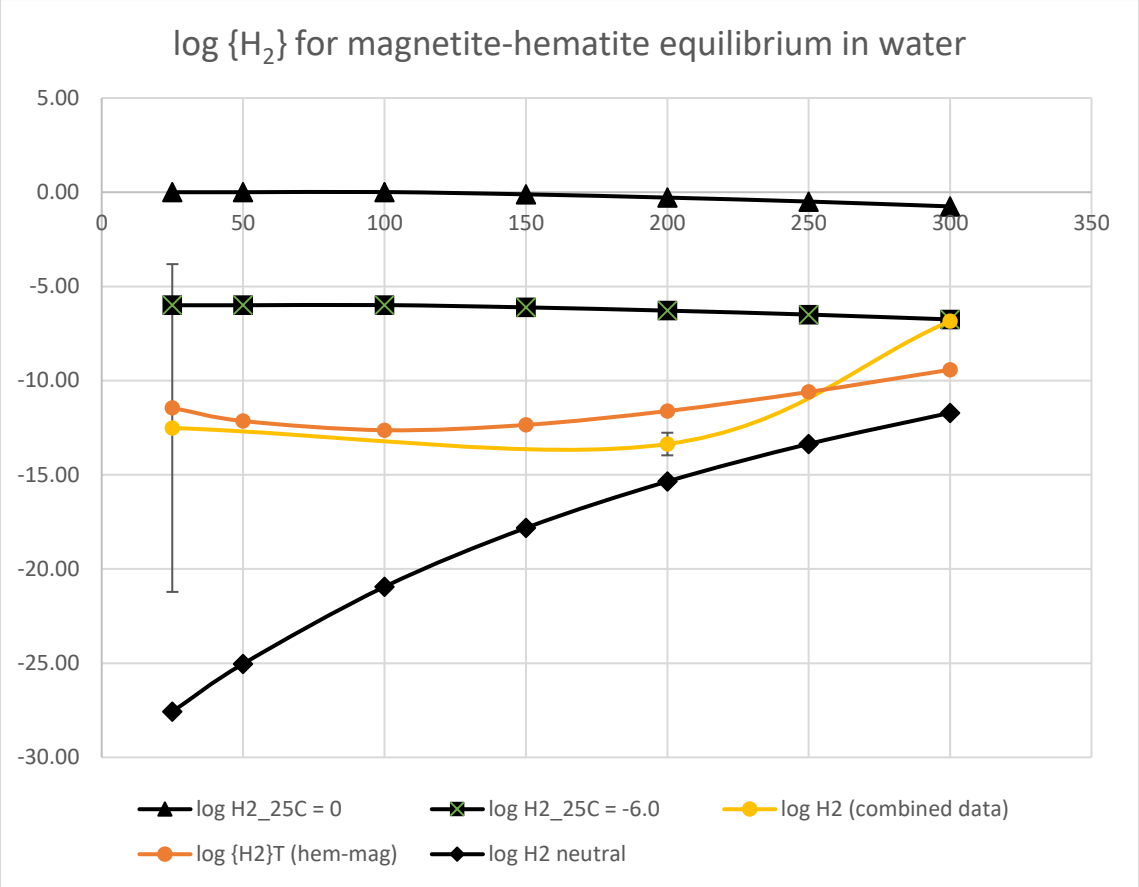

Figure 14.34. Plot showing the approximate temperature dependence of the hydrogen fugacity (as log {H_2}) characteristic of the equilibrium between magnetite and hematite from two different data sources.
Contours of constant hydrogen concentration, and the hydrogen fugacity of pure water, are also shown for reference.

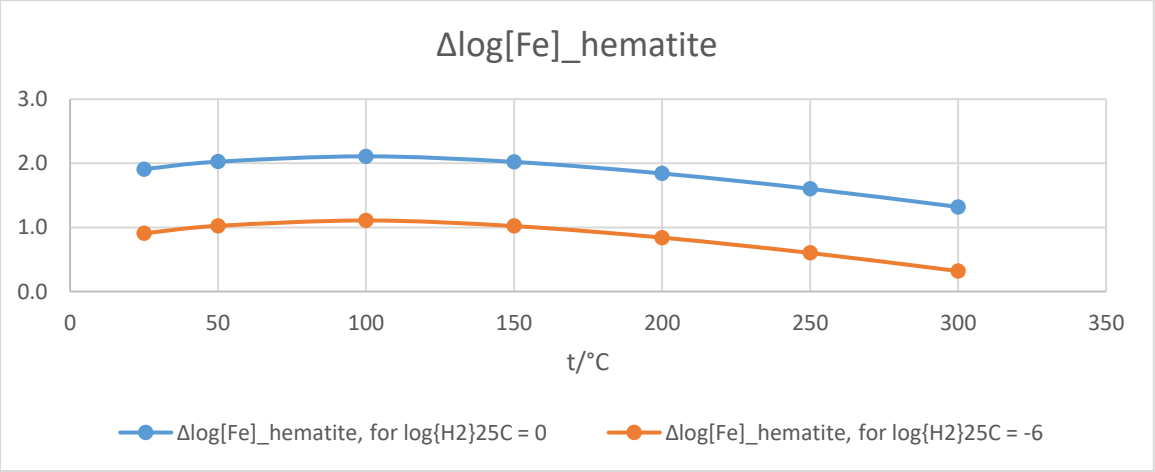

Figure 14.35. Plot showing as a function of temperature the adjustment which must be made to log c as calculated for magnetite, to arrive at the equivalent quantity for hematite solubility.
For every 6 units by which log{H_2}$_{25C}$ decreases, the quantity plotted in the figure decreases by 1 unit. At a value of log{H_2}$_{25C}$ a little above -8, the value of the plotted quantity becomes negative at 300 °C, signifying that hematite replaces magnetite as the stable oxide phase under such conditions.

It can be shown that

$$\left(\log c_{z,l}^{hem} - \log c_{z,l}^{mag}\right) = \frac{1}{6}\log\{H_2\} - \log K_{33} = \frac{1}{6}\left(\log\{H_2\} - \log\{H_2\}_{crit,T}\right) \qquad (34),$$

where $\log K_{z,l}^{phase}$ is for the reaction between an oxide phase (hematite or magnetite) and soluble species as per equations (8) and (9), and ionization coefficients are assumed to equal unity so that $\log c_{z,l}^{phase} = \log K_{z,l}^{phase}$. This was the basis used for calculating $\log\{H_2\}_{crit}$ in the plot above. The blue curve in Figure 14.35 is essentially log K_{33} from equation (33), adjusted by +1/6 Δlog $\{H_2\}$ from Figure 14.10 which changes from 0.000 at 25 °C to -0.125 (-0.75 x 1/6) at 300 °C.

Under oxidising conditions other Fe(III) oxides / hydroxides may occur at room temperature as metastable phases, despite having apparently marginally higher Gibbs energy than Fe_2O_3 at room temperature.

Under sufficiently oxidising conditions for hematite to be stable, solubility in the range pH_{25C} 9 – 11 is dominated by soluble species of oxidation state +3 (ferric). Therefore hematite solubility has minimal or zero sensitivity to hydrogen fugacity, since Fe within hematite is also in the +3 oxidation state. Figure 14.36 shows hematite solubility when hydrogen fugacity is controlled by equilibrium with magnetite. At more oxidising conditions there is minimal difference, though the solubility below about 50 °C is fractionally lower when ferrous (+2) species are entirely absent. Figure 14.37 presents the same data as shown in Figure 14.36, but on a logarithmic scale to allow differences at low ppb concentrations to be discerned. For reference, a value of -8 on the y axis represents 0.6 ppb Fe.

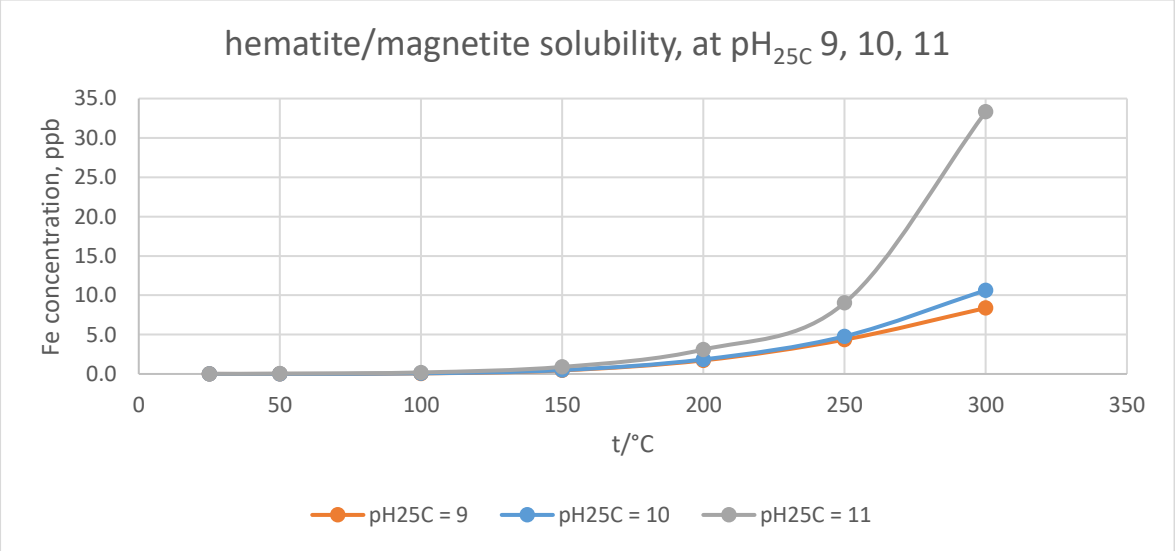

Figure 14.36. Temperature dependent solubility of hematite or magnetite, under hydrogen fugacity conditions present at hematite-magnetite equilibrium, at pH_{25C} 9, 10, and 11.

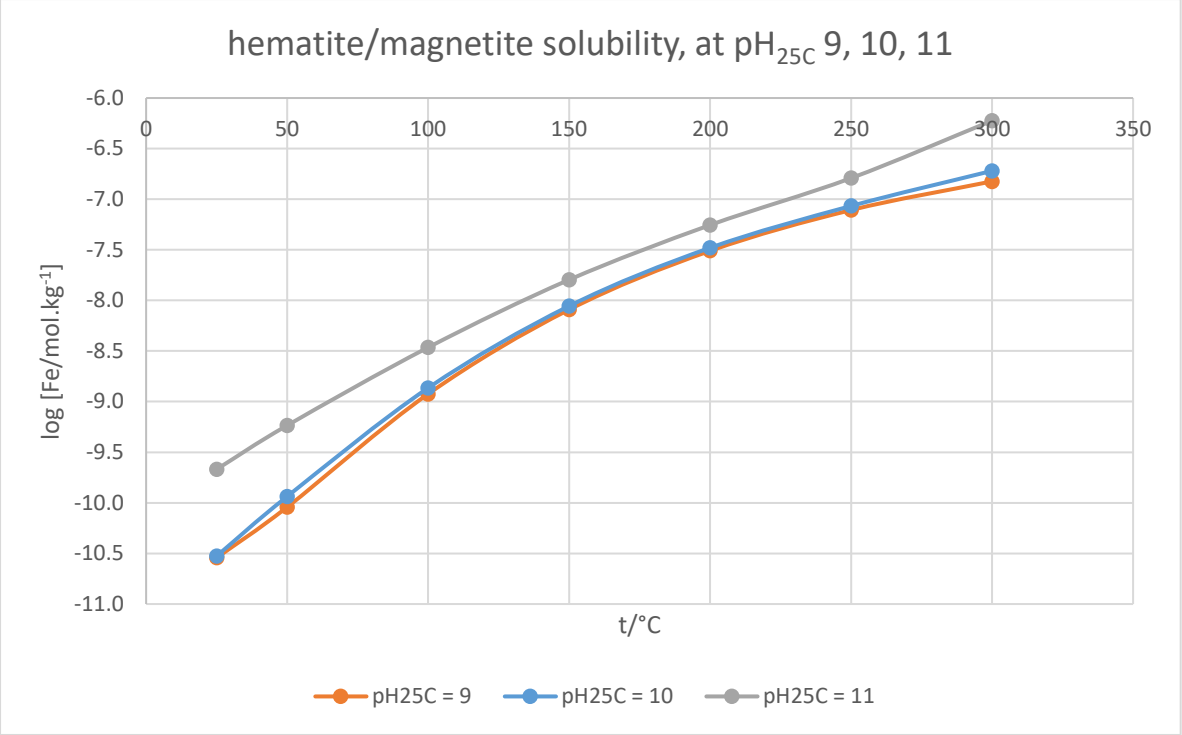

Figure 14.37. The logarithm of temperature-dependent solubility of hematite or magnetite, under hydrogen fugacity conditions present at hematite-magnetite equilibrium, at pH_{25C} 9, 10, and 11.

14.3.7. Ferrous hydroxide, $Fe(OH)_2$

For the reaction

$$Fe(OH)_2(cr) + 2H^+ \leftrightarrows Fe^{2+} + 2H_2O(l)$$

the equilibrium Fe^{2+} ion concentration in solution is given by

$$\log\{Fe^{2+}\} = \log K_{s0}^{Fe(OH)2} - 2pH$$

The equivalent relation for magnetite solubility is given by

$$\log\{Fe^{2+}\} = \log K_{s0}^{Fe3O4} - 2pH - \frac{1}{3}\log\{H_2\}.$$

At a certain hydrogen fugacity, the two phases are in equilibrium with each other and have equal solubility. By equating the two expressions above, one can derive an expression for the critical hydrogen fugacity.

$$\log\{H_2\}_{crit} = 3\left(\log K_{so}^{Fe(OH)2} + \log K_{s0}^{Fe3O4}\right)$$

This is plotted against temperature in Figure 14.38, using data collated in [38] at steam saturation pressure, with representative hydrogen concentrations:

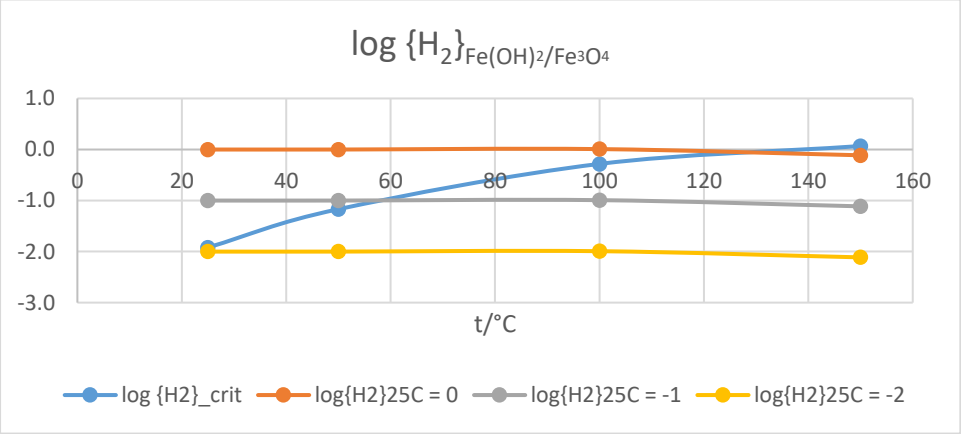

Figure 14.38. Plot showing temperature dependence of the hydrogen fugacity (as log $\{H_2\}$) characteristic of the equilibrium between $Fe(OH)_2$ and Fe_3O_4.
Contours of constant hydrogen concentration are also shown for reference.

It can be seen from Figure 14.38 that $Fe(OH)_2$ is stable to around 120 °C for log $\{H_2\}_{25C}$ = 0, and 60 °C for log $\{H_2\}_{25C}$ = -1. For log $\{H_2\}_{25C}$ values of -2 and below, $Fe(OH)_2$ is not stable at any temperature in the range 25 – 300 °C.

If hydrogen fugacity is controlled at the level of $\{H_2\}_{crit}$, then solubility follows the pattern shown in Figure 14.39 below. Of the pH values shown, only at pH_{25C} = 9 is there an appreciable level of Fe. At higher hydrogen fugacities the solubility is essentially unchanged, since only a fraction of the soluble Fe under such reducing conditions is in the ferric oxidation state.

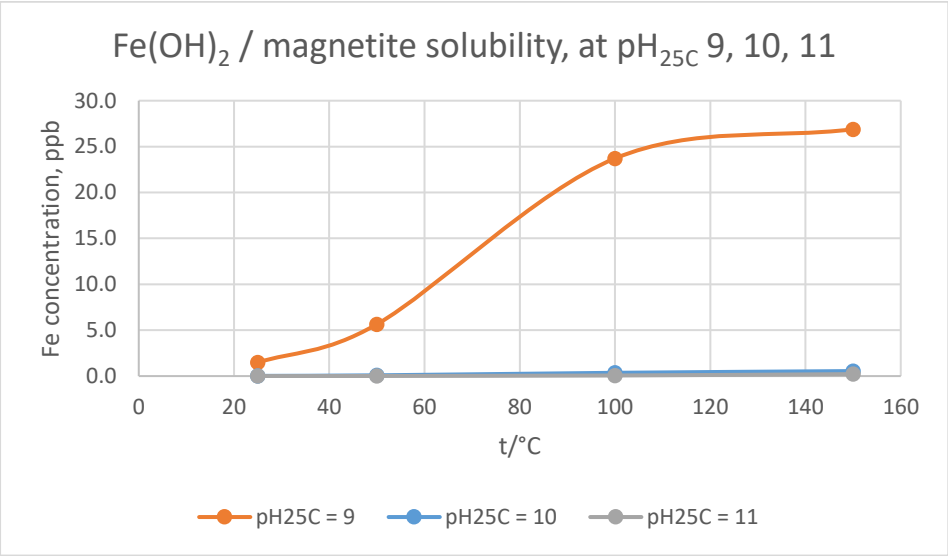

Figure 14.39. Temperature dependent solubility of $Fe(OH)_2$ or Fe_3O_4, under hydrogen fugacity conditions present at equilibrium between the two oxides, at pH_{25C} 9, 10, and 11.
Data only extends as far as 150 °C, as the fit for $Fe(OH)_2$ – Fe_3O_4 equilibrium only extends this far. At these temperatures, the strongly reducing conditions cause a high solubility (i.e. well above 1 ppb) at pH_{25C} 9 due to the predominance of Fe^{2+} ions; at pH 10 and 11, the predominance of more hydrolysed, ferric (Fe(III)) species results in a very low solubility under such reducing conditions.

14.3.8. Ni, NiO and $Ni(OH)_2$

NiO data are taken from [187], as tabulated in [38]. Palmer et al. found a 2-parameter fitting scheme of just two aqueous species, Ni^{2+} and $Ni(OH)_2$, to be sufficient to fit their data from 0 to 350 °C – the improvement gained from fitting with more parameters or aqueous species was not enough to warrant the extra complexity. It should be noted that Ziemniak and Goyette [188] produced a more refined fitting scheme, with more parameters and inclusion of the species $Ni(OH)^+$, and several fits over different temperature ranges The present data are sufficient for the purposes of this thesis, to demonstrate the extent to which levels of Ni in coolant are under or over-saturated with respect to NiO solubility.

Temperature dependent solubility constants, K_{eq}

Data are presented in [38] in the form $\log_{10} K_{sy} = n_1 + n_2(T)^{-1} + n_3 \ln(T) + \ldots$ for various oxides, as selected by the authors having reviewed the literature.

For the reactions

$$NiO(cr) + (2-y)H^+(aq) \leftrightarrows Ni(OH)_y^{2-y}(aq) + (1-y)H_2O(l) \qquad (NiO\ eqn)$$

The coefficients, n_1 and n_2, giving log K(T) for (NiO eqn) are reproduced here in Table 14.4, and plotted in Figure 14.40 below.

Table 14.4. Coefficients for giving log K(T) for NiO solubility [38], [187].

y	Soluble species	n_1	n_2	n_3
0	Ni^{2+}	-9.833	6255.01	-
2	$Ni(OH)_2$	-7.885	-193.49	-

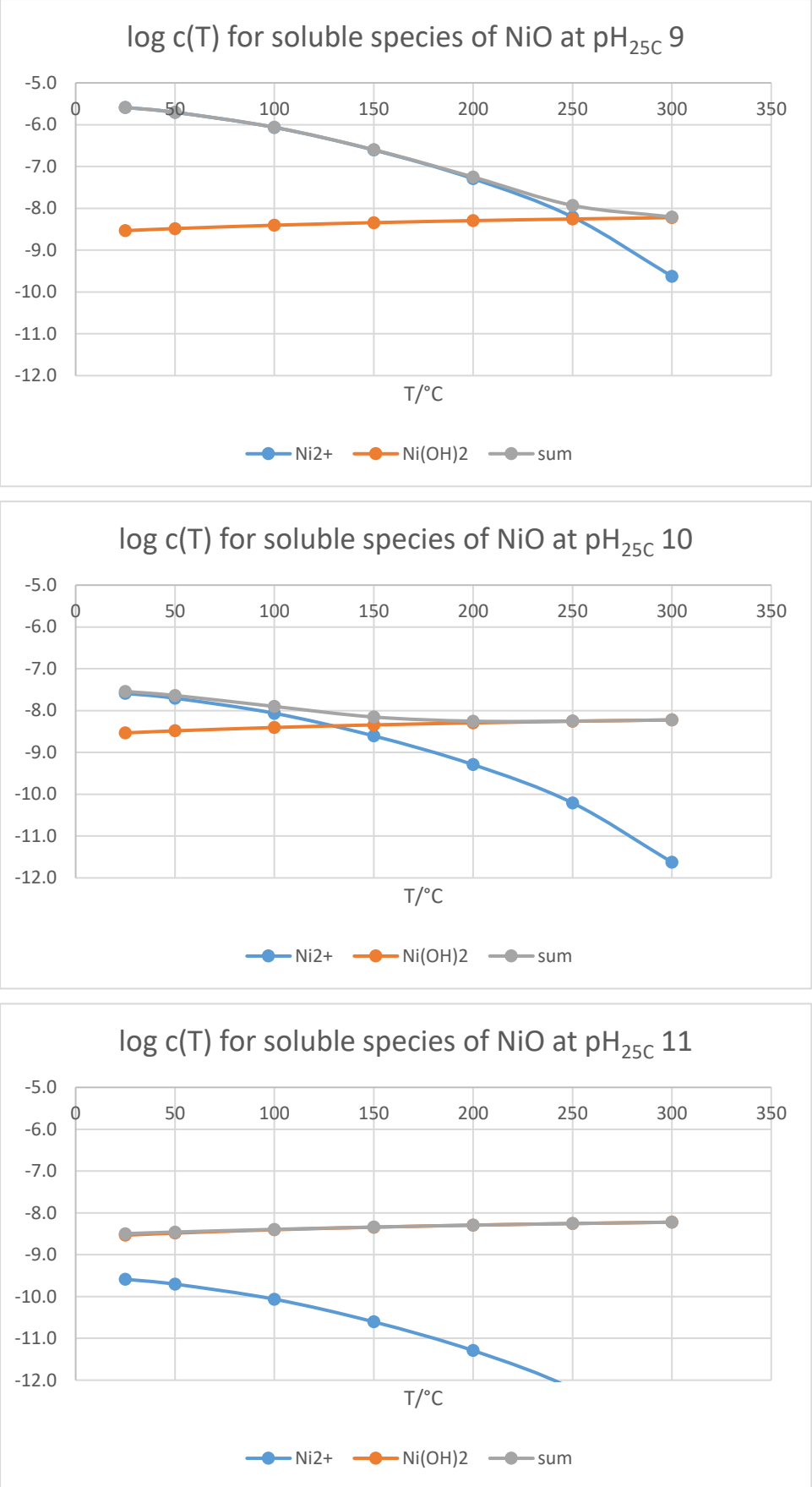

Figure 14.40. log c(T) for soluble species of NiO at pH_{25C} 9, 10, 11

The equilibrium dehydration temperature for β-$Ni(OH)_2$ (to form NiO) is predicted by Palmer et al. to be 77 °C from their solubility results, at 1 bar pressure [187]. However, at temperatures up to 200 °C the reaction rate is slow [189].

NiO solubility is insensitive to hydrogen fugacity, so long as the fugacity is not high enough for reduction to Ni metal. Ni metal has solubility described by the following reactions:

$$Ni(cr) + (2 - y)H^+(aq) + yH_2O \leftrightarrows Ni(OH)_y^{2-y}(aq) + H_2(g)$$

The key point to note is that Ni solubility is inversely proportional to hydrogen fugacity, and so Ni / NiO solubility falls off rapidly with falling hydrogen fugacity, once it falls below the fugacity of the oxidation reaction:

$$Ni(cr) + H_2O(l) \leftrightarrows NiO(cr) + H_2(g)$$

However, it should also be noted that slow kinetics have been found to severely limit the dissolution rate of NiO at temperatures below 200 °C, and transformation between NiO and Ni is also very slow [190]. Figure 14.41 below shows stability of Ni and NiO for representative hydrogen concentrations. Owing to the range of temperatures employed in the rig of the current project, and the variation in hydrogen fugacity due to factors such as changing flow rates, it seems likely that stability fluctuated between the two phases repeatedly during the course of experiments.

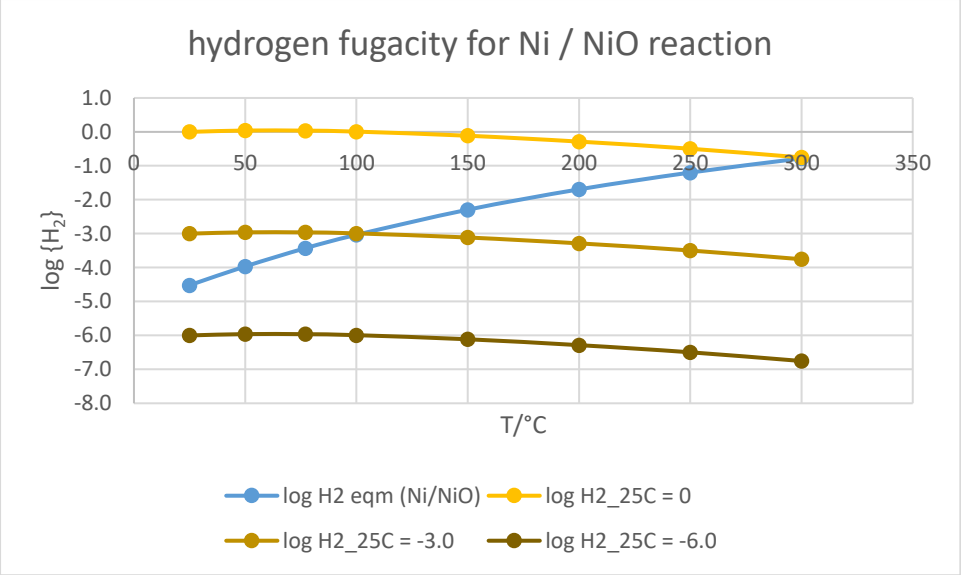

Figure 14.41. Hydrogen fugacity for Ni/NiO reaction, as a function of temperature

Where Ni becomes the stable phase and solubility becomes very low, Ni leaches out of mixed metal oxide phases in which it is present, such as ferrite and chromite.

It can be shown by analogy with the arguments in the section on hematite that

$$\log c_{z,l}^{Ni} = \log c_{z,l}^{NiO} - \log\left(\frac{\{H_2\}}{\{H_2\}_{crit,T}}\right)$$

Using this relation, and the hydrogen fugacity of Ni/NiO equilibrium, Ni solubility is plotted below for selected hydrogen fugacities and pH_{25C} values. NiO / $Ni(OH)_2$ solubility is also shown for comparison. In Figure 14.42 below, Ni metal solubility is shown for three selected values of log $\{H_2\}_{25C}$ (at 0, -3, -6) at pH_{25C} 10 across the full temperature range, 25 to 300 °C. The high solubility of Ni at the lowest hydrogen concentration, and at the intermediate concentration at temperatures over 100 °C is apparent, though such high dissolved levels are unlikely to be observed under PWR-relevant conditions due to precipitation of NiO (or $Ni(OH)_2$ phase at <77 °C), and Ni-bearing mixed oxide phases such as ferrites. At the higher value of hydrogen concentration, and at the intermediate value where T < 100 °C, the presence of Ni metal phase brings equilibrium Ni levels down compared with levels where NiO is present.

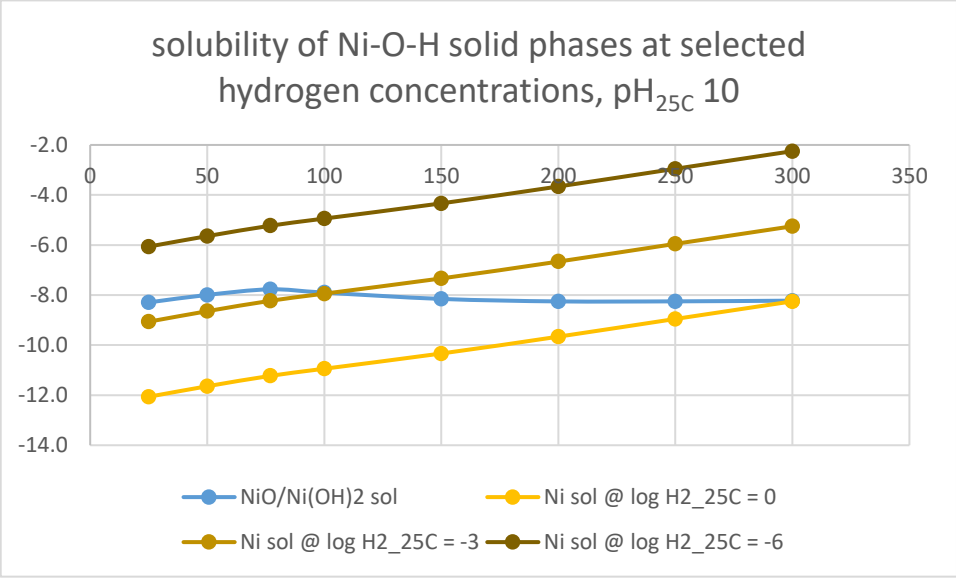

Figure 14.42. solubiity of Ni-O-H solid phases at selected hydrogen concentrations, pH_{25C}10

For clarity, in the plots which follow (Figure 14.43 (i) – (iii)), Ni solubility is only shown for conditions where it is stable relative to NiO / $Ni(OH)_2$. Plots are otherwise displayed in the style of plot above, for pH_{25C} 9, 10 and 11.

In the rig used for conducting the experiments of this PhD project, the Ni(II) solid phases (NiO and $Ni(OH)_2$) or Ni metal, may have been present as solubility controlling phase, with equilibrium solubilities as described above. Due to the relatively low Ni content of SS316L however, it is more likely that all the Ni present in the surface layer of oxide (which controls solubility equilibria with solution) was accommodated fully by mixed ferrite and chromite spinels. The above solubilities therefore represent an upper bound for Ni concentration at given hydrogen concentration. Where observed Ni levels are similar to those levels, it may be an indication that one of the nickel phases treated above was indeed present.

Where hydrogen concentration is not known, as was the case in the rig, Ni levels below those expected for NiO / $Ni(OH)_2$ may be indicative either of a lack of separate Ni-based phase (Ni levels controlled by Ni-bearing ferrite), or of presence of Ni metal, at hydrogen concentration indicated in plots.

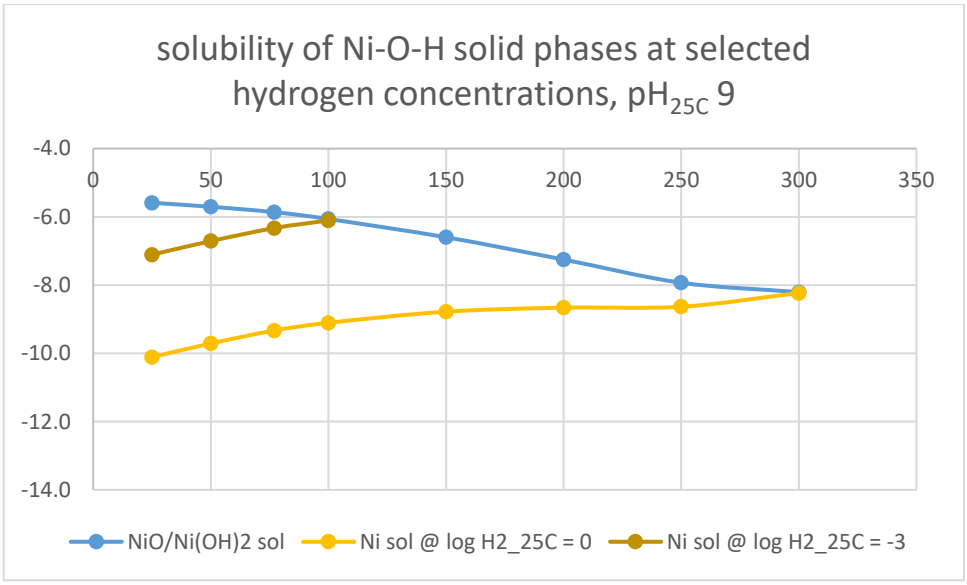

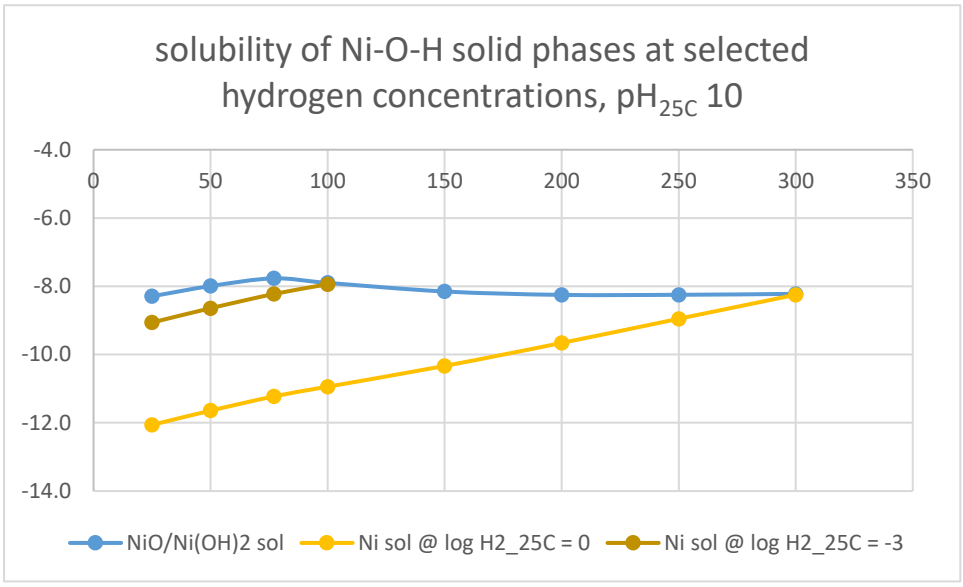

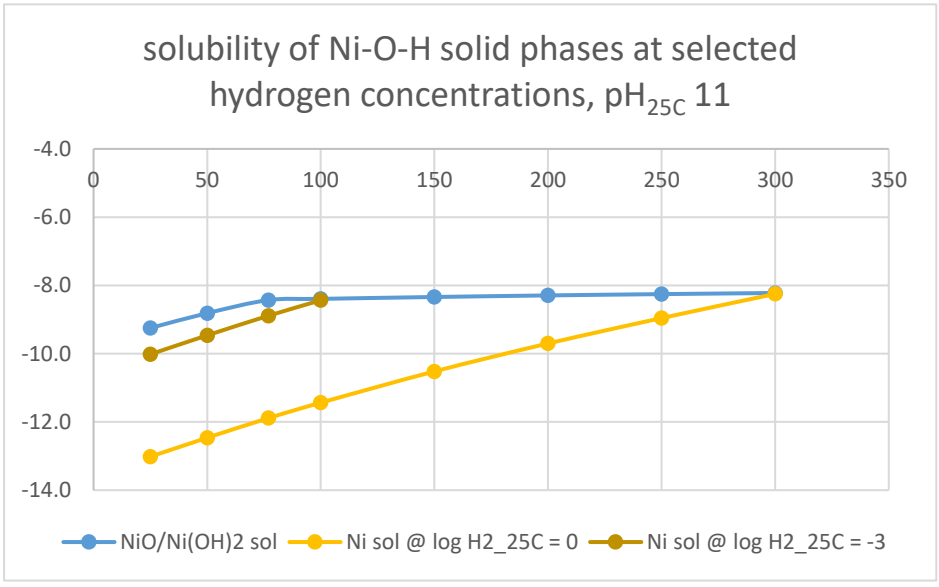

Figure 14.43: solubility of Ni-O-H solid phases at selected hydrogen concentrations, pH_{25C} 9, 10, 11

Summary

In summary, Ni species in solution are dominated by $Ni(OH)_2(aq)$ at pH_{25C} 11 for all temperatures covered, at pH_{25C} 10 for T ~ 150 °C and above, and at pH_{25C} 9 from about 250 °C upwards. Where NiO is the stable phase, this results in a fairly constant Ni concentration with temperature, pH and hydrogen fugacity, being around $10^{-8.3}$ molal (0.3 ppb). At the lower values of pH and temperature, $Ni^{2+}(aq)$ becomes dominant. In addition, the hydrated form of Ni(II) oxide, $Ni(OH)_2$, becomes stable below ~ 77 °C. The two effects combine to produce a solubility peak at ~77 °C, $10^{-5.9}$ molal Ni (74 ppb) at pH 9; and at ~50 °C, $10^{-7.6}$ molal Ni (1.5 ppb) at pH 10.

The maximum hydrogen fugacity for stability of NiO relative to Ni corresponds to log $\{H_2\}_{25C}$ values which fall from 0.0 at 300 °C down to -4.5 at 25 °C. Though the value of log $\{H_2\}_{25C}$ in the rig was uncertain and likely to have fluctuated widely, taking the measured value of -3.0 (see later section) as a representative value this results in stability of nickel metal below about 100 °C. This gives 25 °C soluble Ni levels of $10^{-7.1}$, $10^{-9.1}$ and $10^{-10.0}$ molal (4.7, 0.05 and 0.01 ppb) at pH_{25C} 9, 10, 11 respectively, with the latter two values being less than for NiO at high temp. The latter two values are also comparable with observed levels from the rig at pH 10 and 11, which were significantly lower than for pH_{25C} 9, suggesting that Ni readings may be artificially low in those cases due to precipitation of Ni metal in the cool back-end of the rig, outside the oven.

14.3.9. Cr(III) hydrated oxides, γCrOOH and $Cr(OH)_3.xH_2O$

Temperature dependent solubility constants, K_{eq}

Temperature dependent K_{eq} values for dissolution of CrOOH and $Cr(OH)_3.xH_2O$ to the neutral hydroxocomplex $Cr(OH)_3$ (aq), and for hydrolysis to $Cr(OH)_4^-$, are reproduced here from a study into solubility of Cr(III) oxides and $FeCr_2O_4$ [102]. Least squares fits to the data of the form $\Delta G = A - BT - CT \ln T$, or $\Delta G = A - BT$, were used by the authors of the study: these parameters are included in Table 14.5 below, alongside the fitted value of $\Delta G^0(298)$.

Table 14.5. thermodynamic data for dissolution and hydrolysis of Cr(III) oxides. Data from [102]

Reaction	A (kJ/mol)	B (J /mole /K)	C (J /mole /K)	$\Delta G^0(298)$, kJ/mol
Dissolution				
$Cr(OH)_3.3H_2O(s)=Cr(OH)_3(aq)+3H_2O$ / $K_{s3'}$	15.96±6.48	-136.44±20.48	-	56.64±0.53
$CrOOH(s) + H_2O = Cr(OH)_3$ (aq) / K_{s3}	-20.18±6.48	-433.55±175.05	32.03±24.83	54.66±0.48
Hydrolysis				
$Cr(OH)_3(aq) + H_2O = Cr(OH)_4^- + H^+$ / K_{h3}	145.11±26.40	1514.34±14.30	-223.81±8.46	73.80±11.46

For the scheme of species $\gamma CrOOH\ (s) + (3-y)H^+ \leftrightarrows Cr(OH)_y^{3-y}\ (aq) + (2-y)\ H_2O$,

log K_{sy} versus T for y = 3, 4 are plotted in Figure 14.44. Log K_{s4} was found from log K_{s3} plus log K_{h3}. Equivalent values for the dissolution of $Cr(OH)_3.3H_2O(s)$ are also included at low temperature, showing the transition in stability of the two oxides at around 50 °C.

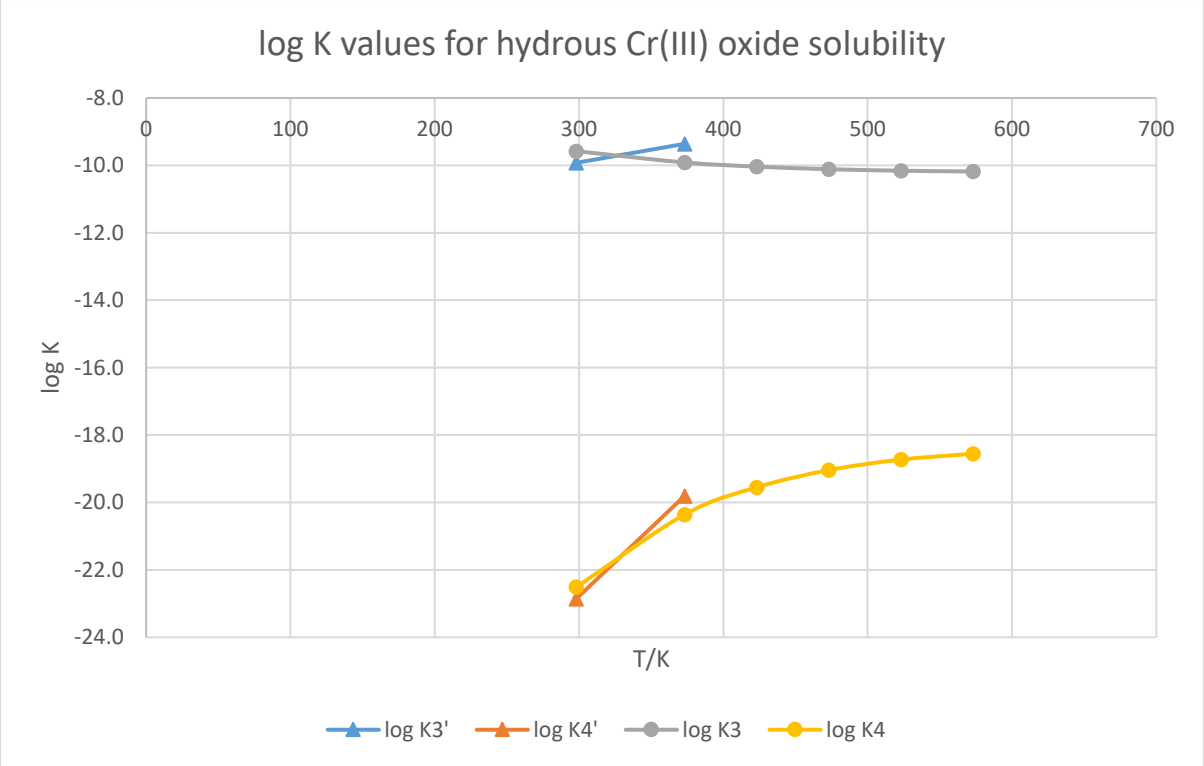

Figure 14.44. log K values for hydrous Cr (III) oxide solubility. Data from [102].
Triangle symbols represent $Cr(OH)_3.xH_2O$ solubility (stable below ~ 50 °C); circles represent CrOOH solubility.

Temperature dependent solubility, for fixed pH_T and log $\{H_2\}_T$

Temperature dependent solubility for fixed pH_T and log $\{H_2\}_T$ are plotted in Figure 14.45. As long as conditions are not oxidising, Cr(VI) ions are not present and so there is no effect of hydrogen fugacity on Cr(III) oxide solubility. Under moderately alkaline conditions the two soluble species considered are sufficient to describe solubility behaviour. For most of the conditions considered $Cr(OH)_3$ (aq) is the dominant species, and so there is little dependence of overall solubility on pH_T. On heating from 25 °C, equilibrium concentration of $Cr(OH)_3$ (aq) rises slightly from 0.12 nm (0.006 ppb) to 0.19 nm (0.010 ppb) at 50 °C, where the stable oxide phase transitions from $Cr(OH)_3.3H_2O$ to CrOOH; concentration then falls to 0.08 nm (0.004 ppb) at 200 °C, and 0.07 nm (0.003 ppb) at 300 °C.

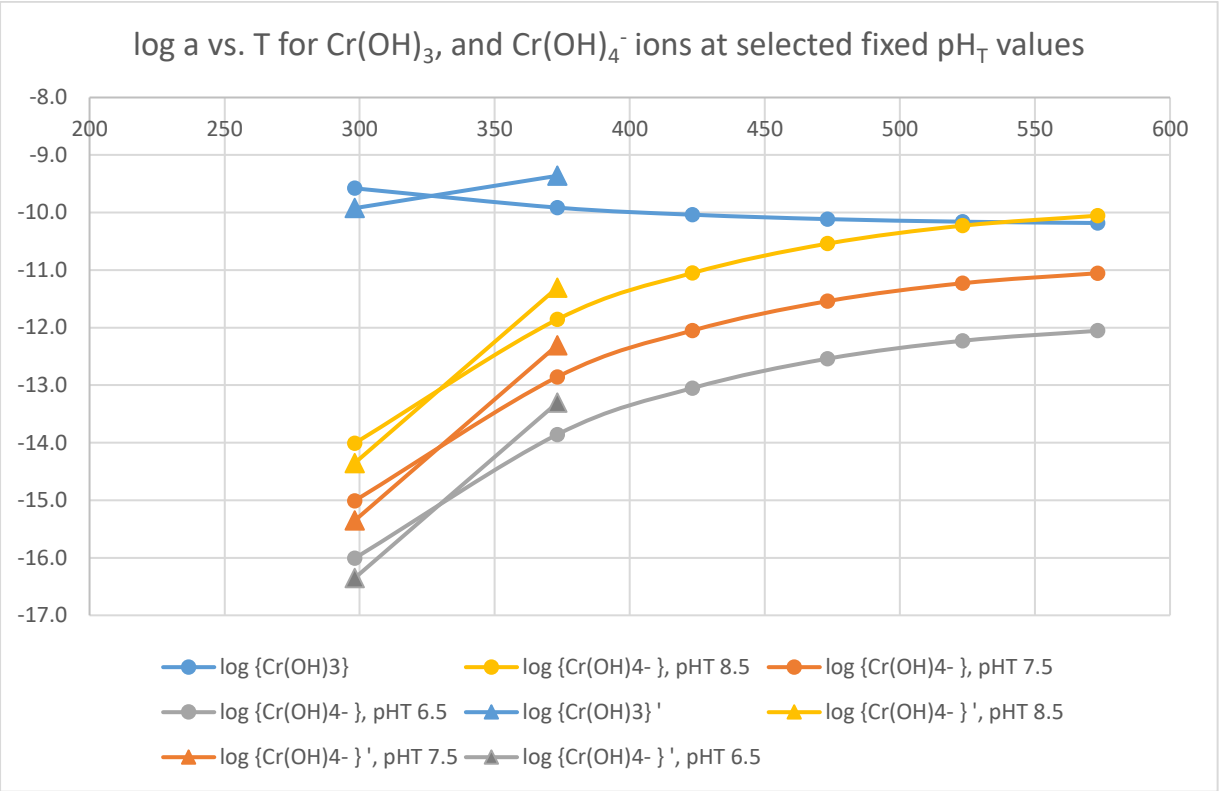

Figure 14.45. Log a vs. T for $Cr(OH)_3$, and $Cr(OH)_4^-$ ions at selected fixed pH_T values. Using thermodynamic data from [102].
Triangle symbols represent $Cr(OH)_3.xH_2O$ solubility (stable below ~ 50 °C); circles represent CrOOH solubility.

14.3.10. Temperature-dependent solubility, for a model solution of fixed composition

Temperature dependent solubility curves are plotted in Figure 14.46 for model solutions of pH_{25C} 9 – 11. For the solution chemistries used in the present study, namely pH_{25C} values of 9, 10 and 11 (LiOH) and reducing conditions, $Cr(OH)_3$ (aq) dominates the overall Cr(III) oxide solubility, except at the very highest values of pH_{25C} and T. At pH 9, solubility is simply given by the curve for $Cr(OH)_3$ (aq), whereas at pH 11 solubility is given by the black curve marked 'log tot', and shows an increase with temperature at higher temperatures due to the contribution from $Fe(OH)_4^-$ ions. At pH_{25C} 11, there is a Cr(III) oxide solubility minimum at around 200 °C.

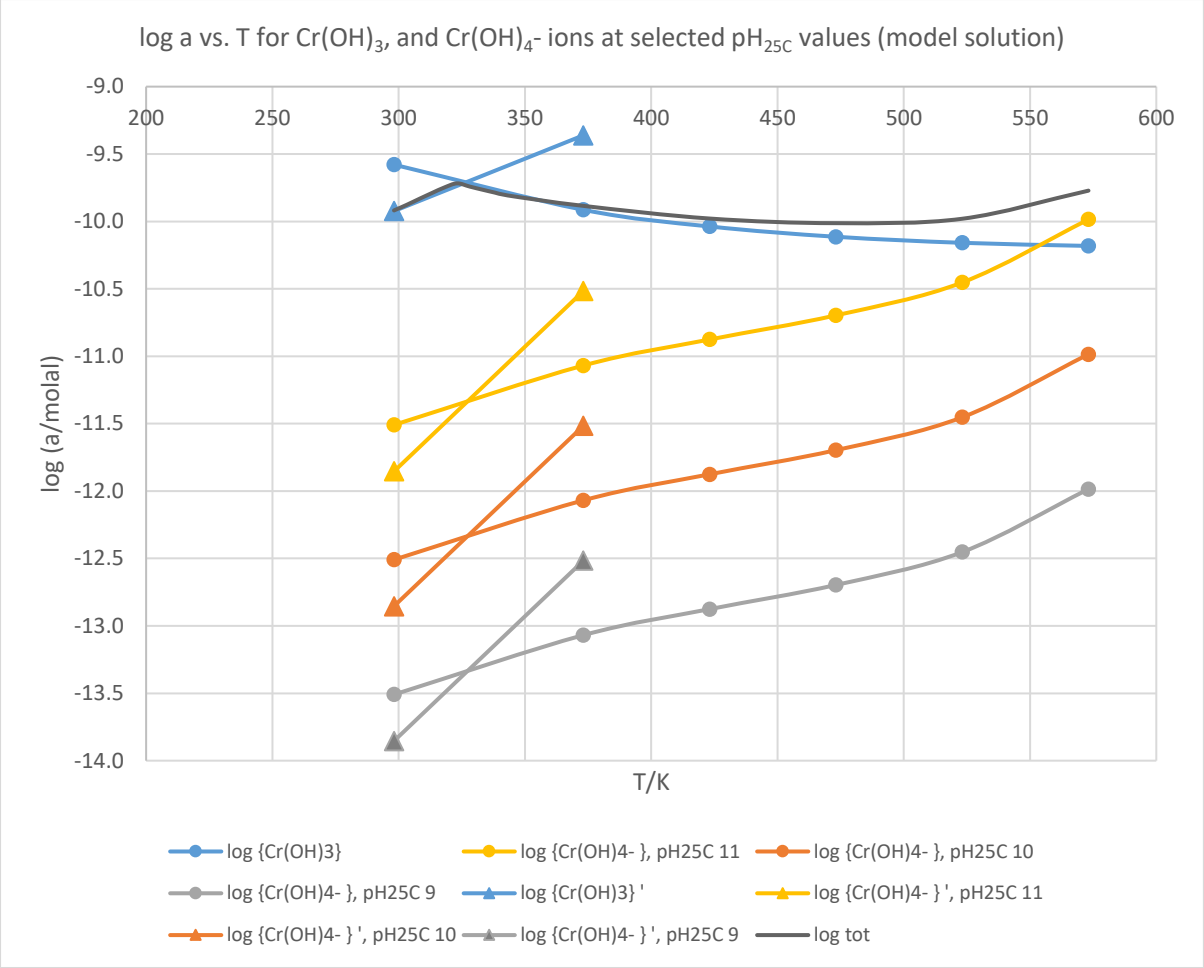

Figure 14.46. Log a vs. T for $Cr(OH)_3$, and $Cr(OH)_4$ ions at selected pH_{25} values (model solution). Using thermodynamic data from [102].
Triangle symbols represent $Cr(OH)_3.xH_2O$ solubility (stable below ~ 50 °C); circles represent CrOOH solubility.

Discussion, and implications for current study

Levels of dissolved Cr coming from the plant would be expected to be around 0.00 to 0.01 ppb for all conditions used in the current study, since this is the range of solubility levels of Cr(III) oxides in both the hot and cold parts of the rig. The very last part of the rig before samples are collected was accessible by the atmosphere at room temperature, and so Cr(VI) species may have become stable in solution, but are unlikely to have had much effect due to kinetics considerations at room temperature.

The rest of the rig, which is not accessible to the atmosphere, was only exposed to deoxygenated feedwater in the normal course of events: if oxygen had temporarily ingressed at any stage of the experimental programme then oxidation of Cr(III) to Cr(VI) ions could have the potential to cause a spike in Cr levels due to desorption of Cr ions adsorbed on any oxide surfaces [184].

14.3.11. Ferrous chromite, $FeCr_2O_4$

As discussed in earlier section, Fe-Cr-Ni spinel-type oxides under equilibrium conditions at PWR-relevant conditions can have a wide range of different compositions. Composition can be characterised by x and y in the following formulation,

$$(Ni_xFe_{1-x})^{(II)}\left(Cr_yFe_{1-y}\right)_2^{(III)}O_4$$

With $0 \leq x \leq 1$. Where y is more than about 0.7 (Cr-rich), the oxide is a normal spinel referred to generically as the chromite phase. Where y is less than about 0.05 or 0.1 (for the extremes of low and high Ni content respectively), the oxide is an inverse spinel and is referred to generically as the ferrite (oxide) phase – not to be confused with the ferrite phase of Fe, α-Fe, which does not feature in this thesis apart from this remark. Any intermediate y value *is* possible at temperatures of interest (room temperature to around 300 °C), by for example quenching from high temperatures of around 1000 °C or above where there is full miscibility between the phases; however, such oxides are unstable to decomposition to the ferrite and chromite phases at the solvus of immiscibility, i.e. y = 0.7 and y ≈ 0.05 to 0.1. Decomposition is extremely slow as a solid-state process, but accelerated by ageing in hydrothermal solutions.

Pure ferrous chromite is thought to be marginally unstable under conditions of PWR coolant, with respect to decomposition to form ferrite (in this case having x = 0, y ≈ 0.05) and CrOOH, but prevalent as the protective oxide layer on corroding stainless steel surfaces for reasons of kinetics [103].

At the limit of stability for ferrous chromite – around 160 °C for a hydrogen concentration 30 scc/kg typical of PWR primary coolant according to Dickinson et al. [103] – a mutual equilibrium between ferrite (x=0, y ≈ 0.05), ferrous chromite (x=0, y ≈ 0.7), and γ-CrOOH is possible. In this case, solution concentrations of Fe and Cr are given simply by the solubility of ferrite (essentially magnetite in this case) and γ-CrOOH. Where chromite is marginally stable, solution levels of Fe and Cr will be similar to those expected by the respective single metal oxides, but with one or both being marginally lower. When conditions change so that ferrous chromite becomes marginally unstable, it will have a tendency to control solution concentrations of Fe and Cr to levels which are slightly supersaturated with respect to the single metal oxides: this tendency is however in competition with precipitation of those oxides – actual solution concentrations will therefore be dependent on kinetics and the relative surface areas of each phase exposed to solution. The composition of ferrous chromite when in equilibrium with ferrite is known to have a value of y of around 0.7; where equilibrium is with CrOOH instead (as was the case for Ziemniak et al.'s study [102]) this could potentially cause y to have slightly higher value, though almost certainly within the level of uncertainty which exists.

Where ferrous chromite is unstable, it is thought that a surface layer of CrOOH forms, through which Fe from the chromite diffuses to reach solution. Ferrite oxide then precipitates from solution. Since the CrOOH is closest to the chromite, it would most likely be more efficient than ferrite at controlling activity of their respective trivalent ions (Cr^{3+} and Fe^{3+}, or equivalently $Cr(OH)_3$ (aq) and $Fe(OH)_3$ (aq)) at the chromite surface, whilst Fe species at that location would have elevated activity compared with ferrite solubility, and so the ratio of Cr(III) to Fe(III) in the (meta stable) chromite in this case could cause y to be lowered slightly from 0.7. A liquid-solid distribution coefficient was cited by the authors as a convenient parameter to express overall equilibrium behaviour, with the implication being that the ratio of Cr(III):Fe(III) in the oxide is directly proportional to the same ratio in solution, all other things being equal:

$$K_d = \frac{[Cr(III)/Fe(III)]_{liquid}}{[Cr(III)/Fe(III)]_{solid}}$$

The discussion at the beginning of the previous paragraph demonstrates that ferrous chromite dissolution must necessarily be incongruent, as was observed, since ferrite solubility is orders of magnitude greater than γCrOOH solubility under PWR-relevant conditions.

In summary, the results from the study of Ziemniak et al. [102] are thought to represent chromite in equilibrium with a thin surface phase of γCrOOH at lower temperatures where chromite is stable; and equilibrium between the surface γCrOOH phase and magnetite crystallites (precipitated from solution) at higher temperatures where chromite is not stable. They did find small unidentified crystals on the surface of the chromite granules under post-test inspection in SEM, but since the chromite bed had been subjected to additional testing under oxidising conditions, it was not certain whether these had been present under the reducing conditions reported in the paper.

According to Ziemniak et al., if their results are to remain consistent with earlier work of Thamer et al. [191] then "a transition between γ and α CrOOH may be expected around 295 °C". Therefore when the rig is held at 300 °C for long periods, it may be the α form of CrOOH which is present if it is present at all.

Temperature dependent solubility constants, Keq

The temperature dependent K_{eq} value for dissolution of chromite (nominally $FeCr_2O_4$) to form the unhydrolysed Fe^{2+} ion and the neutral aquocomplex of Cr^{3+} is reproduced here, from the same study in which CrOOH solubility was determined [102].

A least squares fit to the data of the form ΔG = A – BT was used by the authors of the study [102]: these parameters are included in Table 14.6, alongside the fitted value of $\Delta G^0(298)$, and the resulting temperature dependence of log K is plotted in Figure 14.47. Activities of all the other soluble species

of Fe and Cr can be determined using the equilibrium constants for the respective oxides, Fe_3O_4 and CrOOH.

Table 14.6. thermodynamic data for dissolution of ferrous chromite. Data from [102]

Reaction	A (kJ/mol)	B (J /mole /K)	$\Delta G^0(298)$, kJ/mol
Dissolution			
$FeCr_2O_4(s) + 2H^+ + 2\,H_2O = Fe^{2+} + 2Cr(OH)_3\,(aq)/\,K_{sp}$	-73.42±1.65	-424.04±3.85	53.00±0.58

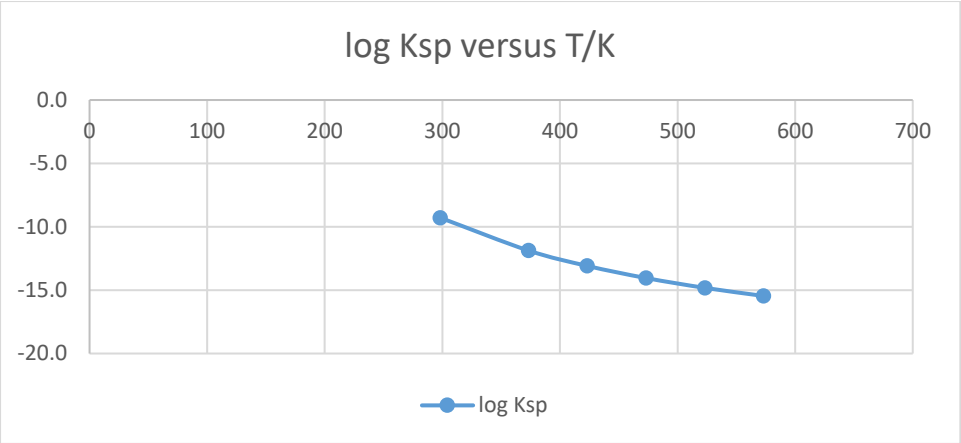

Figure 14.47: log Ksp versus T/K

Temperature-dependent solubility, for a model solution of fixed composition

The dissolution equation above gives

$$\log\{Fe^{2+}\} + 2\log\{Cr(OH)_3\,(aq)\} = \log K_{sp} - 2pH$$

In order to determine activity of one species, the activity of the other must be known. As discussed in the section on stability of oxides, only for a very narrow band of compositions in the solid phase can chromite exist alone – ordinarily it will be in equilibrium either with γCrOOH or ferrite, so that $\{Cr(OH)_3\,(aq)\}$ or $\{Fe^{2+}\}$ is constrained by the solubility of the respective single oxide phase. By extension, activity of all the other species and the overall solubility for that element is also fully described, as per sections 14.3.9, and 14.3.5 to 14.3.7, respectively. Expressions are provided below for the equilibrium activity of the other species, $Cr(OH)_3\,(aq)$ or Fe^{2+}.

Where CrOOH is present:

$$\log\{Fe^{2+}\} = \log K_{sp} - 2\log K_3 - 2pH; \qquad \log\{Cr(OH)_3\,(aq)\} = \log K_3$$

And where ferrite is present:

$$\log\{Cr(OH)_3\ (aq)\} = \frac{1}{2}\left(\log K_{sp} - \log K_{Fe2+}\right); \quad \log\{Fe^{2+}\} = \log K_{Fe2+} - 2pH + \frac{1}{3}\log\{H_2\}$$

Where CrOOH is present, the level of dissolved Fe species from chromite relative to what would be expected from ferrite can be expressed simply as:

$$\log S_{Fe} = \log\left(\frac{\{Fe^{2+}\}_{chromite}}{\{Fe^{2+}\}_{ferrite}}\right) = \left(\log K_{sp} - 2\log K_3 - \log K_{Fe2+} - \frac{1}{3}\log\{H_2\}\right)$$

Where ferrite is present, the level of dissolved Cr species from chromite relative to what would be expected from CrOOH can be expressed simply as the following (which is equal to the expression for log S_{Fe} save for an additional factor of ½):

$$\log S_{Cr} = \log\left(\frac{\{Cr(OH)_3\ (aq)\}_{chromite}}{\{Cr(OH)_3\ (aq)\}_{CrOOH}}\right) = \frac{1}{2}\left(\log K_{sp} - 2\log K_3 - \log K_{Fe2+} - \frac{1}{3}\log\{H_2\}\right)$$

Figure 14.48 (i) - (ii) below show the temperature dependence of log SFe and log SCr at selected hydrogen concentrations. These quantities represent the shift in log [Fe] or log [Cr] relative to the solubility of the single metal oxides. A curve of constant Δ log a = 0 is included to illustrate that only one of the elements experiences a shift in solubilty relative to the single oxide phase, the other is unaffected.

Values of Δlog a greater than zero represent supersaturation with respect to the single metal oxide phase, which therefore is expected to precipitate from solution and control [Fe] or [Cr] to roughly saturation levels (i.e. Δlog a = 0). The extent of supersaturation in Figure 14.48 below represents magnitude of driving force for net dissolution of the chromite phase, but kinetics are known to be very slow, hence the protective nature of the oxide. As can be seen, the stability range of chromite extends to higher temperatures under the more reducing conditions. The relationship between hydrogen fugacity and temperature at the limit of chromite stability, according to the following reaction is plotted in Figure 14.49 below, from [103].

$$FeCr_2O_4 + \frac{4}{3}H_2O = \frac{1}{3}Fe_3O_4 + 2CrOOH + \frac{1}{3}H_2$$

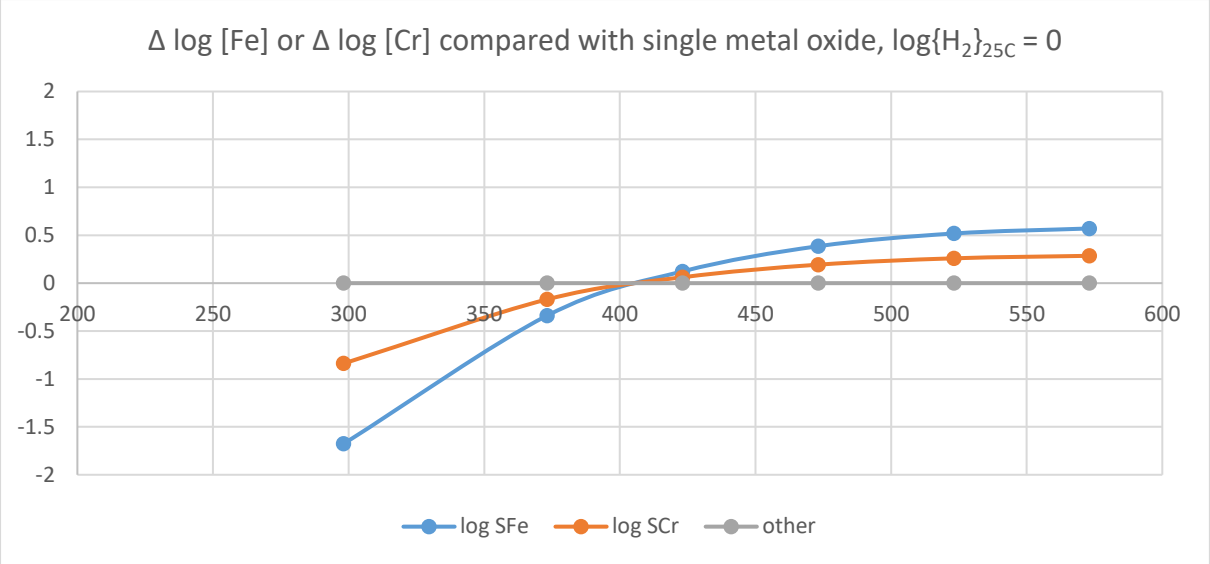

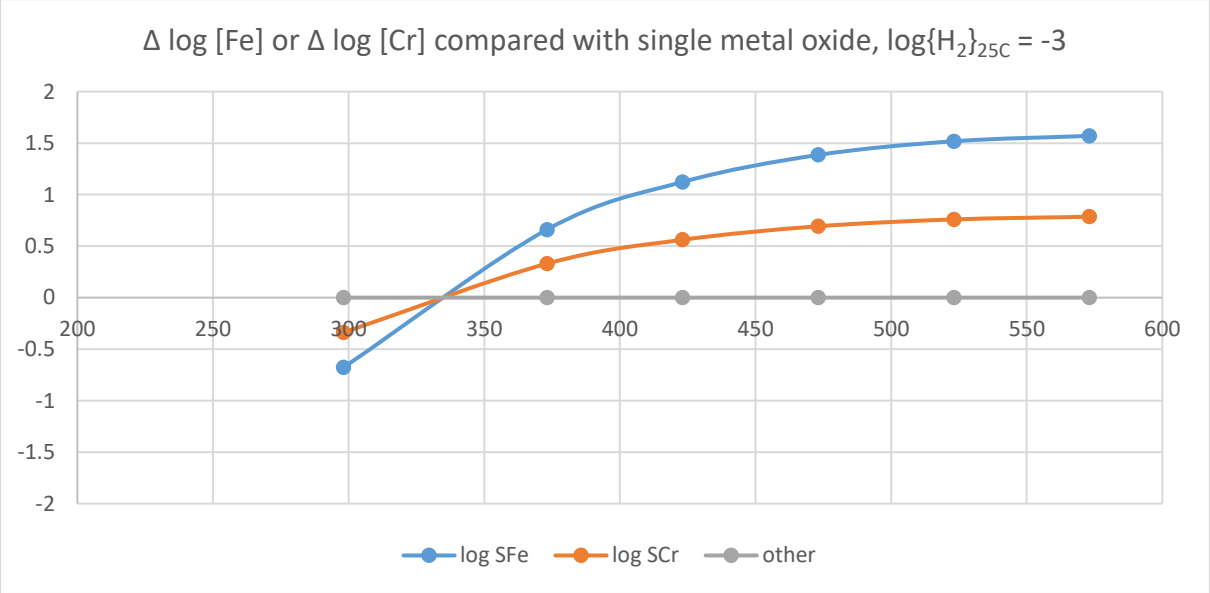

Figure 14.48 Δ log [Fe] or Δ log [Cr] compared with single metal Cr(III) oxide, log{H_2}$_{25C}$ = 0, -3

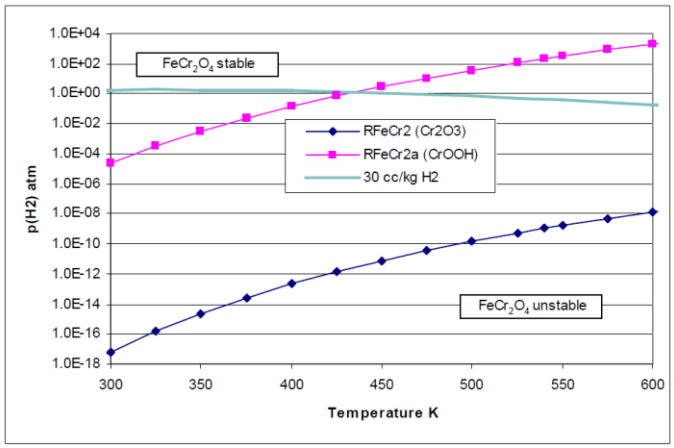

Figure 14.49. Equilibrium H_2 pressure for $FeCr_2O_4$ decomposition reactions. From [103].

14.3.12. Nickel chromite, $NiCr_2O_4$

As discussed in earlier sections, composition of Fe-Cr-Ni spinel-type oxides can be characterised by x and y in the following formulation,

$$(Ni_xFe_{1-x})^{(II)}\left(Cr_yFe_{1-y}\right)_2^{(III)}O_4$$

With $0 \leq x \leq 1$. For x = 1, nickel chromite and nickel ferrite in mutual equilibrium have y = 0.7 and y = 0.1 respectively. No experimental data have been found for solubility of $NiCr_2O_4$ in aqueous solution, but Dickinson et al. [103] have plotted equilibrium hydrogen pressure versus temperature for the decomposition of nickel chromite to Ni metal and CrOOH, using literature thermochemical data, see Figure 14.50.

The plot shows that stoichiometric nickel chromite is stable with respect to decomposition to Ni and CrOOH only for low hydrogen fugacity, below the pink curves (conflicting data from two different studies). Nickel chromite becomes progressively more stable with respect to that reaction as hydrogen fugacity is decreased below the line, and more progressively more unstable with distance above the line. The blue Ni/NiO curve represents hydrogen fugacity where Ni and NiO are present in mutual equilibrium. Below this line, NiO rather than Ni is the stable phase, and so decomposition of $NiCr_2O_4$ (to Ni metal and CrOOH) no longer has any hydrogen dependence. Therefore stoichiometric nickel chromite is not stable under any conditions of hydrogen fugacity between 300 and 600 K: the degree of instability at given temperature is dependent on the extent to which hydrogen fugacity is above the decomposition curve(s) in the plot, above the Ni/NiO curve, and is independent of hydrogen fugacity below it.

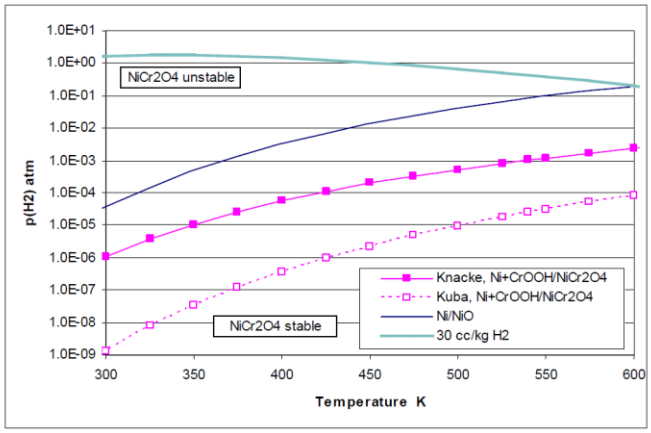

Figure 14.50. Equilibrium H_2 pressure for $NiCr_2O_4$ decomposition and Ni oxidation. Figure from [103].

The implications of these findings are that stoichiometric nickel chromite is not stable with respect to decomposition to Ni (or NiO under sufficiently oxidising conditions) and CrOOH – i.e. soluble levels of either [Ni], [Cr], or both, in equilibrium with dissolving nickel chromite, would be higher than solubility of the respective single metal oxides. It is not clear whether substitution of some of the Ni(II) with Fe(II) in the mixed oxide would lower the Gibbs energy sufficiently to make nickel ferrite stable against decomposition to the two single metal oxides. In any case, decomposition to single metal oxides is a solid state process and therefore extremely slow compared with dissolution / precipitation reactions [14], [74]. In studies of corrosion film on Ni base alloys [75], [86], the equilibrium or meta stable equilibrium between corrosion film and coolant gave Ni(II) content of x = 0.9 for ferrite crystallites (x in $Ni_xFe_{1-x}(Fe_yCr_{1-y})_2O_4$). The equivalent figure for the underlying chromite oxide was x = 0.7.

In a study in which $FeNiCrO_4$ spinel oxide was allowed to decompose to ferrite and chromite phases under air annealing at 600+ °C [74], decomposition of nickel ferrite to respective single metal oxides was not noted. However, an additional unknown oxide phase was observed by XRD analysis, and the kinetics even of the decomposition reaction studied were extremely slow: the reaction was still incomplete after 1 year at 600 °C. Therefore decomposition to single metal oxide phases may or may not have occurred given sufficient time.

As was discussed for ferrous chromite, if the mixed oxide phase is indeed stable then it is likely that the single metal oxides (CrOOH and Ni/NiO) would precipitate on any surfaces of chromite exposed to the coolant, controlling the solubility to low levels, and solid state kinetics mean that new dissolution of the chromite phase is extremely slow.

14.3.13. Nickel ferrite, $NiFe_2O_4$

As discussed, Fe-Cr-Ni spinel-type oxides under equilibrium conditions at PWR-relevant conditions can have a wide range of different compositions. Composition can be characterised by x and y in the following formulation,

$$(Ni_xFe_{1-x})^{(II)}\left(Cr_yFe_{1-y}\right)_2^{(III)}O_4$$

With $0 \leq x \leq 1$.

There is limited solubility data on nickel ferrite solubility, since most of the papers were conducted in 'pure' water for which the pH was not known. In a paper by Bellefleur et al., [130] the hydrogen fugacity was not accurately known, though the quench pH was measured. If an educated guess is made of hydrogen fugacity, solution levels of Fe appeared to have been ~ 10x supersaturated with respect to pure magnetite phase, even at the high end of the range of possible log H_2 values where solubility is highest. Levels of dissolved Ni were close to saturation levels at 150 °C and 200 °C, but only at ~10% of saturation at 100 °C, relative to NiO solubility (which is unaffected by H_2 concentration except where the concentration is sufficiently high to stabilise Ni metal).

The supersaturation with respect to Fe phases is surprising, especially at the lowest temperature of 100 °C, given the concurrent under-saturation with respect to NiO. One possible explanation is that suspended or particulate Fe is being recorded as dissolved. This is common at high pH, but less so at low pH where results from major studies are in good agreement [4], [121]. As Bellefleur et al. note however, Stefànsson and Seward [192] observed a complete precipitation of iron(III) under similar pH and concentration conditions.

Paper by Bellefleur et al. (NPC 2014) [130]

The paper uses log K values from the MULTEQ database, but does not give them quantitatively. Differences between log K values were used by the present author to give estimates of log K_$NiFe_2O_4$, using log K values for Fe_3O_4, Fe_2O_3 and NiO, giving dissolution to the unhydrolysed Me^{2+} cation in each case.

First of all, an upper bound for log $K_{NiFe2O4}$ was found, log $K_{NiFe2O4}$ < log K_{NiO} + log K_{Fe2O3}, above which $NiFe_2O_4$ would be unstable against decomposition to NiO and Fe_2O_3. This is plotted in Figure 14.51.

An estimate of MULTEQ values of log $K_{NiFe2O4}$ was deduced from the values of log $K_{NiFe2O4}$ – log K_{Fe2O3} provided in the paper, at approximately 100, 150 and 200 °C. Another estimate of MULTEQ values of log $K_{NiFe2O4}$ was deduced in an equilvalent way, using the values of log $K_{NiFe2O4}$ – log K_{Fe3O4} provided. In each case the different formulation of the equilibrium equations were taken into account (1 mole of

reaction involves 1 mole of Fe_3O_4 or Fe_2O_3 in the NPC 2014 paper, but 1/3 mole and ½ mole respectively in [38]. These also are plotted in Figure 14.51. Similar data is plotted in Figure 14.52 also.

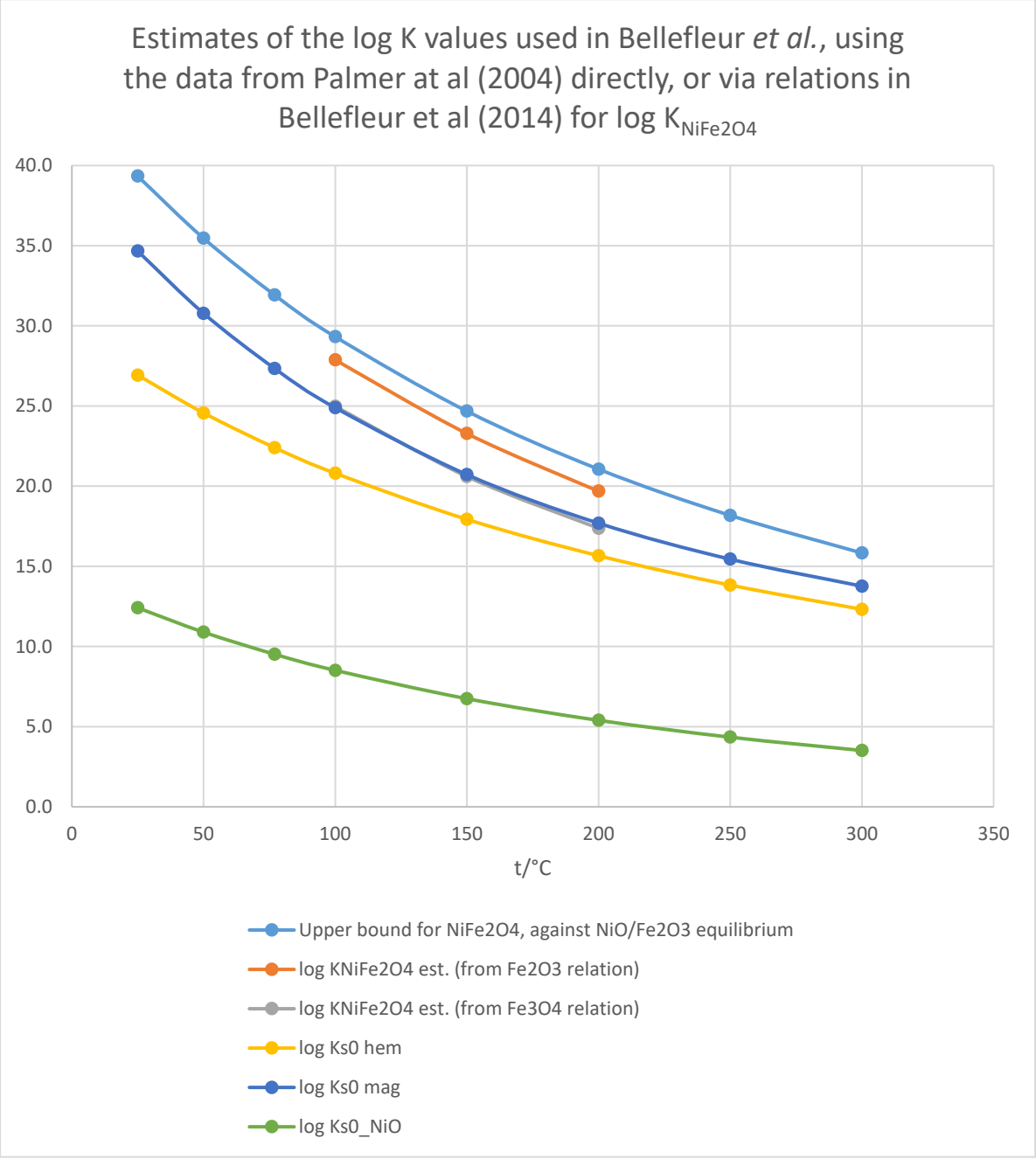

Figure 14.51. Estimates of the log K values used in Bellefleur et al. [130]*, using the data from Palmer at al* [187] *directly, or via relations in Bellefleur et al.* [130] *for log* $K_{NiFe2O4}$

Log K for dissolution of Fe_2O_3 to Fe^{2+} (aq) is a fairly obscure quantity, since hematite is stable under more oxidising conditions where Fe(III) species tend to dominate in solution. It was constructed from the data in [38] for dissolution of hematite to $Fe(OH)_4^-$, dissolution of magnetite to $Fe(OH)_4^-$, and

dissolution of magnetite to Fe^{2+} (referred to here as K_{Fe3O4}). For these reasons it is a less reliable reference point than the value for magnetite, K_{Fe3O4}.

Of the two curves of log $K_{NiFe2O4}$ this produced, the one derived using magnetite solubility is the more reliable. This curve lies very close to the curve of log K_{Fe3O4} itself (and is partially hidden in the plot). It lies around 4 log units below the limit of stability with respect to NiO and Fe_2O_3.

Where decomposition of $NiFe_2O_4$ to NiO and Fe_3O_4 is concerned, hydrogen fugacity becomes an important factor, since some of the Fe(III) in nickel ferrite must be reduced to Fe(II) in order to form Fe_3O_4. Another boundary for nickel ferrite stability can therefore be expressed as $\log K_{NiFe2O4} < \log K_{NiO} + 2/3 \log K_{Fe3O4} - 1/3 \log \{H_2\}$.

The quantity on the RHS of this inequality is plotted for selected values of log $\{H_2\}_{25C}$. Comparison with the more reliable estimate of log $K_{NiFe2O4}$ suggests that $NiFe_2O_4$ is stable against decomposition to NiO and magnetite for log $\{H_2\}_{25C} < 0$, over the temperature range 100 to 200 °C. In any case, for log $\{H_2\}_{25C}$ of above around -3.0 to -1.4 over the same temperature range, Ni becomes stable relative to NiO. Ni solubility is inversely proportional to hydrogen fugacity, so at values of log $\{H_2\}_{25C}$ higher than this, the maximum equilibrium Ni concentration in solution falls off rapidly, this causes nickel ferrite to become unstable with respect to decomposition to Ni and magnetite, or in practice Ni leaches out from the nickel ferrite to form Ni metal deposits by Ostwald ripening, leaving behind a non-stoichiometric ferrite phase with Fe:Ni greater than 2.

For the other curve of estimated log $K_{NiFe2O4}$, a maximum log $\{H_2\}_{25C}$ of around -8 is suggested. The difference between the two values is a reminder of the level of uncertainty.

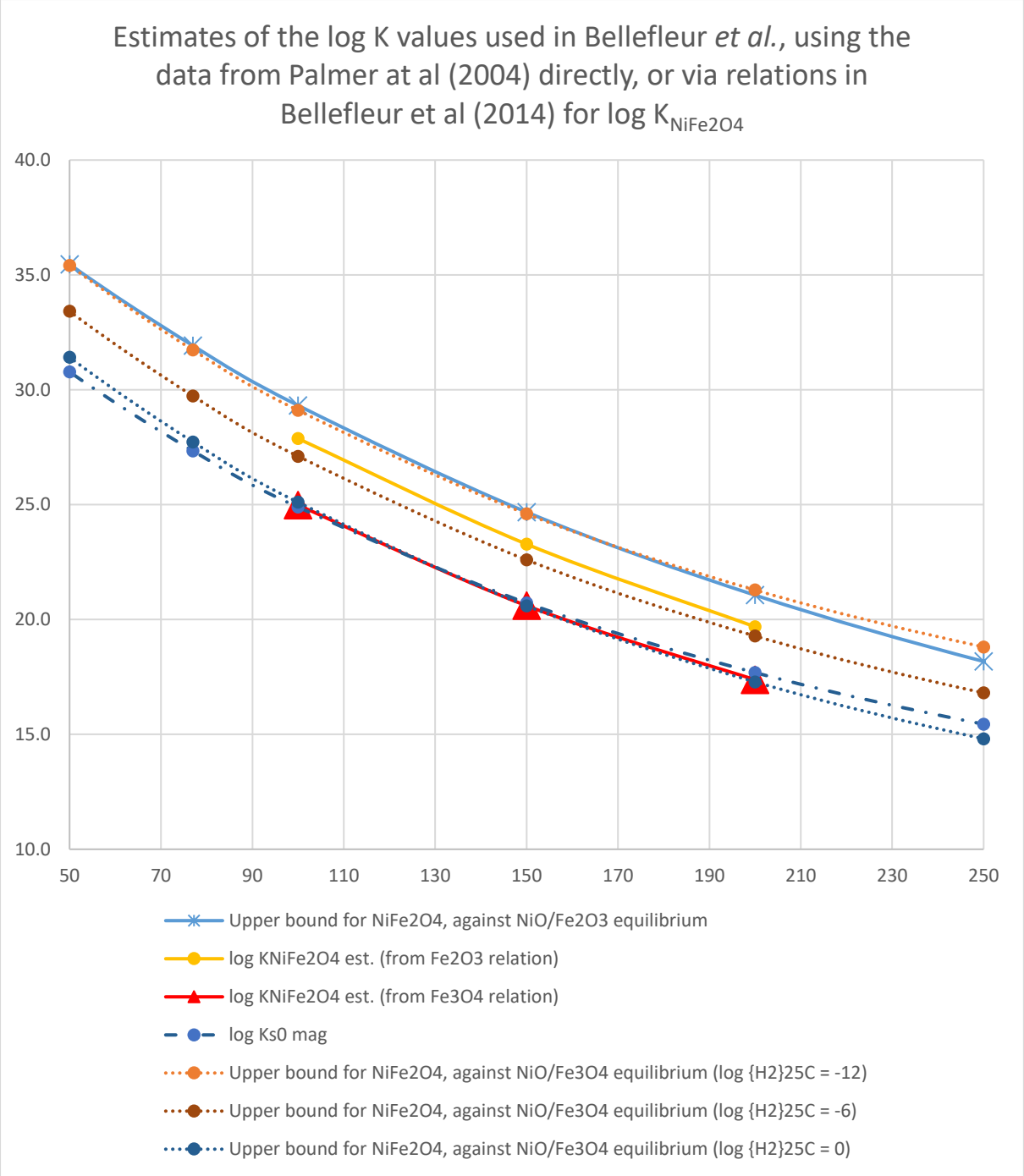

Figure 14.52. Estimates of the log K values used in Bellefleur et al. [130]*, using the data from Palmer at al.* [187] *directly, or via relations in Bellefleur et al.* [130] *for log* $K_{NiFe2O4}$.

Magnetite – nickel ferrite solid solution

Stoichiometric magnetite and stoichiometric nickel ferrite are end-members of a solid solution of inverse spinels known generically as 'ferrite'.

For intermediate values of x in the composition, $Ni_xFe_{3-x}O_4$, partition coefficients may be used [14] to describe the equilibrium between x and the activity of soluble nickel species in solution. There is not in general a linear relationship due to Gibbs energy of mixing between the two phases being non-linear. Little data is available in this field.

For intermediate values of x, the term 'solubility' is used loosely, as the nature of the oxide is poorly defined. The system is at a well-defined equilibrium where the ferrite phase is in equilibrium with whichever Ni phase is stable under prevailing conditions (NiO or Ni under hydrothermal conditions, see Ni, NiO, $Ni(OH)_2$ section). In this case, levels of Ni in solution are controlled by the Ni-based phase, the fixed activity of soluble nickel in turn fixes the composition of the ferrite (i.e. x), and levels of soluble iron are given by the ferrite solubility product together with known levels of Ni. Although there is full miscibility between end members magnetite and nickel ferrite, the maximum value of x at equilibrium in hydrothermal solutions may be less than 1. This is due to instability of stoichiometric nickel ferrite (x=1) with respect to decomposition into the stable Ni-based phase and a ferrite phase poorer in Ni, for example x = 0.9. Where conditions are sufficiently reducing that Ni metal is the stable phase of Ni, solubility of Ni is inversely proportional to hydrogen fugacity, and so drops off rapidly with rising hydrogen fugacity. In accordance with the partition coefficient for $\{Ni^{2+}(aq)\}$ / $Ni_xFe_{3-x}O_4(cr)$, the maximum value of x for equilibrium decreases rapidly (though not linearly) as hydrogen fugacity increases and Ni solubility decreases.

For the elemental make-up $Ni_xFe_{3-x}O_4$, x may take any value from 0 to 1, though for any given set of conditions the maximum value of x at equilibrium may be less than 1.

15. Appendix 2:

Elemental Analysis of Rig Effluent, using ICP-MS – Full Results and In-depth Discussion

15.1. Overview of Chapter

Samples analysed by ICP-MS came from six sessions of use of the MOS rig, as well as a few samples from related rigs in the same laboratory (the 'Hot Loop', and the Corrosion Rate Rigs). They were prepared on a batch basis, to enable relatively accurate assessment of the mean and standard error of contamination introduced in the course of the sample preparation and analysis procedure, via a number of 'blank' samples analysed within each batch. A table summarising all the 'raw' ICP-MS data is included in the appendices, grouped according to batch, along with key data pertaining to each sample such as the coolant pH and temperature.

The contamination and dilution effects of sample preparation were accounted for to give a best estimate of the actual levels in the rig effluent before sampling and analysis; these are the 'processed' data, presented in Section 15.2. To each result was assigned a measurement error, taking into account both the quoted error of the analysis method itself (around 5% for most elements) and the observed error on the blanks. The processed data are grouped according to the sessions of rig use from which they were taken. Sections 15.2.3 to 15.2.8 talk the reader through the results tables, session by session, including any extra information of interest regarding particular samples which may not be obvious or apparent from the tables themselves. An example of such information is the effect of different sampling methods used throughout session 2, and the fact that the effects of sampling and analysis may not be accurately accounted for, for some of these samples. Section 15.2 also discusses some trends which are apparent from the data as displayed in tabular form.

To fully appreciate trends in the data it is necessary to consider the effect that the passage of time has on the results. In Section 15.3, processed data are plotted against 'hot hours' – time at temperatures of 200 °C or more. Time spent at room temperature is excluded from the time

ordinate because corrosion is expected to occur at a negligible rate in comparison with hydrothermal conditions. Periods of zero flow, when held at temperatures of 200 °C or more, are included in the time ordinate because corrosion continues regardless of flow rate. However, these periods were taken into consideration when analysing the data, along with any other disturbances to the normal operation of the rig. For sessions 1 to 3 the same reaction cell was used throughout, and so results were plotted on the same graph against cumulative time. For later sessions, a new reaction cell was used each time, so each session has its own graph with the time ordinate starting at zero when the session commenced.

It was noted that samples taken relatively soon after a disturbance to the flow tended to produce erratic results compared with other samples taken under the same conditions. Section 6.4 details a set of consistent rules which were developed to remove these data points based on the conditions under which they were taken, in order to try to avoid the bias which would be introduced by simply discarding the results with the most extreme values. For example, by removing data from samples taken within 24 h of a change in conditions some of the most erratic results were removed enabling the general trends in data over time to be seen more clearly. Plots of the data thus cleaned are presented. The discarded data points are still of interest, in terms of qualitatively indicating what happens in the rig shortly after each change in conditions or disruption to the flow.

15.2. Processed Results, Presented by Session

15.2.1. Summary of method used to process and display results

In arriving at processed results, the best use was made of information gained from blank samples to give the best possible estimate of the levels actually present in the rig effluent, based on a few assumptions as discussed in Chapter 7. The net effect of sample preparation on the results was accounted for on a batch basis using the following equation:

$$C_a = \frac{15.15}{12}\{C_r - C_b\}$$

Where C_a is the best estimate of the actual concentration before sample preparation ('processed' data), C_r is the sample concentration measured in the ICP-MS ('raw' data), C_b is the mean blank concentration measured in the ICP-MS for the batch in which the sample was analysed, and 15.15/12 is the ratio of masses after and before acidification, to account for dilution.

When accounting for the effect of sample preparation on results as described above, any uncertainty in the level of blanks contributes to uncertainty in processed results. In addition, there is statistical error associated with the analysis process itself, which can vary between ICP-MS instruments, due to factors such as lab and instrument background levels. For the Agilent 7500ce used for batches 1 – 4 of analysis, typical error was known/thought to be around 5% for most elements [193], on top of the errors associated with sample preparation which become significant only at low levels comparable with blanks. Levels in just one pair of duplicate samples, as well as some other samples which turned out to be near-identical, were compared; the figure of 5% was found to be consistent with the results for all of the elements analysed in those samples, apart from Mo and Mn, for which the levels were so similar that a much lower error of 0.5% was adopted. Overall error on each measurement was thus quantified for each sample using the following equation

$$\sigma\{C_a\} = \frac{15.15}{12}\sqrt{\sigma^2\{C_r\} + \sigma^2\{C_b\}}\,,$$

where $\sigma\{X\}$ denotes the standard error of a variable, X; and C_a, C_r, and C_b retain their previous meanings. For $\sigma\{C_r\}$, the value of $0.005 * C_r$ was used for Mo and Mn, and $0.05 * C_r$ was used for all other elements. Error on blanks, $\sigma\{C_b\}$, was calculated from the blanks using the usual formula:

$$\left(\sigma = \sqrt{\frac{\sum(x-\bar{x})^2}{n-1}}\right).$$

All calculations were performed in Microsoft Excel using the full degree of precision available, and only then rounded to a suitable degree of precision for display.

15.2.2. Notes on how the results are displayed

In the following sections, processed results from samples are listed in tables by session. For each session, data on the mean and standard error of blanks which were used in the processing of those results are included, for reference. For session 3 there are two entries for the blanks because samples from that session were analysed across two different batches of analysis. It should be noted that levels presented for the blanks represent an average of raw values, whereas levels for all the other samples are as-processed according to the equations above.

In displaying each result and measurement error, the convention of X (Y) was adopted, where X represents the result and Y is an indication of the standard error. Y represents the error on the last digit of the result value, or where Y has two digits, the last two digits of the result value. For example, 0.7 (1) represents 0.7 +/- 0.1, and 18.79 (94) represents 18.79 +/- 0.94.

For samples analysed in batches 1 and 2 – i.e. all samples from session 1, some from session 3 and both of the hot loop samples – some results were below the reporting limit of 0.1 ppb imposed by the ICP-MS operator, particularly for cobalt, and were reported simply as "< 0.1". For all samples except for blanks this is indicated in the tables by the use of blue text colour, and the value "< 0.1". An estimate of the mean and standard error of blanks was made for each element, even when some or all of the blanks for that element were below the minimum reporting limit – in this case the mean and standard deviation were displayed, but with blue text colour and the letter m. For such blanks, the value of 0.05 ppb was used in calculations of mean and standard error; and where all blanks were < 0.1 ppb for a particular element the value of 0.03 ppb was used for the standard error. For batches 3 onwards, full precision of all data was requested including those below 0.1 ppb, so that blanks could be adjusted for appropriately without having to guess their levels. Caution should be exercised regarding such low levels where they appear in rig effluent samples, and especially regarding the supposed measurement error on these levels. This is illustrated by three samples from session 2 having Ni levels in excess of 7 measurement errors below zero! However, these were perhaps an exceptional case, being also in excess of 3 σ below zero in terms of the raw level from the ICP-MS analysis (before adjusting for blanks), suggesting either a slight mishap during analysis, or that the 5 month prior residence of these samples in glass vials achieved Ni levels consistently lower than blanks prepared both by the author and by the operator of the ICP-MS instrument.

For each batch, for each element, the value of $\mu + 2\sigma$ for the blanks was calculated. These values are listed in appendix A as the 'sample mrv', the minimum reportable value for raw sample data, as calculated from scatter in the blanks rather than the 0.1 ppb limit imposed in early batches by the operator. Assuming a normal distribution of blank levels, raw values at or above this sample mrv could be achieved by a blank about one time in 40 (though in reality outliers may be more common), and progressively more commonly at progressively lower values. In appendix A, raw values which are less than the sample mrv are coloured red and italicised, indicating that there is at least a slim chance that actual level was zero before sample preparation. Such values were processed and presented in the tables of this chapter, along with the other data, but were likewise coloured red and italicised, for indicative purposes. Values of these data points are still of interest as the purpose of the project is to study trends in effluent levels and the effect of various variables, rather than simply to prove the presence or absence of the elements studied.

In the results tables, the following abbreviations have been used.

Column headings:

T = temperature (°C)

$\dot{m}$ = mass flow rate (g/min)

N_2 = nitrogen overpressure in the feed water barrel (barg)

Information in the "Other info" field:

d.l. = dump line – an alternative exit from the rig, only used for samples during sessions 1 and 2

s.c. = sampling cell – a ~ 42 ml sealed cell made from 1" SS316L tubing, only used for samples during sessions 1 and 2 (and the first 2 samples of session 3). For these samples, flow was diverted from the dump line to the sampling line.

scoop = the sampling vessel (glass vial) was used to scoop a sample from the dump beaker, which was used to collect rig effluent primarily for mass flow rate monitoring.

g.v. = glass vial (used as a sampling vessel)

t.t. = test tube (used as a sampling vessel)

15.2.3. Session 1 Results

Just four effluent samples were taken during session 1, which served as a practice for use of the rig, sampling, and sample preparation. These were analysed for Fe, Cr, Ni, Mn and Co, along with a single blank and a deliberately contaminated sample, as batch 1; processed results are shown in Table 15.1.

Table 15.1. Session 1 results

sample	pH	T	$\dot{m}$	N_2	[Fe]	[Cr]	[Ni]	[Mo]	[Mn]	[Co]	Other info
01-01	7*	260	1	0.7	10 *(4)*	1.4 (5)	12 (*1*)	-	240 (*1*)	2.4 (*01*)	25ml, d.l., 75min since start, 30 min at temp.
01-02	7*	260	1	0.7	17 *(4)*	1.0 (4)	4 (*0*)	-	67 (*1*)	0.8 (*01*)	28ml, d.l., 217min since start, 172 min at temp.
01-03	7*	260	1	0.7	16 *(4)*	1.4 (4)	57 (*3*)	-	527 (*3*)	30.1 (*15*)	35ml, s.c., 158min since pump restart
01-04	7*	20	1	0.7	7 *(4)*	1.1 (4)	147 (*7*)	-	83 (*1*)	2.4 (*01*)	36ml, d.l., ~1 h after pump restart
01-con	-	-	-	-	59 *(6)*	0.9 (4)	1 (*0*)	-	2 (*1*)	m 0.0 (*01*)	Deliberately contaminated with fleck of hematite
Blanks	-	-	-	-	19 (3)	2.7 (3)	1 (0)	-	1 (1)	m 0.1 (01)	Batch 1. One blank to cover all session/batch 1 samples.

Since only one blank was analysed, standard error on blanks was estimated using human judgement
*feedwater was pH neutral at time of preparation, but the pH of ultrapure water is susceptible to change via the addition of ions dissolved from rig

Levels in the blank were relatively high, especially for Fe and Cr, and since there was only one blank the error on those levels had to be estimated by human judgement. In addition, there was a lot of uncertainty regarding the actual pH_T in the hot part of the rig, the concentration of hydrogen, and the oxides which would be present at this early stage of corrosion. For all the above reasons, session 1 results have limited applicability outside of this project, but were useful as an indication of the levels to expect in rig effluent samples from later sessions, and also for comparison with later sessions to see how different the levels were during the first few hours of use of the rig, before the duplex oxide film of hydrothermal conditions had become established.

Sample 01-con

The deliberately contaminated sample (01-con) was prepared as a blank, to which were added two tiny flecks of rust from the lab, barely visible to the naked eye. The rust was added to give an idea of the amount of Fe and other elements which could enter samples as airborne contamination. The flecks of rust, although small, were too large to become airborne except in a strong breeze, therefore any contamination likely to affect samples would be much lighter, such as dust particles, and each particle would have a much smaller effect than the flecks of rust. As a precaution, care was taken in subsequent sessions to avoid airborne contamination.

Rig effluent samples 01-01 to 01-04

Each of the four samples is quite different from the others in terms of the circumstances under which they were taken; this is important to explain to give proper context to the results. Table 15.2 provides an overview of rig conditions for session 1. Samples 01-01 and 01-02 were both taken very

early on in the use of the rig – within 4 hours of the rig first being filled with water and flow commencing, and within 3 hours of the oven being heated to 260 °C. Sample 01-03 was taken after about 24 hours at temperature, but only around 2 ½ hours after flow was restarted following a 7 hour period of zero flow. Sample 01-04 was taken towards the end of session 1, which consisted of: 5 days of intermittent flow at 260 °C; 2 days of zero flow at room temperature; one day at 260 °C, including 8 hours of flow; and 11 days of zero flow at room temperature. Flow was resumed, at room temperature, for just one hour before sample 01-04 was taken; after this, flow was stopped and session 1 concluded.

An important point to consider is the residence time in the rig – if one full residence time has not been allowed between the latest changes to rig conditions and the commencement of a sample, then that sample will have spent some of its time in the rig under conditions other than those quoted. If the amount of time which has been allowed is only marginally above the residence time, then the sample still may be influenced by the previous conditions, due to diffusion and mixing of flow within the reaction cell. If the rig is considered to begin at the point at which feed water exits the 50 litre barrel, then the bulk of the rig's volume resides in the oven: that is, in the reaction cell, of ~ 120 ml volume; and in ¼" tubing totalling ~ 10 ml. Together with about 20 ml of ¼" and 1/8" tubing outside of the oven, the total volume of the rig is ~ 150 ml. At 1 g/min flow at room temperature the coolant therefore takes around 150 minutes to pass through the rig. Under hydrothermal conditions the time taken decreases as the specific volume of the coolant increases – at 260 °C for example the time is reduced to 118 minutes – and the time taken also varies according to flow rate.

Samples 01-01 and 01-04 both contain coolant which spent some of its time in the rig at conditions other than those quoted in Table 15.1. For sample 01-01, it was present in the rig at room temperature for 10 minutes (as the rig was filled and pressurised by the pump at a fast flow rate), then for 35 minutes at 1 g/min, as the oven temperature gradually increased to 260 °C. After this just 30 minutes was allowed before the sample commenced. Effluent at the beginning of the sample would have had around 45 minutes at a temperature gradually climbing to around 260 °C, plus 25 minutes at 260 °C, and 5 minutes in the room temperature tubing (some of it plastic, some SS316L), at the back end of the rig. The last few drops of effluent entering the sample would have had an extra 25 minutes at 260 °C. For sample 01-04, the coolant was stationary in the rig for 11 days before flowing for between 60 and 96 minutes (for the start and end of the sample respectively) at 1 g/min. Samples 01-02 and 01-03 were under conditions quoted in Table 15.1 for the full passage through the rig, though only by fairly narrow margins.

Table 15.2. Conditions of the rig and sampling during session 1

Conditions	*Times and dates*	*Samples analysed*	*Notes*
1 g/min; 22 °C rising to 260 °C	12/9/13, ~ **2 hours**	01-01	Air in oven reached 260 °C only 45 minutes after start of session, but SS316L tubing and water in rig is known to take time to heat up initially, see results for session 4.
1 g/min; 260 °C	12/9 – 16/9, **4 days** 12 h flow (7 h no flow) 7 h flow (2 h no flow) 2 h flow (19 h no flow) 2 h flow (19 h no flow) 2 h flow (18 h no flow)	 01-02 01-03	
2 g/min; 260 °C	16/9, **5 hours** 4 h flow (1 h no flow)		
3 g/min; 260 °C	16/9 – 17/9, **1 day** 3 h flow (2 h no flow) 1 h flow (15 h no flow)		
Stagnant, room temperature	17/9 – 19/9, **2 days** (46 h no flow)		
1 g/min; 22 °C rising to 260 °C	19/9, **2 hours** 2 h flow		
(1+1)g/min* 260 °C	19/9 – 20/9, **1 day** 7 h flow (15 h no flow)		
Stagnant, room temperature	20/9 – 1/10, **11 days** (270 h no flow)		
1 g/min; 24 °C	1/10, **2 hours** 2 h flow	 01-04	
Stagnant, room temperature	1/10 – 8/10, **7 days** (169 h no flow)		
(1+1)g/min* 24 °C	8/10, **2 hours** 2 h flow		Session ended after this

For samples 01-01 to 01-03, levels of Ni, Mn and Co follow a clear trend, being highest for 01-03 and lowest for 01-02; differences between 01-01 and 01-02 levels are particularly consistent, with a factor of around 3 separating the samples in each case. This can be understood in terms of the SS316L surfaces releasing particularly high levels of those elements during their first few hours of contact with ultrapure water, even at room temperature. Sample 01-03 was collected in the

sampling cell, and was in contact with the SS316L surfaces of the as-yet unused cell for the 45 minutes during which the sample was taken (of the 45 g collected, 35 g was decanted into a glass vial as a sample and 10 g was discarded). In addition, flow was diverted along the sampling line (see chapter 7.4.1) for the very first time, immediately before sample 01-03 was started. The sampling line is a short section of ¼" SS316L tubing, of just a few (~2-3) ml of volume, taking the effluent from a BPR to the intended sampling point (in this case the sampling cell); the alternative exit from the rig is the dump line, from which some samples were taken during sessions 1 and 2 only, which takes effluent from a different BPR to the dump beaker. Bearing the above points in mind, the effluent in sample 01-03 has passed over SS316L surfaces which have been exposed to ultrapure water for the very first time since being purchased, aside from a quick rinse to clean them, both in the tubing of the sampling line, and in the sampling cell. The SS316L surfaces which sample 01-01 passed over, in the room temperature tubing at the back end of the rig, had only about 75 minutes of prior exposure; and for sample 01-02 the figure was a little higher, at 217 minutes. The resulting decreasing levels of Ni, Mn and Co could be explained by an early leaching of such elements from the surface and near-surface regions of the SS316L surfaces at room temperature in ultrapure water.

Sample 01-04 represents conditions in the rig after 11 days of zero flow at room temperature, plus any transient effects of the flow starting up again – for example particulate matter which built up over those 11 days may become stirred up and sampled. Ni is very high, perhaps as either dissolved or particulate matter which has built to high levels due to the longer residence time. Co is equal to sample 01-01 levels, perhaps due to the flow disturbance stirring up particulates, and Mn is similar to the sample 01-02 level.

For all four samples, levels of Co are far higher than expected for such a low level impurity in the alloy, whose levels are not even quoted in the elemental composition. Levels of Mn are high, given the low alloying %, showing the high solubility of Mn oxides. Levels of Ni were higher than expected. Levels of Cr were much higher than expected, given the solubility of ~ 0.00 to 0.01 for Cr oxides and chromites under hydrothermal conditions and at room temperature, suggesting the presence of particulate matter. Cr levels were also surprisingly consistent across the four samples, especially given that they are likely particulate in form. Levels of Fe were relatively consistent across the four samples, and for samples 01-01 to 01-03 were consistent with literature solubility values, assuming similar hydrogen levels and a pH which was modified to around pH 5.7 (equivalent to room temperature pH of 8).

Overall, levels of Fe were fairly similar for all the samples, and consistent with solubility of ferrites and chromites; levels of Cr and Ni and Co were higher than expected and suggestive of particulate

matter coming from the rig; levels of Mn are the highest of all, and are consistent with the high solubility of Mn.

Estimates of coolant pH_T, accounting for dissolved ions from the rig

Estimates of pH_T were made using the measured levels of each element and dissociation data [ref:], assuming that elements were fully dissolved when present in the rig. Mn was the dominant factor, causing pH_{260C} to increase from 5.6 (neutral) to 6.0, 5.7, and 6.2 for samples 01-01, 01-02, and 01-03. Had these pH values been achieved by a strong base such as LiOH, they would correspond to room temperature pH of 8.9, 8.4 and 9.2, in other words approximately 8 – 9. However, since Mo was not measured it was not possible to determine the effect on pH from dissolved Mo. For sample 01-03, 1760 ppb Mo would be required to neutralise the solution, or 1620 ppb to bring it down to pH_{25C} 8. For sample 01-02 the equivalent values would be 250 and 160 ppb. Thus it cannot be conclusively determined whether pH was modified upwards or downwards.

15.2.4. Session 2 Results

From session 2, ten rig effluent samples and two feedwater samples were analysed (along with samples from other sessions) in batch 3 of analysis. The processed results are displayed in Table 15.3

Table 15.3. Session 2 results

sample	pH	T	$\dot{m}$	N_2	[Fe]	[Cr]	[Ni]	[Mo]	[Mn]	[Co]	Other info
02-07	11	300	2	0.7	0.6 *(4)*	0.8 *(0)*	2.6 *(2)*	451 *(2)*	0.7 *(1)*	-	s.c.-->g.v. 23h after start of session
02-08	11	300	2	0.7	2.2 *(4)*	0.7 *(0)*	4.4 *(3)*	318 *(2)*	0.6 *(1)*	-	s.c.-->g.v. 25h after start of session
02-09	11	300	2	0.7	2.0 *(4)*	1.4 *(1)*	0.1 *(1)*	481 *(2)*	0.3 *(1)*	-	scoop-->g.v. 29h after start of session
02-10					0.2 *(4)*	0.6 *(0)*	0.1 *(1)*	330 *(2)*	0.1 *(1)*	-	s.c.-->g.v. 29h after start of session
02-20	11	300	2	1.0	0.2 *(4)*	0.7 *(0)*	-0.4 *(1)*	78 *(0)*	0.0 *(1)*	-	d.l.-->t.t.* 5 h after latest restart
02-21					0.4 *(4)*	1.2 *(1)*	-0.3 *(1)*	76 *(0)*	-0.1 *(1)*	-	d.l.-->g.v. 5 h after latest restart
02-22					0.4 *(4)*	0.9 *(0)*	3.8 *(2)*	121 *(1)*	0.0 *(1)*	-	s.c.-->g.v. 5 h after latest restart
02-25	11	300	2	1.0	0.9 *(4)*	0.8 *(0)*	-0.4 *(1)*	59 *(0)*	0.0 *(1)*	-	d.l.-->t.t.* 29h after latest restart
02-26a	11	300	2	1.0	0.9 *(4)*	6.3 *(3)*	0.0 *(1)*	61 *(0)*	0.1 *(1)*	-	s.c.-->g.v. 16h after latest restart
02-26b					0.1 *(4)*	2.4 *(1)*	0.3 *(1)*	54 *(0)*	-0.1 *(1)*	-	s.c.-->t.t.* 16h after latest restart
02-f1	11	20	-	0.7	-0.4 *(4)*	0.9 *(0)*	2.3 *(2)*	2.0 *(0)*	-0.1 *(1)*	-	g.v. Feed water from barrel
02-f2	11	20	-	1.0	1.0 *(4)*	0.6 *(0)*	1.3 *(1)*	1.3 *(0)*	-0.1 *(1)*	-	g.v. Feed water from pump inlet
Blanks	-	-	-	-	1.5 *(3)*	0.0 *(0)*	0.2 *(0)*	0.0 *(0)*	0.1 *(0)*	-	Batch 3. Four blanks analysed.

* each of the three polypropylene test tubes was from a different manufacturer, and all were different from the 16.5 ml Sarstedt test tubes used for final sample preparation.

Accounting for blanks

Four blanks were prepared in test tubes and analysed for batch 3, enabling an assessment of error on blanks. All the samples from session 2 were collected either in glass vials or in polypropylene containers which differed from the standard Sarstedt test tubes used for acidifying samples (used in all batches of analysis except batch 1). Therefore in each case ~ 12.0 +/- 0.5 g of the sample was transferred to a Sarstedt test tube before acidification and analysis. For this reason, the session 3 blanks were not fully representative of the samples – some contamination could have been picked up from the sampling vessels, causing additional contamination compared with the blanks; though pH 11 solution is likely to have limited leaching effect in comparison with the ~0.5 pH of solution after acidification. Also, holding samples in the initial sampling vessels for ~ 5 months before transferring to the final vessel for acidification could have caused an under-reading of results, if certain elements were to crystallise or adsorb onto the walls of the vessel, or if particulates were to settle at the bottom and not transfer with the ~12 g of solution taken as a sample.

For the above reasons, there may be biases in the results from session 2, in terms of absolute value (possible contamination from sampling vessel); relative value (a proportion of total levels of some elements may be adsorbed on the vessels for example); and tendency towards a particular value

(room temperature, pH 11 solubility of the relevant oxides, where crystallisation onto vessel walls is concerned). In addition, the effects of the various sampling methods and sampling vessels used may be different in each case, making comparisons between samples problematic. At the flow rate and temperature employed, rig residence time was just 54 minutes; all samples analysed were taken after at least 5 residence times' worth of flow since the latest disruption to the flow (pump stall) in the main part of the rig. However, 6 of the 10 samples were taken using the sampling cell, by diverting flow along the sampling line instead of the dump line for the ~20 minutes it took to collect the sample, then diverting flow back along the dump line as soon as the sample was complete. Thus, for each sample which used the sampling cell, the last few ml of room temperature flow before exiting the rig passed through tubing (with a residence time of a minute or so) which had previously contained stagnant water for a number of hours, and which had only been exposed to flowing coolant for a few hours in total during previous sampling – as little as 44 minutes for sample 02-07 and at most 6 hours (02-26a&b). Also, effluent was resident in the SS316L sampling cell for ~20 minutes while the cell filled, which may have altered the levels of some elements – especially for the first few samples where the sampling cell had not yet had much exposure to the pH 11 coolant.

Summary of rig conditions and sampling during session 2

Temperature, feedwater pH, and mass flow rate were unchanged throughout session 2 (apart from periods of zero flow after pump stalls). Table 15.4 summarises conditions employed during session 2. Samples 02-07 to 02-10 were taken during the 37 hour period of uninterrupted flow following commencement of the session. After this came a 45 h period of intermittent flow (13 h and 10 h), followed by a 35 h period of no flow. Backpressure in the feedwater barrel was then increased from 0.7 to 1.0 barg in an attempt to improve the time to pump stall, then there was intermittent flow for a further 7 days, consisting of 6 periods lasting the following amounts of time: 19 h; 7 h; 24 h; 46 h; 24 h; and 17 h. The remaining samples were taken in the 4th and 6th such periods, and a feedwater sample was taken in the 2nd. The other feedwater sample, 02-f1, was taken directly from the barrel (by temporarily disconnecting the line to the pump and attaching a short line to the sampling vessel), after preparing and sparging the feedwater but before commencement of flow in the rig.

Table 15.4. Conditions of the rig and sampling during session 2

Conditions	*Times and dates*	*Samples analysed*	*notes*
2 g/min; 22 °C rising to 300 °C; 0.7 barg N_2	16/10/13, **2 hours** 2 h flow	[no samples analysed]	Sample F1 taken directly from feed-water barrel before commencement of flow in rig
2 g/min; 300 °C; 0.7 barg N_2	16/10 – 19/10, **3 days** 35 h flow (8 h no flow) 13 h flow (14 h no flow) 10 h flow	#7,8,9,10	
Zero flow; 300 °C	19/10 – 20/10, **1 day** (35 h no flow)		Nitrogen overpressure changed during this time
2 g/min; 300 °C; 1.0 barg N_2	21/10 – 28/10, **7 days** 19 h flow (8 h no flow) 7 h flow (14 h no flow) 24 h flow (4 h no flow) 46 h flow (1 h no flow) 24 h flow (10 h no flow) 17 h flow	 F2 #20, 21, 22, 25 #26, 27	

Discussion of results

Table 15.3 shows that levels of Mo and Mn were significantly higher for the first four samples, when feedwater backpressure was 0.7 barg, than the latter six, for which backpressure was 1.0 barg. For Mo, the same observation can be made regarding the two feedwater samples. A possible explanation could be that air, and thus oxygen, was ingressing to the feedwater barrel or the rig tubing before the pump by some means, and affecting solubility behaviour, and that a larger positive pressure in the feedwater was more effective at minimising this effect. However, it should also be noted that there was a large passage of time between when the first four samples were taken (between 24 and 29 hot hours); and when 02-f2 and the latter six samples were taken (142, and 197 – 288 hot hours respectively), during which the corrosion of the SS316L surfaces in pH 11 coolant, and its effect on chemistry of the corrosion film, will have progressed considerably. Also several more samples were taken in the sampling cell in the intervening days.

For Fe, given the relatively large measurement error of ~0.4 ppb, results are consistent with a constant level of ~ 0.5 ppb throughout, with scatter caused purely by measurement error, with perhaps a genuinely higher level in samples 02-08 and 02-09. The measurement error on Cr readings

is much lower, typically 0.0 to 0.1 ppb, and therefore cannot fully account for the scatter observed in readings. Since the Cr levels do not seem to follow any discernible pattern, results can be described in general as following a distribution which does not change over time, of ~ 0.9 +/- 0.2 ppb (apart from samples 02-26a and 02-26b), with results reflecting genuine changes in sample levels. Solubility of Cr from various oxides is around 0.00 to 0.01 for all the pH values of solution used in this project, at all temperatures from room temperature to 300 °C, thus it can be assumed that more or less all of the Cr is present in particulate form. It is therefore understandable that levels may fluctuate and not follow well defined trends, as opposed to some of the other elements. Comparison of samples 02-20 to 02-22, which were taken in quick succession, illustrates the random nature of scatter in Cr levels, and likewise for samples 02-26a and 02-26b.

Levels of Mn begin very low, at 0.7 ppb for sample 02-07, and soon fall to zero (within two measurement errors). This is in stark contrast to levels observed in session 1, perhaps partly due to the effectiveness of the ultrapure water used during that session in removing Mn ions from the corrosion film and near-surface region of SS316L surfaces, as well as the relative ineffectiveness of pH 11 coolant. The word 'solubility' is not here used, because Mn- and Mo- based oxide phases are not thought to exist on the corrosion films, but rather levels of these elements in the coolant and in the corrosion film reach a balance: in the shorter term dependent on the prevalence of these elements as impurity elements within ferrite and chromite oxides and in the near surface alloy; and in the longer term a steady state, based on a matching of the rate of release to solution with the rate at which Mo and Mn ions are liberated from the alloy by advancing corrosion. Shorter term deviations from the steady state matching of rates are achieved by a latency effect as the inventories of these elements in the corrosion film must either build up or become depleted to achieve a new steady state after any change in rig conditions occurs, during which time the corrosion film impedes or augments the flux of ions diffusing to the surface as a result of ongoing corrosion. On reflection, it seems that the low level of Mn in samples is actually due mostly to the very strong retention of Mn in the corrosion film in contact with pH 11 feed water, and perhaps the non-zero levels in the first few samples were due to particulate matter which had not yet been fully flushed from the sampling cell and rig tubing – this is consistent with the higher levels of Ni in the first two samples, also thought to be particulate.

Levels of Ni suggest a baseline of around 0.0 ppb in around 7 of the effluent samples (distribution: ~ -0.1 +/- 0.2 ppb, with negative values due simply to measurement error), and higher levels in the other three effluent samples and the two feedwater samples – presumably particulate in nature. The low levels of soluble Ni are consistent with the low solubility of NiO, Ni, or non-stoichiometric nickel ferrite (being lower than the pure metal or oxide) with a particulate contribution in some samples.

Several readings were significantly below zero, by more than three supposed measurement errors. This demonstrates that the measurement error has been incorrectly determined, or that the three samples in question were somehow prepared in a way that resulted in systematically less Ni contamination than the blanks. Since the effluent samples and the feed water blanks were prepared contemporaneously, using the same nitric acid and the same method of transferring it, it is difficult to understand how this occurred, unless the process of leaving the pH 11 samples for 5 months in glass vials or plastic test tubes – and the adsorption or crystallisation of Ni/NiO onto the walls of those vessels – somehow brought levels of Ni significantly lower than those present in the type I water drawn from the MIlliQ. The three samples in question had levels that were as low as -0.12 ppb Ni in terms of the raw value from the ICP-MS analysis, therefore they were also lower than the blanks or extrapolated zero value of the ICP-MS calibration. It should be borne in mind that the ICP-MS analysis has a minimum reporting value for each element, which is around 0.1 ppb for Ni. It was arranged that values below this level still be received from the ICP-MS analysis, in order to accurately measure the blanks, but in this case it seems the similarity in levels of all the blanks measured for batch 3 caused the error on sample measurement to be under-estimated.

Levels of Mo showed the clearest trend, with levels decreasing over time. This trend, along with some effects on the other elements, becomes clearer if the idiosyncrasies of some of the samples are taken into account. Table 15.5 below shows only the samples which were taken in the sampling cell and decanted to a glass vial, enabling direct comparisons to be made. Sample 02-08 is separated from the other samples in the table to show that it was affected by being open to the lab atmosphere.

Table 15.5. Session 2 samples taken using sampling cell and glass vial

sample	pH	T	$\dot{m}$	N_2	[Fe]	[Cr]	[Ni]	[Mo]	[Mn]	[Co]	Other info
02-07	11	300	2	0.7	0.6 *(4)*	0.8 *(0)*	2.6 *(2)*	451 *(2)*	0.7 *(1)*	-	s.c.-->g.v.; 23h from start; 2 prev. uses; 18h prior stagnancy
02-10	11	300	2	0.7	0.2 *(4)*	0.6 *(0)*	0.1 *(1)*	330 *(2)*	0.1 *(1)*	-	s.c.-->g.v.; 29h from start; 4 prev. uses; 3h prior stagnancy
02-22	11	300	2	1.0	0.4 *(4)*	0.9 *(0)*	3.8 *(2)*	121 *(1)*	0.0 *(1)*	-	s.c.-->g.v.; 198h f.s.; 5h f.r.; 14 prev.; 5h prior stagnancy
02-26*	11	300	2	1.0	0.5 *(4)*	4.3 *(2)*	0.2 *(1)*	57 *(0)*	0.0 *(1)*	-	s.c.-->... ; 287h f.s.; 16h f.r.; 17 prev.; 71h prior stagnancy
02-08	11	300	2	0.7	2.2 *(4)*	0.7 *(0)*	4.4 *(3)*	318 *(2)*	0.6 *(1)*	-	s.c.-->g.v.; 25h from start; 3 prev.; 2h prior; s.c. left open!

Table 15.6 shows only the samples taken from the dump line, either directly or scooped from the dump water. It should be noted that sample 02-09 was scooped from a dump beaker containing the last 10 hours' worth of flow, and so approximately represents an average over the previous 10 hours.

Table 15.6. Session 2 samples taken directly from dump line, or scooped from dump water

sample	pH	T	$\dot{m}$	N_2	[Fe]	[Cr]	[Ni]	[Mo]	[Mn]	[Co]	Other info
02-09	11	300	2	0.7	2.0 *(4)*	1.4 *(1)*	0.1 *(1)*	481 *(2)*	0.3 *(1)*	-	scoop-->g.v.; 29h from start;
02-20	11	300	2	1.0	0.2 *(4)*	0.7 *(0)*	-0.4 *(1)*	78 *(0)*	0.0 *(1)*	-	d.l.-->t.t.; 197h from start; 5h from restart
02-21					0.4 *(4)*	1.2 *(1)*	-0.3 *(1)*	76 *(0)*	-0.1 *(1)*	-	d.l.-->g.v.; 197h from start; 5h from restart
02-25	11	300	2	1.0	0.9 *(4)*	0.8 *(0)*	-0.4 *(1)*	59 *(0)*	0.0 *(1)*	-	d.l.-->t.t.; 221h from start; 29h from restart

Comparison of Mo levels for samples 20/21 and 22 provides an example of differences between the sampling methods, although in this case it may be particularly large due to lingering effects in the sampling cell and sampling line from the previous s.c. sample (02-19, not analysed), which was collected just 26 minutes after restarting flow following a period of zero flow. Despite these differences, all samples show a consistent trend over time, when plotted against time on the same graph. Such a graph is plotted in Figure 15.1, with samples which are thought to be non-representative shaded in orange (#'s 08, 09, 22); a power law relationship is fitted to the remainder of data points, coloured blue, for illustrative purposes. Observation of Figure 15.1 suggests that over the ~ 12 days (~300 h) of sampling during session 2, the dominant factor affecting [Mo] levels was the cumulative number of hot hours during which the rig was in contact with pH 11 coolant, despite effects from other factors such as details of the sampling method and changing nitrogen overpressure in the feedwater barrel.

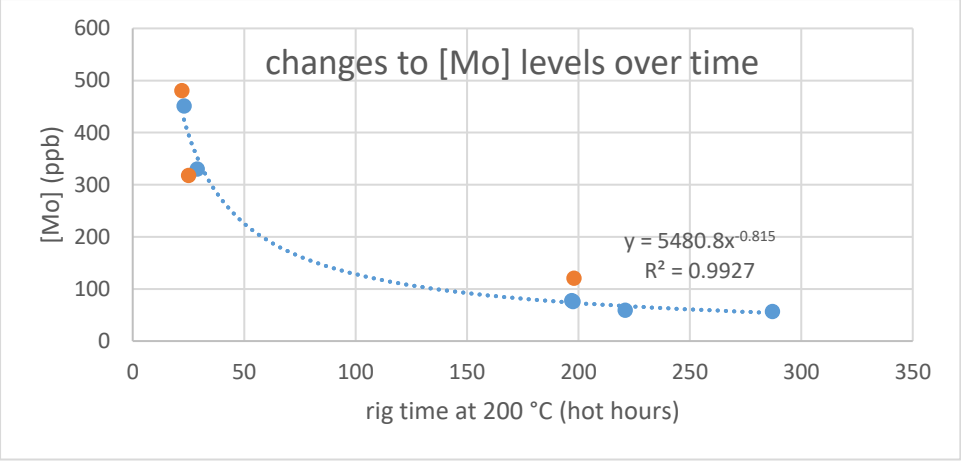

Figure 15.1. Changes to [Mo] levels over time during session 2.

In Table 15.7 and Table 15.8 the levels of each element measured during session 2 are summarised and discussed. In Table 15.9 and Table 15.10 various aspects of the conditions and prior conditions in the rig and sampling line are tabulated and compared, for samples taken via the sampling cell and dump line respectively.

Table 15.7. Overview discussion of levels during session 2 (pH 11, 300 °C, 2 g/min)

Ele-ment	behaviour	Why?
Fe	0.5 +/- 0.4 ppb 2.0, 2.2 ppb	Steady level of ~ 0.5 ppb in rig effluent, obscured by sampling error Higher levels for two samples, due to: s.c. being open to the lab atmosphere (02-08); and method of scooping from dump beaker (02-09)
Cr	0.9 +/- 0.2 ppb 6.3, 2.4 ppb	Fluctuating levels of Cr particulate in rig effluent, but on the whole levels stay fairly steady Both samples (02-26a and b) were decanted from the same s.c. sample. Before this sample was taken, effluent had not flowed along the sampling line since the previous sample 71 hours previously. For the other samples this time was much less (at most 18 h, in the case of 02-07; and 2 h, 3 h and 5 h for the other s.c. samples). The difference between these two samples shows how variable the levels can be, when caused by particulates, even within the volume of a single s.c. sample.
Ni	-0.1 +/- 0.2 ppb 2.6, 4.4, 3.8	Significantly negative levels of Ni suggests problems with the analysis and processing of results for Ni for this session. Ni levels for these 7 samples are approximately zero, reflecting the low solubility under these conditions. 02-07, not sure why – perhaps the recent changing of the nitrogen cylinder caused oxygen ingress? Or more likely simply because the sampling line and s.c. had only been used 2 previous times with pH 11 coolant. 02-08, s.c. left open to lab atmosphere 02-22, only 5 hr of flow allowed after restarting the pump. More importantly, previous use of the s.c. was for a sample taken just 26 min after restarting pump, therefore may have been contaminated by stagnant water.
Mo	Max 451 Min 54	Gradually and smoothly decreasing over time. Obscured a little by the varied sampling methods - trend becomes clearer when this is accounted for. Cold parts of the rig, and the s.c., shown to have a decreasing trend with time. Presumably also true of hot parts of the rig, but since temperature of the hot part of the rig was not varied, this cannot be determined.
Mn	0.7, 0.6, 0.3, then zero for remainder of samples	At pH 11, the SS316L surfaces have a strong tendency for retention of Mn in the corrosion film, especially when Mn was initially depleted due to high solubility in the ultrapure feed water of session 1. By the time the effects from session 1 wore off corrosion rate was too slow for Mn to release to detectable levels. First few samples, perhaps there was a small amount of Mn or mixed particulate. There were also elevated levels of Ni, which certainly seemed to be particulate-based. Another factor: perhaps the Cr oxide of the cold parts of the rig is able to soak up Mn from further upstream and remove it from the effluent?... (this effect is suspected as cause for low levels of Fe in later sessions (sess 3, 4).

Table 15.8. Summary of levels during session 2 (pH 11, 300 °C, 2 g/min)

Behaviour of Fe	Behaviour of Cr	Behaviour of Ni	Behaviour of Mo	Behaviour of Mn
Constant level of 0.5 ppb, Measurement error of ~ 0.4 ppb →0.5+/-0.4	0.9 +/- 0.2 ppb 6.3, 2.4 ppb Genuine fluctuation in effluent particulate levels	-0.1 +/- 0.2 ppb 2.6, 4.4, 3.8 ppb Usually ~ 0.0 sometimes particulates present, because of flow disturbance etc	Max 451 Min 54 Gradually, smoothly decreasing. Partly obscured by variety of sampling methods	0 ppb (first few, up to 0.7 ppb) Perhaps some lingering particulates causing the non-zero values of first few samples

Table 15.9. Comparison of conditions for samples taken in sampling cell

	MOS rig	Sampling Line				
sample	cum. hot days	cum. flow	cum. stag. time	Stag. time since previous	# prev. uses	notes
02-07	1 days	1 h	19 h	18 h	2	
02-08	1 days	1 h	21 h	2 h	3	s.c. left open
02-10	1 days	2 h	24 h	3 h	4	
02-22	8 days	5 h	189 h	5 h	14	abnormal previous use of s.c. *
02-26	12 days	6 h	278 h	71 h	17	

* previous sample using the s.c. (02-19) was taken just 26 mins after pump restart (following ~3 ½ h of zero flow in the rig),

Table 15.10. Comparison of conditions for samples taken from dump line

sample	cum. hot hrs	t since latest pump start	prev. stagnancy time	# prev. stoppages	notes
02-09	29 h	29 h	n/a	0	*[scoop]--> g.v.
02-20 02-21	197 h	5 h	4 h	6	d.l. --> t.t. d.l. --> g.v.
02-25	221 h	29 h	4 h	6	d.l. --> t.t.

* sample 02-09 was not taken directly from the dump line, but scooped from a beaker containing the last ~ 10 hours' worth of flow from the dump line.

15.2.5. Session 3 Results

From session 3, thirty effluent samples were analysed. Samples 03-01 to 03-09 were analysed in batch 2, and the remainder were analysed in batch 3. The processed results are presented in Table 15.11 below.

Accounting for blanks

For each sample, accounting for the levels on blanks was done using the appropriate blanks for that sample, according to which batch the sample was analysed in. In batch 2 there was some uncertainty over the mean and standard error on blanks, because levels below the reporting limit (per the operator) were reported as "< 0.1", and so some estimation of these values was required. This issue was resolved in time for batch 3, where all results were reported to full precision.

Table 15.11. Session 3 results

Sample	pH	T	$\dot{m}$	N_2	[Fe]	[Cr]	[Ni]	[Mo]	[Mn]	[Co]	Other info
03-01	9	22	2	0.8	3.0 *(6)*	18.79 *(94)*	2.4 *(2)*	78.9 *(4)*	0.5 *(1)*	0.28 *(4)*	s.c.-->t.t. 3 min after start
03-02	9	22	2	0.8	3.9 *(7)*	0.66 *(5)*	10.3 *(5)*	19.6 *(1)*	3.2 *(1)*	0.26 *(4)*	s.c.-->t.t. 1.25 h after start
03-03	9	300	2	0.8	2.8 *(6)*	1.11 *(7)*	1.1 *(1)*	11.5 *(1)*	58.0 *(3)*	< 0.1	0.5 h after T reached
03-04	9	300	2	0.8	2.0 *(6)*	0.15 *(4)*	0.4 *(1)*	5.6 *(0)*	26.8 *(2)*	< 0.1	2 h after T reached
03-05	9	300	2	0.8	5.0 *(7)*	0.28 *(4)*	1.3 *(1)*	7.8 *(1)*	48.2 *(3)*	< 0.1	4 h after T reached
03-06	9	300	2	0.8	3.4 *(7)*	0.87 *(6)*	2.3 *(1)*	20.3 *(1)*	104.1 *(5)*	< 0.1	21 h after T reached
03-07	9	300	2	0.8	5.5 *(7)*	0.06 *(4)*	2.1 *(1)*	25.6 *(1)*	22.5 *(2)*	< 0.1	52 h after T reached
03-08	9	300	2	0.8	5.3 *(7)*	0.22 *(4)*	2.7 *(2)*	25.6 *(1)*	18.4 *(2)*	0.13 *(4)*	28 h after pump restart
03-08-du					5.6 *(7)*	0.25 *(4)*	2.6 *(2)*	25.6 *(1)*	18.3 *(2)*	0.11 *(4)*	
03-09	9	300	2	0.8	6.0 *(7)*	0.10 *(4)*	2.5 *(2)*	24.3 *(1)*	19.4 *(2)*	0.26 *(4)*	50 h after pump restart
03-09-du					9.2 *(7)*	0.19 *(1)*	2.7 *(2)*	24.5 *(1)*	22.2 *(1)*	-	
03-10	9	300	2	0.8	3.4 *(5)*	0.09 *(1)*	2.8 *(2)*	23.7 *(1)*	24.5 *(1)*	-	79 h after pump restart
03-11	9	300	2	0.8	5.9 *(5)*	0.10 *(1)*	3.4 *(2)*	22.9 *(1)*	24.5 *(1)*	-	104 h after pump restart
03-12	9	300	2	0.8	9.8 *(7)*	0.05 *(1)*	2.7 *(2)*	24.7 *(1)*	19.6 *(1)*	-	3 min after second restart
03-13	9	300	2	0.8	5.2 *(5)*	0.05 *(1)*	5.3 *(3)*	21.5 *(1)*	29.6 *(2)*	-	44 h after second restart
03-15	9	300	0.5	0.8	5.2 *(5)*	0.10 *(1)*	6.7 *(4)*	27.9 *(1)*	43.4 *(2)*	-	21 h after change in flow rate
03-16	9	300	0.5	0.8	2.5 *(4)*	1.75 *(1)*	8.6 *(4)*	38.5 *(2)*	66.1 *(3)*	-	27 h after change in flow rate. 03-16 taken immediately after flow was diverted to drip line. N_2 cylinder recently replaced.
03-17					4.7 *(5)*	0.14 *(1)*	6.8 *(4)*	33.1 *(2)*	36.5 *(2)*	-	
03-18					8.4 *(6)*	0.10 *(1)*	6.1 *(3)*	36.1 *(2)*	26.7 *(1)*	-	
03-19	9	300	0.5	0.8	3.8 *(5)*	0.08 *(1)*	5.1 *(3)*	54.9 *(3)*	34.4 *(2)*	-	27 h after pump restart
03-20	9	300	0.5	0.8	4.6 *(5)*	0.08 *(1)*	4.0 *(2)*	63.3 *(3)*	25.3 *(1)*	-	52 h after pump restart
03-23	9	300	0.1	0.8	1.8 *(4)*	0.16 *(1)*	2.2 *(1)*	77.7 *(4)*	16.5 *(1)*	-	76 h after change in flow rate
03-24	9	300	0.1	0.8	2.2 *(4)*	0.12 *(1)*	1.8 *(1)*	79.4 *(4)*	14.6 *(1)*	-	95 h after change in flow rate
03-25	9	300	0.1	0.8	1.6 *(4)*	0.10 *(1)*	1.5 *(1)*	92.5 *(5)*	13.2 *(1)*	-	117 h after change in flow rate
03-31	9	250	1	0.8	6.1 *(6)*	0.00 *(1)*	0.3 *(1)*	47.5 *(2)*	4.8 *(1)*	-	4 h after new T reached
03-32	9	250	1	0.8	1.1 *(4)*	0.00 *(1)*	0.5 *(1)*	38.5 *(2)*	8.8 *(1)*	-	22 h after new T reached
03-33	9	250	1	0.8	1.4 *(4)*	0.01 *(1)*	0.5 *(1)*	34.3 *(2)*	5.6 *(1)*	-	23 h after new T reached
03-39	9	200	1	0.8	1.5 *(4)*	-0.01 *(1)*	0.6 *(1)*	12.2 *(1)*	18.0 *(1)*	-	11 h after pump restart
03-40	9	200	1	0.8	0.6 *(4)*	0.00 *(1)*	0.7 *(1)*	8.8 *(0)*	13.4 *(1)*	-	22 h after second restart
03-41	9	200	1	0.8	1.6 *(4)*	0.00 *(1)*	0.7 *(1)*	8.3 *(0)*	14.2 *(1)*	-	24 h after second restart
Blanks	-	-	-	-	1.5 *(5)*	m 0.05 *(3)*	0.2 *(1)*	m0.1 *(0)*	m 0.1 *(1)*	m0.1 *(0)*	Batch 2. Relevant to samples up to 03-09
Blanks	-	-	-	-	1.5 *(3)*	0.00 *(1)*	0.2 *(0)*	0.0 *(0)*	0.1 *(1)*	-	Batch 3. Relevant to samples 03-09-du onwards

By assuming a level of 0.05 ppb for any blank samples having < 0.1 ppb for a given element, a bias could have been introduced in the reporting of that blank, of anything between -0.05 ppb (where the actual level was 0.10 ppb) and +0.05 ppb (where the actual level was 0.00 ppb). Where an average is taken from four blanks, each blank which is reported as "<0.1 ppb" introduces a possible range of bias of +/- 0.0125 ppb, which translates to +/- 0.0158 ppb in effluent samples once dilution has been accounted for. The magnitude of possible bias introduced to batch 2 samples in this way

has the following values, in ppb, for the elements analysed (Fe, Cr, Ni, Mo, Mn, Co): 0.00; 0.06; 0.00; 0.05; 0.03; and 0.06 respectively. For Mo and Mn, this is generally within the overall error, and represents only a small proportion of the measured values. For Co and Cr, it is larger than the overall supposed error, which itself is crudely estimated, and is a significant proportion of measured values, so results should be treated with caution. Blanks of both batches were prepared in the same way, and achieved similar results where directly comparable (i.e. for Fe and Ni, which had no "<0.1" results), therefore it is likely that Cr levels in batch 2 were similar to the 0.00 +/- 0.01 ppb measured for batch 3, which would mean actual Cr levels for samples 03-01 to 03-09 are up to 0.06 ppb higher than reported in Table 15.11 above.

Summary of rig conditions and sampling during session 3

Table 15.12 below summarises the conditions used and samples taken during session 3. At the beginning of session 3, the sampling cell was used to collect two samples within two hours of flow commencing, whilst the oven was still at room temperature. These samples were decanted into two thoroughly rinsed Sarstedt 16.5 ml test tubes. All subsequent samples were taken directly from the sampling line into Sarstedt 16.5 ml test tubes, all water-rinsed by the same procedure.

Table 15.12. Conditions of the rig and sampling during session 3

Conditions	*Times and dates*	*Samples analysed*	*notes*
2 g/min; ~22 °C	*22/11/13,* ***3 hours***	*1, 2*	*Used the s.c.*
2 g/min; 300 °C	*22/11 – 2/12,* ***10 days*** *65 h flow* *(3 h no flow)* *112 h flow* *(18 h no flow)* *44 h flow*	 *3,4,5,6,7* *8,9,10,11* *12,13*	*12 g samples, diverted to s.l. shortly before each sample*
0.5 g/min; 300 °C	*2/12 – 6/12,* ***4 days*** *33 h flow* *(8 h no flow)* *53 h flow*	 *15,16,17,18* *19,20*	*12 g samples, diverted to s.l. shortly before each sample. Samples 16,17,18 only 4 g each, taken in quick succession*
0.1 g/min; 300 °C	*6/12 – 11/12,* ***5 days*** *119 h flow*	 *23,24,25*	*Flow diverted to s.l. several days prior to sampling. 4 g samples.*
1 g/min; 250 °C	*11/12 – 12/12,* ***1 day*** *24 h flow*	 *31,32,33*	*Flow continued in s.l. until after #31, then #32,33 followed 17 h stagnancy*
1 g/min; 200 °C	*12/12 – 16/12,* ***4 days*** *10 h flow* *(13 h no flow)* *34 h flow* *(16 h no flow)* *24 h flow*	 *39* *40,41*	*Diverted to s.l. within a few hours of starting each sample*
0.1 g/min; 200 °C	*16/12 – 18/12,* ***2 days*** *48 h flow*		*No samples analysed.*

The rig was operated at 300 °C at three different flow rates – 2, 0.5, and 0.1 g/min – in order to explore the effect of flow rate on results. Several samples were taken over several days at each flow rate, to account for anticipated high levels of scatter, outliers, and changes over time, based on results from session 1. The rig was then set to 1 g/min flow rate, and the temperature set to 250 °C for one day and 200 °C for 4 days, during which further samples were taken, in order to explore the effect of temperature.

For the majority of session 3, flow at the back end of the rig was routed along the dump line, at the end of which was space for a large beaker to collect effluent for mass monitoring and to prevent spillage onto the laboratory floor; space was limited at the end of the sampling line. Flow was generally only diverted to the sampling line for sample collection, except for the full duration at 300 °C, 0.1 g/min and the first few hours at 250 °C. This procedure may have affected the results, where insufficient time was allowed for stagnant effluent in the sampling line to be flushed through by fresh effluent.

Other factors which may have affected results – besides the major variables of pH, temperature and flow rate – include periods of stagnancy caused by pump stalls; disruptions to the flow caused by

pump restarts and changes to temperature or flow rate; and the passage of time, as characterised for example by total time since the beginning of session 3. Table 15.13 summarises the key data on these secondary factors for each sample, dealing with: time since the session began; time since the latest disruption to the flow; time since the pump was last restarted (following a stagnant period in the whole rig); and the amount of time and flow that was allowed in the sampling line before starting the sample (following a stagnant period in the sampling line).

Discussion in the following sections draws on the information in Table 15.12 and Table 15.13 as well as the results in Table 15.11.

Since the sampling line contained around 6 ml of volume, and could therefore hold 6 g of coolant, the amount of wait time between diverting flow to the sampling line and commencing sample collection was important, especially when the amount of flow passing prior to sample commencement was less than or comparable to 6 g – see the last 5 columns of Table 15.13 for relevant data from session 2, and the captions below the table for more explanation.

Ideally a much longer wait time would have been allowed, to enable thorough flushing of any stagnant solution remaining in the sampling line; the fact that it often was not was a major flaw in the operation procedures of session 2, which was addressed in later sessions. However, comparison of different samples for which greater or lesser prior flushing of the stagnant solution had been performed enabled some information about conditions in the cool back end of the rig (sampling line) to be inferred. In Table 15.14, samples during flow of 0.5 – 2 g/min are sorted into two categories for comparison – those for which 'sufficient' flushing was allowed (6 g or more before sample commencement) and those for which it was not. Samples are also sorted further, to allow for the effect of flow rate, and transient effects from being sampled within the first 24 hours. Some limited differences were found in results according to the amount of flushing allowed, but there were so many variables potentially affecting the results that it was difficult to isolate any one effect from all the others.

Table 15.13. Stagnant periods, and other disruptions to flow during session 3

Sampling sequence α		Disruptions to flow β		Pump restarts, and prior stagnancy γ			Diversion to sampling line, and prior stagnancy δ				
t_{sess} (h)	Sample #	t_{change} (h)	†Latest change	$t_{restart}$ (h)	re-start #	t_{stag_1} (h)	t_{wait} (min)	t_{stag_2} (h)	m_{wait} (g)	$m_{initial}$ (g)	m_{final} (g)
3	03-03	1	T	3	#0	n/a	0.	2	0	-6.	6.
5	03-04	2	T	5	#0	n/a	7.	1	14	8.	20.
7	03-05	4	T	7	#0	n/a	5.	2	10	4.	16.
24	03-06	21	T	24	#0	n/a	0.5	17	1	-5.	7.
55	03-07	52	T	55	#0	n/a	5.	30	10	4.	16.
99	03-08	28	r-s	28	#1	3 h	2.	44	4	-2.	10.
121	03-09	51	r-s	51	#1	3 h	2.5	22	5	-1.	11.
150	03-10	79	r-s	79	#1	3 h	3.	29	6	0.	12.
174	03-11	104	r-s	104	#1	3 h	5.	25	10	4.	16.
201	03-12	0	r-s	0	#2	18 h	5.	26	10	4.	16.
245	03-13	44	r-s	44	#2	18 h	6.	43	12	6.	18.
266	03-15	21	$\dot{m}$	65	#2	18 h	7.	18	3.5	-2.5	9.5
272	03-16	27	$\dot{m}$	71	#2	18 h	0.	5	0	-6.	-2.
272	03-17	27	$\dot{m}$	71	#2	18 h	9.	5	4.5	-1.5	2.5
272	03-18	27	$\dot{m}$	71	#2	18 h	19.	5	9.5	3.5	7.5
313	03-19	27	r-s	27	#3	8 h	14.	40	7	1.	13.
338	03-20	52	r-s	52	#3	8 h	19.	24	9.5	3.5	15.5
416	03-23	77	$\dot{m}$	130	#3	8 h	73 h	4	438	432.	436.
436	03-24	97	$\dot{m}$	149	#3	8 h	92 h	4	555	549.	553.
457	03-25	118	$\dot{m}$	171	#3	8 h	114 h	4	683	677.	681.
464	03-31	4	T	177	#3	8 h	269.‡	4	269‡	263.‡	275.‡
482	03-32	22	T	195	#3	8 h	7.	17	7	1.	13.
483	03-33	23	T	196	#3	8 h	71.	17	71	65.	77.
518	03-39	12	r-s	12	#4	13 h	8.	6	8	2.	14.
578	03-40	22	r-s	22	#5	16 h	35.	59	35	29.	41.
580	03-41	24	r-s	24	#5	16 h	165.	59	165	159.	171.

α: 't_{sess} (h)' represents cumulative time in hours since session 3 started. Remove three from this number to give cumulative hours at 200 °C or more.

β: 't_{change} (h)' gives time in hours since the latest change which caused disruption to flow in the rig.
† Abbreviations for latest change: T=temperature; r-s = pump restart (after stall); $\dot{m}$ =mass flow rate.

γ: '$t_{restart}$ (h)' is the time in hours since the latest pump restart following a period of stagnancy (zero flow). 'restart #' gives the cumulative number of times the pump has been restarted, and 't_{stag_1} (h)' gives the length of time in hours of the stagnancy prior to pump stall

δ: 't_{wait} (min)' is the time in minutes between diverting flow to the sampling line and commencement of the sample (for samples 03-23 to 03-25 time is given in hours); 't_{stag_2} (h)' is the length of time in hours that the sampling line was left stagnant before commencement of the sample; 'm_{wait} (g)' is the mass of fresh effluent which *entered* the sampling line before commencement of the sample (the product of t_{wait} and mass flow rate); and '$m_{initial}$ (g)' and 'm_{final} (g)' represent the total mass of fresh effluent which have *exited* the sampling line on commencement and finishing of the sample (respectively) - $m_{initial}$ is 6 g less than m_{wait} to account for flushing of 6 g stagnant water from the line; negative numbers represent direct inclusion of stagnant effluent in the sample.
‡ 't_{wait} (min)' for sample 03-31 represents time since the current *temperature* was set, as the flow had already been diverted to the sampling line previously.

Table 15.14. Effect of insufficient rinsing of sampling line on 300 °C results. Samples with italicised red text may be considered outliers due to other reasons (#12 soon after pump stall; #09-du sample left acidified at room temperature for 5 months).

Sample	m_i	m_f	[Fe]	[Cr]	[Ni]	[Mo]	[Mn]
1st 24 h: Insufficient rinsing → Higher levels for all but Fe; Fe more consistent. For all elements but Mn, stagnancy brings levels closer to those of 03-02 (at 22 °C)							
1st 24 h, sufficient rinsing			2 – 5	0.1 – 0.3	0.4 – 1.3	6 – 8	27 – 48
03-04	8	20.	2.0 (6)	0.15 (4)	0.4 (1)	5.6 (0)	26.8 (2)
03-05	4	16.	5.0 (7)	0.28 (4)	1.3 (1)	7.8 (1)	48.2 (3)
1st 24 h, insufficient rinsing			~3	0.9 – 1.1	1.1 – 2.3	12 – 20	58 – 104
03-03	-6	6	2.8 (6)	1.11 (7)	1.1 (1)	11.5 (1)	58.0 (3)
03-06	-5	7	3.4 (7)	0.87 (6)	2.3 (1)	20.3 (1)	104.1 (5)
				more consistent/			more cons. /
>24 h: Insufficient rinsing →			sim.	higher	lower	sim.	lower
Higher Cr, other elements similar (simply changing over time, plus Mn extra lower, by ~ 3 – 6 ppb). 03-12 is interesting as it shows effects of stagnancy in hot part of rig and recent pump restart (7 mins) → causes slightly lower Mn & higher Mo. Higher Fe.							
>24 h, sufficient rinsing			3 – 10	0.05 – 0.10	2.1 – 5.3	22 – 26	20 – 30
03-07	4	16. .	5.5 (7)	0.06 (4)	2.1 (1)	25.6 (1)	22.5 (2)
03-10	0	12	3.4 (5)	0.09 (1)	2.8 (2)	23.7 (1)	24.5 (1)
03-11	4	16. .	5.9 (5)	0.10 (1)	3.4 (2)	22.9 (1)	24.5 (1)
03-12	4	16. .	9.8 (7)	0.05 (1)	2.7 (2)	24.7 (1)	19.6 (1)
03-13	6	18. .	5.2 (5)	0.05 (1)	5.3 (3)	21.5 (1)	29.6 (2)
>24 h, insufficient rinsing			5 – 9	0.10 – 0.25	2.5 – 2.7	24 – 26	18 – 22
03-08	-2	10	5.3 (7)	0.22 (4)	2.7 (2)	25.6 (1)	18.4 (2)
03-08-du	-2	10	5.6 (7)	0.25 (4)	2.6 (2)	25.6 (1)	18.3 (2)
03-09	-1	11	6.0 (7)	0.10 (4)	2.5 (2)	24.3 (1)	19.4 (2)
03-09-du	-1	11	9.2 (7)	0.19 (1)	2.7 (2)	24.5 (1)	22.2 (1)
0.5 g/min: Insufficient rinsing → lower?			higher	higher	lower	higher	
Higher Cr, higher Ni (?) other elements similar (simply changing over time)							
0.5 g/min, sufficient rinsing			4 – 8	0.08 – 0.10	4.0 – 6.1	36 – 63	25 – 34
03-18	3.5	7.5	8.4 (6)	0.10 (1)	6.1 (3)	36.1 (2)	26.7 (1)
03-19	1	13	3.8 (5)	0.08 (1)	5.1 (3)	54.9 (3)	34.4 (2)
03-20	3.5	15.5	4.6 (5)	0.08 (1)	4.0 (2)	63.3 (3)	25.3 (1)
0.5 g/min, insufficient rinsing			3 – 5	0.10 – 1.75	6.7 – 8.6	28 – 39	37 – 66
03-15	-2.5	9.5	5.2 (5)	0.10 (1)	6.7 (4)	27.9 (1)	43.4 (2)
03-16	-6	-2. .	2.5 (4)	1.75 (1)	8.6 (4)	38.5 (2)	66.1 (3)
03-17	-1.5	2.5	4.7 (5)	0.14 (1)	6.8 (4)	33.1 (2)	36.5 (2)

Discussion of the results

Samples 03-01 and 03-02 were taken at the start of session 3 using the sampling cell, to give an indication of the levels released from the rig at room temperature, within just a few hours of first being exposed to pH 9 feedwater. As such, they are not representative of typical levels for the rig at room temperature, and represent the initial reaction of the SS316L surfaces to pH 9 coolant, both in the 'hot' part of the rig (where a duplex oxide layer exists from prior exposure in sessions 1 and 2) and the tubing at the back end of the rig (where a protective Cr oxide or hydroxide is thought to exist, see section 3.5). Levels of Cr were extremely high, especially in the first sample, and may represent the release of Cr-based particulates from Cr oxides either in the R.C. or the cold parts of the rig, or the sampling cell, as the new coolant chemistry causes changes to the chemistry and morphology of the oxide film potentially causing stresses and strains and the release of particulates. Levels of Mn were particularly low compared with all the later samples of session 3, and increased by a factor of around 6 between the first and second samples. Levels in the first sample were comparable with those measured during session 2, suggesting a 'memory' of levels from the end of session 2. This could be achieved by for example an equilibrium between Mn ions in solution and in the oxide film of the back end of the rig and sampling cell (if the chief source of Mn in effluent is ionic), or the requirement of a lead time for Mn-containing particulates to propagate/travel along the tubing to reach the sampling point (if the Mn in effluent is particulate). The same memory effect may also be true of Mo, which decreased by a factor of around 4 from first to second sample, starting at a high level similar to those seen in session 2. Behaviour of Ni has been difficult to characterise in the previous two sessions, except by assuming a low solubility and a level of particulate matter which seems to vary unpredictably – levels of Ni here were consistent with those findings. Levels of Fe for these two samples were similar to those from samples taken at high temperature.

Two pairs of duplicate samples were analysed (samples 08, 08-du, 09 and 09-du) to give an indication of whether supposed sampling errors were appropriate, as discussed in chapter 3 and earlier in this chapter. Sample 03-09-du had higher levels of each element, particularly Fe, Cr and Mn, which may be due to the period of 5 months that it was left acidified at room temperature before being refrigerated and then analysed. Therefore this sample could be considered an outlier. The magnitude of the differences between 09 and 09-du levels could be indicative of the susceptibility of each element to errors caused by differences in the length of time that samples were left acidified at room temperature. Since the differences are relatively small for all elements except for Fe and Cr, it could be inferred that susceptibility is low, especially considering that all samples within a batch were refrigerated within 12 to 24 hours of being acidified. The lower levels of

03-09 could be due to incomplete dissolution of some particulates, which had time to fully dissolve in 03-09-du. In that case 03-09-du accurately reflects the full inventory for each element whereas 03-09 represents the full inventory of each element that was in solution at the moment of acidification, plus a partial amount of the particulate inventory – however much the acid was able to dissolve in the time available. Alternatively, excess levels in 03-09-du may be merely due to additional leaching from the test tubes over the 5 additional months the test tube was left at lab temperature, compared with the 12- 24 hours of blanks. No long-term blanks were analysed to test this hypothesis.

Samples 03-08 and 03-08-du had values within the supposed measurement error of each other for all elements analysed. For Mo and Mn, results were so close that they were considered inconsistent with the 5% supposed error on analysis in the ICP-MS instrument. A value of 0.5% was instead chosen – this value was used when determining overall measurement errors as they appear for Mo and Mn in session 3 results as well as all the other sessions and results from other rigs. 08 and 08-du remain within one measurement error of each other using the 0.5% value for Mo and Mn, as do several samples taken under the same conditions as each other from the corrosion rate rigs.

A set of three 4 g samples were taken in quick succession (16, 17, 18), to show the effect of allowing insufficient flow in the sampling line before taking a sample. There was a clear trend in results for all elements except Mo; this is discussed along with the full discussion for each element.

Chromium

Where sufficient flushing of the sampling line was allowed, Cr levels were more or less constant for each given set of conditions, with ~ 0.05 – 0.15 ppb being typical at 300 °C. Levels were slightly higher at slower flow than at 2 g /min, though the difference was subtle and could also have been caused by random scatter or evolution of the corrosion film over time. Levels were also slightly elevated (0.15 and 0.28) when taken within 4 hours of 300 °C temperature being reached (and therefore within 7 hours of session 3 starting). At 250 °C and 200 °C, Cr levels dropped to 0.00 +/- 0.01 ppb, consistent with solubility expectations.

Since the rig is capable of producing such low Cr levels, this provides evidence that the source of the (relatively) much higher levels of Cr at 300 °C is particulate matter, from the hot part of the rig, and not the cold tubing at the back end of the rig. However, where sufficient flushing of the sampling line was *not* achieved (or where the sampling cell was used), levels of Cr were found to be consistently higher, with the three most extreme cases and the two sampling cell samples yielding the five highest results (samples #1, 2, 3, 6, 16). One possible explanation for this could be that during the

periods when the sampling line is left stagnant between samples, corrosion progresses at room temperature under oxidising conditions at the end of the sampling line, or possibly even in contact with damp air as some of the effluent in the sampling line evaporates or drips out under gravity, to be replaced by air. Under the disturbance produced when flow first passes over these corroding surfaces again some Cr(III) oxide or hydroxide (such as Cr_2O_3 or CrOOH) crystals become entrained in the flow, but as flow continues it becomes more uniform, with boundary layers near the walls, and a situation is soon reached where any oxide loose enough has already been swept away by the flow. A similar argument could explain the high Cr level resulting from the first use of the sampling cell in session 3, sample 03-01.

The condition of 'sufficient flushing of the sampling line' has been defined as samples where $m_{initial}$ is at least zero – i.e. at least the 6 g of stagnant effluent which had been sat in the sampling line since the last sample was allowed to exit the rig before sampling started. This criterion has yielded clear differences between those samples which pass or fail the test, as discussed above. In addition, results suggest that the first 2 g of effluent yield particularly high levels of Cr. Aside from the two samples taken at room temperature, the highest three Cr results were from samples which began with the first gram of effluent to exit the rig – 03-03 and 03-16, with levels of 1.1 and 1.7 ppb respectively; or the second gram of effluent to exit the rig – 03-06, with 0.9 ppb Cr. The next-highest Cr level of an 'insufficiently flushed' sample was 03-08-du, at 0.2 ppb, which was lower than one of the 'sufficiently flushed' samples, 03-05, at 0.3 ppb Cr.

It is suggested that none of the 250 °C and 200 °C samples suffered insufficient flushing of the sampling line judging by the fact that elevated levels of Cr were not observed, although unfortunately this cannot be confirmed.

Presence of Cr particulates in the form of a pure Cr(III) oxide (Cr_2O_3 or CrOOH), and not as ferrous chromite (which is about 50% Fe by mass on a metals basis under relevant hydrothermal conditions [85],[2]) – would also explain why Fe levels were not also elevated in line with Cr for the samples mentioned above. Since such oxides are not expected to exist in significant quantity in the corrosion film, it is conceivable that ferrous chromite particulates once released from the corrosion film into coolant could lose their Fe content over time through leaching, leaving pure Cr oxide behind, especially under conditions where chromite is not stable. In fact, the sequence of samples #16 – 18 demonstrates that whilst Cr levels were elevated in the first 4 g of effluent exiting the sampling line (03-16), levels of Fe in the same sample were particularly low; and as Cr levels fell over the next two samples, Fe level increased. The extent to which Fe increased is surprising, with sample 03-18 being the second highest of all session 3 samples. However, levels of Fe are seen to suffer a high degree of scatter overall (see next section), and the collection of three 4 g samples is likely to increase the level

of scatter relative to the typical sample size of 12 g. If a single 12 g sample had been taken instead of the three smaller samples, one would expect [Fe] to equal the average of the three samples, 5.2 g. This value is typical of the other samples, with the implication being that within each of the 12 g samples, levels of Fe may fluctuate wildly from one gram to the next – or from one drip to the next – as the effluent exits the rig. The Cr level averaged in this way is 0.7 ppb – still among the three highest samples of those which were not collected in the sampling cell.

In contrast, for sample 03-12, sampling within 7 minutes of flow recommencing after an 18 hour period of stagnancy in the rig as a whole caused no elevation in Cr level, but the Fe level was elevated to 9.8 ppb, the highest of all results in session 3. Also Ni levels were not elevated, and were slightly lower than the preceding and following sample. Combined with other observations (the likely presence of Fe-containing particulates, due to scatter of Fe levels and levels being lower for the slower flow rates), this suggests the presence of particulates of a fairly pure Fe oxide such as magnetite from the hot part of the rig.

Iron

At 300 °C, at the faster flow rates of 2 and 0.5 g/min, levels of iron were consistently within the bounds of ~ 2 to 10 ppb, though fairly erratic within those bounds. The two highest Fe levels, of 9.8 and 9.2 ppb, can be considered as coming from non-representative samples. Sample 03-09-du was left for a prolonged period at room temperature after acidification, and 03-12 was taken just 7 minutes after a pump restart following 18 hours of stagnant conditions.

As discussed in the Cr section, the sequence of samples #16 – 18 suggests that insufficient flushing of the sampling line resulted in lower Fe levels for the first few grams of flow (around 6 g), this could be due to adsorption or otherwise incorporation into the Cr(III) oxide film in the cold part of the rig, or settling of particulates, since Fe solubility should increase at room temperature.

At 300 °C, 0.1 g/min, levels of Fe were lower, which may be due to: less particulate matter from the hot part of the rig; longer opportunity in the sampling line for particulates from the hot part of the rig to settle; or longer residence time in the sampling line for dissolved Fe to be adsorbed by or incorporated into the room temperature corrosion film.

At 250 °C and 200 °C, levels of Fe dropped to around 1.1 +/- 0.5 ppb, apart from one outlier at 6.1 ppb, despite flow rate being lifted to 1 g/min and despite the fact that higher solubility is expected at those temperatures, again drawing attention to the effect of the back-end of the rig.

Other elements

Apart from cobalt, where the data were fairly limited, the other elements displayed interesting trends over time, due to more than just changes in the controlled variables of temperature and flow rate. Trends are described approximately below, but in more detail in the next section where plots of results versus time make the trends clearer.

Levels of Co, where analysed for (samples 03-01 to 03-09), were ~ 0.0 – 0.3 ppb. It is interesting that levels were so high, even after the full duration of sessions 1 and 2, from an element whose contribution to the alloy is so low that it is not mentioned as an impurity in the elemental analysis (Table 7.1). It may be a contribution from one of the valves, or from the pump or some other coolant-facing surface whose composition had been overlooked. The levels are relatively consistent compared with those observed in session 1.

Levels of Ni were around 1 – 9 ppb at 300 °C, but seemed to increase over time up to sample 03-16 (soon after the flow rate was decreased to 0.5 g/min), and then decrease over time from there onwards. Levels were lowest for the last 6 samples, taken at 250 and 200 °C, despite flow rate being lifted to 1 g/min. It is difficult to tell to what extent the low levels of the last 6 samples were due to the temperature, and how much was due to a decreasing trend in Ni levels which was already occurring.

At 300 °C, levels of Mo were unsettled for the first 4 samples, then followed a gradual fall-off at 2 g/min. At 0.5 and 0.1 g/min, Mo levels climbed to over four times their previous value; then as the flow rate was increased again, to 1 g/min (and temperatures decreased to 250 then 200 °C), Mo levels decreased again – this suggests that levels of Mo are controlled by a rate of release rather than a solubility. The high levels of Mo that were in some cases observed, and the smooth variation of Mo levels over time (see Figure 15.1) suggest that Mo is fully dissolved rather than in particulate form, and that solubility of the most stable Mo oxide is relatively high – especially compared with Fe and Cr from ferrite and chromite – supporting the view that molybdenum levels in solution are constrained only by solid state diffusion through the oxide layers, rather than solubility limitations. Levels of Mo are thus expected to be proportional to the rate at which Mo is released to the coolant, and inversely proportional to the rate at which it is diluted by the coolant (i.e. flow rate).

Levels of Mo did not climb as high as expected as flow rate was changed, but were still in the process of changing over several days when conditions in the rig were changed, therefore they may have changed to the expected levels if given sufficient time. Pourbaix diagrams [112], [194] indicate that MoO_2 (cr) would be the stable single oxide phase at room temperature under reducing conditions, with MoO_4^{2-} (aq) being the dominant ion in solution [194]. The oxidative (Mo(IV) → Mo(VI)) and

basic (2 OH^- ions consumed per MoO_4^{2-} (aq) ion released) nature of the dissolution means that more effective leaching of Mo from the oxide film at room temperature might be expected at the higher end of the pH range used, and at times and locations when conditions were most oxidising – assuming Mo is present as Mo(IV) within the Cr(III) oxide-based corrosion film (see section 4.1.7). The actual oxidation state of Mo in the oxide film in the rig is expected to be at most +4, but possibly even lower at +2 or +3 (see the paragraph below), which would make the oxidative nature of Mo dissolution in this case even more pronounced than it is for MoO_2.

At elevated temperature MoO_2 (cr) remains the stable solid phase for Mo under reducing conditions ([195] see figure 1 therein). The present author could not find literature regarding MoO_2 solubility in conditions appropriate to the current study, aside from [196], [197], which were not accessible: reference [195] was at salinity and low pH. Data contained in [132] for ionisation of molybdic acid (H_2MoO_4) indicate that at 300 °C, MoO_4^{2-} and $HMoO_4^-$ are about equal in concentration at pH_{25C} 10, whereas the former ion dominates at pH_{25C} 11 and the latter at pH_{25C} 9. However, at the more reducing conditions employed in the current study, soluble molybdenum in the lower (+4) valency state might dominate instead ([197], in [132]). In this case, decreasing the potential of the solution, to ever more reducing conditions, would cease to cause solubility to decrease beyond a certain point as soluble Mo(IV) species start to dominate, having the same oxidation state as the Mo in the oxide (MoO_2). However, it might be expected that in the current project Mo was present in the (II) and (III) oxidation states, incorporated into magnetite structure. Mo_3O_4 (hausmannite), a spinel type oxide [198], is known to form solid solutions with ferrite, with up to 54% mole fraction of Mo_3O_4 being soluble in Fe_3O_4 [199]. The Mo in hausmannite is in a mixed (II) / (III) oxidation state [198], analogously with Fe in magnetite. Therefore it is possible that Mo will continue to leach more readily from magnetite with increasing hydrogen fugacity, even up to high hydrogen fugacities. On the other hand, Mo has been reported to take on the (+4) valence state in the oxide film of NiCrMo Alloy 625 [86].

A step change increase to Mo leaching (an increase in pH) would be expected to cause the first few samples of the following run to be high, then settle to a moderate value, and vice-versa for a step change decrease to Mo leaching (decrease in pH) – starting low then settling to a moderate value. Even if there is a corresponding major change to Fe solubility, this will have no effect since more or less 100% of the Fe released from the alloy is retained in the outer oxide layer in any case due to the slow volume flow rate and low Fe solubility.

The anticipated effect of changing up to a higher pH was indeed observed, with high Mo levels at the beginning of sessions 2 (pH 11 following a pH neutral run) and 6 (pH 10 following a pH 9 run); and low Mo levels at the beginning of session 3 (pH 9 following a pH 11 run).

At 300 °C, levels of Mn were unsettled for the first 4 samples, as for Mo. Levels then climbed steadily over the course of flow at 2 g/min, in much the same manner as Ni, if the effects of insufficient flow in the sampling line or in the rig as a whole are accounted for. This can be seen clearly in Table 15.14, for 2 g/min samples after >24 h of flow – both for the samples with sufficient flushing of the sampling line and those with insufficient flushing – if the samples 03-12 and 03-09-du are excluded. Also roughly in line with behaviour of Ni, levels if Mn were at their highest during 0.5 g/min flow before falling when flow decreased to 0.1 g/min. Levels at 250 °C were the lowest (apart from 03-01 and 03-02), and levels at 200 °C were fairly low, but noticeably higher than for 250 °C.

15.2.6. Session 4 Results

From session 4, forty-three effluent samples, five feed-water samples and a feed-water syringe blank were analysed along with the 11 blanks and other samples of batch 4. The processed results are presented in Table 15.15 below.

Accounting for blanks

After a successful trial of the acid soak procedure in batch 3 of analysis, all test tubes for samples and blanks were prepared by this procedure before use, from batch 4 onwards – this includes sessions 4, 5 and 6, and latter samples from the corrosion rate rigs. As can be seen in Table 15.15, there was a marked improvement in the levels and standard error on blanks; this in turn resulted in smaller measurement error on samples.

Table 15.15

Session 4 results

Sample	*pH*	*T*	$\dot{m}$	N_2	*[Fe]*	*[Cr]*	*[Ni]*	*[Mo]*	*[Mn]*	*[Co]*	*Other info*
04-01	9	300	0.1	0.8	1.7 *(1)*	0.16 *(1)*	40.8 *(20)*	22.6 *(1)*	88.7 *(4)*	-	3.5 h after T reached. (4 h after start)
04-02	9	300	0.1	0.2	7.2 *(4)*	0.08 *(1)*	7.6 *(4)*	36.6 *(2)*	22.1 *(1)*	-	26 h after T reached. N_2 0.2, this & next few samples
04-03	9	300	0.1	0.2?	0.3 *(1)*	0.04 *(0)*	5.1 *(3)*	55.8 *(3)*	14.9 *(1)*	-	31 h after T reached
04-04	9	300	0.1	0.2?	1.9 *(1)*	0.09 *(1)*	4.5 *(2)*	86.8 *(4)*	11.0 *(1)*	-	47 h after T reached
04-06	9	300	0.1	0.8?	0.7 *(1)*	0.11 *(1)*	1.6 *(1)*	95.0 *(5)*	7.0 *(0)*	-	75 h after T reached
04-08	9	300	0.1	0.8?	1.5 *(1)*	0.15 *(1)*	1.5 *(1)*	73.8 *(4)*	5.5 *(0)*	-	99 h after T reached
04-12	9	300	0.1	0.8	*0.1 (1)*	0.20 *(1)*	2.0 *(1)*	55.3 *(3)*	5.1 *(0)*	-	154 h after T reached
04-15	9	300	0.1	0.8	0.4 *(1)*	0.22 *(1)*	2.5 *(1)*	46.4 *(2)*	4.8 *(0)*	-	196 h after T reached
04-18	9	300	0.1	0.8	0.7 *(1)*	0.14 *(1)*	2.2 *(1)*	43.1 *(2)*	4.7 *(0)*	-	243 h after T reached
04-19	9	300	0.1	0.8	0.3 *(1)*	0.04 *(0)*	2.6 *(1)*	54.0 *(3)*	6.9 *(0)*	-	288 h after T reached
04-22	9	300	0.1	0.8	1.0 *(1)*	0.02 *(0)*	2.9 *(2)*	49.8 *(2)*	8.4 *(0)*	-	343 h after T reached
04-24	9	300	0.1	0.8	0.7 *(1)*	0.02 *(0)*	1.2 *(1)*	57.6 *(3)*	3.4 *(0)*	-	391 h after T reached
04-25	9	300	0.1	0.8	0.7 *(1)*	0.02 *(0)*	1.3 *(1)*	57.2 *(3)*	3.5 *(0)*	-	392 h after T reached
04-27	9	300	0.1	0.8	2.8 *(2)*	0.06 *(1)*	4.2 *(2)*	52.7 *(3)*	18.8 *(1)*	-	1 h after restart
04-28	9	300	0.1	0.8	0.9 *(1)*	*0.01 (0)*	1.6 *(1)*	62.6 *(3)*	5.3 *(0)*	-	32 h after restart
04-29	9	300	0.1	0.8	0.6 *(1)*	*0.00 (0)*	1.2 *(1)*	61.7 *(3)*	4.1 *(0)*	-	48 h after restart
04-30	9	250	0.1	0.8	1.3 *(1)*	0.04 *(0)*	4.4 *(2)*	33.4 *(2)*	12.5 *(1)*	-	2.5 h after T reached. (0.5 h after flow recommenced)
04-31A	9	250	0.1	0.8	0.3 *(1)*	0.03 *(0)*	0.5 *(0)*	33.7 *(2)*	3.7 *(0)*	-	21 h after T reached
04-31B	9	250	0.1	0.8	0.2 *(1)*	0.03 *(0)*	0.5 *(0)*	31.9 *(2)*	3.4 *(0)*	-	27 h after T reached
04-32	9	250	0.1	0.8	0.4 *(1)*	0.06 *(1)*	0.6 *(1)*	28.2 *(1)*	3.1 *(0)*	-	44 h after T reached

04-34	9	250	0.1	0.8	0.3 *(1)*	0.06 *(1)*	0.7 *(1)*	26.5 *(1)*	3.1 *(0)*	-	69 h after T reached. N_2 cylinder recently replaced
04-36	9	250	0.1	0.8	0.2 *(1)*	0.06 *(1)*	0.9 *(1)*	21.4 *(1)*	2.6 *(0)*	-	123 h after T reached
04-39	9	250	0.1	0.8	0.2 *(1)*	0.08 *(1)*	0.9 *(1)*	20.7 *(1)*	2.3 *(0)*	-	173 h after T reached
04-42	9	250	0.1	0.8	0.3 *(1)*	0.21 *(1)*	0.8 *(1)*	20.1 *(1)*	2.1 *(0)*	-	208 h after T reached
04-45	9	250	0.1	0.8	0.4 *(1)*	0.22 *(1)*	1.0 *(1)*	19.6 *(1)*	2.3 *(0)*	-	240 h after T reached
04-46	9	250	0.1	0.8	*0.1 (1)*	0.26 *(1)*	1.0 *(1)*	19.5 *(1)*	2.0 *(0)*	-	304 h after T reached
04-47	9	250	0.1	0.8	*0.0 (1)*	0.30 *(1)*	0.9 *(1)*	18.3 *(1)*	2.1 *(0)*	-	311 h after T reached
04-48	9	200	0.1	0.8	*0.0 (1)*	0.19 *(1)*	3.2 *(2)*	15.2 *(1)*	4.4 *(0)*	-	2 h after T reached. (0.5 h after flow recommenced)
04-49	9	200	0.1	0.8	1.1 *(1)*	*0.01 (0)*	0.8 *(1)*	13.2 *(1)*	6.1 *(0)*	-	17 h after T reached
04-50	9	200	0.1	0.8	0.3 *(1)*	*0.01 (0)*	0.8 *(1)*	11.8 *(1)*	7.2 *(0)*	-	24 h after T reached
04-51	9	200	0.1	0.8	*0.2 (1)*	*0.01 (0)*	0.8 *(1)*	10.9 *(1)*	9.2 *(0)*	-	39 h after T reached
04-55	9	200	0.1	0.8	0.3 *(1)*	*0.01 (0)*	1.2 *(1)*	8.0 *(0)*	13.0 *(1)*	-	93 h after T reached. N_2 cylinder recently replaced
04-56	9	200	0.1	0.8	*0.1 (1)*	*0.00 (0)*	1.1 *(1)*	8.1 *(0)*	11.1 *(1)*	-	148 h after T reached
04-59	9	200	0.1	0.8	0.3 *(1)*	0.01 *(0)*	1.3 *(1)*	9.6 *(1)*	13.6 *(1)*	-	187 h after T reached
04-62	9	200	0.1	0.8	2.7 *(2)*	0.02 *(0)*	1.6 *(1)*	8.1 *(0)*	21.1 *(1)*	-	264 h after T reached
04-64	9	200	0.1	0.8	0.3 *(1)*	*0.01 (0)*	1.8 *(1)*	9.6 *(1)*	23.9 *(1)*	-	341 h after T reached
04-66	9	200	0.1	0.8	0.4 *(1)*	*0.01 (0)*	1.9 *(1)*	10.1 *(1)*	24.5 *(1)*	-	405 h after T reached
04-68	9	200	0.1	0.8	1.4 *(1)*	0.01 *(0)*	2.4 *(1)*	10.8 *(1)*	23.6 *(1)*	-	508 h after T reached. N_2 cylinder recently replaced
04-69	9	200	0.1	0.8	0.9 *(1)*	*0.00 (0)*	1.7 *(1)*	12.2 *(1)*	19.7 *(1)*	-	554 h after T reached
04-70	9	200	0.1	0.8	0.6 *(1)*	*0.00 (0)*	1.5 *(1)*	13.0 *(1)*	19.8 *(1)*	-	555 h after T reached
04-71	9	200	0.1	0.8	0.4 *(1)*	*0.00 (0)*	1.4 *(1)*	11.6 *(1)*	18.2 *(1)*	-	600 h after T reached
04-73	9	200	0.1	0.8	1.3 *(1)*	*0.00 (0)*	1.1 *(1)*	7.4 *(0)*	13.0 *(1)*	-	750 h after T reached. N_2 cylinder recently replaced
04-75	9	200	0.1	0.8	0.4 *(1)*	*0.00 (0)*	1.2 *(1)*	9.7 *(1)*	13.3 *(1)*	-	886 h after T reached
04-f1	9	-	0.1	0.8	0.6 *(1)*	*0.01 (0)*	2.2 *(1)*	0.4 *(0)*	3.0 *(0)*	-	Feed water. Taken 2.5 h after sample 04-29
04-f3	9	-	0.1	0.8	0.3 *(1)*	*0.00 (0)*	0.3 *(0)*	0.4 *(0)*	2.4 *(0)*	-	Feed water. Taken 3.5 h after sample 04-29
04-f4	9	-	0.1	0.8	0.5 *(1)*	*0.01 (0)*	2.4 *(1)*	0.5 *(0)*	3.9 *(0)*	-	Feed water. Taken 13 h after sample 04-51
04-f5	9	-	0.1	0.8	0.2 *(1)*	*0.00 (0)*	*0.1 (0)*	*0.0 (0)*	0.1 *(0)*	-	Feed water syringe blank. 2 h after sample 04-75
04-f6	9	-	0.1	0.8	0.7 *(1)*	0.01 *(0)*	0.8 *(1)*	0.6 *(0)*	5.7 *(0)*	-	Feed water. Taken 2.5 h after sample 04-75
04-f7	9	-	0.1	0.8	1.0 *(1)*	0.02 *(0)*	1.2 *(1)*	0.6 *(0)*	5.0 *(0)*	-	Feed water. Taken 3 h after sample 04-75
Blanks	-	-	-	-	0.1 *(1)*	-0.02 *(0)*	0.0 *(0)*	0.0 *(0)*	-0.0 *(0)*	-	Batch 4. Eleven blanks analysed

Overview of rig use for session 4

Table 15.16 gives an overview of the conditions of the rig and samples taken during session 4. The sampling line was used throughout the session, and never closed off. Samples of 4 g (with two exceptions, of 6 and 9 g) were collected directly into acid-soaked Sarstedt test tubes. Table 15.17 lists the sequence and timings of samples taken during session 4, and details of any disruptions to the flow relevant to sampling

Table 15.16. Conditions of the rig and sampling during session 4

Conditions	*Times and dates*	*Samples analysed*	*notes*
1 g/min; 22 °C rising to 300 °C	7/5/14, **0.5 hours**	[no samples analysed]	
0.1 g/min; 300 °C	7/5 – 27/5, **20 days** 432 h flow (3 h no flow) 51 h flow	13 samples from #1-25 3 samples (27,28,29)	
0.1 g/min; 250 °C	27/5 – 9/6, **13 days** 310 h flow	11 samples from #30-47	
0.1 g/min; 200 °C	9/6 – 16/7, **37 days** 887 h flow	16 samples from #48-75	

Table 15.17. Stagnant periods, and other disruptions to flow during session 4

Sampling sequence α		Disruptions to flow β	
t_{sess} *(h)*	*Sample #*	t_{change} *(h)*	†*Latest change*
4	04-01	1	T_w
27	04-02	24	T_w
32	04-03	29	T_w
47	04-04	45	T_w
75	04-06	73	T_w
100	04-08	97	T_w
155	04-12	152	T_w
197	04-15	194	T_w
244	04-18	241	T_w
288	04-19	286	T_w
344	04-22	341	T_w
392	04-24	389	T_w
393	04-25	390	T_w
437	04-27	1	r-s.
468	04-28	32	r-s.
484	04-29	48	r-s.
490	04-30	0	r-s. (T1)
509	04-31A	19	r-s. (T1)
515	04-31B	25	r-s. (T1)
531	04-32	42	r-s. (T1)
557	04-34	68	r-s. (T1)
610	04-36	121	r-s. (T1)
660	04-39	171	r-s. (T1)
695	04-42	206	r-s. (T1)
728	04-45	238	r-s. (T1)
791	04-46	302	r-s. (T1)
799	04-47	310	r-s. (T1)
802	04-48	1	r-s. (T2)
817	04-49	16	r-s. (T2)
824	04-50	22	r-s. (T2)
839	04-51	38	r-s. (T2)
893	04-55	91	r-s. (T2)
948	04-56	146	r-s. (T2)
987	04-59	186	r-s. (T2)
1064	04-62	263	r-s. (T2)
1141	04-64	340	r-s. (T2)
1205	04-66	404	r-s. (T2)
1309	04-68	507	r-s. (T2)
1354	04-69	552	r-s. (T2)
1355	04-70	553	r-s. (T2)
1400	04-71	599	r-s. (T2)
1550	04-73	748	r-s. (T2)
1686	04-75	884	r-s. (T2)

For reference, residence time for session 4 is 1 h in the cold tubing at the back end of the rig, and 15.5 h, 17.5 h and 18.9 h respectively in the hot part of the rig at 300, 250, and 200 °C.

α: 't_{sess} (h)' represents cumulative time in hours since session 4 started. Remove two from this number to give cumulative hours at 200 °C or more.

β: 't_{change} (h)' gives time in hours since the latest change which caused disruption to flow.

† Abbreviations for latest change: T_w = temperature of water reaching 300 °C (as judged by flow rate at rig exit returning to normal); r-s = pump restart (after stall, stagnant for only 3 h 20 min); r-s (T1)/r-s (T2) = recommencement of flow after a stagnant period following transition from 300 to 250 °C (T1, stagnant for 2 h 04 min) or from 250 to 200 °C (T2, stagnant for 1 h 40 min).

After just a few minutes of flow at room temperature, the oven was set to 300 °C. During heating, the water expanded and therefore exited from the rig at a rate which was considerably faster than the 0.1 g/min feed from the pump. The air in the oven reached 300 °C after around half an hour, but effluent left the rig at an elevated flow rate for a time after this, around two hours, as the water in the hot part of the rig was brought fully to temperature. After a further hour-and-a-half the first sample was taken. A further twelve samples were taken during 432 h of uninterrupted flow before a

pump stall left the rig stagnant for a period of around 3 h. Three samples were taken during the following 51 h of flow.

After setting the oven to 250 °C, air in the oven took around 15 mins to reach the new temperature, but the water within the rig took longer to cool. As it cooled, the water had a tendency to contract (despite the supply of 0.1 g/min from the pump) which manifested as a decrease in pressure and a cessation of flow from the rig exit. The pressure dropped relatively rapidly from 102 to 82 bara, over the course of 4 minutes, see Figure 15.2, whereupon there was a step change (decrease) in the rate of decline. The saturation temperature for pure water under 82 bara pressure is 297 °C, therefore it is apparent that boiling commenced at this point, with the vapour phase preventing the pressure falling much below the saturation pressure. The saturation pressure, in turn, fell in line with the gradually decreasing temperature in the rig.

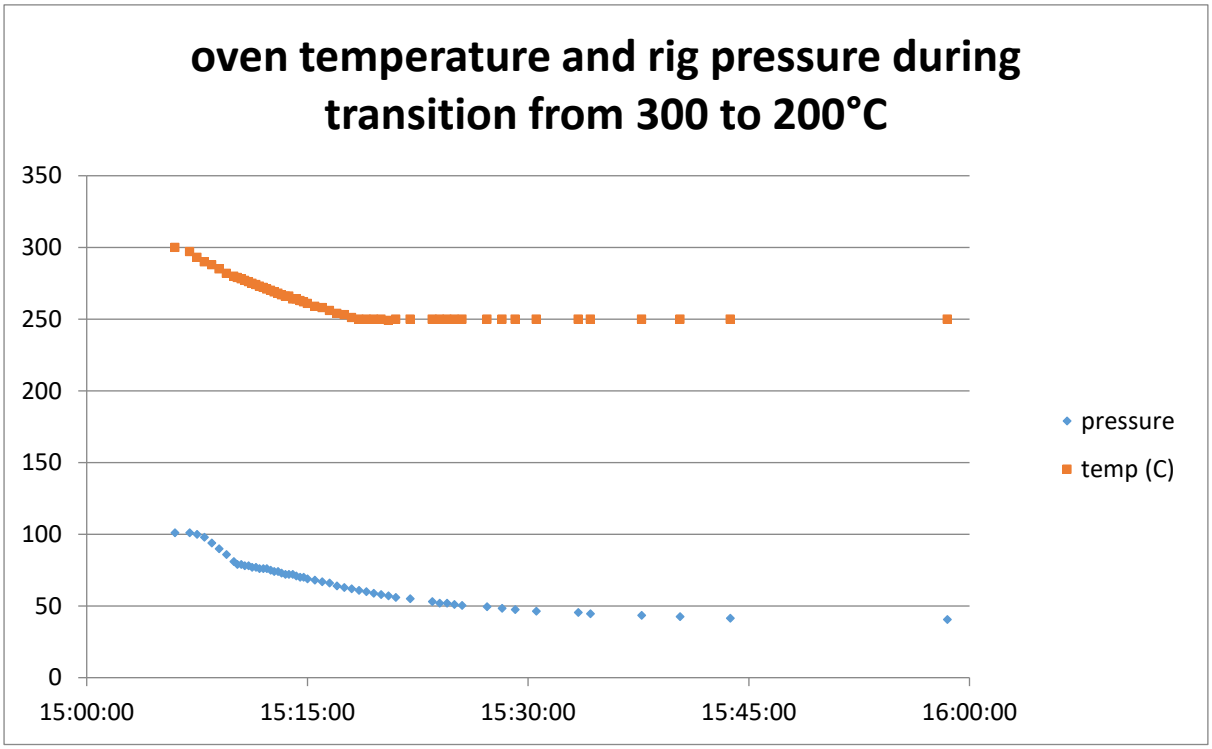

Figure 15.2: oven temperature and rig pressure during transition from 300 to 200 °C

In Figure 15.3, the equivalent saturation temperatures are plotted in place of the observed pressure values as plotted in Figure 15.2. When the first 8 data points were taken the vapour phase was not yet present, so an alternative curve has been included for those points, where the actual water temperature is approximated. The lowest pressure observed was 41 bara, to the nearest bara, which corresponds to 251.1 to 252.5 °C. It is not known why the pressure did not drop to the 39.8 bara expected for 250 °C, it may be down to error in the manometric module, a pressure differential

between the manometric module and the part of the rig in the oven, or an effect of LiOH on the boiling properties of water. Since the pressure stopped decreasing after around 45 minutes to one hour, it can be assumed that the temperature of 250 °C was reached on a similar timescale, even though the plot indicates a slightly higher temperature. The vapour phase was calculated to have reached a maximum of around 8.3 ml after 34 minutes (at 15:40) – after this point the 0.1 g/min injection of water more than compensated for the thermal contraction of the water, and the vapour phase began to shrink as it condensed back to the liquid phase. This fact may be another reason for the pressure not falling as low as expected, since a slight over-pressure above the saturation pressure would be required to drive the condensation of the vapour phase.

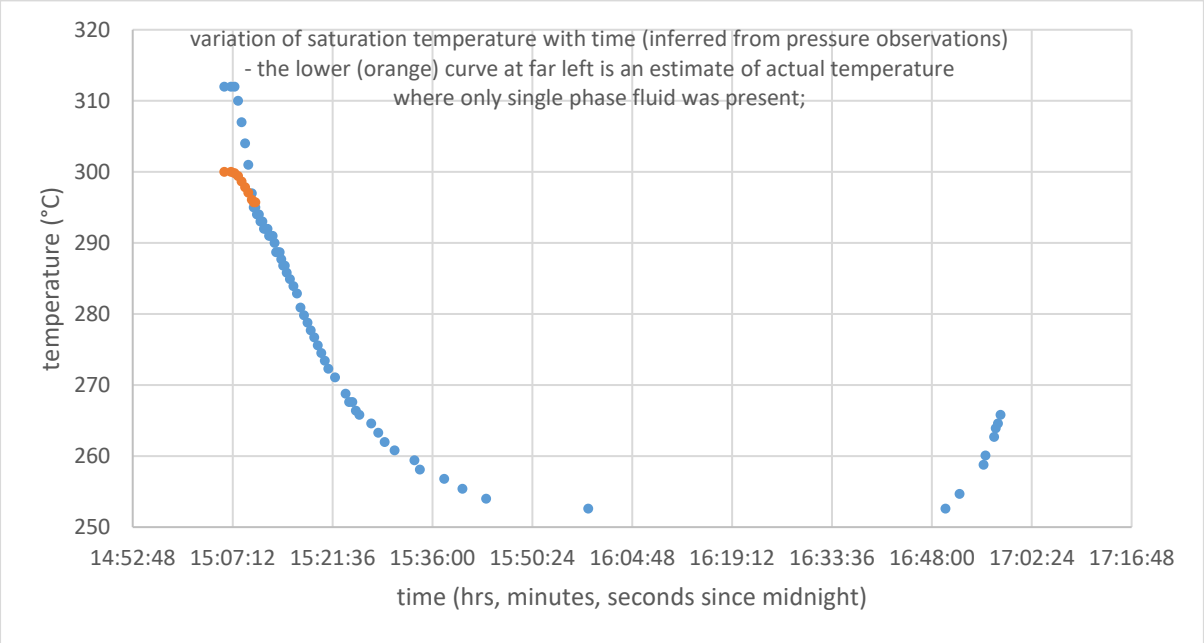

Figure 15.3 Variation of saturation temperature with time (inferred from pressure observations) the lower (orange) curve at far left is an estimate of actual temperature where only single phase fluid was presen

The vapour phase would have resided mostly in the top ~2 - 3 cm of the reaction cell, as well the short section of ¼" tubing above it. After about an hour and forty-five minutes since the oven was set to 250 °C, the vapour phase had fully condensed and the pressure began to rise again. After a further 15 minutes, pressure reached 102 bara and flow re-commenced from the exit of the rig. Sample 04-30 was taken just 26 minutes after this, and so represents water which resided in the rig for ~20 hours at 300 °C before sitting in the cold tubing at the back end of the rig for an extra two hours on top of the one hour it normally takes to pass through that region. Additionally the disturbance to the flow and the variation in pressure are likely to have affected this sample. A further ten samples were taken over 13 days at 250 °C before dropping the temperature to 200 °C.

After setting to 200 °C, the air in the oven took a similar amount of time to cool as for the transition to 250 °C (~15 minutes), as did the water (around 45 minutes to an hour in this case) – see Figure 15.4. The total time until flow recommenced was slightly shorter, around 1.5 hours. This is consistent with the density change of the ~130 ml of water in the hot part of the rig, which gains 11.7 g mass on cooling from 300 to 250 °C (about 2 hours of flow at 0.1 g/min) and 8.47 g on cooling from 250 to 200 °C (about 1.5 hours of flow). As with the previous transition, the pressure did not drop quite as far as expected for a full transition to 200 °C, with the lowest pressure reading being 17 bara (corresponding to 204 °C) as opposed to the 15 bara expected for 200 °C. Sample 04-48 was taken after 40 minutes of flow recommencing, and so represents flowing rig conditions at 250 °C plus an additional 1.5 h residence at the back end of the rig under stagnant conditions, and any effects that the disturbance to the flow may have. A further 15 samples were taken at 200 °C.

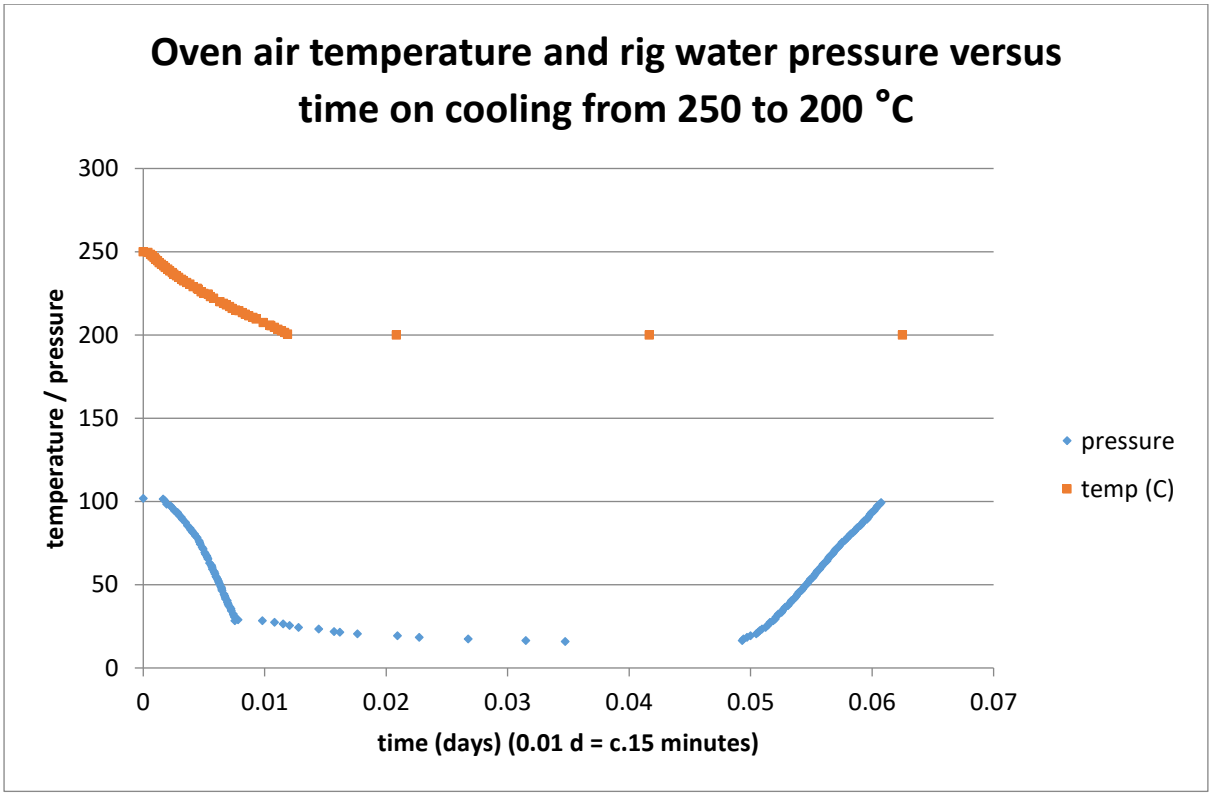

Figure 15.4. Oven air temperature and rig water pressure versus time on cooling from 250 to 200 °C

In addition to effluent samples, five feed-water samples were taken at various times. These samples were taken from the 3-way valve at the pump inlet, using a plastic syringe. The syringe was rinsed by drawing and discarding several ~10 ml quantities of feed-water before collecting each sample for analysis. In order to test for residual contamination coming from the syringe itself, a blank sample was prepared using ultrapure water drawn via the syringe.

Discussion of results

As has been the case for the other sessions, results were atypical for the first few days of the session for most of the elements analysed, and soon after a restart (for example within around 24 h) following a pump stall. Results were also atypical soon after a change in temperature, which for session 4 was accompanied by a period of ~1.5 – 2 h of stagnant conditions, and boiling or evaporation in the hot part of the rig. Apart from these phenomena, the rig conditions and the manner in which samples were taken were kept constant, so that the sampling procedure could be eliminated as a variable.

At 300 °C, samples #1-4 and #27 could be considered atypical, being taken within 48 h of the start of the session, and within 24 h of pump restart, respectively. For Mn and Ni, these represent the highest 5 of the 300 °C results; for Fe they include the top 4 results at 300 °C. The effects, if any, on Mo and Cr are not so clear. Results at 300 °C can be compared with the three samples taken under the same conditions during session 3 (03-23 to 03-25). Results are comparable across the two sessions for each of the elements apart from Fe and Mn. Levels of Fe, aside from the 5 atypical samples, range from 0.1 to 1.5 ppb, compared with session 3 results of 1.6, 1.8 and 2.2. For Mn also, results are consistently lower for the session 4 results save for the 5 atypical samples mentioned above. The difference in Mn results is not of great concern, it is consistent with findings from previous sessions that the levels of Mo and Mn vary with time. Levels of Cr were lower from sample #19 onwards, with those samples making up seven of the lowest eight samples at 300 °C. It is not known why this occurred – it seems that particulate levels of Cr settled to around zero over the course of many days under the same set of conditions.

At 250 °C, two samples were taken within 24 h of flow recommencing following the change in temperature, but only the one taken within an hour (#30) had atypical results. As was the case at 300 °C, Fe, Ni and Mn were the elements whose results were visibly different, with sample #30 having the highest of all the 250 °C levels in each case. As discussed in the previous subheading, sample #30 was already resident in the cold back-end of the rig when temperature in the rig was changed, and so is representative of the previous (300 °C) conditions as far as the hot part of the rig is concerned. Levels of Mn and Ni are higher than all the results at 300 °C also, apart from the 5 atypical samples. The same is almost true for Fe, but sample #8 has a slightly higher level.

Interestingly, the level of Mo in sample #30 is much more consistent with the samples that followed at 250 °C than those taken at 300 °C. This could be a co-incidence, or it could be that the level of dissolved Mo equilibrated between the hot and cold pressurised parts of the rig by diffusion.

At 200 °C, three samples were taken within 24 h of flow recommencing following the change in temperature, but again, only the one taken within an hour (#48) had atypical results. This time it was the levels of Ni and Cr which differed most significantly, with Ni having a higher level than any of the typical results at either 250 or 200 °C. Levels of Cr were much higher than any of the other samples taken at 200 °C, but comparable with the last samples taken at 250 °C.

Aside from sample #48, levels of Cr at 200 °C were extremely low, comparable with the expected solubility of chromite or Cr(III) oxide under hydrothermal conditions. This shows that the rig is capable of providing correct solubility results for Cr, without the back end of the rig altering Cr levels – even with such a long residence time at the back end of the rig – and that the higher Cr levels present during conditions of 250 °C and 300 °C represent Cr-based particulates originating from the hot part of the rig. These low levels of Cr at 200 °C are consistent with results from session 3 at the faster flow rate of 1 g/min; it is not known why the equally low levels at 250 °C from session 3 were not replicated in session 4.

Some trends over time were clearly visible, particularly for Mo and Mn – these are treated in the next section, with reference to a plot of results against time.

15.2.7. Session 5 Results

From session 5, thirty-nine effluent samples, five feed-water samples and three feed-water syringe blanks were analysed along with the eighteen blanks and other samples of batch 5. The processed results are presented in Table 15.23.

As was the case for previous batches, blank samples were interspersed with effluent samples, and the levels recorded in earlier blanks compared with those acidified later to test for any drift in contamination levels over the course of the acidification process. Samples were shuffled so that they were not analysed in consecutive order, in order to mitigate against any drift in background levels should it occur (whether detected or not).

Accounting for blanks

The levels and standard error on blanks were similar to those obtained by the same (acid soak) procedure in previous batches (batches 4 and 3), once the results from 5 problematic blanks were excluded from analysis. The mean and standard error on these rejected blanks are shown in Table 15.23 as 'rejects'; values were particularly high for Ni, owing to one sample having 8.3 ppb, which demonstrates that one-off outliers having exceptionally high levels of one element may be as a result of contamination during the sample preparation process and does not necessarily reflect circumstances in the rig. Three of these blanks were the first three test tubes prepared on 25 August 2015, when the latter portion of batch 5 were acidified, and the other two were the first two test tubes prepared after a break of over three hours, during the acidification of the former portion of batch 5 samples on 30 April 2015. Since these blanks were not representative of the majority of blank samples, their values were not included in the mean and standard error used to correct rig effluent samples for sample preparation effects. The source of this contamination is not known, and one possible source could potentially be related to the process of adding water to the blank samples – a process which was not present during acquisition of effluent samples. This possible scenario could explain why levels of some elements in feedwater blanks (for which water was drawn directly from the water stream provided by the MilliQ into a plastic syringe, to test whether this syringe was contributing metallic cations to feedwater samples taken using the same syringe) were significantly lower than in ordinary blanks.

Also note that from session 6 (pH 10), raw data for the 16 samples taken at 1 g/min, 300 °C, and the 12 samples taken at 0.5 g/min, 300 °C had a lower variance in each case than the 13 accepted blanks.

Assessing whether acidification process may have introduced bias (affecting some results more than others)

Samples which were acidified within a few places before or after those blanks with anomalously high results were compared with like samples (collected under same rig conditions) acidified earlier or later in the process: results were found to be consistent regardless of their position in the acidification process.

Effluent sample levels tended to be either so close to background levels as to be considered effectively zero, or at much greater levels so that error on blanks was immaterial in comparison. Nevertheless the levels of rejected blanks were significantly higher than the other blanks, showing clear contamination – as high as 8 ppb Ni in one case. In addition, levels of Fe were consistently lower for feedwater syringe blanks than for ordinary blanks: of the 18 blanks and 4 feedwater syringe blanks, syringe blanks accounted for the 1st, 2nd, 4th and 9th lowest levels of Fe; and for Mo the figures were 1st 2nd, 3rd and 5th. For this reason it is concluded that the elevated levels of the rejected blanks compared with other blanks was due to the slightly higher than normal levels of contamination present in the MilliQ water at that time, and so these blanks are not representative of contamination levels present in effluent samples for which the water component was drawn from the rig. However these results also show that anomalously high levels of, for example Ni, are possible from the acidification process alone, and this should be borne in mind when considering one-off extremely high results from effluent samples.

Overall, for the reasons discussed above, no overall bias was found to be present in relation to the time at which samples were acidified, and a mean and standard deviation was taken from the thirteen accepted blanks to correct for background levels of all samples analysed in batch 5 (session 5, session 6, and some CRR samples).

Overview of rig use for session 5

Table 15.18 gives an overview of the conditions of the rig and samples taken during session 5. Table 15.19 shows the full sampling sequence, including time since the session started and time since the latest disruption to flow for each sample. The sampling line was used throughout the session, and never closed off – except briefly during the process of taking two sealed samples for analysis of hydrogen gas content. Effluent samples of between 4 and 12 g mass were collected directly into acid-soaked Sarstedt test tubes.

Table 15.18. Conditions of the rig and sampling during session 5

Conditions	*Times and dates*	*Samples analysed*	*notes*
1 g/min; 22 °C rising to 300 °C	27/11/14, **1 hour**	1	After 1 h, oven air had just reached 300 °C, water temperature probably not yet at 300 °C
1 g/min; 300 °C	27/11 – 4/12, **7 days** 56 h flow (10 h no flow) 104 h flow	 2, 3 4-10, f2-f5	f1, a syringe blank, taken prior to f2-f5
0.5 g/min; 300 °C	4/12–18/12, **14 days** 149 h flow (40 h no flow) 9 h flow (10 h no flow) 60 h flow (12 h no flow) 43 h flow	 11-16 18 19, 20	
0.1 g/min; 300 °C	18/12/14–15/02/15, **59 days** 117 h flow (15 h no flow) 203 h flow (6 h no flow) 223 h flow (0.5 h no flow) 81 h flow (4 h no flow) 222 h flow (0.5 h no flow) 269 h flow (24 h no flow) 31 h flow (7 h no flow) 192 h flow (26 h no flow) 2 h flow	 21-24 26-29 30-32 33 34 35 36 (with 3.0 µm filter) 37 (with 3.0 µm filter)	 [preliminary H_2 sample taken] [0.45 µm and 3.0 µm filters attached in series briefly, then 0.45 µm filter removed] [H_2 sample #1 taken]
0.1 g/min; 250 °C	15/2 – 17/2, **2 days** 49 h flow	 f8, 38, 39	f6,f7, syringe blanks, taken prior to f8.
0.1 g/min; 200 °C	17/2 – 20/2, **3 days** 77 h flow (504 h no flow)	 40, 41	

Table 15.19. Stagnant periods, and other disruptions to flow during session 5

Sampling sequence α		Disruptions to flow β	
t_{sess} (h)	Sample #	t_{change} (h)	†Latest change
1	05-01	-1	T_w
17	05-02	15	T_w
47	05-03	45	T_w
67	05-04	0	r-s 1
99	05-05	31	r-s 1
124	05-06	57	r-s 1
140	05-07	73	r-s 1
140	05-08	73	r-s 1
140	05-09	73	r-s 1
170	05-10	103	r-s 1
189	05-11	17	flow (.5)
220	05-12	48	flow (.5)
238	05-13	66	flow (.5)
266	05-14	95	flow (.5)
285	05-15	114	flow (.5)
304	05-16	133	flow (.5)
425	05-18	46	r-s 3
454	05-19	3	r-s 4
476	05-20	26	r-s 4
523	05-21	29	flow (.1)
547	05-22	53	flow (.1)
576	05-23	82	flow (.1)
595	05-24	101	flow (.1)
640	05-26	14	r-s 5
713	05-27	87	r-s 5
788	05-28	162	r-s 5
813	05-29	187	r-s 5
836	05-30	1	r-s 6
888	05-31	53	r-s 6
934	05-32	99	r-s 6
1100	05-33	41	r-s 7
1413	05-34	47	r-s 9
1679	05-35	20	r-s 10
1751	05-36	54	r-s 11
1774	05-37	76	r-s 11
1947	05-38	25	r-s (250)
1967	05-39	45	r-s (250)
1995	05-40	25	r-s (200)
2020	05-41	50	r-s (200)

For reference, residence time at 0.1 g/min (sample 05-21 onwards) is 1 h in the cold tubing at the back end of the rig, and 15.5 h, 17.5 h and 18.9 h respectively in the hot part of the rig at 300, 250, and 200 °C. Residence times at 0.5 g/min, 300 °C *(05-11 through 05-20) are 0.2 h and 3.1 h respectively, and at 1.0 g/min, 300* °C *(05-01 through 05-10) are 0.1 h and 1.6 h respectively for the back end of the rig and the hot part of the rig.*

α: 't_{sess} (h)' represents cumulative time in hours since session 5 started. Remove two from this number to give cumulative hours at 200 °C or more.

β: 't_{change} (h)' gives time in hours since the latest change which caused disruption to flow in the rig.

† Abbreviations for latest change: T_w = temperature of water reaching 300 °C (as judged by flow rate at rig exit returning to normal); r-s (no.) = pump restart (after stall; cumulative no. of restarts is indicated); r-s (250) and r-s (200) = recommencement of normal flow after a transient period following transition to 250 °C (1 h 40 min) or to 200 °C (flow rate increased for for 1 h 20 min to prevent stagnation and pressure loss)

The first sample was taken after air in the oven had reached 300 °C, but the water had not yet done so and was exiting the rig at a faster rate than the pump flow rate due to thermal expansion. A further 38 samples were taken during over a period of around 2000 hours. Three flow rates were employed at 300 °C, and data at 0.1 g / min flow rate were taken at 300 °C, 250 °C and 200 °C, for comparison with previous sessions. As with previous sessions, some samples were taken too soon

after a change in conditions to yield representative results, but their results were of interest in showing the nature and extent of transient effects during changes to the conditions in the rig.

Feed-water samples

Syringe blanks, 05-f1, 05-f6 and 05-f7, were taken to investigate whether the PP syringe used for collecting feedwater samples was introducing any contamination – this was shown not to be the case. Feedwater samples 05-f2 to 05-f5 were taken within an hour of each other, whilst the pump was working at 1 g/min; and 05-f8 was taken at a later date, whilst the pump was working at 0.1 g/min. Levels of each element for these samples were similar to those obtained during session 4, at the same pH value (9). As with session 4, levels in the feedwater were significantly higher than in the type I water and LiOH used in its preparation, showing that metals were released from the SS316L tubing and feedwater barrel at room temperature, under neutral redox conditions. Levels of Cr were consistent with expected solubility, ~ 0.01 ppb. Levels of Fe were much higher than the expected solubility of ~ 0.00 ppb (goethite): this may be due to the presence of particulate matter releasing from walls of the rig, or due to release of soluble Fe from the alloy at supersaturated levels, at a faster rate than iron oxide is able to precipitate from solution on the tubing walls. Levels of Ni, Mn and Mo are below the solubility of the respective pure oxides (check this/ ref: for Mn and Mo) and so are likely to be controlled by rate of release from the alloy, and by the extent of their tendency to incorporate in the corrosion film as impurity elements. Levels of each element in the feedwater are worthy of study, since the coolant passes through room temperature SS316L tubing in the sampling line before samples can be taken, and so feedwater samples – having passed through SS316L tubing at room temperature – give some indication of the levels to which each element may tend as a result of passing along the sampling lines. Where levels in the rig effluent are indistinguishable from feedwater samples, caution should be exercised in drawing conclusions about solubility equilibria, and other processes occurring in the heated part of the rig, from effluent samples.

Samples taken within 24 h of a disturbance to the flow, and outliers with particularly high levels of Fe and Ni, compared with the remainder of samples

In order to explore transient effects resulting from flow disturbances, results from session 5 were separated into two categories: early – from samples taken within 24 h of a disturbance to the flow, i.e. pump restart after a stall, or change in flow rate or temperature conditions; and normal – from all other samples, save for extreme outliers. Samples 05-18, 05-34, 05-36 and 05-37 were considered outliers due to their high levels of some elements, particularly Fe, compared with other samples taken under the same conditions. Sampling mean for each element, and an estimate of the

uncertainty on this mean value (i.e. $\frac{\sigma_{n-1}}{\sqrt{n}}$), were provided for the various categories, at each set of conditions in Table 15.20 below. For Fe, at 300 °C, 1 g/min and 0.5 g/min, early samples had lower values than normal, then after the flow rate was decreased to 0.1 g/min early samples had much higher values than normal. Solubility of magnetite is ~ 0.5 to 1 ppb at temperatures of 200 to 300 °C, and ~ 0.6 ppb at 25 °C, at levels of hydrogen fugacity in the range of those modelled or measured. Solubility of the stable Fe oxide phase at 25 °C under neutral to oxidising conditions, goethite (FeOOH), is also 0.0 ppb. Levels of Fe in the feedwater, of up to 2.5 ppb are therefore indicative of particulate matter: this may be as oxide particles released from the oxide film, or colloidal particles precipitated directly from supersaturated solution (due to dissolution of Fe^{2+} ions released from the corroding SS316L tubing through the protective oxide film). Likewise, levels of Fe in effluent are also indicative of particulate matter. This may include a component released from the room temperature tubing of the sampling line, but a significant proportion is likely to come from the heated part of the rig, since such higher levels are observed in the effluent compared with feedwater. At least some is known to have come from the heated part if the rig under some circumstances, as high temperature oxide crystallites were observed on the filter holders during session 6.

A possible interpretation of the results would be that some process which evolved over time was responsible for the high levels of Fe, >10 ppb, observed for 6 of the samples at 300 °C, 0.1 g/min and both of the samples taken under the conditions of 250 °C, 0.1 g/min which followed. The low room temperature solubility of stable Fe oxide suggests that particulates must be involved. However, high levels, of 36 ppb and 42 ppb, were observed in samples taken whilst a 3 µm filter was in place, suggesting that particulates were mostly small. A few large particulates were observed on this filter. The filter, which was 13 mm across, caused effluent to exit the rig unevenly, with sporadic bursts of flow followed by periods of several minutes of no flow. This could have caused any loosely adherent oxide near the end of the sampling line to release into the effluent. Levels of Cr were ~0.00 ppb throughout.

Rig effluent samples

Table 15.21 summarises typical levels of each element under each condition employed in session 5 (pH 9, with chips), and levels from sessions 3 and 4 (also at pH 9, but with no chips) for comparison. Levels of Cr were around 0.00 to 0.01 ppb throughout session 5, consistent with the solubility of Cr oxides under the full range of conditions likely to be present during session 5. Levels of Fe were variable during session 5, as in previous sessions, ranging from around 2 to 7 ppb for most of the samples Session 4 data showed that by allowing the rig to settle over long periods of flow exclusively

at 0.1 g/min, Fe could be maintained at low levels, consistent with those of the feedwater, at all three temperatures employed in the heated part of the rig. During session 5, after falling slightly on slowing from 1 to 0.5 g/min (300 °C), levels of Fe rose to a comparatively very high peak of 30 – 40 ppb whilst flowing at 0.1 g/min, 300 °C, and gradually fell over time under the lower temperature conditions that followed. This is suggestive of some kind of large release of particulates, by analogy with 'CRUD burst' [118] phenomena observed in PWRs, and so the prevailing temperature and flow rate conditions become irrelevant compared with the effects of the crud burst. Session 3 data had higher levels of Fe than session 4 at 300 °C, 0.1 g/min, but if more than 3 samples were taken and over a longer time period this might have settled to lower values. Levels of Fe were variable, as in previous sessions, but 300 °C values were typically ~ 3 to 4 ppb at 1 g/min; 2 ppb at 0.5 g/min, and 6 ppb at 0.1 g/min, rising to 30 to 40 ppb over the last few samples.

Table 15.20. Summary table for Session 5 data: early versus normal samples, filter samples, and outliers

Sample	[Fe]	[Ni]	[Cr]	[Mo]	[Mn]
300 °C, 1, early	2.2 ± 0.8	0.7 ± 0.3	0.01 ± 0.00	39 ± 23	3.4 ± 1.1
300 °C, 1, normal	**3.5 ± 0.2**	**0.3 ± 0.0**	**-0.01 ± 0.01**	**94 ± 4**	**1.5 ± 0.0**
300 °C, 0.5, early	1.7 ± 0.3	0.4 ± 0.1	0.00 ± 0.01	70 ± 19	1.7 ± 0.2
300 °C, 0.5, normal	**2.3 ± 0.1**	**0.3 ± 0.0**	**0.00 ± 0.01**	**97 ± 2**	**1.9 ± 0.0**
Outlier	12.4	1.2	0.00	68	5.2
300 °C, 0.1, early	21.0 ± 3.7	6.4 ± 5.3	0.03 ± 0.01	46 ± 4	4.2 ± 0.7
300 °C, 0.1, normal	**5.9 ± 0.4**	**0.5 ± 0.1**	**0.01 ± 0.00**	**49 ± 4**	**3.2 ± 0.2**
Outlier	12.2	0.7	-0.01	48	2.9
3 µm filter	38.8 ± 2.9	1.5 ± 0.1	0.01 ± 0.01	38 ± 2	3.4 ± 0.1
250 °C, 0.1, normal	**19.6 ± 0.5**	**1.3 ± 0.1**	**0.01 ± 0.01**	**19 ± 2**	**8.3 ± 0.1**
200 °C, 0.1, normal	**3.6 ± 0.3**	**0.6 ± 0.1**	**0.01 ± 0.00**	**10 ± 0**	**20.5 ± 0.1**

Table 15.21 Summary table for pH 9 results. Session 5 data, with session 3 and 4 data below for comparison

Element *(solubility , 25 °C)* †	**T:300 $\dot{m}$: 2**	**T:300 $\dot{m}$: 1**	**T:300 $\dot{m}$: 0.5**	**T:300 $\dot{m}$: 0.1**	**T:250 $\dot{m}$: 1**	**T:250 $\dot{m}$: 0.1**	**T:200 $\dot{m}$: 1**	**T:200 $\dot{m}$: 0.1**	**Feed-water**
[Fe], ppb *(0.00)*		3 to 4	2	6, rising to 30-40		20		4	~.5 – 2.5
(sess 3)	6		5	2	1-1.5		1-1.5		
(sess 4)				~0.8 (.3–1.5)		~0.2 (.0-.4)		~0.5 (.1-1.4)	~0.1-1.0
[Cr], ppb *(0.01)*		0.00	0.00	0.01		0.02	0.01		~0.02
(sess 3)	.3 falls to .05		0.1	.16 falls to .10	0.00		0.00		
(sess 4)				.1-.2, falls to 0.01		0.03 climbs to 0.30		0.01 falls to 0.00	.00-.02
[Ni], ppb *(27)*		0.4	0.3	~0.65 (0.4 to 0.9)		1.3		0.7	~0.4 – 0.9
(sess 3)	1-3, climbs to 5		7, falls to 4	2.2 falls to 1.5	0.4		0.7		
(sess 4)				~2, (5-8 early on)		0.5 climbs to 1.0		~1.4 (.8-2.4)	~0 – 2.5
[Mo], ppb		1 rises to 100	~90 – 100	~ 40 – 70		20		10	~0.7
(sess 3)	Rises to 25, falls to 20		30 rises to 60	80 rises to 90	50 falls to 35		12 falls to 8		
(sess 4)				40-100, settles at ~ 55		30, falls to 20		10	~0.5
[Mn], ppb		1.5	1.9	3.2		8.3		20.5	~4 – 7
(sess 3)	30-100, settles at 20		40, falls to 25	17, falls to 13	7		14		
(sess 4)				90, settles at 5.3		3, falls to 2		4, rises to 25, falls to 13	~2 – 6

† For Fe, Cr and Ni, solubility of the most stable oxide phase at pH9, 25 °C, under neutral redox conditions is provided for reference. Solubility of magnetite is 0.3 ppb under those conditions; 0.00 ppb under mildly reducing conditions (hematite/magnetite equilibrium); and 58 ppb in the presence of air (i.e. 0.2 bar oxygen)

Table 15.22 provides a briefer summary of session 5 results.

Table 15.22 Summary table for session 5 results

Element / conditions	**300 °C, 1 g/min**	**300 °C, 0.5 g/min**	**300 °C, 0.1 g/min**	**250 °C, 0.1 g/min**	**200 °C, 0.1 g/min**	**feedwater**	**solubility**
[Fe], ppb	3 to 4	2	6, rising to 30-40	20	4	~0.5 – 2.5	0.00
[Cr], ppb	0.00	0.00	0.01	0.02	0.01	~0.02	0.01
[Ni], ppb	0.4	0.3	~0.65 (0.4 to 0.9)	1.3	0.7	~0.4 – 0.9	27
[Mo], ppb	1 rising to ~100	~90 – 100	~ 40 – 70	20	10	~0.7	?
[Mn], ppb	1.5	1.9	3.2	8.3	20.5	~4 – 7	?

Table 15.23 Session 5 results. Feedwater of pH_{25C} 9 was used for session 5

Sample	T	ṁ	[Fe]	[Cr]	[Ni]	[Mo]	[Mn]	Other info
05-01	300	1	12.0 *(6)*	0.12 *(1)*	12.9 *(6)*	24 *(0)*	19.2 *(1)*	water in oven not yet reached 300 °C
05-02	300	1	1.7 *(2)*	*0.01 (1)*	0.2 *(0)*	36 *(0)*	1.4 *(0)*	15 h after T reached
05-03	300	1	4.3 *(3)*	*-0.01 (1)*	0.3 *(0)*	70 *(0)*	1.4 *(0)*	45 h after T reached
05-04	300	1	3.7 *(3)*	*0.01 (1)*	0.8 *(0)*	81 *(0)*	3.9 *(0)*	<1 h after pump restart
05-05	300	1	3.5 (3)	*-0.01 (1)*	0.3 *(0)*	92 *(0)*	1.4 *(0)*	31 h after pump restart
05-06	300	1	3.1 *(2)*	*-0.04 (1)*	0.3 *(0)*	95 *(0)*	1.5 *(0)*	57 h after pump restart
05-07	300	1	3.8 *(3)*	0.04 *(1)*	0.4 *(0)*	101 *(1)*	1.6 *(0)*	73 h after pump restart (3 samples in quick succession)
05-08	300	1	3.5 *(3)*	*-0.02 (1)*	0.4 *(0)*	100 *(0)*	1.7 *(0)*	73 h after pump restart
05-09	300	1	3.2 *(2)*	*0.00 (1)*	0.3 *(0)*	100 *(1)*	1.6 *(0)*	73 h after pump restart
05-10	300	1	2.8 *(2)*	*-0.01 (1)*	0.4 *(0)*	101 *(1)*	1.5 *(0)*	103 h after pump restart
05-11	300	0.5	2.0 *(2)*	*-0.01 (1)*	0.3 *(0)*	89 *(0)*	2.0 *(0)*	17 h after change in flow rate
05-12	300	0.5	2.2 *(2)*	*-0.02 (1)*	0.3 *(0)*	91 *(0)*	1.9 *(0)*	48 h after change in flow rate
05-13	300	0.5	2.2 *(2)*	*-0.01 (1)*	0.2 *(0)*	95 *(0)*	2.1 *(0)*	66 h after change in flow rate
05-14	300	0.5	1.9 *(2)*	*-0.01 (1)*	0.3 *(0)*	100 *(1)*	1.9 *(0)*	95 h after change in flow rate
05-15	300	0.5	2.5 *(2)*	0.02 *(1)*	0.2 *(0)*	101 *(1)*	1.8 *(0)*	114 h after change in flow rate
05-16	300	0.5	2.2 *(2)*	*0.01 (1)*	0.4 *(0)*	100 *(0)*	2.0 *(0)*	133 h after change in flow rate
05-18	300	0.5	12.4 *(2)*	*0.00 (1)*	1.2 *(1)*	68 *(0)*	5.2 *(0)*	46 h after pump restart
05-19	300	0.5	1.3 *(2)*	*0.01 (1)*	0.5 *(0)*	51 *(0)*	1.5 *(0)*	3 h after pump restart
05-20	300	0.5	2.4 *(2)*	*0.00 (1)*	0.3 *(0)*	94 *(0)*	1.8 *(0)*	26 h after pump restart
05-21	300	0.1	5.4 *(3)*	*0.01 (1)*	0.9 *(0)*	74 *(0)*	4.4 *(0)*	29 h after change in flow rate
05-22	300	0.1	5.2 *(3)*	*0.01 (1)*	0.4 *(0)*	61 *(0)*	2.8 *(0)*	53 h after change in flow rate
05-23	300	0.1	3.5 *(3)*	*0.01 (1)*	0.5 *(0)*	53 *(0)*	3.2 *(0)*	82 h after change in flow rate
05-24	300	0.1	7.4 *(4)*	*0.02 (1)*	0.9 *(0)*	46 *(0)*	4.2 *(0)*	101 h after change in flow rate
05-26	300	0.1	18.9*(10)*	*0.02 (1)*	1.4 *(1)*	43 *(0)*	4.1 *(0)*	14 h after pump restart
05-27	300	0.1	6.3 *(4)*	*0.00 (1)*	0.4 *(0)*	37 *(0)*	2.5 *(0)*	87 h after pump restart
05-28	300	0.1	6.5 *(4)*	0.03 *(1)*	0.4 *(0)*	42 *(0)*	3.0 *(0)*	162 h after pump restart
05-29	300	0.1	4.9 *(3)*	*0.00 (1)*	0.4 *(0)*	42 *(0)*	3.0 *(0)*	187 h after pump restart
05-30	300	0.1	15.8 *(8)*	0.02 *(1)*	0.8 *(0)*	54 *(0)*	5.4 *(0)*	1 h after pump restart
05-31	300	0.1	5.7 *(3)*	*0.00 (1)*	0.3 *(0)*	41 *(0)*	2.7 *(0)*	53 h after pump restart
05-32	300	0.1	5.8 *(3)*	0.04 *(1)*	0.2 *(0)*	45 *(0)*	2.8 *(0)*	99 h after pump restart
05-33	300	0.1	8.3 *(5)*	*0.01 (1)*	0.3 *(0)*	50 *(0)*	2.7 *(0)*	41 h after pump restart
05-34	300	0.1	12.2 *(6)*	*-0.01 (1)*	0.7 *(0)*	48 *(0)*	2.9 *(0)*	47 h after pump restart
05-35	300	0.1	28.2*(14)*	0.04 *(1)*	17.1 *(9)*	41 *(0)*	3.1 *(0)*	20 h after pump restart
05-36	300	0.1	35.8*(18)*	*0.00 (1)*	1.5 *(1)*	40 *(0)*	3.5 *(0)*	54 h after pump restart
05-37	300	0.1	41.7*(21)*	*0.02 (1)*	1.6 *(1)*	37 *(0)*	3.4 *(0)*	76 h after pump restart
05-38	250	0.1	20.1*(10)*	*0.00 (1)*	1.2 *(1)*	21 *(0)*	8.4 *(0)*	25 h after change in temperature
05-39	250	0.1	19.2*(10)*	0.03 *(1)*	1.4 *(1)*	17 *(0)*	8.2 *(0)*	45 h after change in temperature
05-40	200	0.1	3.3 *(2)*	*0.01 (1)*	0.5 *(0)*	11 *(0)*	20.4 *(1)*	25 h after change in temperature
05-41	200	0.1	3.9 *(3)*	*0.01 (1)*	0.8 *(0)*	10 *(0)*	20.6 *(1)*	50 h after change in temperature
05-f2	-	1	0.6 *(2)*	0.02 *(1)*	0.4 *(0)*	0.7 *(0)*	4.2 *(0)*	Feedwater, 0.5 h after sample #10
05-f3	-	1	0.5 *(2)*	0.02 *(1)*	0.4 *(0)*	0.6 *(0)*	4.3 *(0)*	Feedwater, 0.5 h after sample #10
05-f4	-	1	0.4 *(2)*	0.03 *(1)*	0.4 *(0)*	0.7 *(0)*	4.3 *(0)*	Feedwater, 1 h after sample #10
05-f5	-	1	0.4 *(2)*	*0.02 (1)*	0.4 *(0)*	0.6 *(0)*	4.7 *(0)*	Feedwater, 1 h after sample #10
05-f8	-	0.1	2.5 *(2)*	0.03 *(1)*	0.9 *(0)*	0.8 *(0)*	7.2 *(0)*	Feedwater, 25 h before sample #38
05-f1	-	-	*-0.1 (2)*	*0.00 (1)*	0.10 *(1)*	*-0.03(3)*	0.05 *(1)*	Syringe blank, for samples f2-f5
05-f6	-	-	*-0.3 (2)*	*0.00 (1)*	*-0.01 (1)*	*-0.06(3)*	*0.01 (1)*	Syringe blanks, for sample f8
05-f7	-	-	*-0.2 (2)*	*-0.01 (1)*	*-0.01 (1)*	*-0.06(3)*	*-0.01 (1)*	Syringe blanks, for sample f8
Rejects	-	-	0.5 *(4)*	0.05 *(5)*	1.3 *(29)*	0.04 *(5)*	0.02 *(2)*	Rejected blanks
Blanks	-	-	0.04*(14)*	-0.01 *(1)*	-0.01 *(1)*	0.02 *(2)*	0.00 *(1)*	Batch 5.

15.2.8. Session 6 Results

From session 6, eighty-six effluent samples (including 7 special samples having been taken from waste effluent vessels using a syringe), a syringe blank for the syringe used to collect special samples, nine feed-water samples, two samples of type 1 water having passed through a used filter, and one feed-water syringe blank were analysed along with the eighteen blanks and other samples of batch 5. The processed results are presented in Table 15.26.

Filters were in place for around half (46) of the samples. There was no significant difference between results taken when the filter was in place compared with those taken when no filter was in place. The filters themselves were analysed under SEM and only one particulate was found.

As for the results of previous sessions, conditions of the rig and sampling during the session (Table 15.24) and details of any disruptions to flow (Table 15.25) are included in tables below.

Table 15.24 Conditions of the rig and sampling during session 6

Conditions	*Times and dates*	*Samples analysed*	*notes*
1 g/min; 22 °C rising to 300 °C	14/4/15, **1 hour**		
1 g/min; 300 °C	14/4 – 5/5, **21 days** (74 h no filter) 72 h, 0.45µm filter (20 h no filter) 153 h, 0.05 µm filter (91 h no filter) 92 h, 3.0 µm filter	 1, 2 (& dump vessels) 3, 4 (& dump vessels) 5, 6 7, 8, 9, 10, 10B 11, 12, 13 14, 15	On 23/4, after 216 h of flow, samples were taken from dump water (effluent) vessels: 400-ml beaker (first 6 h flow); 1000-ml beaker (6 – 22 h); 250-ml beaker (22 – 27 h); round barrel (27 – 74 h); square barrel (78 – 146 h).
0.5 g/min; 300 °C	5/5 – 20/5, **15 days** 149 h, 3.0 µm filter (68 h no filter) 56 h 0.05 µm filter (20 h no filter) 67 h 0.45 µm filter	 16, 17, 18 19, 20 21, 22, 23 24 25, 26, 27	
0.1 g/min; 300 °C	20/5 – 5/6, **16 days** 51 h, 0.45 µm filter (94 h no filter) 49 h, 3.0 µm filter (24 h no filter) 93 h, 0.05 µm filter (70 h no filter)	 28, 29, 30 31, 32 (& filter1, 2) 33, 34, 35 36, 37 38, 39, 40 41, 42, 43	After 0.45 µm filter was removed from rig, still enclosed in its plastic housing, it was rinsed with type 1 water and two samples of ~5 g each (filter1,2) were taken of type 1 water which was allowed to slowly pass through filter.
0.1 g/min; 250 °C	5/6 – 19/6, **14 days** (102 h no filter) 48 h 0.05 µm filter (22 h no filter) 98 h 3.0 µm filter (22 h no filter) 50 h, 0.45 µm filter (1 h no filter)	 44, 45, 46, 47 48, 49, 50 51, 52 53, 54, 55 56, 57 58, 59, 60 61	
0.1 g/min; 200 °C	19/6 – 3/7, **14 days** (94 h no filter) 48 h, 0.45 µm filter (25 h no filter) 95 h, 0.05 µm filter (26 h no filter) 47 h, 3.0 µm filter (4 h no filter)	 41, 42	

Table 15.25. Disruptions to flow during session 6

Sampling sequence α		Disruptions to flow β	
t_{sess} (h)	Sample #	t_{change} (h)	†Latest change
7	06-01	6	T_w
72	06-02	71	T_w
79	06-03	78	T_w
146	06-04	145	T_w
148	06-05	147	T_w
166	06-06	165	T_w
169	06-07	168	T_w
170	06-08	169	T_w
197	06-09	196	T_w
226	06-10	225	T_w
319	06-10B	318	T_w
319	06-11	318	T_w
357	06-12	356	T_w
387	06-13	386	T_w
457	06-14	456	T_w
501	06-15	500	T_w
554	06-16	52	flow (.5)
574	06-17	73	flow (.5)
650	06-18	149	flow (.5)
653	06-19	151	flow (.5)
718	06-20	217	flow (.5)
722	06-21	220	flow (.5)
744	06-22	243	flow (.5)
775	06-23	273	flow (.5)
776	06-24	275	flow (.5)
819	06-25	317	flow (.5)
841	06-26	339	flow (.5)
862	06-27	360	flow (.5)
867	06-28	4	flow (.1)
889	06-29	27	flow (.1)
912	06-30	50	flow (.1)
914	06-31	52	flow (.1)
1006	06-32	144	flow (.1)
1010	06-33	148	flow (.1)
1033	06-34	171	flow (.1)
1055	06-35	193	flow (.1)
1059	06-36	196	flow (.1)
1079	06-37	217	flow (.1)
1082	06-38	220	flow (.1)
1150	06-39	288	flow (.1)

Sampling sequence α		Disruptions to flow β	
t_{sess} (h)	Sample #	t_{change} (h)	†Latest change
1172	06-40	310	flow (.1)
1177	06-41	314	flow (.1)
1204	06-42	342	flow (.1)
1242	06-43	380	flow (.1)
1245	06-44	1	T (250)
1250	06-45	5	T (250)
1320	06-46	76	T (250)
1342	06-47	97	T (250)
1349	06-48	105	T (250)
1369	06-49	124	T (250)
1392	06-50	147	T (250)
1396	06-51	152	T (250)
1413	06-52	168	T (250)
1418	06-53	174	T (250)
1488	06-54	244	T (250)
1511	06-55	267	T (250)
1514	06-56	270	T (250)
1534	06-57	289	T (250)
1537	06-58	293	T (250)
1564	06-59	320	T (250)
1581	06-60	337	T (250)
1584	06-61	340	T (250)
1587	06-62	1	T (200)
1654	06-63	68	T (200)
1677	06-64	91	T (200)
1682	06-65	96	T (200)
1703	06-66	117	T (200)
1726	06-67	140	T (200)
1729	06-68	143	T (200)
1749	06-69	163	T (200)
1751	06-70	165	T (200)
1824	06-71	238	T (200)
1845	06-72	259	T (200)
1850	06-73	264	T (200)
1870	06-74	284	T (200)
1874	06-75	288	T (200)
1896	06-76	310	T (200)
1917	06-77	331	T (200)
1920	06-78	334	T (200)

For reference, residence time at 0.1 g/min (sample 05-21 onwards) is 1 h in the cold tubing at the back end of the rig, and 15.5 h, 17.5 h and 18.9 h respectively in the hot part of the rig at 300, 250, and 200 °C. Residence times at 0.5 g/min, 300 °C (05-11 through 05-20) are 0.2 h and 3.1 h respectively, and at 1.0 g/min, 300 °C (05-01 through 05-10) are 0.1 h and 1.6 h respectively for the back end of the rig and the hot part of the rig.

α: 't_{sess} (h)' represents cumulative time in hours since session 5 started. Remove two from this number to give cumulative hours at 200 °C or more.

β: 't_{change} (h)' gives time in hours since the latest change which caused disruption to flow in the rig.

† Abbreviations for latest change: T_w = temperature of water reaching 300 °C (as judged by flow rate at rig exit returning to normal); r-s (no.) = pump restart (after stall; cumulative no. of restarts is indicated); r-s (250) and r-s (200) = recommencement of normal flow after a transient period following transition to 250 °C (1 h 40 min) or to 200 °C (flow rate increased for for 1 h 20 min to prevent stagnation and pressure loss)

Table 15.26. Session 6 results. Feedwater of pH_{25C} 10 was used for session 6

Sample	T	ṁ	[Fe]	[Cr]	[Ni]	[Mo]	[Mn]	Other info
400-top	300	1	0.4 *(2)*	0.44 *(2)*	1.7 *(1)*	400 *(2)*	8.4 *(0)*	From top of dump vessel (0-6 h)
400-bot	300	1	1.2 *(2)*	0.45 *(2)*	2.4 *(1)*	400 *(2)*	8.6 *(0)*	From bottom of dump vessel (0-6 h)
1000	300	1	*-0.2 (2)*	1.04 *(5)*	*0.0 (0)*	768 *(4)*	0.0 *(0)*	From top of dump vessel (0-22 h)
250-top	300	1	*-0.1 (2)*	1.35 *(7)*	*0.0 (0)*	951 *(5)*	0.0 *(0)*	From top of dump vessel (22-27 h)
250-bot	300	1	*-0.1 (2)*	1.36 *(7)*	*0.0 (0)*	946 *(5)*	0.0 *(0)*	Bottom of dump vessel (22-27 h)
round	300	1	*-0.2 (2)*	1.18 *(6)*	0.8 *(0)*	445 *(2)*	0.1 *(0)*	From top of dump vessel (27-74 h)
square	300	1	*-0.2 (2)*	1.96*(10)*	*0.0 (0)*	318 *(2)*	0.0 *(0)*	From top of dump vessel (78-146 h)
06-B1	-	-	2.0 *(2)*	0.21 *(1)*	0.3 *(0)*	*-0.03 (3)*	0.05 *(1)*	Syringe blank, for 7 specials above
06-01	300	1	*0.1 (2)*	1.03 *(5)*	0.7 *(0)*	688 *(3)*	0.1 *(0)*	6 h after T reached
06-02	300	1	*0.1 (2)*	0.91 *(5)*	0.1 *(0)*	408 *(2)*	0.1 *(0)*	71 h after T reached
06-03	300	1	*0.2 (2)*	0.86 *(4)*	*0.0 (0)*	392 *(2)*	0.1 *(0)*	78 h after T reached
06-04	300	1	*0.4 (2)*	1.35 *(7)*	*0.0 (0)*	303 *(2)*	0.1 *(0)*	145 h after T reached
06-05	300	1	*0.1 (2)*	1.40 *(7)*	0.0 *(0)*	304 *(2)*	0.1 *(0)*	147 h after T reached
06-06	300	1	*0.1 (2)*	1.00 *(5)*	*0.0 (0)*	285 *(1)*	0.1 *(0)*	165 h after T reached
06-07	300	1	*0.2 (2)*	1.07 *(5)*	*0.0 (0)*	282 *(1)*	0.0 *(0)*	168 h after T reached
06-08	300	1	*0.2 (2)*	0.98 *(5)*	0.0 *(0)*	281 *(1)*	0.0 *(0)*	169 h after T reached
06-09	300	1	*0.0 (2)*	0.98 *(5)*	0.0 *(0)*	261 *(1)*	0.0 *(0)*	196 h after T reached
06-10	300	1	*0.0 (2)*	0.83 *(4)*	*0.0 (0)*	240 *(1)*	0.0 *(0)*	225 h after T reached
06-10B	300	1	*0.1 (2)*	0.56 *(3)*	*-0.1 (0)*	159 *(1)*	0.1 *(0)*	318 h after T reached
06-11	300	1	*0.2 (2)*	0.55 *(3)*	*0.0 (0)*	156 *(1)*	0.1 *(0)*	318 h after T reached
06-12	300	1	*0.1 (2)*	0.54 *(3)*	*0.0 (0)*	123 *(1)*	0.1 *(0)*	356 h after T reached
06-13	300	1	*0.0 (2)*	0.50 *(3)*	*0.0 (0)*	104 *(1)*	0.0 *(0)*	386 h after T reached
06-14	300	1	*0.0 (2)*	0.47 *(3)*	0.0 *(0)*	72 *(0)*	0.1 *(0)*	456 h after T reached
06-15	300	1	*0.1 (2)*	0.47 *(3)*	*0.0 (0)*	59 *(0)*	0.1 *(0)*	500 h after T reached
06-16	300	0.5	0.4 *(2)*	0.82 *(4)*	0.0 *(0)*	93 *(0)*	0.1 *(0)*	52 h after change in flow rate
06-17	300	0.5	*0.2 (2)*	0.90 *(5)*	*0.0 (0)*	93 *(0)*	0.1 *(0)*	73 h after change in flow rate
06-18	300	0.5	*0.1 (2)*	0.63 *(3)*	0.1 *(0)*	84 *(0)*	0.1 *(0)*	149 h after change in flow rate
06-19	300	0.5	*0.1 (2)*	0.67 *(3)*	0.0 *(0)*	82 *(0)*	0.2 *(0)*	151 h after change in flow rate
06-20	300	0.5	*0.0 (2)*	0.60 *(3)*	0.0 *(0)*	74 *(0)*	0.1 *(0)*	217 h after change in flow rate
06-21	300	0.5	*0.1 (2)*	0.55 *(3)*	*0.0 (0)*	72 *(0)*	0.0 *(0)*	220 h after change in flow rate
06-22	300	0.5	*0.0 (2)*	0.70 *(4)*	*0.0 (0)*	69 *(0)*	0.0 *(0)*	243 h after change in flow rate
06-23	300	0.5	*0.1 (2)*	0.60 *(3)*	0.0 *(0)*	66 *(0)*	0.0 *(0)*	273 h after change in flow rate
06-24	300	0.5	*0.2 (2)*	0.57 *(3)*	*0.0 (0)*	66 *(0)*	0.1 *(0)*	275 h after change in flow rate
06-25	300	0.5	*0.2 (2)*	0.54 *(3)*	*0.0 (0)*	60 *(0)*	0.1 *(0)*	317 h after change in flow rate
06-26	300	0.5	*0.0 (2)*	0.50 *(3)*	0.0 *(0)*	57 *(0)*	0.1 *(0)*	339 h after change in flow rate
06-27	300	0.5	*0.3 (2)*	0.51 *(3)*	*0.0 (0)*	55 *(0)*	0.1 *(0)*	360 h after change in flow rate
06-28	300	0.1	*0.2 (2)*	2.21*(11)*	*0.0 (0)*	59 *(0)*	0.1 *(0)*	4 h after change in flow rate
06-29	300	0.1	0.7 *(2)*	2.72*(14)*	*0.0 (0)*	91 *(0)*	0.1 *(0)*	27 h after change in flow rate
06-30	300	0.1	*0.2 (2)*	2.32*(12)*	0.1 *(0)*	126 *(1)*	0.1 *(0)*	50 h after change in flow rate
06-31	300	0.1	0.5 *(2)*	2.50*(13)*	0.5 *(0)*	130 *(1)*	0.5 *(0)*	52 h after change in flow rate
06-32	300	0.1	*0.2 (2)*	2.10*(10)*	0.1 *(0)*	170 *(1)*	0.1 *(0)*	144 h after change in flow rate
06-33	300	0.1	0.4 *(2)*	2.05*(10)*	*0.0 (0)*	170 *(1)*	0.0 *(0)*	148 h after change in flow rate
06-34	300	0.1	*0.1 (2)*	2.05*(10)*	0.0 *(0)*	157 *(1)*	0.1 *(0)*	171 h after change in flow rate
06-35	300	0.1	*0.2 (2)*	1.94*(10)*	0.0 *(0)*	164 *(1)*	0.1 *(0)*	193 h after change in flow rate
06-36	300	0.1	*0.1 (2)*	1.98*(10)*	0.2 *(0)*	161 *(1)*	0.2 *(0)*	196 h after change in flow rate
06-37	300	0.1	*0.1 (2)*	1.90*(10)*	0.1 *(0)*	159 *(1)*	0.1 *(0)*	217 h after change in flow rate
06-38	300	0.1	0.7 *(2)*	1.74 *(9)*	0.0 *(0)*	151 *(1)*	0.4 *(0)*	220 h after change in flow rate
06-39	300	0.1	*0.2 (2)*	1.71 *(9)*	*0.0 (0)*	156 *(1)*	0.0 *(0)*	288 h after change in flow rate
06-40	300	0.1	*0.2 (2)*	2.21*(11)*	*-0.1 (0)*	184 *(1)*	0.0 *(0)*	310 h after change in flow rate
06-41	300	0.1	*0.1 (2)*	2.20*(11)*	0.3 *(0)*	165 *(1)*	0.4 *(0)*	314 h after change in flow rate
06-42	300	0.1	1.0 *(2)*	2.13*(11)*	0.0 *(0)*	158 *(1)*	0.1 *(0)*	342 h after change in flow rate
06-43	300	0.1	*0.0 (2)*	1.82 *(9)*	*0.0 (0)*	154 *(1)*	0.0 *(0)*	380 h after change in flow rate
06-44	250	0.1	0.7 *(2)*	3.54*(18)*	0.1 *(0)*	157 *(1)*	0.3 *(0)*	1 h after change in temperature
06-45	250	0.1	0.7 *(2)*	2.05*(10)*	0.0 *(0)*	98 *(0)*	0.1 *(0)*	5 h after change in temperature
06-46	250	0.1	1.0 *(2)*	2.24*(11)*	*0.0 (0)*	77 *(0)*	0.1 *(0)*	76 h after change in temperature
06-47	250	0.1	0.8 *(2)*	2.04*(10)*	*0.0 (0)*	74 *(0)*	0.1 *(0)*	97 h after change in temperature
06-48	250	0.1	*0.4 (2)*	2.11*(11)*	*0.0 (0)*	72 *(0)*	0.1 *(0)*	105 h after change in temperature
06-49	250	0.1	2.6 *(2)*	2.49*(12)*	*0.0 (0)*	76 *(0)*	0.3 *(0)*	124 h after change in temperature

06-50	250	0.1	0.9 *(2)*	2.25*(11)*	*0.0 (0)*	72 *(0)*	0.1 *(0)*	147 h after change in temperature
06-51	250	0.1	*0.3 (2)*	2.56*(13)*	0.2 *(0)*	71 *(0)*	0.2 *(0)*	152 h after change in temperature
06-52	250	0.1	0.8 *(2)*	2.23*(11)*	*0.0 (0)*	72 *(0)*	0.1 *(0)*	168 h after change in temperature
06-53	250	0.1	*-0.1 (2)*	2.27*(11)*	*0.0 (0)*	72 *(0)*	0.0 *(0)*	174 h after change in temperature
06-54	250	0.1	1.5 *(2)*	2.41*(12)*	*0.0 (0)*	79 *(0)*	0.1 *(0)*	244 h after change in temperature
06-55	250	0.1	1.3 *(2)*	2.19*(11)*	*0.0 (0)*	80 *(0)*	0.1 *(0)*	267 h after change in temperature
06-56	250	0.1	*0.3 (2)*	2.33*(12)*	0.4 *(0)*	80 *(0)*	0.3 *(0)*	270 h after change in temperature
06-57	250	0.1	*0.4 (2)*	2.02*(10)*	0.0 *(0)*	81 *(0)*	0.1 *(0)*	289 h after change in temperature
06-58	250	0.1	*0.2 (2)*	2.21*(11)*	*0.0 (0)*	80 *(0)*	0.1 *(0)*	293 h after change in temperature
06-59	250	0.1	1.0 *(2)*	2.14*(11)*	0.0 *(0)*	84 *(0)*	0.1 *(0)*	320 h after change in temperature
06-60	250	0.1	0.6 *(2)*	1.99*(10)*	*0.0 (0)*	83 *(0)*	0.1 *(0)*	337 h after change in temperature
06-61	250	0.1	0.7 *(2)*	2.20*(11)*	0.3 *(0)*	82 *(0)*	0.2 *(0)*	340 h after change in temperature
06-62	200	0.1	*0.0 (2)*	2.04*(10)*	0.1 *(0)*	84 *(0)*	0.1 *(0)*	1 h after change in temperature
06-63	200	0.1	*0.0 (2)*	1.97*(10)*	*0.0 (0)*	50 *(0)*	0.1 *(0)*	68 h after change in temperature
06-64	200	0.1	*-0.1 (2)*	1.97*(10)*	*0.0 (0)*	42 *(0)*	0.1 *(0)*	91 h after change in temperature
06-65	200	0.1	0.6 *(2)*	2.07*(10)*	*0.0 (0)*	40 *(0)*	0.1 *(0)*	96 h after change in temperature
06-66	200	0.1	*0.0 (2)*	2.21*(11)*	*0.0 (0)*	35 *(0)*	0.0 *(0)*	117 h after change in temperature
06-67	200	0.1	0.7 *(2)*	2.05*(10)*	*0.0 (0)*	31 *(0)*	0.1 *(0)*	140 h after change in temperature
06-68	200	0.1	0.6 *(2)*	2.09*(10)*	0.1 *(0)*	30 *(0)*	0.2 *(0)*	143 h after change in temperature
06-69	200	0.1	*-0.2 (2)*	1.97*(10)*	*0.0 (0)*	28 *(0)*	0.1 *(0)*	163 h after change in temperature
06-70	200	0.1	0.8 *(2)*	2.08*(10)*	*0.0 (0)*	28 *(0)*	0.0 *(0)*	165 h after change in temperature
06-71	200	0.1	0.5 *(2)*	2.02*(10)*	*0.0 (0)*	24 *(0)*	0.0 *(0)*	238 h after change in temperature
06-72	200	0.1	0.4 *(2)*	1.90*(10)*	*0.0 (0)*	23 *(0)*	0.0 *(0)*	259 h after change in temperature
06-73	200	0.1	*0.1 (2)*	2.71*(14)*	0.3 *(0)*	23 *(0)*	0.2 *(0)*	264 h after change in temperature
06-74	200	0.1	*0.0 (2)*	2.38*(12)*	0.4 *(0)*	23 *(0)*	0.1 *(0)*	284 h after change in temperature
06-75	200	0.1	*0.2 (2)*	2.45*(12)*	*0.0 (0)*	23 *(0)*	0.0 *(0)*	288 h after change in temperature
06-76	200	0.1	*0.3 (2)*	1.94*(10)*	*0.0 (0)*	24 *(0)*	0.1 *(0)*	310 h after change in temperature
06-77	200	0.1	*0.1 (2)*	1.88 *(9)*	*0.0 (0)*	23 *(0)*	0.1 *(0)*	331 h after change in temperature
06-78	200	0.1	0.4 *(2)*	2.82*(14)*	0.2 *(0)*	24 *(0)*	0.2 *(0)*	334 h after change in temperature
06-f2	-	1	0.4 *(2)*	*0.00 (1)*	0.1 *(0)*	*0.04 (3)*	0.03 *(1)*	Feedwater, 4 h before sample #12
06-f3	-	1	*0.0 (2)*	*-0.01 (1)*	0.0 *(0)*	*0.04 (3)*	*0.01 (1)*	Feedwater, 4 h before sample #12
06-f4	-	1	*0.0 (2)*	*-0.01 (1)*	0.0 *(0)*	*0.03 (3)*	*0.00 (1)*	Feedwater, 4 h before sample #12
06-f5	-	1	*0.0 (2)*	*0.02 (1)*	0.4 *(0)*	*0.03 (3)*	*0.01 (1)*	Feedwater, 4 h before sample #12
06-f6	-	1	*-0.1 (2)*	*0.00 (1)*	0.0 *(0)*	*0.04 (3)*	0.02 *(1)*	Feedwater, 0.3 h before sample #12
06-f7	-	1	1.1 *(2)*	0.02 *(1)*	0.1 *(0)*	*0.03 (3)*	*0.01 (1)*	Feedwater, 0.2 h before sample #12
06-f8	-	0.1	0.5 *(2)*	*-0.01 (1)*	0.1 *(0)*	0.17 *(3)*	0.08 *(1)*	Feedwater, during 0.1 g/min flow
06-f9	-	0.1	*0.0 (2)*	*0.01 (1)*	0.0 *(0)*	0.16 *(3)*	0.05 *(1)*	Feedwater, during 0.1 g/min flow
06-f10	-	0.1	*0.0 (2)*	*0.01 (1)*	0.0 *(0)*	0.16 *(3)*	0.05 *(1)*	Feedwater, during 0.1 g/min flow
06-f1	-	-	*-0.2 (2)*	*0.02 (1)*	0.2 *(0)*	*-0.06 (3)*	0.11 *(1)*	Syringe blank, for samples f2-f7
Filter1			*0.2 (2)*	0.04 *(1)*	*0.01 (1)*	1.1 *(0)*	0.1 *(0)*	Used filter blank, 1 h after #31
Filter2			*0.1 (2)*	0.03 *(1)*	*0.00 (1)*	0.2 *(0)*	0.2 *(0)*	Used filter blank, 4 h after #31
Rejects	-	-	0.5 *(4)*	0.05 *(5)*	1.3 *(29)*	0.04 *(5)*	0.02 *(2)*	Rejected blanks
Blanks	-	-	0.04*(14)*	-0.01 *(1)*	-0.01 *(1)*	0.02 *(2)*	0.00 *(1)*	Batch 5.

15.3. Results plotted against cumulative time under hydrothermal conditions, and cleaning of the data

Some of the more obvious trends with time or sampling sequence were discussed in section 15.2, along with discussion of why some of the particular data points may not be representative. In this section, results are plotted against cumulative time under hydrothermal conditions, here taken as temperatures of 200 °C or more, to enable trends with time to been seen more clearly. A consistent method was developed to remove non-representative data points, as discussed in more detail in section 15.3.1 below. Plots of the resulting 'cleaned' data are presented in the subsections which follow, alongside plots which include all the data, for comparison, since there is a degree of judgement in deciding which points should be removed and some information or insight may be lost in doing so. For sessions 1 – 3, which shared a reaction cell, results are plotted together on one plot so that the previous session's influence on early results of the next session can be appreciated; session 4 is dealt with separately.

15.3.1. Method for cleaning the data

As discussed in at the beginning of this appendix, a systematic method was developed in which unrepresentative or anomalous results were removed.

It was observed that samples taken soon after a change in conditions (temperature, flow rate, or restart after a pump stall) often gave erratic results, typically much higher than the other results. Deciding on a cut-off time based purely on the extent to which results were atypical risked introducing a bias to results, therefore a physical basis was sought for the cut-off time. The initial criterion used was that "the time since the latest change in conditions must be sufficient for feed-water to have flowed through the reaction chamber for the full residence time at the current conditions, prior to commencement of the sample, taking into account also the lag time between exiting the oven and exiting the rig." Some erratic data points remained, particularly sample 03-31 in terms of its Fe content, and this can be explained physically in terms of diffusion and mixing of the flow within the reaction chamber, enabling transient effects – such as increased particulate or dissolved concentrations – to persist for longer. Therefore, a time period of *two* residence times in the hot part of the rig (~130 ml), plus time taken to pass through the room temperature tubing forming the back-end of the rig, was chosen as the cut-off. In this way, the cut-off time was dependent on flow rate, and also on temperature via its effect on density and thus residence time in the reaction cell. The mass of water in the hot part of the rig was calculated as 93.0 g, 104.8 g, and

113.2 g, at the temperatures of 300, 250 and 200 °C respectively, with the residence times having the same values in minutes for a flow rate of 1 g/min. The 6 ml room temperature tubing at the back-end of the rig had a residence time of ~ 6 minutes at 1 g/min, regardless of temperature in the oven.

By application of the above rule, all results from session 1 were removed, along with samples # 1, 2, 3, 4, 12 and 31 from session 3. All results from session 2 were retained, since they passed the criteria of the rule; however, these results were problematic in general, since they came from a variety of sampling techniques, it's just that it was unclear which sampling technique was least representative and therefore which points to remove. Results from session 2 should thus be treated with caution, as discussed later.

In addition, duplicates (03-08-du and 03-09-du) were removed, and an average was taken from the set of three 4 ml samples taken back to back (03-16 to 03-18), to form a data point equivalent to the 12 ml samples which were typically used under the same conditions.

15.3.2. Sessions 1 to 4

Plots are presented below in five figures, one for each element. Each figure follows the same format, with four plots as follows:

(a) Sessions 1-3, all data. All data points are plotted, so that results can be seen in the context of earlier or later sessions – for example in Figure 15.8 (a), low initial [Mo] readings at pH 9 can be seen as a consequence of depletion of Mo in the oxide film as a result of high levels released at pH 11.

(b) Sessions 1-3, 'cleaned' data. Non-representative points are removed, in order to more clearly see trends due to processes occurring within the rig, as opposed to artefacts of the sampling method. In the case of Mo, data from session 2 are also removed in order to better see the behaviour of [Mo] over the range of 0 – 100 ppb in session 3.

(c) Session 4, all data. All data points are plotted so that any lingering effect of the previous temperature condition, or the flow disturbance associated with the temperature change, can be observed for the early 250 °C and 200 °C data points. Also, elevated levels after the session's sole pump stall and restart can be observed for reference.

(d) Session 4, 'cleaned' data. As per part b, data from early non-representative samples are removed.

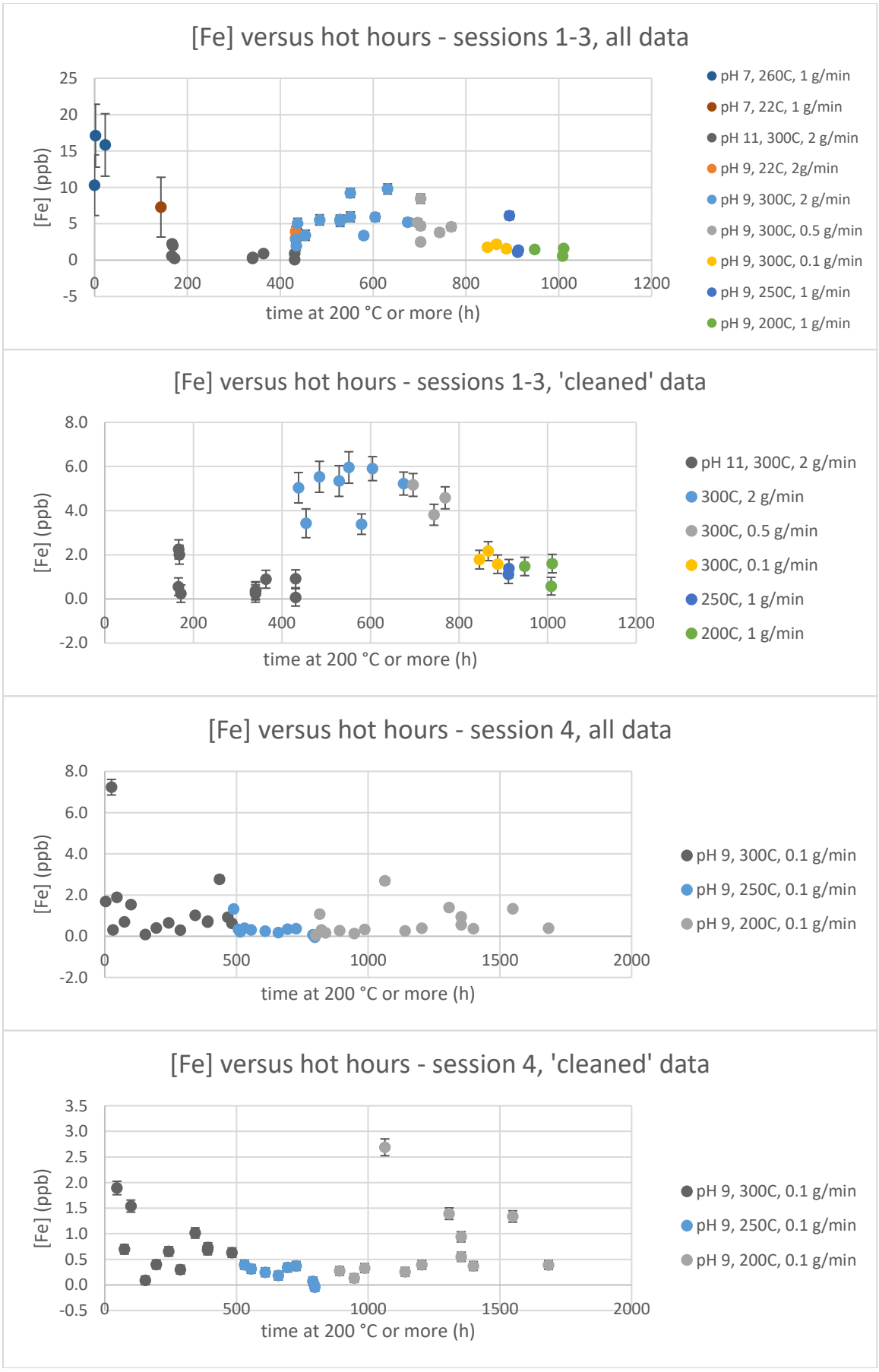

Figure 15.5 Results versus time under hydrothermal conditions for Fe, sessions 1 to 4

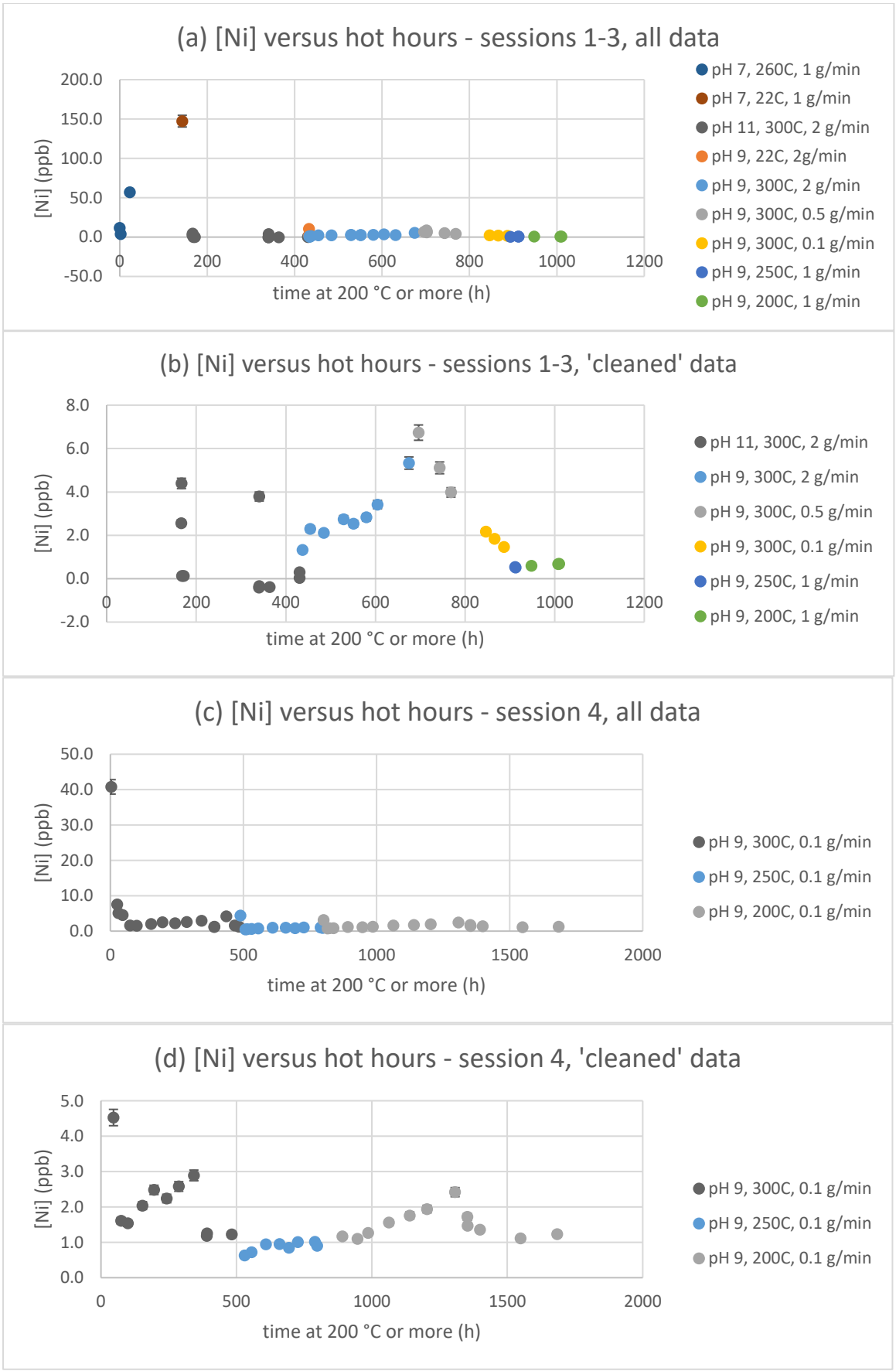

Figure 15.6 Results versus time under hydrothermal conditions for Ni, sessions 1 to 4

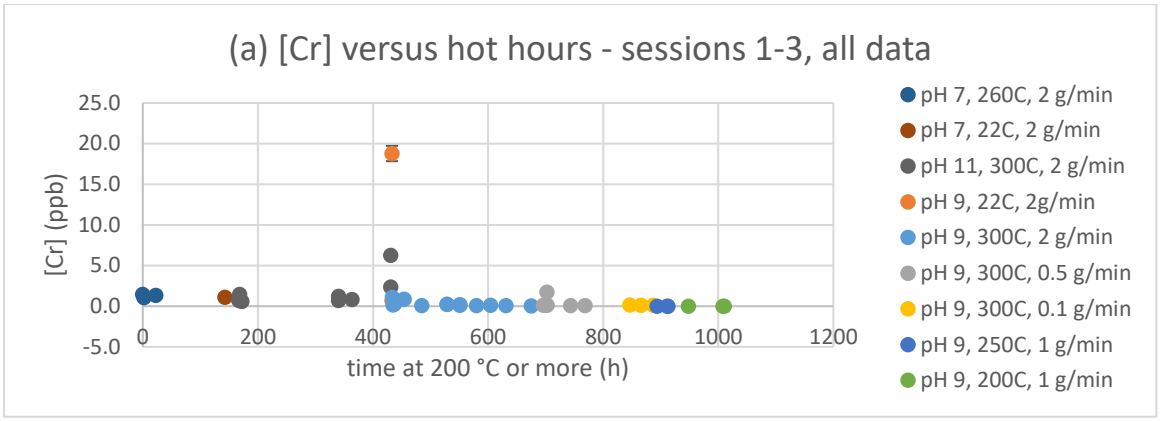

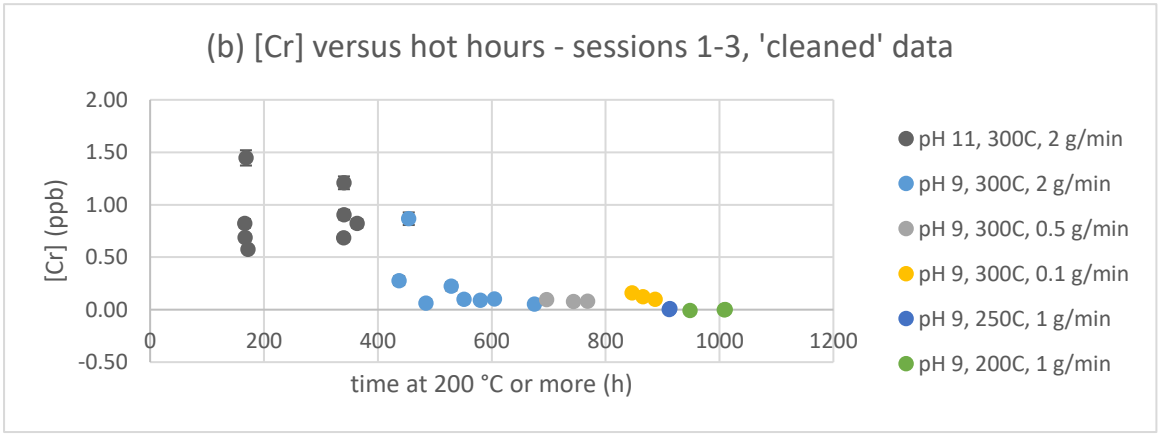

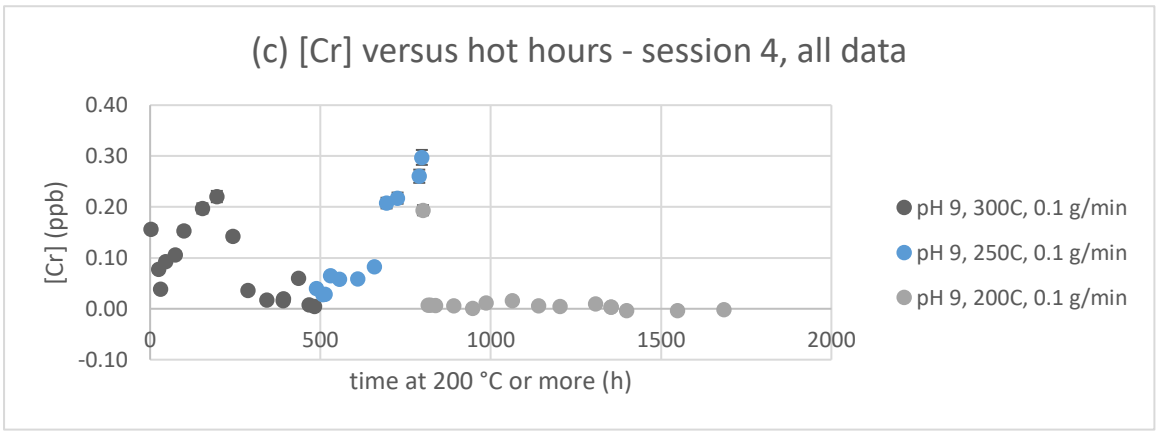

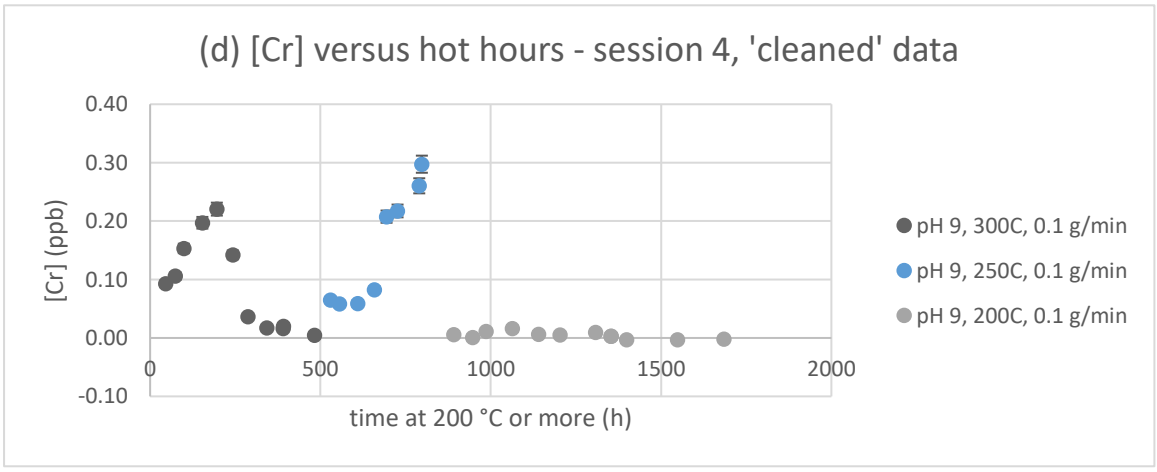

Figure 15.7. Results versus time under hydrothermal conditions for Cr, sessions 1 to 4

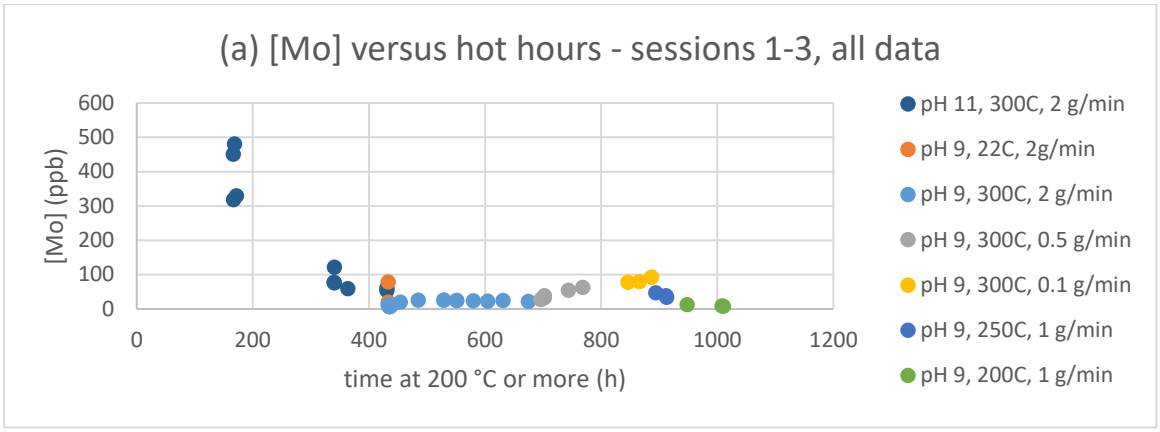

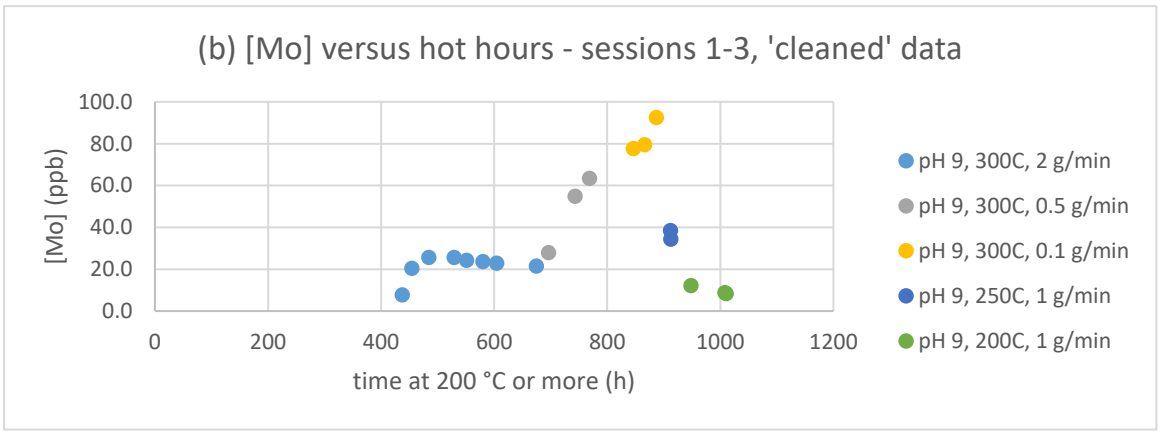

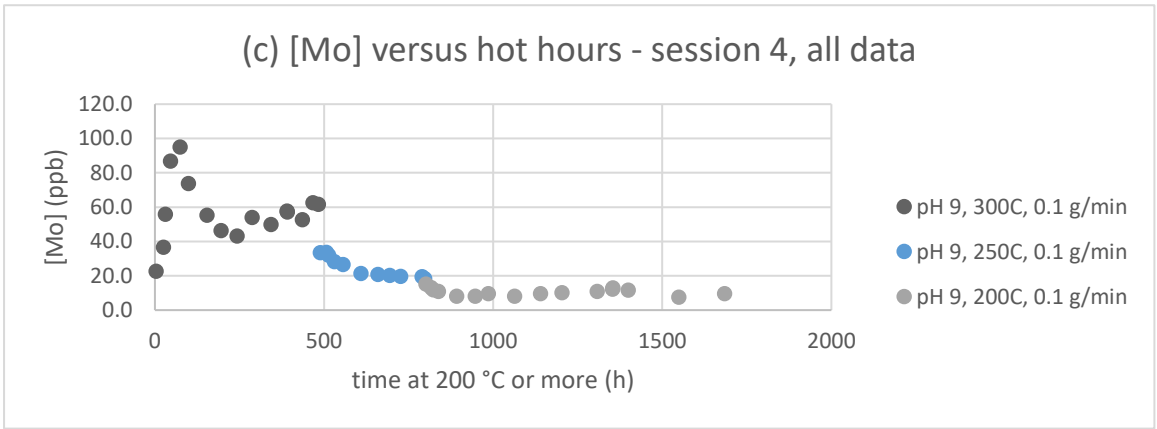

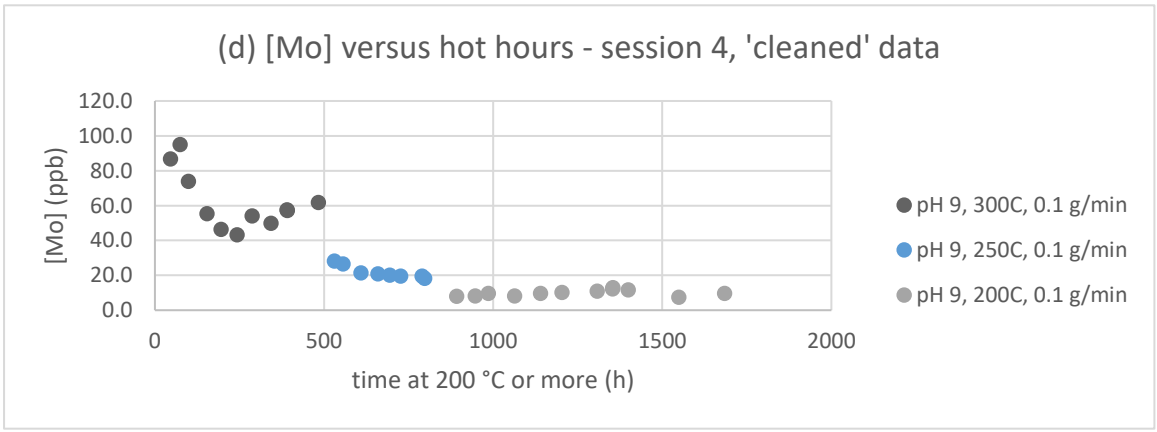

Figure 15.8. Results versus time under hydrothermal conditions for Mo, sessions 1 to 4

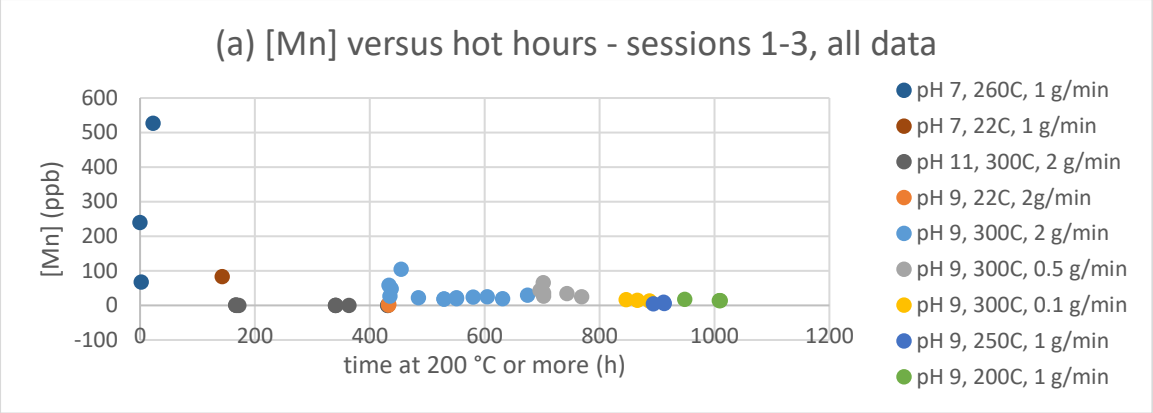

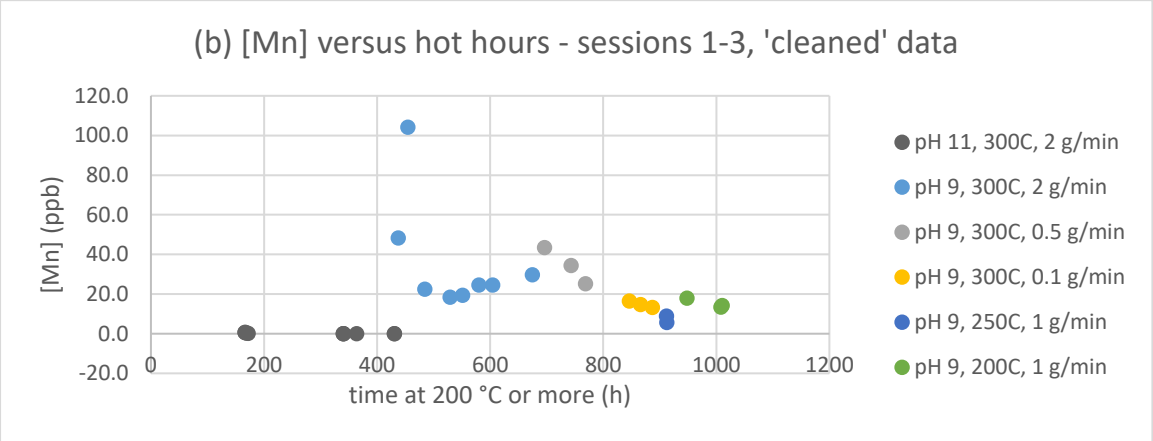

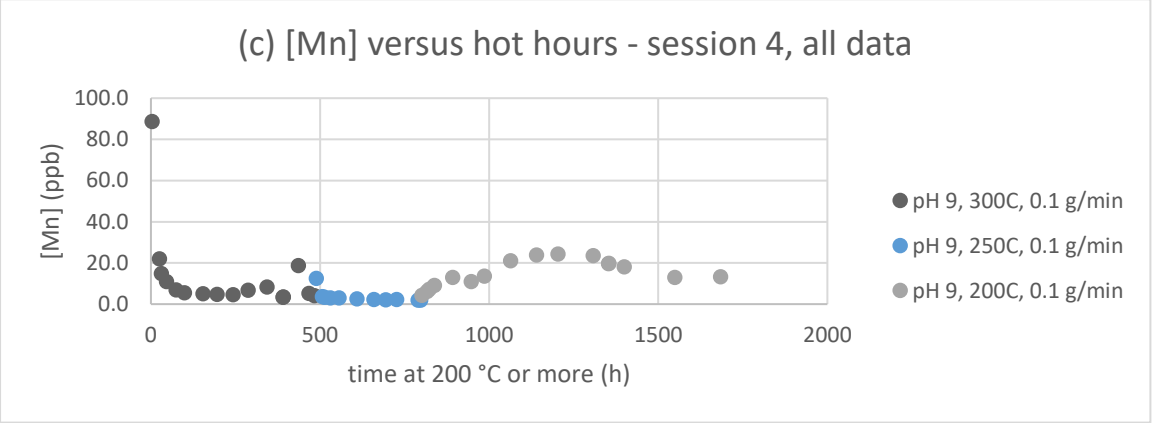

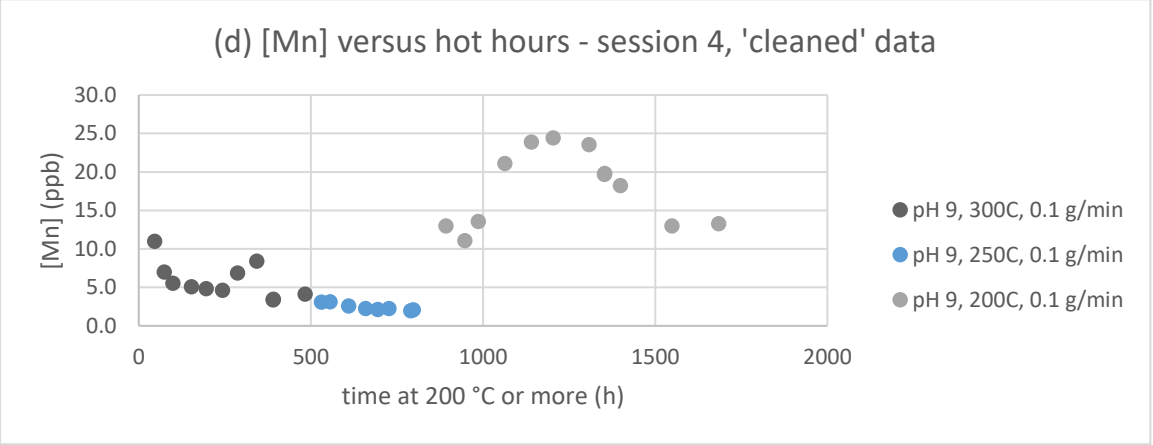

Figure 15.9. Results versus time under hydrothermal conditions for Mn, sessions 1 to 4

Iron

In Figure 15.5 we see the session 1 (pH 7) Fe results in context of their large supposed measurement uncertainty – nevertheless, the three samples taken at pH 7, 260 °C have higher [Fe] than all the data from sessions 2 and 3. pH 11 coolant provides the lowest results, though for various of those samples subtraction of blank levels may have over- or under- compensated for contamination, due to the variety of sampling methods used.

At pH 9, various flow rates were used at 300 °C, then 1 g/min was used at 250 and 200 °C. At 300 °C, the samples taken at 0.1 g/min, at around 2 ppb, had much lower results than those taken at the faster flow rates of 0.5 and 2 g/min, at around 5 ppb. This effect cannot be explained by incomplete saturation in the hot part of the rig (indeed complete saturation is expected to be easily achieved there for any flow rate below ~ 5 g/min, and therefore must be due to either one or both of the following:

(i) A higher level of Fe-based particulates carried in the flow at faster flow rates; or

(ii) partial progress, in the room temperature SS316L tubing at the back-end of the rig, towards a new equilibrium between Fe in solution in the coolant and Fe adsorbed onto or incorporated into the Cr(III) oxide film, resulting in lower levels of dissolved Fe at the slowest flow rate (0.1 g/min), where residence time is sufficient for significant progress to be made, but having little effect at the faster flow rates of 0.5 to 2 g/min.

Note that the presence of Cr(III) oxide phase at the back end of the rig (and the lack of access to an Fe-based oxide) is a requirement for scenario (ii), and results in dissolved [Fe] levels being controlled by equilibrium with Fe impurity levels in the Cr(III) oxide (rather than Fe oxide solubility which would cause *higher* Fe levels at the 0.1 g/min flow rate). As such, the resulting concentration of dissolved Fe in solution would not be well controlled as in the case of solubility, but dependent on levels of Fe in the Cr(III) oxide. Scenario (ii) would require an activity of Fe in the Cr(III) oxide film that is lower than that of Fe in the coolant, which in turn is lower than that of Fe in a saturated solution (with respect to the stable Fe-based solid phase at room temperature, hematite), which in turn is lower than the activity of Fe in the underlying stainless steel alloy.

Nickel

In Figure 15.6, outliers at 150 ppb and 40 ppb can be clearly seen. Data at pH 11 are seen to be sporadic, possibly due to the mix of sampling techniques. At pH 9 during sessions 3 and 4, levels can be seen to rise to a peak then fall again over the course of days and weeks, following a definite trend over time. It is not clear to what extent this behaviour is affected by the temperature of the oven (200, 250, or 300 °C), if at all.

At pH 9, for a hydrogen concentration of 10-3 atm at 25 °C, and below, NiO solubility rises from 0.4 ppb to 3.3 ppb as temperature is decreased from 300 to 200 °C. NiO solubility would be expected to form an upper limit of high temperature Ni levels, which may be much lower from non-stoichiometric nickel ferrite. Levels higher than this are presumably due to particulates, either directly or through ionic release from particulates deposited in the sampling line. Solubility of [Ni] in the sampling line from the most stable solid phase at room temperature is highly dependent on hydrogen concentration, being 0.005 ppb, from Ni, at log $\{H_2\}_{25C}$ = 0; 4.6 ppb, from Ni, at log $\{H_2\}_{25C}$ = -3; and 27 ppb, from $Ni(OH)_2$, at log $\{H_2\}_{25C}$ = -6. Solubility from oxide particulates transported from the high temperature part of the rig high may be higher.

Chromium

For Cr, Figure 15.7, it can be seen that there were some outliers, at 20 ppb and 6 ppb. As with Ni, there was a clear trend of levels building to a peak over a period of days and then tailing off again. Again, there was perhaps no clear trend effect of temperature, although during session 4 the sudden transition from rising Cr levels back to the baseline levels of ~ 0.01 ppb co-incided exactly with the transition from 250 °C to 200 °C. At pH 11, levels were consistently high at around 0.5 - 1.5 ppb. This may be due to oxidising conditions in the sampling line when left stagnant between taking samples.

At pH 9, levels had a baseline of ~0.01 ppb as expected, building to peaks of around 0.2 to 0.3 ppb during session 4.

Molybdenum

For Mo, Figure 15.8, in contrast with other elements, there was never an outlier observed in the midst of much lower readings taken at a similar time. However, levels at the start of session 2, pH 11, were extremely high compared with other elements, up to 500 ppb. On changing to pH 9, levels were initially low, then built to ~ 25 ppb before falling slightly.

This can be understood in terms of a strong dependence of Mo solubility on pH, being greater at high pH. If it is assumed that solubility from corrosion film is low at pH 7 (where Mo data were not taken), then a significant proportion of the Mo in corrosion release flux would have been retained in the corrosion film. Under the high solubility at pH 11, one would expect Mo which built up under prior conditions to release to solution at high concentrations initially, before tailing off to lower levels as was observed (due to approaching a steady state between supply of Mo to the corrosion film from corrosion release flux, and release of Mo to solution). At the lower solubility prevailing at pH 9, results at the beginning of session 3 can be explained by the opposite effect: A Mo-depleted corrosion film, due to prior conditions, initially releases Mo to low levels, until a steady state is

established between Mo ions supplied to the film by corrosion release flux and those released from the corrosion film to the coolant.

Approaching a new steady state can also be used to explain the delayed progress towards higher levels on decreasing flow rate, and then lower levels on speeding the flow up again.

Data from session 4 suggest a lower solubility of Mo from corrosion film at lower temperatures.

Manganese

Levels of Mn, Figure 15.9, were very high in a few samples, one sample was over 500 ppb at pH 7, and two samples were around 100 ppb at pH 9. These samples were all taken fairly soon after a change in conditions and disturbance to the flow. In contrast with Mo, the very highest levels were observed at pH 7 and the very lowest at pH 11, suggesting the opposite dependence of solubility on pH. Although levels at 250 °C, session 4 continued in the same trend as under the prior conditions of 300 °C, levels were much higher at 200 °C, suggesting the opposite dependence of solubility on temperature compared with Mo.

15.4. Variability of Results

Since the results have shown trends over time, they do not represent a static quantity, such as equilibrium solubility under a fixed set of conditions. Therefore, it is difficult to ascertain how much of the variability is due to genuine changes in the rig over time, how much is due to statistical scatter introduced by the rig, and how much is due to statistical scatter introduced by the sampling process.

A few samples were selected to give an indication of the variability of results, or the repeatability of the experiments, and were intended to give some insight into the source of these variances.

15.4.1. Variance due to the ICP-MS instrument

Typical standard error due to the ICP-MS instrument is known to be around 5% [193], though this increases for low concentrations as the detection limit of the instrument is approached.

One sample taken from the rig was divided into two samples at the time of sampling: JH-03-08 and JH-03-08-dupl. For each element analysed, Table 15.27 and Table 15.28 compare the difference in the raw values (i.e., before adjusting for dilution and mean blank levels) of levels measured in the two duplicate samples, against the expected standard error. For Fe for example, the difference between levels of two samples would be expected to follow a distribution given by 0.00 +/- 0.78 ppb. The measured size of this difference was 0.18 ppb, or 44% of one sigma, which is consistent with expectations. The equivalent ratio for Mo and Mn was only 1% and 3% respectively. Although not a meaningful result on its own, this confirmed other observations that levels of Mo and Mn were much more consistent from one sample to the next than the other elements, in relative terms. Therefore, a revised estimate of error, of 0.5%, was used in this thesis, for example when plotting results with error bars.

Table 15.27. Comparison of variances.
Errors are combined by adding in quadrature.

Sample	[Fe]	σ (5%, sample)	σ (due to blanks)	σ (combined)
JH-03-08	5.70	0.29	0.47	0.55
JH-03-08-dupl	5.88	0.29	0.47	0.55
difference	0.18	0.41	0.66	0.78

Table 15.28. Difference in raw results (JH-03-08 vs JH-03-08-dupl), compared with that expected by 5% error; error in samples; and combined error.
Errors are combined by adding in quadrature.

Quantity	[Fe]	[Ni]	[Cr]	[Mo]	[Mn]	[Ti]	[Co]
JH-03-08 (RAW)	5.70	2.42	0.226	20.36	14.67	0.155	0.155
JH-03-08-dupl (RAW)	5.88	2.27	0.245	20.34	14.64	0.160	0.139
difference	0.18	0.15	0.019	0.02	0.03	0.005	0.016
σ_{diff} (5%, samples)	0.41	0.17	0.017	1.44	1.04	0.011	0.010
σ_{diff} (due to blanks)	0.66	0.07	0.042	0.04	0.15	0.182	0.042
σ_{diff} (combined)	0.78	0.18	0.046	1.44	1.05	0.182	0.043
Diff / σ_{diff}(5%,samples)	44%	88%	112%	1%	3%	45%	160%
Diff / σ_{diff}(combined)	23%	83%	41%	1%	3%	3%	37%
Consistent with 5% model?	Yes	Yes	Yes	No	No	Yes	Yes
Revised estimate of error	-	-	-	0.5%	0.5%	-	-

Levels from samples taken from the corrosion rate rig showed remarkable self-consistency. Two of these are compared in Table 15.29. This confirms the choice of measurement error on all elements except Mn, assuming that both samples had identical levels of each element. If the revised measurement error on Mn, of 0.5%, is correct, then this shows that the difference in levels between the two samples, though small, is statistically significant.

These calculations were performed to give indicative values of measurement error, on the understanding that rigorous statistical assessments cannot be made on just two pairs of samples.

Table 15.29. Difference in raw results (JH-corr-01-02 vs JH-corr-01-04), compared with that expected by 5% error; error in samples; and combined error.
Errors are combined by adding in quadrature.

Quantity	[Fe]	[Ni]	[Cr]	[Mo]	[Mn]
C2-s1-dir (RAW)	2.63	.154	.0242	12.08	.347
C2-s1-dump (RAW)	2.69	.170	.0178	12.09	.309
Difference	0.06	.016	.0064	0.01	.038
σ_{diff} (5%, samples)	0.19	.011	.0015	0.85	.023
σ_{diff} (due to blanks)	0.42	.054	.0096	0.01	.064
σ_{diff} (combined)	0.46	.055	.0097	0.85	.068
Diff / σ_{diff}(5%,samples)	32%	145%	427%	1%	165%
Diff / σ_{diff}(combined)	13%	29%	66%	1%	56%
Consistent with 5% model?	Yes	Yes	Yes	No	Yes *
Revised estimate of error	-	-	-	0.5%	-

* Also remains consistent with 0.5% model proposed earlier – overall standard error is dominated by the error on the blanks in either case.

16. Appendix 3:

Model to describe gases within sampling cell

16.1. Overview

In order to measure dissolved hydrogen concentration in the oxide solubility rig, sealed samples of rig effluent were taken in a sampling cell. These were analysed for hydrogen content of gases released on opening the cell, as described in section 7.6.

A model was developed to predict the transfer of hydrogen and nitrogen gases between the aqueous and gaseous phases within the cell, and the build-up of pressure, as the cell filled with effluent.

Note – when pressure of the cell is measured, can pretend we are measuring nitrogen pressure, any effect of hydrogen on total pressure will not be discernible.

Note – for water flow I've used the variable "f_water", but I also considered using "flow_water", or just "f".

16.2. Variables and parameters of the model

V_cell	volume of the cell (cm^3)
f_water	volume flow rate of effluent entering the cell (ml/min)
sol_N2	solubility of nitrogen in water (scc/ml/bar):– amount of nitrogen (scc) dissolved in each ml of water per bara of partial pressure of nitrogen in the gas phase
P_feedwater	Pressure of feedwater, maintained by nitrogen cover gas (bara)
H2_effluent	hydrogen concentration in effluent from rig (scc/ml)
t	time since filling commenced (min)
V_water (t) †	time varying volume of water within the cell (ml)
F (t) †	time varying fill ratio (unit-less) F (t) = V_water (t) / V_cell

P (t) † time varying partial pressure of nitrogen (bara)

N2_tot (t) † time varying total amount of nitrogen within cell (scc)

N2_aq (t) † time varying amount of nitrogen in the aqueous phase within cell (scc)

N2_gas (t) † time varying amount of nitrogen in the gas phase within cell (scc)

N2_prompt (t)† time varying amount of nitrogen in the gas phase within cell, which would release promptly from the cell on equilibrating with a pressure of 1 bara (scc)

N2_prompt (t) = N2_gas (t) . (P(t) – 1) / P(t)

N2_frac (t) † time varying faction of total nitrogen which is in the gaseous phase

N2_frac (t) = N2_gas (t) / N2_tot (t)

† Parameter names ending with " (t)" represent equilibrium values of time varying quantities during filling. Where the t is dropped, values of the same quantities on completion of sample acquisition are represented.

Note – to differentiate between different quantities/measures, volume in general is measured in cm^3, quantities of gas are measured in scc, and quantities of water are given in ml (though 1 ml is identical in magnitude to 1 cm^3).

16.3. The model

16.3.1. Assumptions

In the model it has been assumed that equilibrium is obtained instantaneously at each instant in time as the cell fills. The implications of finite kinetics have been considered in terms of how observations would differ from those predicted by the model.

Differences between atmospheric pressure and 1 bara are neglected. It is assumed that the cell is initially filled with 1 bara nitrogen gas, and slowly fills with effluent from the rig. Quantities of hydrogen are assumed to be sufficiently low that hydrogen partial pressure has no observable impact on overall pressure (determined solely from nitrogen partial pressure). Dissolved nitrogen is present in the coolant at levels controlled by the equilibrium of feedwater with a 1.7 bara nitrogen cover gas, namely 0.025 scc/ml.

16.3.2. Values of parameters

On each occasion that effluent samples were taken for hydrogen measurement, the flow rate was 0.1 g/min, and pressure in the feedwater barrel was 1.7 bara.

f_water	0.1 g/min
sol_N2	0.015 scc/ml/bar
sol_H2	0.018 scc/bar/ml
P_feedwater	1.7 bara
N2_effluent	1.7 x 0.015 = 0.025 scc/ml
H2_effluent	[values as measured were input, to check for any effect on results]
V_cell	51.5 cm^3

16.3.3. Fill ratio as master variable, and simple expressions to track total hydrogen and nitrogen quantities

The fill ratio, F (t), can be treated as the master variable as the cell fills. F(t) is defined in terms of other variables as follows:

$$F(t) = \frac{V_{water}(t)}{V_{cell}} = \frac{f_{water} * t}{V_{cell}} = \frac{0.1t}{V_{cell}}$$

From F (t), time varying quantities of nitrogen gas and hydrogen gas are given by:

$$N2_{tot}(t) = V_{cell}(1 + 0.025.F(t))$$
$$H2_{tot}(t) = V_{cell}.F(t).H2_{effluent}$$

16.3.4. Expressing pressure as a function of fill ratio

The following method is used to express the equilibrium pressure of the cell, in terms of fill ratio, and time invariant parameters, only. It is assumed that the small amounts of hydrogen present do not materially affect overall pressure.

1. The total amount of nitrogen in the cell is related to cell pressure, $P(t)$, and fill fraction, $F(t)$, by summing contributions from the two phases, and using the relations $V_{water} = F(t).V_{cell}$ and $V_{gas} = (1 - F(t)).V_{cell}$. The parameter sol_{N2} is replaced by its numerical value.

$$N2_{gas}(t) = \quad P(t).V_{gas}(t) \quad = P(t).(1 - F(t)).V_{cell}$$
$$N2_{aq}(t) \; = P(t).sol_{N2}.V_{water}(t) = P(t).0.015.F(t).V_{cell}$$
$$N2_{tot}(t) = \; P(t).V_{cell}.\big((1 - F) + 0.015.F\big) = P(t).V_{cell}.(1 - 0.985.F(t))$$

2. The relation for $N2_{tot}(t)$ thus obtained is equated with the simple equation for the same quantity derived earlier, and re-arranged to give an expression for P(t) in terms of F(t) (and time invariant parameters) only:

$$P(t).V_{cell}.(1 - 0.985.F(t)) = V_{cell}(1 + 0.025.F(t))$$
$$\Rightarrow P(t) = \frac{1 + 0.025.F(t)}{1 - 0.985.F(t)}$$

In this way, if one knows the value of just one of the two key variables – $F(t)$ and $P(t)$ – one can uniquely determine the value of the other one (the function above has one-to-one correspondence for F(t) between 0 and 1), and also the quantities of nitrogen in each phase: $N2_{aq}(t)$; and $N2_{gas}(t)$.

16.3.5. Accounting for hydrogen gas

By analogy with the calculations performed for nitrogen gas, quantities of hydrogen in the two phases and in total can be expressed in terms of hydrogen partial pressure as follows:

$$H2_{gas}(t) = \quad P_{H2}(t).\big(1 - F(t)\big).V_{cell}$$
$$H2_{aq}(t) = \quad P_{H2}(t).sol_{H2}.F(t).V_{cell}$$
$$H2_{tot}(t) = \quad P_{H2}(t).V_{cell}.\big(1 - 0.982.F(t)\big),$$

and the relation for $H2_{tot}(t)$ thus obtained is equated with the relation derived earlier to give an expression of $P_{H2}(t)$ in terms of $F(t)$ and time-invariant parameters only:

$$P_{H2}(t).V_{cell}.\big(1 - 0.982.F(t)\big) = \; V_{cell}.F(t).H2_{effluent}$$

$$\Rightarrow P_{H2}(t) = \frac{F(t).H2_{effluent}}{1 - 0.982.F(t)}.$$

16.3.6. Useful outputs from the model

The model was developed for several purposes.

1. To provide relationships between pressure, fill ratio, and time
    a. So that the **rapidity of pressurisation** as the cell fills up could be anticipated

b. So that online monitoring of cell pressure could be used as an **indication of fill ratio**

2. To estimate quantities of each gas (scc) in aqueous phase and gas phase as the cell fills, and derived values such as fraction in the gaseous phase, and quantities of each gas which would be released 'promptly' (i.e. H2_prompt and N2_prompt) on pressure equilibration to 1 bara.
    a. So that the **optimum fill ratio** (or pressure) could be determined in order to maximise the volume of gas (or hydrogen part thereof) released promptly to the MS
    b. So that ratio of hydrogen to nitrogen measured in the MS could be used to estimate
        i. Volumes of each gas released to MS (or balloon for sample "0")
        ii. Concentration of dissolved hydrogen in rig effluent at time of sampling

Points 1. a and b can be addressed by a plot of P versus F. See fig A1.1. It should be borne in mind, however, that the model assumes equilibrium at all times. Compression of the gas phase, caused by increasing water volume, results in increasing pressure which is mitigated by transfer of some of the nitrogen from gas to water phase (i.e. dissolution). Finite kinetics of dissolution mean that in reality the pressure at any fill ratio may be greater than predicted by the model whilst the cell is still filling, but will settle over time to the equilibrium value predicted by the model once filling ceases. This is especially true as the gas volume in the cell starts to diminish, at a fill ratio of around 0.8 to 0.9 and above. At a fill ratio of 1, the indicated pressure of 70 bara represents partial pressure of nitrogen – the actual (hydrostatic) pressure would in this situation rapidly rise to that of the BPR (back-pressure regulator), ~100 bara, preventing any further filling of the cell (the rig was protected by a maximum pressure cut-off on the pump, and a burst disc!), because of the relative incompressibility of water.

In order to address point 2.a, further quantities – derived from those already obtained – are required, namely:

$$N2_{prompt}(t) = N2_{gas}(t).\frac{P(t)-1}{P(t)};$$

$$H2_{prompt}(t) = H2_{gas}(t).\frac{P(t)-1}{P(t)}$$

In figures A1.2 and A1.3 these are plotted along with related quantities – total amounts of each gas in the cell overall; and in the gas phase – as a function of fill ratio. A value for $H2_{effluent}$ of 9.1 x 10^{-4} scc/ml was assumed, in order that the plot for hydrogen could be expressed in terms of numerical values. For different values of $H2_{effluent}$ the form of the plot remains unchanged, aside from having a different scale on the y axis. It can be seen from the plots that the expected quantity of hydrogen released promptly peaks at a fill ratio around F = 0.9 to 0.925, and at a similar but

slightly lower value of F for nitrogen. A fill ratio of F = 0.9 to 0.925 is therefore deemed to be the optimum fill ratio to maximise the quantity of hydrogen available for measurement in the MS.

Point 2.b.i is answered for nitrogen by values of $N2_{prompt}$ as plotted in Figure A1.2. In order to estimate the volume of hydrogen released, the ratio of hydrogen to nitrogen measured in the MS is multiplied by $N2_{prompt}$.

To answer Point 2.b.ii, differences in the solubility of hydrogen and nitrogen must be addressed as the presence of the gases in the aqueous phase must be accounted for. The total amounts of hydrogen and nitrogen in the cell are given from measured amounts by:

$$H2_{tot} = \frac{H2_{prompt}}{H2_{frac}} . \frac{P}{P-1} \; ; \quad and \quad N2_{tot} = \frac{N2_{prompt}}{N2_{frac}} . \frac{P}{P-1}$$

$$H2_{frac} = \frac{H2_{gas}}{H2_{tot}} = \frac{1-F(t)}{1-(1-sol_{H2}).F(t)} = \frac{1-F(t)}{1-0.982.F(t)}$$

$$N2_{frac} = \frac{N2_{gas}}{N2_{tot}} = \frac{1-F(t)}{1-(1-sol_{N2}).F(t)} = \frac{1-F(t)}{1-0.985.F(t)}$$

The ratio of $2_{tot} : N2_{tot}$ is thus related to measured ratio, $H2_{prompt} : N2_{prompt}$, by:

$$\frac{H2_{tot}}{N2_{tot}} = \frac{H2_{prompt}}{N2_{prompt}} . \frac{N2_{frac}}{H2_{frac}}$$

In this way, the measured ratio of hydrogen to nitrogen can be multiplied by a 'ratio modifier' to give the ratio of total hydrogen to total nitrogen in the cell; multiplied by total nitrogen content of the cell to give total hydrogen content; and divided by the volume of water in the cell to give dissolved hydrogen concentration in the rig effluent at the time of sampling:

$$H2_{effluent} = \frac{H2_{tot}}{N2_{tot}} . \frac{N2_{tot}}{V_{water}} = \left(\frac{H2_{prompt}}{N2_{prompt}}\right)_{MS} . \left(\frac{N2_{frac}}{H2_{frac}}\right) . \left(\frac{N2_{tot}}{V_{water}}\right)$$

The first term in parentheses represents hydrogen to nitrogen ratio measured in the mass spectrometer (hence the subscript 'MS'); the second term in parentheses is a 'ratio modifier', accounting for slightly greater tendency for hydrogen to reside in the aqueous phase compared with nitrogen – its value is close to 1; the third term in parentheses enables the conversion from hydrogen to nitrogen ratio into effluent dissolved hydrogen concentration – its value is also close to 1 for the fill ratios employed in this study.

Values of $N2_{frac}$ and $H2_{frac}$ are plotted against F in fig A1.4, and their ratio is plotted against F in fig A1.5. The ratio $\frac{N2_{tot}}{V_{water}}$ is plotted against F in fig A1.6.

The product of $\left(\frac{N2_{frac}}{H2_{frac}}\right)$ and $\left(\frac{N2_{tot}}{V_{water}}\right)$ is plotted against F in fig A1.7. This shows that the value of the measured ratio of hydrogen to nitrogen in the MS is close to the value of hydrogen concentration in scc/ml, $H2_{frac}$, according to the model, for values of F around 0.9 to 0.95 as used in this study.

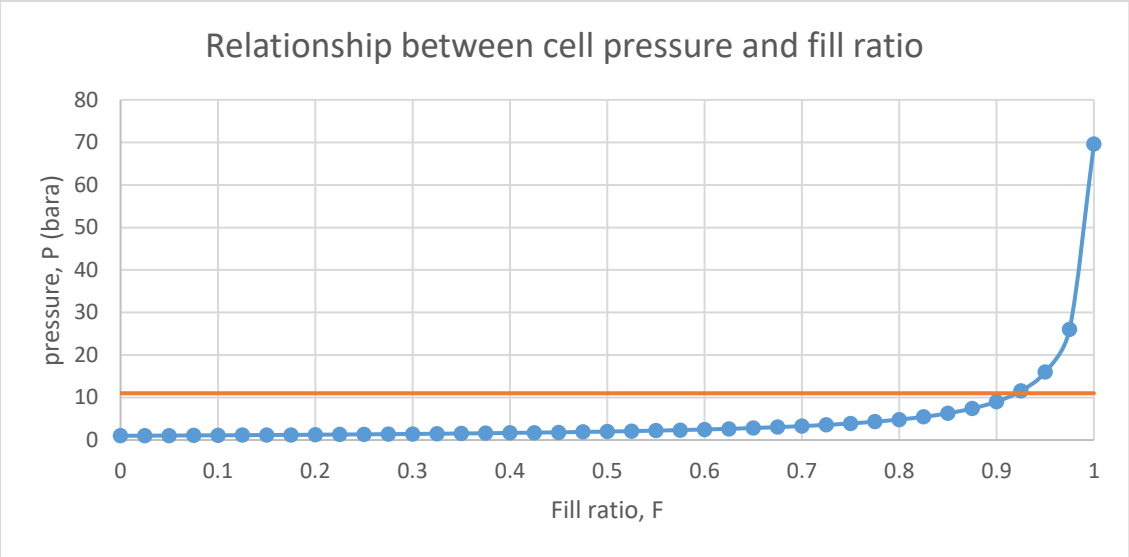

Figure 16.1. Relationship between P (pressure) and F (fill ratio).
The orange line shows the approximate pressure to which the cell settled after a few days of filling, after it was allowed to reach equilibrium via dissolution of gas into under-saturated aqueous phase

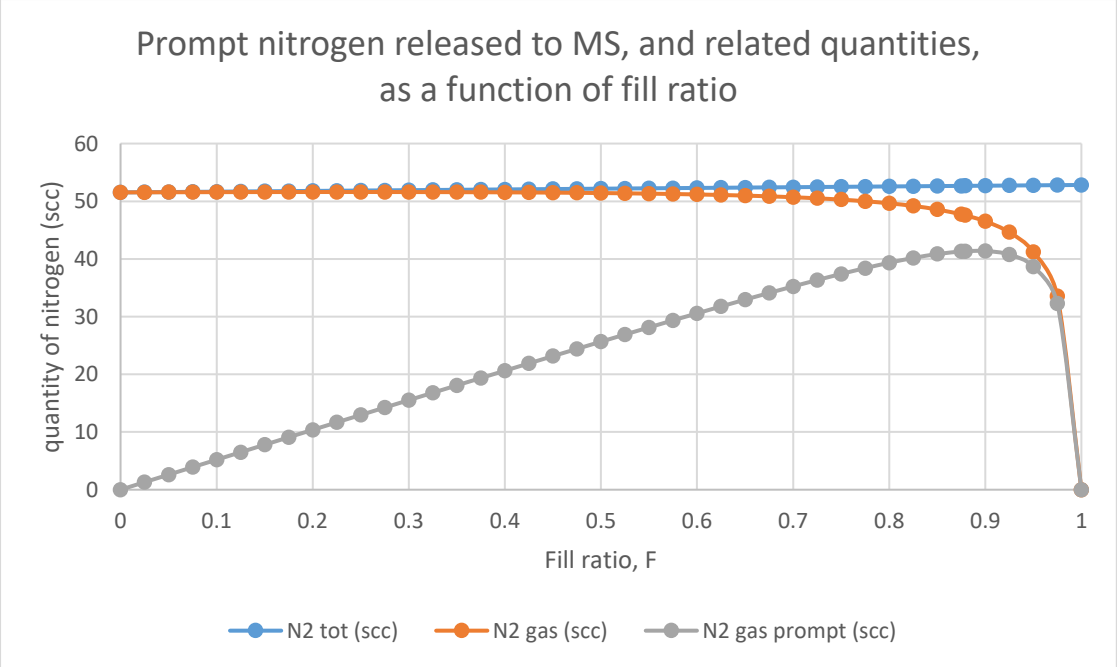

Figure 16.2. Changes to total quantity of nitrogen in the cell, and equilibrium values of total and 'prompt' quantities of nitrogen in the gas phase as fill ratio, F, varies from 0 to 1.

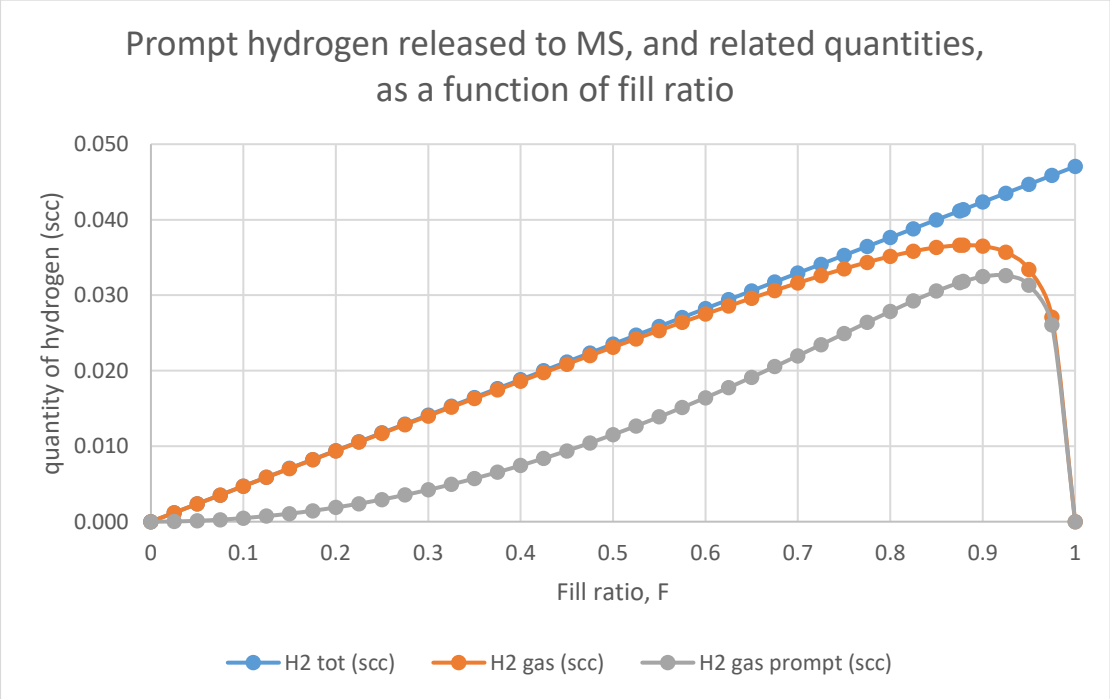

Figure 16.3. Changes to total quantity of hydrogen in the cell, and equilibrium values of total and 'prompt' quantities of nitrogen in the gas phase as fill ratio, F, varies from 0 to 1.

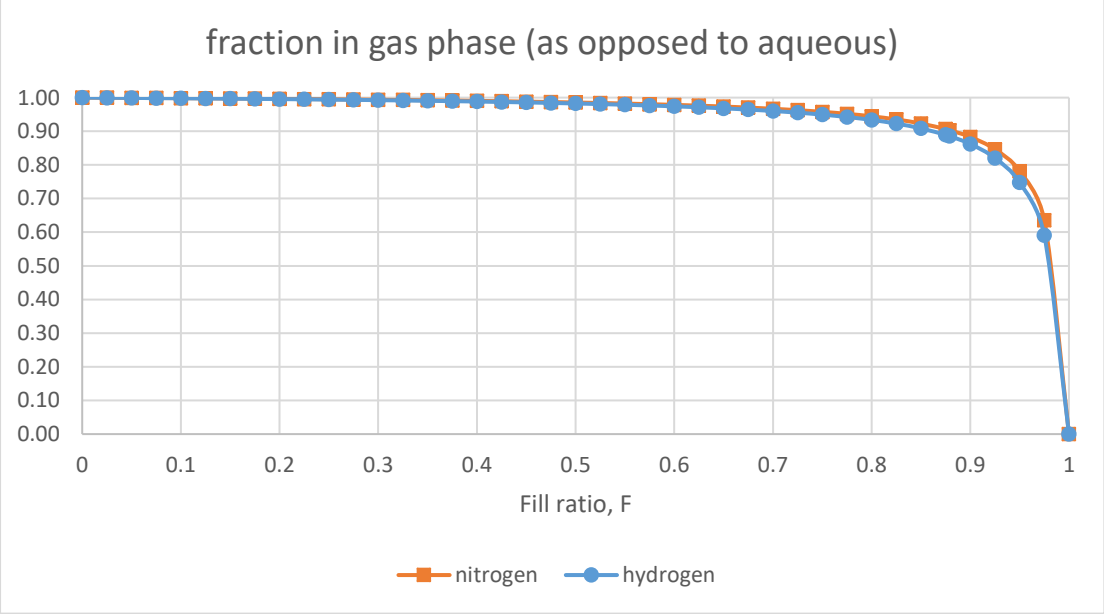

Figure 16.4. Fraction of each gas residing in the gas phase, $N2_{frac}$ and $H2_{frac}$, as fill ratio, F, varies from 0 to 1.
As can be seen, the fraction of gas residing in aqueous phase becomes appreciable only for fill ratio above about 0.9.

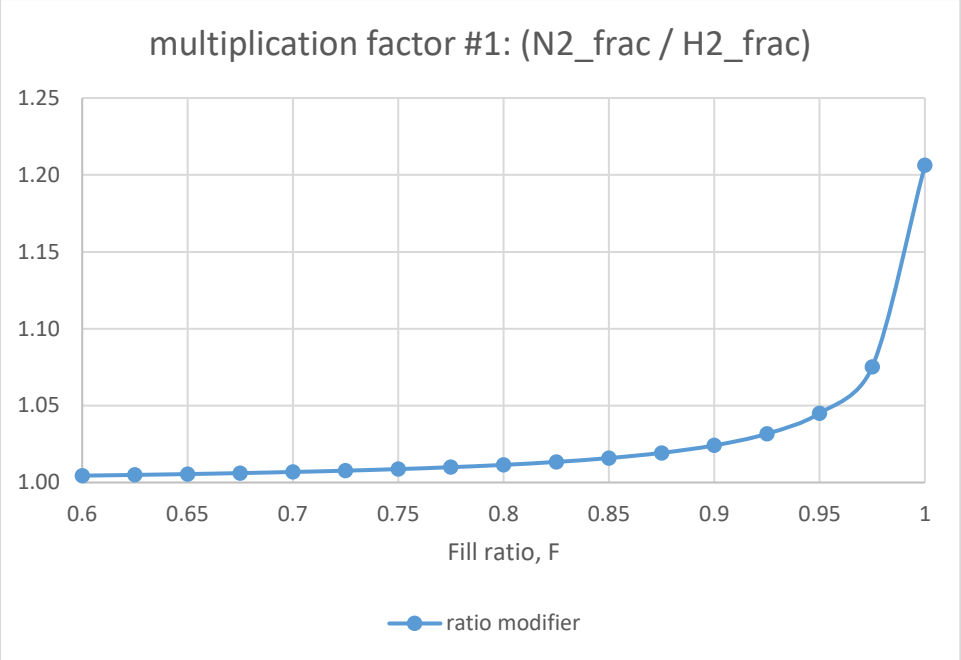

Figure 16.5. Plot of the ratio $\frac{N2_{frac}}{H2_{frac}}$, for F between 0.6 and 1, as calculated by model.

The ratio of hydrogen to nitrogen measured by the MS (as released from the gas phase) is multiplied by this factor to yield an estimate of the ratio of total quantities of hydrogen and nitrogen in the cell (which includes aqueous phase). Values are greater than 1, reflecting the slightly greater solubility of hydrogen compared with nitrogen.

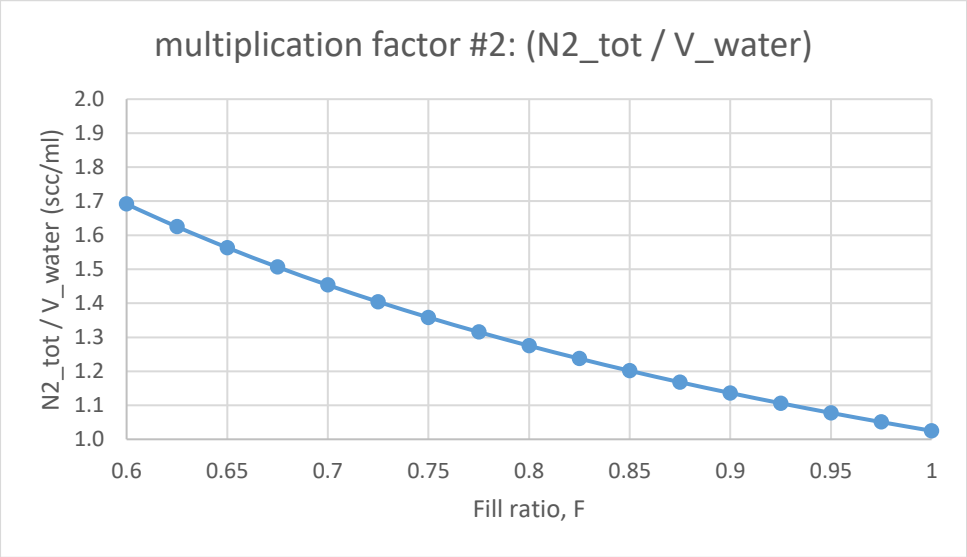

Figure 16.6. Plot of the ratio $\frac{N2_{tot}}{V_{water}}$, for F between 0.6 and 1, as calculated by model.

Ratio of total amounts of the two gases, H_2/N_2, is multiplied by this factor to give an estimate of hydrogen concentration of effluent as it exits from the rig.

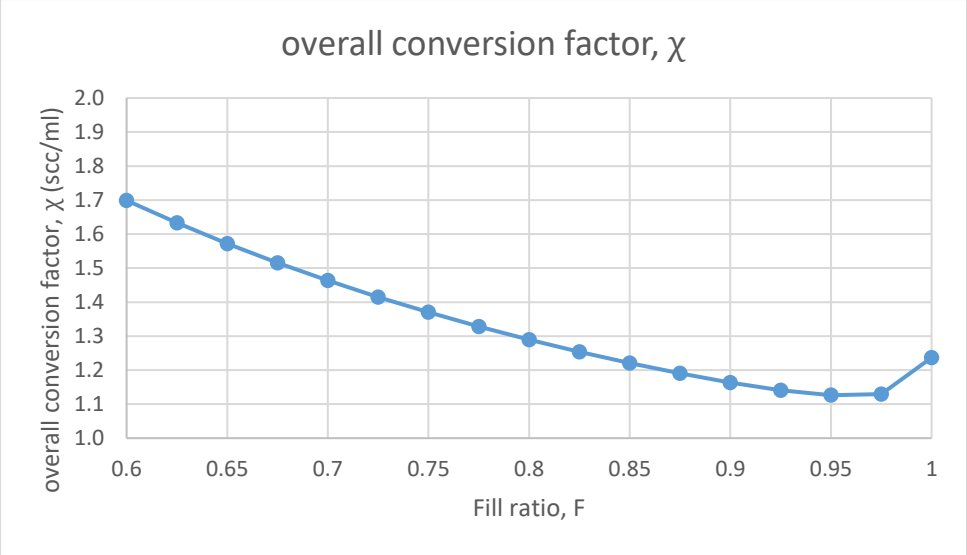

Figure 16.7. Plot of the overall conversion factor, χ, for F between 0.6 and 1, as calculated by model. This is simply the product of the two multiplication factors given in Figure 16.5 and Figure 16.6. The ratio of hydrogen to nitrogen as measured in the MS is multiplied by χ to give an estimate of hydrogen concentration in rig effluent.

16.4. Limitations of the model

The model does not take into account the finite kinetics of dissolution, therefore the pressure during filling is expected to be higher than the steady state value predicted by the model, to which it decays over time once filling is ceased. This effect was indeed observed as pressure fell by several bar over the course of a few hours after filling ceased.

16.5. Measurement of gas volume released from preliminary sample, to verify model

The model was not developed until after samples 1 and 2 had been analysed. From sample 2, accurate recording of the filling time and multiple readings of pressure during and after filling enabled an accurate determination of the fill ratio to be made, which allowed total volume of the cell to be accurately estimated. The cell volume thus obtained was used as a fixed parameter in the model. The water volume and pressure (and thus also fill ratio and cell volume) recorded for the preliminary sample were very similar to those recorded for sample 2. The measured volume of gas from the preliminary sample was identical to that predicted by the model, within error, thus providing verification of the model. Gas volume was measured by releasing gas from the cell into a latex balloon. After filling, the balloon was sealed by tying a knot in the end, and fully submersed in a

beaker of water by pressing down using several thin rods of negligible volume, so that water overflowed from the sides of the beaker. The mass of water displaced by gases within the balloon (i.e. excluding the mass displaced by volume of the latex of the balloon itself) was determined by weighing the beaker on a mass balance after water displacement by the balloon, and comparing with the mass obtained in like manner using the empty balloon. In each case the outside of the beaker was dried with paper towel before weighing. Finally, mass of displaced water was converted to volume using the ratio 1 g = 1 ml.

Sample 1 recorded higher pressure from less filling time compared with the other two samples. The reason for this is unknown. It could be due to a greater proportion of water already present in the tubing leading up to the cell. If the total cell volume as calculated for sample 2 is assumed, then the fill ratio is 0.88. If pressure readings are taken to be consistent with those for sample 2 (a difference of only 0.8 bar immediately on fill completion) then the fill ratio can be assumed to be 0.91. As an upper bound, if it is assumed that pressure did not fall off over time for sample 1 a fill ratio of 0.95 could be assumed. Even across this full range, the value of the ratio modifier – which is ultimately the key output from the model which affects the estimate of hydrogen concentration –varies only little, from 1.19 to 1.13 scc/ml. Therefore the model is relatively insensitive to error in pressure readings or the fill ratio determined. [187].

A table of key information is provided in Table 16.1

Table 16.1. Table of key information

Sample #	Time to fill	Pressure when first filled	Subsequent readings (time since sample taken)	Other information according to model	
Sample "0"	469 min	15.8 bara immediately	N2_prompt gas volume measured (26d) 43 +/- 2 scc *	V_liquid = 47 cc Fill fraction, F, = 0.91 ⇒ V_gas = 5 cc ⇒ V_tot = 52 cc N2_tot = 54 scc N2_gas = 47 scc N2_prompt = 42 scc	
Sample 1	452 min	15.8 bara immediately	Mass spec (0.75d)	V_liquid = 45 cc Fill fraction, F, = 0.88 ⇒ V_gas = 6 cc ⇒ V_tot = 52 cc N2_tot = 53 scc N2_gas = 48 scc N2_prompt = 42 scc H2_prompt =	Ratio: 5.3E-5 revision: 1.15 x DH: 6.1E-5 scc/ml Log H_2 = –2.46
Sample 2	470 min	15.2 bara immediately 14.4 bara after 46 min	11.2 bara (5d) 11.2 bara (18d) 11.0 bara (113d) Mass spec (114d)	V_liquid = 47 cc Fill fraction, F, = 0.91 ⇒ V_gas = 5 cc ⇒ V_tot = 52 cc N2_tot = 54 scc N2_gas = 46 scc N2_prompt = 42 scc	Ratio: 5.5E-3 Revision 1.16 x DH: 6.4E-3 scc/ml Log H_2 = –0.44

*included a small amount of water

17. Appendix 4:

Modeling conditions and processes in the rig, to predict measurable outputs

17.1. Overview of the current appendix chapter

Four aspects of outputs from the rig were experimentally observed, measured, or characterised, as shown in Table 17.1. In each case, research literature was reviewed, and either a simplified summary of findings, or a mathematical model, were used to make predictions of anticipated results. The models were adapted where appropriate considering results as they came in: for example, where there were several different underlying processes which could explain the same results, subsequent experiments were designed to resolve the issue by choosing conditions in which the different processes were expected to give markedly different results.

The four models mentioned in Table 17.1 are treated in following sections here. The effluent hydrogen model (section 17.2.5), and the corrosion rate model on which it is built (section 17.2.3), have a simple numerical output (hydrogen concentration and corrosion film thickness respectively), whilst the other two models are perhaps more accurately collections of literature findings or data tables. In addition, a micromodel of the whole rig is presented, in which local conditions throughout the rig were considered with regards to their effect on corrosion product build-up in the coolant, and as deposited particles on rig walls.

A separate model was also developed specifically for interpreting results of hydrogen gas measurements, since a measured hydrogen to nitrogen gas ratio had to be converted to provide an estimate of hydrogen concentration in rig effluent – this is in chapter 16

Table 17.1. Experimental observations made during the project, and predictive models used to anticipate and interpret results.

Experimental aspect	Observable quantity	Model / literature sources	Results chapters
Corrosion	Corrosion film morphology	Literature (see chapter 3)	Chapter 10
	Elemental composition of each oxide layer	Literature (see chapter 3, and Table 10.1)	Chapter 10
	Thickness of oxide film	CORROSION MODEL (section 17.2.3)	Chapter 10
Hydrogen build-up in rig coolant	Effluent hydrogen concentration	EFFLUENT HYDROGEN MODEL (section 17.2)	Chapter 9
Overall corrosion product (CP) concentrations in rig coolant	Effluent corrosion product concentrations (ICP-MS)	SOLUBILITY MODEL, sect. 17.3 (Various solubility scenarios), and PARTICULATES MODEL, sect. 17.4 (Largely qualitative)	Chapter 8
CP particles in rig coolant	Direct: observation of particles on filters	SOLUBILITY MODEL, and PARTICULATES MODEL	Chapter 11
	Indirect: effect of filters on ICP-MS readings	SOLUBILITY MODEL, and PARTICULATES MODEL	Chapter 8
	Any deposits on samples from the hot part of the rig	PARTICULATES MODEL, and literature on particulate deposition and re-entrainment etc (chapter 5, 6)	Chapter 10

17.2. Model to predict effluent hydrogen levels at steady state

17.2.1. Assumptions, and applicability of model

To estimate levels of dissolved hydrogen in the rig coolant, a simple model was developed based upon the following assumptions:

1. Feed-water (coolant) was free from any dissolved oxygen and hydrogen before entering the high temperature part of the rig
2. Corrosion of the stainless steel at high temperature (≥ 200 °C) produced hydrogen gas, via reactions such as 3 Fe + 4 H_2O = Fe_3O_4 + 4 H_2, of which a fixed proportion (10%) was released to the coolant. The remainder was assumed to be retained within the steel, trapped under the protective oxide film (see section 3.2).
3. There was no leakage of hydrogen gas from the coolant.
4. Sufficient time had been allowed at the current conditions for a steady state to be reached in terms of hydrogen concentration in the rig effluent.

The model predicts average hydrogen concentration in rig effluent, at steady state, as this was the only quantity which could be verified by physical measurements. Within the rig, local concentrations of hydrogen may be expected to have varied with lateral position in the tubing (being higher closer to the corroding surfaces) and longitudinal position (building steadily from zero to the level present in effluent, on progressing through the rig), to an extent which depended on factors such as the degree of hydrogen diffusion occurring, and whether there were any deviations from normal Hagen-Poiseuille flow. At the slow flow rates employed, there would likely have been fast enough dissolution / precipitation kinetics that dissolved levels of Fe and other metals in coolant leaving the hot part of the rig were controlled by *final* (effluent) hydrogen concentration, rather than the lower levels farther back in the rig, so in this sense the model-predicted levels are directly relevant. However, lateral variations in hydrogen concentration may mean that local hydrogen concentration at the rig walls might be expected to be higher than the model predictions, especially during sessions 1 to 4. During sessions 5 and 6, in the reaction cell the presence of SS316L chips would have negated this effect.

17.2.2. Steady state equation involving hydrogen release rate and mass flow rate

At steady state, for a given corrosion rate and coolant flow rate, the rate at which hydrogen is released by corroding surfaces, $\dot{H}$ (mole h^{-1}), must necessarily be matched by the rate at which it leaves the rig as effluent. The rate of dilution is known from mass flow rate, $\dot{M}$ (kg h^{-1}); the ratio of these two quantities gives steady state hydrogen concentration of coolant, C (mole kg^{-1}) as it leaves the hot part of the rig (and as it leaves the rig entirely as effluent):

$$C = \dot{H}/\dot{M}$$

17.2.3. Modeling corrosion rate versus time, using data from a sister rig

The oxide film on SS316L tubing in the heated parts of the rig (~2 dm^2), and on the SS316L chips (~20 dm^2), where present, is expected to have grown progressively over time, with roughly parabolic kinetics after the first few hundred hours of exposure. The corrosion rate of rig walls (tubing) was modelled for sessions 1 to 4 of rig use; for session 4 corrosion film growth for the freshly added replacement oxide chamber are shown alongside that for the rest of the rig. The SS316L chips added freshly for both session 5 and session 6 – having a factor of 10 greater nominal surface area than the rig walls, and no prior exposure to hydrothermal solution – are expected to have accounted for the bulk of corrosion growth, and thus hydrogen build-up, during their respective sessions of use, and so corrosion of the chips alone was modelled during those sessions.

Corrosion of stainless steels in hydrothermal solutions has been shown to follow parabolic kinetics [26], [76], [80], [84], which is characterised by a parabolic rate constant, k_p. For SS316L, values of k_p were measured by J. Morrison [26], under a range of conditions comparable to those employed in the rig of the current study – see Table 3.1. Averaged values of 0.52, 0.43, and 0.23 mg dm^{-2} $h^{-1/2}$ were taken from those results, for pH 9, 10 and 11 respectively at 300 °C. Due to a lack of directly comparable data at lower temperatures, and since there was no clear trend with temperature for an equivalent set of data from the same study using a different analysis method [26], and a different study using SS304 [80], these values were used in the model for 200 and 250 °C conditions also.

Equations (7.1) and (7.2) below show the dependence of mass of alloy corroded, w (mg dm^{-2}), on time, t (h); and the dependence of corrosion rate dw/dt on time [37]. By substituting the

expression for $t^{-1/2}$ from (7.1) into (7.2), a further expression for dw/dt is derived in terms of w, (7.3).

$$w = k_p t^{\frac{1}{2}} \quad \Rightarrow \quad t^{-\frac{1}{2}} = \frac{k_p}{w} \qquad (14.1)$$

$$\frac{dw}{dt} = \frac{1}{2} k_p t^{-\frac{1}{2}} \qquad (14.2)$$

$$\frac{dw}{dt} = \frac{1}{w} . \frac{k_p^2}{2} \qquad (14.3)$$

As SS316L (or any similar alloy) corrodes, a certain proportion (about half) [37], [73], [76] is retained in the protective oxide film, and the remainder is released into coolant, from where it forms outer oxide crystallites. Therefore, the thickness of the protective oxide film is proportional to w. Equation (7.3) follows necessarily from an assumption that corrosion growth rate is inversely proportional to the thickness of the protective oxide film. Where the corrosion film is exposed to different conditions, having different characteristic values of k_p, equation (7.3) becomes the appropriate equation to use.

Figure 17.1 to Figure 17.4 illustrate the expected effects on corrosion film growth, and corrosion rate, from operating under differing conditions at different times during sessions 1 to 4 – namely the use of pH 11 coolant during session 2, for which corrosion rate is thought to be slower than at other times when pH 9 coolant was used. For session 1 (neutral pH feedwater) corrosion rate data for a pH of 9 was used due to lack of data at neutral pH. The fact that ultrapure water with no pH reagent or buffer is susceptible to changes in pH_T, due to dissolution of impurities, adds to uncertainty over the true value of pH in this case.

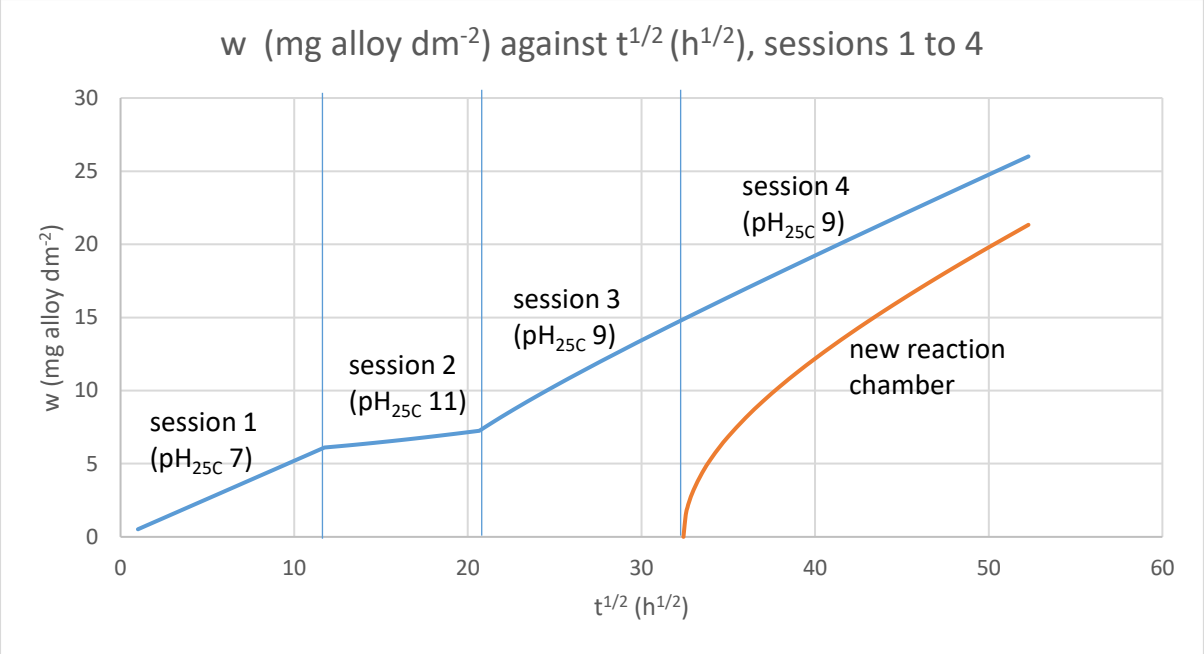

Figure 17.1. Corrosion growth during sessions 1 to 4, with $t^{1/2}$ as the x coordinate

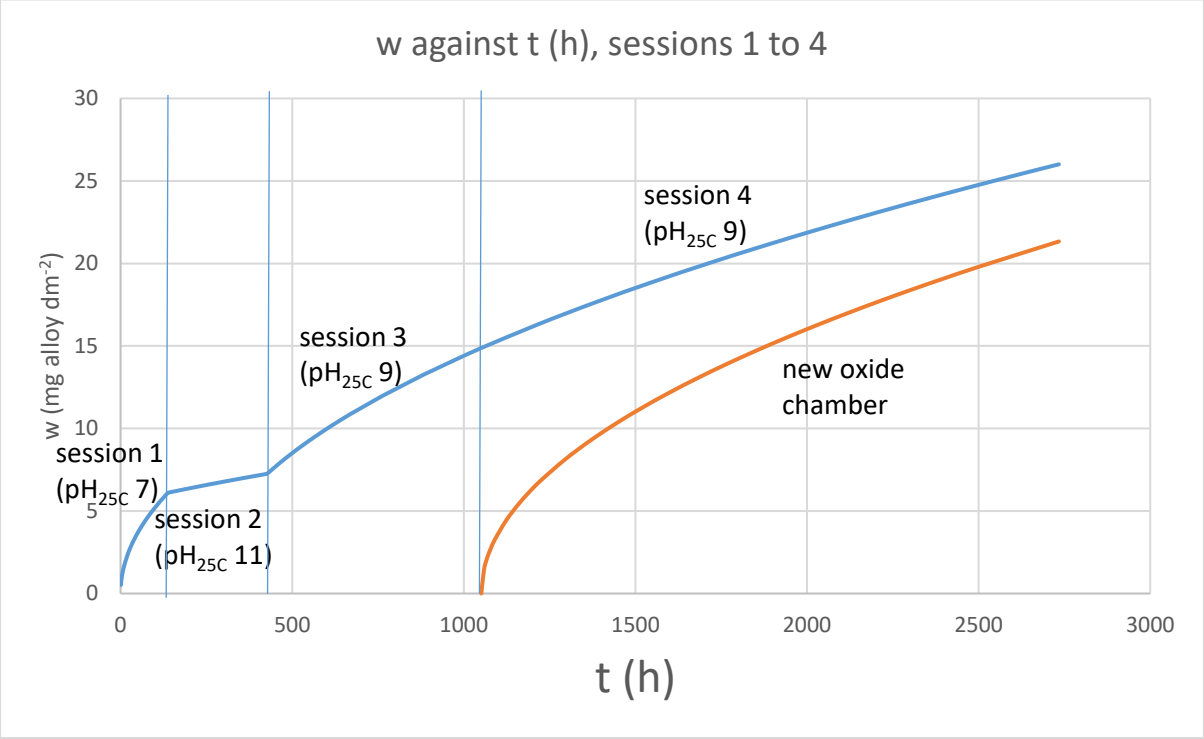

Figure 17.2. Corrosion growth during sessions 1 to 4, with t as the x coordinate

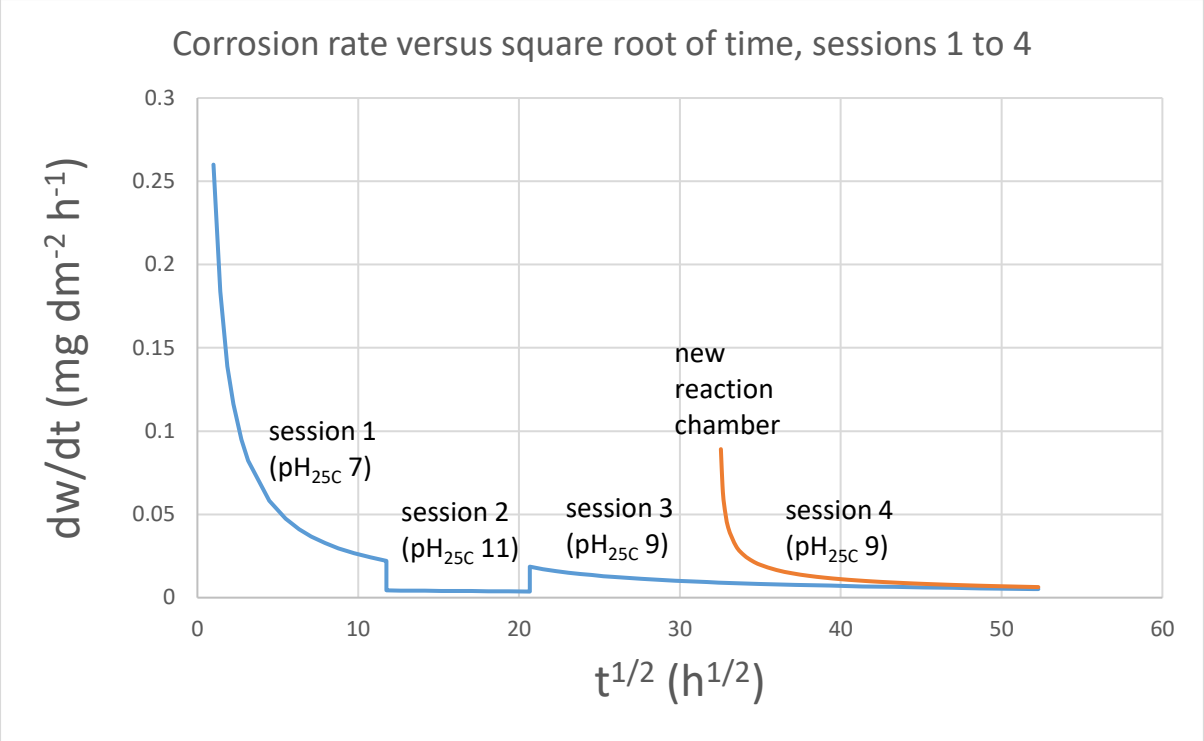

Figure 17.3. Corrosion rate during sessions 1 to 4, with $t^{1/2}$ as the x coordinate

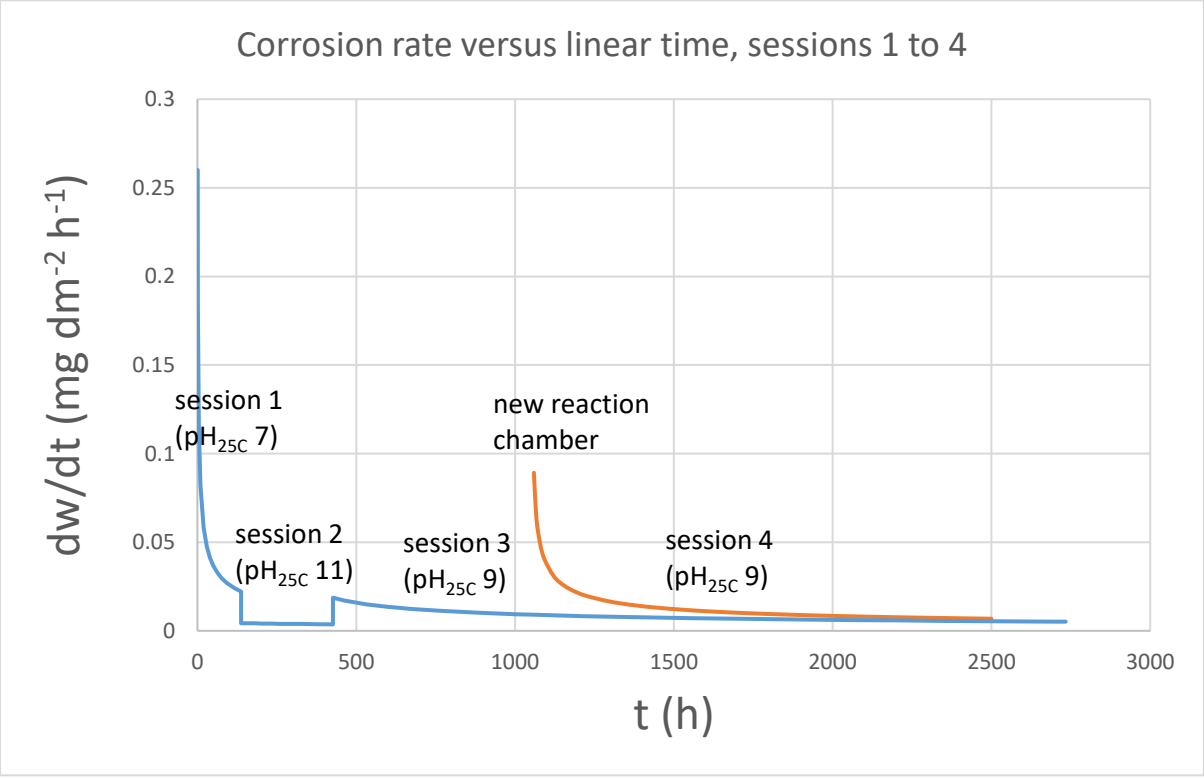

Figure 17.4. Corrosion rate during sessions 1 to 4, with t as the x coordinate

17.2.4. Estimating hydrogen release rate, from corrosion rate

The molar mass of SS316L was calculated, and used to determine the number of moles of hydrogen gas produced per mg of alloy corroded, via by the reaction $3Me + 4H_2O \rightarrow Me_3O_4 + 4H_2$, as shown in Table 17.2. The number was multiplied by 0.1, to account for retention of hydrogen within the metal [95] (in [94]) (see section 3.2), giving the value of 2.4 x 10^{-6} moles of hydrogen released to solution per mg of alloy corroded.

Table 17.2. Calculating the number of moles of hydrogen gas released to solution per mg of corroding alloy.

Key element	Relative conc, wt%			Molar mass (g)	No. of moles per 100 g of alloy	
Fe	65.3			55.845	1.17	
Cr	17.4			51.9961	0.33	
Ni	13.2			58.6934	0.22	
Mo	2.5			95.94	0.03	
Mn	1.7			58.6934	0.03	
			Sum total:		1.78	moles
			1 mole alloy		56.06	g
			metal in 1 mole Me_3O_4		168.17	g
			metal per mole of H_2		42.04	g
			moles H_2 per mg metal		2.37849E-05	mole H_2 per mg alloy
			of which, released:		2.37849E-06	mole H_2 released per mg alloy

In Figure 17.5 is plotted the modelled rate of hydrogen release to the coolant during sessions 1 – 4, using the nominal total surface area of corroding walls in the hot part of the rig, 2 dm^2. During session 1 the modelled rate was very fast, though the assumption of parabolic kinetics is not necessarily correct during the early stages of corrosion. During session 2, modelled corrosion rate was slow because of slower corrosion kinetics in pH_{25C} 11 coolant, and was fairly steady at ~25 – 30 nano moles per hour. During session 3 and 4, faster corrosion kinetics at pH_{25C} 9 meant a higher modelled rate of ~40 – 100 nano moles per hr (session 3) and 25 – 40 nanomoles / hr (session 4).

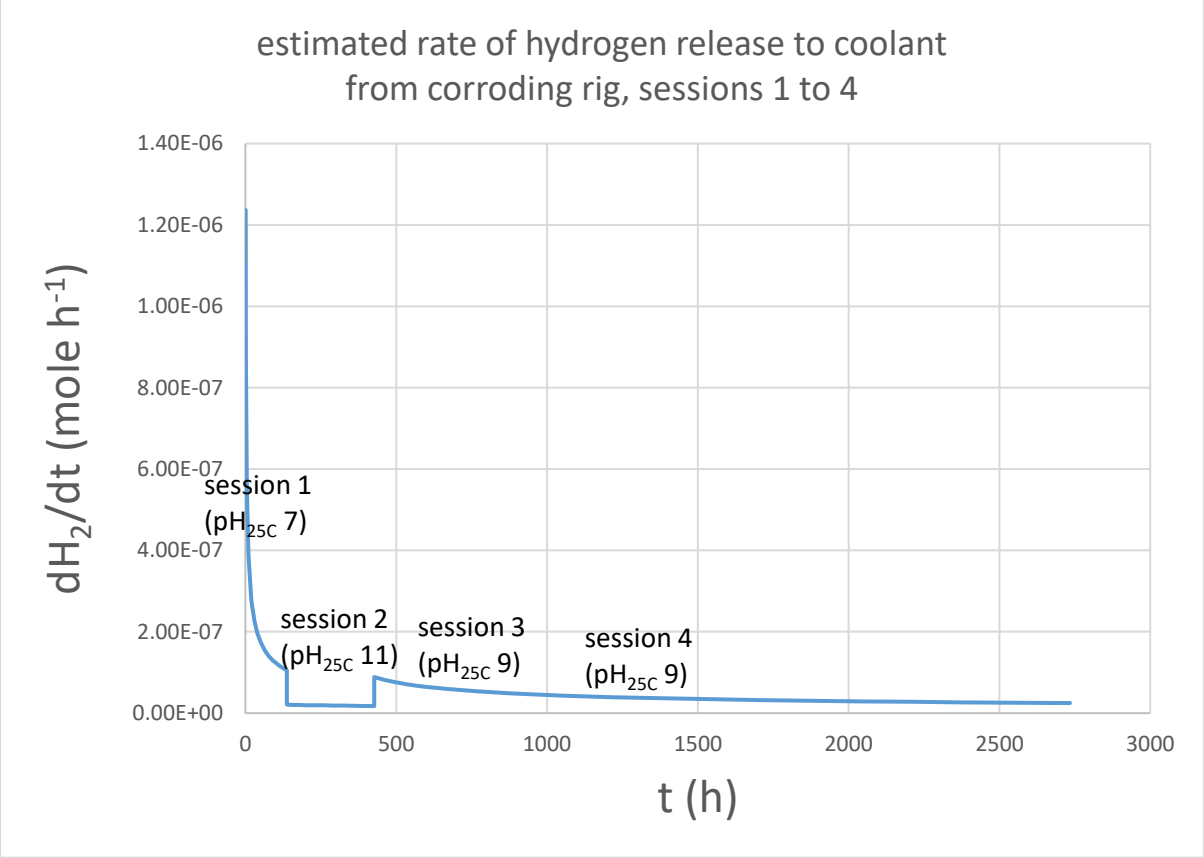

Figure 17.5. Estimated rate of hydrogen release from rig into coolant, during sessions 1 to 4.

17.2.5. Model-predicted levels of hydrogen in rig effluent

The amount of dissolved hydrogen in the coolant is expected to have reached a steady state, as the number of moles of hydrogen released each hour was diluted according to the number of kilograms of water entering the hot part of the rig each hour (mass flow rate). Calculated steady state hydrogen concentration is plotted in Figure 17.6 for sessions 1 – 4, taking into account the variation of flow rate with time. The finite release rate of hydrogen, and finite rate of dilution, means that the actual hydrogen concentration is expected to approach steady state levels exponentially whenever there is an abrupt change to the steady state level, with characteristic time period being the coolant residence time in the hot part of the rig. This assumes that hydrogen diffuses rapidly throughout the coolant, and that water and dissolved hydrogen pass congruently through the BPR towards the rig exit. At the slowest flow rate used, 0.1 g/min, residence time in the hot part of the rig was at least 15 hours, depending on temperature, and so there was an appreciable delay in reaching steady state, which is not shown in the figures. Expected transients of hydrogen build-up during periods of zero flow, due to pump stalls, are also not shown.

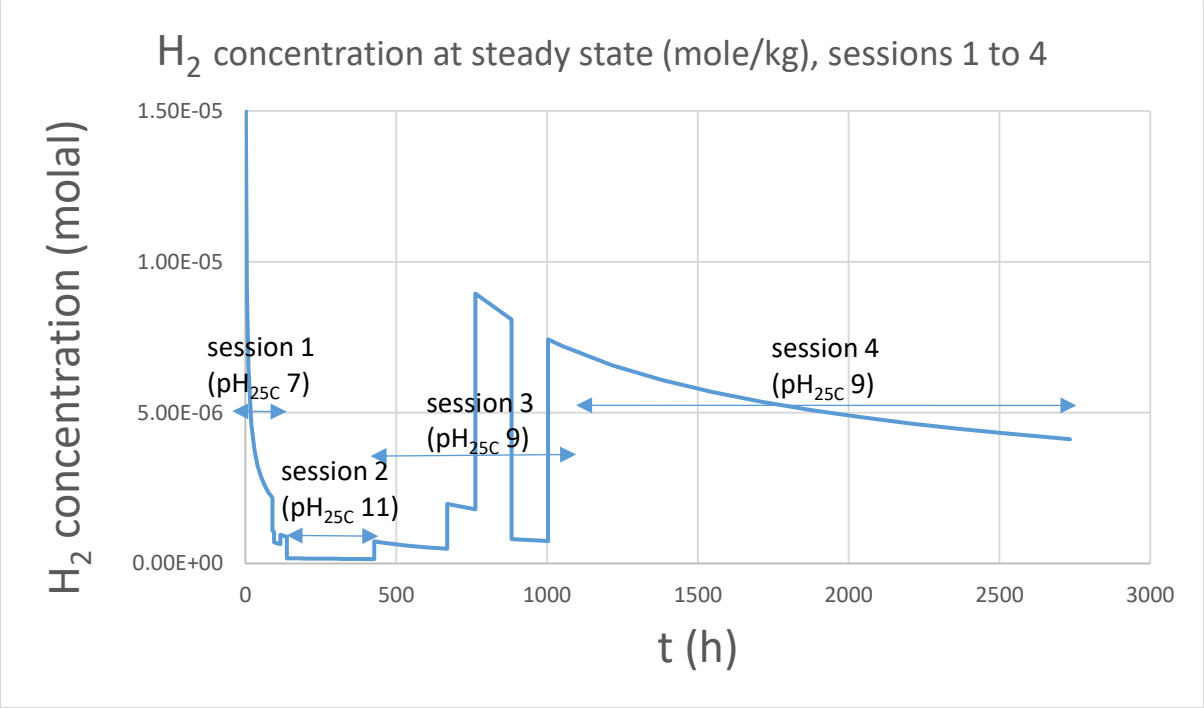

Figure 17.6. Estimated hydrogen concentration in the hot part of rig during sessions 1 – 6, based on corrosion rate data, flow rate, and assumption that 90% of hydrogen produced is retained in metal.

In Figure 17.7 and Figure 17.8 are plotted steady state hydrogen concentrations expected during sessions 5 and 6, using the same method as above, due to the addition in each case of fresh as-yet un-corroded SS316L chips of nominal total surface area 20 dm^2. For reference, 1 atm of hydrogen in equilibrium with water at 25 °C has a concentration of 7.8 x 10^{-4} molal. In Figure 17.9, estimated hydrogen concentrations are compared across all 6 sessions of rig use on a log scale. Results from hydrogen measurements, and selected values of log $\{H_2\}_{25C}$, are included for reference.

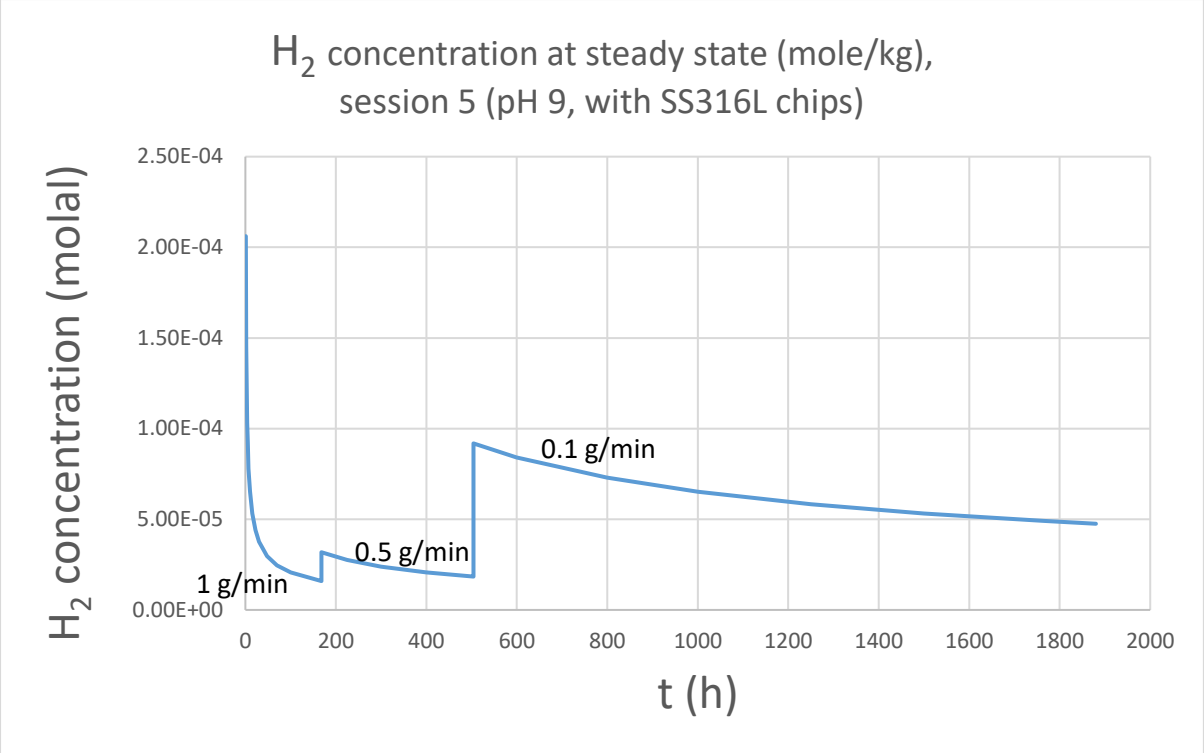

Figure 17.7. Estimated hydrogen concentration, session 5

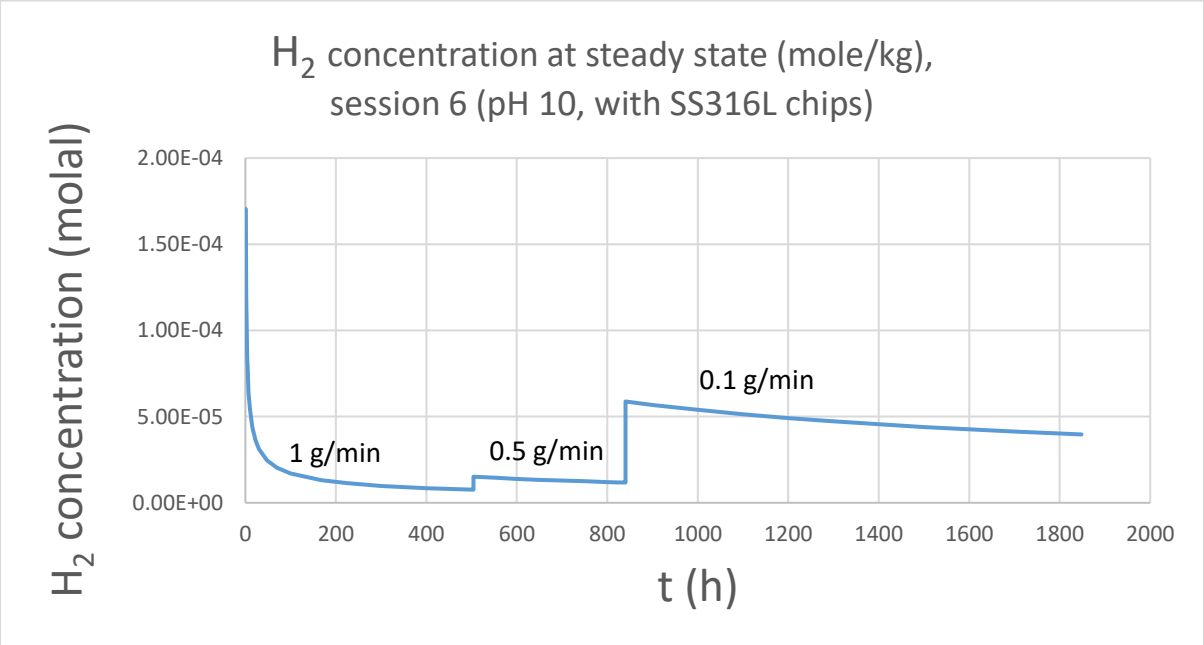

Figure 17.8. Estimated hydrogen concentration, session 6

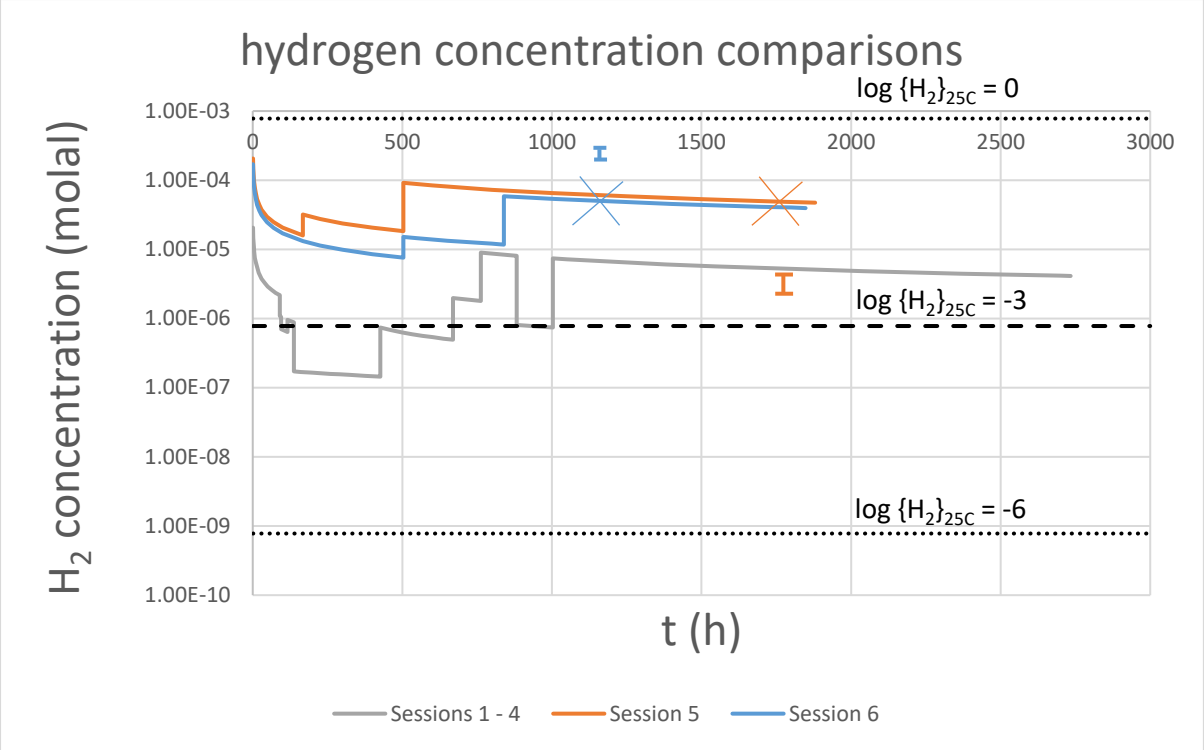

Figure 17.9. Comparison of modelled steady state hydrogen concentrations in the rig during sessions 1 to 6.
Approximate values from the two measurements are also indicated, by error bars, and for each measurement the corresponding modelled hydrogen concentration is marked with a colour-coded cross – the orange cross at ~1750 h represents the first reading, taken during session 5, and the blue cross at ~ 1200 h represents the second reading, taken during session 6. Lines are plotted at selected values of log{H_2}$_{25C}$ for ease of reference.

17.3. Models to predict soluble concentrations of each species in rig effluent

As a first approximation, soluble levels may be expected to follow exactly the equilibrium solubility of the most stable oxide phases under the prevailing conditions. In the context of expected or possible conditions in the rig, a summary of findings from the literature review in chapters 0 and 14 is provided, regarding stability of oxide phases (sections 17.3.1 and 17.3.2), and equilibrium solubility levels of Fe, Cr and Ni from their respective oxides as a function of conditions, for a representative selection of coolant conditions (section 17.3.3).

To move beyond a deterministic, thermodynamics-based, initial approach, the effects of finite kinetics must be considered. In section 17.3.4 the relatively rapid kinetics of equilibration in the high temperature parts of the rig, and the much slower kinetics with which coolant attempts to reach equilibrium with walls of the sampling line, are considered, as well as the effect of any particles of high temperature oxides on soluble effluent levels after they have been transported to the room-temperature tubing of the sampling line, where their metastability causes enhanced solubility. The effect of corrosion film crystallite aging is also considered.

An overall model is outlined in section 17.3.5. The model has quantitative elements in terms of the solubility levels under various conditions at high temperature and at ambient temperature, but only treats in a qualitative manner the relative impact of the heated and ambient portions on final effluent soluble concentrations expected, and the impact of other effects such as the presence of metastable phases.

17.3.1. Stability of oxides at high temperature

Figure 17.10 summarises the stability of crystalline phases in the system Fe-Cr-Ni-H-O. The range of conditions expected in the heated part of the rig are indicated by a red rectangle, and the oxides expected as a function of hydrogen concentration at 250 °C (the mid-point of the temperature range) are tabulated in Table 17.3, for ease of reference.

Fe and Cr exist stably as ferrite and chromite in the bulk of the corrosion film, whilst the presence of water at the oxide-coolant interface causes CrOOH to be stable as a thin layer on coolant-facing surfaces of chromite.

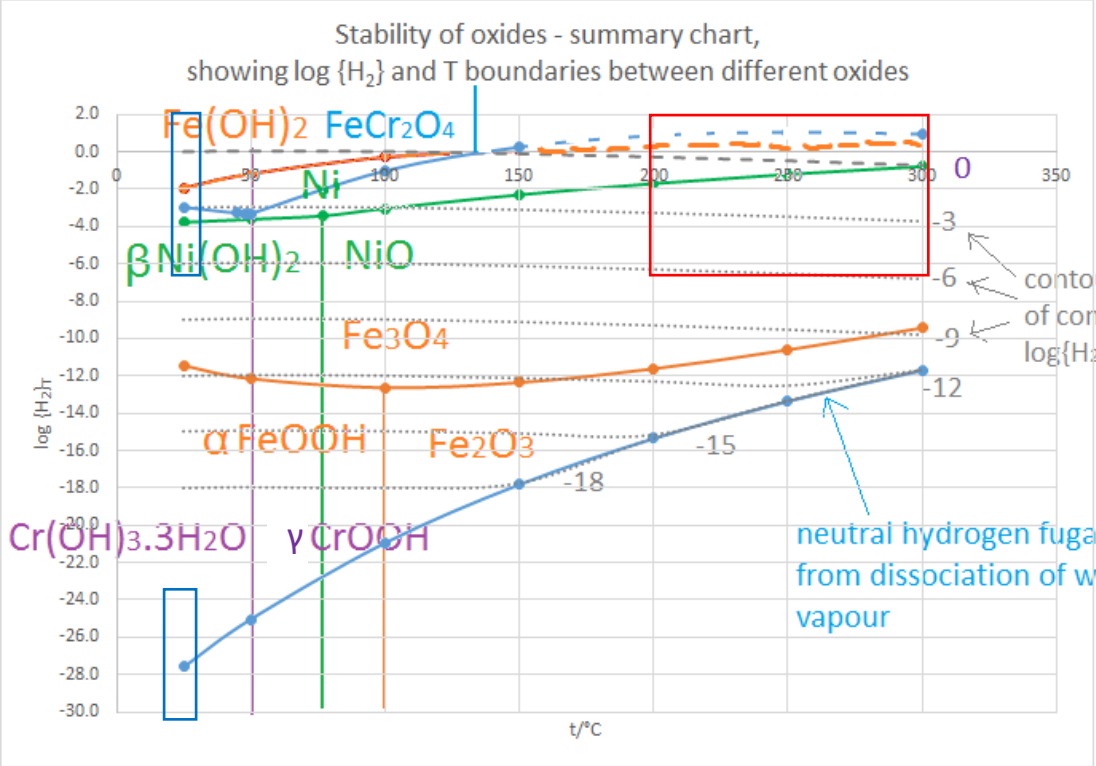

Figure 17.10. Stability fields of oxides of Fe (colour-coded orange), Cr (purple) and Ni (green), in terms of temperature (T/K) and the logarithm of hydrogen fugacity (in multiples of 1 bar).
Plotted from solubility data in Appendix 1 (Chapter 14), by considering which phase has the lowest solubility as conditions vary. Coloured boxes indicate conditions in heated regions of the rig (red) and in the sampling line (upper blue). The lower blue box indicates possible conditions in the last few cm of the sampling line, due to oxygen ingress and hydrogen egress to the laboratory atmosphere. Whilst hydrogen fugacity may extend beyond the bottom of the graph, there is no change in stability of the oxides at any possible hydrogen concentration below log {H_2} = c. -13.

These three phases are expected to be the only ones present at temperature in the rig for the majority of conditions (besides the underlying alloy), according to thermodynamics considerations alone, with nickel incorporated into the two spinel phases as illustrated in Figure 17.12.

Early in the use of the rig, or soon after part of the high temperature tubing had been replaced, rapid corrosion would likely have caused particularly high hydrogen levels for a limited time, before the protective corrosion film developed further. At this stage, nickel would have been highly stable in its pure metallic state, having extremely low solubility at such high hydrogen concentration. Therefore, the nickel metal phase would likely be present, as outer layer (and possibly inner layer) crystallites and as colloids forming from supersaturated solution. A large release of particulate Ni to coolant is indeed typically observed during commissioning and early use of new PWRs (though is largely attributed to the much more Ni-rich Ni base alloys of the SGs [43], [120]). In addition to high hydrogen levels, the poorly developed corrosion film enables rapid dissolution of metals from the alloy at the same time as limited surface area of outer layer crystallites on which dissolved ions may

Table 17.3. Approximate values of hydrogen fugacity for transition between solid phases at 250 °C.

Transition	Hydrogen fugacity of transition. Log $\{H_2\}_{25C}$ approx..	comments
$FeCr_2O_4$ → CrOOH and Fe_3O_4	1.5	Per data used in preparing the plot, $FeCr_2O_4$ is not truly stable in the presence of water above around 130 °C – at any hydrogen fugacity – against decomposition to CrOOH and $Fe(OH)_2$. Where water is absent (beneath corrosion film surface) CrOOH cannot form and so $FeCr_2O_4$ remains stable. In the absence of $Fe(OH)_2$ phase, $FeCr_2O_4$ may be present at oxide-coolant interface at high hydrogen fugacity (> c. $10^{1.5}$ atm), but unstable against decomposition to CrOOH + Fe_3O_4 at lower hydrogen fugacity. If CrOOH is indeed present under these conditions, it is likely to be just a very thin layer on top of the chromite at the oxide-coolant interface.
$Fe(OH)_2$ → Fe_3O_4	0.5	
Ni and Fe_3O_4 → $NiFe_2O_4$	0	
Ni → NiO	-1	
Ferrite, $FeCr_2O_4$, Ni →Ferrite, $NiCr_2O_4$,Ni	-1 (at 290 °C)	

precipitate. Under these conditions, kinetics considerations may favour the nucleation and growth of metastable hydroxide phases, especially when particle size is still small (the difference in Gibbs energy of oxide versus hydroxide phases tends to get smaller with smaller particle size, with hydroxide expected to become the more stable phase for particles < 10 nm [38]): $Ni(OH)_2$ (which is stable only below about 77 °C, but can exist metastably at much higher temperatures [3], [187]); and $Fe(OH)_2$ (which favours high hydrogen fugacity, and is thought to be stable only below about 150 °C, but can also exist metastably at higher temperature [5], [38], [121]). Both phases have been observed on corrosion films of Fe-Cr-Ni alloys ([133], and [200] in [133]).

Later, with falling hydrogen concentration, equilibrium levels of soluble Ni in equilibrium with Ni metal would rise, allowing greater retention in the spinel-type oxides, as described below. This would also enable any separate Ni-based phase to fully dissolve, with the Ni being incorporated into the spinel oxides, if kinetics allow. With hydrogen concentration falling further, the stable phase of Ni transitions from Ni metal to NiO. Kinetics of phase transition are slow, so that any of the phases

Ni, NiO, $Ni(OH)_2$, and $Fe(OH)_2$ may persist for a time under conditions for which they are not the most stable forms. Some studies have observed Cr_2O_3 inclusions at the oxide-alloy interface (for example, [133]), though this is not expected to influence either soluble or particulate levels of corrosion product in the rig effluent samples.

Partition of Ni between spinel-type oxides, Ni-based phases, and coolant

In general, the stable Ni-based phase would be nickel metal above a certain hydrogen fugacity, or otherwise NiO. Due to the high ratio of (Fe + Cr) to Ni in SS316L, about 5.9, one would not expect a separate Ni-based phase, with nickel instead being incorporated in spinel-type phases ferrite and chromite, as illustrated in Figure 17.11 and the top part of Figure 17.12, provided the hydrogen fugacity is not too high.

At around 300 °C (290 °C), nickel ferrite is stable up to more-or-less stoichiometric composition ($x > 0.9$ in $Ni_xFe_{3-x}O_4$) for hydrogen concentrations up to ~ 1 atm at 25 °C (that is, ~18 scc/kg), see Figure 17.11. At higher hydrogen concentrations, as nickel metal becomes increasingly stable, nickel leaches from the ferrite causing the saturation nickel content of the oxide to fall, from $x = 0.9$ at ~ 1 atm, to $x = 0.2$ at 10 atm hydrogen. Nickel ferrite can be said to be unstable against decomposition to magnetite and nickel metal above a certain threshold hydrogen concentration, whose temperature dependence is shown in Figure 4.5; though for ferrite with a lower nickel content, stability against leaching of nickel persists to a higher hydrogen fugacity than for the stoichiometric oxide.

Nickel chromite exhibits similar behaviour, but stability doesn't extend to as high a hydrogen concentration as for nickel ferrite, with nickel content falling from $x = 0.8$ at ~0.01 atm to $x = 0.05$ at 1 atm hydrogen at 25 °C in $Ni_xFe_{1-x}(Cr_yFe_{1-y})_2O_4$ according to the Kurepin model.

The Kurepin model predicts that the partition of nickel is heavily favoured towards the ferrite phase, at least where excess nickel is present. This agrees with the conclusion of Dickinson et al. that nickel ferrite is stable under PWR primary conditions whilst nickel chromite is not [103]. However, studies of the duplex oxides on corrosion films have shown fairly equal partition of nickel between the two phases. This may be due to the slower diffusivity of Ni^{2+} ions through the chromite lattice than that of either Fe^{2+} or Mn^{2+} [73], coupled with the mechanism by which the corrosion film forms, by diffusion of divalent cations across the chromite oxide layer from alloy to coolant. Oxide composition reflects kinetics considerations and not just thermodynamic stability.

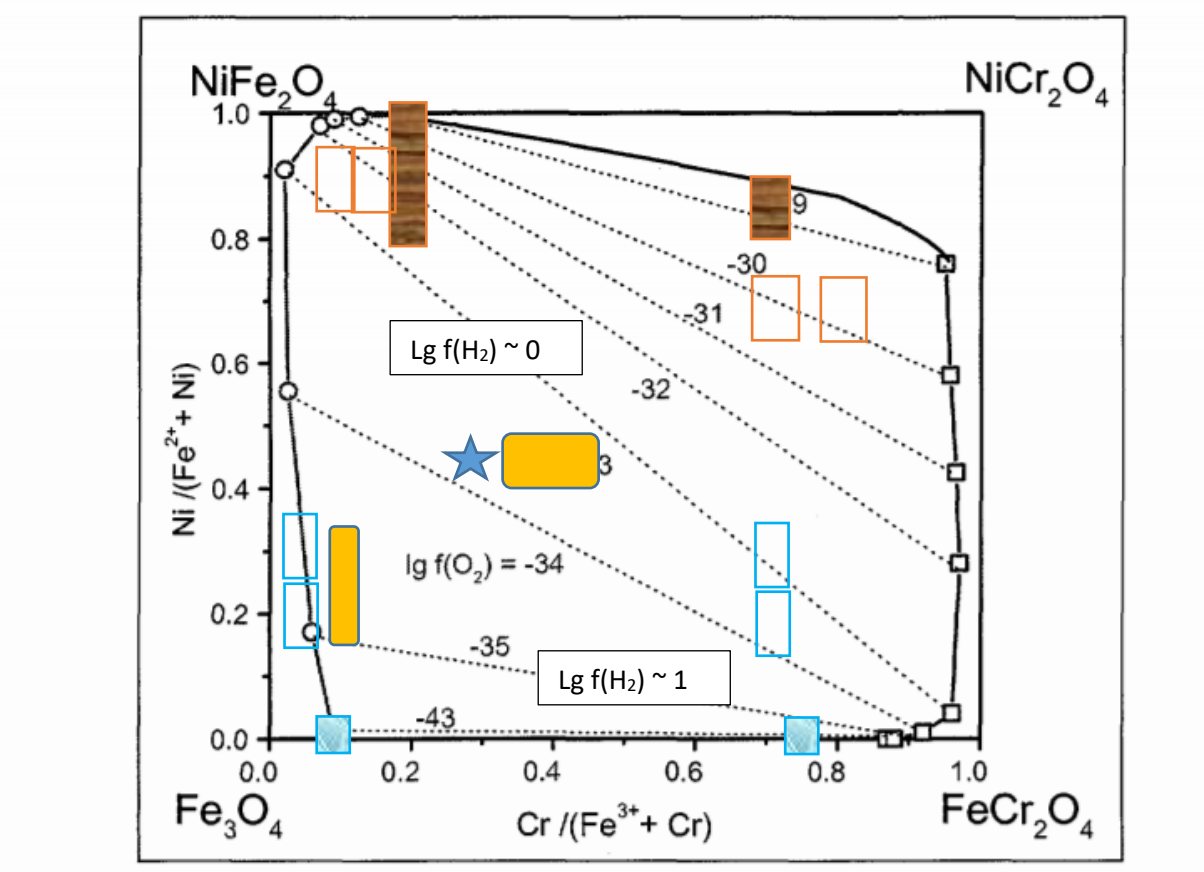

Figure 17.11. Calculated phase equilibria in the system Fe_3O_4 – $FeCr_2O_4$ – $NiFe_2O_4$ – $NiCr_2O_4$ at 290 °C, per the model of Kurepin et al. From [12].
The central bounded region indicates compositions which are thermodynamically unstable against decomposition into separate Fe-rich (ferrite) and Cr-rich (chromite) phases, at the left and right boundaries of the central region respectively. Lines of equal oxygen fugacity are shown, the two ends of which represent the pair of spinel compositions which are stable for that particular level of oxygen fugacity, in the presence of excess nickel (where there is a deficit of nickel, levels in the oxide are necessarily lower). This indicates that nickel content diminishes as conditions become increasingly reducing, due to the precipitation of Ni metal as a separate phase – under these conditions there is a much greater stability of Ni in ferrite than chromite, as shown. Very approximate equivalent hydrogen fugacities are indicated for reference. The boundary shown between single phase and two-phase stability is called the 'solvus of immiscibility'. Experimental determinations of the solvus, as plotted in Table 4.1, are plotted here as coloured boxes for comparison – open boxes for corrosion film studies (orange - Ni base alloys; blue – stainless steels), and shaded boxes for oxide decomposition studies (orange – $NiFeCrO_4$; blue – Fe_2CrO_4). In corrosion studies on Ni base alloys, there was excess Ni metal present in the inner oxide layer, demonstrating that the spinels were saturated with the highest concentration of Ni possible for the prevailing redox conditions, at least for the chromite phase. For the stainless steels, it can be seen that partition of Ni between ferrite and chromite was equal, within errors. The star symbol shows approximate composition of the SS316L used in the current project, if it were to oxidise as a single spinel phase, and the yellow rectangles show measured composition of inner and outer layer oxides, see Table 10.1, though the former may have been distorted by interference from underlying outer layer oxides.

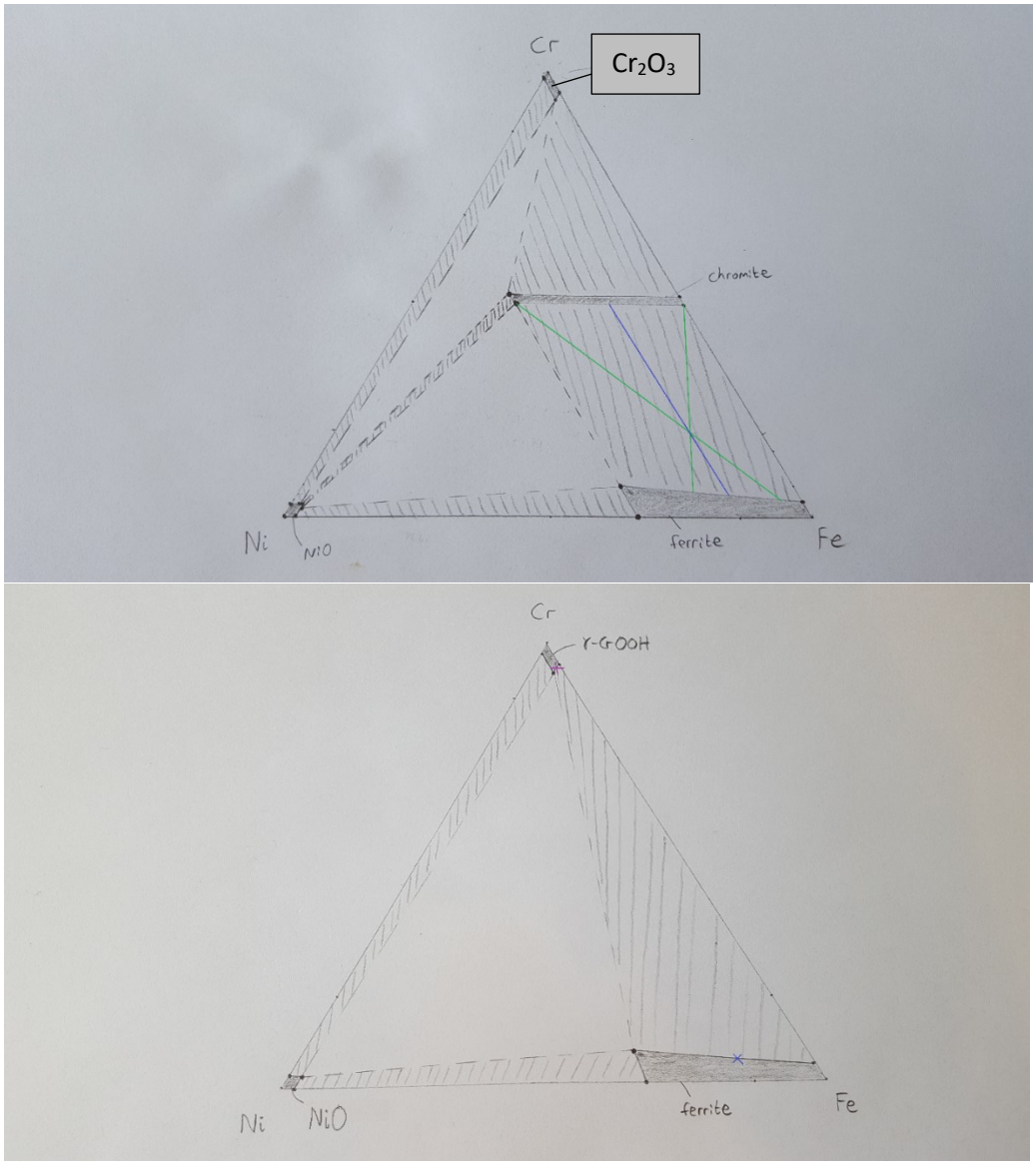

Figure 17.12. Approximate phase diagrams for the system Fe-Cr-Ni-H-O, at conditions expected in hot part of rig (200 – 300 °C, moderately reducing conditions having log $\{H_2\}_{25C}$ ~ -5 to 0).
At the top end of the range of hydrogen fugacities covered, Ni metal is expected to be the stable phase rather than NiO, and the stability field of ferrite would not be expected to extend as far left as depicted.
Top: Solid phases in which the bulk *of metal ions from the alloy reside after oxidation. Assuming congruent oxidation, and neglecting any loss to rig effluent (inconsequential for Fe, Cr and Ni), components of the alloy pass to the oxide film in the same proportions that they are present in the alloy. The two ends of green and blue tie lines, whose intersection marks the composition of SS316L, show the range of possible chromite and ferrite compositions, assuming Ni/NiO is absent as a separate phase. Experimental studies have tended to show equi-partition of Ni (blue line)* [76], [84] *or a slight preference for the ferrite phase* [75], [86]*, whilst the model of Kurepin* [12] *suggests a strong preference for the ferrite phase under certain redox conditions (see Figure 4.4). Bottom: Solid phases thought to be present at coolant facing surfaces, as solubility-controlling phases. Chromite is not present as it is unstable (see section 14.3.11). Incongruent dissolution of Fe from $FeCr_2O_4$ is thought to occur, leaving a thin layer of γCrOOH at the surface* [103].

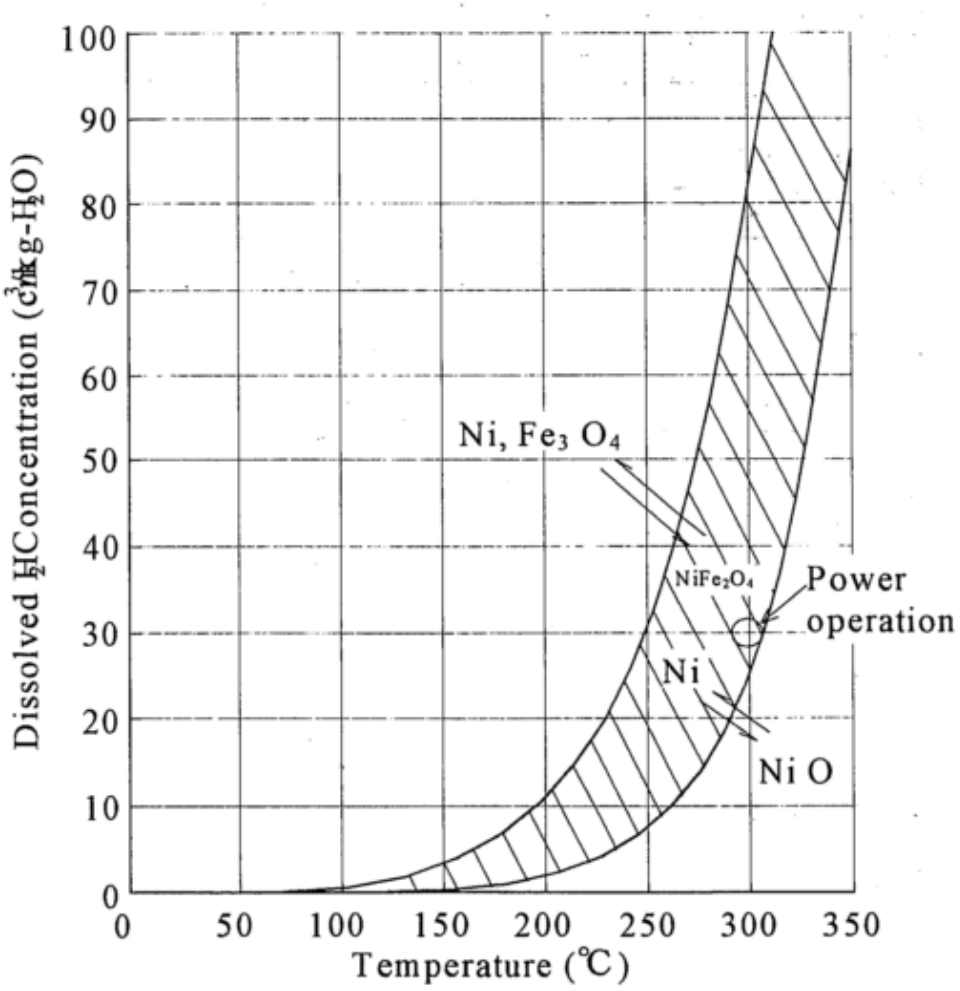

Figure 17.13. Region of stability of Ni metal and nickel ferrite, against oxidation to NiO and decomposition to nickel metal and magnetite respectively. From [118].

Some possible scenarios regarding oxides present at selected hydrogen levels

Table 17.4 to Table 17.6 present some possible scenarios regarding which oxides may have been present in the hot part of the rig at 300 °C.

Table 17.4. Expected surface and bulk phases at 300 °C, allowing presence of nickel chromite as a meta-stable phase, in the presence of excess Ni metal and where formation of NiO is suppressed. Data from the Kurepin model were used. This table shows upper limits of Ni contents of ferrite and chromite phases at equilibrium with each other and a Ni phase (Ni metal) – lower Ni contents are possible at equilibrium where there is no excess Ni, or where NiO is present instead of metastable Ni metal. Lower or higher Ni contents are also possible in practice due to non-equilibrium conditions.

$Lg\{H_2\}_{25C}$	Cr-based	Fe-based	Ni-based
3	$FeCr_2O_4$	Fe_3O_4	Ni metal
2	CrOOH / $FeCr_2O_4$	Ferrite, x < 0.1	Ni metal
1	s: CrOOH (b: $FeCr_2O_4$)	Ferrite, x = 0.2	Ni metal
0	s: CrOOH (b: $FeCr_2O_4$)	Ferrite, x = 0.9	NiO / Ni
-1	s: CrOOH (b: chromite, x = 0.5 *)	$NiFe_2O_4$	NiO (Ni*)
-2	s: CrOOH (b: chromite, x = 0.8 *)	$NiFe_2O_4$	NiO (Ni*)

Table 17.5. Expected surface and bulk phases, using the data from Table 17.4, but with limited inventory of Ni – limited to x = 0.45 to match the composition of SS316L used in the rig.
Equal volumes of inner and outer oxide are assumed, so that overall 'x' for the oxide film is simply the mean of the values from the inner and outer oxides.

$Lg\{H_2\}_{25C}$	Cr-based	Fe-based	Ni-based	notes
3	$FeCr_2O_4$	Fe_3O_4	Ni metal	Oxide 100% Ni saturated
2	CrOOH / $FeCr_2O_4$	Ferrite, x < 0.1	Ni metal	Oxide 100% Ni saturated
1	s: CrOOH (b: $FeCr_2O_4$)	Ferrite, x = 0.2	Ni metal	Oxide 100% Ni saturated
0	s: CrOOH (b: $FeCr_2O_4$)	Ferrite, x = 0.9	NiO / Ni	Oxide 100% Ni saturated
-1	s: CrOOH (b: chromite, x = 0.3 *)	Ferrite, x = 0.6	-	Oxide 60% Ni saturated
-2	s: CrOOH (b: chromite, x = 0.4 *)	Ferrite, x = 0.5	-	Oxide 50% Ni saturated

Table 17.6. Expected surfaces phases at 300 °C, based on an assumption that a value of x = 0.25 is present in both the inner and outer oxides (as measured in chapter 10), except at the highest hydrogen concentrations where almost no Ni is retained in the ferrite phase.
Only surface-facing phases, which can affect solubility, are included. This table reflects empirical evidence wherein spinels settle to a relatively equal partition of Ni between ferrite and chromite in corrosion films.

$Lg\{H_2\}_{25C}$	Cr-based	Fe-based	Ni-based	Possible meta-stable phases
3	chromite	Fe_3O_4	Ni metal	$Fe(OH)_2$*, $Ni(OH)_2$*, NiO*
2	CrOOH / chromite	Ferrite, x < 0.1	Ni metal	$Fe(OH)_2$*, $Ni(OH)_2$*, NiO*
1	CrOOH	Ferrite, x = 0.2	Ni metal	$Fe(OH)_2$*, $Ni(OH)_2$*, NiO*
0	CrOOH	Ferrite, x< ~0.25	NiO / Ni	$Fe(OH)_2$*, $Ni(OH)_2$*
-1	CrOOH	Ferrite, x< ~0.25	NiO	$Fe(OH)_2$*, $Ni(OH)_2$*, Ni*
<= -2	CrOOH	Ferrite, x< ~0.25	NiO	$Fe(OH)_2$*, $Ni(OH)_2$*, Ni*

17.3.2. Stability of oxides at room temperature

In Figure 17.10, a blue box indicates conditions in the sampling line, having the same hydrogen concentration as the heated portions, but lower temperature. Another blue box illustrates the oxidising conditions at the very of the sampling line, where oxygen from the laboratory atmosphere can diffuse a few mm upstream against the flow. As hydrogen fugacity is decreased, stability shifts from $Fe(OH)_2$, $FeCr_2O_4$ and Ni metal to Fe_3O_4, $Cr(OH)_3.3H_2O$, $Ni(OH)_2$ controlling levels of Fe, Cr, and Ni respectively. At room temperature, kinetics are far slower than at high temperature, and so metastable or unstable phases could readily have persisted in the sampling line. This could be on the natively formed oxides, or as particles carried downstream from the hot part of the rig. Therefore, any of the oxides discussed at high temperature could also have been present at room temperature.

17.3.3. Equilibrium solubility of Fe, Cr and Ni oxides as a function of conditions

Reducing conditions present in most regions of the rig

Combining solubility data from chapter 14 with the expected stability and composition of phases as treated above, Table 17.7 summarises the maximum dissolved levels of the elements Fe, Cr, and Ni which would be expected in the coolant under selected conditions of pH_{25C}, log $\{H_2\}_{25C}$, and temperature.

Dissolved levels are given in mass parts per billion (ppb), at 300 °C, 200 °C, and 25 °C, representing the highest and lowest temperature employed in the hot part of the rig, and the approximate temperature of the room-temperature back end of the rig through which the coolant flows before passing through the BPR into the non-pressurised tubing leading to the sampling or ejection point. In addition, where levels of a given element pass through a minimum or maximum level in between the selected temperatures, the ppb level at that extremum is displayed in parentheses.

Levels given for Fe are taken directly from fits to magnetite solubility data, and so probably represent a slight overestimate in comparison to a mixed phase containing Ni and Cr.

Levels given for Cr are for CrOOH, $Cr(OH)_3.3H_2O$, or $FeCr_2O_4$ solubility (in the presence of the stable Fe-based phase, ferrite or $Fe(OH)_2$) – whichever is lowest. Levels of Cr from CrOOH or $Cr(OH)_3.3H_2O$ are independent of hydrogen fugacity, but levels of Cr fall with increasing hydrogen fugacity where

$FeCr_2O_4$ and ferrite are the stable phases. Where $FeCr_2O_4$ and $Fe(OH)_2$ are the stable phases, there is no appreciable hydrogen dependence of Cr and Fe levels from the respective phases, and so levels

Table 17.7. Expected solubility of the most stable, solubility controlling phase for each element under the reducing conditions expected in the pressurised parts of the rig, at selected values of temperature, hydrogen fugacity, and pH_{25C}.

Ele-Ment	**controlling surface phase / effect**	Log $\{H_2\}_{25C}$ = 0 ppb at 300 °C, *200 °C*, and 25 °C, at selected pH_{25C}, (plus max/min at intermediate temperatures)			Log $\{H_2\}_{25C}$ = -3 ppb at 300 °C, *200 °C*, and 25 °C, at selected pH_{25C}, (plus max/min at intermediate temperatures)			Log $\{H_2\}_{25C}$ = -6 ppb at 300 °C, *200 °C*, and 25 °C, at selected pH_{25C}, (plus max/min at intermediate temperatures)		
		9	10	11	9	10	11	9	10	11
Fe	Ferrite solubility (values shown are for Fe_3O_4, may be lower for mixed oxide) **$Fe(OH)_2$ solubility (in bold)**	≲ 1.1 *9.4* **(24)** **1.5**	≲ 1.1 *0.47* **0.02**	≲ 2.3 *0.37* **0.003**	≲ 1.0 (0.5) *1.0* (3.0) 0.64	≲ 1.3 *0.12* 0.01	≲ 3.9 *0.16* 0.002	≲ 3.0 *0.32* (0.30) 0.06	≲ 3.8 *0.24* 0.001	≲ 12.0 *0.4* 0.002
Cr	CrOOH / $Cr(OH)_3.3H_2O$ Solubility, **chromite solubility (in bold)**	.003 *.004* **(.005)** **.004**	.004 *.004* **(.005)** **.004**	.009 *.005* **(.005)** **.004**	.003 *.004* **(.009)** .006	.004 *.004* **(.009)** .006	.009 *.005* **(.009)** .006	.003 *.004* (.010) .006	.004 *.004* (.010) .006	.009 *.005* (.010) .006
Ni	**Ni** / NiO / $\beta Ni(OH)_2$ Solubility (equilibrium levels of Ni may be much lower, controlled by composition of ferrite, and partition coefficient)	≤ **0.34** ***0.13*** **0.005**	≤ **0.33** ***0.01*** **0.000**	≤ **0.33** ***0.01*** **0.000**	≤ 0.37 *3.3* **(46)** **4.6**	≤ 0.35 *0.33* **(0.67)** **0.05**	≤ 0.35 *0.30* **0.006**	≤ 0.37 *3.3* (79) 27	≤ 0.35 *0.33* (1.0) 0.30	≤ 0.35 *0.30* 0.03
Mo	Mo composition near surface of ferrite; Mo partition coefficient									
Mn	Mn composition near surface of ferrite; Mn partition coefficient									

Table 17.8. A qualitative description of the processes expected to control levels of the major elements Fe, Cr and Ni in the coolant over different timescales. Conditions assumed: 200 - 300 °C, log {H_2} = 0. Whilst levels of Fe and Cr are simply controlled by the sparing solubility of their oxide phases

Ele-Ment	**Bulk phases where the element is located after oxidation**	**Longer-term trend:**	**Immediate: controlling surface phase / effect**
Fe	Ferrite, chromite *Fast diffusion.* *Over half the oxidised Fe is released to solution,* *almost completely retained as re-precipitated ferrite due to low solubility.* *The remainder is retained in chromite phase.*	[none]	Ferrite solubility
Cr	Chromite, (ferrite) *Slow diffusion.* *Majority of Cr stays in original location,* *forming chromite as leaching Fe(II) is replaced by oxygen (via O^{2-} ions or H_2O), and the associated build-up of hydrogen (via H^+ ions or H_2O).*	[none]	$FeCr_2O_4$ solubility (in equilibrium with ferrite or $Fe(OH)_2$) where stable. $Cr(OH)_3.3H_2O$ / CrOOH solubility , precipitated as surface phase where $FeCr_2O_4$ is not stable
Ni	Ferrite, chromite *Having intermediate diffusivity, but slower than Fe, the Ni component has been observed in literature studies to be similar across the two phases. This may represent a balance between slow diffusion relative to other divalent ions, tending to cause higher concentration in the inner layer, and the relative instability of Ni in chromite as opposed to in ferrite (see e.g.* Figure 17.11*,* Table 17.4*), tending to cause decreased concentration in the inner oxide.*	Ni may be retained in the ferrite and chromite oxides, in roughly equal proportion, up to x = 0.45 (in $Ni_x(Fe/Cr)_{3-x}O_4$), at sufficiently low hydrogen concentration. At higher hydrogen concentration, separate Ni metal phase present – over the longer term, this metal should incorporate into spinels whenever hydrogen levels are low enough, though Ni and NiO phases may persist over fairly long timescales.	Solubility of separate Ni / NiO / $Ni(OH)_2$ phase where present. Otherwise solubility of Ni from mixed spinel phases, dependent on Ni content near surface and partition coefficient. Can be related to a proportion of Ni metal solubility using Figure 17.11

are effectively frozen at the values given by ferrite / chromite at the hydrogen fugacity at which stability transitions from Fe_3O_4 to $Fe(OH)_2$. Where the data represent $FeCr_2O_4$ solubility, this is indicated by bold typeface.

Near-neutral to oxidising conditions in the last few mm of the sampling line

After the simulated coolant passed through the BPR, it was accessible by oxygen from the laboratory atmosphere as well as carbon dioxide gas which may have modified solution pH. Slow diffusion means that appreciably altered conditions were only likely to have been present in the last few millimetres of the sampling line. In this small section of the rig, a marked change to solubility may have caused dissolution or re-precipitation in this region if the solution was strongly under- or super-saturated with respect to the stable oxide phases under such conditions.

Table 17.9. Expected solubility of the most stable, solubility controlling phase for each element under the near-neutral to oxidising conditions expected in the non-pressurised parts of the rig, close to the exit from the rig, for selected pH values at 25 °C.

Element	**Controlling surface phase, process**	**Concentration at 25 °C at selected pH_{25C}, ppb...** ...for redox conditions of ferrite/goethite equilibrium, $log\ \{H_2\}_{25C} \approx -12$ (...for near-neutral to oxidising conditions, $log\ \{H_2\}_{25C} \lessapprox -28$, where different).			
		8	9	10	11
Fe	αFeOOH (goethite), solubility	0.09 (0.001)	0.002 (0.001)	0.002	0.01
Cr	$Cr(OH)_3.3H_2O$, Solubility.	0.006	0.006	0.006	0.006
Ni	$\beta Ni(OH)_2$ (theophrastite), Solubility	2700	27	0.30	0.03
Mo / Mn	αFeOOH (goethite)? Partition coefficient in conjunction with solid state composition at oxide surface	Over long timescales, expected to reach steady state where dissolved levels of Mo and Mn are unchanged by passage through cool part of rig. Over shorter timescale, after a change in conditions causing differing levels of Mo and Mn in hot part of rig (and different room temperature partition coefficient), expect net transfer of Mo and Mn between solution and oxide until new steady state is set up			

17.3.4. Kinetics considerations

High temperatures

Kinetics of dissolution and diffusion are relatively rapid at high temperatures of 200 °C and above. If the coolant immediately adjacent to rig walls is assumed to be saturated, diffusion towards the centre of the coolant flow is sufficient to comfortably achieve saturation at any of the flow rates employed in the rig. Kinetics in the solid state involving phase transformations may be slow even at high temperature, so that unstable or metastable phases can persist. Even for the most stable phase, metastable forms of that phase are to be expected, having for example smaller crystallite size and less crystallinity than the true equilibrium forms, to which they slowly age over a period of weeks or months. This latter effect may cause measured solubility to be higher than expected from equilibrium solubility, for the earliest samples.

Room temperature

If mass transport is again considered to be the rate controlling step of dissolution and precipitation processes, then significant progress can be expected towards a new equilibrium with oxides present in the sampling line at room temperature, depending on the flow rate. On the other hand, progress towards room temperature equilibrium may be much less than predicted in this way, since the surface reaction stage of dissolution and precipitation processes can be kinetically limited at room temperature.

In addition to the stable oxide phases at room temperature, metastable phases may be present if kinetically favoured, and other phases may be present in the form of particles transported from the high temperature parts of the rig. The last few millimetres or centimetres of the sampling line are expected to have oxidising conditions, in which the solubility of any oxide particles transported from elsewhere in the rig may be very high, but dissolution is limited by kinetics and a short residence time. Soluble levels may be proportional to particulate number density in this region as well as solubility.

The corroding walls of the sampling line may contribute their own corrosion products also, at supersaturated levels.

Effect of flow rate

Expected soluble levels can be expected to depend on three locations, as shown in Table 17.10. Slower flow rates would cause an increased influence of the latter two locations on effluent soluble concentrations.

Table 17.10. influence of key regions of the rig on dissolved concentrations

Location	Residence time	kinetics	Progress to new equilibrium
Hot parts of rig	long	fast	Full
Sampling line - reducing	Medium	Slow	intermediate
Sampling line - oxidising	short	slow	Small (unless high density of particles on filter). May have significant impact where solubility is great.

Effect of time since latest addition of new steel components

Soluble levels in the effluent can in general be expected to fall gradually over time, especially for the first days and weeks, as oxides age to more stable forms. Under conditions where Mo or Mn have very high solubility, their concentration in effluent may be limited by the rate of solid state diffusion to the oxide surfaces, as they are leached from the oxides.

Effect of stagnant conditions in sampling line

Where the sampling line was left stagnant between runs, the influence of the sampling line on effluent levels could be observed by comparison against other samples.

Effect of particulates

When filters were in place at the sampling point, particulates could not affect effluent levels directly. Instead, they appear to have entered samples as soluble ions, dissolved from filters. Bolz found that almost all particles dissolved on filters over a period of several hours [36]. In this way filters may help even out fluctuations in overall effluent levels (particulate plus soluble together) caused by the stochastic nature of particulate transport.

On a few occasions a large deposit of particles was found in the filter housing, a little further upstream from the rig exit (see chapter 11). These particles, apparently high temperature oxides from the hot part of the rig, may have been far enough from the rig exit to avoid strongly oxidising conditions, but would likely have affected soluble levels since they are not stable phases at room temperature.

A particle observed on a filter during the last session of rig use (see chapter 11) was found to be similar in composition to the outer layer oxide at high temperature, but heavily depleted in Ni and enriched in Mn. This suggests that leaching of Ni from mixed spinel phases could be a source of Ni in effluent samples. This mechanism is a plausible explanation for the high ratio of Ni:Fe, around 3, seen in the effluent during session 4 of rig use, which would not be expected for high temperature

dissolution from non-stoichiometric nickel ferrite, nor from direct inclusion of ferrite particles in effluent samples.

17.3.5. summary of model

hydrogen concentration as given by the hydrogen concentration model applies to the latter portions of the heated part of the rig, and almost the whole length of the sampling line. Oxidising conditions apply for the last few mm or cm. Expected solubility of Fe, Cr, and Ni from respective stable phases are given in Table 17.7 for reducing conditions, and in Table 17.9 for oxidising conditions at room temperature. Ni levels represent an upper bound, as levels may be lower in equilibrium with mixed ferrite phase.

Levels of Fe, Cr and Ni may be similar to levels in the table, suggesting that simple dissolution and precipitation reactions dominate the effluent levels. In some cases effluent levels are much greater, and vary in a stochastic manner, or build and fall over time in a way which does not correlate with changing solubility. In this case the presence of particulates is implied. These may enter effluent samples directly, or indirectly by dissolution of high temperature oxide particles in the sampling line (particularly in the oxidising conditions near the end or on filters) where they are metastable or unstable phases.

17.4. Models to predict nature and behaviour of particulates

The model can be summarised as follows:

- Particles are created in several ways
    - early on, colloids formed at high temperature from supersaturated solution, particularly for Ni-based phases.
    - Larger particles caused by erosion of outer layer crystallites from high temperature parts of rig, particularly during events such as boiling in the hot part of the rig.
    - Particles also caused by corrosion in the room temperature part of rig – Fe and Ni (not Cr) seem to be fully released to coolant, perhaps as supersaturated csolution, forming colloids.
- Inventory of particles builds and changes over time
    - This is partly because the source of circulating particles – outer layer crystallites – become larger, more numerous, and more chemically stable over time
    - Also, inventory of eroded and re-deposited particles grows over time until reaching steady state – these become re-entrained in the flow much more readily than outer layer crystallites which have not yet eroded.
- Across a particular size range, may expect a fairly flat distribution of contribution to mass concentration, per unit size range. I.e. 0 – 0.5 µm, 0.5 – 1 µm, 1 – 1.5 µm and 1.5 – 2 µm equally important contributions to the total.
    - At very small sizes, around 10 nm, colloids may have a significant contribution to overall mass concentration (e.g. similar contribution from 5 – 15 nm colloids as from 0.5 – 2 µm particles)?
- Where the coolant travels upwards, only particles below a certain size can be sustained in the flow (dependent on factors such as particle density and flow velocity).
- Where the coolant flows horizontally, gravitational settling occurs, preferentially for larger particles.
- Flow disturbances cause a spike in levels of particulates in coolant, which gradually falls over time.
- Particles may take time to propagate along the tubing through multiple release and deposition events, causing a gradual build-up over time in some circumstances.

17.5. Overview of models and assumptions which feed into overall model

From the three tightly controlled parameters – pH, temperature (T), and mass flow rate ($\dot{m}$) – as well as elapsed time, t, and parameters describing the geometry of the rig (such as the length, inner radius, and orientation of the different sections of tubing), dependent parameters can be calculated simply from literature data and fitting functions, such as water density and velocity, and diffusivity of aqueous species, with a reasonably high degree of certainty.

Other parameters are subject to a greater degree of uncertainty, and their values are to some extent subjects of the study. Primary among these is the hydrogen fugacity, upon which many other variables depend. Hydrogen fugacity, in turn, is dependent on corrosion characteristics such as corrosion rate, and mechanism (namely the proportion of corrosion hydrogen retained in the walls), for which there is some uncertainty and variability, as well as the possibility of leakage from the rig.

The greatest degree of uncertainty accompanies the presence of corrosion products in the coolant, and in the effluent (as measured), their make-up in terms of soluble and particulate fractions, and phenomena governing their behaviour – particularly the influence of the sampling line in adding or removing corrosion products present at high temperature. These quantities are all influenced by the foregoing parameters such as hydrogen fugacity, zeta potential and flow characteristics.

Table 17.11 below represents the different sources and categories of parameter, starting with the controlled and simply dependent parameters and working through intermediate modelled parameters to the parameters of most interest – but highest uncertainty – regarding soluble and particulate corrosion products. In the first column of the table, categories are assigned a level from 1 to 5, with each subsequent level building on all the preceding levels, resulting in a great deal of uncertainty over expected levels in the effluent and the mechanisms responsible.

Table 17.11. An overview of all quantities considered in rig models, grouped by category, 'level' and by the route by which they were determined (sources). Each level builds on the preceding levels. Some quantities covered were considered in more detail than others – some were simply calculated, some were calculated according to models, some were considered qualitatively according to a model or assumptions, and some (such as nucleation and growth of colloids) were considered only briefly.

Level / sources:	*Category*	*Quantities covered*
1. Literature data and known parameters of the rig	Controlled parameters, and time	pH; temperature (T); mass flow rate ($\dot{m}$); time (t)
	Rig geometry	Displacement from beginning of rig, z; Inner radius, R(z); orientation (horizontal/ascending/descending); presence or lack of chips
	Derived coolant parameters	Density (ρ); Reynolds number (Re); average velocity, $v_{av}(z)$; velocity profile, $v(r/R, z)$; diffusivity of species A (D_A)
1. Literature studies, particularly the study by Morrison [26], as summarised in Table 3.1	Corrosion	High T corrosion kinetics (200 – 300 °C); room T corrosion kinetics; approximate morphology and composition of corrosion film
2. Simple models (see models, in this chapter, for references)	Hydrogen (and oxygen) fugacity	Steady state hydrogen concentration in effluent (C_{ss}); location-dependence of hydrogen concentration in rig: dC/dz, dC/dr, C(z,r,t)
3. Literature data, assumptions, above hydrogen models	Electrostatic potentials	Coolant reduction potential; Corrosion potential, E_{corr}; zeta potential (and the related pH_{PZC})
	Equilibrium solubility	Equilibrium solubilities, at high temperature and room temperature, for metal oxides, at hydrogen levels calculated in models; Qualitative aspects of Mo and Mn partition between solution and spinels (as minor components) which might be expected per some simple assumptions See chapters 4 and 14, and section 17.3
4. Literature studies, simple qualitative modeling and assumptions, all above modeled quantities	particulates	erosion of outer layer crystallites on corrosion film; precipitation and growth of colloids in solution; flocculation (dependent on zeta potentials); deposition and re-entrainment
5. Modeling and assumptions taking account of all the above	Overall concentrations of elements in effluent	Interaction between particulate and soluble forms (elevated solubility due to small particles, dissolution/precipitation reactions between solution and particles or walls); effects of sampling line; effects of flow rate on particles; deposition on filter holders; dissolution of particles trapped on filters; expected overall behaviour of effluent concentrations

17.6. Micro-model to account for localised conditions and geometry of the rig

This model treats the changing conditions experienced by coolant as it progresses through the rig, and the ways in which this may ultimately affect effluent concentrations of corrosion products.

The geometry of the rig is modeled, including the speed and direction of flow (horizontal, upwards or downwards), and any impacts on particle behaviour are discussed. Diffusivity data is used to estimate concentration profiles for hydrogen, and assess kinetics of mass transport of dissolved cations (a key step in the process of oxide-coolant equilibration). The impact of solubility gradients, set up by hydrogen concentration gradients, is discussed.

The local effects of temperature gradients where coolant enters and exits the oven are considered. The diffusion of oxygen upstream from the point of exit from the rig is also considered.

In summary, the following effects are considered:

- Rig geometry, and effect on flow velocity and particulate behaviour
- Corrosion products in feedwater
- Hydrogen concentration as a function of position in rig, and impact on CP transport
- Temperature gradients, and effect on flow, solubility, and particulate behaviour
- Oxygen ingress (and hydrogen egress) at the sampling point
- Transient conditions, including boiling on a few occasions

17.6.1. Overview of model

In this simple model, the rig is divided into eight regions, starting with the feedwater barrel and finishing with the sampling line. Conditions in each region as predicted by the model are listed and described in Table 17.12. A key point to consider is that the model assumes a gradual build-up of hydrogen fugacity on passage through the rig. This is because upstream diffusion is limited in Hagen-Poiseuille (fully developed laminar) flow, even for dissolved hydrogen in very slowly flowing coolant (see section 17.6.4). Transient effects and other disruptions to the flow pattern (such as convection currents) could cause more efficient mixing than the model predicts, particularly at 0.1 g/min where residence time in the flowing part of the rig is on the order of 20 hours.

Table 17.12. Predicted conditions in each section of the rig, according to model.

Region / conditions	**T, p**	**Hydrogen fugacity**	**Mean flow velocity**	**Concentration of selected elements (ppb)**
Feedwater barrel	~25 °C, 1.7 bara	~neutral? (~ 10^{-28} bar)	No flow; agitation by nitrogen bubbling	Expected: effectively zero (same as blank samples) Measured: pH 11 (just one sample) Fe, Ni, Cr, Mo, Mn -0.4, 2.3, 0.9, 2.0, -0.1
1/8" tubing to pump inlet	~25 °C, 1.7 bara	building to ~1 x 10^{-6} bar at 1 g/min ~1 x 10^{-5} bar at 0.1 g/min or ~ neutral if O_2 removal was not 100% effective.	Up to 11 mm/s (at 1 g/min)	Expected: kinetics too slow for equilibrium solubility? Cations are released from steel, may form colloidal particles from solution Measured: Fe (pH 9): 0.5 ($\dot{m}$=1); 2.5 ($\dot{m}$=0.1) Fe (pH 10): 0.0 ($\dot{m}$= 0.1 and 0.1), outliers at 0.4, 0.5, 1.1. Fe (pH 11): 1.0 ($\dot{m}$=2) Model: Fe (pH 9 and 10): up to 0.2 ($\dot{m}$=1); 2.0 ($\dot{m}$=0.1)
¼" tubing from pump to oven	~25 °C, 100 bara	building to ~ double the levels reached in 1/8" tubing (or ~ neutral if O_2 persists)	Up to 2.3 mm/s (at 1 g/min)	Model: Fe (pH 9 and 10): up to 0.4 ($\dot{m}$=1); up to 4.0 ($\dot{m}$=0.1)
¼" tubing in oven leading to reaction cell	200 to 300 °C, 100 bara	Building to ~ 20% of effluent levels	Up to 3.2 mm/s (at 1 g/min) at 300 °C. Thermal	Building to equilibrium levels for prevailing conditions. Intermediate temperatures on entering oven, and relatively low hydrogen concentration may cause supersaturation

		(section 17.2.5)	Convection?	with respect to conditions downstream, resulting in colloidal particulates.
1" tubing: reaction cell	200 to 300 °C, 100 bara	Building to ~ 80% of effluent levels	Up to 67 µm/s (1 g/min, 300 °C)	Dissolved Fe should reach equilibrium easily, but particulates may also be present. Slow velocity may cause particulates above a certain size to settle out, to an extent which depends on flow rate.
¼" tubing in oven downstream of reaction cell	200 to 300 °C, 100 bara	Building to ~ 100% of effluent levels	Up to 3.2 mm/s (at 1 g/min) at 300 °C. Thermal Convection?	equilibrium levels of dissolved Fe and Ni, plus particulate matter. Particulates may become caught up in flow due to convection currents in the vicinity where tubing exits oven. Higher levels of particulates expected at faster flow
¼" tubing leading to BPR	~25 °C, 100 bara	~ 100% of effluent levels	Up to 2.3 mm/s (at 1 g/min)	Solubility is generally much lower than in the heated portion of the rig, therefore dissolved Fe is likely to precipitate from solution as colloidal particles, or be lost from the coolant by precipitating on tube walls. Less settling of particulates and less precipitation of dissolved Fe on rig walls expected at faster flow
¼" tubing leading to rig exit	~25 °C, 1 bara	~ 100% of effluent levels for the majority of the length, falling to zero over the last few cm. oxygen present in last cm or so.	Up to 2.3 mm/s (at 1 g/min)	As for pressurised tubing leading to BPR, but oxidising conditions near the exit point could cause very high solubility of any ferrite particulates residing there (up to 58 ppb Fe at pH 9; up to 160 ppb Fe and pH 10; up to ~ 1000 ppb at pH 11)

17.6.2. Hydrogen production in room temperature parts of rig.

Corrosion rate of SS316L at room temperature has been taken to be a steady value of 0.8 ng dm^{-2} h^{-1}, as a very approximate reference value, based on a corrosion rate of ~ 10^{-6} cm over the course of 1000 h in pure water for a corrosion film of constant thickness of 4 nm, see figure 3 in reference [73], and the density of SS316L, ~8 g/cc.

1/8" tubing

The 1/8" tubing has an inner radius of 0.6985 mm, and length of ~2 m, giving a surface area of 0.88 dm^2, and an absolute corrosion rate of 0.70 ng h^{-1}. Using the molar weight of the alloy, 56.1 g, this can be expressed alternatively as 0.013 nano mole alloy h^{-1}. The approximate stoichiometry of the corrosion reaction can be written as follows, having a molar ratio of hydrogen molecules to metal atoms of 1.5:

$$2Me + 3H_2O \rightarrow Me_2O_3 + 3H_2$$

The majority of metal will be in the trivalent oxidation state, regardless of whether it is in the aqueous or solid state – apart from nickel, which is in the divalent state in either case, but this will have only a small effect which is neglected for the purposes of the model.

Using the ratio of 1.5, this gives 0.019 nano mole H_2 h^{-1}. However, it is assumed that 90% is retained within the alloy (see section 5.4 on hydrogen production), giving 0.0019 nano mole h^{-1} released to solution. At a flow rate of 1 g/min, this results in a hydrogen concentration of 3.1 x 10^{-11} molal by the time the feedwater enters the pump – that is, 4.0 x 10^{-8} bar H_2. In this case, the stable Fe species will actually be Fe_3O_4, for anything above ~ 10^{-12} bar hydrogen, which would be reached at about one-thousandth of the way along the tubing (~2 mm). The average oxidation state in solution is close to that of magnetite, i.e. 2.67+, at hydrogen concentrations in this range. Therefore a hydrogen to metal molar ratio of 4/3 should instead be used, giving 2.8 x 10^{-11} molal (3.6 x 10^{-8} bar) H_2. If nitrogen sparging was not 100% efficient at removing oxygen gas, then some may remain to be used in oxidation of the steel – in this case conditions would remain oxidising.

If all the Fe, Ni and Cr produced were released to the feedwater, this would result in 0.008 ppb Fe, 0.002 ppb Cr, and 0.002 ppb Ni at 1 g/min, rising to 0.08, 0.02 and 0.02 respectively at 0.1 g/min. Observed levels of Cr in feedwater were at similar values, but levels of Fe and Ni were much greater. This implies either that a much faster effective corrosion rate occurred, with correspondingly higher

hydrogen levels; or that pieces of unoxidised steel broke off from the tubing, providing the bulk of the Fe and Ni recorded in feedwater samples, but without the corresponding hydrogen production.

In either case, solubility of Fe is very low and the Fe observed in feedwater is almost entirely in particulate form. Table 17.13 compares the level of Fe expected from corrosion rates, against levels observed, and an adjusted corrosion rate is proposed to account for observed Fe levels.

Table 17.13. Comparison of expected Fe levels with observed levels in feedwater samples, and a suggested correction to the assumed corrosion rate and hydrogen levels as a result of discrepancies therein.
$Fe_{\_corr}$ represents the expected (upper limit) concentration of Fe in the feedwater according to corrosion at the assumed rate, and is calculated by assuming 100% of corroded material releases to coolant; $Fe_{\_sol}$ is solubility of magnetite at assumed hydrogen fugacity (resulting from corrosion at the assumed rate).
An adjustment is made to the assumed corrosion rate such that the resulting adjusted value of Fe_{corr} is consistent with observed levels. A typical adjustment factor employed was 25x for pH 9 and 10, and 250x for pH 11. The adjusted Fe_{corr} and hydrogen pressure are tabulated. Adjusted Fe_{sol} is also tabulated, and is in each case considerably lower than Fe_{corr}, demonstrating the presence of particulates, or at least of a very high degree of supersaturation, of Fe in the feedwater.

	Expected Fe_{corr}, (Fe_{sol})	Observed Fe	Adjusted Fe_{corr}	Adjusted H_2, (adjusted Fe_{sol})	
pH 9, 1 g/min	.008 (.02)	.5 +/- .1 (sess 5)	(50x) → 0.4	2E-6 bar, (.08)	
pH 9, 0.1 g/min	.08 (.05)	2.5 (sess 5) .6 +/- .3 (sess 4)	(50x) → 4.0 (10x) → 0.8	2E-5 bar, (.17) 4E-6 bar, (.10)	
pH 10, 1 g/min and 0.1 g/min	.008 (.001) and .08 (.001)	.0 typical; .4, .5, 1.1 outliers; .2 average (sess6)	(25x) → 0.2 (25x) → 2.0	1E-6 bar (.00) 1E-5 bar (.00)	
pH 11, 2 g/min	.004 (.003)	1.0 +/- 0.4 (sess2)	(250x)→1.0	5E-6 bar (.00)	

1/4" tubing

Based on the adjusted room temperature corrosion rate of 25 x 0.8 = 20 ng dm^{-2} h^{-1}, the 1 metre of ¼" tubing leading to the oven, of surface area ~ 1.0 dm^2, corrodes at an absolute rate of 20 ng h^{-1}, providing 0.05 nano mole h^{-1} of hydrogen to the feedwater. Combined with the 0.9 dm^2 of 1/8" tubing treated above, levels of hydrogen, and potential levels of Fe and Ni if they are fully released to the coolant, are approximately doubled.

17.6.3. Hydrogen production in heated parts of rig.

The volume flow rate in the heated parts if the rig, and thus the residence times in each part, varies according to temperature, because of the temperature dependence of water density. The sections of ¼" tubing before and after the reaction cell each have volume of 4.4 ml, and the reaction cell itself has volume of around 120 ml. Residence times in each portion are thus (in minutes, for a flow rate of 1 g/min) 3.1, 85.8, and 3.1 at 300 °C; 3.5, 96.7, and 3.5 at 250 °C; and 3.8, 104.5, and 3.8 at 200 °C.

Each 60 cm section of ¼" tubing has internal surface area 0.6 dm^2, and the reaction cell has internal surface area 2.2 dm^2. The corrosion rate slows over time, as the protective oxide film grows thicker, as modelled in chapter 7.6.

Corrosion rate is given by $\frac{dw}{dt} = \frac{1}{2} k_p t^{-\frac{1}{2}}$. To give a representative value of corrosion rate, the rate constant selected from literature data for conditions of pH_{25C} 9, 300 °C is used (k_p = 0.52 mg dm^{-2} $h^{-1/2}$ [26], see Table 3.1), with t = 1000 h total corrosion time at pH 9, 300 °C. Corrosion rate under these conditions is 0.0082 mg dm^{-2} h^{-1}. This gives absolute corrosion rate of 0.0047 mg h^{-1} in each section of ¼" tubing, and 0.018 mg h^{-1} in the reaction cell. Modelled levels of Fe released would in this case increase from 0.4 ppb in the room temperature sections pre-oven, with addition of a further 51 ppb contribution from each section of ¼" tubing and 196 ppb from the reaction chamber (about 300 ppb in total), though in the high temperatures of the heated parts of the rig kinetics are fast enough that thermodynamic equilibria become important, and coolant is controlled at saturation levels by the precipitation of oxide crystallites, which is where the majority of oxidised Fe, Cr and Ni ends up. The full amounts of Cr, Ni, Mo and Mn passing to the oxide film per hour at this corrosion rate, in ppb are 80, 60, 11, and 8.

The amount of hydrogen produced is 1.9 x 10^{-10} molal in each section of ¼" tubing, and 7.1 x 10^{-10} molal in the reaction cell. That's 11 x 10^{-10} molal in total, or 1.4 x 10^{-5} bar H_2, in addition to the 4 x 10^{-8} bar already present.

Hydrogen will have built to one tenth its final value a little over half-way (~35 cm) through the first section of ¼" tubing, and one hundredth its final value after around 3.5 cm, though in reality this may occur a little further along the pipe as it takes a few cm for temperature to settle at the rig temperature. It is expected that very close to 100% saturation of dissolved iron may be achieved by the end of the hot part of the rig, and that coolant near the rig walls will reach saturation within a few mm of entering the oven, therefore the lower hydrogen fugacity and temperature in this region could be a cause for saturated Fe levels to soon become supersaturated as advection takes the Fe to regions of higher temperature and hydrogen fugacity where in some situations the solubility is

lower. This is the case in the example under consideration here: once the temperature gets close to 300 °C (there is a positive temperature coefficient of solubility under these conditions), the lower hydrogen fugacity in the upstream portion of the heated part of the rig causes greater solubility, with hydrogen fugacity being at least a factor of 10 lower than its final value for the first half of the first section of ¼" tubing. At 1 g/min, residence time in this region is only about a minute and a half, but at 0.1 g/min the residence time increases to 15 minutes and the ratio of local hydrogen fugacity to final hydrogen fugacity at any given point is the same regardless of flow rate and corrosion rate, therefore the propensity to dissolve Fe to levels which are subsequently supersaturated may increase at slower flow rates. At slower flow however there is also additional time for particulates to dissolve or settle out, and in the slower upwards velocity in the reaction cell there is decreased ability to carry particulates upwards against gravity. A similar effect is expected in the region where the ¼" tubing downstream of the reaction cell leads out of the oven, as intermediate temperatures result in higher or lower solubility (lower, for the conditions illustrated above), yet still fast enough corrosion kinetics that outer layer crystallites are available for dissolution. In addition, the ¼" tubing enters and exits the oven at a horizontal orientation, and so convection currents are possible at these locations, as the hotter, less dense water at the underside of the tube on entering the oven (or in the centre of flow on exiting the oven) exchanges with cooler, denser water in the centre of flow on entering the oven (or against the top surface of the tube on exiting the oven). Since the fully developed (Hagen-Pouiseuille) flow at the flow rates employed has such a slow velocity, these flow disturbances could be significant in terms of the release and deposition of particulate matter from the tubing walls. Fully developed flow is restored after just a few cm, see following section.

17.6.4. Properties of the flow

Reynolds number

Dimensionless parameters can be used to describe characteristics of a flow, such as the well-known Reynolds number, Re, given by:

$$Re = \rho . U . L / \mu$$

Where ρ is fluid (water) density, U is the free stream velocity (mean flow velocity), L is a characteristic length scale selected according to the context, and μ is dynamic viscosity of the fluid. For flow in a cylindrical pipe, L is the inner diameter of the pipe, D_H. Transition from laminar to turbulent flow begins at Re_{crit} of 2300 in a straight tube, or higher in pipe bends [136].

For a fixed mass flow rate, $\dot{m}$, average velocity is given by

$$U = \frac{4\dot{m}}{\pi\rho D_H^2}$$

And therefore Re is given by

$$Re = \frac{4\dot{m}}{\pi\mu D_H}$$

Table 17.14 shows values of Re and other relevant quantities at selected temperatures, for a 1 g/min flow rate. For the reaction cell filled with chips, the average velocity is almost unchanged (the volume fraction of chips within the cell is only 0.04), but the relevant length scale in this case is the gap between chips, estimated at 0.5 mm, resulting in a much lower Re in this region. Flow in the rig is comfortably within the range for laminar flow under all conditions employed.

Table 17.14. Reynolds number and related quantities for selected conditions, at 1 g/min flow rate.

	25 °C	50 °C	200 °C	250 °C	300 °C
μ (kg m^{-1} s^{-1})	8.99 x 10^{-4}	5.57 x 10^{-4}	1.41 x 10^{-4}	1.14 x 10^{-4}	9.01 x 10^{-5}
Re (1/8" tubing)	16.9	-	-	-	-
Re (1/4" tubing)	7.7	12.5	49.4	61.1	77.3
Re (1" tubing: reaction cell)	1.1	1.8	7.1	8.8	11.2
Re (reaction cell, with chips)	-	-	0.002	0.002	0.003

Diffusivity, and related quantities

Findings from a literature paper on upstream diffusion [201] were used to assess the extent to which oxygen from the laboratory air could be expected to diffuse into the sampling line, causing conditions to become oxidising and affecting any dissolution or precipitation processes there.

The authors of the paper used separation of variables to solve for concentration at any position (r, x), where r is radial distance from centre of pipe and x is distance upstream from the pipe exit. It was found that the solution must be an infinite series of the form:

$$c = \sum_{i=1}^{\infty} a_i R_i(r).\exp(-\lambda_i x)$$

Where a_i are scaling factors to normalise the solution, $R_i(r)$ give the radial form of each term, $\exp(-\lambda_i x)$ is the axial form of each term, and each λ_i gets successively larger (i.e. $\lambda_{i+1} > \lambda_i$). However, it was also found that the contribution from terms beyond the first term becomes vanishingly small within a small distance from the pipe exit, with $\frac{\exp(-\lambda_2 x)}{\exp(-\lambda_1 x)}$ decreasing below 0.01 within one tube radius, under conditions within the range for which the result is deemed to be valid.

By neglecting all terms other than the first, and setting $a_i = 1$, the asymptotic solution is given:

$$c = R_1(r).\exp(-\lambda_1 x)$$

If the boundary conditions are set up such that the contour for which c=1 follows a specific form, i.e. $x = \lambda_1^{-1}.\ln R_1(r)$, then the asymptotic solution is exact, and contours of equal c follow the same form, shifted along the x-axis:

$$x = \lambda_1^{-1}.\ln R_1(r) + \Delta x; \quad c = \exp(-\lambda_1 \Delta x)$$

If boundary conditions employ a contour of $c = 1$ having a different form, then higher order terms are required to describe contours of constant c near the tube exit, but these contours rapidly conform to the asymptotic form, $x = \lambda_1^{-1}.\ln R_1(r) + \Delta x$. The asymptotic solution is thus fully described by λ_1 and the contour $x = \lambda_1^{-1}.\ln R_1(r)$, and these two quantities are uniquely determined by a dimensionless parameter of the flow: the product of Reynolds number, Re, and Schmidt number, Sc. The solution is deemed to be valid for values of ReSc > 10, and only under fully developed (Hagen-Pouiseuille) laminar flow.

The value of λ_1 is approximately $\lambda_1 = 1.4\ (ReSc)^{1/2}$, and the form of $x = \lambda_1^{-1}.\ln R_1(r)$ is a function of ReSc, as plotted for several values of ReSc in Figure 17.14 below.

Sc is given by the following, where μ is dynamic viscosity of the fluid, ρ is fluid density, and D is diffusivity of the species of interest:

$$Sc = \frac{\mu}{\rho D}$$

Using the relation derived earlier for Re at fixed mass flow rate, gives:

$$ReSc = \frac{4\dot{m}}{\pi \rho D_H D}$$

Table 17.15 tabulates ReSc, and related parameters, for 1 g/min flow in the rig. The situation of most interest to this project is for oxygen diffusing upstream from the rig exit. At 1 g/min, this yields ReSc ≈ 400, with contours of equal oxygen concentration having a form somewhere between that of the contours for ReSc = 250 and ReSc = 1000. The value of λ_1 in this case is 24 mm^{-1}, which corresponds to a factor of 10 decrease in oxygen fugacity every 96 µm. That results in a decrease in oxygen fugacity from up to 10^{-1} bar at the rig exit to 10^{-83} bar – the oxygen fugacity in equilibrium with 1 bar of hydrogen fugacity – in a distance of just 7.9 mm; or to neutral oxygen fugacity of 10^{-28} bar in just 2.6 mm. magnetite solubility falls to below 0.01 at oxygen fugacity below ~ 10^{-50}, at pH 9; ~ 10^{-55}, at pH 10; and ~ 10^{-60}, at pH 11 (before climbing again at sufficiently high hydrogen fugacity, as conditions become more reducing).

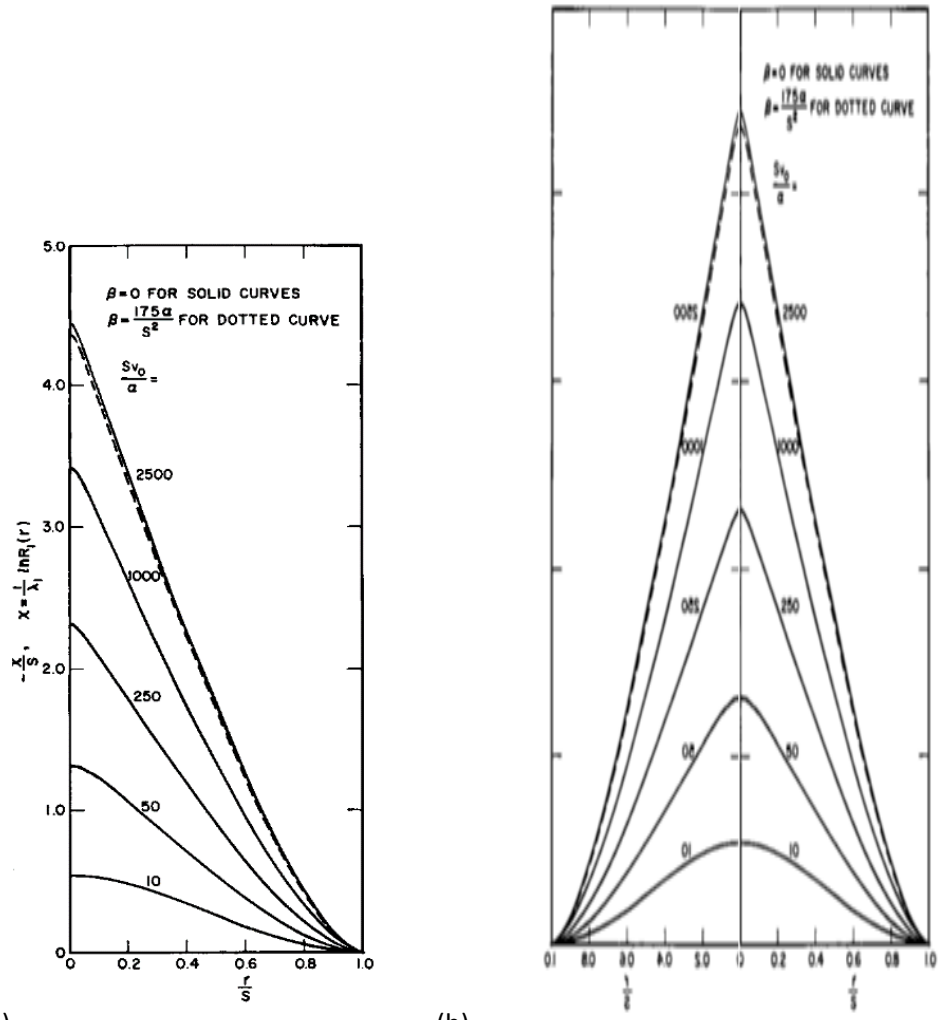

(a) (b)

Figure 17.14. Contours of equal concentration, for the asymptotic solution of the problem of upstream diffusion at the point of exit of Hagen-Poiseuille flow from a pipe to a reservoir. From Passell and Perry [201].

(a) Form of the contour of equal concentration, $x = \lambda_1^{-1}.ln\ R_1(r)$, for the asymptotic solution, versus radial distance from centre of tube, r, for selected values of ReSc (written here as Sv_0/α). Both ordinate (x) and abscissa (r) are expressed in normalised unitless form, by dividing by tube radius, s. The dashed line represents the effect of loss through radioactive decay, and is not relevant for the current study. (b) – the plot from (a) is reflected in the y-axis, and stretched so that distances in the x- and y- directions are to the same scale, to facilitate visualisation.

At 0.1 g/min, ReSc ≈ 40, and a factor of 10 decrease in oxygen fugacity occurs every 136 μm.

1. The solution provided in the paper, [201], is valid for fully developed laminar flow. Flow disturbances created as drips form and fall at the end of the sampling line may allow oxygen to diffuse a few mm further upstream.
2. The shape of equal concentration contours means that oxygen may penetrate a further 7.7 mm at 1 g/min, or 3.7 mm at 0.1 g/min, along the pipe walls where flow is slowest.

The diffusivity of hydrogen is about 2.5 times greater than that of oxygen, giving a value of λ_1 which is $\sqrt{2.5} = 1.6$ times smaller, so in the equivalent situation for hydrogen gas, hydrogen would penetrate about 1.6 times further. This model is not directly applicable to the degassing of hydrogen at the exit line, but the similar diffusivity suggests that hydrogen would remain present to a high concentration for most of the length of the tube.

Table 17.15. ReSc, and related parameters, for 1 g/min flow in the rig

	25 °C **	100 °C	200 °C	250 °C	300 °C
ρ (kg m^{-3}) †	1001 (997)	963	871	806	715
μ (10^{-3} Pa s) [29]	0.889 (0.890)	0.284	0.137	0.108	0.0864
D_{water} (10^{-9} m^2 s^{-1}) ‡	2.50 (2.44)	7.44	17.5	24.1	33.1
$D_{O2(aq)}$ (10^{-9} m^2 s^{-1}) ‡	2.38 (2.56)	7.78	16.5	22.6	32.1
$D_{H2(aq)}$ (10^{-9} m^2 s^{-1}) ‡	6.42 (6.37)	15.6	33.3	46.2	66.5
$D_{CO2(aq)}$ (10^{-9} m^2 s^{-1}) [202], [203]	1.7				
$D_{Fe2+(aq)}$ (10^{-9} m^2 s^{-1}) *	0.6 [20]	2.4	6.2	8.7	12
$D_{Ni2+(aq)}$ (10^{-9} m^2 s^{-1}) *	0.7 [204]	2.7	7.0	9.8	13
ReSc (1/8” tubing), H_2	2364 (2392)	1011	524	407	319
ReSc (1/4” tubing), H_2	1083 (1096)	463	240	187	146
ReSc (1” tubing: reaction cell), H_2	157 (158)	67	35	27	21
ReSc (1/8” tubing), O_2	6376 (5952)	2027	1057	834	662
ReSc (1/4” tubing), O_2	2922 (2728)	929	484	382	303
ReSc (1” tubing: reaction cell), O_2	423 (394)	134	70	55	44
ReSc (reaction cell, with chips)					
$(ReSc)^{1/2}$ (1/4” tubing), O_2	54 (52)	30	22	20	17

† using the fit provided in [19], [173]

‡ calculated from the 14 parameter fit from [205], using density as determined in the table

* 25 °C data extrapolated to higher temperatures using the relation $D \propto T/\mu$ from the Wilke-Chang correlation [21], [22]

** figures in parentheses are for 1 bara pressure.

17.6.5. Solubility of Ni from Ni metal, nickel oxides, and spinels

Table 17.7 shows Ni solubility from various crystalline phases. At low levels of hydrogen, NiO is the stable Ni-based phase, having solubility of ~ 0.4 ppb at 300 °C across a wide range of pH values. Above approximately the level of hydrogen resulting from saturation with 1 atm at 25 °C (~17.7 scc/kg), Ni metal becomes the stable phase, having solubility which rapidly falls with increasing hydrogen fugacity, as [Ni] $\propto \frac{1}{\{H_2\}}$. With 25 – 50 scc/kg dissolved hydrogen, Ni is the stable phase, having solubility ~0.2 ppb at 300 °C. Transition between Ni and NiO is characterised by slow kinetics, particularly below 200 °C, so the high solubility of Ni under less reducing conditions is relevant even where it is not the thermodynamically stable phase.

Where spinel oxides are present alongside nickel metal, it is the nickel metal which controls Ni levels in the coolant, with Fe levels from the mixed ferrite oxide being comparable to or a little lower than that for magnetite. With increasing hydrogen fugacity, nickel solubility decreases; in turn, the lower Ni levels in solution reach equilibrium with a lower saturation concentration of NiO in solid solution in the ferrite (falling x in $Ni_xFe_{3-x}O_4$) – this can be seen in the Fe-rich solvus composition of Figure 4.4: At log $\{O_2\}$ = -33 (log $\{H_2\}$ ~ 0, ~ 18 scc/kg H_2), x = 0.9; whilst at log $\{O_2\}$ = -35 (log $\{H_2\}$ ~ 1, ~ 180 scc/kg H_2), x = 0.15. If the Ni content of the spinels is below saturation, then equilibrium levels of Ni in solution decrease accordingly from Ni solubility levels.

Table 17.16. A comparison of solubilities of Ni-based crystalline phases.
For NiO(cr), the stable phase under sufficiently oxidising conditions, hydrogen fugacity has no effect on solubility. The dominant ion in solution is indicated in the table, with $Ni(OH)_2(aq)$ providing a steady solubility having no dependence on pH and limited dependence on temperature. At lower temperatures and pH values Ni^{2+} dominates, having much higher solubility.
At higher hydrogen fugacities (as indicated in table), crystalline Ni becomes the stable phase, having a solubility which steeply diminishes to negligible values with increasing hydrogen fugacity, as shown in the table for 3 selected hydrogen fugacities. Red font is used to show conditions where Ni metal is not the most stable phase.
Below ~77 °C, $Ni(OH)_2(cr)$ replaces NiO as the stable phase in the presence of water, resulting in slightly lower solubility at 25 °C where present.

[Ni] (ppb) from NiO	*25 °C*	*200 °C*	*300 °C*	$Ni(OH)_2$(cr) at 25 °C
pH 9	150 Ni^{2+}	3 Ni^{2+}	0.4 $Ni(OH)_2$(aq)	20
pH 10	2 Ni^{2+}	0.3 $Ni(OH)_2$(aq)	0.4 $Ni(OH)_2$(aq)	0.3
pH 11	0.2 $Ni(OH)_2$(aq)	0.3 $Ni(OH)_2$(aq)	0.4 $Ni(OH)_2$(aq)	0.03

Critical log $\{H_2\}_{25C}$ of Ni/NiO transition	*25 °C*	*200 °C*	*300 °C*	
	-4.5	-1.4	0	

[Ni] (ppb) from Ni. $\{H_2\}_{25C} = 10^0$ atm.	*25 °C*	*200 °C*	*300 °C*	
pH 9	0.004	0.1	0.4	
pH 10	0.00004	0.01	0.4	
pH 11	0.000006	0.01	0.4	

[Ni] (ppb) from Ni. $\{H_2\}_{25C} = 10^{-3}$ atm.	*25 °C*	*200 °C*	*300 °C*	
pH 9	4	100	400	
pH 10	0.04	13	400	
pH 11	0.006	13	400	

[Ni] (ppb) from Ni. $\{H_2\}_{25C} = 10^{-6}$ atm.	*25 °C*	*200 °C*	*300 °C*	
pH 9	4000	100,000	400,000	
pH 10	40	13,000	400,000	
pH 11	10	13,000	400,000	

17.6.6. Solubility of Mo from MoO_2 and from mixed ferrites

Wang et al. [131] analysed solubility and thermochemical data for Mo and Mo oxides from various studies, including their own. They produced potential pH diagrams, reproduced here in Figure 4.12. The boundary between MoO_2 oxide and soluble MoO_4^{2-} ions represents solubility of ~100 ppb in the

upper plot and 1000 ppm in the lower plot. At pH 9-11, close to the hydrogen line, Mo solubility could therefore be similar to 100 ppb, or higher, and increases with increasing pH. Mo solubility also appears to increase with increasing pH. Mo solubility also appears to increase with potential, i.e. at low hydrogen fugacities. This is because on dissolving Mo is oxidised from Mo(IV) in the oxide to Mo(VI) in solution.

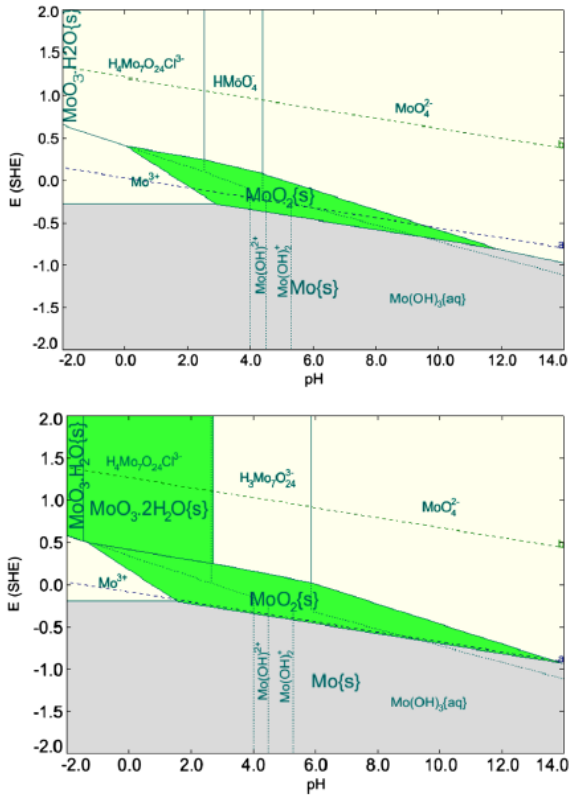

Figure 17.15. Potential-pH diagrams for Mo at 25 °C, for molal activities of dissolved Mo at 10^{-6} (top) and 10^{-2} (bottom). From [131].

17.6.7. Dissolution / precipitation behaviour of other elements within spinels

Other metallic elements can become incorporated within the spinel structure in small amounts, such as Co, Mn and Mo. Concerning coolant-oxide equilibria, there are some studies regarding Co and Zn in spinels, but a literature search did not yield any for Mn or Mo. In the absence of data, a simple assumption is that levels in solution are proportional to their composition in the oxide, for a given set of coolant conditions. For Ni in Co-Ni-ferrites, this assumption seems to hold reasonably well. However, for Co in Co-Ni-ferrites, this assumption does not seem to hold, as two oxides with very different Co compositions were found to have similar Co solubility [66].

17.7. Mass balance of corrosion product transport in the rig

In this subsection it is shown that, due to the slow flow rates employed in the rig, and low levels of corrosion products in the coolant (dissolved or otherwise), metal oxide corrosion products were almost entirely retained locally in the corrosion film. The only exception to this was the element molybdenum, the release of which was strongly dependent on coolant conditions, especially pH. During several of the sessions of rig use, the cumulative mass of molybdenum released to the effluent from SS316L surfaces (the rig walls, and also the chips added in sessions 5 and 6) exceeded the maximum amount that could have been released by non-selective oxidation of the alloy, according to modeled corrosion rates using Morrison [26] data, and total surface area with and without chips of ~ 20 dm^2 and ~ 2 dm^2 respectively; on one occasion this discrepancy was at least a factor of ten (session 2, discussed later). This degree of extra Mo, in excess of that expected from non-selective oxidation of the alloy, suggests either: leaching from the underlying alloy (i.e. selective oxidation); release from some other source, such as pump bearings; or a gross underestimate of corrosion rates. It is argued below that the former explanation is the most likely. Surveys of particle distribution of the outer layer oxide crystallites were conducted, from SEM images, providing some corroborating evidence that corrosion rates were indeed approximately consistent with those calculated using Morrison [26] data.

17.7.1. Particle size distribution on outer layer oxide

From SEM images of representative regions of the corrosion film, on walls of the rig and on SS316L chips, independent measurements of the outer layer average thickness were made approximately, by surveying the percentage area covered by particles of several size ranges. From this, approximate size distributions were also acquired. Figure 17.16 and Figure 17.17 illustrate the method that was used: a regular grid of around 100 lattice points was drawn (in this case, 13 x 10 = 130); the approximate size of the particle at each intersection point on the grid was noted, according to the size range categories indicated in Table 17.17 and Table 17.18 below; and these data were tabulated and used to calculate other values such as % coverage and contribution to total (mean) film thickness of the outer oxide layer. For calculations, the size of “1 µm” particles was taken to be 1.125 µm – the mid-point of the size range, and 0.1 µm was selected as a representative size of the < 0.25 µm size range. For the smooth side of chips used during session 5, the < 0.25 µm size range contributed around half of the total mass, as calculated, therefore this result is quite sensitive to the assumed representative size of the small particles. This fact together with the fact that the corrosion film can vary with location (such as rough or smooth sides of chips) means that results are indicative

only; in this sense, there is good agreement between these results and calculated values of corrosion film thickness using Morrison [26] data. Comparisons were made between this method of particle counting and a much more thorough method, performed by Ziemniak et al. in their study of electro-polished SS304 corrosion [76], by surveying SEM images included in the paper, and the results compared favourably, with the calculated mass thickness of the outer oxide layer agreeing to within 25% for all 4 instances performed.

The size distribution in Table 17.17 is consistent with that found in the circulating corrosion product particles in PWR primary coolant [120], in that the mass contribution per micron width of size range is approximately equal across a range of sizes, in this case up to ~ 4 µm, though in the PWR study it continued up to ~30 µm (see Figure 5.3 Figure 5.4 of this thesis).

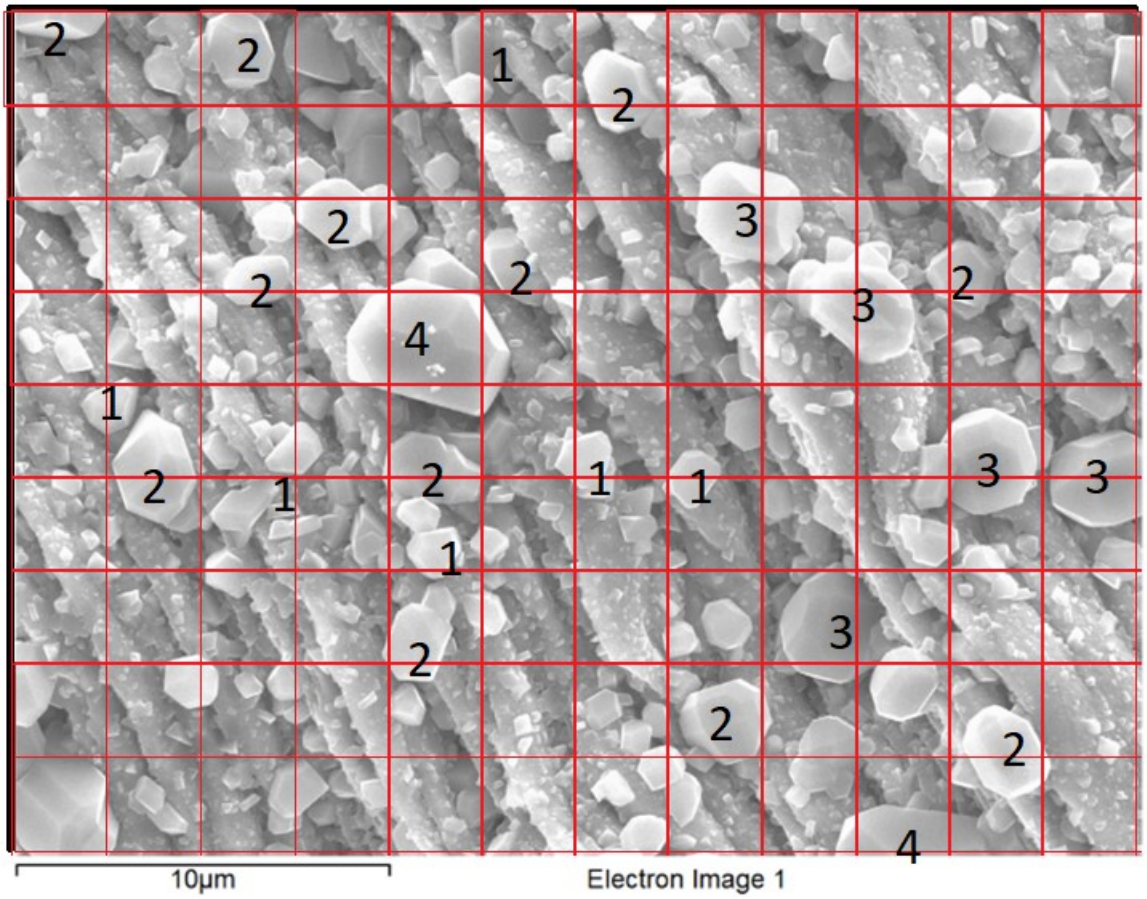

Figure 17.16. Example of a particle coverage survey, from the rough side of one of the SS316L chips used during session 5.
The SEM image used also appears in Figure 10.12. Nominal sizes of some of the crystallites were added to the diagram to facilitate the process.

Table 17.17. Particle Size distribution and coverage, from a survey of the image in Figure 17.16. The number of counts of each particle size (columns 1 and 2) are the only data that were measured, the rest of the table is calculated from those data. Crystallites are modelled as spheres, having mean height of 2/3 x diameter, and density 5.2 g/cm^3.

Size (diameter, µm)	#	Coverage (%)	Thickness (µm)	Thickness (mg dm^{-2})	No. density (# mm^{-2})
5 (4.5 – 5.5)	0	-	-	-	-
4 (3.5 – 4.5)	5	3.8	0.10	5.3	3.1 x 10^3
3 (2.5 – 3.5)	8	6.2	0.12	6.4	8.7 x 10^3
2 (1.5 – 2.5)	12	9.2	0.12	6.4	2.9 x 10^4
1 (0.75 – 1.5)	18	13.8	0.10	5.4	1.8 x 10^5
0.5 (0.25 – 0.75)	14	10.8	0.04	1.9	5.5 x 10^5
0.1 (0 – 0.25)	73	56.2	0.04	1.9	7.1 x 10^7
Sum	*130*	*100.0*	*0.53*	*27.3*	*7.2 x 10^7*

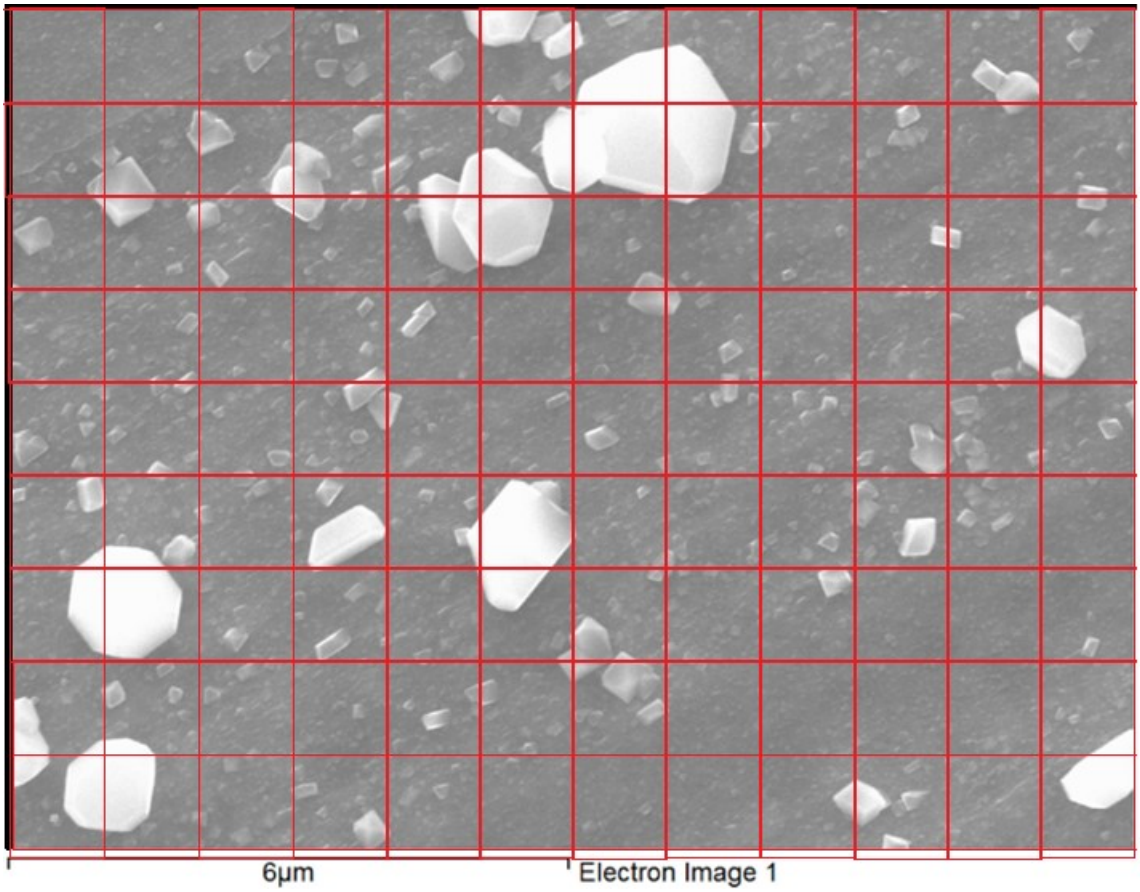

Figure 17.17. Particle size survey, from the smooth side of one of the SS316L chips used during session 5.
The SEM image used also appears in Figure 10.12.

Table 17.18. Particle size distribution and coverage, from a survey of the image in Figure 17.17. The number of counts of each particle size (columns 1 and 2) are the only data that were measured, the rest of the table is calculated from those data. Crystallites are modelled as spheres, having mean height of 2/3 x diameter, and density 5.2 g/cm^3.

Size (diameter, µm)	#	Coverage (%)	Thickness (µm)	Thickness (mg dm^{-2})	No. density (# mm^{-2})
5 (4.5 – 5.5)	0	-	-	-	-
4 (3.5 – 4.5)	0	-	-	-	-
3 (2.5 – 3.5)	0	-	-	-	-
2 (1.5 – 2.5)	2	1.5	0.02	1.1	4.9 x 10^3
1 (0.75 – 1.5)	7	5.4	0.04	1.9	5.4 x 10^4
0.5 (0.25 – 0.75)	5	3.8	0.01	0.7	2.0 x 10^5
0.1 (0 – 0.25)	116	89.2	0.06	3.1	1.1 x 10^8
Sum	*130*	*100.0*	*0.13*	*6.7*	*1.1 x 10^8*

17.7.2. Mass pickup or loss to coolant, per ICP-MS data

By comparing effluent concentrations against feedwater concentrations for each element, per ICP-MS data, it was possible to estimate the mass pickup or loss to coolant for each element, for each session of rig use. These data are presented in Table 17.19, alongside other pertinent information such as the modelled corrosion film mass thickness (see section 17.2.3).

ICP-MS data were grouped according to temperature and flow rate for each session, mean average concentrations were found for each element, and appropriate levels for feedwater were subtracted, to give the net increase in coolant concentration on passing the hot part of the rig. These values were weighted according to the mass of coolant which passed through the rig at the given temperature and flow rate conditions, and combined to give an average coolant concentration change for the session. In some cases, the value of this quantity was negative, indicating net pickup from the coolant for a particular element for a particular session.

Averaged values of coolant concentration change were multiplied by the total coolant flow for each session, and divided by total corroding surface area (~ 2 dm^2 for sessions 1 – 4; ~20 dm^2 in sessions 5 – 6 due to SS316L chips) to give the mass loss (or pickup) for each element. These are presented in Table 17.19 alongside the calculated total mass of each element that would be present in the corrosion film, in the case of zero release to effluent. The ratios of these two values are presented to give an indication of what proportion of the corroded material of each element was released to the effluent. Cases where this proportion was ~ 100% or higher occurred for Mo and Mn, and have been highlighted in the table. For most of these cases the release occurred most rapidly at the start of the session, with release rate steadily falling over the course of the session, see for example Figure 8.11 for session 6.

For each session #, some pertinent details are included for ease of reference, including the total flow of coolant (which was used in calculating the mass loss for each element); the pH_{25C}; and total time at ≥ 200 °C. From the latter two quantities, total mass of alloy oxidised was calculated, taking account of the corrosion in previous sessions for the case of sessions 2 and 3, where the tubing and reaction cell were not replaced. To convert the mass of oxidised alloy to mass of metal oxide, the mass of metal in one mole of Me_3O_4 (168.17g, from Table 17.2) and the mass of oxygen in one mole of Me_3O_4 (4 mol x 15.999 g/mol = 63.996 g) were used, to find the mass ratio of oxide to alloy, being (168.17+63.996)/168.17 = 1.3805. Using the density of SS316L, 8.0 g/cm^3, and the density of spinel type oxides of the inner and outer layers as 5.2 g/cm^3, the thickness of the inner layer and of the full oxide layer were calculated (see * and ** notes below Table 17.19). These calculations suggest that the two layers have roughly equal mass thickness.

Table 17.19. Mass balance, by element, by session (#) of rig use, using averaged ICP-MS data and modelled corrosion kinetics. Cases equivalent to ≳100% release from corrosion film are highlighted.

#	Details	Conc. / mass balance	**Fe**	**Cr**	**Ni**	**Mo**	**Mn**
1	pH: neutral, 1 - 3 g/min	feedwater (ppb)	0.6	0.0	1.5	-	3.9
	T: 260 °C. No chips	effluent (ppb)	12.6	1.2	55.0	-	229.4
	time at ≥ 200 °C: 140 h	net (ppb)	12.0	1.2	53.6	-	225.4
	total flow: 4.1 kg	mass oxidised (µm dm^{-2})	4030	1073	812	155	105
	m_{film}: 6.2 / 8.5 mg dm^{-2} *	Loss to effluent (µm dm^{-2})	25	3	111	-	467
	h_{film}: 0.08 / 0.16 µm **	*% of film mass released*	*0.6%*	*0.2%*	*14%*	-	*443%*
2	pH: 11, 2 g/min	feedwater (ppb)	0.3	0.7	1.8	1.7	-0.1
	T: 300 °C. No chips	effluent (ppb)	0.8	1.6	1.0	202.8	0.2
	time at ≥ 200 °C: 289 h	net (ppb)	0.5	0.9	-0.8	201.2	0.2
	total flow: 23.4 kg	mass oxidised (µm dm^{-2})	4745	1263	956	183	124
	m_{film}: 7.3 / 10.1 mg dm^{-2} *	Loss to effluent (µm dm^{-2})	6	10	-9	2354	3
	h_{film}: 0.09 / 0.19 µm **	*% of film mass released*	*0.1%*	*0.8%*	*-1.0%*	*1290%*	*2.0%*
3	pH: 9, 0.1 - 2 g/min	feedwater (ppb)	0.6	0.0	1.5	0.5	3.9
	T: 200 - 300 °C. No chips	effluent (ppb)	4.6	0.3	2.4	22.8	29.8
	time at ≥ 200 °C: 624 h	net (ppb)	4.0	0.3	1.0	22.3	25.9
	total flow: 35.7 kg	mass oxidised (µm dm^{-2})	9685	2578	1952	373	253
	m_{film}: 14.9 / 20.6 mg dm^{-2} *	Loss to effluent (µm dm^{-2})	71	6	17	397	462
	h_{film}: 0.19 / 0.40 µm **	*% of film mass released*	*0.7%*	*0.2%*	*0.9%*	*107%*	*183%*
4	pH: 9, 0.1 g/min	feedwater (ppb)	0.6	0.0	1.5	0.5	3.9
	T: 200 - 300 °C. No chips	effluent (ppb)	0.8	0.1	2.5	26.5	12.5
	time at ≥ 200 °C: 1683 h	net (ppb)	0.2	0.0	1.0	26.1	8.6
	total flow: 10.1 kg	mass oxidised (µm dm^{-2})	13845	3685	2790	533	362
	m_{film}: 21.3 / 29.5 mg dm^{-2} *	Loss to effluent (µm dm^{-2})	1	0	5	131	43
	h_{film}: 0.27 / 0.57 µm **	*% of film mass released*	*0.0%*	*0.0%*	*0.2%*	*25%*	*12%*
5	pH: 9, 0.1 - 1 g/min	feedwater (ppb)	0.9	0.0	0.5	0.7	4.9
	T: 200 - 300 °C. Chips.	effluent (ppb)	6.8	0.0	1.3	70.3	3.4
	time at ≥ 200 °C: 2317 h	net (ppb)	6.0	0.0	0.8	69.6	-1.5
	total flow: 26.2 kg	mass oxidised (µm dm^{-2})	16250	4325	3275	625	425
	m_{film}: 25.0 / 34.6 mg dm^{-2} *	Loss to effluent (µm dm^{-2})	8	0	1	91	-2
	h_{film}: 0.31 / 0.66 µm **	*% of film mass released*	*0.0%*	*0.0%*	*0.0%*	*15%*	*-0.5%*
6	pH: 10, 0.1 - 1 g/min	feedwater (ppb)	5.3	0.1	2.3	1.0	0.4
	T: 200 - 300 °C. Chips.	effluent (ppb)	5.2	1.1	2.3	193.5	0.5
	time at ≥ 200 °C: 1925 h	net (ppb)	-0.1	1.0	-0.1	192.5	0.1
	total flow: 47.3 kg	mass oxidised (µm dm^{-2})	11960	3183	2410	460	313
	m_{film}: 19.3 / 26.7 mg dm^{-2} *	Loss to effluent (µm dm^{-2})	0	2	0	455	0
	h_{film}: 0.24 / 0.51 µm **	*% of film mass released*	*0.0%*	*0.1%*	*-0.0%*	*99%*	*0.0%*

* m_{film} gives the total mass of oxidised alloy; followed by the total mass of oxide, assuming zero loss to the coolant (the former is multiplied by 1.3805 to give the latter, see above)

** h_{film} gives the thickness of the inner film (according to mass of alloy corroded, and SS316L density of 8.0 g/cm^3), assuming it replaces the volume of alloy oxidised and there is zero loss to the coolant; followed by average thickness of the full corrosion film, of both layers (according to total mass of oxide, and oxide density of 5.2 g/cm^3), again assuming zero loss to the coolant.

18. Appendix 5:
Tables of ICP-MS Results

Table 18.1. to Table 18.8 below provide all ICP-MS results from effluent of the Metal Oxide Solubility (MOS) rig, and similar rigs in the same laboratory. Other results are also provided, such as levels in blanks and feedwater samples. Data are grouped by session of rig use for the MOS rig, or by rig for other rigs. Data presented are the best estimate of ppb levels of Fe and other elements in the effluent at the point of sampling, after accounting for the dilution effect of acidification, and the summative contamination effect of the sampling and sample preparation procedures (as judged by mean levels in blanks) – see chapters 7 and 15 for more details.

Table 18.1. Session 1 results

sample	pH	T	$\dot{m}$	N_2	[Fe]	[Cr]	[Ni]	[Mo]	[Mn]	[Co]	Other info
01-01	7*	260	1	0.7	10 *(4)*	1.4 (*5*)	12 (*1*)	-	240 (*1*)	2.4 (*01*)	25ml, d.l., 75min since start, 30 min at temp.
01-02	7*	260	1	0.7	17 *(4)*	1.0 (*4*)	4 (*0*)	-	67 (*1*)	0.8 (*01*)	28ml, d.l., 217min since start, 172 min at temp.
01-03	7*	260	1	0.7	16 *(4)*	1.4 (*4*)	57 (*3*)	-	527 (*3*)	30.1 (*15*)	35ml, s.c., 158min since pump restart
01-04	7*	20	1	0.5	7 *(4)*	1.1 (*4*)	147 (*7*)	-	83 (*1*)	2.4 (*01*)	36ml, d.l., ~1 h after pump restart
01-con	-	-	-	-	59 *(6)*	0.9 (*4*)	1 (*0*)	-	2 (*1*)	m 0.0 (*01*)	Deliberately contaminated with fleck of hematite
Blanks	-	-	-	-	19 (3)	2.7 (3)	1 (0)	-	1 (1)	m 0.1 (01)	Batch 1. Just 1 blank to cover all session/batch 1 samples.

Table 18.2. Session 2 results

sample	pH	T	$\dot{m}$	N_2	[Fe]	[Cr]	[Ni]	[Mo]	[Mn]	[Co]	Other info
02-07	11	300	2	0.7	0.6 *(4)*	0.8 *(0)*	2.6 *(2)*	451 *(2)*	0.7 *(1)*	-	s.c.-->g.v. 24h after temp first reached and pump started
02-08	11	300	2	0.7	2.2 *(4)*	0.7 *(0)*	4.4 *(3)*	318 *(2)*	0.6 *(1)*	-	s.c.-->g.v. 26h after temp first reached and pump started
02-09a	11	300	2	0.7	2.0 *(4)*	1.4 *(1)*	0.1 *(1)*	481 *(2)*	0.3 *(1)*	-	scoop-->g.v. 29h … collected simultaneously with 02-09b
02-09b					0.2 *(4)*	0.6 *(0)*	0.1 *(1)*	330 *(2)*	0.1 *(1)*	-	s.c.-->g.v. 29h … collected simultaneously with 02-09a
02-20a	11	300	2	1.0	0.2 *(4)*	0.7 *(0)*	-0.4 *(1)*	78 *(0)*	0.0 *(1)*	-	d.l.-->t.t. ("universal" tube). 5 h after multiple restarts
02-20b					0.4 *(4)*	1.2 *(1)*	-0.3 *(1)*	76 *(0)*	-0.1 *(1)*	-	d.l.-->g.v. 5 h after multiple restarts
02-20c					0.4 *(4)*	0.9 *(0)*	3.8 *(2)*	121 *(1)*	0.0 *(1)*	-	s.c.-->g.v. 5 h after multiple restarts
02-25	11	300	2	1.0	0.9 *(4)*	0.8 *(0)*	-0.4 *(1)*	59 *(0)*	0.0 *(1)*	-	d.l.-->t.t. (other centrifuge tube). 29h after mult. restarts
02-26a	11	300	2	1.0	0.9 *(4)*	6.3 *(3)*	0.0 *(1)*	61 *(0)*	0.1 *(1)*	-	s.c.-->g.v. 49h after mult. restarts
02-26b					0.1 *(4)*	2.4 *(1)*	0.3 *(1)*	54 *(0)*	-0.1 *(1)*	-	s.c.-->t.t. (Sarstedt centrifuge tube) 49h after mult. restarts
02-f1	11	20	-	0.7	-0.4 *(4)*	0.9 *(0)*	2.3 *(2)*	2.0 *(0)*	-0.1 *(1)*	-	g.v. Feed water from barrel
02-f2	11	20	-	0.7	1.0 *(4)*	0.6 *(0)*	1.3 *(1)*	1.3 *(0)*	-0.1 *(1)*	-	g.v. Feed water from pump inlet
Blanks	-	-	-	-	1.5 *(3)*	0.0 *(0)*	0.2 *(0)*	0.0 *(0)*	0.1 *(0)*	-	Batch 3. Four blanks analysed.

Table 18.3. Session 3 results

Sample	pH	T	$\dot{m}$	N_2	[Fe]	[Cr]	[Ni]	[Mo]	[Mn]	[Co]	Other info
03-01	9	22	2	0.8	3.0 *(6)*	18.79 *(94)*	2.4 *(2)*	78.9 *(4)*	0.5 *(1)*	0.28 *(4)*	s.c.-->t.t. 3 min after start
03-02	9	22	2	0.8	3.9 *(7)*	0.66 *(5)*	10.3 *(5)*	19.6 *(1)*	3.2 *(1)*	0.26 *(4)*	s.c.-->t.t. 1.25 h after start
03-03	9	300	2	0.8	2.8 *(6)*	1.11 *(7)*	1.1 *(1)*	11.5 *(1)*	58.0 *(3)*	< 0.1	0.5 h after T reached
03-04	9	300	2	0.8	2.0 *(6)*	0.15 *(4)*	0.4 *(1)*	5.6 *(0)*	26.8 *(2)*	< 0.1	2 h after T reached
03-05	9	300	2	0.8	5.0 *(7)*	0.28 *(4)*	1.3 *(1)*	7.8 *(1)*	48.2 *(3)*	< 0.1	4 h after T reached
03-06	9	300	2	0.8	3.4 *(7)*	0.87 *(6)*	2.3 *(1)*	20.3 *(1)*	104.1 *(5)*	< 0.1	21 h after T reached
03-07	9	300	2	0.8	5.5 *(7)*	0.06 *(4)*	2.1 *(1)*	25.6 *(1)*	22.5 *(2)*	< 0.1	52 h after T reached
03-08	9	300	2	0.8	5.3 *(7)*	0.22 *(4)*	2.7 *(2)*	25.6 *(1)*	18.4 *(2)*	0.13 *(4)*	28 h after pump restart
03-08-du					5.6 *(7)*	0.25 *(4)*	2.6 *(2)*	25.6 *(1)*	18.3 *(2)*	0.11 *(4)*	
03-09	9	300	2	0.8	6.0 *(7)*	0.10 *(4)*	2.5 *(2)*	24.3 *(1)*	19.4 *(2)*	0.26 *(4)*	50 h after pump restart
03-09-du					9.2 *(7)*	0.19 *(1)*	2.7 *(2)*	24.5 *(1)*	22.2 *(1)*	-	
03-10	9	300	2	0.8	3.4 *(5)*	0.09 *(1)*	2.8 *(2)*	23.7 *(1)*	24.5 *(1)*	-	79 h after pump restart
03-11	9	300	2	0.8	5.9 *(5)*	0.10 *(1)*	3.4 *(2)*	22.9 *(1)*	24.5 *(1)*	-	104 h after pump restart
03-12	9	300	2	0.8	9.8 *(7)*	0.05 *(1)*	2.7 *(2)*	24.7 *(1)*	19.6 *(1)*	-	3 min after second restart
03-13	9	300	2	0.8	5.2 *(5)*	0.05 *(1)*	5.3 *(3)*	21.5 *(1)*	29.6 *(2)*	-	44 h after second restart
03-15	9	300	0.5	0.8	5.2 *(5)*	0.10 *(1)*	6.7 *(4)*	27.9 *(1)*	43.4 *(2)*	-	21 h after change in flow rate
03-16	9	300	0.5	0.8	2.5 *(4)*	1.75 *(1)*	8.6 *(4)*	38.5 *(2)*	66.1 *(3)*	-	27 h after change in flow rate. 03-16 taken immediately after flow was diverted to drip line. N_2 cylinder recently replaced.
03-17					4.7 *(5)*	0.14 *(1)*	6.8 *(4)*	33.1 *(2)*	36.5 *(2)*	-	
03-18					8.4 *(6)*	0.10 *(1)*	6.1 *(3)*	36.1 *(2)*	26.7 *(1)*	-	
03-19	9	300	0.5	0.8	3.8 *(5)*	0.08 *(1)*	5.1 *(3)*	54.9 *(3)*	34.4 *(2)*	-	27 h after pump restart
03-20	9	300	0.5	0.8	4.6 *(5)*	0.08 *(1)*	4.0 *(2)*	63.3 *(3)*	25.3 *(1)*	-	52 h after pump restart
03-23	9	300	0.1	0.8	1.8 *(4)*	0.16 *(1)*	2.2 *(1)*	77.7 *(4)*	16.5 *(1)*	-	76 h after change in flow rate
03-24	9	300	0.1	0.8	2.2 *(4)*	0.12 *(1)*	1.8 *(1)*	79.4 *(4)*	14.6 *(1)*	-	95 h after change in flow rate
03-25	9	300	0.1	0.8	1.6 *(4)*	0.10 *(1)*	1.5 *(1)*	92.5 *(5)*	13.2 *(1)*	-	117 h after change in flow rate
03-31	9	250	1	0.8	6.1 *(6)*	0.00 *(1)*	0.3 *(1)*	47.5 *(2)*	4.8 *(1)*	-	4 h after new T reached
03-32	9	250	1	0.8	1.1 *(4)*	0.00 *(1)*	0.5 *(1)*	38.5 *(2)*	8.8 *(1)*	-	22 h after new T reached
03-33	9	250	1	0.8	1.4 *(4)*	0.01 *(1)*	0.5 *(1)*	34.3 *(2)*	5.6 *(1)*	-	23 h after new T reached

03-39	9	200	1	0.8	1.5 *(4)*	-0.01 *(1)*	0.6 *(1)*	12.2 *(1)*	18.0 *(1)*	-	11 h after pump restart
03-40	9	200	1	0.8	0.6 *(4)*	0.00 *(1)*	0.7 *(1)*	8.8 *(0)*	13.4 *(1)*	-	22 h after second restart
03-41	9	200	1	0.8	1.6 *(4)*	0.00 *(1)*	0.7 *(1)*	8.3 *(0)*	14.2 *(1)*	-	24 h after second restart
Blanks	-	-	-	-	1.5 *(5)*	m 0.1 *(0)*	0.2 *(1)*	m0.1 *(0)*	m 0.1 *(1)*	m0.1 *(0)*	Batch 2. Relevant to samples up to 03-09
Blanks	-	-	-	-	1.5 *(3)*	0.0 *(0)*	0.2 *(0)*	0.0 *(0)*	0.1 *(1)*	-	Batch 3. Relevant to samples 03-09-du onwards

Table 18.4. Session 4 results

Sample	***pH***	***T***	***ṁ***	***N_2***	***[Fe]***	***[Cr]***	***[Ni]***	***[Mo]***	***[Mn]***	***[Co]***	***Other info***
04-01	9	300	0.1	0.8	1.7 *(1)*	0.16 *(1)*	40.8 *(20)*	22.6 *(1)*	88.7 *(4)*	-	3.5 h after T reached. (4 h after start)
04-02	9	300	0.1	0.2	7.2 *(4)*	0.08 *(1)*	7.6 *(4)*	36.6 *(2)*	22.1 *(1)*	-	26 h after T reached. N_2 0.2, this & next few samples
04-03	9	300	0.1	0.2?	0.3 *(1)*	0.04 *(0)*	5.1 *(3)*	55.8 *(3)*	14.9 *(1)*	-	31 h after T reached
04-04	9	300	0.1	0.2?	1.9 *(1)*	0.09 *(1)*	4.5 *(2)*	86.8 *(4)*	11.0 *(1)*	-	47 h after T reached
04-06	9	300	0.1	0.8?	0.7 *(1)*	0.11 *(1)*	1.6 *(1)*	95.0 *(5)*	7.0 *(0)*	-	75 h after T reached
04-08	9	300	0.1	0.8?	1.5 *(1)*	0.15 *(1)*	1.5 *(1)*	73.8 *(4)*	5.5 *(0)*	-	99 h after T reached
04-12	9	300	0.1	0.8	0.1 *(1)*	0.20 *(1)*	2.0 *(1)*	55.3 *(3)*	5.1 *(0)*	-	154 h after T reached
04-15	9	300	0.1	0.8	0.4 *(1)*	0.22 *(1)*	2.5 *(1)*	46.4 *(2)*	4.8 *(0)*	-	196 h after T reached
04-18	9	300	0.1	0.8	0.7 *(1)*	0.14 *(1)*	2.2 *(1)*	43.1 *(2)*	4.7 *(0)*	-	243 h after T reached
04-19	9	300	0.1	0.8	0.3 *(1)*	0.04 *(0)*	2.6 *(1)*	54.0 *(3)*	6.9 *(0)*	-	288 h after T reached
04-22	9	300	0.1	0.8	1.0 *(1)*	0.02 *(0)*	2.9 *(2)*	49.8 *(2)*	8.4 *(0)*	-	343 h after T reached
04-24	9	300	0.1	0.8	0.7 *(1)*	0.02 *(0)*	1.2 *(1)*	57.6 *(3)*	3.4 *(0)*	-	391 h after T reached
04-25	9	300	0.1	0.8	0.7 *(1)*	0.02 *(0)*	1.3 *(1)*	57.2 *(3)*	3.5 *(0)*	-	392 h after T reached
04-27	9	300	0.1	0.8	2.8 *(2)*	0.06 *(1)*	4.2 *(2)*	52.7 *(3)*	18.8 *(1)*	-	1 h after restart
04-28	9	300	0.1	0.8	0.9 *(1)*	0.01 *(0)*	1.6 *(1)*	62.6 *(3)*	5.3 *(0)*	-	32 h after restart
04-29	9	300	0.1	0.8	0.6 *(1)*	0.00 *(0)*	1.2 *(1)*	61.7 *(3)*	4.1 *(0)*	-	48 h after restart
04-30	9	250	0.1	0.8	1.3 *(1)*	0.04 *(0)*	4.4 *(2)*	33.4 *(2)*	12.5 *(1)*	-	2.5 h after T reached. (0.5 h after flow recommenced)
04-31A	9	250	0.1	0.8	0.3 *(1)*	0.03 *(0)*	0.5 *(0)*	33.7 *(2)*	3.7 *(0)*	-	21 h after T reached
04-31B	9	250	0.1	0.8	0.2 *(1)*	0.03 *(0)*	0.5 *(0)*	31.9 *(2)*	3.4 *(0)*	-	27 h after T reached
04-32	9	250	0.1	0.8	0.4 *(1)*	0.06 *(1)*	0.6 *(1)*	28.2 *(1)*	3.1 *(0)*	-	44 h after T reached

04-34	9	250	0.1	0.8	0.3 *(1)*	0.06 *(1)*	0.7 *(1)*	26.5 *(1)*	3.1 *(0)*	-	69 h after T reached. N_2 cylinder recently replaced
04-36	9	250	0.1	0.8	0.2 *(1)*	0.06 *(1)*	0.9 *(1)*	21.4 *(1)*	2.6 *(0)*	-	123 h after T reached
04-39	9	250	0.1	0.8	0.2 *(1)*	0.08 *(1)*	0.9 *(1)*	20.7 *(1)*	2.3 *(0)*	-	173 h after T reached
04-42	9	250	0.1	0.8	0.3 *(1)*	0.21 *(1)*	0.8 *(1)*	20.1 *(1)*	2.1 *(0)*	-	208 h after T reached
04-45	9	250	0.1	0.8	0.4 *(1)*	0.22 *(1)*	1.0 *(1)*	19.6 *(1)*	2.3 *(0)*	-	240 h after T reached
04-46	9	250	0.1	0.8	*0.1 (1)*	0.26 *(1)*	1.0 *(1)*	19.5 *(1)*	2.0 *(0)*	-	304 h after T reached
04-47	9	250	0.1	0.8	*0.0 (1)*	0.30 *(1)*	0.9 *(1)*	18.3 *(1)*	2.1 *(0)*	-	311 h after T reached
04-48	9	200	0.1	0.8	*0.0 (1)*	0.19 *(1)*	3.2 *(2)*	15.2 *(1)*	4.4 *(0)*	-	2 h after T reached. (0.5 h after flow recommenced)
04-49	9	200	0.1	0.8	1.1 *(1)*	*0.01 (0)*	0.8 *(1)*	13.2 *(1)*	6.1 *(0)*	-	17 h after T reached
04-50	9	200	0.1	0.8	0.3 *(1)*	*0.01 (0)*	0.8 *(1)*	11.8 *(1)*	7.2 *(0)*	-	24 h after T reached
04-51	9	200	0.1	0.8	*0.2 (1)*	*0.01 (0)*	0.8 *(1)*	10.9 *(1)*	9.2 *(0)*	-	39 h after T reached
04-55	9	200	0.1	0.8	0.3 *(1)*	*0.01 (0)*	1.2 *(1)*	8.0 *(0)*	13.0 *(1)*	-	93 h after T reached. N_2 cylinder recently replaced
04-56	9	200	0.1	0.8	*0.1 (1)*	*0.00 (0)*	1.1 *(1)*	8.1 *(0)*	11.1 *(1)*	-	148 h after T reached
04-59	9	200	0.1	0.8	0.3 *(1)*	0.01 *(0)*	1.3 *(1)*	9.6 *(1)*	13.6 *(1)*	-	187 h after T reached
04-62	9	200	0.1	0.8	2.7 *(2)*	0.02 *(0)*	1.6 *(1)*	8.1 *(0)*	21.1 *(1)*	-	264 h after T reached
04-64	9	200	0.1	0.8	0.3 *(1)*	*0.01 (0)*	1.8 *(1)*	9.6 *(1)*	23.9 *(1)*	-	341 h after T reached
04-66	9	200	0.1	0.8	0.4 *(1)*	*0.01 (0)*	1.9 *(1)*	10.1 *(1)*	24.5 *(1)*	-	405 h after T reached
04-68	9	200	0.1	0.8	1.4 *(1)*	0.01 *(0)*	2.4 *(1)*	10.8 *(1)*	23.6 *(1)*	-	508 h after T reached. N_2 cylinder recently replaced
04-69	9	200	0.1	0.8	0.9 *(1)*	*0.00 (0)*	1.7 *(1)*	12.2 *(1)*	19.7 *(1)*	-	554 h after T reached
04-70	9	200	0.1	0.8	0.6 *(1)*	*0.00 (0)*	1.5 *(1)*	13.0 *(1)*	19.8 *(1)*	-	555 h after T reached
04-71	9	200	0.1	0.8	0.4 *(1)*	*0.00 (0)*	1.4 *(1)*	11.6 *(1)*	18.2 *(1)*	-	600 h after T reached
04-73	9	200	0.1	0.8	1.3 *(1)*	*0.00 (0)*	1.1 *(1)*	7.4 *(0)*	13.0 *(1)*	-	750 h after T reached. N_2 cylinder recently replaced
04-75	9	200	0.1	0.8	0.4 *(1)*	*0.00 (0)*	1.2 *(1)*	9.7 *(1)*	13.3 *(1)*	-	886 h after T reached
04-f1	9	-	0.1	0.8	0.6 *(1)*	*0.01 (0)*	2.2 *(1)*	0.4 *(0)*	3.0 *(0)*	-	Feed water. Taken 2.5 h after sample 04-29
04-f3	9	-	0.1	0.8	0.3 *(1)*	*0.00 (0)*	0.3 *(0)*	0.4 *(0)*	2.4 *(0)*	-	Feed water. Taken 3.5 h after sample 04-29
04-f4	9	-	0.1	0.8	0.5 *(1)*	*0.01 (0)*	2.4 *(1)*	0.5 *(0)*	3.9 *(0)*	-	Feed water. Taken 13 h after sample 04-51
04-f5	9	-	0.1	0.8	0.2 *(1)*	*0.00 (0)*	*0.1 (0)*	*0.0 (0)*	0.1 *(0)*	-	Feed water syringe blank. 2 h after sample 04-75
04-f6	9	-	0.1	0.8	0.7 *(1)*	0.01 *(0)*	0.8 *(1)*	0.6 *(0)*	5.7 *(0)*	-	Feed water. Taken 2.5 h after sample 04-75
04-f7	9	-	0.1	0.8	1.0 *(1)*	0.02 *(0)*	1.2 *(1)*	0.6 *(0)*	5.0 *(0)*	-	Feed water. Taken 3 h after sample 04-75
Blanks	-	-	-	-	0.1 *(1)*	-0.02 *(0)*	0.0 *(0)*	0.0 *(0)*	-0.0 *(0)*	-	Batch 4. Eleven blanks analysed

Table 18.5. Session 5 results. Feedwater of pH_{25C} 9 was used for session 5

Sample	*T*	*ṁ*	*[Fe]*	*[Cr]*	*[Ni]*	*[Mo]*	*[Mn]*	*Other info*
05-01	300	1	1.1 *(2)*	*0.00 (1)*	1.3 *(1)*	1 *(0)*	5.0 *(0)*	water in oven not yet reached 300 °C
05-02	300	1	1.7 *(2)*	*0.01 (1)*	0.2 *(0)*	36 *(0)*	1.4 *(0)*	15 h after T reached
05-03	300	1	4.3 *(3)*	*-0.01 (1)*	0.3 *(0)*	70 *(0)*	1.4 *(0)*	45 h after T reached
05-04	300	1	3.7 *(3)*	*0.01 (1)*	0.8 *(0)*	81 *(0)*	3.9 *(0)*	<1 h after pump restart
05-05	300	1	3.5 (3)	*-0.01 (1)*	0.3 *(0)*	92 *(0)*	1.4 *(0)*	31 h after pump restart
05-06	300	1	3.1 *(2)*	*-0.04 (1)*	0.3 *(0)*	95 *(0)*	1.5 *(0)*	57 h after pump restart
05-07	300	1	3.8 *(3)*	0.04 *(1)*	0.4 *(0)*	101 *(1)*	1.6 *(0)*	73 h after pump restart ⎫ 3 samples
05-08	300	1	3.5 *(3)*	*-0.02 (1)*	0.4 *(0)*	100 *(0)*	1.7 *(0)*	73 h after pump restart ⎬ in quick
05-09	300	1	3.2 *(2)*	*0.00 (1)*	0.3 *(0)*	100 *(1)*	1.6 *(0)*	73 h after pump restart ⎭ succession
05-10	300	1	2.8 *(2)*	*-0.01 (1)*	0.4 *(0)*	101 *(1)*	1.5 *(0)*	103 h after pump restart
05-11	300	0.5	2.0 *(2)*	*-0.01 (1)*	0.3 *(0)*	89 *(0)*	2.0 *(0)*	17 h after change in flow rate
05-12	300	0.5	2.2 *(2)*	*-0.02 (1)*	0.3 *(0)*	91 *(0)*	1.9 *(0)*	48 h after change in flow rate
05-13	300	0.5	2.2 *(2)*	*-0.01 (1)*	0.2 *(0)*	95 *(0)*	2.1 *(0)*	66 h after change in flow rate
05-14	300	0.5	1.9 *(2)*	*-0.01 (1)*	0.3 *(0)*	100 *(1)*	1.9 *(0)*	95 h after change in flow rate
05-15	300	0.5	2.5 *(2)*	0.02 *(1)*	0.2 *(0)*	101 *(1)*	1.8 *(0)*	114 h after change in flow rate
05-16	300	0.5	2.2 *(2)*	*0.01 (1)*	0.4 *(0)*	100 *(0)*	2.0 *(0)*	133 h after change in flow rate
05-18	300	0.5	12.4 *(2)*	*0.00 (1)*	1.2 *(1)*	68 *(0)*	5.2 *(0)*	46 h after pump restart
05-19	300	0.5	1.3 *(2)*	*0.01 (1)*	0.5 *(0)*	51 *(0)*	1.5 *(0)*	3 h after pump restart
05-20	300	0.5	2.4 *(2)*	*0.00 (1)*	0.3 *(0)*	94 *(0)*	1.8 *(0)*	26 h after pump restart
05-21	300	0.1	5.4 *(3)*	*0.01 (1)*	0.9 *(0)*	74 *(0)*	4.4 *(0)*	29 h after change in flow rate
05-22	300	0.1	5.2 *(3)*	*0.01 (1)*	0.4 *(0)*	61 *(0)*	2.8 *(0)*	53 h after change in flow rate
05-23	300	0.1	3.5 *(3)*	*0.01 (1)*	0.5 *(0)*	53 *(0)*	3.2 *(0)*	82 h after change in flow rate
05-24	300	0.1	7.4 *(4)*	*0.02 (1)*	0.9 *(0)*	46 *(0)*	4.2 *(0)*	101 h after change in flow rate
05-26	300	0.1	18.9*(10)*	*0.02 (1)*	1.4 *(1)*	43 *(0)*	4.1 *(0)*	14 h after pump restart
05-27	300	0.1	6.3 *(4)*	*0.00 (1)*	0.4 *(0)*	37 *(0)*	2.5 *(0)*	87 h after pump restart
05-28	300	0.1	6.5 *(4)*	0.03 *(1)*	0.4 *(0)*	42 *(0)*	3.0 *(0)*	162 h after pump restart
05-29	300	0.1	4.9 *(3)*	*0.00 (1)*	0.4 *(0)*	42 *(0)*	3.0 *(0)*	187 h after pump restart
05-30	300	0.1	15.8 *(8)*	0.02 *(1)*	0.8 *(0)*	54 *(0)*	5.4 *(0)*	1 h after pump restart
05-31	300	0.1	5.7 *(3)*	*0.00 (1)*	0.3 *(0)*	41 *(0)*	2.7 *(0)*	53 h after pump restart
05-32	300	0.1	5.8 *(3)*	0.04 *(1)*	0.2 *(0)*	45 *(0)*	2.8 *(0)*	99 h after pump restart
05-33	300	0.1	8.3 *(5)*	*0.01 (1)*	0.3 *(0)*	50 *(0)*	2.7 *(0)*	41 h after pump restart
05-34	300	0.1	12.2 *(6)*	*-0.01 (1)*	0.7 *(0)*	48 *(0)*	2.9 *(0)*	47 h after pump restart
05-35	300	0.1	28.2*(14)*	0.04 *(1)*	17.1 *(9)*	41 *(0)*	3.1 *(0)*	20 h after pump restart
05-36	300	0.1	35.8*(18)*	*0.00 (1)*	1.5 *(1)*	40 *(0)*	3.5 *(0)*	54 h after pump restart
05-37	300	0.1	41.7*(21)*	*0.02 (1)*	1.6 *(1)*	37 *(0)*	3.4 *(0)*	76 h after pump restart
05-38	250	0.1	20.1*(10)*	*0.00 (1)*	1.2 *(1)*	21 *(0)*	8.4 *(0)*	25 h after change in temperature
05-39	250	0.1	19.2*(10)*	0.03 *(1)*	1.4 *(1)*	17 *(0)*	8.2 *(0)*	45 h after change in temperature
05-40	200	0.1	3.3 *(2)*	*0.01 (1)*	0.5 *(0)*	11 *(0)*	20.4 *(1)*	25 h after change in temperature
05-41	200	0.1	3.9 *(3)*	*0.01 (1)*	0.8 *(0)*	10 *(0)*	20.6 *(1)*	50 h after change in temperature
05-f2	-	1	0.6 *(2)*	0.02 *(1)*	0.4 *(0)*	0.7 *(0)*	4.2 *(0)*	Feedwater, 0.5 h after sample #10
05-f3	-	1	0.5 *(2)*	0.02 *(1)*	0.4 *(0)*	0.6 *(0)*	4.3 *(0)*	Feedwater, 0.5 h after sample #10
05-f4	-	1	0.4 *(2)*	0.03 *(1)*	0.4 *(0)*	0.7 *(0)*	4.3 *(0)*	Feedwater, 1 h after sample #10
05-f5	-	1	0.4 *(2)*	*0.02 (1)*	0.4 *(0)*	0.6 *(0)*	4.7 *(0)*	Feedwater, 1 h after sample #10
05-f8	-	0.1	2.5 *(2)*	0.03 *(1)*	0.9 *(0)*	0.8 *(0)*	7.2 *(0)*	Feedwater, 25 h before sample #38
05-f1	-	-	*-0.1 (2)*	*0.00 (1)*	0.10 *(1)*	*-0.03(3)*	0.05 *(1)*	Syringe blank, for samples f2-f5
05-f6	-	-	*-0.3 (2)*	*0.00 (1)*	*-0.01 (1)*	*-0.06(3)*	*0.01 (1)*	Syringe blanks, for sample f8
05-f7	-	-	*-0.2 (2)*	*-0.01 (1)*	*-0.01 (1)*	*-0.06(3)*	*-0.01 (1)*	Syringe blanks, for sample f8
Rejects	-	-	0.5 *(4)*	0.05 *(5)*	1.3 *(29)*	0.04 *(5)*	0.02 *(2)*	Rejected blanks
Blanks	-	-	0.04*(14)*	-0.01 *(1)*	-0.01 *(1)*	0.02 *(2)*	0.00 *(1)*	Batch 5.

Table 18.6. Session 6 results. Feedwater of pH_{25C} 10 was used for session 6.

Sample	T	ṁ	[Fe]	[Cr]	[Ni]	[Mo]	[Mn]	Other info
400-top	300	1	0.4 *(2)*	0.44 *(2)*	1.7 *(1)*	400 *(2)*	8.4 *(0)*	From top of dump vessel (0-6 h)
400-bot	300	1	1.2 *(2)*	0.45 *(2)*	2.4 *(1)*	400 *(2)*	8.6 *(0)*	From bottom of dump vessel (0-6 h)
1000	300	1	*-0.2 (2)*	1.04 *(5)*	*0.0 (0)*	768 *(4)*	0.0 *(0)*	From top of dump vessel (0-22 h)
250-top	300	1	*-0.1 (2)*	1.35 *(7)*	*0.0 (0)*	951 *(5)*	0.0 *(0)*	From top of dump vessel (22-27 h)
250-bot	300	1	*-0.1 (2)*	1.36 *(7)*	*0.0 (0)*	946 *(5)*	0.0 *(0)*	Bottom of dump vessel (22-27 h)
round	300	1	*-0.2 (2)*	1.18 *(6)*	0.8 *(0)*	445 *(2)*	0.1 *(0)*	From top of dump vessel (27-74 h)
square	300	1	*-0.2 (2)*	1.96*(10)*	*0.0 (0)*	318 *(2)*	0.0 *(0)*	From top of dump vessel (78-146 h)
06-B1	-	-	2.0 *(2)*	0.21 *(1)*	0.3 *(0)*	*-0.03 (3)*	0.05 *(1)*	Syringe blank, for 7 specials above
06-01	300	1	*0.1 (2)*	1.03 *(5)*	0.7 *(0)*	688 *(3)*	0.1 *(0)*	6 h after T reached
06-02	300	1	*0.1 (2)*	0.91 *(5)*	0.1 *(0)*	408 *(2)*	0.1 *(0)*	71 h after T reached
06-03	300	1	*0.2 (2)*	0.86 *(4)*	*0.0 (0)*	392 *(2)*	0.1 *(0)*	78 h after T reached
06-04	300	1	*0.4 (2)*	1.35 *(7)*	*0.0 (0)*	303 *(2)*	0.1 *(0)*	145 h after T reached
06-05	300	1	*0.1 (2)*	1.40 *(7)*	0.0 *(0)*	304 *(2)*	0.1 *(0)*	147 h after T reached
06-06	300	1	*0.1 (2)*	1.00 *(5)*	*0.0 (0)*	285 *(1)*	0.1 *(0)*	165 h after T reached
06-07	300	1	*0.2 (2)*	1.07 *(5)*	*0.0 (0)*	282 *(1)*	0.0 *(0)*	168 h after T reached
06-08	300	1	*0.2 (2)*	0.98 *(5)*	0.0 *(0)*	281 *(1)*	0.0 *(0)*	169 h after T reached
06-09	300	1	*0.0 (2)*	0.98 *(5)*	0.0 *(0)*	261 *(1)*	0.0 *(0)*	196 h after T reached
06-10	300	1	*0.0 (2)*	0.83 *(4)*	*0.0 (0)*	240 *(1)*	0.0 *(0)*	225 h after T reached
06-10B	300	1	*0.1 (2)*	0.56 *(3)*	*-0.1 (0)*	159 *(1)*	0.1 *(0)*	318 h after T reached
06-11	300	1	*0.2 (2)*	0.55 *(3)*	*0.0 (0)*	156 *(1)*	0.1 *(0)*	318 h after T reached
06-12	300	1	*0.1 (2)*	0.54 *(3)*	*0.0 (0)*	123 *(1)*	0.1 *(0)*	356 h after T reached
06-13	300	1	*0.0 (2)*	0.50 *(3)*	*0.0 (0)*	104 *(1)*	0.0 *(0)*	386 h after T reached
06-14	300	1	*0.0 (2)*	0.47 *(3)*	0.0 *(0)*	72 *(0)*	0.1 *(0)*	456 h after T reached
06-15	300	1	*0.1 (2)*	0.47 *(3)*	*0.0 (0)*	59 *(0)*	0.1 *(0)*	500 h after T reached
06-16	300	0.5	0.4 *(2)*	0.82 *(4)*	0.0 *(0)*	93 *(0)*	0.1 *(0)*	52 h after change in flow rate
06-17	300	0.5	*0.2 (2)*	0.90 *(5)*	*0.0 (0)*	93 *(0)*	0.1 *(0)*	73 h after change in flow rate
06-18	300	0.5	*0.1 (2)*	0.63 *(3)*	0.1 *(0)*	84 *(0)*	0.1 *(0)*	149 h after change in flow rate
06-19	300	0.5	*0.1 (2)*	0.67 *(3)*	0.0 *(0)*	82 *(0)*	0.2 *(0)*	151 h after change in flow rate
06-20	300	0.5	*0.0 (2)*	0.60 *(3)*	0.0 *(0)*	74 *(0)*	0.1 *(0)*	217 h after change in flow rate
06-21	300	0.5	*0.1 (2)*	0.55 *(3)*	*0.0 (0)*	72 *(0)*	0.0 *(0)*	220 h after change in flow rate
06-22	300	0.5	*0.0 (2)*	0.70 *(4)*	*0.0 (0)*	69 *(0)*	0.0 *(0)*	243 h after change in flow rate
06-23	300	0.5	*0.1 (2)*	0.60 *(3)*	0.0 *(0)*	66 *(0)*	0.0 *(0)*	273 h after change in flow rate
06-24	300	0.5	*0.2 (2)*	0.57 *(3)*	*0.0 (0)*	66 *(0)*	0.1 *(0)*	275 h after change in flow rate
06-25	300	0.5	*0.2 (2)*	0.54 *(3)*	*0.0 (0)*	60 *(0)*	0.1 *(0)*	317 h after change in flow rate
06-26	300	0.5	*0.0 (2)*	0.50 *(3)*	0.0 *(0)*	57 *(0)*	0.1 *(0)*	339 h after change in flow rate
06-27	300	0.5	*0.3 (2)*	0.51 *(3)*	*0.0 (0)*	55 *(0)*	0.1 *(0)*	360 h after change in flow rate
06-28	300	0.1	*0.2 (2)*	2.21*(11)*	*0.0 (0)*	59 *(0)*	0.1 *(0)*	4 h after change in flow rate
06-29	300	0.1	0.7 *(2)*	2.72*(14)*	*0.0 (0)*	91 *(0)*	0.1 *(0)*	27 h after change in flow rate
06-30	300	0.1	*0.2 (2)*	2.32*(12)*	0.1 *(0)*	126 *(1)*	0.1 *(0)*	50 h after change in flow rate
06-31	300	0.1	0.5 *(2)*	2.50*(13)*	0.5 *(0)*	130 *(1)*	0.5 *(0)*	52 h after change in flow rate
06-32	300	0.1	*0.2 (2)*	2.10*(10)*	0.1 *(0)*	170 *(1)*	0.1 *(0)*	144 h after change in flow rate
06-33	300	0.1	0.4 *(2)*	2.05*(10)*	*0.0 (0)*	170 *(1)*	0.0 *(0)*	148 h after change in flow rate
06-34	300	0.1	*0.1 (2)*	2.05*(10)*	0.0 *(0)*	157 *(1)*	0.1 *(0)*	171 h after change in flow rate
06-35	300	0.1	*0.2 (2)*	1.94*(10)*	0.0 *(0)*	164 *(1)*	0.1 *(0)*	193 h after change in flow rate
06-36	300	0.1	*0.1 (2)*	1.98*(10)*	0.2 *(0)*	161 *(1)*	0.2 *(0)*	196 h after change in flow rate
06-37	300	0.1	*0.1 (2)*	1.90*(10)*	0.1 *(0)*	159 *(1)*	0.1 *(0)*	217 h after change in flow rate
06-38	300	0.1	0.7 *(2)*	1.74 *(9)*	0.0 *(0)*	151 *(1)*	0.4 *(0)*	220 h after change in flow rate
06-39	300	0.1	*0.2 (2)*	1.71 *(9)*	*0.0 (0)*	156 *(1)*	0.0 *(0)*	288 h after change in flow rate
06-40	300	0.1	*0.2 (2)*	2.21*(11)*	*-0.1 (0)*	184 *(1)*	0.0 *(0)*	310 h after change in flow rate
06-41	300	0.1	*0.1 (2)*	2.20*(11)*	0.3 *(0)*	165 *(1)*	0.4 *(0)*	314 h after change in flow rate
06-42	300	0.1	1.0 *(2)*	2.13*(11)*	0.0 *(0)*	158 *(1)*	0.1 *(0)*	342 h after change in flow rate
06-43	300	0.1	*0.0 (2)*	1.82 *(9)*	*0.0 (0)*	154 *(1)*	0.0 *(0)*	380 h after change in flow rate
06-44	250	0.1	0.7 *(2)*	3.54*(18)*	0.1 *(0)*	157 *(1)*	0.3 *(0)*	1 h after change in temperature
06-45	250	0.1	0.7 *(2)*	2.05*(10)*	0.0 *(0)*	98 *(0)*	0.1 *(0)*	5 h after change in temperature
06-46	250	0.1	1.0 *(2)*	2.24*(11)*	*0.0 (0)*	77 *(0)*	0.1 *(0)*	76 h after change in temperature
06-47	250	0.1	0.8 *(2)*	2.04*(10)*	*0.0 (0)*	74 *(0)*	0.1 *(0)*	97 h after change in temperature
06-48	250	0.1	*0.4 (2)*	2.11*(11)*	*0.0 (0)*	72 *(0)*	0.1 *(0)*	105 h after change in temperature
06-49	250	0.1	2.6 *(2)*	2.49*(12)*	*0.0 (0)*	76 *(0)*	0.3 *(0)*	124 h after change in temperature

06-50	250	0.1	0.9 *(2)*	2.25*(11)*	*0.0 (0)*	72 *(0)*	0.1 *(0)*	147 h after change in temperature
06-51	250	0.1	*0.3 (2)*	2.56*(13)*	0.2 *(0)*	71 *(0)*	0.2 *(0)*	152 h after change in temperature
06-52	250	0.1	0.8 *(2)*	2.23*(11)*	*0.0 (0)*	72 *(0)*	0.1 *(0)*	168 h after change in temperature
06-53	250	0.1	*-0.1 (2)*	2.27*(11)*	*0.0 (0)*	72 *(0)*	0.0 *(0)*	174 h after change in temperature
06-54	250	0.1	1.5 *(2)*	2.41*(12)*	*0.0 (0)*	79 *(0)*	0.1 *(0)*	244 h after change in temperature
06-55	250	0.1	1.3 *(2)*	2.19*(11)*	*0.0 (0)*	80 *(0)*	0.1 *(0)*	267 h after change in temperature
06-56	250	0.1	*0.3 (2)*	2.33*(12)*	0.4 *(0)*	80 *(0)*	0.3 *(0)*	270 h after change in temperature
06-57	250	0.1	*0.4 (2)*	2.02*(10)*	0.0 *(0)*	81 *(0)*	0.1 *(0)*	289 h after change in temperature
06-58	250	0.1	*0.2 (2)*	2.21*(11)*	*0.0 (0)*	80 *(0)*	0.1 *(0)*	293 h after change in temperature
06-59	250	0.1	1.0 *(2)*	2.14*(11)*	0.0 *(0)*	84 *(0)*	0.1 *(0)*	320 h after change in temperature
06-60	250	0.1	0.6 *(2)*	1.99*(10)*	*0.0 (0)*	83 *(0)*	0.1 *(0)*	337 h after change in temperature
06-61	250	0.1	0.7 *(2)*	2.20*(11)*	0.3 *(0)*	82 *(0)*	0.2 *(0)*	340 h after change in temperature
06-62	200	0.1	*0.0 (2)*	2.04*(10)*	0.1 *(0)*	84 *(0)*	0.1 *(0)*	1 h after change in temperature
06-63	200	0.1	*0.0 (2)*	1.97*(10)*	*0.0 (0)*	50 *(0)*	0.1 *(0)*	68 h after change in temperature
06-64	200	0.1	*-0.1 (2)*	1.97*(10)*	*0.0 (0)*	42 *(0)*	0.1 *(0)*	91 h after change in temperature
06-65	200	0.1	0.6 *(2)*	2.07*(10)*	*0.0 (0)*	40 *(0)*	0.1 *(0)*	96 h after change in temperature
06-66	200	0.1	*0.0 (2)*	2.21*(11)*	*0.0 (0)*	35 *(0)*	0.0 *(0)*	117 h after change in temperature
06-67	200	0.1	0.7 *(2)*	2.05*(10)*	*0.0 (0)*	31 *(0)*	0.1 *(0)*	140 h after change in temperature
06-68	200	0.1	0.6 *(2)*	2.09*(10)*	0.1 *(0)*	30 *(0)*	0.2 *(0)*	143 h after change in temperature
06-69	200	0.1	*-0.2 (2)*	1.97*(10)*	*0.0 (0)*	28 *(0)*	0.1 *(0)*	163 h after change in temperature
06-70	200	0.1	0.8 *(2)*	2.08*(10)*	*0.0 (0)*	28 *(0)*	0.0 *(0)*	165 h after change in temperature
06-71	200	0.1	0.5 *(2)*	2.02*(10)*	*0.0 (0)*	24 *(0)*	0.0 *(0)*	238 h after change in temperature
06-72	200	0.1	0.4 *(2)*	1.90*(10)*	*0.0 (0)*	23 *(0)*	0.0 *(0)*	259 h after change in temperature
06-73	200	0.1	*0.1 (2)*	2.71*(14)*	0.3 *(0)*	23 *(0)*	0.2 *(0)*	264 h after change in temperature
06-74	200	0.1	*0.0 (2)*	2.38*(12)*	0.4 *(0)*	23 *(0)*	0.1 *(0)*	284 h after change in temperature
06-75	200	0.1	*0.2 (2)*	2.45*(12)*	*0.0 (0)*	23 *(0)*	0.0 *(0)*	288 h after change in temperature
06-76	200	0.1	*0.3 (2)*	1.94*(10)*	*0.0 (0)*	24 *(0)*	0.1 *(0)*	310 h after change in temperature
06-77	200	0.1	*0.1 (2)*	1.88 *(9)*	*0.0 (0)*	23 *(0)*	0.1 *(0)*	331 h after change in temperature
06-78	200	0.1	0.4 *(2)*	2.82*(14)*	0.2 *(0)*	24 *(0)*	0.2 *(0)*	334 h after change in temperature
06-f2	-	1	0.4 *(2)*	*0.00 (1)*	0.1 *(0)*	*0.04 (3)*	0.03 *(1)*	Feedwater, 4 h before sample #12
06-f3	-	1	*0.0 (2)*	*-0.01 (1)*	0.0 *(0)*	*0.04 (3)*	*0.01 (1)*	Feedwater, 4 h before sample #12
06-f4	-	1	*0.0 (2)*	*-0.01 (1)*	0.0 *(0)*	*0.03 (3)*	*0.00 (1)*	Feedwater, 4 h before sample #12
06-f5	-	1	*0.0 (2)*	*0.02 (1)*	0.4 *(0)*	*0.03 (3)*	*0.01 (1)*	Feedwater, 4 h before sample #12
06-f6	-	1	*-0.1 (2)*	*0.00 (1)*	0.0 *(0)*	*0.04 (3)*	0.02 *(1)*	Feedwater, 0.3 h before sample #12
06-f7	-	1	1.1 *(2)*	0.02 *(1)*	0.1 *(0)*	*0.03 (3)*	*0.01 (1)*	Feedwater, 0.2 h before sample #12
06-f8	-	0.1	0.5 *(2)*	*-0.01 (1)*	0.1 *(0)*	0.17 *(3)*	0.08 *(1)*	Feedwater, during 0.1 g/min flow
06-f9	-	0.1	*0.0 (2)*	*0.01 (1)*	0.0 *(0)*	0.16 *(3)*	0.05 *(1)*	Feedwater, during 0.1 g/min flow
06-f10	-	0.1	*0.0 (2)*	*0.01 (1)*	0.0 *(0)*	0.16 *(3)*	0.05 *(1)*	Feedwater, during 0.1 g/min flow
06-f1	-	-	*-0.2 (2)*	*0.02 (1)*	0.2 *(0)*	*-0.06 (3)*	0.11 *(1)*	Syringe blank, for samples f2-f7
Filter1			*0.2 (2)*	0.04 *(1)*	*0.01 (1)*	1.1 *(0)*	0.1 *(0)*	Used filter blank, 1 h after #31
Filter2			*0.1 (2)*	0.03 *(1)*	*0.00 (1)*	0.2 *(0)*	0.2 *(0)*	Used filter blank, 4 h after #31
Rejects	-	-	0.5 *(4)*	0.05 *(5)*	1.3 *(29)*	0.04 *(5)*	0.02 *(2)*	Rejected blanks
Blanks	-	-	0.04*(14)*	-0.01 *(1)*	-0.01 *(1)*	0.02 *(2)*	0.00 *(1)*	Batch 5.

Table 18.8. Results from hot loop rig

Sample	*pH*	*T*	*ṁ*	*N_2*	*[Fe]*	*[Cr]*	*[Ni]*	*[Mo]*	*[Mn]*	*[Co]*	*Other info*
HL-1a HL-1b	7*	300 ?	fast	?	348 *(18)* 334 *(17)*	0.30 *(4)* 0.25 *(4)*	132 *(7)* 82 *(4)*	754 *(4)* 699 *(3)*	87.5 *(5)* 83.6 *(4)*	3.6 *(2)* 2.4 *(1)*	
Blanks	-	-	-	-	1 *(0)*	m0.05 *(3)*	0 *(0)*	m 0 *(0)*	m0.1 *(1)*	m0.1 *(0)*	Batch 2. Relevant to HL samples

Table 18.7. Results from corrosion rate rigs

Sample	*pH*	*T*	*ṁ*	*N_2*	*[Fe]*	*[Cr]*	*[Ni]*	*[Mo]*	*[Mn]*	*Other info*
C1-s1-dir C1-s1-dump	10	300	2	0.8?	0.7 *(4)* 2.9 *(5)*	0.01 *(1)* 0.03 *(1)*	-0.2 *(0)* 0.1 *(1)*	15.26 *(8)* 16.13 *(8)*	0.2 *(1)* 0.4 *(1)*	12/8/14. Corrosion rig #1. dir = sampled directly, dump = sample decanted from dump water barrel
C2-s1-dir C2-s1-dump	10	300	2	0.8?	1.5 *(4)* 1.6 *(4)*	0.03 *(1)* 0.02 *(1)*	-0.1 *(0)* 0.0 *(0)*	15.23 *(8)* 15.24 *(8)*	0.3 *(1)* 0.3 *(1)*	12/8/14. Corrosion rig #2. dir = sampled directly, dump = sample decanted from dump water barrel
C1-s2-fltr1 C1-s2-fltr2 C1-s2-dir	9	300	1.5	0.8?	-0.0 *(2)* -0.4 *(2)* -0.1 *(2)*	0.12 *(1)* 0.12 *(1)* 0.13 *(1)*	-0.0 *(0)* -0.0 *(0)* -0.0 *(0)*	18.78 *(10)* 18.48 *(10)* 18.45 *(10)*	0.07 *(1)* 0.06 *(1)* 0.07 *(1)*	23/1/15. 0.45 µm, 1.3cm filter installed 7 days previously, caused sporadic flow. "dir" sample taken within 5 mins of filter removal
C2-s2-dir	11	300	1.5	0.8?	-0.1 *(2)*	0.06 *(1)*	-0.0 *(0)*	20.41 *(11)*	0.08 *(1)*	23/1/15. Sample taken directly
Blanks	-	-	-	-	1.5 *(3)*	0.0 *(0)*	0.2 *(0)*	0.0 *(0)*	0.1 *(1)*	Batch 3. relevant to C#-s1 samples
Blanks	-	-	-	-	0.04 *(14)*	-0.01 *(1)*	-0.01 *(1)*	0.02 *(2)*	0.00 *(1)*	Batch 5 (b). Relevant to C#-s2 samples